

# Hand Sign Language Recognition for Bangla Alphabet using Support Vector Machine

Md Azher Uddin  
Computer Science & Engineering  
Kyung Hee University  
South Korea  
azher006@yahoo.com

Shayhan Ameen Chowdhury  
Computer Science & Engineering  
International Islamic University Chittagong  
Chittagong, Bangladesh  
shayhan@yahoo.com

**Abstract**— The sign language considered as the main language for deaf and dumb people. So, a translator is needed when a normal person wants to talk with a deaf or dumb person. In this paper, we present a framework for recognizing Bangla Sign Language (BSL) using Support Vector Machine. The Bangla hand sign alphabets for both vowels and consonants have been used to train and test the recognition system. Bangla sign alphabets are recognized by analyzing its shape and comparing its features that differentiates each sign. In proposed system, hand signs are first converted to HSV color space from RGB image. Then Gabor filters are used to acquire desired hand sign features. Since feature vector obtained using Gabor filter is in a high dimension, to reduce the dimensionality a nonlinear dimensionality reduction technique that is Kernel PCA has been used. Lastly, Support Vector Machine (SVM) is employed for classification of candidate features. The experimental results show that our proposed method outperforms the existing work on Bengali hand sign recognition.

**Keywords**—sign language; Bangla sign language; HSV; Gabor filter; Kernel PCA; Support Vector Machine.

## I. INTRODUCTION

Between the deaf and dumb people, Sign language is the basic communication method. This means using hand gestures instead of sound or spoken words. The deaf and dumb people use hand gestures, which is a pictorial procedure of communication including the mixture of hand positioning, shapes and movement of the hands. They share many similarities with spoken languages, however there are also few major differences between signed and spoken languages. On the other hands, there is no worldwide hand sign language for deaf and dumb people. Different nations use different hand sign languages. Various hand sign languages are American, Australian, and Japanese hand sign languages, etc. In Bangladesh, it is called Bangla Sign Language Anthology (BSLA). The formation of Bangla Sign Language is structurally dissimilar from other nation sign languages. Generally, both hands are used to accomplish the Bangla Sign Language. Various types of Bangla sign language alphabets are shown in Figure 1. However in Bangladesh, 2.4 million deaf people are living [3].

In this paper we have used a database for collecting images for hand sign recognition, which contains some critical factors such as lighting illumination, different angle and scale variability of hand sign. In this paper, we present a framework for Bangla sign language recognition. The framework

composed of two processing steps: 1) segmentation of hand sign and 2) recognition of hand sign by extracting the features from the hand sign.



Figure 1: Bangla Sign Language Alphabets

In first phase, our method focuses on a solution for image disturbance resulting from non-uniform lighting condition. Additionally, our approach has numerous inherent advantages over other feature extraction technique. In feature extraction phase, features are extracted from the hand signs by Gabor filter, which is invariant to non-uniform lighting condition, rotation, scaling, and translation. After that, KPCA is employed to decrease the high dimensionality of feature vector that is gained by Gabor filter. Finally, SVM classifier is used to recognize the hand sign. The experimental result shows an accuracy of 97.7% for the recognition of hand gestures. Moreover, our experimental result also compared with existing works performed for the recognition of Bangla hand sign language. The paper is ordered as follows. The next segment composes a discussion of related researches that have been implemented. Proposed framework is described in section III. Segment IV presents evaluation of result. At the end, conclusion is given in segment V.

## II. RELATED WORK

Different techniques are developed for sign language recognition. This section presents some previous related works

for sign language recognition which is significant to propose approach.

Muhammad Aminur Rahman et al [1] proposed a technique for Bengali hand gesture recognition that focus on computer vision. Here the technique extracts the hand gesture based on Hue and Saturation value from HSI color model. Then K-nearest neighbors (KNN) classifier used for recognition. 96.46% recognition rate is achieved by the system. In [2], authors used LDA and LBP to obtain the features from hand sign. Finally, for hand sign classification Nearest Neighbor algorithm is used. In [3], LDA and ANN used by the authors to recognize the two-handed hand sign for BSL. In [4], authors proposed hand gesture recognition system for Bengali characters based on the fuzzy rule. In [5], authors proposed a framework for Bangladeshi Sign Language recognition system using computer vision-based technique. Here, for Bengali vowels and Bengali numbers recognition distinct PCA (Principal Component Analysis) has been used. In [6], low cost method for real time hand gesture recognition has been proposed. Shreyashi Narayan Sawant et al [7] proposed real time Sign Language recognition system using PCA. For hand gesture recognition the PCA procedure was employed and recognized hand gesture is transformed into user friendly way.

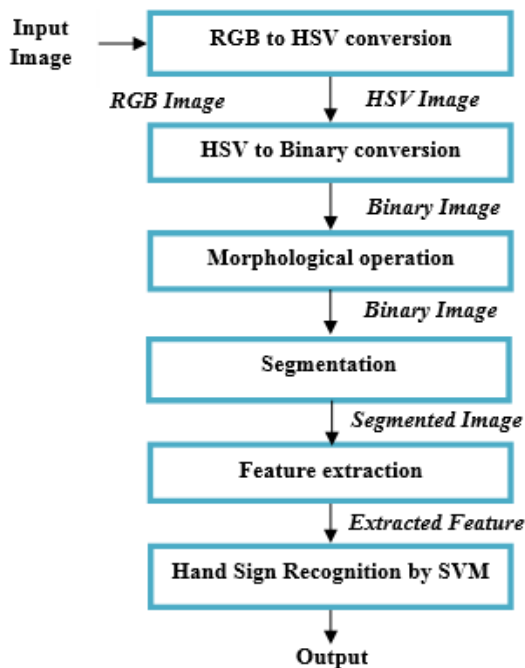


Figure 2: Proposed Framework

### III. PROPOSED FRAMEWORK

The proposed Bangla Sign Language recognition algorithm consists of two main stages: (1) segmentation of hand sign and (2) recognition of hand sign. The block diagram in figure 2 shows the working approach towards the solution of the stated problem.

#### A. RGB to HSV conversion

The Bangla hand sign alphabets are first captured using digital camera and stored in .jpg format. The each hand sign alphabets were collected four times from 30 different peoples

with different angles (<60 degree) and lighting conditions. The size of the input images is 480×360 pixels.

The RGB color model consists of the three additive colors: red, green, and blue. In this process we converted the RGB image into HSV image, since it is less sensitive to illumination variations compared to RGB. In HSV color model, colors are expressed in terms of hue, saturation, and value. In particular, hue is expressed from 0 to 360 degrees, expressing hues of red begins at 0°, yellow begins at 60°, green begins at 120° and blue begins at 240°. Saturation is the amount of gray in the color, it ranges from 0 to 100%. Value refers to the brightness or intensity of the color (0 to 100%).

#### B. HSV to Binary conversion

In digital image processing, a binary image has only two potential colors (i.e. black and white) for every pixel. In this section, based on hand skin color the hand region is segmented. Hand area is found out by implementing threshold value on Hue and Saturation channel. The hand sign in component H is determined by values from 0 to 50 and in the component S from 0.23 to 0.68.

#### C. Morphological operation

During morphological operation, a structuring element is applied to an input image that produces an output image of the same size. Dilation and erosion are the most basic morphological operation. Here we performed morphological operation in order to remove the noises from processed binary image, first by performing dilation operation, then followed by erosion and smoothing operation. After that removing all connected components (objects) that have fewer than 50 pixels.

#### D. Segmentation

Image segmentation is the method of partitioning a digital image into several parts. In this phase, vertical and horizontal line segmentation is performed through y-axis and x-axis of the region respectively.

#### E. Feature Extraction

Selecting good features is a critical phase in any object recognition system. Here the segmented binary image is resized to 80×60. In this phase, we implemented a Gabor filter with the intention of gaining a feature vector. It is a band-pass filter, where a harmonic function multiplied by a Gaussian function is used to define the impulse response of the Gabor filter. Hence, a two-dimensional Gabor filter establishes a complex sinusoidal plane of particular frequency and orientation modulated by a Gaussian envelope [8]. The greatest significant benefit of Gabor filters is their invariance to different lighting conditions, translation, scaling, and rotation. For the spatial domain, a two-dimensional Gabor filter [9], defined as:

$$G(x, y) = \frac{f^2}{\pi\gamma\eta} \exp\left(-\frac{x'^2 + \gamma^2 y'^2}{2\sigma^2}\right) \exp(j2\pi f x' + \phi) \quad (1)$$

$$x' = x \cos\theta + y \sin\theta \quad y' = -x \sin\theta + y \cos\theta \quad (2)$$

Where,  $f$  is the frequency of the sinusoidal factor,  $\sigma$  is the standard deviation of the Gaussian envelope,  $\phi$  is the phase offset,  $\theta$  denotes the orientation of the normal to the parallel stripes of a Gabor function and  $\gamma$  is the spatial aspect ratio which

identifies the ellipticity. Our proposed framework implements thirty-two Gabor filters in four scales with eight orientations. Then downsampling is done, here column downsampling factor is (5×5). Thus the size of the Gabor feature vector obtained is (80×60×4×8) / (5×5) which is 6144. However, even after downsampling the feature vector achieved using Gabor filter is still large. Therefore, dimensionality decrease approach has been implemented. For dimensionality reduction Kernel PCA (KPCA) has been employed. KPCA is a nonlinear dimensionality decrease approach which is an updated version of Principle component analysis (PCA). On the other hand, PCA is a linear feature extraction method frequently used in numerous pattern classification methods. Kernel oriented approaches have been used in various applications for example in [10-11]. KPCA maps the features from a low dimensional space to a more high dimensional space. By doing this, the features become linearly separable. Kernel PCA [12] calculates the principal eigenvectors of the kernel matrix, as an alternative of those of the covariance matrix. The reconstruction of conventional PCA in kernel space is easy, due to a kernel matrix is similar to the product of the features in the high-dimensional space that is built using the kernel function. The application of PCA in kernel space gives Kernel PCA the property of constructing nonlinear mappings. Kernel PCA calculates the kernel matrix K of the features  $x_i$ . The kernel matrix can be defined by,

$$k_{ij} = \kappa(x_i, x_j) \quad (3)$$

where  $\kappa$  is a kernel function. Then, the kernel matrix K is centered using the following alteration of the entries

$$k_{ij} = k_{ij} - \frac{1}{n} \sum_l k_{il} - \frac{1}{n} \sum_l k_{jl} + \frac{1}{n^2} \sum_{lm} k_{lm} \quad (4)$$

The centering process corresponds to deducting the mean of the features in conventional PCA. It makes guaranteed that the features in the high-dimensional space defined by the kernel function are zero-mean. Then, the principal  $d$  eigenvectors  $v_i$  of the centered kernel matrix are calculated. It can be shown that, the eigenvectors of the covariance matrix  $\alpha_i$  are scaled forms of the eigenvectors of the kernel matrix  $v_i$

$$\alpha_i = \frac{1}{\sqrt{\lambda_i}} v_i \quad (5)$$

The feature is projected onto the eigenvectors of the covariance matrix to obtain the low-dimensional data representation. The result of the projection is given by,

$$Y = \{\sum_j \alpha_1 \kappa(x_j, x), \sum_j \alpha_2 \kappa(x_j, x), \dots, \sum_j \alpha_d \kappa(x_j, x)\} \quad (6)$$

where  $\kappa$  is the kernel function, used in the calculation of the kernel matrix. Since Kernel PCA is a kernel-based technique, the mapping done by Kernel PCA vastly depends on the choice of the kernel function  $\kappa$ . In our work, we used Gaussian kernel function. The dimension of the feature vector has been reduced to 180 from 6144 using Kernel PCA.

#### F. Hand Sign Recognition

Support Vector Machine (SVM) classifier is implemented for the training and classification processes. SVM [13] is a classification tool that uses machine learning idea to maximize

predictive accuracy while spontaneously avoiding over-fit to the data.

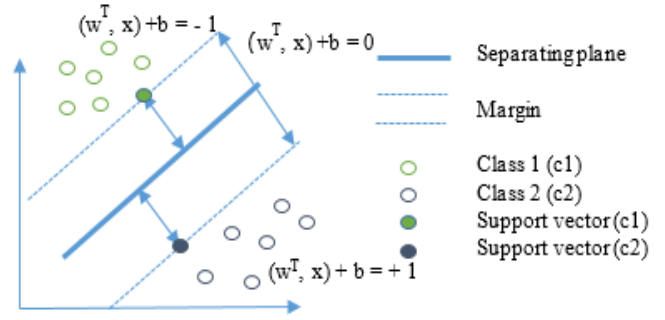


Figure 3: Linear separating hyperplanes for the separable case

We are given a set of  $n$  data points  $\{x_i, y_i\}$ ; where,  $i = 1, \dots, n$ ,  $y_i \in \{-1, +1\}$  and  $x_i \in \mathbb{R}^n$ . SVM method targets at finding a classifier of form,

$$y(x) = \text{sign}(\sum_{i=1}^n \alpha_i y_i k(x, x_i) + b) \quad (7)$$

Where  $\alpha_i$  are positive real constants and  $b$  is a real constant;  $k(x, x_i)$  is the kernel function that can be defined by,

$$k(x, x_i) = \varphi(x)^T \varphi(x_i) \quad (8)$$

$\varphi$  is a nonlinear mapping function used to map input data point  $x_i$  into a higher dimensional space. In our proposed framework, the Gaussian radial basis function is used. It is defined by,

$$k(x, z) = e^{-\gamma \|x - z\|^2} \quad (9)$$

In the high dimensional space, the data can be divided by a linear hyperplane, according to the following equations,

$$\begin{cases} w^T \cdot x_i + b \geq +1, & \text{if } y_i = +1 \\ w^T \cdot x_i + b \leq -1, & \text{if } y_i = -1 \end{cases} \quad (10)$$

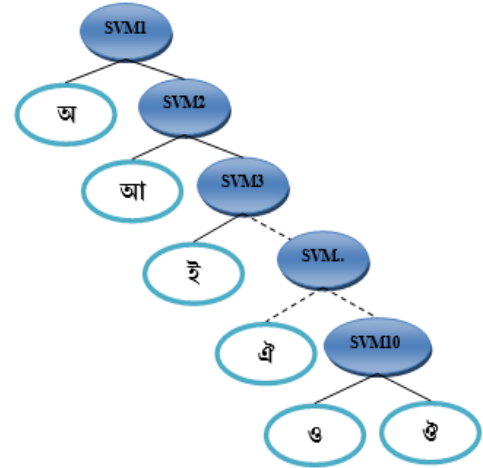


Figure 4: Binary tree based vowels classifier

In our work, we build two big SVM classifiers for vowels and consonants respectively. Both classifiers implement a binary tree structure and apply one against rest to build sub-classifiers. Let us consider vowels classifier as an instance, it contains 10 sub-classifiers. Figure 4 shows the vowel classifier.

Each layer contains a vowel as a leaf node and a sub-classifier except for the last layer that contains two vowels as a leaf nodes and the root node is a classifier. Each leaf node is a vowel and a positive output ( $y_i = +1$ ), on the other hand each sub-classifier is a negative output ( $y_i = -1$ ).

#### IV. RESULT EVALUATION

We have used MATLAB tool to complete our experiments. In the experiments, we have used 4800 images with the size  $480 \times 360$  pixels. The images were taken from different illuminations, diverse angle. The database is separated into two datasets. The first dataset contains 2400 images and are used for training the SVM character classifiers. On the other hand, another dataset contains 2400 images and are used for testing the performance of the classifiers. The Bangla Sign Language recognition rate of success is 97.7%. Table I and II shows the result of Bangla Sign Language recognition.

TABLE I. Recognition Result in Different Condition for Training

Condition	No. of Training Images	No. of Correctly Recognized Images	Success rate (%)
Normal situation	1200	1200	100 %
Different angles	600	592	98.6 %
Different illuminations	600	597	99.5 %
Total	2400	2389	99.5 %

In [3], the system can work very satisfactorily when LDA feature extraction process is used, but the size of the dataset is very small, only 330 images were used. In our proposed approach, we used a large dataset for training and testing with different conditions. We can see from figure 5 that, our proposed framework outperforms the existing works for Bangla Sign Language recognition.

TABLE II. Recognition Result in Different Condition for Testing

Condition	No. of Testing Images	No. of Correctly Recognized Images	Success rate (%)
Normal situation	1200	1182	98.5 %
Different angles	600	557	92.8 %
Different illuminations	600	564	94.0 %
Total	2400	2303	95.9 %

#### V. CONCLUSION

In this paper, we showed a framework for Bangla hand sign recognition method using support vector machine. Here, first images are converted to HSV color space. Subsequently, features are extracted from the segmented image by Gabor filter and then KPCA is applied to reduce the dimensionality. Finally, SVM is used to recognize the hand sign. Here we used a large dataset for training and testing purpose. The recognition results confirm the effectiveness and dominance of the proposed framework. In future, we will extend our work by recognizing the hand sign from the video data.

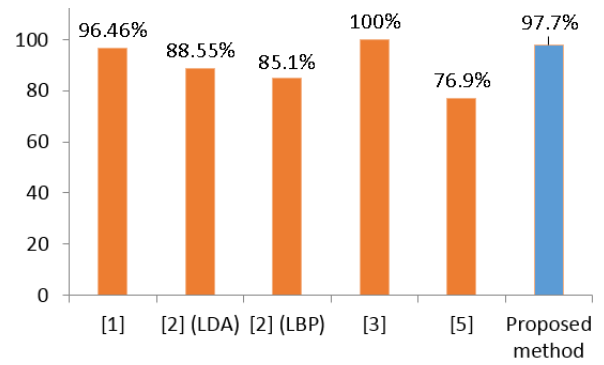


Figure 5: Comparison of overall system performance between our proposed method and other related works

#### REFERENCES

- [1] Muhammad Aminur Rahaman, Mahmood Jasim, Md. Haider Ali and Md. Hasanuzzaman, "Real-Time Computer Vision-Based Bengali Sign Language Recognition", 2014 17th International Conference on Computer and Information Technology (ICIT), pp. 192-197, 2014.
- [2] Mahmood Jasim and Md. Hasanuzzaman, "Sign Language Interpretation using Linear Discriminant Analysis and Local Binary Patterns", 2014 International Conference on Informatics, Electronics & Vision (ICIEV), pp. 1-5, 2014.
- [3] Rahat Yasir and Riasat Azim Khan, "Two-Handed Hand Gesture Recognition for Bangla Sign Language using LDA and ANN", 2014 8th International Conference on Software, Knowledge, Information Management and Applications (SKIMA), pp. 1-5, 2014.
- [4] Tanzila Ferdous Ayshee, Sadia Afrin Raka, Quazi Ridwan Hasib, Md. Hossain and Rashedur M Rahman, "Fuzzy Rule-Based Hand Gesture Recognition for Bengali Characters", 2014 IEEE International Advance Computing Conference (IACC), pp. 484-489, 2014.
- [5] Salma Begum and Md. Hasanuzzaman, "Computer Vision-based Bangladeshi Sign Language Recognition System", 12th International Conference on Computers and Information Technology (ICIT), 2009, pp. 414-419, 2009.
- [6] Matheesha Fernando and Janaka Wijayanayaka, "Low cost approach for Real Time Sign Language Recognition", 2013 8th IEEE International Conference on Industrial and Information Systems (ICIIS), pp. 637-642, 2013.
- [7] Shreyashi Narayan Sawant and M. S. Kumbhar, "Real Time Sign Language Recognition using PCA", 2014 International Conference on Advanced Communication Control and Computing Technologies (ICACCCT), pp. 1412-1415, 2014.
- [8] J.R. Movellan, "Tutorial on Gabor Filters," 2008. Available: <http://mplab.ucsd.edu/tutorials/gabor.pdf> [Accessed: December 12th 2014].
- [9] M. Haghghat, S. Zonouz and M. Abdel-Mottaleb, "Identification using encrypted biometrics", Computer analysis of images and patterns (CAIP), Springer, pp. 440-448, 2013
- [10] Milad Moghaddam, Manoochehr Nahvi and Reza Hassanzadeh Pak, "Static Persian Sign Language Recognition Using Kernel-Based Feature Extraction", 7th Iranian conference on Machine Vision and Image Processing (MVIP), pp. 1-5, 2011.
- [11] A. Kocsor and L. Toth, "Kernel-based feature extraction with a speech technology application," Signal Processing, IEEE Transactions on, vol. 52, pp. 2250-2263, 2004.
- [12] L.J.P. van der Maaten, E.O. Postma, and H.J. van den Herik, "Dimensionality Reduction: A Comparative Review. Tilburg University Technical Report", TiCC-TR 2009-005, 2009.
- [13] Md Azher Uddin, Joolakha Bibi Joollee and Shayhan Ameen Chowdhury, "Bangladeshi Vehicle Digital License Plate Recognition for Metropolitan Cities Using Support Vector Machine", in Proc. International Conference on Advanced Information and Communication Technology, 2016.

# An Integrated Approach to Classify Gender and Ethnicity

Md Azher Uddin  
Computer Science & Engineering  
Kyung Hee University  
South Korea  
azher006@yahoo.com

Shayhan Ameen Chowdhury  
Computer Science & Engineering  
International Islamic University Chittagong  
Chittagong, Bangladesh  
shayhan@yahoo.com

**Abstract**— Faces express many social indications, including gender, ethnicity, age, expression and identity, most of them have drawn thriving attention from various research communities, for instance neuroscience, computer science and psychology. In this paper, we propose a new approach to classify gender and ethnicity by merging both texture and shape features extracted from face images. Gabor filter is used to extract the texture features and histogram of oriented gradients (HOG) is used to extract the shape features from face images. In order to achieve higher performance we combined both texture and shape features. After combining, the size of feature vector obtained is in a high dimension, to decrease the dimensionality Kernel PCA has been implemented. Finally, to classify the gender and ethnicity we used Support Vector Machine. The experimental result shows the effectiveness of proposed framework.

**Keywords**- Gender Recognition; Ethnicity Recognition; Gabor filter; Histogram of oriented gradients; Kernel PCA; Support Vector Machine.

## I. INTRODUCTION

In the area of computer vision, facial image investigation is one of the important research issue. The faces of human beings provide various demographic properties for example identity, gender, ethnicity and age, significantly contributing in this area. From the different demographic properties, gender and ethnicity remains unchanged throughout whole life and significantly supports face recognition systems. Moreover, it also has a high degree of interest to be applied for development in various areas including access control, image retrieval and surveillance etc.

This paper proposes a framework to classify gender and ethnicity. The framework composed of three processing steps: 1) feature extraction by utilizing histogram of oriented gradients (HOG) and Gabor filter, 2) dimensionality reduction using Kernel PCA and 3) classification using Support Vector Machine (SVM). Our method has several benefits compared to other feature extraction method as Gabor filter is invariant to translation, scaling, rotation and illumination problem. We use FERET dataset [1] to test our system. In FERET dataset, the ethnicity classification is divided into three class: Caucasian, African, and Asian oriental with male and female gender for each ethnicity.

The remaining paper is structured as follows. The following section introduces a review of related works that have been applied. In section III, we discuss the System overview. Section

IV shows results evaluation of our system. Lastly, we draw conclusion in section V.

## II. RELATED WORK

Several systems has been already developed to classify gender and ethnicity. This section presents some previous related works to classify gender and ethnicity which is significant to our framework.

In [2], authors used Gabor wavelet features and SVM classifier to classify ethnicity with an average accuracy of 96%, 93% and 94% for Asian, European, and African respectively. They used HOIP dataset for their experiments. LBPH (Local Binary Pattern histogram) features and Adaboost are used in [3], to classify gender, ethnicity and age. In [4], a method is proposed by using Oriented Gradient Maps (OGMs) to focus local geometry with texture information of whole faces and feature selection is done using Adaboost. The proposed method achieved 98.3% accuracy on FRGC v2.0 dataset. Local Binary Patterns and SVM classifier used by authors in [5] and they also used FRGC face dataset. In [6], experimental comparison has been performed for gender classification.

## III. SYSTEM OVERVIEW

Our approach is decomposed into three steps: feature extraction, dimensionality reduction and classification. In feature extraction phase, we extract both shape and texture information by histogram of oriented gradients (HOG) and Gabor filter respectively. Then we combined both feature vector into one. The block diagram in figure 1 illustrates the framework to classify gender and ethnicity.

### A. Pre-processing

Pre-processing is a process which is done on the input image before feature extraction phase. Preprocessing phase contains image enhancement, image conversion, image resize etc. To improve the picture contrast image enhancement is used so that picture can become clear. Image conversion is used to convert the RGB image to gray scale image. The RGB model contains of the three colors: red, blue and green whereas the subsequent gray level image are composed of black and white pixels. The range of resultant gray level image will be between 0 to 255 values. Image resize is used to resize image into a fixed size. All images are scale normalized to  $100 \times 120$  pixels.

## B. Feature extraction

Choosing important features is a crucial phase in any recognition or classification system. In our work, we extracted both texture and shape features. Histogram of oriented gradients (HOG) and Gabor filter are used to extract features from the gray scale image.

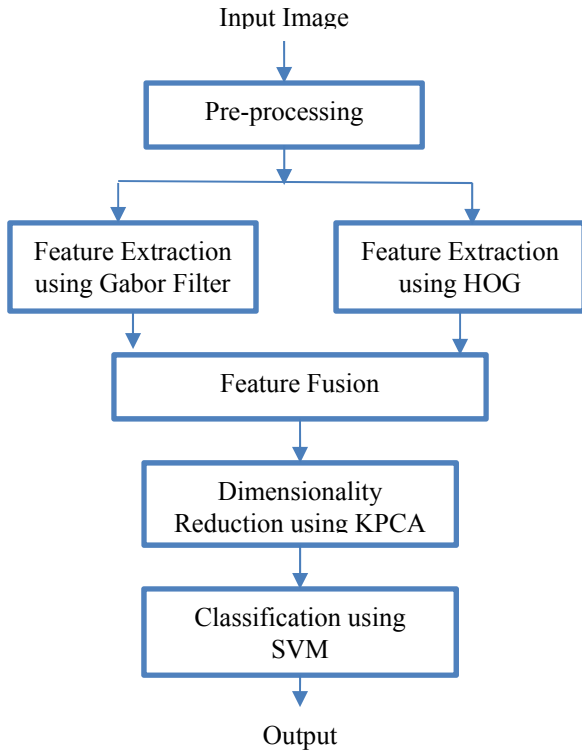


Fig. 1. Proposed framework

### 1) Gabor Filter

Gabor filter is a robust feature vector. This technique extracts texture information. Gabor filtering is effectively implemented in several computer vision fields including texture analysis, image smoothing, face recognition, fingerprint recognition etc. The Gabor filter is a band-pass filter, where a harmonic function multiplied by a Gaussian function is used to define the impulse response of the Gabor filter. Hence, a two-dimensional Gabor filter establishes a complex sinusoidal plane of certain frequency and orientation modulated by a Gaussian envelope [8]. Gabor filter is invariance to translation, scaling, non-uniform lighting condition and rotation. In spatial domain, a 2D Gabor filter [9] is defined as:

$$G(x, y) = \frac{f^2}{\pi\gamma} \exp\left(-\frac{x'^2 + \gamma^2 y'^2}{2\sigma^2}\right) \exp(j2\pi f x' + \phi) \quad (1)$$

$$x' = x \cos\theta + y \sin\theta \quad (2)$$

$$y' = -x \sin\theta + y \cos\theta \quad (3)$$

Where,  $\theta$  denotes the orientation of Gabor function,  $\sigma$  is the standard deviation,  $f$  is the frequency of the sinusoidal factor,  $\gamma$  is the spatial aspect ratio and  $\phi$  is the phase offset. Our framework implements twenty-four Gabor filters in eight orientation angles and three scales. Then based on  $(5 \times 5)$

downsampling factor, downsampling is done. The dimension of the feature vector obtained by Gabor filter is  $(100 \times 120 \times 3 \times 8) / (5 \times 5)$  which is 11520. However, even after downsampling the dimension of feature vector achieved is still huge.

### 2) Histogram of oriented gradients (HOG)

The Histogram of Oriented Gradients (HOG) by Dalal et al. [10] is a powerful descriptor for human detection and tracking. HOG features has various application in image processing. HOG use intensity gradient distribution to describe the local feature of an object and its shape. They are calculated by the following steps:

- i. For every pixel  $I(x, y)$ , the horizontal and vertical gradient are calculated according to the following equation:

$$G_x = I(x + 1, y) - I(x - 1, y)$$

$$G_y = I(x, y + 1) - I(x, y - 1) \quad (4)$$

- ii. Then, the gradient magnitude and orientation are found by:

$$|G| = \sqrt{G_x^2 + G_y^2} \quad (5)$$

$$\theta = \arctan\left(\frac{G_y}{G_x}\right) \quad (6)$$

- iii. Lastly, the histogram of gradient orientations is evaluated to get the HOG features.

In our work, face images are divided into numerous blocks and for every block a local histogram of the gradient orientations is calculated. Then, HOG features are obtained by combining all local histograms. In this research, the HOG over  $100 \times 120$  images is calculated where each block contain  $2 \times 2$  cells with size  $8 \times 8$  and 9 histogram bins. The dimension of HOG feature vector is  $(11 \times 14 \times 4 \times 9) = 5544$ .

In the feature fusion phase, the both feature vector for Gabor filter and HOG are combined into one feature vector simply by concatenation. This feature fusion yields a feature vector for the face image with size 17064.

### C. Dimensionality reduction

Since the size of feature vector is so large, it not only requires more computational time sometime it may also reduce the accuracy of classification. Therefore, dimensionality reduction technique has been applied. Although there are different dimensionality reduction method are available but we used Kernel PCA (KPCA) as it offers a better understanding about what nonlinear features are needed to extract. KPCA is a nonlinear dimensionality technique and it is an extended type of Principle component analysis (PCA). PCA is a linear feature extraction process frequently applied in various pattern recognition system, such as [11]. Kernel based tactics has been applied in numerous systems such as in [12-13]. The features from a low dimensional space is group into a more high dimensional space by KPCA. Due to this, the features can be linearly separable. Kernel PCA [14] calculates the principal eigenvectors of a matrix, as an alternative of those of the covariance matrix. The re-establishment of conventional PCA in kernel space is simple, due to a kernel matrix is identical to the product of the features in the high-dimensional space that is

built by utilizing kernel function. The utilization of PCA in kernel space gives Kernel PCA the estate to handle nonlinear mappings. The kernel matrix  $K$  calculated by Kernel PCA can be defined as,

$$k_{ij} = \kappa(x_i, x_j) \quad (7)$$

Where  $\kappa$  is a kernel function. Then, the following alteration of the entries are employed to centralize the kernel matrix  $K$

$$k_{ij} = k_{ij} - \frac{1}{n} \sum_l k_{il} - \frac{1}{n} \sum_l k_{jl} + \frac{1}{n^2} \sum_{lm} k_{lm} \quad (8)$$

The centering process coincides to deducting the mean of the features in conventional PCA. It guaranteed that the features in the high-dimensional space are zero-mean. Then, the principal  $d$  eigenvectors  $v_i$  are calculated. The eigenvectors of the covariance matrix  $\alpha_i$  are scaled forms of the eigenvectors of the kernel matrix  $v_i$

$$\alpha_i = \frac{1}{\sqrt{\lambda_i}} v_i \quad (9)$$

The feature is projected onto the eigenvectors of the covariance matrix to obtain the low-dimensional data demonstration. The result of the projection is specified by,

$$Y = \{\sum_j \alpha_1 \kappa(x_j, x), \sum_j \alpha_2 \kappa(x_j, x), \dots, \sum_j \alpha_d \kappa(x_j, x)\} \quad (10)$$

Where  $\kappa$  is the kernel function. As Kernel PCA is a kernel-based method, the mapping done by Kernel PCA very much relies on the selection of the kernel function  $\kappa$ . Feasible choices for the kernel function consist of polynomial kernel, Gaussian kernel and linear kernel. Gaussian kernel function has been used in our research work. The size of the feature vector has been decreased to 320 from 17064 using nonlinear dimensionality reduction approach Kernel PCA.

#### D. Classification

The training and testing procedures are finished by utilizing Support Vector Machine (SVM) classifier to classify gender and ethnicity. SVM [15] is a classification tool that uses machine learning idea.

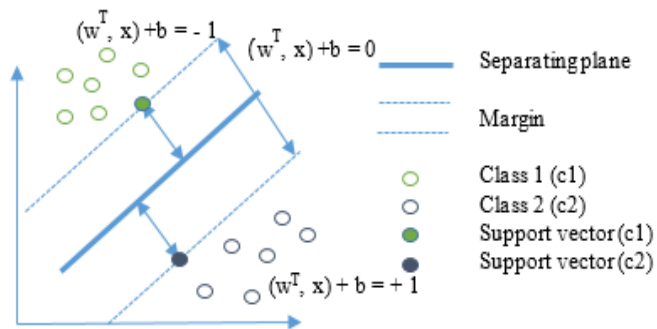


Fig. 2. SVM classifier using linear separating hyperplanes

We are given a set of  $n$  data points  $\{x_i, y_i\}$ ; where,  $i = 1, \dots, n$ ,  $y_i \in \{-1, +1\}$  and  $x_i \in \mathbb{R}^n$ . SVM method goals at finding a classifier of form,

$$y(x) = \text{sign}(\sum_{i=1}^n \alpha_i y_i k(x, x_i) + b) \quad (11)$$

Where  $\alpha_i$  are positive real constants and  $b$  is a real constant;  $k(x, x_i)$  is the kernel function which can be defined by,

$$k(x, x_i) = \varphi(x)^T \varphi(x_i) \quad (12)$$

Where  $\varphi$  is a nonlinear mapping. In our work, we used the Gaussian radial basis function that can be defined by,

$$k(x, z) = e^{-\gamma \|x - z\|^2} \quad (13)$$

In high dimensional space, the data can be divided by a linear hyperplane, depending to the following equations,

$$\begin{cases} w^T \cdot x_i + b \geq +1, & \text{if } y_i = +1 \\ w^T \cdot x_i + b \leq -1, & \text{if } y_i = -1 \end{cases} \quad (14)$$

In this research, we develop one SVM classifiers to classify gender and ethnicity. The classifier employs binary tree structure and applies one against rest for sub-classification. The classifier contains 5 sub-classifiers. Figure 3 shows the SVM classifier. Each level contains a leaf node and a sub-classifier except the final level that contains two leaf nodes. Every leaf node denotes positive output ( $y_i = +1$ ), on the other hand each sub-classifier is a negative output ( $y_i = -1$ ).

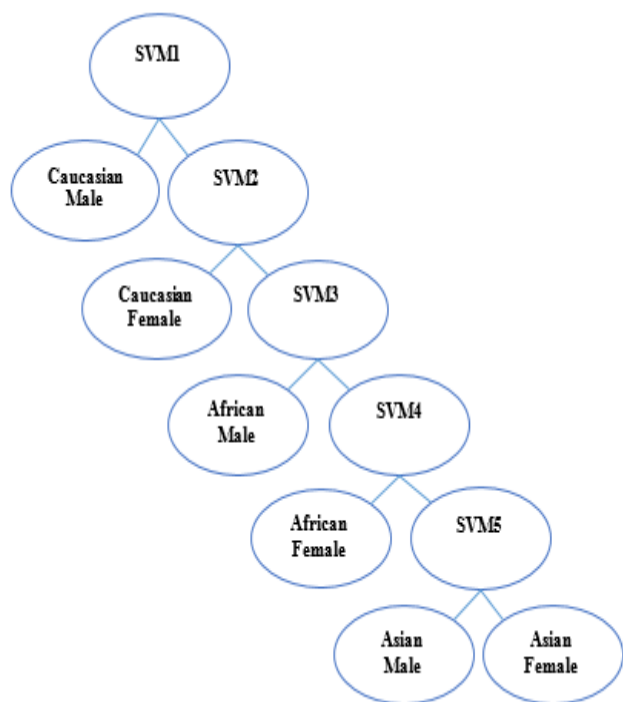


Fig. 3. Binary tree based SVM classifier

## IV. RESULT EVALUATION

In this segment, we perform experiments to illustrate the efficiency of the framework for gender and ethnicity classification. We have used FERET dataset for training and testing our system. Dataset contains 403 male individuals and 403 female individuals with a total of 2400 images. In our work, we have employed 1010 images for training and 1390 images for testing the efficiency of the framework. Fig. 4 shows some sample images. Before the training processing we have done few preprocessing on the original dataset, for instance cropping, rotating and scaling. And the Table I shows the result for training set. Here we have compared the result for Gabor filter features and HOG features. And also we have showed the result after combining both features.



Fig. 4. Sample images for gender and ethnicity classification

TABLE I. Classification Result for Different Groups

Condition	Number of Images used for testing	Gabor Filter + KPCA	HOG + KPCA	Integrated Approach + KPCA
Caucasian Male	240	93.6 %	91.1 %	97.3 %
Caucasian Female	230	94.2 %	87.6 %	95.9 %
African Male	240	91.5 %	89.3 %	93.6 %
African Female	230	88.7 %	84.8 %	96.8 %
Asian Male	230	93.2 %	82.6 %	93.4 %
Asian Female	220	89.6 %	90.1 %	95.6 %

## V. CONCLUSION

In our work, we have used an integrated approach to classify gender and ethnicity that combines Gabor filter features and Histogram of Oriented Gradients (HOG) features of a face image. The experimental result shows that integrated approach works better than the single feature method. To extract the texture features Gabor filter features are used and to extract shape features HOG features are used. Since dimensionality reduction technique is used in our system, so it requires less computation time.

## REFERENCES

- [1] P. J. Phillips, H. Moon, S. Rizvi, and P. Rauss, "The FERET evaluation methodology for face-recognition algorithms," *IEEE Transactions on Pattern Analysis and Machine Intelligence*, vol. 22, no. 10, 2000, pp. 1090-1104.
- [2] S. Hosoi, E. Takikawa, and M. Kawade, "Ethnicity estimation with facial images," in *Proc. IEEE International Conference on Automatic Face and Gesture Recognition*, 2004, pp. 195-200.
- [3] Z. Yang and H. Ai, "Demographic classification with local binary patterns," in *Proc. International Conference on Biometrics*, 2007, pp. 464-473.
- [4] H. X. Ding, D. Huang, Y. H. Wang, and L. M. Chen, "Facial ethnicity classification based on boosted local texture and shape descriptions," in *Proc. IEEE Int. Conf. Workshops Autom. Face Gesture Recognition*, 2013, pp. 1-6.
- [5] J. R. Lyle, P. E. Miller, S. J. Pundlik, and D. L. Woodard, "Soft biometric classification using periocular region features," in *Proc. IEEE 4th Int. Conf. Biometrics: Theory Appl. Syst.*, 2010, pp. 1-7.
- [6] E. M'akinen and R. Raisamo, "An experimental comparison of gender classification methods," *Pattern Recognition Letters.*, vol. 29, pp. 1544-1556, July 2008.
- [7] Md Azher Uddin, Joolekha Bibi Joolee and Shayhan Ameen Chowdhury, "Bangladeshi Vehicle Digital License Plate Recognition for Metropolitan Cities Using Support Vector Machine", in *Proc. International Conference on Advanced Information and Communication Technology*, 2016.
- [8] R. Movellan, "Tutorial on Gabor Filters," 2008. Available: <http://mplab.ucsd.edu/tutorials/gabor.pdf> [Accessed: December 12th 2014].
- [9] M. Haghghat, S. Zonouz and M. Abdel-Mottaleb, "Identification using encrypted biometrics", *Computer analysis of images and patterns (CAIP)*, Springer, pp. 440-448, 2013.
- [10] N. Dalal and B. Triggs, Histograms of oriented gradients for human detection, in: *Proceedings of the Conference on Computer Vision and Pattern Recognition (CVPR)*, vol. 1, pp. 886 - 893, 2005.
- [11] M. Kirby and L. Sirovich, "Application of the Karhunen-Loeve procedure for the characterization of human faces," *Pattern Analysis and Machine Intelligence*, *IEEE Transactions on*, vol. 12, pp. 103- 108, 1990.
- [12] Milad Moghaddam, Manoochehr Nahvi and Reza Hassanzadeh Pak, "Static Persian Sign Language Recognition Using Kernel-Based Feature Extraction", 7th Iranian conference on Machine Vision and Image Processing (MVIP), pp. 1-5, 2011.
- [13] A. Kocsor and L. Toth, "Kernel-based feature extraction with a speech technology application," *Signal Processing*, *IEEE Transactions on*, vol. 52, pp. 2250-2263, 2004.
- [14] L.J.P. van der Maaten, E.O. Postma, and H.J. van den Herik, "Dimensionality Reduction: A Comparative Review. Tilburg University Technical Report", TiCC-TR 2009-005, 2009.
- [15] Christopher J. C. Burges, "A tutorial on support vector machines for pattern recognition," *Data Mining and Knowledge Discovery*, Vol. 2, pp.121-167, 1998.



# Prospects and potential of biogas technology in Bangladesh

Md. Rafsan Nahian

Department of Mechanical Engineering  
Rajshahi University of Engineering & Technology  
Rajshahi, Bangladesh  
samsrafsan@gmail.com

Md. Nurul Islam

Department of Mechanical Engineering  
Rajshahi University of Engineering & Technology  
Rajshahi, Bangladesh  
nurul50.ruet@gmail.com

**Abstract**—The issues of energy crisis, depletion of fossil fuel and global warming are growing concern in the world. To cope up with this situation, the role of renewable energy is becoming more and more significant to meet partially demand of global energy. Biogas is an auspicious renewable energy source that can solve the energy crisis problem at a great extent. As Bangladesh is an agricultural country, it has blessed with plenty of biomass which has been used for extracting energy by generating biogas. Animal manures being accessible in the rural areas are greatly used in producing biogas to be used for cooking and electricity. In Bangladesh around 59.6% of the total population is covered by electricity and 6% is covered under natural gas network. About 62.59% of total electricity develops from natural gas. The main concern of this paper is to quantify the solution of energy crisis through biogas and assess the economical, environmental and social impacts of biogas technology in Bangladesh.

**Keywords**—Renewable energy, biogas, poultry waste, cattle manure, municipal waste, prospects of biogas.

## I. INTRODUCTION

Fossil fuels are extensively used in transportation, power generation and machinery energy source due to its high heating power, availability and quality of combustion characteristics, but its reserve is draining day by day. Bangladesh, as a developing nation has been struggling to keep up with the energy demand for its large population. Bangladesh has installed power plants having the generating capacity of 11877 MW where maximum generation is 8177 MW and 93.9% power comes from fossil fuel [1]. Bangladesh government envisions that 5% & 10% of total energy production will have to be achieved from renewable energy sources by the year 2015 & 2020 respectively [1]. Biogas is one of the auspicious renewable energy sources which refer to a mixture of different gases generated by the decomposition of organic matter like agricultural waste, municipal waste and animal manure in the absence of oxygen. About 102.6 million tons Cattle dung from 25.5 million cows and buffaloes, 12.9 million tons poultry waste from 291.5 million chickens and ducks and 8.65 million tons municipal waste are produced in Bangladesh every year [2]. Such a large amount of these wastes have great economical value which can be utilized to produce biogas for cooking, heating and electricity generation. Besides, production of

biogas from organic waste avoids emitting of methane and nitrous oxide in the environment. The intergovernmental panel reports on climate change that nitrous warms the atmosphere 310 times more than carbon dioxide and methane does so 21 times more [3].

## II. BIOGAS AND ITS COMPOSITION

Biogas is a combustible mixture of gases. Methane (CH<sub>4</sub>) and carbon dioxide (CO<sub>2</sub>) are the main components of biogas which is formed by the anaerobic bacterial decomposition of organic compounds in absence of oxygen. The gases are produced from the waste products of the respiration of these decomposer microorganisms. The composition of the gases depends on the substances that are being decomposed [4]. It has burning properties like natural gas. It is about 20% lighter than air and calorific value is (5000-7000) kcal per cubic meter. It usually burns with 60% efficiency in a conventional biogas stove [5].

TABLE I. COMPOSITION OF BIOGAS [6]

Components	Percentage
Methane (CH <sub>4</sub> )	60-70
Carbon dioxide (CO <sub>2</sub> )	30-40
Hydrogen (H <sub>2</sub> )	2-2.5
Nitrogen (N <sub>2</sub> )	1-1.5
Oxygen (O <sub>2</sub> )	0.3-0.4
Hydrogen Sulfide (H <sub>2</sub> S)	0.1-0.2

## III. ANAEROBIC DIGESTION

It is an oxygen-free complex biological process, in which the feeding material is decomposed partially by the combined action of several types of microorganisms to generate biogas.

Biogas production by anaerobic digestion depends on various factors such as temperature, pH condition of feeding material, nutrient of charge, organic loading rate etc. The temperature range required for anaerobic digestion is 30°C-70°C but optimum range is between 35°C-38°C. Besides the

optimum range of pH value is 6 to 7 [4]. The anaerobic digestion process and utilization of biogas are given below:

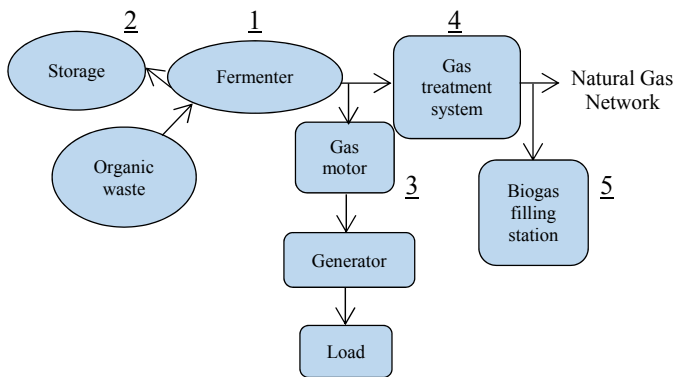


Fig. 1. Energy production in a biogas plant.

1. The digester contains biomass that anaerobically digest by the action of micro-organisms to produce the biogas and carbon dioxide.
2. Residual materials from the digester called slurry can be utilized as fertilizer, substantially reducing the use of fertilizer.
3. In a Combined Heat and Power (CHP) plant the biogas is combusted to produce both electricity and heat
4. The Gas upgrading plant increases the overall quality of the biogas by removing CO<sub>2</sub>, S and other impurities.
5. The upgraded biogas can be utilized in gas engine.

#### IV. TEMPERATURE CONTROL SYSTEM

The temperature control system enhances the rate of biogas production for large scale biogas plant. The temperature range required for anaerobic digestion is 30°C- 70°C. Temperature between 35°C-38°C is considered optimum. A temperature control system can be utilized to maintain the optimum temperature between 30°C-40°C in digester.

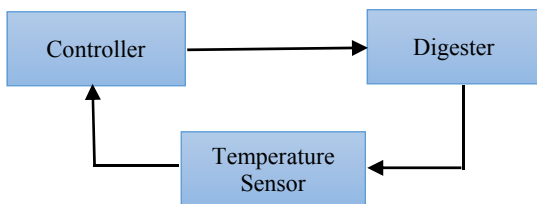


Fig. 2. Temperature control system in digester.

Temperature control system consists of control panel, an electric heater in digester and a temperature sensor. The temperature sensor is used to sample digester temperature. The electric heater is controlled through the controller. When the temperature of digester is below 30°C, the temperature sensor sends a signal to the controller to switch on the electric heater. Similarly when the temperature of digester is above 40°C, the temperature sensor sends a signal to the controller to switch off the electric heater.

#### V. STATISTICS AND ENERGY ANALYSIS OF ORGANIC WASTE IN BANGLADESH

##### A. Poultry waste

As Bangladesh is a promising place for poultry industry, the number of poultry farms have increased continually. The main objective of the poultry industry was to assist only food supply against a highly dense population. In 2013, the country had approximately 245 million chickens and 46 million ducks respectively that produced 12.9 million tons of waste [2]. This poultry waste can be extracted by anaerobic digestion (AD) process which has huge energy value.

TABLE II. ENERGY CALCULATION CHART [7]

Waste and droppings per chicken/duck per day	Amount of biogas produced from 1 kg of poultry waste	Amount of biogas for 1 KW electricity generation
0.1 kg	0.074 m <sup>3</sup>	0.71 m <sup>3</sup>

Total number of chickens and ducks= 291000000

So, Total amount of poultry waste= (0.1×291000000) kg  
= 29100000 kg

Total amount of produced biogas= (29100000×0.074) m<sup>3</sup>  
= 2153400 m<sup>3</sup>

Total electricity generation= (2153400÷0.71) KW  
= 3032957 KW= 3033 MW

##### B. Cattle dung

Traditionally cattle dung is utilized as a fertilizer. Nowadays dung is collected and used to produce biogas. The international energy agency reports that bioenergy has the potential to meet more than a quarter of the world demand for transportation fuels by 2050. In 2013, the country had approximately 24 million cows and 1.5 million buffaloes respectively that produced 102.6 million tons of waste [2].

TABLE III. ENERGY CALCULATION CHART [6]

Dung from one cattle per day	Amount of biogas produced from 1 kg of cattle dung	Amount of biogas for 1 KW electricity generation
10 kg	0.034 m <sup>3</sup>	0.71 m <sup>3</sup>

Total number of cattle's= 25500000

So, Total amount of cattle waste= (10×25500000) kg  
= 255000000 kg

Total amount of produced biogas= (255000000×0.034) m<sup>3</sup>  
= 8670000 m<sup>3</sup>

Total electricity generation= (8670000÷0.71) KW  
= 12211267 KW= 12211 MW

### C. Municipal waste

Municipal waste disposal is one of the main problems being confronted by all nations across the world. The daily per capita per person solid waste produced in Bangladesh is about (300-400) gram and approximately 8.65 million tons municipal waste was generated in 2013. If we carefully analyze these waste, we will realize that most of these are biodegradable.

TABLE IV. ENERGY CALCULATION CHART

Amount of municipal waste per day	Amount of biogas produced from 1 kg of municipal waste	Amount of biogas for 1 KW electricity generation
21500000 kg	0.076 m <sup>3</sup>	0.71 m <sup>3</sup>

Total amount of municipal waste= 21500000 kg  
 Total amount of produced biogas= (21500000×0.076) m<sup>3</sup>  
 = 1634000 m<sup>3</sup>  
 Total electricity generation=(1634000÷0.71) KW  
 = 2301408 KW= 2301 MW

From the above calculations TABLE V has been drawn that shows the possibility of total amount of biogas production and electricity generation from organic waste in Bangladesh.

TABLE V. ENERGY FROM ORGANIC WASTE (2013)

Source of organic waste	Amount of produced biogas in cubic meter	Amount of generated electricity in MW	Percentage of generated electricity
Poultry waste	2153400	3033	17.3
Cattle dung	8670000	12211	69.6
Municipal waste	1634000	2301	13.1
Total amount	12457400	17545	100

From TABLE V, we can draw a pie chart which shows the percentage of possibility of electricity generation from poultry waste, cattle dung and municipal waste in Bangladesh.

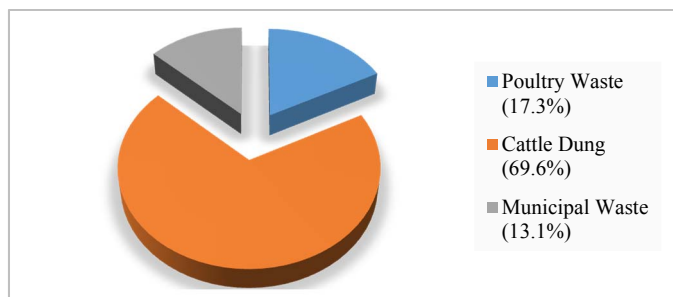


Fig. 3. Possibility of electricity generation from organic waste (2013)

## VI. ECONOMICAL, ENVIRONMENTAL AND SOCIAL PROSPECTS

Biogas technologies have great significance for energy access, energy security, deplete dependency on fossil fuels, moderating climate change, sustainability and socio-economic benefits.

### A. Economical prospects

Biogas has great potential to cover a variety of markets, including electricity, heat, transportation fuels and also to use the gas for direct combustion in household stoves and gas lamps. Bangladesh has installed power plants having electricity generating capacity of 11877 MW where maximum generation is 8177 MW and peak demand is 10283 MW until 2015 [1]. From TABLE V, total electricity generated from organic waste is 17420 MW. In 2013 if we could utilize at least 10% of total amount of organic waste, 1754 MW electricity would be produced which was able to fulfill 21% of peak demand out of 8339 MW in Bangladesh [1].

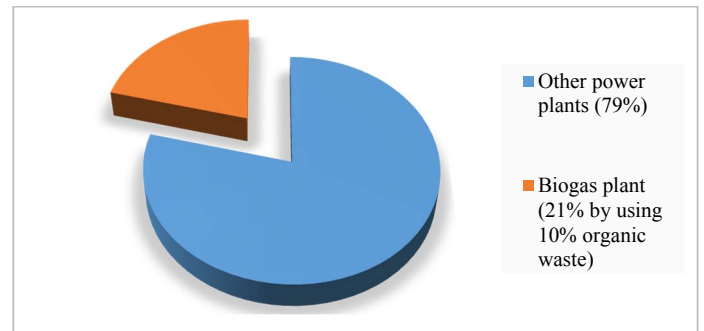


Fig. 4. Possibility of electricity generation in Bangladesh (2013)

Fig. 4 shows how biogas could play a vital role to fulfill 21% of peak demand if 10% of total amount of organic waste was utilized in 2013.

Biogas enables us to save the energy cost and earn money by selling biogas to the neighbors. Soil fertility in Bangladesh is gradually diminishing. One of the major factors is excessive utilization of chemical fertilizers. The by-product of a biogas plant is called bio-slurry. It is the best alternative supplement to chemical fertilizers for maintaining soil fertility. It is nontoxic. The nutrient quality of bio-slurry is higher than compost manure and chemical fertilizer.

### B. Environmental prospects

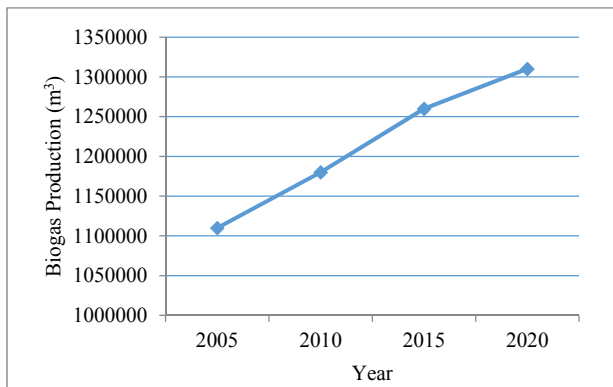
There are increasing concerns about growing greenhouse gas (GHG) emissions and their impact on worldwide climate change. GHG reduction require strategies in different production sectors but the existing strategies are not yet effective.

Only in United States, over one billion tons of cattle manure is produced from livestock yearly [8]. Ammonia, VOCs, hydrogen sulfide and particulate matter are emitted from manure which can create health problems [9]. Ammonia can also contaminate ground water and lead to eutrophication of the soil [10]. Biogas plants have environmental benefits to the

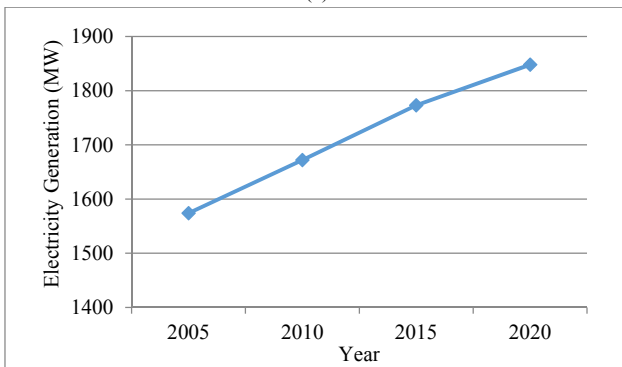
reduction of greenhouse gas emissions and air pollutants in the atmosphere. This is possible through the controlled capture of CH<sub>4</sub> and the saving of fossil fuels by biogas replacement [11]. Unbalancing the eco-system is the main cause of natural disasters. Biogas technology can play a powerful role to keep the balance of eco-system as it will encourage farming and reduce deforestation.

## VII. FUTURE PROSPECTIVE

Production of biogas from organic waste exposes massive interest around the world. Biogas technology offers vital environmental benefits in term of bioenergy. It provides different final products such as a renewable energy source, electricity production, heat generation, transportation fuel and a good fertilizer.



(a)



(b)

Fig. 5. Graphical representation of possibility of (a) biogas production, (b) electricity generation; from 10% of total amount of organic waste in Bangladesh.

Bangladesh has possibility to produce 13100000 cubic meter biogas by utilizing total amount (100%) of organic waste in 2020. If we ensure to utilize at least 10% of it, it will produce

1848 MW electricity which will cover 10.7% of peak electricity demand in 2020. To solve energy crisis in third world countries such as in Bangladesh and save the planet from the effects of climate change and greenhouse gases, we need investments in biogas technologies. In this regard, the developing countries have the opportunity to leapfrog conventional energy options in favor of cleaner energy alternatives such as biogas energy.

## VIII. CONCLUSION

The outcome of this paper expresses that there is substantial scope for Bangladesh to fulfill its future power demand through biogas. Biogas energy sources conferred above can aid Bangladesh to generate more power in order to minimize load-shedding problem. It is high time to work with biogas technology to generate electricity rather than depending entirely on conventional method. Therefore, the government and non-government organizations should work together on biogas and biogas technology to solve energy crisis problem.

## REFERENCES

- [1] Bangladesh Power Development Board. [http://www.bpdb.gov.bd/bpdb/index.php?option=com\\_content&view=article&id=126&Itemid=17](http://www.bpdb.gov.bd/bpdb/index.php?option=com_content&view=article&id=126&Itemid=17)
- [2] FAOSTAT.-2013 <http://faostat3.fao.org/browse/Q/QA/E>
- [3] Cow power: the energy and emissions benefits of converting manure to biogas by Amanda D Cuellar and Michael E Webber. IOP Publishing Ltd, Volume 3, Number 3. 2008
- [4] Peter Jacob Jorgensen, "Biogas- Green Energy." pp. 4
- [5] A. D. Obozov, and Asankulova, "Biogas in Kyrgyzstan" in *Applied Solar Energy*(2007), Vol. 43, No. 4, pp.262–265,
- [6] Feasibility study on electricity generation from poultry litter based biogas in Bangladesh. DOI: 10.1109/ICDRET.2014.6861661
- [7] Design and Benefit Analysis of Biogas Plant for Rural Development in Bangladesh. International Journal of Engineering and Advanced Technology (IJEAT) ISSN: 2249 – 8958, Volume-3, Issue-3, 2014
- [8] Kellogg R L, Lander C H, Moffitt D C and Gollehon N 2000 Manure Nutrients Relative to the Capacity of Cropland and Pastureland to Assimilate Nutrients: Spatial and Temporal Trends for the United States (March, 2007)
- [9] National Research Council 2003 Ad hoc committee on air emissions from animal feeding, O Air Emissions from Animal Feeding Operations: Current Knowledge, Future Needs vol xxi (Washington, DC: National Academies Press) pp. 263
- [10] Doorn M R J, Natschke D F and Meeuwissen P C 2002 Review of Emission Factors and Methodologies to Estimate Ammonia Emissions from Animal Waste Handling US Environmental Protection Agency.
- [11] Environmental analysis of biogas production systems by Caterina Tricase & Mariarosaria Lombardi. Volume 3, issue 6. Pages 749-760, 2012. DOI:10.4155/bfs

# Land Cover Change Detection Using GIS and Remote Sensing Techniques

A Spatio-Temporal Study on Tanguar Haor, Sunamganj, Bangladesh.

Md. Inzamal Haque  
Masters Student, Department of Geography and  
Environment  
Shahjalal University of Science & Technology  
Sylhet-3114, Bangladesh.  
sazal.edu@outlook.com

Rony Basak  
Assistant professor, Department of Geography &  
Environment  
Shahjalal University of Science & Technology  
Sylhet-3114, Bangladesh  
rbasak-gee@sust.edu

**Abstract**— Tanguar Haor undergoes a radical change in its form over the decades. This study illustrated that, about 40% land cover of the total study area has been converted. Forested and High land vegetation's are disappearing rapidly, deep water bodies consist of large lakes are becoming the rare feature of the study area. Widespread development of settlement and dominant shallow water feature are converting the natural wetland a permanent low lying agricultural land. Both pre classification and post classification change detection approach was used to assess the change. Several satellite images were taken as the fundamental secondary data for detail analysis from USGS satellite data archive. Change Vector Analysis (CVA), Natural Difference Vegetation Index (NDVI) and Natural Difference Water Index (NDWI) analysis were implemented to assess the change dynamics. Maximum likelihood supervised classification technique was performed to create the signature class of significant land cover category (Deep Water, Shallow Water, Vegetation and Settlement). Image differencing, Statistical change detection techniques (transition probability matrix), change dynamics analysis was operated to evaluate the past change relative to present.

**Keywords**— Tanguar Haor; Wetland; Anthropogenic influence; Satellite Image; Land Cover Change;

## I. INTRODUCTION

According to Blasco and Aizpuru (1997), wetlands include world heritage sites with significant values to ecological, biologic, zoological, limnological, or hydrological settings, including such phenomena as thermal features and underground rivers [1]. Tanguar Haor is one of the largest wetland systems in the northeast region of Bangladesh. It is also said to be a part of world's largest geosynclines. Tanguar Haor plays a vital part in the economy of Bangladesh with its natural richness and diversity. Both human-induced and natural land cover changes can influence the global change because of its interaction with terrestrial ecosystem [2], biodiversity and landscape ecology [3]. In addition, it reflects the human impacts on environment at various temporal and spatial scales [4]. Therefore, accurate and up-to-date land use/cover information is essential for environmental planning, to understand the impact on terrestrial ecosystem [5] and to achieve sustainable development [6]. Remote Sensing (RS) and Geographic Information System (GIS) are now providing

effective tools for advanced ecosystem and socio economic management. The collection of remotely sensed data facilitates the synoptic analyses of Earth - system function, patterning, and change at local, regional and global scales over time; such data also provide an important link between intensive, localized ecological research and regional, national and international conservation and management of biological diversity [7].

This study used geospatial technology (GIS, RS) to signify the importance of land cover changes over the Tanguar Haor basin, which possibly help to assess the change dynamics of the area. Scientific change assessment may also help the policymakers to understand the natural state of the area and the complex relation between the physiographic and man-made features.

The main objective of the study is to evaluate the nature, significance and rate of wetland change from 1980-2010. The study also tried to find out the areas of rapid change and magnitude of change around the study area.

## II. MATERIALS AND METHODS

### A. Study Area

Tanguar Haor is located in the northeastern part of Bangladesh, between 25° 12' 2.572" and 25° 5' 47.989" North Latitude and 90° 58' 49.426" and 91° 10' 0.018" East Longitude. The total area of Tanguar Haor is approximately 160 square kilometers including all Geographic features and land cover. It is Northwestern part of Sunamganj district of Sylhet division. Within total area of Tanguar Haor there are two upazila of Sunamganj district e.g. Tahirpur and Dharmapasha and four unions e.g. Uttar Bangshikunda, Dakshin Bangshikunda, Uttar Sreepur, Dakhsin Sreepur. Within its geographic boundary Tanguar Haor possesses 88 villages.

### B. Data Collection

The present study is in view of both primary and secondary information. The primary information was gathered through the poll review, organized and unstructured meeting with key witnesses, direct field perception and dialogs with

the common individuals of the study area. On the other hand, the preliminary secondary data for this study was collected from free available satellite image archives.

Base maps for this study include- Tanguar Haor Area map, Mouza map, Union map, Upazila map and available land use map of the study area. Main Base map was collected from Community Based Sustainable Management of Tanguar Haor Program (CBSMTHP) by the Government of Bangladesh. Freeware satellite data was downloaded from Landsat archive of United States Geological Survey (USGS) official website (earthexplorer.usgs.gov). Every satellite imagery represents the dry season. The information about downloaded satellite data are represented in (table 1).

TABLE 1. DETAILS OF ACQUIRED SATELLITE IMAGES

Satellite Id	Sensor Id	Path/Row	Acquisition Date	Spatial Resolution	Quality
Landsat 3	MSS	147/43	02-02-1980	60 meter	0
Landsat 4	TM	137/43	28-01-1989	30 meter	9
Landsat 7	ETM	137/43	29-01-2001	30 meter	9
Landsat 5	TM	137/43	30-01-2010	30 meter	9

### C. Data Analysis

The total analysis is based on transforming ideas into maps and graphs. The raw satellite images contain cell value called Digital Number. The digital numbers for each cell of each images first converted into reflectance value. After preprocessing the study area had been masked or clipped from the whole image. This is an optional step, subset or masking reduce the image size which help the user to flexibly and precisely go through the forward steps. After preprocessing a classification scheme have made to classify the image. The true color image is transferred to false color composite image after in detail classification. A detail change detection analysis was assessed by implementing pre and post change detection techniques. The critical change areas were identified by integration of several techniques.

## III. RESULT AND DISCUSSION

### A. Preprocessing

Common forms of noise include systematic striping or banding and dropped lines. The overall appearance was thus a 'striped' effect (Jacqueline, NASA). Discrete Fourier Transform (DFT) method was used to reduce the noise from 1978 image. The quantity of frequencies compares to the quantity of pixels in the spatial space picture, i.e. the picture in the spatial and Fourier space is of the same size. For a square image of size  $N \times N$ , the two-dimensional DFT is given by (equation 1):

$$F(k, l) = \sum_{i=0}^{N-1} \sum_{j=0}^{N-1} f(i, j) e^{-i2\pi(\frac{ik}{N} + \frac{j l}{N})}$$

(1)

where  $f(i,j)$  is the image in the spatial domain and the exponential term is the basis function corresponding to each point  $F(k,l)$  in the Fourier space. The satellite image of 1980 includes some of this stripped effect. The band 4 among the all

bands contained excessive noise. The noise was reduced at a level via Fourier analysis using ERDAS Imagine 9.1.

Landsat Satellite sensors capture images of Land cover as Digital Number (DN) value rather than Top of Atmosphere (ToA) reflectance units. The main purpose of this step is to convert the digital numbers to Top of Atmosphere reflectance units. Equations and parameters to convert calibrated Digital Numbers (DNs) to physical units, such as at-sensor radiance or Top-Of-Atmosphere (TOA) reflectance, have been presented in a "sensor-specific" manner elsewhere, e.g., MSS [8], TM [9] [10], ETM+(Handbook2), and ALI. Different calibration values differ according to sensor id and acquisition date. These calibration procedures consist of two steps- Converting DN(Qcal) to Radiance( $L\lambda$ ) and then Converting Radiance ( $L\lambda$ ) to Reflectance ( $\rho\lambda$ ).

The whole radiometric calibration process was implemented following some relevant equation using Erdas Imagine model maker tool and Environment for Visualizing Images (ENVI) Landsat calibration tool.

### B. Classification

The Supervised Maximum Likelihood classification used in this study is the most common method in remote sensing image data analysis. It used the means and variances of the training data to estimate the probability that a pixel is a member of a class. The pixel was then placed in the class with the highest probability of membership [11]. A classification scheme was developed for further analysis of the images, based on the characteristics of the area (Table 2).

TABLE 2 DETAIL OF CLASSIFICATION SCHEME

Code	Land Cover Type	Description
1	Deep Water	River, Permanent open water, Perennial lakes and reservoirs.
2	Vegetation	High land agriculture, Forest, Trees, Shrub lands
3	Shallow Water	Semi inundated land filled with marshy vegetation.
4	Settlement	Temporary and permanent houses, Villages, Artificial infrastructure, Roads, Bare land.

Digital spectral signatures were developed based on classification scheme. Maximum likelihood parametric rule was applied during classification as mentioned before. Based on statistics (mean; variance/covariance), a (Bayesian) Probability Function is calculated from the inputs for classes established from training sites. Each pixel is then judged as to the class to which its most probably belong (Figure 1).

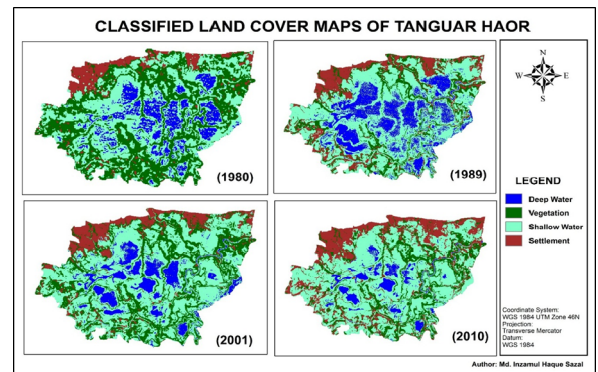


Figure 1. Classified Land Cover Maps of Tanguar Haor (1980-2010)

### C. Land Cover Change Detection

There are two broad methods of Change Detection Techniques includes- a) Pre Classification Method, b) Post Classification Method. Pre Classification method analyze the change without classifying the image. The most common and widely used pre classification method is “Vegetation Index Differencing (NDVI)”. Various index has developed after NDVI e.g. NDWI, MNDWI, Change Vector Analysis(CVA) etc. On the other hand, post Classification method is the most widely used change detection method of modern times. Post classification evaluate the change in land cover based on a detail categorized classification of land cover. Post Classification comparison, Aerial Difference calculation, Image Differencing, Image rationing, Image regression etc. are some of the common post classification Change detection approaches.

NDVI is calculated on a per-pixel basis as the normalized difference between the red and near infrared bands from an image (equation 2):

$$NDVI = \frac{NIR - RED}{NIR + RED} \quad (2)$$

The NDWI is derived using similar principles to the NDVI. The equation is as follows (equation 3):

$$NDWI = \frac{GREEN - NIR}{GREEN + NIR} \quad (3)$$

After successful production of both NDVI and NDWI maps unsupervised classification had used for every output to classify the result dataset. Isodata algorithms with Maximum Iteration 6 and Convergence Threshold 0.950 used to classify each Vegetation Differentiating Image and Water Differentiating Image. Only positive values were take in count to classify each image. After classification area was calculated for each land cover category for both NDVI and NDWI image. After aerial calculation linear regression line was constructed for each category. Time was taken as the independent factor (x) and area was taken as the dependent factor during the calculation

A significant decline in forested high land vegetation; a significant incline in Mix vegetation consist of various anthropogenic elements e.g. settlement; and a moderate incline in Bushy or low land vegetation includes crop fields, marshy vegetation (figure 2). Result of linear Regression Analysis for each Vegetation Cover Category have shown in (figure 2). At the mean time The linear regression (figure 3) shows a clear decline trend line for the deep water class when a positive increase found in case of Shallow Water class.

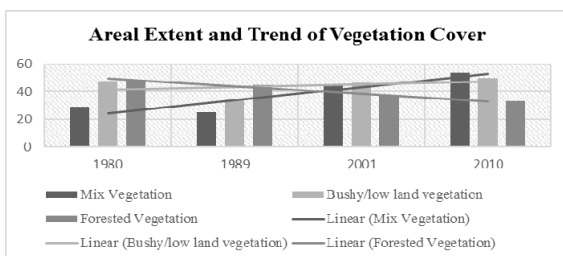


Figure 2. Change in Vegetation Cover of Tanguar Haor (sq. km)

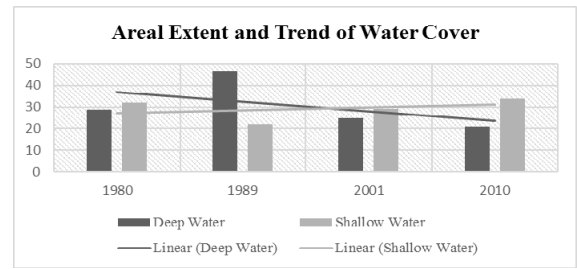


Figure 3. Change in Water Cover of Tanguar Haor (sq. km)

Change Vector Analysis (CVA) is another specialized change detection technique that evaluate the magnitude and direction of Change in spectral space between two times. A change vector is the difference vector between two vectors in n-dimensional feature space defined for two observations of the same geographical location (i.e. corresponding pixels) during two dates [12]. The Study have taken 8 bands comprises of 2 bands for each year (1980, 1989, 2001, 2010). RED and NIR channels for each date are taken for the analysis. As the raster bands of 1980 comprises different values and pixel components, band 5 and 6 are taken as the RED and NIR bands. To CVA analysis with raster bands of 1980, principle component analysis executed to segregate noise components and to normalize the band images (band 5 and band 6) to 30m. (Figure 4) describes the magnitude of land cover change of Tanguar Haor from 1980-2010. More than 50% of the total landscape of Tanguar Haor has been changed or shifted within 30 years. The most gradual changes taken place in the middle part consist of various beels and lakes. The upper part shows lower magnitude of change and the south eastern part shows a moderate change. Most significant change happens in the eastern part of Tanguar Haor.

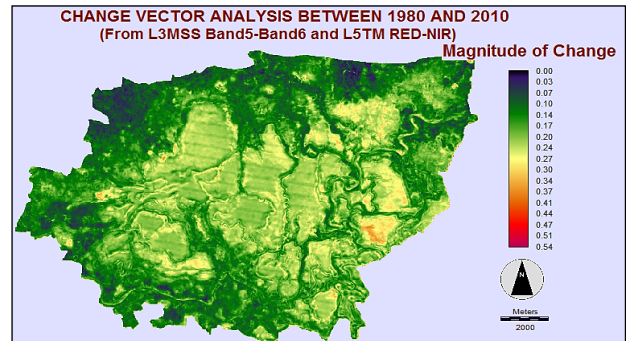


Figure 4. CVA Showing the Magnitude of Change

A convenient way to assess the post classification change dynamics is identifying the thematic change based on change statistics. ENVI thematic change workflow tool was used to portray the dynamics of land cover change that have taken place in Tanguar Haor from 1980 to 2010. The tool measures the transition dynamics of a land cover class to another class at a given extent. Total 24 unique classes were introduced as a change factor between the two-time span. The study only considered the valid classes which carry a significant change resultant. 12 classes were eliminated as they have no valid change value to visualize. After the execution an optional clean-up or Refine operation was done to strengthen the output. Smooth Kernel Size was specified as 3x3 pixel. The square

kernel's center pixel will be replaced with the majority class value of the kernel. At the final stage three distinct output file was created from which the first one is thematic change image (figure 5), second one is thematic change vector file and the final output consist of thematic change statistics (table 3).

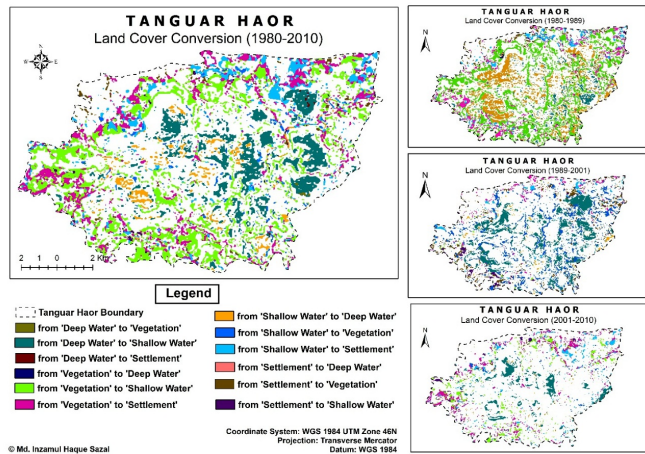


Figure 5. Resultant output of Thematic Change Workflow Analysis

TABLE 3 THEMATIC CHANGE STATISTICS: FROM-TO CHANGE MATRICES

1980	2010	Changed Area (sq. km)	Percent Change
From No Change	to No change	99.386800	62.11675
From Deep Water	to Vegetation	.094500	0.0590625
From Deep Water	to Shallow Water	12.989700	8.1185625
From Deep Water	to Settlement	.104400	0.06525
From Vegetation	to Deep Water	.081000	0.050625
From Vegetation	to Shallow Water	22.464000	14.04
From Vegetation	to Settlement	11.402100	7.1263125
From Shallow Water	to Deep Water	3.289500	2.0559375
From Shallow Water	to Vegetation	2.160900	1.3505625
From Shallow Water	to Settlement	6.342300	3.9639375
From Settlement	to Deep Water	0	0
From Settlement	to Vegetation	1.259100	0.7869375
From Settlement	to Shallow Water	.425700	0.2660625

#### D. Discussion

Impact of land cover change influence approximately 40% of the total landscape of the study area within 1980 to 2010. Present land cover distribution shows that only 6.29% of the total land cover still remain the deep water body, the value was much higher in earlier years. Around 50% of the total deep water extent already degraded in last 30 years. The NDWI analysis shows around 25.4583 square kilometer of deep water body has degraded within 1989-2010. The change dynamics analysis identifies that, most of the deep water part has converted to shallow water consist of emergent or semi emergent vegetation or crop fields. Within 30 years from 1980 forested vegetation decreased more than 50%. The NDVI analysis evaluate a more precise result. Around 15.9967

square kilometer of forested vegetation land has degraded in 30 years from 1980. The transition matrix shows that; the forested vegetation land was either transferred to shallow water or settlement. Population pressure and insufficient land is the main cause of settlement expansion in the adjacent area of Haor Basin. The doubling rate of settlement is only 20-25 year. In the past settlement was condensed only in the upper and lower corner of the Haor Basin but at present time the feature seems to be dominated extensively all over the haor basin.

#### ACKNOWLEDGMENT

Firstly, I would like to express my sincere gratitude to my supervisor Mr. Rony Basak, Assistant professor, Dept. of GEE, SUST for the constant support during this research and also for his patience, motivation, and profuse knowledge. I also wish to express my grateful thanks to Dr. Md. Sirajul Islam, Associate professor, Department of Geography and Environment, University of Dhaka, Md Mostafizur Rahman, Specialist, Database, ICT and System Management Division of CEGIS, A.B.M. Sarowar Alam and Animesh Ghosh from IUCN for their consistent support during my project pursuit. I take this opportunity to express gratitude to all the faculty members and stuffs of dept. of GEE, SUST for their kind help and sincere support.

#### REFERENCES

- [1] Blasco, F., & Aizpuru, M. (1997). Classification and evolution of the mangroves of India. *Tropical Ecology*, 38(2), 357-374.
- [2] Houghton, R. A. (1994). The worldwide extent of land-use change. *BioScience*, 44(5).
- [3] Reid, R. S., Kruska, R. L., Muthui, N., Taye, A., Wotton, S., Wilson, C. J., & Mulatu, W. (2000). Land-use and land-cover dynamics in response to changes in climatic, biological and socio-political forces: the case of southwestern Ethiopia. *Landscape Ecology*, 15(4), 339-355.
- [4] Lopez, A. D., Mathers, C. D., Ezzati, M., Jamison, D. T., & Murray, C. J. (2006). Global and regional burden of disease and risk factors, 2001: systematic analysis of population health data. *The Lancet*, 367(9524), 1747-1757.
- [5] Muttitanon, W., & Tripathi, N. K. (2005). Land use/land cover changes in the coastal zone of Ban Don Bay, Thailand using Landsat 5 TM data. *International Journal of Remote Sensing*, 26(11), 2311-2323.
- [6] Alphan, H. (2003). Land-use change and urbanization of Adana, Turkey. *Land degradation & development*, 14(6), 575-586.
- [7] Wilkie, D. S., & Finn, J. T. (1996). Remote sensing imagery for natural resources monitoring: a guide for first-time users. Columbia University Press.
- [8] Markham, B. L., & Barker, J. L. (1987). Thematic Mapper bandpass solar exoatmospheric irradiances. *International Journal of remote sensing*, 8(3), 517-523.
- [9] Chander, G., & Markham, B. (2003). Revised Landsat-5 TM radiometric calibration procedures and postcalibration dynamic ranges. *Geoscience and Remote Sensing, IEEE Transactions on*, 41(11), 2674-2677.
- [10] Chandler, D. M., & Hemami, S. S. (2007). VSNR: A wavelet-based visual signal-to-noise ratio for natural images. *Image Processing, IEEE Transactions on*, 16(9), 2284-2298.
- [11] Ozesmi, S. L., & Bauer, M. E. (2002). Satellite remote sensing of wetlands ecology and management, 10(5), 381-402.
- [12] Nackaerts, K., Vaesen, K., Muys, B., & Coppin, P. (2005). Comparative performance of a modified change vector analysis in forest change detection. *International Journal of Remote Sensing*, 26(5), 839-852.



# Design and Practical Implementation of Universal Driver Circuit for LED Lamps

Md. Tanvir Hossan, Md. Nayeem Shakkhar

*Department of Electrical & Electronic Engineering*

*Khulna University of Engineering & Technology, Bangladesh*

Email: tanvir.hossan.shaon@gmail.com, nayeem-eee@hotmail.com

**Abstract— This paper presents a universal driver circuit using linear current regulation technology for Light Emitting Diode (LED) operating from either wide-range of voltage (180 to 240V) in Alternating Current (AC) or voltage (12 to 15V) in Direct Current (DC). Available LED driver circuits in the market have some drawbacks like higher cost, higher self-power consumption, a lower load driving technique, designed separately for AC and DC power supply, using too many inductive components. In this scenario the proposed LED driver circuit shows universality in both power supplies with leading power factor (near to unity) as well as its cost & self-power consumption is lower with greater efficiency. To verify the feasibility, a laboratory prototype for LED driver circuit is designed and performance is tested with 3 to 30 LEDs.**

**Keywords— Universal Driver Circuit, Constant Load Current Driver, Double Pole Double Throw (DPDT), Light Emitting Diode (LED).**

## I. INTRODUCTION

Conventionally, compact fluorescent lamps (CFL), fluorescent, and incandescent are being used as general lighting technique in our daily life. "Lumen per watt" or "efficacy" is used as the unit to calculate the efficiency of the light sources. CFL lamp has the efficiency of around 7% - 8% whereas incandescent bulb has 2% [1]. Nowadays, light emitting diodes (LEDs) are drawing industrial and academic consideration due to the advancement of new technologies. LED has huge advantages over conventional lighting sources such as it radiates less mercury and is difficult to break that makes it environment-friendly lighting source. Moreover, it is improvised to shock, vibration or quick environment change. LED has the efficiency of 30% as well as shows longer lifespan ( 100,000 hours) which is ten times greater than conventional lighting sources. It has fast switching times that human eye cannot detect, produces less heat, and projects higher light in the solicited way. LED is compact, and it is easy to install on PCB [2].

As LEDs have become a promising technologies, it has been used widely not only for illumination but also communication purposes. Among which visible light is an uprising technique in modern wireless communication where LEDs are used as transmitter. This communication technique is also known

as optical wireless communication (OWC). Vehicle-to-vehicle communication and LED or digital signage based advertisement are the important application of OWC. In [3], the authors proposed a spatial-temporal resolution based vehicular communication technique which can detect and process multiple objects simultaneously. In [4], the performance of smart digital signage has been analyzed. These are also the great application of LED based communication. However, we are not focusing on these topics. In this paper, we design a universal driver circuit for LED lamps with practical implementation. These driver circuit can be used in vehicular communication or LED signage to ensure reliable and efficient system.

The overall efficiency of LEDs can be affected by adjusting its brightness [5]. LEDs can be connected in parallel and/or series that is driven by high voltage and current. The lumen of LED is directly proportional to the current. Therefore, the operating current can control the brightness of the LEDs. It is preferable to use fewer components to ensure compact, highly efficient, and reliable system.

There are several drivers and driving techniques to drive LED with some drawbacks. Most of the driver circuits are using a large inductor in order to reduce the ripple current through the LEDs successfully [6]. Because of the high inductive resistance, inductor consumes much power. This energy can be dissipated as heat or developed as voltage or current stress to the connected devices. Henceforth, the efficiency of the driver is affected [7].

Pulse-Width Modulation (PWM) is one of the favorite techniques for LEDs in switched-mode driver circuits. Traditional non-isolated step-down PWM buck converters may suffer from reduced efficiency due to the long diode freewheeling time at small duty cycles [8]. The major drawback of PWM dimming is that if all the LED strings are turned on or off simultaneously, the input-output power periodically undergoes abrupt changes, causing massive pulsating input/output current, degraded EMI performance, decreased operating efficiency and increased power bus ripple [9], [10]. There are some non-isolated converter topologies can be used as power factor pre-regulator, such as buck-boost, single-ended primary inductor, CUK and flyback converters or offer universality [11]. Usually, these converters are suitable for small power applications [1]. Conventionally LED is driven by DC voltage. Recently, some paper propose AC utility source which is directly driving LED (e.g., AC-LED). However, it has some disadvantages like

conduction angle causes harmonic distortion and low power factor [12].

This paper proposes a novel architecture and its practical implementation for both AC and DC power supplies in order to keep load current constant in all cases. The proposed scheme is applicable for a wide voltage range of any power supply. The rest of the paper are organized as follows. Section II presents the I-V characteristics of Taylor Series Expression. Whereas Section III of the paper represents the overall system requirements for the proposed architecture, circuit topology where we point out the design considerations for the LED drivers circuit. Then Section IV presents the practical implementation for LED drivers. Section V shows the performance analysis of our proposed approach with a discussion. Finally, Section VI concludes the paper.

## II. I-V CHARACTERISTIC OF LED USING TAYLOR SERIES

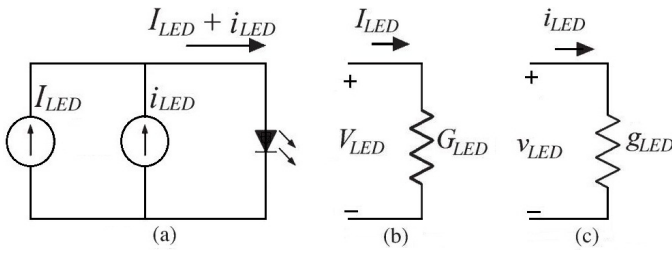


Fig. 1. (a) A DC current source and a low frequency current source with LED, (b) DC, and (c) low frequency equivalent circuits

Taylor series explains the nonlinear I-V characteristics of LEDs [13]. Moreover, current and conductance of both AC and DC domain is calculating from the same series:

$$i_{LED} = I_{Sat} \left( \sum_{n=1}^{\infty} \frac{\left( \frac{q \cdot v_{LED}}{k \cdot T} \right)^n}{n!} \right) \quad (1)$$

where,

$v_{LED}$  LED terminal voltage;

$i_{LED}$  forward current;

$I_{Sat}$  LEDs saturation current;

$q$  electron charge magnitude ( $= 1.602 \times 10^{-19}$ );

$k$  Boltzmann's constant ( $= 1.38 \times 10^{-23}$ );

$T$  absolute temperature ( $= 273 + T_a$ );

Fig. 1(a) represents a DC current source,  $I_{LED}$  and a low frequency current source,  $i_{LED}$  connected to a LED. Therefore, (1) can be expressed regarding DC and AC components, as shown in (2).

$$I_{LED} + i_{LED} = I_{Sat} \left( e^{\frac{V_{LED} + v_{LED}}{V_T}} \right) \quad (2)$$

where,  $V_T = \frac{k \cdot T}{q}$

Therefore, the Taylor series can be expressed as follows:

$$I_{LED} + i_{LED} = I_{Sat} \left( \sum_{n=1}^{\infty} \frac{\left( \frac{V_{LED}}{V_T} \right)^n}{n!} \right) \left( 1 + \frac{v_{LED}}{V_T} + \frac{(v_{LED})^2}{2 \cdot V_T^2} \right) \quad (3)$$

By neglecting the term  $(v_{LED})^2$  above equation can be written as the dc and low frequency components which is shown in (4)

$$I_{LED} + i_{LED} = I_{Sat} \left( \sum_{n=1}^{\infty} \frac{\left( \frac{V_{LED}}{V_T} \right)^n}{n!} \right) + \frac{I_{Sat} * v_{LED}}{V_T} \left( \sum_{n=1}^{\infty} \frac{\left( \frac{V_{LED}}{V_T} \right)^n}{n!} \right) \quad (4)$$

The equivalent dc conductance  $G_{LED}$  of the Fig. 1(b), can be calculated from:

$$G_{LED} = \frac{I_{LED}}{V_{LED}} = \frac{I_{Sat}}{V_{LED}} \left( \sum_{n=1}^5 \frac{\left( \frac{q \cdot V_{LED}}{k(273 + T_a)} \right)^n}{n!} \right) \quad (5)$$

where,  $T_a$  is the ambient temperature. The equivalent small-signal conductance,  $g_{LED}$  of the low frequency equivalent circuit in Fig. 1(c), can be calculated from (6)

$$g_{LED} = \frac{i_{LED}}{v_{LED}} = \frac{q \cdot I_{Sat}}{k(273 + T_a)} \left( \sum_{n=1}^5 \frac{\left( \frac{q \cdot V_{LED}}{k(273 + T_a)} \right)^n}{n!} \right) \quad (6)$$

## III. PROPOSED MODEL

The proposed model of the universal driver circuit for LED lamp is shown in Fig. 2. Tripping of relay 01 (DPDT in Fig. 3) depends on the types of the power source (AC or DC source). Table 1 shows supply voltage ranges of AC & DC supply for the proposed model.

TABLE I  
SPECIFICATION OF PROTOTYPE

Specification	Values
AC Supply	
Input Voltage	180 ~ 240V
Input Line Frequency	50Hz
DC Supply	
Input Voltage	12V ~ 15V

From Fig. 2, if the supply power is AC, then DPDT relay is tripped, AC pass through path 02 (from Fig. 3) and provides required voltage to the current regulator (LM317) after it rectifies to DC. In contrast, if the supply power is DC, then DPDT relay is not tripped, and DC drives the current regulator through path 01 (from Fig. 3). An inductor & relay 02 (SPDT in Fig. 3) is used in path 01 after the DPDT relay to mitigate the effect of voltage spikes on the performance.

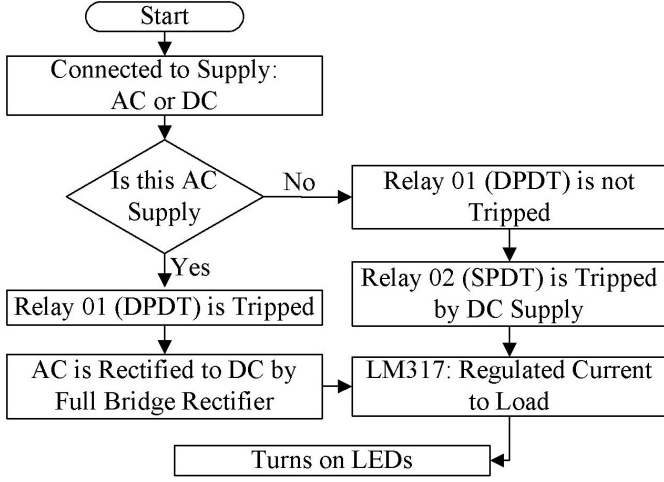


Fig. 2. Flow diagram of universal driver circuit for LEDs.

#### IV. PRACTICAL IMPLEMENTATION

##### A. Delivering constant current to the load

From Table 2, a 3-terminal positive voltage regulator (LM317) is supplying more than 1.5A over a range of output voltage (approximately 1.2V to 37V). By connecting a fixed resistor between the adjustable and output pins, the LM317 has used as a precision current regulator, can be calculated from  $R_{Adj} = \frac{V_{ref}}{I}$ . The regulator gets constant output voltage from a zener diode which is connected in parallel. The zener diode protects the regulator from the ripple of the supply voltage or the load current variation till its current drops below the reverse breakdown region.

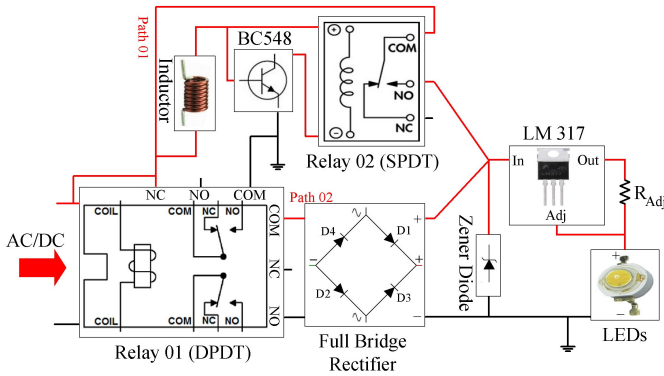


Fig. 3 Block diagram of universal driver circuit.

##### B. Working methodology of universal part

Initially, DPDT relay is starting its work function by input power. It has two rows of change over terminals, and each row has four terminals. Out of these two are the control coil terminals which surround an iron core. The power supply energizes the electromagnet. In a row, the 'Common (COM)' terminal connects with the 'Normally Closed (NC)' terminal and similar construction are in another row. There is another

TABLE II  
BASIC CIRCUIT PARAMETER

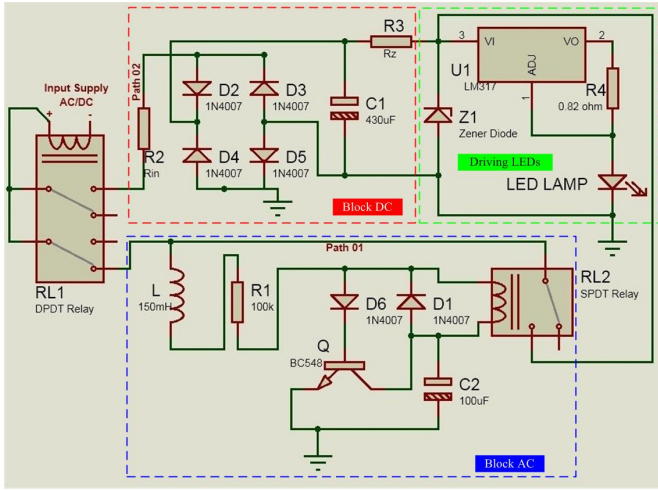
Component	Value
White LED	3.2V, 300mA, 1W
Diode (D1-D5)	600V/0.5A
Zener Diode (1N4744A)	15V
Reservoir Cap	330 $\mu$ F, 400V
Inductor	150mH
Transistor (BC548)	$V_{EBO} : 5V, I_C : 100mA$
Current Regulator (LM317)	$V_o : 1.2 \sim 37V, I_o > 1.5A$
Relay 01 (DPDT)	$V_{in} \leq 240V, I_{in} \leq 10A$
Relay 02 (SPDT)	$V_{in} \leq 12 \sim 28V, I_{in} \leq 15A$

terminal named the 'Normally Open (NO)' in each row. Fig. 3 shows that two paths are starting from two terminals of the relay where path 01 allows DC power but isolate AC power and path 02 acts in opposite way of path 01 to both power domains. Path 01 is connecting in between 'COM' and 'NC' terminals of DPDT relay to isolate AC and path 02 is connecting in between 'COM' and 'NO' terminals of DPDT relay to separate DC.

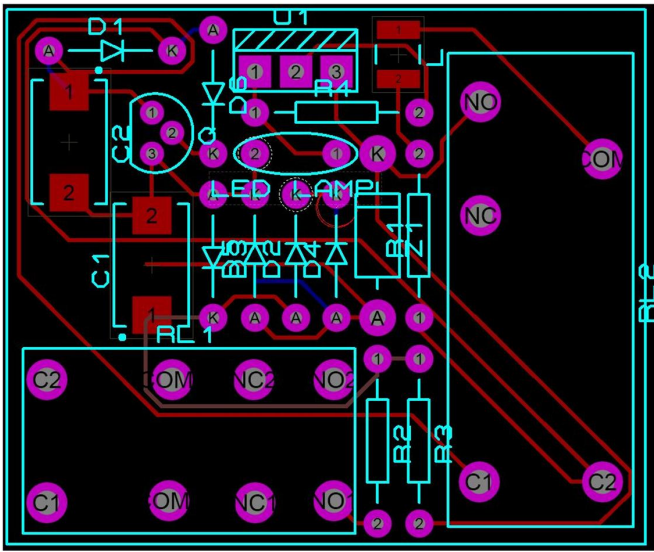
*Isolate AC power:* When rated AC energize control coil, 'COM' terminal starts to be attracted to 'NO' terminal. So the chance of passing AC power through path 01 is zero. An inductor and later a switching transistor (BC548) to switch SPDT relay are placed in path 01 which will mitigate any chance of voltage spikes pass through it. A chance of DPDT relay switching is zero due to chosen voltage range for DC operation (12V to 15V) is lower than rated voltage range of DPDT. To understand the performance of inductor in AC power supply, consider the equation of inductive reactance:  $X_L = 2\pi fL$ . Where  $f$  is the frequency in Hertz and  $L$  is the inductance in Henries. Reactance will increase if frequency or inductance increase. Therefore inductance shows impedance in AC power supply and short in DC power supply. An NPN transistor (BC548) is connected in series with the inductor which rating is shown in Table 2. Transistor switch SPDT relay and control coil of SPDT is energized. 'COM' terminal starts to be attracted to 'NO' terminal and though the load is connected to the 'NO' terminal of the relay; power flows to the load.

*Isolate DC power:* The chosen range of DC power supply is not enough to energize the control coil compare with AC. AC is carried by path 02 to the full bridge rectifier through 'NO' terminal of DPDT relay. The full-wave bridge serves to convert single phase AC input into a DC output; supplies an output of pulsed DC. A capacitor, known as a reservoir (or smoothing) capacitor is added to lessen the variation in the rectified AC output voltage waveform from the bridge. This ripple free pure DC is then deployed to the load.

Schematic diagram and PCB layout of our proposed universal driver circuit for led lamp are shown in Fig. 4(a) and 4(b) respectively. The voltage regulator IC LM317 is attached to



(a)



(b)

Fig. 4. (a) schematic diagram, (b) printed circuit board (PCB) layout of universal driver circuit for LED lamp

a heat sink. It can help the regulator to radiate the heat from its surface. A diode is connected to the SPDT relay to protect the switching transistor from the instantaneous current of the relay coil, and the task is done the diode by providing a path for that current when the coil is switched off.

## V. RESULT AND DISCUSSION

### A. Performance Analysis

From Table 3, input current ( $I_{in}$ ) is increased with the increasing demand of load current ( $I_L$ ), but load voltage ( $V_L$ ) is not varying throughout the whole performance.  $R_{in}$  is the resistor connected in series with the full bridge rectifier. The chosen value of zener diode voltage ( $V_Z$ ) is fixed throughout the whole operation and a resistor  $R_Z$  is connected before zener diode which is also varying with the load. Power factor is decreased with the increase of load, but it is still near to the

unity up to 30W load. Another diode is connected with the transistor (BC548) in series to discard the half cycle of AC voltage spikes.

TABLE III  
PERFORMANCE EVALUATION DATA

Load (W)	$R_{in}$ ( $\Omega$ )	$R_Z$ ( $\Omega$ )	$C_1$ ( $\mu F/V$ )	$I_{in}$ (A)	$V_Z$ (V)	$V_L$ (V)	$I_L$ (A)	pf
3	470	220	100/400	0.35	15	9.6	0.3	0.998
6	240	100	100/400	0.7	15	9.6	0.6	0.998
9	150	68	330/400	1.1	15	9.6	0.9	0.998
12	130	56	330/400	1.3	15	9.6	1.2	0.996
15	100	47	330/400	1.6	15	9.6	1.5	0.995
18	91	36	330/400	1.9	15	9.6	1.8	0.993
21	75	33	430/400	2.2	15	9.6	2.1	0.993
24	68	27	430/400	2.5	15	9.6	2.4	0.993
27	62	22	430/400	2.8	15	9.6	2.7	0.993
30	51	24	430/400	3.15	15	9.6	3.0	0.991

From the performance curve of Fig. 5 shows that drive deliver constant current to the lighter load from a wide range of input voltage (180V to 240V) in AC and the performance is deteriorated for a higher load. Another important thing is after 210V supply the driver shows fixed performance for all types of load used in the experiment in AC power supply.

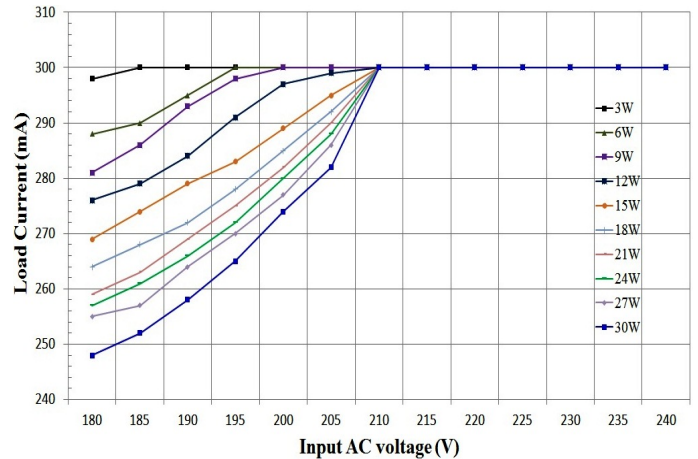


Fig. 5 Input AC voltage versus load current for 3W to 30W load

TABLE IV  
DATA FOR SINGLE LM317 (3W TO 15W LOAD)

$V_{in}$ (V)	Load	$R_{Adj}$ ( $\Omega$ )	$V_{Adj}$ (V)	$V_L$ (V)	$I_L$ (A)
15	3W	3.9	1.2	9.6	0.3
15	6W	2.0	1.2	9.6	0.6
15	9W	1.3	1.2	9.6	0.9
15	12W	1.0	1.2	9.6	1.2
15	15W	0.82	1.2	9.6	1.5

From Table 4, by adjusting the value of  $R_{Adj}$ , it is possible to increase or decrease load. Here,  $V_{Adj}$  is the voltage across  $R_{Adj}$ . Single current regulator (LM317) can handle 3 to 15 LEDs at a time. There should implement at least two regulators to handle 30 LEDs. This adjustment is applicable for both AC and DC power supply.

## B. Cost Analysis

One of the important issues of this paper is to focus on a driver circuit for led which is universal, efficient and profitable. The components which are used in the led driver circuit is very cheap but effective. The overall cost for the 30W load of the implemented driver circuit is around \$1.5 (including the price of 30 LEDs, power rating of each and every LED is 1W), where the price of the DPDT relay is higher than the other components (near about \$0.25). This cost is calculating from 30W LED lamp. On the contrary, the price of the open driver circuit in the market or online shop is much higher than the proposed driver circuit in this paper. As an illustration, the amount of available driver circuit is varying from \$10 to \$15 for around 30W load [14], [15]. On the other hand, availability of the required components for the proposed driver circuit made it more convenient than other driver circuits.

## VI. CONCLUSION

A low-cost universal driver circuit for high power LED lamp is proposed, designed, and constructed. In this study created driver circuit drives 3 to 30 LEDs. The experimental values show that this driver circuit can provide constant current with a broad range of input voltage in AC or DC. Using less inductive component keeps power factor of the driver circuit leading. The self-power consumption of the circuit is about 4%. Moreover, the open driver circuit is working either in AC power domain or DC power domain. Thither the universality of this driver circuit allows a user to connect the lighting load with either DC or AC power supply without any hassle. Therefore the proposed design will remove the conventional circuit design barrier for not the LED driver but also the other available loads.

## REFERENCES

- [1] Z. Ye, F. Greenfeld and Z. Liang, "Design considerations of a high power factor SEPIC converter for high brightness white LED lighting applications," 2008 IEEE Power Electronics Specialists Conference, Rhodes, pp. 2657-2663, 2008.
- [2] C. Y. Wu, T. F. Wu, J. R. Tsai, Y. M. Chen and C. C. Chen, "Multistring LED Backlight Driving System for LCD Panels With Color Sequential Display and Area Control," *IEEE Transactions on Industrial Electronics*, vol. 55, no. 10, pp. 3791-3800, Oct. 2008.
- [3] A. Islam, M. A. Hossain, T. Nguyen, and Y. M. Jang, "High Temporal-Spatial Resolution Optical Wireless Communication Technique using Image Sensor," IEEE International Conference on Information and Communications Technology Convergence 2016, Oct. 2016. [Accepted]
- [4] M. A. Hossain, A. Islam, N. T. Le, H. Lee, Y. T. Lee, and Y. M. Jang, "Performance Analysis of Smart Digital Signage System Based on software-defined IoT and Invisible Image Sensor Communication," *International Journal of Distributed Sensor Networks*, vol. 12, no. 7, pp. 1-14, Jul. 2016.
- [5] Dallas, Charge pump and step up DC-DC converter solutions for powering white LEDs in series or parallel connections. USA: Maxim Integrated Products, <http://www.maximic.com>, 2002.
- [6] J. A. Villarejo, J. Sebastian, F. Soto, and E. de Jodar, "Optimizing the Design of Single-Stage Power-Factor Correctors," *IEEE Transactions on Industrial Electronics*, vol. 54, no. 3, pp. 1472-1482, June 2007.
- [7] X. Qu, S. C. Wong, and C. K. Tse, "Resonance-Assisted Buck Converter for Offline Driving of Power LED Replacement Lamps," *IEEE Transactions on Power Electronics*, vol. 26, no. 2, pp. 532-540, Feb. 2011.

- [8] C. Zhao, X. Xie, and S. Liu, "A simple precise capacitive current balancing method for the multi-output LED drivers," 2012 IEEE Energy Conversion Congress and Exposition (ECCE), Raleigh, NC, pp. 3257-3263, 2012.
- [9] M. Doshi and R. Zane, "Digital Architecture for Driving Large LED Arrays with Dynamic Bus Voltage Regulation and Phase Shifted PWM," APEC 07 - Twenty-Second Annual IEEE Applied Power Electronics Conference and Exposition, Anaheim, CA, USA, pp. 287-293, 2007.
- [10] C. C. Chen, C. Y. Wu, Y. M. Chen, and T. F. Wu, "Sequential Color LED Backlight Driving System for LCD Panels," *IEEE Transactions on Power Electronics*, vol. 22, no. 3, pp. 919-925, May 2007.
- [11] I. Abbasi and N. Z. Yahaya, "Development of Universal LED Driver for Low Power Application," 2014 8th Asia Modelling Symposium, Taipei, pp. 229-234, 2014.
- [12] M. Miskin, J.N. Anderson, "AC light emitting diode and AC LED drive methods and apparatus," U.S. PAT. No. 20070273299.
- [13] R. L. Lin, Y. C. Chang, and C. C. Lee, "Optimal Design of LED Array for Single-Loop CCM Buck-Boost LED Driver," *IEEE Transactions on Industry Applications*, vol. 49, no. 2, pp. 761-768, March-April 2013.
- [14] "Products." Techshop Bangladesh. Available: [Online]. <https://www.techshopbd.com/>
- [15] "LED Driver from India." indiamart. Available: [Online]. <http://dir.indiamart.com/impcat/led-driver.html>

# Design Evolution of Planar Slot Antennas for Ultra-wideband Wireless Communication

Rezaul Azim

Department of Physics  
University of Chittagong, Chittagong 4331, Bangladesh  
razim71@gmail.com

Mohammad Tariquul Islam

Dept. of Electrical, Electronic and Systems Engineering  
Universiti Kebangsaan Malaysia, 43600 Bangi, Malaysia  
tariquul@ukm.edu.my

**Abstract**—The design evolution of planar ultra-wideband slot antennas is presented in this paper. The basic antenna with a T-shaped radiator and ground plane with wide slot is able to exhibit UWB characteristics. Insertion of a curve slit in the front side of the basic antenna helps to generate a stop band at around 3.5GHz while etching of a pair of symmetric slits in the rear side helps to produce a stop band for WLAN. Dual stop band centered at 3.5GHz and 5.5GHz can be obtained by putting both types of slits together. The insertion of slits does not alter the size and shape of basic antenna which gives us an upper hand in the designing of UWB antenna with notch band/s.

**Keywords**—Antenna; ultra-wideband(UWB); wireless communication; WiMAX; WLAN.

## I. INTRODUCTION

Ultra-wideband (UWB), being a communication technology with distinctive characteristics is widely used in numerous wireless communication. The effectiveness of this technology is completely depends upon the performance of antenna, a vital component of any communication system. A suitable UWB antenna must have to an operating frequency band ranges from 3.1 - 10.6 GHz. At the same time UWB antenna have to have the capability to filter out narrow bands of WiMAX and WLAN.

Good number of antennas with UWB operating band are reported in open literature. When compared with other types of antennas, slot antennas possesses large magnetic field and appropriate for UWB communications where minimum near field coupling is necessary [1]. Recently, different UWB slots antennas with narrow and wide slot are reported. Different methods are employed to achieve UWB impedance bandwidth.

Despite of FCC allocation, UWB (3.1-10.6GHz) may electromagnetically interfere with WiMAX (3.3 - 3.8GHz) and WLAN (5.15 - 5.825GHz) which may degrade the system performance. Therefore it is necessary to notch these narrow bands within UWB. Different techniques are already employed to design band notch UWB antennas. Insertion of different shapes of slot/s in the patch or in the ground plane is commonly used to generate notch band/s. For example to produce two notch bands for WiMAX and WLAN, in [2] a concentric partial annular slot and a semi-circular slot were inserted in the ring shaped radiator. To notch a frequency band centered at 5.5GHz, a partial annular slot was embedded in the design reported in [3]. Another technique of notch is to use

different types of slit/s along with patch or ground plane. For example, to notch dual frequency band centered at 3.5GHz and 5.5GHz a single tri-arm parasitic element was etched beneath the patch [4]. In [5], a pair of U-shaped strip was inserted in the radiator to produce two notch bands. The design proposed in [6] use three parasitic strips above the ground to produce triple stop bands for WiMAX, lower and upper WLAN. Defection of ground plane is also observed to produce stop band/s. For example in [7] three notches centered at 3.5, 5.68 and 7.48GHz were achieved by defected ground structure and fork-shaped stub. In [8] two pairs of meandered ground stubs were used to notch lower and upper WLAN band. To filter out undesired frequency spectrum, some reported design uses complex filter element/s which may create fabrication difficulties.

In this paper the design evolution of UWB slot antennas without and with band notch characteristics is presented. The basic design comprises a T-shaped patch and a wide slotted ground plane, and is able to exhibits UWB characteristics. To generate a notch band for WiMAX, a curve slit is placed in the front side while to generate a stop band for WLAN a pair of slits is etched in the rear side. Insertion of both these types of slits together can produce dual notch bands at around 3.5GHz and 5.5GHz and can effectively suppress the interference between WiMAX, WLAN and UWB systems.

## II. ANTENNA LAYOUT

### A. Basic slot antenna with UWB operating band

The layout of the basic wideband slot antenna is displayed in Fig. 1(a). It consists of a T-shaped radiating stub and a ground plane, and is etched on the both sides of an inexpensive standard epoxy resin reinforced woven glass substrate of 1.6mm thick. The relative permittivity of the substrate material is 4.6 and its loss tangent is 0.02. The radiating stub has a dimension of  $13 \times 7 \text{ mm}^2$  and for signal transmission it is fed by a microstrip feed line of  $50\Omega$  characteristic impedance. The antenna occupies a very small area of  $22 \times 24 \text{ mm}^2$ .

It is found using method of moment based full wave EM simulator IE3D that T-shaped radiating stub coupled strongly with the ground plane with tapered slot and a tapered-shape slot matched with a T-shaped tuning stub can exhibit an impedance bandwidth ( $S_{11} \leq -10\text{dB}$ ) of 2.97 to 10.77 GHz as shown in Fig. 2. This achieved band covers the entire UWB frequency spectrum and that is why the designed antenna is very suitable for ubiquitous UWB wireless communication.

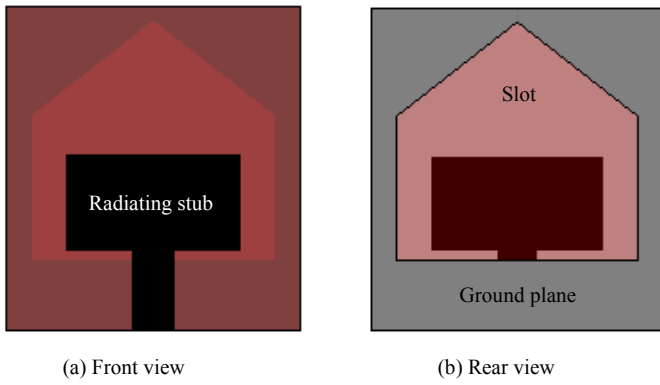


Fig. 1. Design layout of the basic UWB slot antenna.

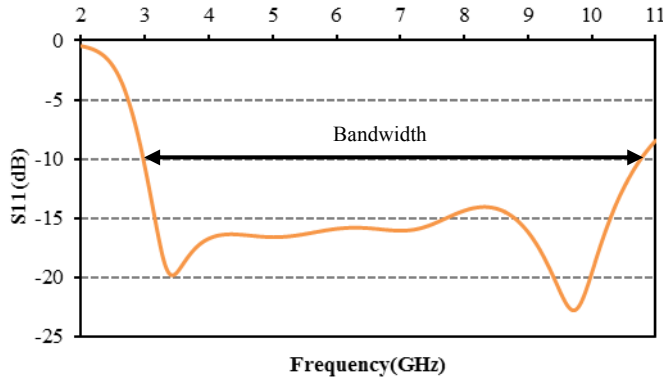


Fig. 2. Performance of the basic UWB slot antenna.

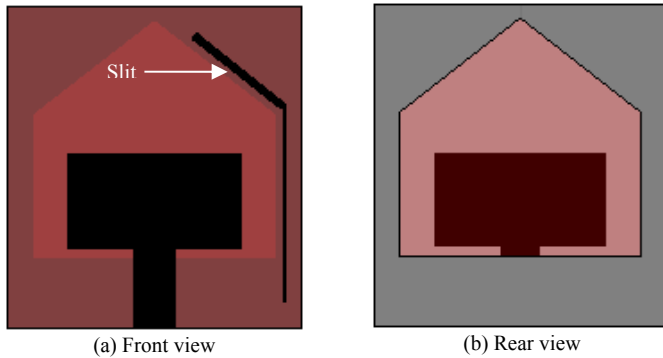


Fig. 3. Geometry of the antenna with notch band for WiMAX.

### B. UWB antenna with notch band for WiMAX

In order to lessen the electromagnetic interference (EMI) between WiMAX and UWB, it is necessary to notch the frequency band of 3.3 - 3.8GHz. To generate a notch band at 3.5GHz, a slit has symmetrically been placed in the front side of the substrate as shown in Fig. 3. Other than the inclusion of this slit, all other parameters are as same as the basic design of Fig. 1.

The etched slit strongly couple with the radiating stub which leads to high impedance at around 3.5GHz. At the notch frequency band, the current concentrates strongly at around the slit. The flows of current in the slit are oppositely

directed to the radiator and ground structure as depicted in Fig. 4. Thus, the overall radiation fields canceled out each other. Therefore at 3.5GHz, the antenna with a slit (filter element) does not radiate effectively resulting in generation of a notch band ranging from 3.27 - 3.83GHz as displayed in Fig. 5.

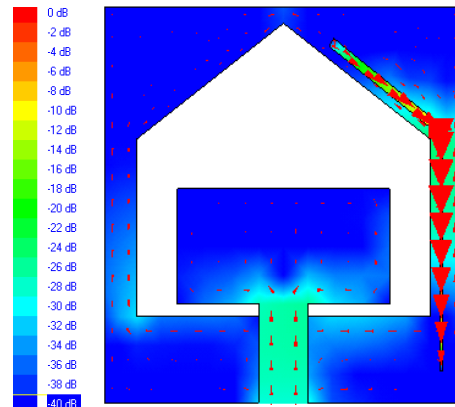


Fig. 4. Current distribution on the radiator and ground plane at 3.5GHz.

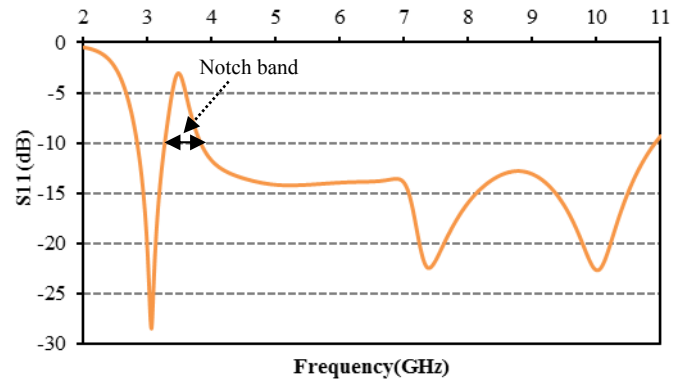


Fig. 5. S-parameter of the antenna with notch band for WiMAX.

### C. UWB antenna with notch band for WLAN

To create a notch band with an aim to eliminate the EMI between UWB and WLAN, a pair of parasitic slits has been inserted in the ground plane (rear side) as shown in Fig. 6. This slits are symmetrical to the inner edges of the tapered slot and placed in the rear side of the substrate.

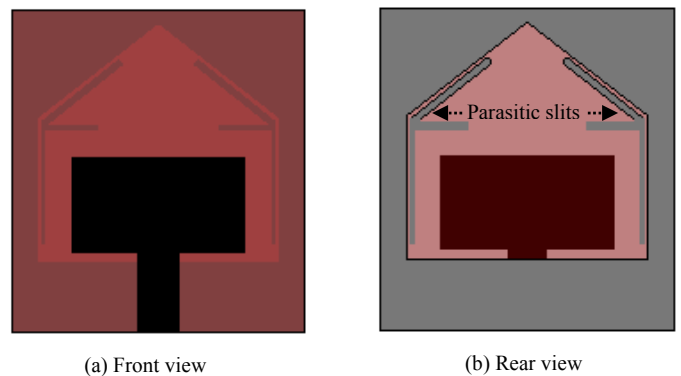


Fig. 6. Layout of the antenna with notch band for WLAN.

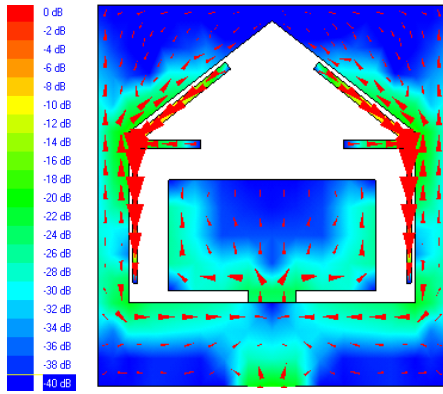


Fig. 7. Current distribution in the ground plane and radiator at 5.5GHz.

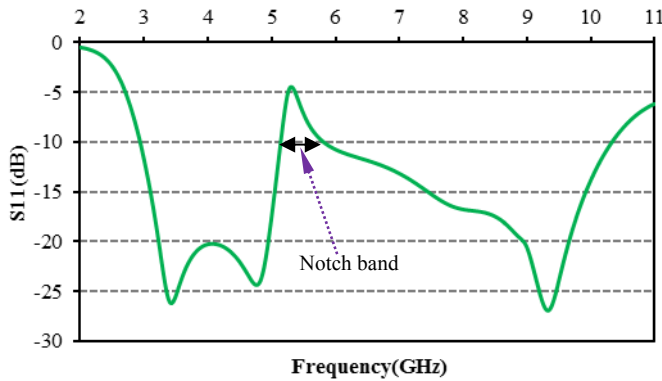


Fig. 8. S-parameter of the antenna with notch band for WLAN.

To understand the phenomenon of the creation of the notch band at around 5.5GHz, the surface current on the radiator and ground is shown in Fig. 7. It is observed from the plot that the current concentration around the parasitic slits is higher than the current on the other parts of the antenna. It is also seen that the current in the parasitic slits are oppositely directed to the currents in the ground plane and radiator. Thus the resultant radiation at around 5.5GHz is very weak and a notch band covering frequency band of 5.14 - 5.81GHz is produced as shown in Fig. 8. Except the exhibition of notch band characteristics, the operating bandwidth of this design is almost similar to that of basic UWB antenna.

#### D. UWB antenna with dual notch band for WiMAX and WLAN

The geometry of the UWB antenna with two notch band is depicted in Fig. 9. The antenna structure is similar to the design presented in Fig. 1. To filter out WiMAX band, a curve parasitic slit is placed in the front side of the antenna along with the radiator as shown in Fig. 9(a). To generate another notch band for WLAN, a pair of slits is symmetrically etched on the rear side of the antenna as depicted in Fig. 9(b).

From the simulated vector current distribution it can be revealed that at 3.5GHz, the currents are strongly concentrated around the slit that has been etched in the front side of the antenna whereas at 5.5GHz, the currents are stronger near the slits that are placed in the rear side of the

antenna. At both these frequencies, the directions of the currents in the slits are opposite to the currents in the radiator and ground plane. As a result, the effective radiation fields eliminate each other and dual notch bands at around 3.5GHz and 5.5GHz are produced as displayed in Fig. 10.

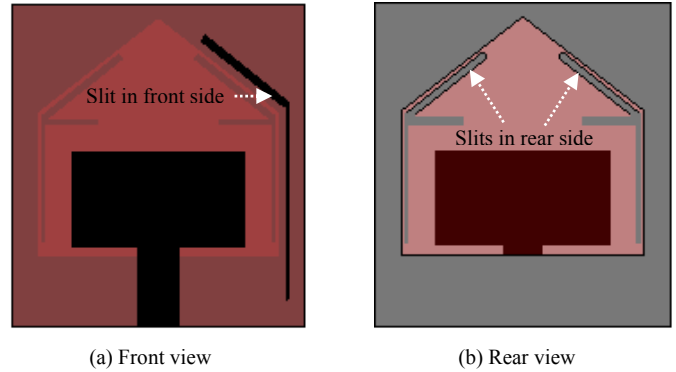


Fig. 9. Geometry of the antenna with dual notch band.

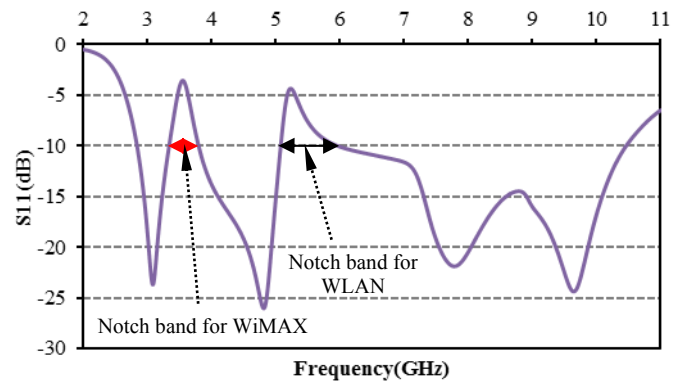


Fig. 10.  $S_{11}$  of the antenna with dual notch band for WiMAX and WLAN.

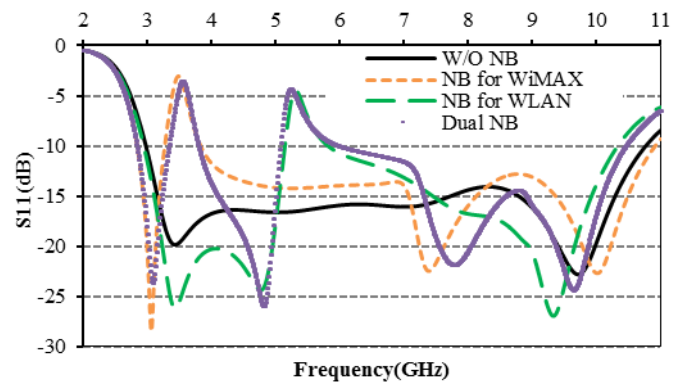


Fig. 11. S-parameter responses of the designed antennas.

### III. COMPARISON OF THE PERFORMANCE OF DESIGN ANTENNAS

The performances of the designed antennas are plotted in Fig. 11. It can be revealed that without any slit (W/O NB), the basic slot antenna achieved an operating band ( $S_{11} \leq -10$ dB) of 2.97 to 10.77GHz which can cover the entire UWB. The insertion of a curved slit in the front side of the basic antenna produces a notch band of 3.27 - 3.83GHz while the etching of



a pair of slits in the rear side notched a band ranging from 5.14 - 5.81GHz. By adding these two types of slits in the front and rear sides, dual notch bands centered at 3.5GHz and 5.5GHz can be created. Despite the inclusion of parasitic slits, the overall dimension of the basic antenna is remaining same.

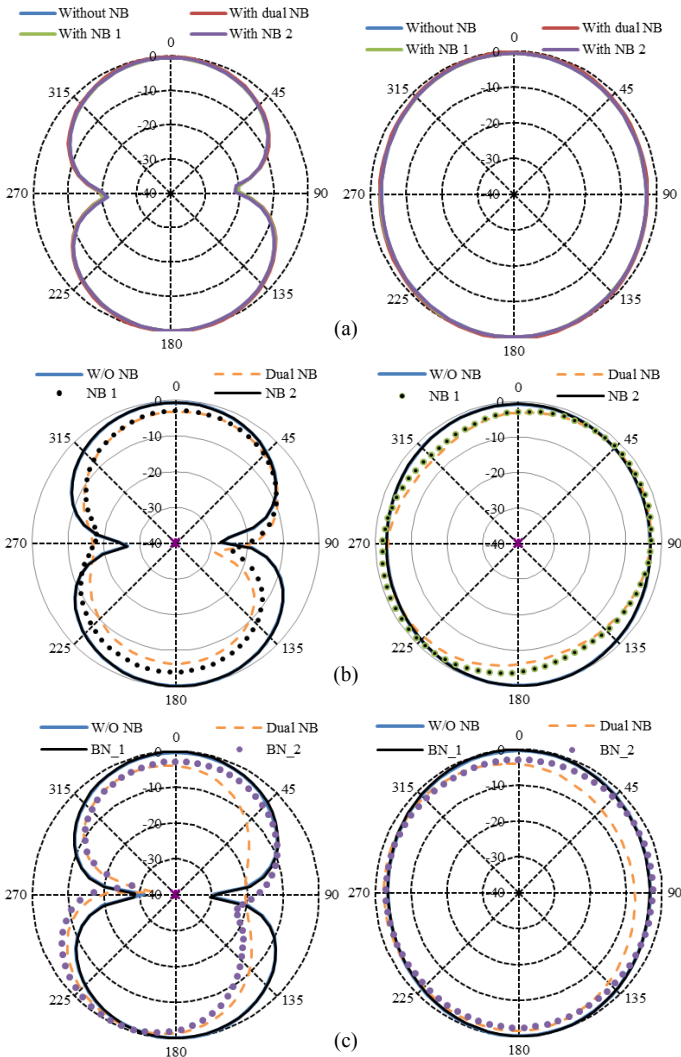


Fig. 12. Radiation patterns at (a) 3GHz, (b) 3.5GHz and (c) 5.5GHz.

The radiation patterns plotted in Fig. 12 shows that at passband frequency of 3GHz, the  $E$ -field pattern is similar to “8” shape while the  $H$ -field pattern is omnidirectional as in Fig. 12(a). It remarkable to mention that at pass band frequency of 3GHz, the gain for all the antennas are almost same. At notch frequencies of 3.5GHz and 5.5GHz, the radiation patterns are similar to that of passband frequencies as shown in Fig. 12(b) and 12(c). However, there is decrement in the gain for the antenna with slit/s i.e. inclusion of slit/s decreases the gain by filtering the desired portion of the signal.

The peak gain the designed antennas is plotted in Fig. 13 from where it can be commented that all the antennas achieved good gain. Without the exhibition of sharp decrement in the respective notch band, the peak gain of all the antennas almost similar. However, at frequencies more than 9GHz, there is fall of the gain and gain of the basic

antenna (W/O NB) is much lower than that of antennas with parasitic slit/s. This may be due to fact at higher frequencies the parasitic slit/s act as a radiator as explained in [9].

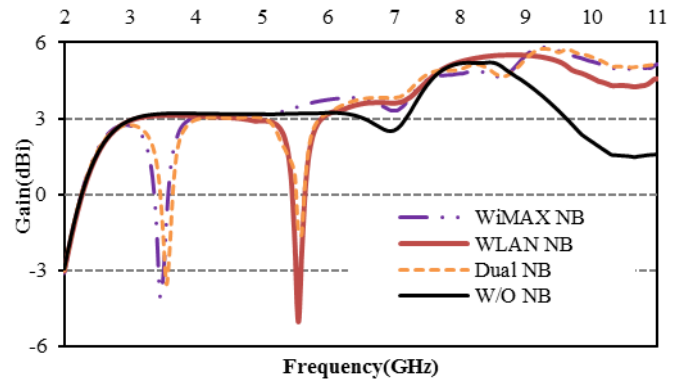


Fig. 13. Peak gain of the designed antennas.

#### IV. CONCLUSION

In this paper small size slot antennas are proposed for UWB applications. The ways to create notch band/s without sacrificing the UWB performance and without altering the size of the basic antenna are presented. It is demonstrated that a curve parasitic slit in the front side of basic antenna can produce a notch band for WiMAX while insertion of a pair of symmetrical slits in the rear side can notch WLAN band. The design with these two types of slits can exhibits UWB characteristics with dual notch bands at 3.5GHz and 5.5GHz.

#### REFERENCES

- [1] H. G. Schantz, “UWB Magnetic Antennas,” in *Proc. of the IEEE Antennas Prop. Soc. Int. Symp.*, 22 - 27 June 2003, USA, pp. 604 - 607.
- [2] R. Azim, M. T. Islam, J. S. Mandeep, and A. T. Mobashsher, “A planar circular ring ultra-wideband antenna with dual band-notched characteristics,” *J. Electromagnet. Wave.*, vol. 26, nos. 14 - 15, pp. 2022 - 2032, 2012.
- [3] R. Azim and M. T. Islam, “Compact planar UWB antenna with band notch characteristics for WLAN and DSRC,” *Prog. Electromagn. Res.*, vol. 133, pp. 391 - 406, 2013.
- [4] R. Azim, M. T. Islam, and A. T. Mobashsher, “Dual band-notch UWB antenna with single tri-arm resonator,” *IEEE Antennas Wirel. Propag. Lett.*, vol. 13, pp. 670 - 673, 2014.
- [5] M. Ojaroudi, N. Ojaroudi, and N. Ghadimi, “Dual band-notched small monopole antenna with novel coupled inverted U-ring strip and novel fork-shaped slit for UWB applications,” *IEEE Antennas Wirel. Propag. Lett.*, vol. 12, pp. 182 - 185, 2013.
- [6] M. T. Islam, R. Azim and A. T. Mobashsher, “Triple band-notched planar UWB antenna using parasitic strips,” *Prog. Electromagn. Res.*, vol. 129, pp. 161 - 179, 2012.
- [7] C. Zhang, J. Zhang, and L. Li, “Triple band-notched UWB antenna based on SIR-DGS and fork-shaped stubs,” *Electron. Lett.*, vol. 50, no. 2, pp. 67 - 69, 2014.
- [8] Y. F. Weng, W. J. Lu, S. W. Cheung, and T. I. Yuk, “UWB antenna with single or dual band-notched characteristic for WLAN band using meandered ground stubs,” in *Proc. of the Loughborough Antennas Prop. Conf.*, 16 - 17 November 2009, Loughborough, UK, pp. 557 - 560.
- [9] R. Azim, M. T. Islam, and A. T. Mobashsher, “Design of a dual band-notch UWB slot antenna by means of simple parasitic slits,” *IEEE Antennas and Wireless Propagation Letters*, vol. 12, pp. 1412-1415, 2013.

# Design and implementation of a digital calling bell with door lock security system using fingerprint.

<sup>1</sup>M.A. Kader, <sup>2</sup>Md. Yousuf Haider, <sup>3</sup>Md.Rezaul Karim, <sup>4</sup>Md. Saiful Islam, <sup>5</sup>Mohammad Mamun Uddin

<sup>1</sup>Assistant Professor, <sup>2-5</sup>Student, Dept. of EEE

International Islamic University Chittagong (IIUC), Chittagong, Bangladesh

kader05cuet@gmail.com, yousufhaider7@gmail.com, ssuton71@gmail.com, si.iiuc@yahoo.com, eee.mamunctg@gmail.com

**Abstract**—The term ‘Home Security’ numerously growing as a major concerning issue in today’s life. The challenge of developing a home security device is to make it user friendly which can reduce human effort as well as ensure safety and security of people and their home. In this paper, a security device is proposed which is developed from the concept of conventional calling bell. The device analyzes the fingerprint of a person and matches it with stored fingerprint database to categorize the person as home member or known guest or unknown guest. When it detects a home member the entrance door automatically opens. In case, the person categorize as known guest, the device sounds a tune but don’t open the door automatically rather people inside home can open the entrance door from anywhere of the home. As guest is known people don’t need to walk towards door to open it. And when device detects the person as unknown guest, it generates a tunes which is different from previous one making aware the people inside that an unknown person wish to enter your home.

**Keywords**— *Fingerprint module, Arduino Uno; microcontroller; wireless control; RF Tx-Rx; UART.*

## I. INTRODUCTION

In rapidly developing technological world, people are searching devices to ensure security and convenience in their home. Considering the increasing demand researchers are trying to develop security devices for smart home with more intelligence and convenience to user. Devices are developed from different perspective based on application. Some security devices are concerned about the entrance of unauthorized person in home [1]-[3], some concern about safety from gas leakage or fire [4] and some are developed based on password or biometric lock at entrance door [5]-[7]. In this paper, a security device is proposed considering the home security and reduction of human effort. The device act as finger print based calling bell and door lock as well as users inside home can open the entrance door from any place of home by a remote controller through this device. The device takes the finger print from a person wish to enter the home by a finger print scanning module. The module match it with finger print data base stored in its memory and categorize the person among any one of three categories indicated as ‘home member’, ‘known guest’ and ‘unknown guest’. Here we define ‘home member’ as regular family member who are staying at home, ‘known guest’ are those relatives or people who frequently visit at home. The finger print of home member and known guest should be stored in the database of fingerprint module. ‘Unknown guest’ are

those people who are rarely visit at home and their finger prints are not stored in database. For a home member the device directly opens the door and generates no sound. When device gets a known guest it does not open the door but generates a sound which indicates the sound of known guest. In this case people inside home should not come towards door to open it as the visitor is known to them. So, they can open the door from any place of home by using a remote. For unknown guest the device doesn’t open the door but generates a sound different from the sound produced for known guest. In this case, people inside home cannot open the door by remote. As the guest is unknown so they have to come towards door and after getting identity they can open the door by pressing a switch beside it. The device reduces human effort in the sense people inside home should not go towards door in most of the time to open the door.

## II. SYSTEM OVERVIEW

The block diagram of the system is shown in ‘Fig. 1’. The fingerprint scanner captures the fingerprint of a person and verifies it. It communicates with microcontroller via universal asynchronous receiver-transmitter (UART) module of microcontroller. After getting verification result from fingerprint module microcontroller takes decision to make sound from any of the buzzers or opening door based on

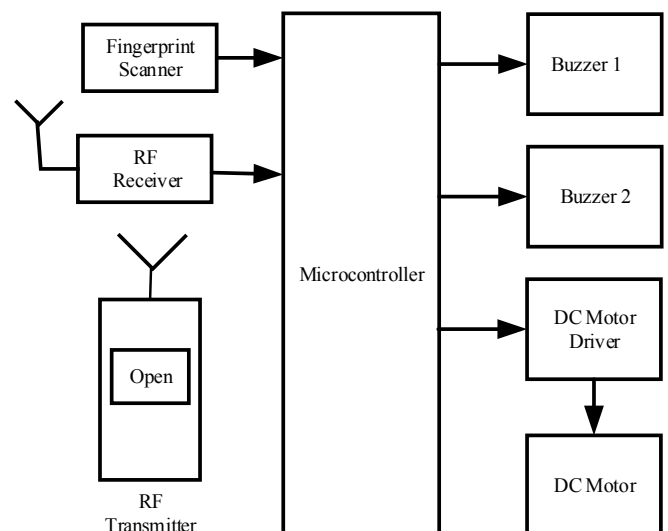


Fig. 1: System block diagram.

person's identity. RF receiver-transmitter pair is used to control entrance door from any place inside home incase finger print module identify a known guest. RF transmitter uses a push buttons to open and close the door.

### III. SYSTEM DESIGN

This section describes the different component used in the system, interfacing the components with microcontroller and circuit diagram of the system.

#### A. Fingerprint Scanner

Fingerprint scanner used here is an optical fingerprint recognition embedded module GT-511C3 developed by ADH technology as shown in "Fig. 2". The module itself does all of the heavy lifting behind reading and identifying the fingerprints with an on-board optical sensor and 32-bit CPU. The module can store up to 200 different fingerprints and is capable of 360° recognition. The device can be operated and configured by sending some simple commands. Some important commands are given in "Table-1". To get started, user can register each fingerprint by sending corresponding commands and pressing finger against the reader three times. The fingerprint scanner can store different fingerprints and the database of prints can even be downloaded from the unit and distributed to other modules. Some key technical specification of fingerprint scanner is given in "Table-2". [8]

TABLE I. SOME IMPORTANT COMMANDS FOR GT-511C3

Number (HEX)	Alias	Description
01	Open	Initialization
02	Close	Termination
22	EnrollStart	Start an enrollment
23	Enroll-1	Make 1 <sup>st</sup> template for an enrollment
24	Enroll-2	Make 2 <sup>nd</sup> template for an enrollment.
25	Enroll-3	Make 3 <sup>rd</sup> template for an enrollment, merge three templates into one template, save merge template to database.
26	IsPressFinger	Check if a finger is placed on the screen.
40	DeleteID	Delete the fingerprint with the specified ID
41	DeleteAll	Delete all fingerprints from the database.
50	Verify	1:1 Verification of the capture fingerprint image with the specified ID.
51	Identify	1:N identification of the capture fingerprint image with the database
52	VerifyTemplate	1:1 Verification of a fingerprint template with the specified ID
61	MakeTemplate	Make template for transmission

TABLE II. TECHNICAL SPECIFICATIONS OF GT-511C3

Item	Value
CPU	ARM Cortex M3 Core
Sensor	Optical Sensor
Effective area of the sensor	14X12.5 (mm)
Image Size	202X258 Pixels
Resolution	450 dpi
The maximum number of fingerprint	200 fingerprints
Matching Mode	1:1, 1:N
The size of template	496 Bytes (template)+ 2 Bytes (checksum)
Communication Interface	UART, default baud rate 9600bps
Identification Time	<1 sec (200 fingerprints)
Enrollment time	<3 sec (3 fingerprints)
Operating Voltage and Current	DC 3.3-6 V and <130 mA



Fig. 2: Fingerprint Scanner - TTL (GT-511C3).

#### B. Universal Asynchronous Receiver-Transmitter (UART)

The finger print scanner has four pins: Vcc, Tx, Rx and Gnd. The module sends data serially through transmit (Tx) pin and receive data or commands serially by receive (Rx) pin. The serial communication used here is asynchronous serial communication. Microcontroller (ATmega328P) used in this project has inbuilt UART module. Microcontroller communicates with fingerprint scanner through this UART module. The UART transmits and receives data using a standard non-return-to-zero (NRZ) format [9].

#### C. RF Transmitter and Receiver Module

The RF module, as the name suggests, operates at Radio Frequency. The digital data is represented as variation in the amplitude of carrier wave which is known as Amplitude Shift Keying (ASK). RF transmitter can transmit digital data through radio frequency carrier wave. RF receiver receives this data mixed with radio frequency carrier wave and separates digital data from it. In this application, RF remote is suitable than IR remote, as RF signal can travel through larger distance than IR

signal and RF signal can travel even when there is an obstruction between transmitter and receiver. Here, the receiver and transmitter pair operates at a frequency of 434 MHz.

#### D. Circuit Diagram

The complete circuit diagram of the system is shown in “Fig. 3”. The circuit consists three parts: Power supply circuit, Transmitter circuit (RF remote controller) and Receiver circuit. The function of power supply circuit is to convert 9V DC voltage into 5V DC. This 5V DC source acts as power source for microcontroller, fingerprint scanner and other components. The transmitter circuit is shown in dotted box in the figure. Transmitter circuit sends 12-bit data to the receiver circuit. These 12 bits are classified into 8 address bits (A0-A7) and 4

data bits (D0-D3). HT12E is an encoder IC used in transmitter which converts 12 bit parallel data inputs into serial outputs. This serial data is provided to TX pin of RF transmitter module. A push button SW1 connected with D0 pin of HT12E. D0 pin is pulled down to ground through a 1K resistor. Normally D0 pin is LOW, but when SW1 is pressed D0 becomes HIGH and this data is send to the receiver circuit. The receiver unit is the main part of this system. It has fingerprint scanner, ATmega328P microcontroller, RF receiver module, buzzers to produce sound and a DC motor to open or close the door. Microcontroller communicates with fingerprint scanner through TX and RX pins. PB5 pin controls the relay which further controls the DC motor. Buzzer-1 and Buzzer-2 are connected with PB3 and PB4 respectively.

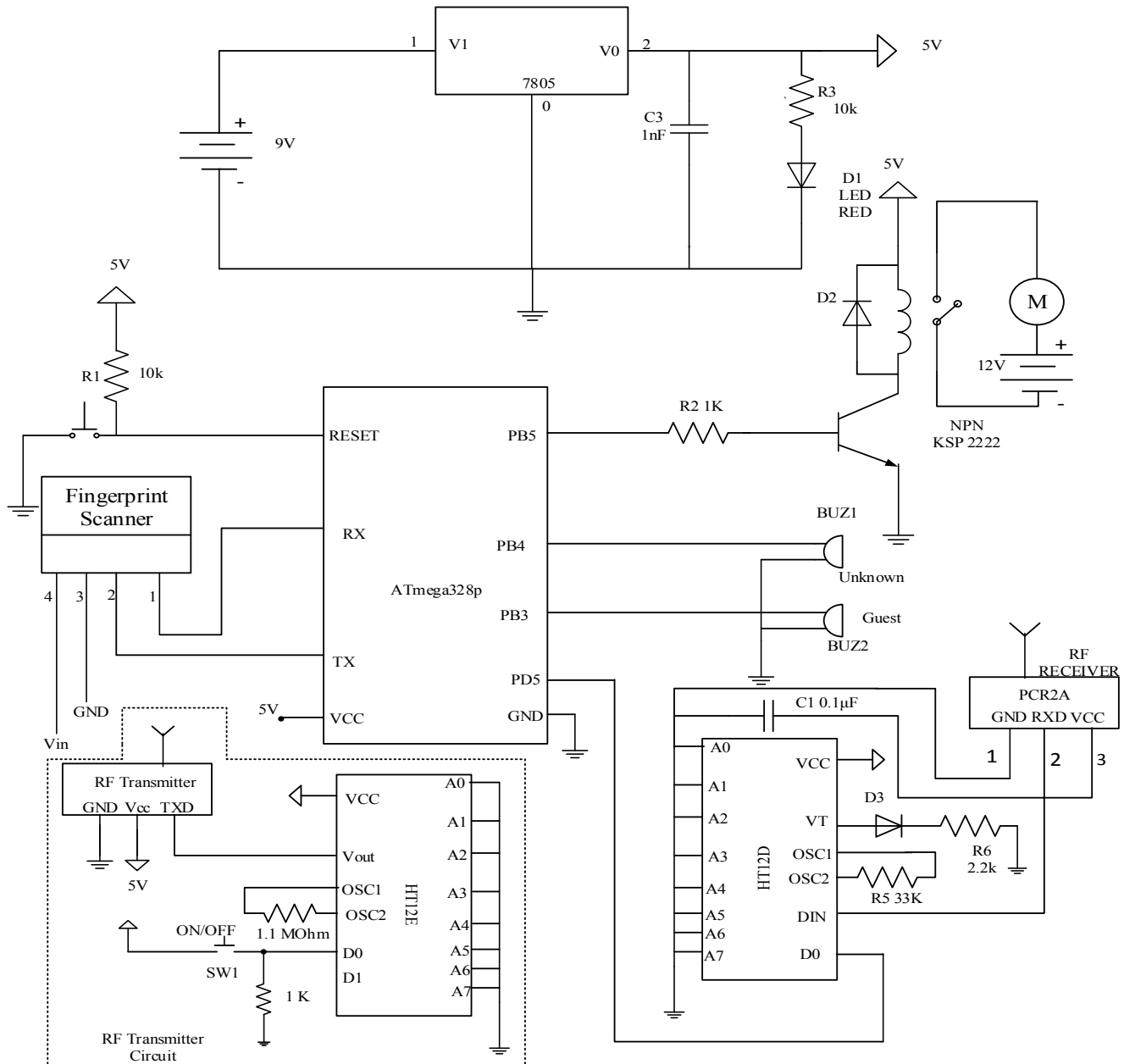


Fig. 3: Complete circuit diagram of the system.

#### IV. PROGRAMMING AND IMPLEMENTATION

This section represents the programming algorithm and practical implementation of our system.

##### A. Programming Algorithm

The flow chart of the program loaded in microcontroller is given in “Fig. 4”. The system initialize by scanning finger print of visitor. Then it processes the finger print image to get the finger print template. After that this finger print template is matched with stored fingerprint. If finger print is not matched with stored fingerprint sound generated from buzzer 2. On the other hand, if finger print is matched, the system further checks whether the visitor is home member or not. If it gets home member the door opens automatically. In other case, system generates sound from buzzer 1 and check received data from RF receiver. The appropriate data of RF receiver opens the door. This process repeatedly runs by microcontroller.

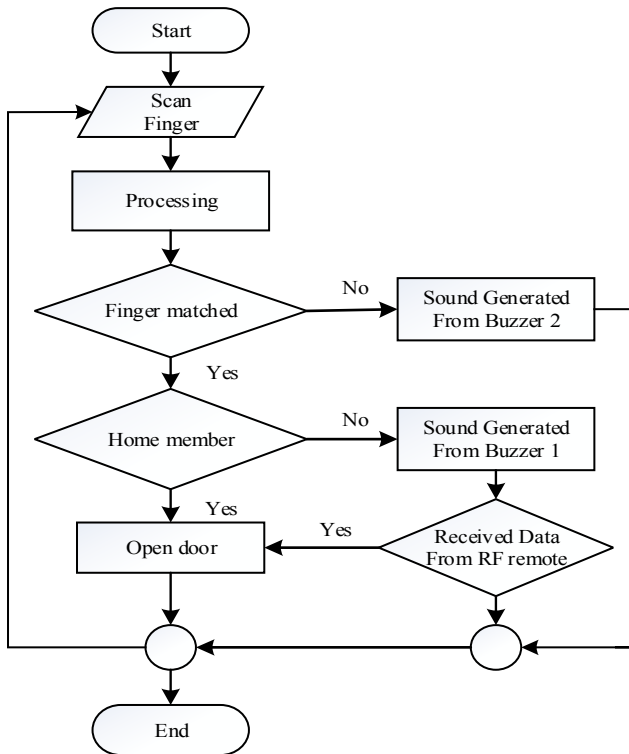


Fig. 4: Flow chart of program.



Fig. 5: Prototype of the system, finger placed on finger print scanner.

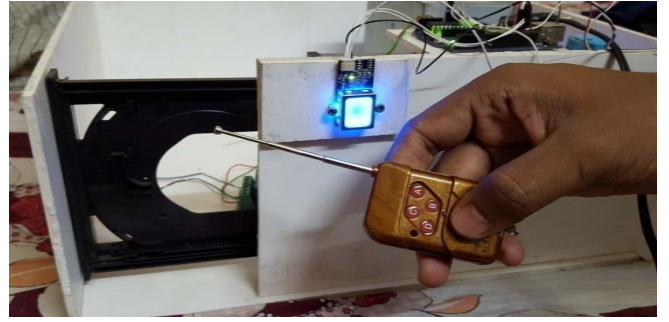


Fig. 6: Prototype of system and RF remote to open the door from inside of home .

##### B. Implementation

A prototype of the system is developed. “Fig. 5” and “Fig. 6” shows some images of the prototype. The prototype is checked for a home living a family of 6 members and considering 12 people as frequently coming guest categorized as known guest in this system. The system worked properly as described earlier. Some specifications are listed in “Table-III”, which are obtained from analysis of implemented system. Total cost of the implemented prototype is about 3800 BDT (around 47 USD) as shown in “Table-IV”. To implement a real system instead of prototype cost will increased up to 80 USD approximately. Mass production of real system will decrease the cost about 15 USD i.e. the cost of the system will be 65 USD.

TABLE III. SYSTEM SPECIFICATIONS

Action Name	Required Time	Field	Specification
Finger print identification	<1 sec	Number of fingerprint storage	200 people
Fingerprint identification and opening door	< 2sec	Range of RF remote	Approx.. 100m in indoor
Closing door	< 1 sec	Power required	1.2 W

TABLE IV. COST CALCULATION OF PROTOTYPE

Field	Cost (BDT)
Fingerprint scanner	2500
Microcontroller	200
RF receiver and transmitter pair	1000
DC motor, power supply circuit and others	100
Total	3800 (around 47 USD)

#### V. CONCLUSION

The purpose of this system is to ensure home security and to reduce human effort. When peoples inside home are busy in cooking, reading, sleeping, bathing or any other daily activity opening or closing door in conventional way can break their concentration in activity. So, the use of this system may help them to concentrate their daily activity in more secured and

reliable way as this system prevent them to go towards entrance door in most of the cases.

#### REFERENCES

- [1] Jayashri Bangali1 and A. Shaligram, "Design and Implementation of Security Systems for Smart Home based on GSM technology", *International Journal of Smart Home*, Vol.7, No.6 (2013), pp.201-208.
- [2] Raqibull Hasan et al., "Microcontroller Based Home Security System with GSM Technology", *Open Journal of Safety Science and Technology*, Vol. 5, pp. 55-62, June 15, 2015.
- [3] Mehek Potnis et al., "Home Security System Using Gsm Modem", *Journal of Engineering Research and Applications*, Vol. 5, Issue 4, April 2015, pp.143-147
- [4] Luay Fraiwan et al., "A wireless home safety gas leakage detection system", 1st Middle East Conference on Biomedical Engineering, Feb. 21-24, 2011, IEEE, DOI: 10.1109/MECBME.2011.5752053
- [5] A. Aditya Shankar et al., "Finger Print Based Door Locking System", *International Journal Of Engineering And Computer Science*, Volume 4 Issue 3 March 2015, pp. 10810-10814.
- [6] K.Wazed Nafi et al., "An Advanced Door Lock Security System using Palmtop Recognition System", *International Journal of Computer Applications*, Volume 56– No.17, October 2012.
- [7] Ajinkya Kawale, "Fingerprint based locking system" *International Journal of Scientific & Engineering Research*, Volume 4, Issue 5, May-2013.
- [8] ADH Technology Company Ltd. "Optical fingerprint recognition embedded module", GT-511C3 Datasheet, March 26, 2013.
- [9] Milan Verle, PIC Microcontroller, 1st edition, mikroElectrica, 2009.

# Short Term Wind Speed Forecasting Using Artificial Neural Network: A Case Study

Hasan Masrur, Meas Nimol  
Energy field of study, SERD  
Asian Institute of Technology  
Pathumthani-12120, Thailand  
hmasrur@gmail.com

Mohammad Faisal, Sk. Md. Golam Mostafa  
Department of Electrical and Electronic Engineering  
International Islamic University Chittagong  
Chittagong-4203, Bangladesh

**Abstract**—The intermittency of wind speed is very challenging in order to produce wind energy via wind turbine to synchronize with the power system. The accurate wind forecasting models are very important for effective power system management. There are many ways have been introduced for short term accurate wind forecasting. In this paper, Artificial Neural Network (ANN) is used with feed forward back propagation algorithm to forecast short-term wind speed of Asian Institute of Technology (AIT). After simulating the model in MATLAB, the result shows that the mean absolute percentage error (MAPE) between the predicted and measured wind speed is quite low and noteworthy. It represents the high prediction correctness of short-term wind speed forecasting using the above mentioned model.

**Keywords**—component; formatting; style; styling; insert (key words)

## I. INTRODUCTION

In order to reduce fuel energy, one country needs to exploit energy from renewable energy sources. Wind energy is important source for power generation because a wind power plant is operated without fuel consumption, has economical operation [1]. The investment cost of wind power plant depends on various factors including the location, the type of wind turbine and its generator. Wind power generation has total installed capacity of 318.5GW in 103 countries in 2013 and is projected to share one third of the world's electricity by 2030. Currently, wind power contributes nearly 4% to the world electricity demand [2]. Thailand just started using electricity generated by wind turbine in 2010 when the first wind power plant was built. The total capacity of all wind power plants in December 2013 was 193 MW, while the peak demand in year 2014 was 26,942.10 MW [3]. Among all the renewable energy sources wind (speed) needs more forecasting approach due to its higher intermittency rate. In order to ensure the efficient installation, operation and continuation and to have reduced influence on wind power projects in severe weather, the magnitude of wind power forecasting has become a vital issue. Again due to forecasting in energy market trading one gets a heads up and can decrease imbalance charges and fines.

## II. BACKGROUND

The randomness of wind speed is very challenging in order to produce wind energy via wind turbine to harmonize with the power system. The precise wind predicting models are very important for effective power system management.

Many ways for short-term accurate wind forecasting have been instigated to get the most out of wind power. However, it is a very tough problem due to the high uncertainties from surrounding environment and the current weather forecast capability. The most straightforward and traditional solution is using the wind variables from real time forecasts of a full-physics atmospheric model, but it is very limited to meet the requirement of a local wind farm. Recently, several attempts have been made by using full physics atmospheric models, statistical approaches or neural network (NN) varieties [4].

An ANN contains of simple processing units called neuron [5]. The computational capabilities are excellent determined by the connection weights, network architecture and training algorithm. ANN is excellent tool for researching field; it can solve non-linear function, data classification, clustering, simulation, prediction, and load forecasting and restoring missing wave measure [6]. ANNs have been used in different fields of science and technology including prediction of different environmental parameters like solar radiation, wind speed etc. and power forecasting [7]. ANN extracts information from data to develop complex relationship between input and output. The inputs variables are multiplied by connection weights and its products, biases are added and delivered through transfer functions for generating output. The network is decided by architecture, exciting function and training algorithm. The architecture determines connection pattern among neurons. During training, the values of connection weights and biases are updated to reduce the mean square of output error. The wind speed prediction accuracy is determined by mean absolute percentage error (MAPE).

The hourly mean wind speed data of January 2016 is used in the ANN model. The data are taken from the automatic wind monitoring station of the Energy field building, School of Environment Resources and Development (SERD), Asian Institute of Technology (AIT), Pathumthani, Thailand (latitude:14.0796<sup>0</sup>N, longitude:100.6127<sup>0</sup>E, altitude:14m above mean sea level). The wind speed range during that period was recorded from 0.04m/s to 4.04 m/s (figure 1).

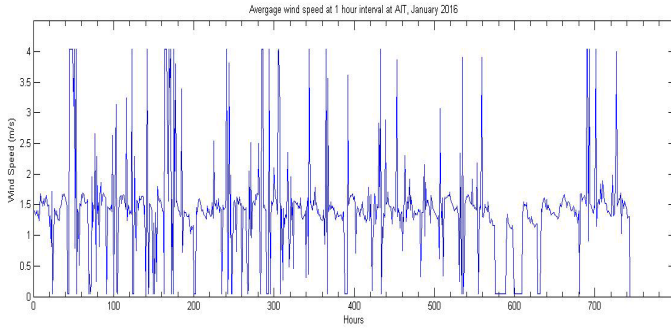


Fig. 1. The hourly variation of wind speed averaged in 01hour interval at AIT Energy building during January, 2016.

### III. SYSTEM MODEL

In this project, neural network toolbox (**nntool**) of MATLAB R2014a is used to forecast hourly 24 hour ahead wind speed with Levenberg-Marquardt Feed forward Back Propagation Algorithm.

The input contains 24 samples which is exactly the same as time period in one day (putting in column of the workspace in MATLAB. Each sample (column) has 30 rows representing the wind speed in the past 30days. Among these 24 samples, there are three groups of data. First group is train data, which contains 60% sample and is selected randomly by nntool. Second group is the validation data which contains 20%sample; it measures the network in general by feeding it with new data. The last group is the test data which contains 20% sample and measures the neural network performance independently in terms of Mean Square Error (MSE). MSE is the square of the difference between predicted value and target value. Thus, it is always positive.

Therefore, this model has 3 layers-first layer is input layer which has 30 neurons corresponding to 30 days of January 2016, second layer is hidden layer which has 20 neurons and the third is output layer which has 1 neuron corresponding to the predicted day. The model simulation is implemented in four scenarios which 01<sup>st</sup>, 11<sup>th</sup>, 22<sup>nd</sup> and 31<sup>th</sup> day of January 2016 is set as the target accordingly.

#### Proposal Formulation

The wind speed forecasting accuracy is determined by MAPE attained from the following equation:

$$MAPE = \left( \frac{1}{n} \sum_{i=1}^n \frac{|WS_{i(ANN)} - WS_{i(measured)}|}{|WS_{i(measured)}|} \right) \times 100$$

Where, n is input and output pair numbers (which can be vector quantities);  $WS_{i(measured)}$  is measured wind speed for i hour;  $WS_{i(ANN)}$  is predicted wind speed for i hour.

The level of prediction accuracy judged by MAPE are less than 10% (high prediction), 10%-20% (good prediction) and over 50% (inaccurate prediction) [8].

## IV. RESULT AND DISCUSSION

### A. Scenario 01

The performance plot of ANN model demonstrates that the MSE is 0.0002 as shown in figure 2. It means the error between predicted value and the measured value is very small correlation coefficient (R-value) shows the association among output and target value of ANN model The perfect fit indicates the data should fall along 45° line (Slope is equal to 1), means network output is equal to target. The R-value is 0.98 and slope is 0.98, achieve during whole data set, proved that the prediction close to measured value as shown in figure 3.

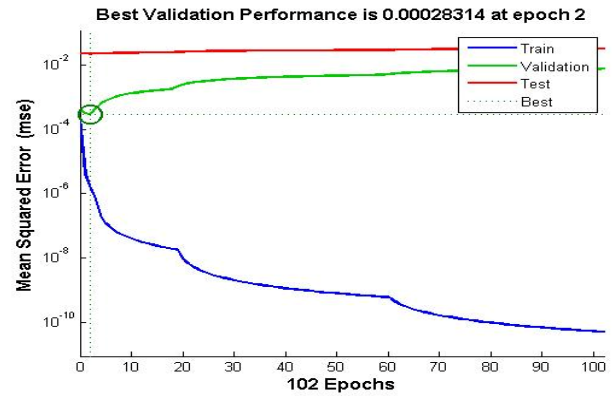


Fig. 2. Performance plot of wind speed prediction in 01<sup>st</sup> January 2016.

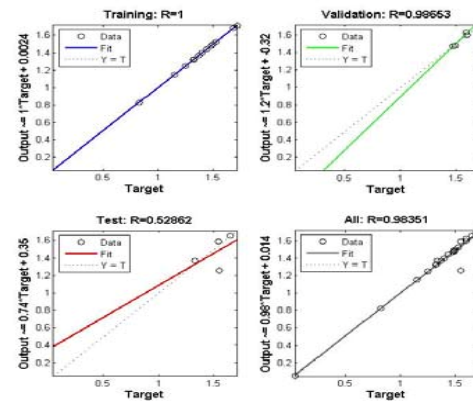


Fig. 3. Regression plot of wind speed prediction 01<sup>st</sup> January 2016.

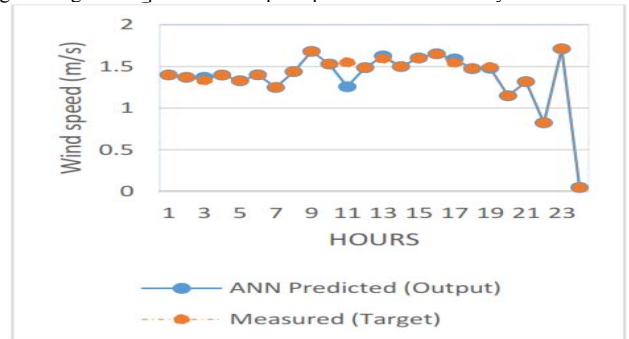


Fig. 4. Comparison between predicted and measured wind speed in AIT on 01<sup>st</sup> January 2016.



TABLE I  
CALCULATION OF MAPE IN 01<sup>st</sup> JANUARY 2016

Hour	Wind Speed (m/s)	
	Predicted	Measured
1	1.40	1.40
2	1.37	1.37
3	1.37	1.33
4	1.40	1.40
5	1.33	1.33
6	1.40	1.40
7	1.25	1.25
8	1.44	1.44
9	1.68	1.68
10	1.53	1.53
11	1.26	1.55
12	1.48	1.49
13	1.62	1.59
14	1.50	1.50
15	1.60	1.60
16	1.65	1.65
17	1.59	1.54
18	1.47	1.48
19	1.48	1.49
20	1.15	1.15
21	1.32	1.32
22	0.82	0.82
23	1.71	1.71
24	0.05	0.05
<b>MAPE</b>	<b>1.1%</b>	

In this table, there are three columns; the first column shows the number of hours in that day while the second column presents the predicted wind speed value that is prepared using nntool and the measured wind speed value is in last column. The result is 1.1% which indicates high accuracy prediction.

### B. Scenario 02

The performance plot of ANN model shows that Mean Square Error (MSE) is 0.014 (figure 5). It means the error between prediction value and the measure value is very small. The R-value is 0.86 and slope is 1, achieved during whole dataset, proved that the prediction close to measured value as shown in figure 6. The MAPE is calculated by comparing predicted and measured data which is 13.7%, showing good prediction of ANN model.

In this table, there are three columns; the first column shows the number of hours in that day while the second column presents the predicted wind speed value that is prepared using nntool and the measured wind speed value is in last column. The result is 1.1% which indicates high accuracy prediction.

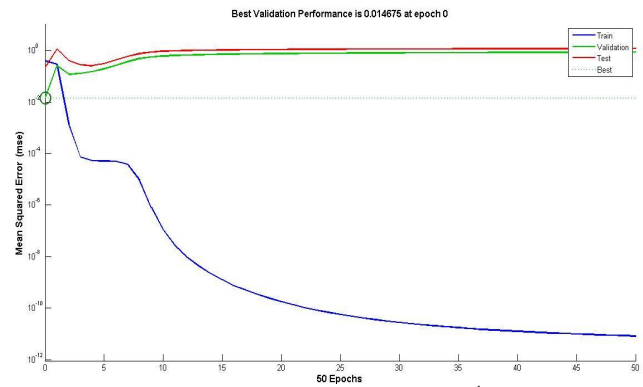


Fig. 5. Performance plot of wind speed prediction on 11<sup>th</sup> January, 2016.

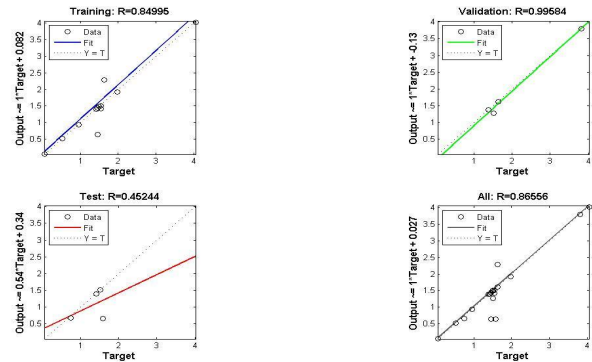


Fig. 6. Regression plot of wind speed prediction on 11<sup>th</sup> January 2016.

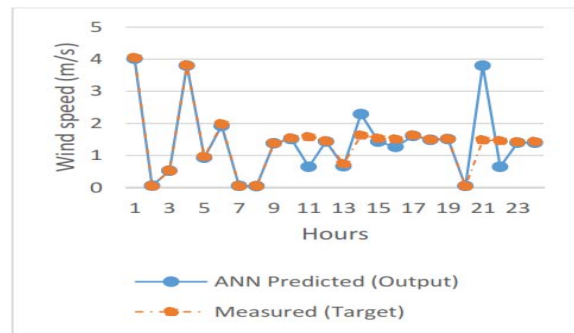


Fig. 7. Comparison between predicted and measured wind speed.

### C. Scenario 03

The performance plot of ANN model demonstrates that the mean square error (MSE) is 0.004 as shown in figure 8. It means the error between prediction value and the measure value is very small. The correlation coefficient (R-value) shows the association among output and target value of ANN model. R value is 0.9 and slope is 0.85 which leads to MAPE of 5.1%.

TABLE II  
CALCULATION OF MAPE IN 31<sup>st</sup> JANUARY 2016

Hour	Wind speed(m/s)	
	Predicted	Measured
1	1.26	1.26
2	1.32	1.32
3	0.79	0.61

4	2.76	3.07
5	1.64	1.64
6	1.04	1.18
7	1.45	1.62
8	0.42	0.34
9	0.76	1.59
10	1.63	1.63
11	1.60	1.60
12	1.62	1.62
13	1.63	1.63
14	1.66	1.66
15	1.72	1.64
16	1.71	1.71
17	1.60	1.60
18	1.82	1.55
19	1.52	1.52
20	1.50	1.50
21	1.46	1.46
22	1.41	1.41
23	1.45	1.45
24	1.42	1.42
<b>MAPE</b>	<b>5.1%</b>	

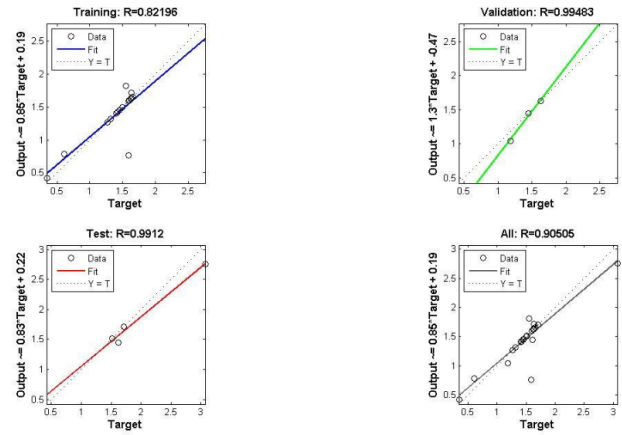


Fig. 9. Regression plot of wind speed prediction on 22<sup>nd</sup> January 2016.

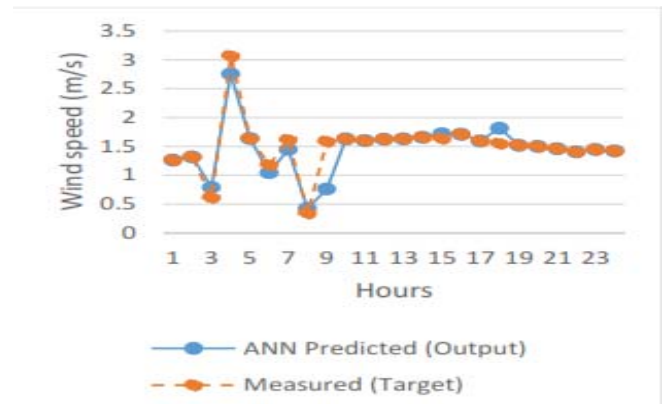


Fig. 10. Comparison between predicted and measured wind speed.

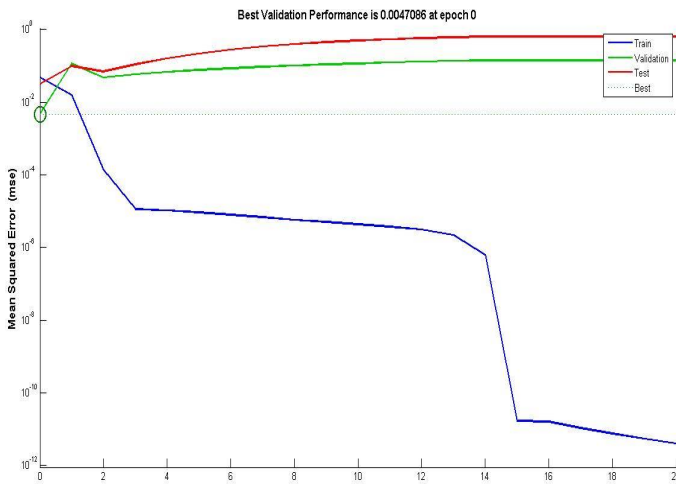


Fig. 8. Performance plot of wind speed prediction on 22<sup>nd</sup> January, 2016.

#### D. Scenario 04

It is clear from the performance plot of ANN model that Mean Square Error is 0.0167 which is very less. The R-value is 0.97 and slope is 0.88, achieved during whole dataset, proved that the prediction close to measured value as shown in figure 9. The MAPE is 4.08%, showing high accuracy of ANN model as shown in figure 10 and table III.

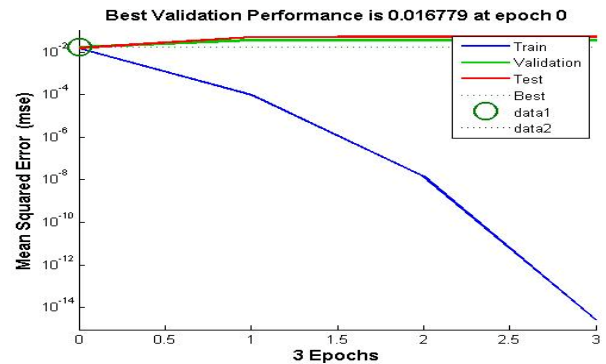


Fig. 11. Performance plot of wind speed prediction on 31<sup>st</sup> January 2016.

TABLE III  
CALCULATION OF MAPE IN 31<sup>st</sup> JANUARY 2016

Hour	Wind Speed (m/s)
------	------------------

	<i>Predicted</i>	<i>Measured</i>
1	1.26	1.31
2	1.47	1.41
3	1.98	1.98
4	1.28	1.32
5	1.39	1.35
6	1.49	1.37
7	2.19	2.61
8	3.89	4
9	1.51	1.48
10	1.67	1.54
11	1.53	1.60
12	1.63	1.59
13	1.74	1.69
14	1.28	1.03
15	1.49	1.60
16	1.47	1.51
17	1.49	1.45
18	1.53	1.56
19	1.49	1.51
20	1.45	1.45
21	1.38	1.41
22	1.36	1.29
23	1.31	1.31
24	1.53	1.31
<b>MAPE</b>	<b>4.08%</b>	

### V. CONCLUSION

ANN model with feed-forward back propagation algorithm is used to forecast hourly wind speed in AIT. The MAPE of the day 01, 11, 22 and 31 are 1.1%, 13.7%, 5.1% and 4.08% respectively which indicates the high prediction accuracy. It means that this model works well with short-term wind speed prediction. Future study can be focused not only on wind velocity prediction but also on parameters of other renewable sources prediction. Furthermore, the comparison between this method and other methods like Levenberg-Marquardt with Bayesian Regularization or Scale Conjugate Gradient or Support Vector Machine (SVM), Decision tree and Random Forest (RF) can be studied for forecasting.

### ACKNOWLEDGMENT

The authors would like to thank their advisor of Energy FoS, AIT for his valuable guideline. They would also like to appreciate Senior Laboratory Supervisor of Energy FoS, AIT for providing necessary data.

### REFERENCES

- [1] A. D. Sahin, "Progress and recent trends in wind energy," *Progress in Energy and Combust Science*, 30(5), 2004, pp. 501-543.
- [2] <http://wwinddea.org/home/index.php>, last accessed on September, 2014.
- [3] Electricity Generating Authority of Thailand (EGAT) <http://www.egat.co.th/index.php?option> Retrieved on March 20, 2016.
- [4] C. Surussavadee, W. Wanchen, "A neural network-based wind forecasting model for wind power management in north eastern Thailand," Milan, *IEEE*, July 2015.
- [5] S. Sumathi and S. Paneerselvam, *Computational intelligence paradigms theory and applications using MATLAB*, Suite300 Boca Raton, FL: CRC Press Taylor and FrancisGroup, 2010.
- [6] O. Makarynsky, D. Makarynska, E. Rusu and A. Gavrilov, *Filling gaps in wave records with artificial neural networks*. Maritime transportation and exploitation of ocean and coastal resources, London: Taylor & Francis Publications, 2005.
- [7] A. U. Haque, P. Mandal, M. E. Kaye, J. Meng, L. Chang and T. Senjyu, "A new strategy for predicting short-term wind speed using soft computing models," *Renewable and Sustainable Energy Review*, 16(7), 2012, pp. 4563-4573.
- [8] C. D. Lewis, *International and business forecasting methods*, London: Butterworths, 1982.

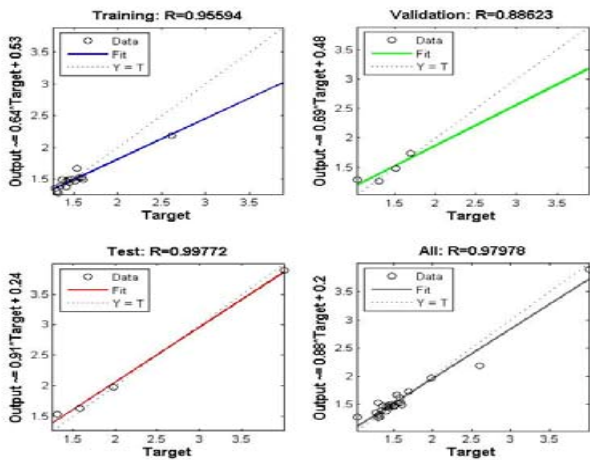


Fig. 12. Regression plot of wind speed prediction on 31<sup>st</sup> January 2016.

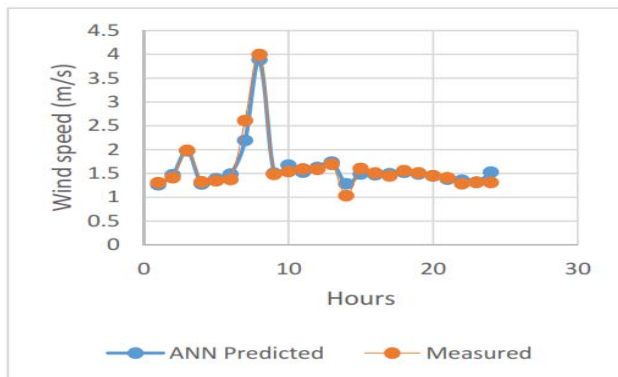


Fig. 13. Comparison between predicted and measured wind speed on

# Design of an universal numeric segmented display and implementation of its decoder circuit in FPGA

M.A. Kader, Kazi Sahadat Hossain, Mohammad Serajum Munir, Rajvi Sutra Dhar, Md. Arifur Rahaman

Dept. of Electrical and Electronic Engineering  
International Islamic University Chittagong (IIUC)  
Chittagong, Bangladesh

{Kader05cu, khsahadat91, mamuneeiiuc201132, tanmoy.sd333iiuc, arifrahman1971}@gmail.com

**Abstract**— Segment display is very important in displaying numeric data. Although matrix display can be used to show any number with better font but it has some major disadvantages compared to segment display. Matrix display uses scanning techniques to show something, this technique is complex to implement and needs more memory. Here, a 20-segment display is proposed which can show numbers and mathematical symbols of 14 different languages. Also a decoder circuit is proposed which takes BCD input and generates output binary combination for 20-segment display of selected language. Finally a prototype of 20-segment display is implemented by LED's and the decoder circuit is implemented in FPGA. The system is checked for 14 different languages and some mathematical symbols.

**Keywords**—FPGA, decoder, numeric display, universal numeric display.

## I. INTRODUCTION

Numeric display is very useful to show the value of different parameters of an electronic system. To show English digit we mostly use seven-segment display. An 11 or 10 or 8 segment display can be used to show both English and Bengali numbers [1]-[5]. A 12-segment display is proposed to show Arabic display [6]. Similarly, numeric segment displays are proposed for other languages. But these segment architectures are different to each other and we cannot use the same architecture for uniform display of multiple languages. In some applications, we need a display where users have option to select their own language. For example, if we can design a universal numeric LCD display, it will be very much useful for the product developers or researchers as they have options to make it compatible with people using different language. For this reason, a 20-segment display is proposed here which may be used to design different universal numeric display. The proposed display can show numeric of 14-languages and mathematical symbols. The languages are Bengali, English, Arabic, Devanagari, Chines, Greek, Hebrew, Gujrati, Tamil, Telegu, Tiben, Roman, Persi and Urdu. In this paper, a decoder circuit is also proposed for 20-segment display.

Finally, both the display and decoder circuit is implemented as a prototype. The display circuit is made by using several LEDs in each segment. Commonly a segment display may be two types: Common Anode and Common Cathode. The implemented one is a common cathode display. The decoder circuit is implemented in a FPGA (Field Programmable Gate

Array) chip. A FPGA chip consists of programmable logic block, programmable interconnections and programmable I/O pins. The decoder circuit is constructed by programming FPGA chip using Verilog hardware description language.

## II. SYSTEM OVERVIEW

The block diagram of the system is shown in "Fig. 1". Decoder circuit has four input lines indicated as S0, S1, S2 and S3 to select language. Another four input lines of the decoder indicated as b0, b1, b2 and b3 is used to provide the BCD input. The CS pin of the decoder circuit is used to enable or disable the decoder circuit. Segments of the display are leveled as a, b, c, d, e, f, g, h, i, j, k, l, m, n, o, p, q, r, s and t. Selection of different language is shown in "Table. I".

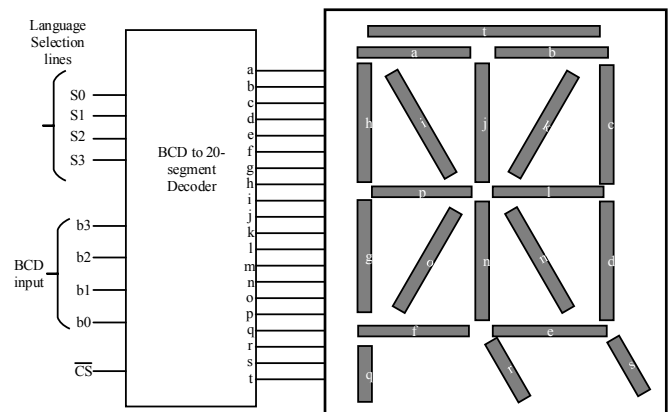


Fig. 1: Block diagram of the system.

TABLE I. DISPLAYED DIGIT PATTERN

S3	S2	S1	S0	Language	S3	S2	S1	S0	Language
0	0	0	0	Bengali	0	1	1	1	Gujrati
0	0	0	1	English	1	0	0	0	Tamil
0	0	1	0	Arabic	1	0	0	1	Telegu
0	0	1	1	Devanagari	1	0	1	0	Tibeten
0	1	0	0	Chinese	1	0	1	1	Roman
0	1	0	1	Greek	1	1	0	0	Persi
0	1	1	0	Hebrew	1	1	0	1	Urdu

### III. SYSTEM DESIGN

This segment describes the procedure of developing the system.

#### A. Patterns of numeric in 20-segment display

In common cathode display a segment glows when segment input line is HIGH. Glowing different segments of the display we can generate patterns for different numeric. The patterns of numeric for different languages are shown in Table-II, Table-III, Table-IV, Table-V, Table-VI, Table-VII, Table-VIII, Table-IX, Table-X, Table-XI, Table-XII, and Table-XIII [7].

TABLE II. BENGALI NUMBERS

Selection Lines: S3=0, S2=0, S1=0, S0=0					
BCD Value	Numeric Symbol	Active Segment	BCD Value	Numeric Symbol	Active Segment
0000	০		0101	৫	
0001	১		0110	৬	
0010	২		0111	৭	
0011	৩		1000	৮	
0100	৪		1001	৯	

TABLE III. ENGLISH NUMBERS

Selection Lines: S3=0, S2=0, S1=0, S0=1					
BCD Value	Numeric Symbol	Active Segment	BCD Value	Numeric Symbol	Active Segment
0000	0		0101	5	
0001	1		0110	6	
0010	2		0111	7	
0011	3		1000	8	
0100	4		1001	9	

TABLE IV. DEVANAGARI NUMBERS

Selection Lines: S3=0, S2=0, S1=1, S0=0					
BCD Value	Numeric Symbol	Active Segment	BCD Value	Numeric Symbol	Active Segment
0000	०		0101	५	

0001	१		0110	६	
0010	२		0111	७	
0011	३		1000	८	
0100	४		1001	९	

TABLE V. GREEK NUMBERS

Selection Lines: S3=0, S2=0, S1=1, S0=1					
BCD Value	Numeric Symbol	Active Segment	BCD Value	Numeric Symbol	Active Segment
0001	α		0110	ς	
0010	β		0111	ζ	
0011	γ		1000	η	
0100	δ		1001	θ	
0101	ε		1010	ι	

TABLE VI. TELEGU NUMBERS

Selection Lines: S3=0, S2=1, S1=0, S0=0					
BCD Value	Numeric Symbol	Active Segment	BCD Value	Numeric Symbol	Active Segment
0000	౦		0101	౫	
0001	౧		0110	౬	
0010	౨		0111	౭	
0011	౩		1000	౮	
0100	౪		1001	౯	

TABLE VII. TIBETAN NUMBERS

Selection Lines: S3=0, S2=1, S1=0, S0=1					
BCD Value	Numeric Symbol	Active Segment	BCD Value	Numeric Symbol	Active Segment
0000	༠		0101	༥	
0001	༡		0110	༦	

0010	۲		0111	۲	
0011	۳		1000	۳	
0100	۴		1001	۴	

TABLE VIII. MATHEMATICAL SYMBOLS

Selection Lines: S3=0, S2=1, S1=1, S0=0					
BCD Value	Numeric Symbol	Active Segment	BCD Value	Numeric Symbol	Active Segment
0000	+		0101	=	
0001	-		0110	<	
0010	*		0111	>	
0011	/		1000	$\pi$	
0100	%		1001	$\square$	

TABLE IX. GUJRATI NUMBERS

Selection Lines: S3=0, S2=1, S1=1, S0=1					
BCD Value	Numeric Symbol	Active Segment	BCD Value	Numeric Symbol	Active Segment
0000	૦		0101	૨	
0001	૧		0110	૩	
0010	૨		0111	૪	
0011	૩		1000	૫	
0100	૪		1001	૬	

TABLE X. ARABIC NUMERIC

Selection Lines: S3=1, S2=0, S1=0, S0=1					
BCD Value	Numeric Symbol	Active Segment	BCD Value	Numeric Symbol	Active Segment
0000	٠		0101	٥	
0001	١		0110	٦	

0010	۲		0111	۷	
0011	۳		1000	۸	
0100	۴		1001	۹	

TABLE XI. CHINESE NUMERIC

Selection Lines: S3=1, S2=0, S1=1, S0=0					
BCD Value	Numeric Symbol	Active Segment	BCD Value	Numeric Symbol	Active Segment
0000	零		0101	五	
0001	一		0110	六	
0010	二		0111	七	
0011	三		1000	八	
0100	四		1001	九	

TABLE XII. HEBREW NUMERIC

Selection Lines: S3=1, S2=0, S1=1, S0=1					
BCD Value	Numeric Symbol	Active Segment	BCD Value	Numeric Symbol	Active Segment
0001	א		0110	ב	
0010	ב		0111	ג	
0011	ג		1000	ד	
0100	ד		1001	ה	
0101	ה		1010	ו	

### B. Design of Segments

A prototype of 20-segment display is developed here. In the developed 20-segment display each segment consists of 6 LED's. Two LED's are connected in series with a 120 ohm resistor. Three such groups are connected in parallel to form a

segment shown in “Fig. 2”. The input voltage of the segment should be 5V and each segment needs 60 mA of current for a good light intensity. The power drop in each resistor is (20 mA \* 20 mA \* 120 Ohm) or, 0.048 W. When all segments of this display glows, it takes about (60\*20) or, 1.2 Amp current.

TABLE XIII. PERSI AND URDU NUMERIC

Selection Lines: S3=1, S2=1, S1=0, S0=0					
BCD Value	Numeric Symbol	Active Segment	BCD Value	Numeric Symbol	Active Segment
0000	۰		0101	۵	
0001	۱		0110	۶	
0010	۲		0111	۷	
0011	۳		1000	۸	
0100	۴		1001	۹	

TABLE XIV. PERSI AND URDU NUMERIC

Selection Lines: S3=1, S2=1, S1=0, S0=1					
BCD Value	Numeric Symbol	Active Segment	BCD Value	Numeric Symbol	Active Segment
0001	۱		0110	۶	
0010	۲		0111	۷	
0011	۳		1000	۸	
0100	۴		1001	۹	
0101	۵		1010	۰	

TABLE XV. ROMAN NUMERIC

Selection Lines: S3=1, S2=1, S1=1, S0=0					
BCD Value	Numeric Symbol	Active Segment	BCD Value	Numeric Symbol	Active Segment
0000	I		1101	D	
0101	V		1110	M	
1010	X		1100	C	
1011	L				

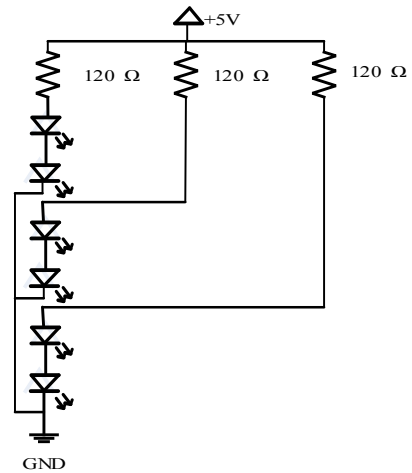


Fig. 2: LED connection in segments.

### C. Field Programmable Gate Array (FPGA)

The field-programmable gate array (FPGA) is a programmable semiconductor device where user can develop any digital electronic circuit inside it by using Verilog Hardware Description Language. FPGA contains configurable logic blocks, programmable interconnections, configurable I/O blocks and clock circuitry [8]. In this project, ALTERA Development and Education Board-2 (DE-2) are used to develop the decoder circuit.

### D. Circuit Diagram

“Fig. 3” shows the circuit diagram of the system. Here, P1 is a 20-pin connector of FPGA where pins can be configured as input or output. The decoder circuit inside FPGA chip is developed by Verilog Hardware Description Language and pins of P1 is leveled as shown in “Fig. 3”. Current provided by I/O pins is not enough to glow all LEDs of a segment, so ULN2003A chip is used to increase the current of a I/O pin.

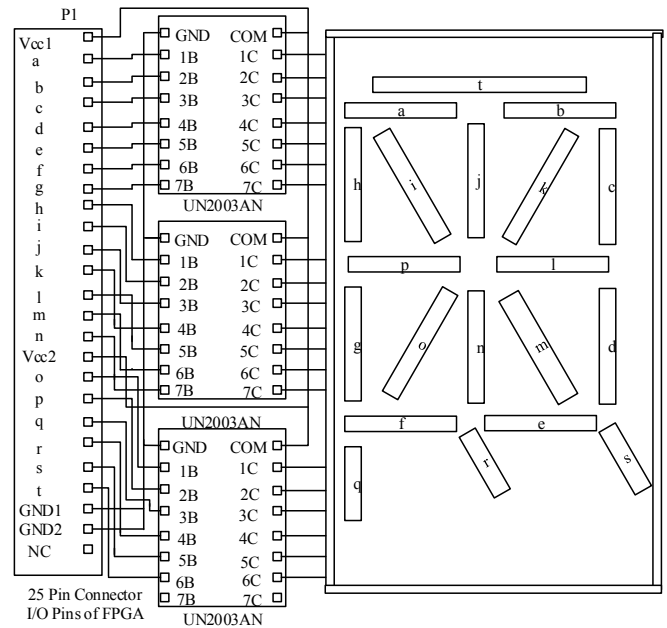


Fig. 3: Circuit diagram of the system.

#### IV. IMPLEMENTATION AND RESULTS

A prototype of 20-segment display is implemented. The PCB layout of display circuit is designed in PROTEUS as shown in “Fig.4”. The connection of 20-segment display with FPGA DE-2 board is shown in “Fig. 5”.

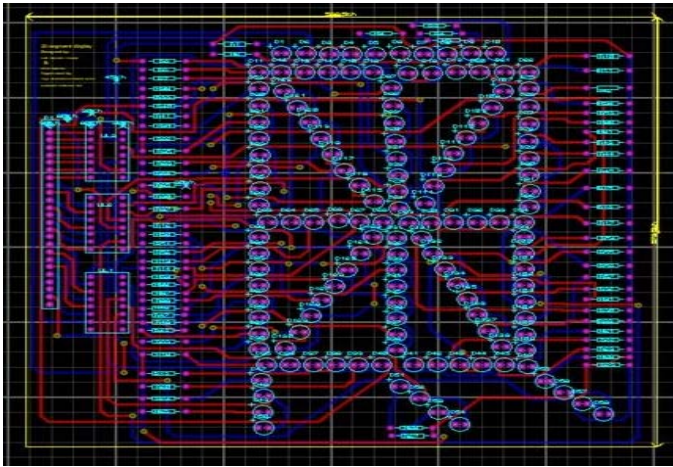


Fig. 4: PCB Layout of display circuit.

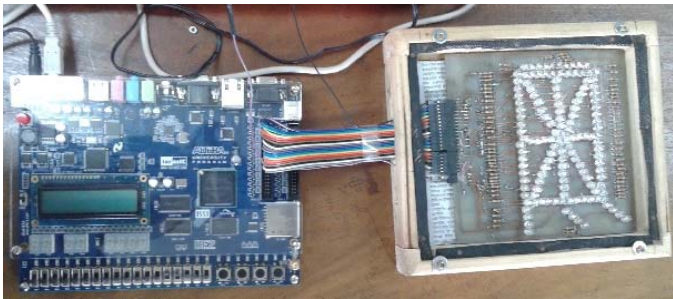


Fig. 5: Connection of 20-segment display with FPGA.

Numeric of different languages obtained in 20-segment display is shown in “Table- XVI” and “Table-XVII”

TABLE XVI. NUMERIC OBTAINED FROM IMPLEMENTED DISPLAY

Bengali	English	Devngri	Greek	Telegu	Tibetan	Gujrati
০	0	०	Α	౦	༠	૦
১	1	१	Β	౧	༡	૧
২	2	२	Γ	౨	༢	૨
৩	3	३	Δ	౩	༣	૩
৪	4	४	Ε	౪	༤	૪
৫	5	५	Ζ	౫	༥	૫
৬	6	६	Θ	౬	༦	૬
৭	7	७	Ι	౭	༧	૭
৮	8	८	Κ	౮	༨	૮
৯	9	९	Λ	౯	༩	૯

TABLE XVII. NUMERIC OBTAINED FROM IMPLEMENTED DISPLAY

Arabic	Chiness	Hebrew	Tamil	Roman	Persi	Sign
۰	0	א	௦	0	۰	+
۱	1	ב	௧	1	۱	-
۲	2	ג	௨	2	۲	X
۳	3	ד	௩	3	۳	/
۴	4	ה	௪	4	۴	%
۵	5	ו	௫	5	۵	~
۶	6	ז	௬	6	۶	<
۷	7	ח	௭	7	۷	>
۸	8	ט	௮	8	۸	π
۹	9	י	௯	9	۹	□

#### V. CONCLUSION

The decoder circuit is implemented in FPGA by using Verilog HDL. The same Verilog code can be used to design an Integrated Circuit (IC) of this decoder using CADENCE tool. The 20-segment display proposed here can also be used to show all English alphabets. Display and decoder circuit can be interfaced with microcontroller or other electronic components to show any numeric parameter in 14 different languages.

#### REFERENCES

- [1] Md. Abul Kalam et al., "A unique 10 Segment Display for Bangla Numerals", proceedings of 8th International Conference on Computer and Information Technology (ICCIT), 2005, Dhaka, Bangladesh.
- [2] M. Osiur Rahman et al., "Different Segment displays for Bangla, English and Arabic digits", proceedings of 6th International Conference on Computer and Information Technology (ICCIT), pp. 299-302, 2003, Dhaka, Bangladesh.
- [3] M.A. kader et al., "Bengali character based digital clock using 13 segment LED display", 17th International Conference on Computer and Information Technology (ICCIT), Dec. 2014, IEEE, DOI: 10.1109/ICCITechn.2014.7073101.
- [4] Fazle Rabbi et al., "An 8-segment display for both English and Bangla digits", proceedings of 6th Int.Conference on Computer and Information Technology (ICCIT), pp.338-341, 2003, Dhaka, Bangladesh.
- [5] S.M Niaz Arifin et al., "Segmented display for Bangla Numerals. Simplicity vs. Accuracy", proceedings of 6th International Conference on Computer and Information Technology (ICCIT-2003), pp. 119-125
- [6] Gahangir Hossain. "Designing Segmented Display for Arabic Numerals",Asian Journal of Information Technology, Volume: 4, Issue-10, pp. 907-909, 2005.
- [7] Md. Abul Kalam Azad, Rezwana Sharmeen and S. M. Kamruzzaman, "Universal Numeric Segmented display", proceedings of 7th International Conference on Computer and Information Technology (ICCIT), pp. 887-892, 2004, Dhaka, Bangladesh.
- [8] U. Farooq et al.,"FPGA Architectures: An Overview" in Tree-Based Heterogeneous FPGA Architectures, Springer Science+Business Media New York 2012, pp. 7-10.



# Human Facial Feature Detection Based on Skin Color and Edge Labeling

Md. Khaliluzzaman\*, Md. Faisal Alam and Tanveer Ahsan

Dept. of Computer Science and Engineering, International Islamic University Chittagong, Chittagong-4203, Bangladesh  
\*khalil\_021@yahoo.co.in, md.alamfaisal@gmail.com and tanveer.ahsan@gmail.com

**Abstract**— In the recent years facial feature detection and recognition is an interesting and challenging work in the field of image processing in which facial region detection is the most basic step. This paper proposes a framework for detecting the facial region and facial features from a frontal facial image. Initially, an RGB facial image is used to detect the facial region. In the next step, the facial features, i.e. eyebrows, eyes, nose, and lips regions are detected from the extracted facial region. For that, the binary information is used to detect the facial region from the input facial image. After that, the RGB image is converted into YCbCr based skin color image from where the edges of the facial features are extracted. In the next step, labeling operation is performed on the edge image to identify the location of the facial features region. Various frontal facial images are utilized to evaluate the proposed framework and presented outcomes demonstrate the adequacy.

**Keywords**— facial features; skin color conversion; RGB; YCbCr

## I. INTRODUCTION

Software and hardware applications for human face image processing are becoming more ubiquitous. Human face recognition has attracted substantial attention from various disciplines from the past ten years. It has seen a tremendous growth in researches. It is done for identifying or verifying a person's identity. Its main uses are in security systems, surveillance systems, credit card verification, and many other applications of artificial intelligence. Facial feature detection has become important for face recognition. In many computer vision applications such as expression recognition, face recognition, face tracking, animation, red-eye correction, and localizing of facial feature act as a critical component. Facial feature detection is also plays an important role in personal identification security and user verification. As images can be acquired in non-intrusive and humans can use in their visual interactions, so face recognition is one of the most acceptable biometrics. But in faces has a lot of difficulties because of not only various environments as like as a background and brightness for lighting conditions, but also vary in scale, location, orientation, pose, ethnicity, gender and age.

This section provides a descriptive summary of some methods that have been implemented and tested for facial region and features detection from facial images. Recent years, various methods have been proposed for facial feature detection. This classified into three categories [1]. Knowledge based method, Template based method, and appearance based method. Devadethan et al. [2] proposed a system that contains two stages. Firstly, the eye regions are detected using the morphological operation technique and rule based methodology. In the next, the facial regions are located and facial features are extracted. But this approach is sensitive with glasses and different lighting conditions.

Md. Mehedi Hasan et al. [3] proposed a framework to detect facial features. Initially, face region is detected and then the facial features i.e. eyes, lips are localized in the detected facial region. For that, authors used morphological and pixel color segmentation procedure. Tanmay Rajpathak et al. [4] introduced a process to detect eyes. The process is based on color image processing and morphological operation. Following that manner, skin color operation is performed for facial region detection. After that, eye pair is exploited by the reflecting feature of pupil. This Method failed when any eye or eye pair is closed. Rong Liu et al. [5] proposed a procedure to extract the nose features. This consists of the three major steps. Firstly, obtains three average nose models (ANM) which corresponds to the nose region and divides the nose into left and right part. Then extract the depth image features from the 3D face image. Finally, utilizing the depth features through the ANM to detect the nose region. The time complexity is high for finding frontal view direction with brutal force search. This method has only worked with only 3D images.

This paper presents a framework to detect the facial region and features based on binary and skin color information. The facial region is detected by utilizing the facial binary information. The facial features are detected by using the skin color conversion method.

The paper is organized as follows. Proposed facial detection framework is described step by step in Section II. In Section III, the experimental results are explained. Finally, the conclusion is given in Section IV.

## II. PROPOSED FRAMEWORK

Basically proposed facial feature detection framework is divided into two parts, i.e. facial region and facial feature detection. The proposed framework is divided into seven primary stages, i.e. (1) RGB to gray scale conversion, (2) binary representation, (3) facial region detection, (4) color conversion, (5) edge detection, (6) labeling, and (7) facial feature detection. Fig. 1 shows the proposed framework.

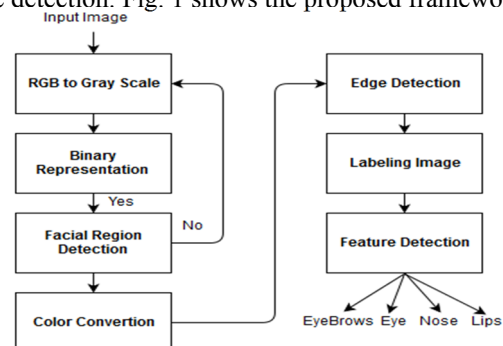


Fig. 1. Proposed facial features detection framework.

### A. RGB to gray scale conversion

In this section, the input facial image is converted into the gray scale image to reduce the computational complexity. The input image is an RGB image. The RGB color model is an additive color model [6]. Gray scale image known as intensity image or gray level image. Each pixel of gray scale image is a single value which carries only intensity information. The equation to get a gray scale image from RGB image is given in (1).

$$Gray\ Image = R * 0.299 + G * 0.587 + B * 0.114 \quad (1)$$

### B. Binary representation

After getting the gray scale image, it is converted to binary image to get the classification between face and non-face region by two labels: 0 and 1. So that various region of the facial gets by the binary values. Since, processing binary image has been faster than any other color space. Therefore face region detection is firstly performed on the binary image where the input is a color image to reduce the computational complexity. Fig. 2 shows the processing example of converting gray scale image into a binary image.



Fig. 2. Experimental example of the binary representation: (a) Input gray scale image, (b) binary image.

### C. Facial Region Detection

This section describes the process of facial region detection in details. Facial region detection is the major part for facial feature detection because of the facial region contains all the features of the facial.

After getting the binary image from the gray image with having the facial portion and non-facial portion of two different labels of zeros and ones. So, easily ignoring the non facial portions and detect the facial region that contains all the facial features like eyebrows, eyes, hairs, nose and lips. The facial region detection procedure is shown in Fig 3. Fig 4 shows the experimental example of detecting facial region from facial image.

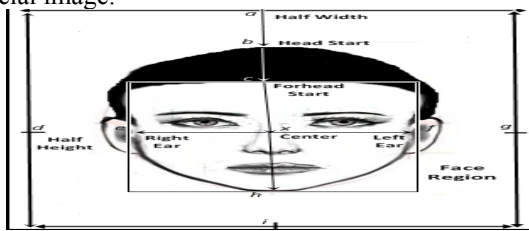


Fig. 3. Facial region detection procedure.

The procedure for facial region detection is described below.

#### Procedure: Detecting facial region

- Step1** Input frontal image
- Step2** Getting height (a to i) and width (d to g) of the input image
- Step3** Then determine the half value of height (d) and width (a)
- Step4** Generate gray scale image and then create binary image  
For j = a to i
- Step5** If binary image (j, half\_width) is equal 1  
starting point of head i.e. b is found and break

- For j= b to i
- Step6** If binary image (j, half\_width) is equal 0  
starting point of forehead i.e. c is found and break
- For j = i to a
- Step7** If binary image (j, half\_width) is equal 1  
ending point of face i.e. h is found and break
- For j = d to g
- Step8** If binary image (j, half\_width) is equal 1  
right ear found and break.
- For j = g to d
- Step9** If binary image (j, half\_height) is equal 1  
left ear found and break.  
Minimum value of x = right ear.  
Maximum value of x = left ear.
- Step10** Minimum value of y = starting point of forehead.  
Maximum value of y = ending point of head.
- Step11** Generate face region with the values of x and y axis

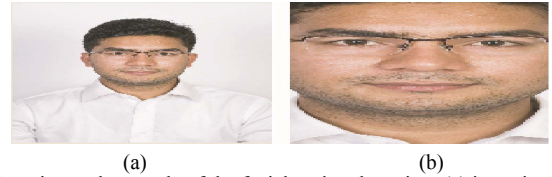


Fig. 4. Experimental example of the facial region detection: (a) input image and (b) extracted facial region.

### D. Skin Color Conversion

As color conversion is a way of encoding of RGB image, so color conversion is obtained here to get the skin color. This paper considered the YCbCr coordinate system, which has relatively stable distribution about skin color. It is a way of encoding RGB information. The information is range from 16 to 235 for Y and 16 to 240 for Cb and Cr [8]. Y means Luminance, where Y component is actually the gray scale conversion of the facial portion. Cb and Cr stand for the blue-difference and red-difference of chrominance components. Since, the face region is in RGB color space. So, YCbCr color space is derived from RGB by (2), (3), and (4).

$$Y = 16 + (65.481 * R + 128.553 * G + 24.966 * B) \quad (2)$$

$$Cb = 128 + (-37.797 * R - 74.203 * G + 112 * B) \quad (3)$$

$$Cr = 128 + (112 * R + 93.786 * G + 18.214 * B) \quad (4)$$

After conversion, thresholding is needed for getting actual skin color which only contains necessary regions of face.

If (140 < Cr < 170 and 105 < Cb < 150)

Facial Skin image = 0

Else

Facial Skin image = 255

Fig. 5 shows the experimental example of skin color conversion from the RGB facial region.



Fig. 5. Experimental example of the skin color conversion: (a) facial region and (b) converted skin color image.

### E. Edge Detection

This section extracts the edges from the skin color image. There are many methods of edge detection. Most of them are grouped into two categories, one is Gradient and another one is Laplacian [9]. The gradient method is used to detect the

edges by looking for the maximum and minimum in the first derivative of the image. The Laplacian method is used to perform searches for zero crossings in the second derivative of the image to find edges. Sobel, Prewitt and Roberts operators come under gradient method. Marrs-Hildreth is a Laplacian method. In this paper uses Canny edge detector with Sobel operator. Among edge detector method, the Canny detector with Sobel operator is fast, detects edges at finer scales, and has smoothing along the edge direction, which avoids noisy edges. By analysis, it is shown that only x-axis of Sobel kernel is enough for detecting edges to detect features accurately. The experimental example of the edge detection is shown in Fig 6.

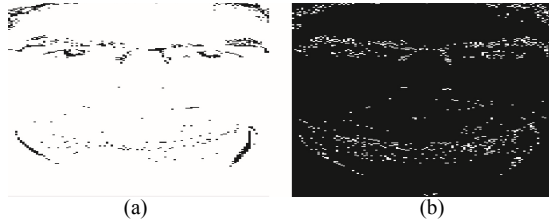


Fig. 6. Experimental example of the edge detection: (a) skin color image and (b) extracted edge image.

### F. Labeling Image

This section performs the labeling operation in the Canny edge image. Feature detection process is proceeded after labeling the facial region. Here, a top pass labeling algorithm is used [10]. After that, the filtering operation is performed over the labeling image to reduce the remaining noise from facial region. Median filtering [11] is applied for noise reduction. The median filter is a nonlinear technique to remove noise. This filter runs through the image matrix and then renews the value with the median of neighboring pixels. It is noted that, 8-connected labeling is also applied. The labeling image represents all the connected regions such as an eye, eyebrow, nose, lips etc. with different individual labels. Fig. 7 shows the processing example of labeling image from the Canny edge image.



Fig. 7. Experimental example of the Labeling Image: (a) Canny edge image and (b) extracted labels in image.

### G. Facial feature Detection

This section detecting the facial features from the labeling image. In this case considered that if the value of the edge and binary image both are equal one value, then consider this value as its corresponding label. It is the starting of the label. Then get the approximate value of the label where it starts or where it ends. Then store the labeling starting and ending pixel values. The particular feature can be detected from the starting and ending point. It may be an eye, an eyebrow or any other feature. It only depends on the localization of the label on the facial region.

For detecting the eyebrows in the facial region, scan the labeling image in the one-fourth of the facial region from the top of the head on the both sides of the facial region. The

procedure and processing example of the eyebrow detection is shown in Fig. 8(a). Actually the eyes are located just below of the eyebrow. Using this idea for eye detection scans the labels just below the eyebrows. The procedure and experimental example of the eye detection is as shown in Fig. 8(b). According to the facial structure the nose is located in the half of the total height of the facial region. For detecting the nose, scanning is started from the half of the width top of the head and continue to the half of the height. The procedure and experimental example of the nose detection is as shown in Fig. 8(c). The lips are located almost same y coordinate value of the nose. However, it is just below the nose. For nose detection, the scanning is done from the bellow of the height by the half of the width. The procedure and experimental example of the lips detection is as shown in Fig. 8(d). Here, edge and labelling binary information is used simultaneously to detect eyes, eyebrows, nose, and lips from a facial image region.

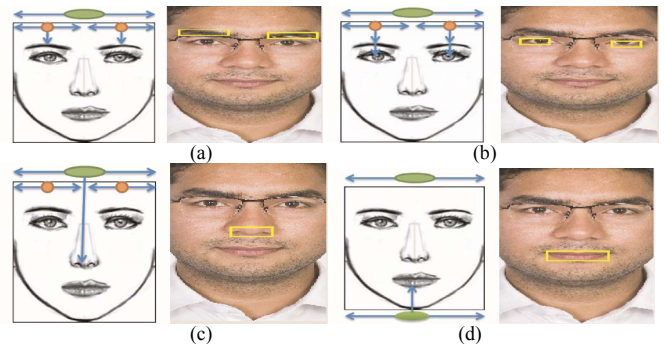


Fig. 8. Experimental example of the feature detection with the procedure: (a) eyebrows detection; (b) eye detection; (c) nose detection and (d) lips detection.

## III. EXPERIMENTAL RESULTS

The experimental results of some frontal facial images are explained in this section. All experiments were performed on Intel(R) Core(TM) i3-3120M@2.5GHZ processor with 4GB RAM. The images are captured by the Canon D700 DSLR camera with the size of 1889x2568. In the experiments, 75 facial images were used. These images are captured from different environments with different illumination conditions, i.e., normal, uneven, and noisy to consider various types. Different illumination type's facial images is shown in Fig. 9. All facial images are captured from the front side of the face.

Fig. 10(a) shows the results of processing sample images. Facial region detection, labeling facial image, eyebrows detection, eye detection, nose detection, lip detection is shown in Fig. 10(b), Fig. 10(c), Fig. 10(d), Fig. 10(e), Fig. 10(f), and Fig. 10(g) respectively.

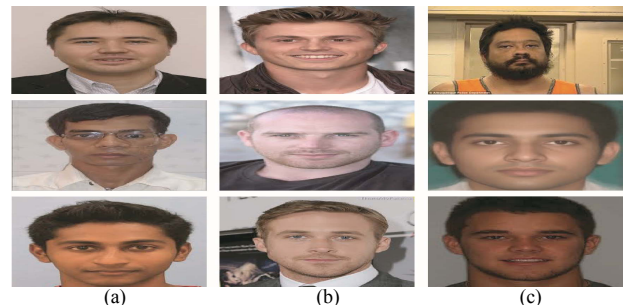


Fig. 9. Various types of facial images: (a) with normal illumination, (b) with uneven illumination and (c) with the noisy background.

In Fig. 10, facial sample 1 is captured at normal illumination conditions where the face is long enough. Facial sample 2 is also captured from the normal illumination where the face is round shaped enough and the person is baldhead. Facial sample 3 is short shaped face with comparing to others. All these images are captured from indoor environments. Facial sample 4 and 5 are captured from outdoor environments with uneven illumination and noisy background respectively. The example shown as the experimental example contains a picture where the person used normal eye glass. The proposed framework can detect the all of these images efficiently.

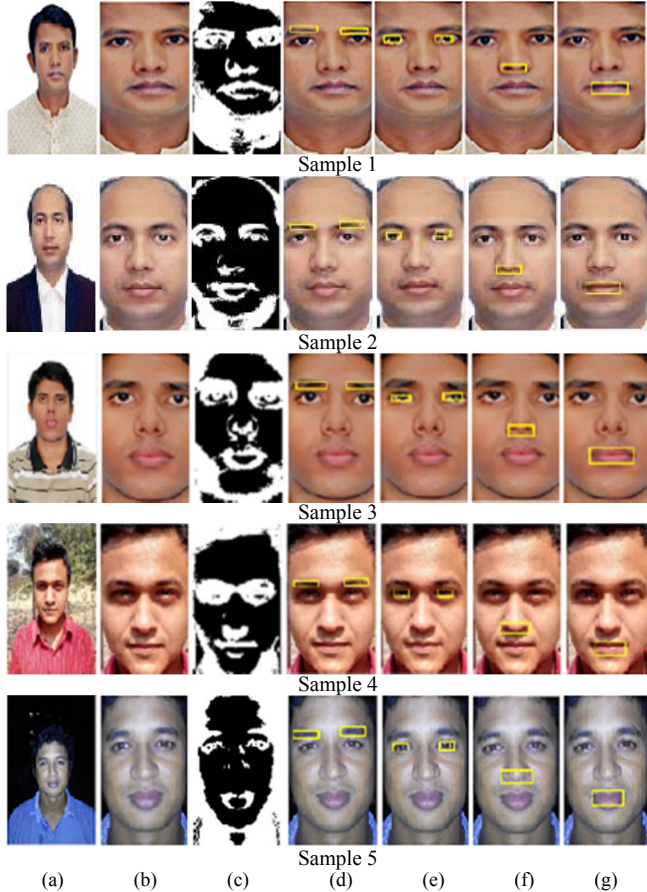


Fig. 10. Experimental example of the facial region and features detection: a) input image, b) facial region detection, c) labeling image, d) eyebrows detection; e) eyes detection; f) nose detection and g) lips detection.

In Table I shows the detection accuracy of the facial images that are measured from different types of facial images. The experimental result shows that the detection accuracy under different illumination is 94.66%.

TABLE I: FACIAL FEATURE DETECTION ACCURACY

Environmental Condition	Total Input Image	Correctly Detected	Detection Accuracy (%)
Normal illumination	40	39	97.5
Uneven illumination	20	17	85
Noisy background	15	12	80
<b>Average</b>	<b>75</b>	<b>68</b>	<b>94.66</b>

Table II shows the comparison of the proposed framework with [2] for facial image detection. The number of features is extracted by [2] and proposed method is 3 and 4 respectively.

TABLE II: COMPARISON OF FACIAL FEATURE DETECTION PERFORMANCE

Method	Number of Facial Feature Extraction	Average Success Rate (%)	Average Error rate (%)
[2]	3	80	20
<b>Proposed framework</b>	<b>4</b>	<b>94.66</b>	<b>5.33</b>

#### IV. CONCLUSIONS

A skin color based facial feature detection framework has been proposed in this paper. The goal of this paper is to detect facial features, i.e. eyes, eyebrows, nose and lips from an RGB image. Most of the facial feature detection is used for personal identity verification. Hence frontal images are considered where each of the features is well identified. In the case of facial region detection binary information is utilized. Facial features are detected by using the binary and skin color information where labeling has identified the facial feature's location. This framework was tested successfully on a group of facial images with a varying style and different illumination conditions. The proposed framework detected facial region and facial features from these facial images with acceptable accuracy of 94.66%. The error rate is 5.33% because of various circumstances like brightness, poses, and orientations. In future, this work will be extended for detecting facial region and features from different poses and orientations facial images.

#### References

- [1] Zeynep Orman, Abdulkadir Battal and Erdem Kemer, "A Study On Face, Eye Detection And Gaze Estimation", International Journal of Computer Science and Engineering Survey (IJCSSES) Vol.2, No.3, August 2011.
- [2] Devadethan, S., Geevarghese Titus, and S. Purushothaman. "Face detection and facial feature extraction based on a fusion of knowledge based method and morphological image processing." Emerging Research Areas: Magnetics, Machines and Drives (AICERA/iCMMDD), 2014 Annual International Conference on. IEEE, 2014.
- [3] Md. Mehedi Hasan, and Md. Foisal Hossain. "Facial features detection in color images based on skin color segmentation." Informatics, Electronics & Vision (ICIEV), 2014 International Conference on. IEEE, 2014.
- [4] Tanmay Rajpathak, Ratnesh Kumar and Eric Schwartz, "Eye Detection Using Morphological and Color Image Processing" Proceedings of Florida Conference on Recent Advances in Robotics, FCRAR, 2009.
- [5] Rong Liu, Rose Hu, and Huimin Yu. "Nose detection on 3D face images by depth-based template matching." Image and Signal Processing (CISP), 2014 7th International Congress on. IEEE, 2014.
- [6] Basu, Mitra. "Gaussian-based edge-detection methods-a survey." IEEE Transactions on Systems, Man, and Cybernetics, Part C, Vol. 32, No.3, pp. 252-260, 2002.
- [7] Yuan, Liying, and Xue Xu. "Adaptive Image Edge Detection Algorithm Based on Canny Operator." 2015 4th International Conference on Advanced Information Technology and Sensor Application (AITS). IEEE, 2015.
- [8] S. Kannumuri, and A. N. Rajagopalan. "Human face detection in cluttered color images using skin color and edge information." Indian Conference on Computer Vision, Graphics and Image Processing (ICVGIP'02),(Ahmedabad, India). 2002.
- [9] Yuan, Liying, and Xue Xu. "Adaptive Image Edge Detection Algorithm Based on Canny Operator." 2015 4th International Conference on Advanced Information Technology and Sensor Application (AITS), IEEE, 2015.
- [10] Crow, Ian, David Tock, and Alan Bennett. "Finding face features." Computer Vision—ECCV'92. Springer Berlin Heidelberg, 1992.
- [11] Fan, Wei. "Median filtered image quality enhancement and anti-forensics via variational deconvolution." IEEE Transactions on Information Forensics and Security, Vol. 10, No.5, pp. 1076-1091, 2015.
- [12] Anima Majumder, Laxmidhar Behera, and Venkatesh K. Subramanian. "Automatic and robust detection of facial features in frontal face images." Computer Modelling and Simulation (UKSim), 2011 UkSim 13th International Conference on. IEEE, 2011.

# Effect of Acceptor Concentration on Performance of CdTe Solar Cell from Numerical Analysis

M.A.A. Noman<sup>a</sup>, M.S. Islam<sup>a</sup>, M.J. Abden<sup>a,\*</sup>,  
M. Arifuzzaman<sup>a</sup>

<sup>a</sup>Department of Electrical and Electronic Engineering  
International Islamic University Chittagong  
Chittagong-4314, Bangladesh

\*Corresponding author. Email address: mjaynul@gmail.com

M.A. Islam<sup>b</sup>

<sup>b</sup>Graduate School of Material Science,  
NARA Institute of Science and Technology,  
Ikoma, Nara 630-0101, Japan

**Abstract**— In this study, the absorber layer of Cadmium Telluride (CdTe) ultra-thin solar cell was analyzed by using the one dimensional simulator Analysis of Microelectronic and Photonic Structures (AMPS 1D) software. A novel structure of ultra-thin CdS:O/CdTe solar cell is suggested in this research that emphasizes on conversion efficiency. The maximum conversion efficiency of  $\sim 26.24\%$  ( $J_{SC} = 27.05 \text{ mA/cm}^2$ ,  $V_{OC} = 1.2 \text{ V}$ ,  $FF = 0.886$ ) is achieved with 600 nm CdTe absorber layer at the acceptor concentration of  $5 \times 10^{19} \text{ cm}^{-3}$ . The temperature effect is also examined with an aim to realize the environmental impact on performance of the cell. Our outcomes offer innovative research guidelines for resolving persistent challenges of CdTe photovoltaics.

**Keywords**— Carrier concentration; CdTe solar cell; numerical analysis; AMPS 1D

## I. INTRODUCTION

Polycrystalline cadmium telluride (CdTe) has already been found wide acceptance as an absorber material for thin film solar cells owing to its ideal band gap energy (1.45 eV), excellent absorption coefficient ( $> 5 \times 10^5 \text{ cm}^{-1}$ ) and good electronic properties [1,2]. Moreover, the layer of CdTe solar cells can be deposited using various cost effective methods, including chemical bath deposition (CBD), sputtering and close-spaced sublimation (CSS) etc. [3]. Oxygenated cadmium sulphide (CdS:O) appears to be an attractive candidates for window layer. It should be noted that nanocrystalline CdS:O has larger optical band gap (2.5-3.1 eV) and excellent lattice match with the absorber layer of CdTe which decrease inter-diffusion affinity at the PN junction [4]. The first CdTe solar cell was fabricated by Bonnet and Rabenhorst in 1972 with efficiency  $\sim 5\%$  [3]. In 1982, Tyan et al. [5] prepared CdTe/CdS thin-film solar cells and reported an efficiency of around 10%. Then, an efficiency of 15.8% has been achieved by Britt and Ferekides [6]. The current record one-of-a-kind laboratory research cell was fabricated in 2015 by First Solar (FSLR) and has an efficiency of 21.5%. Indeed, the key focus of today's PV study is to using fewer semiconductor materials by producing the thinner cells. Thinning will save materials usage thus reduce the fabrication cost required to make the cells. All of these factors mentioned above may lead to produce inexpensive and affordable solar cells. Careful investigation of the reported results display that high efficiency CdTe cells (say  $>10\%$ ) have doping concentrations

between  $\sim 1.0 \times 10^{14}$  and  $\sim 5.0 \times 10^{15} \text{ cm}^{-3}$  [1,6]. However, to mitigate the manufacturing cost of this cell a lower thickness is required along with appreciable conversion efficiency. So, if the doping concentration of the CdTe layer can be raised above  $5 \times 10^{15} \text{ cm}^{-3}$  the maximum conversion efficiency can be found with a thinner absorber layer.

Hence, the aims of the present investigation is to find out an optimum carrier concentration for more stable and high efficient ultra-thin CdTe based solar cells. In addition, the influence of temperature is also considered to realize the environmental impact on performance of the cell. All of the simulations was done using AMPS 1D program.

## II. MODELING AND SIMULATION

Numerical models have already been widely accepted as important tools for the fabrication of any kind of feasible solar cells. Numerical modeling of ultra-thin solar cells is a significant approach to test the possibility of suggested physical explanations and to expect the effect of physical changes on cell performance. Assumed the complex nature of CdS:O/CdTe ultra-thin solar cells, the requirement for numerical modeling is obvious. Numerical simulations give understanding into the mechanism of structures, thus allowing the fabrication of novel structures with good performance and

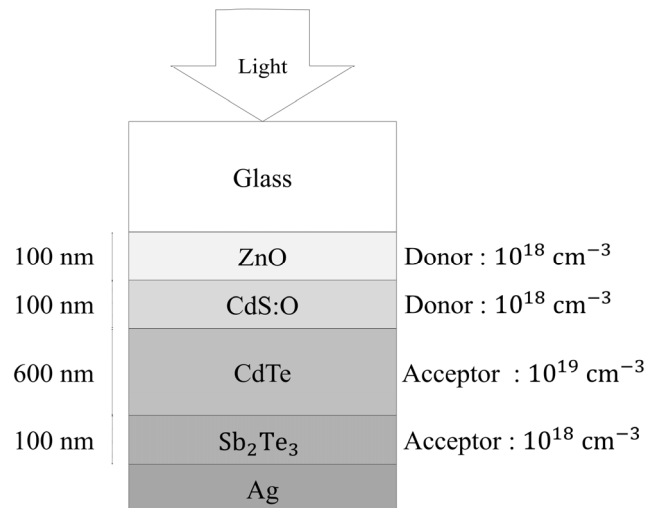


Fig. 1 Schematic structure of the CdTe solar cell.

Table I

Values of different parameters used in simulation [7].

Parameters	ZnO	CdS:O	CdTe	Sb <sub>2</sub> Te <sub>3</sub>
$\epsilon/\epsilon_0$	9.00	10.00	9.40	55.00
$\mu_N - \text{cm}^2/\text{Vs}$	100	100	320	1094
$\mu_P - \text{cm}^2/\text{Vs}$	25	25	40	320
$N_A - 1/\text{cm}^3$	-	-	$5.0 \times 10^{16} - 5.0 \times 10^{22}$	$6.8 \times 10^{19}$
$N_D - 1/\text{cm}^3$	$1.0 \times 10^{18}$	$1.0 \times 10^{18}$	-	-
$E_g - \text{eV}$	3.30	2.75	1.50	0.42
$N_C - 1/\text{cm}^3$	$2.2 \times 10^{18}$	$2.2 \times 10^{18}$	$7.5 \times 10^{17}$	$1.0 \times 10^{16}$
$N_V - 1/\text{cm}^3$	$1.8 \times 10^{19}$	$1.8 \times 10^{19}$	$1.8 \times 10^{19}$	$1.0 \times 10^{17}$
$\chi - \text{eV}$	4.50	4.50	4.28	4.15
W (nm)	100	100	100-2000	100

efficiency. The accepted methods to enhance the performance of CdS:O/CdTe cells have been explored using AMPS 1D. The key functional aspect of AMPS 1D is to solve the fundamental semiconductor equations, such as Poisson's equation and carrier continuity equations. Fig. 1 shows the modified cell structures for superior conversion efficiency which have been used in our present investigation.

In this study, we used the one dimensional (1D) simulation software AMPS to examine the effect of acceptor concentration of absorber layer on the performance of CdTe ultra-thin solar cells with modified structure. The effect of temperature and thickness of absorber layer on the performance of CdTe cells are investigated. Here, ZnO and Sb<sub>2</sub>Te<sub>3</sub> have been used as the front contact and back surface field (BSF) layer, respectively. The thickness of the ZnO is kept 100 nm. During the simulation, the hole concentration of absorber layer is varied from  $5 \times 10^{16}$  to  $5 \times 10^{22} \text{ cm}^{-3}$ , the CdTe layer thickness is ranging from 100 to 2000 nm and operating temperature range of 298 to 500 K. The short-circuit current ( $J_{SC}$ ), open circuit voltage ( $V_{OC}$ ), fill factor ( $FF$ ) and efficiency was investigated with respect to the variation of doping concentrations, temperature and the thickness of CdTe layer. The values of different material parameters used in 1D software AMPS are illustrated in Table I.

### III. RESULT AND DISCUSSION

#### A. Effect of acceptor concentration

The acceptor concentration of the CdTe layer has been changed from  $5 \times 10^{16}$  to  $5 \times 10^{22} \text{ cm}^{-3}$  and simulated results is illustrated in Fig. 2 for the fixed CdTe thickness of 600 nm. It

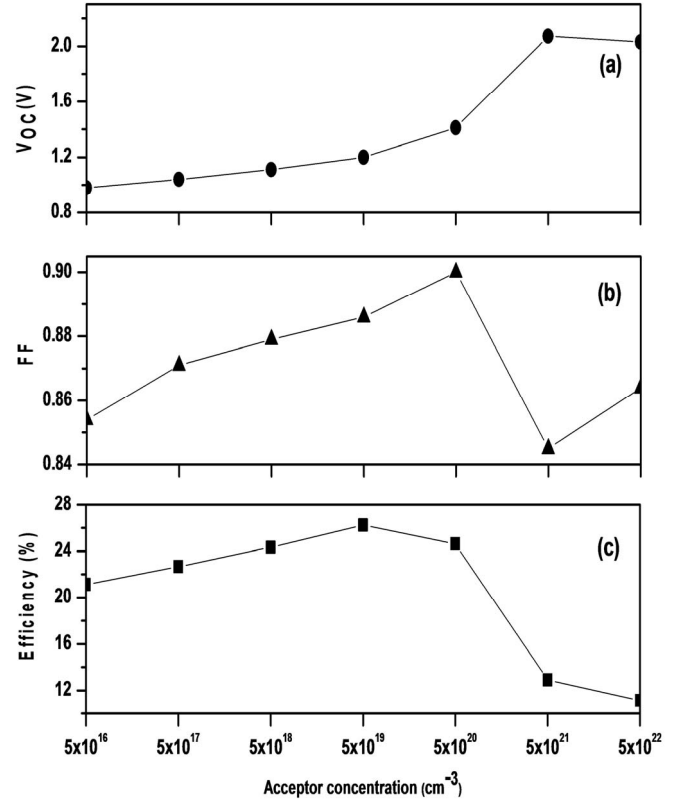
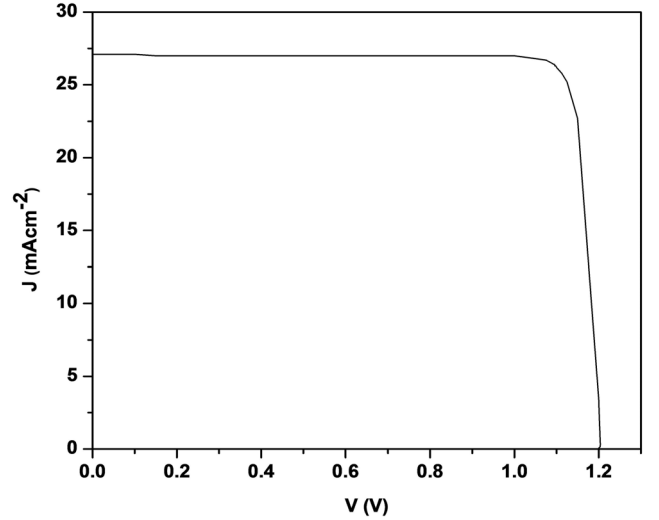
Fig. 2 Effect of acceptor concentration on (a)  $V_{OC}$ , (b)  $FF$  and (c) efficiency.

Fig. 3 Light J-V characteristics curve.

can be seen from Fig. 2 that the maximum efficiency of 26.24% is achieved for the acceptor concentration of  $5 \times 10^{19} \text{ cm}^{-3}$ . It is important to focus that the efficiency of CdS:O/CdTe solar cell increases with the acceptor concentration from  $5 \times 10^{16}$  to  $5 \times 10^{19} \text{ cm}^{-3}$ , for further increment of acceptor concentration the efficiency decreased considerably. Higher doping concentration reduces the diode's saturation current and hence increases the open-circuit voltage ( $V_{OC}$ ) (Fig. 2(a)) and the fill-factor ( $FF$ ) (Fig. 2(b)) [8]. However, for the acceptor concentration above  $5 \times 10^{19} \text{ cm}^{-3}$

the efficiency (Fig. 2(c)) decreased sharply. In this case  $R_s$  seems to decrease with increasing the doping concentration up to the optimum level,  $N_A = 5 \times 10^{19} \text{ cm}^{-3}$ . The  $J-V$  characteristics curve of CdS:O/CdTe ultra-thin solar cell is shown in Fig. 3. From this curve, it is clearly observed that the higher shunt resistance and lower series resistance with maximum  $J_{SC}$ ,  $V_{OC}$  and  $FF$ . Compared with previously reported cells, our proposed CdS:O/CdTe solar cell exhibited superior efficiency owing to the improvement of  $V_{OC}$  (1.2 V).

### B. Effect of Thickness of CdTe Layer

It is suggested that the reduction of thickness of CdTe absorber layers not only helpful to minimize the cost of materials in the process of cell production but also lead to improve the properties of cell by decreasing recombination losses in the bulk [3]. At this stage, the thickness of CdTe layer is ranging from 100 to 2000 nm to achieve the optimum thickness of absorber layer for the fixed acceptor concentration of  $5 \times 10^{19} \text{ cm}^{-3}$ . The highest efficiency of 26.24% is achieved for 600 nm of CdTe as observed in Fig. 4(b). Further increase in the thickness causes the efficiency to decrease. Fig. 4(a) shows the highest  $V_{OC}$  of 1.2 V is found for CdS:O/CdTe cell. It signifies that although the thicker CdTe layer has greater spectral response, it increases the carrier recombination also.

### C. Effect of Temperature

Operating temperature is playing a vital role in thin-film solar cell's performance and stability. It is suggested that the operating temperature on the cell surface can be prolonged from 283 to 373 K under the sun light [9]. CdTe has comparatively low temperature coefficient which can protect the cell performance at higher temperature [10]. For this cell operating temperature is varied from 298 to 500 K. Fig. 5 shows the efficiency with respect to the variation of the operating temperature on the cell. From our results the temperature coefficient is found to be 0.031% / K which shows the stability and reliability of the proposed cell. From

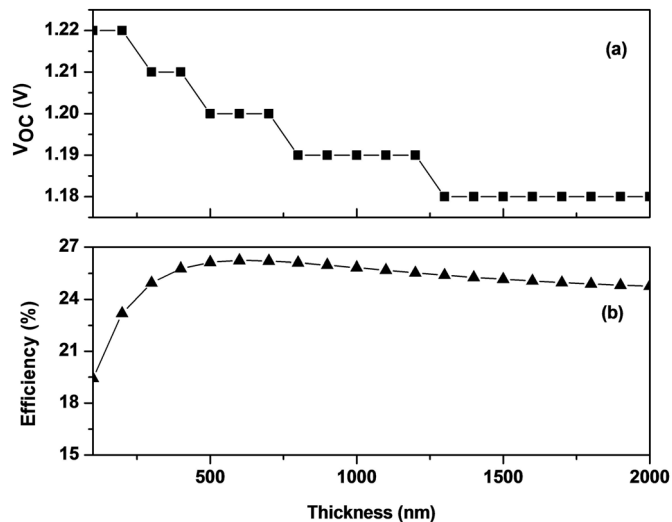


Fig. 4 Effect of thickness on (a)  $V_{OC}$  and (b) efficiency of CdTe solar cell.

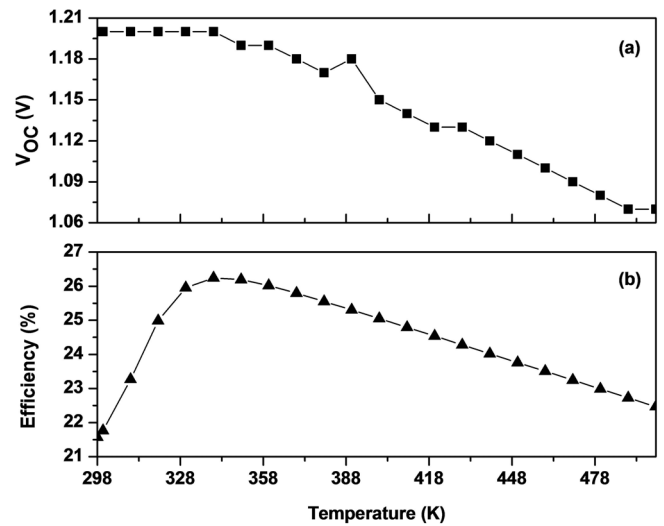


Fig. 5 Effect of temperature on (a)  $V_{OC}$  and (b) efficiency.

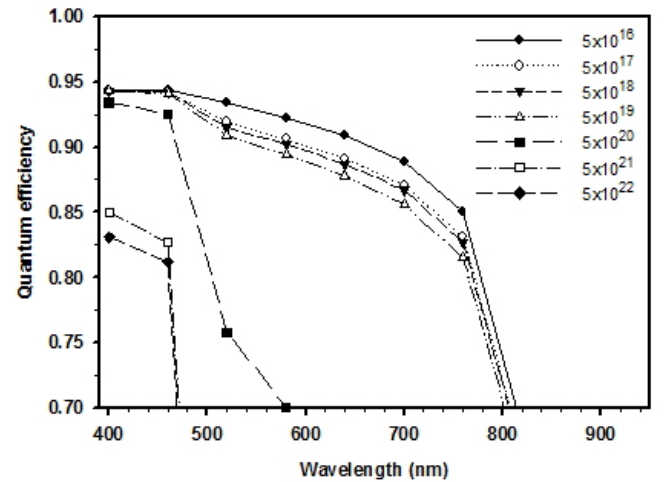


Fig. 6 Quantum efficiency of CdTe solar cell.

Fig 5(b), it can be observed that the efficiency increases with increasing the temperature and achieved highest value at 340 K, for further increment of temperature the efficiency decreased sharply. As observed the  $V_{OC}$  (Fig. 5(a)) at this stage for which the efficiency is increased. As the band gap in the semiconductor decreases with the increase of temperature which helps to enhance the cell efficiency by increasing the electrons flow rate in the material. On the other hand, the results as shown in Fig. 5 indicating that over the temperature 340 K, the carrier collision and recombination is dominated over the carrier flow rate and the efficiency start to reduce.

### D. Quantum Efficiency

The quantum efficiency ( $QE$ ) can be defined as the ratio of the current of photo-generated carriers to the incident photon flux. The  $QE$  of a solar cell strongly depends on the energy of the individual photon. This may be due to both the wavelength dependency of the optical absorption coefficients in semiconductors and the depth dependency of the carrier collection probability. Fig. 6 shows the  $QE$  vs. wavelength

characteristics curve for different acceptor concentration on the absorber layer. For different concentration of CdTe layer the spectral response exhibited different characteristics. The wavelength of the cell is varied from 400 to 850 nm. For the various acceptor concentrations the  $QE$  exhibits almost same characteristics. The results in a change in the quantum efficiency as shown in Fig. 6 indicates that CdTe thin film solar cell provides more stable spectral response.

#### IV. CONCLUSION

In this study, an ultra-thin high efficiency CdS:O/CdTe solar cell is suggested with a reduced CdTe absorber layer thickness. The performance of CdS:O/CdTe cell was numerically simulated by using AMPS 1D package. The maximum conversion efficiency of 26.24% ( $J_{SC} = 27.05$  mA/cm<sup>2</sup>,  $V_{OC} = 1.2$  V and  $FF = 88.6\%$ ) is achieved with the proposed cell consisting of 600 nm CdTe layer and with acceptor concentration of  $5 \times 10^{19}$  cm<sup>-3</sup>. The greater values of  $J_{SC}$ ,  $V_{OC}$ ,  $FF$  as well as  $QE$  curves are demonstrated the lower pinholes and shallow defect density, outstanding absorption range and strength. Our findings not only open up new research instructions but also cover the way for the industrialization of very cost-efficient solar modules.

#### ACKNOWLEDGEMENT

This work has been supported by the Department of Electrical and Electronic Engineering, International Islamic University Chittagong, Chittagong 4314, Bangladesh.

#### REFERENCES

- [1] M.A. Green, K. Emery, Y. Hishikawa, W. Warta and E.D. Dunlop, Solar cell efficiency tables (Version 45), *Progress in Photovoltaics: Research and Applications*, **23** (2015) 1–9.
- [2] A. Morales-Acevedo, Can we improve the record efficiency of CdS/CdTe solar cells? *Solar Energy Materials and Solar Cells*, **90** (2006) 2213-2220.
- [3] N. Amin, K. Sopian, and M. Konagai, Numerical modeling of CdS/CdTe and CdS/CdTe/ZnTe solar cells as a function of CdTe thickness, *Solar Energy Materials and Solar Cells*, **91** (2007) 1202-1208.
- [4] R.W. Birkmire and P.E. Meyers, Processing issues for thin-film CdTe cells and modules, *Proceedings of the 24th IEEE Photovoltaic Specialists Conference*, ISSN: 01608371, Waikoloa, HI, USA, (1994) 76-76.
- [5] Y.S. Tyan, E.A. Perez-Albuerne, Efficient thin film CdS/CdTe solar cells, *Proceedings of the 16th IEEE Photovoltaic Specialists Conference*, New York. (1982) 794-798.
- [6] J. Britt, C. Ferekides, Thin-film CdS/CdTe solar cell with 15.8% efficiency, *Applied Physics Letters*, **62** (1993) 2851-2852.
- [7] M.A. Islam, Y. Sulaiman, N. Amin, A Comparative study of BSF layers for ultra-thin CdS:O/CdTe solar cell, *Chalcogenide Letters*, **8** (2011) 65-75.
- [8] F. Troni, R. Menozzi, E. Colegrove, C. Buurma, Simulation of current transport in polycrystalline CdTe solar cells, *Journal of Electronic Materials*, **42** (2013) 3175-3180.
- [9] M.A. Islam, S. Hossain, N. Amin, M.M. Aliyu, Y. Sulaiman, K. Sopian, Investigation for Optimum Structure of CdS:O/CdTe Solar Cell from Numerical Analysis, *Advanced Materials Research*, **622** (2012) 1194-1198.
- [10] P. Singh, N.M. Ravindra, Temperature dependence of solar cell performance an analysis, *Solar Energy Materials and Solar Cells*, **101** (2012) 36-45.



# Search and Rescue System for Alive Human Detection by Semi-autonomous Mobile Rescue Robot

**Zia Uddin**

Dept. of Electronic and Telecommunications Engineering  
International Islamic University Chittagong (IIUC)  
Chittagong, Bangladesh  
([ziauddin.kcpsc@gmail.com](mailto:ziauddin.kcpsc@gmail.com))

**Mojaharul Islam**

Dept. of Electronic and Telecommunications Engineering  
International Islamic University Chittagong (IIUC)  
Chittagong, Bangladesh  
([mojahar.bd@gmail.com](mailto:mojahar.bd@gmail.com))

**Abstract**— In this modern era, technological development lead the creation of sky scraper buildings and dwellings which increase risks of losing life due to natural and manmade disasters. Many people died by trapping under debris as their presence cannot detect by the rescue team. Sometimes, it is impossible to reach in certain points of the disasters in such calamity hit zones. The situation is worst for developing country like Bangladesh because of low quality design and construction. In this paper, PIR sensor based semi-autonomous mobile rescues robot is developed which can detect live human being from an unreachable point of the disaster area. Joystick and RF technology is used to control the semi-autonomous robot and communicate with control point. Ultrasonic sensor is used for obstacle detection in navigation path of robot and gas sensor is used to detect gas leak inside the building. IP Camera is also integrated to observe and analyze conditions that will facilitate human detection in reliable manner with highest probability of success rate in that kind of situation.

**Keywords:** Semi-autonomous robot, RF technology, rescue robot, PIR sensor

## I. INTRODUCTION

Technology is evolving day by day to make life easy and comfortable. Because of technological development, information about different natural disaster can predict earlier. But man cannot prevent natural disaster from happening. Sometimes they themselves bring disaster to others in the shape of war or bombing or transportation accident or major fire etc. Now a day, Natural disaster like flood, earthquake and cyclone keep happening frequently because people are disrupting the natural balance by cutting trees, destroying hills and unplanned urbanization. During catastrophes, many people lose their life and property. The situation is even worse for developing country like Bangladesh because of their dense population and low

quality building and structure. After any disaster, first 48 hours is crucial to rescue defectors. Police, fire service and paramedics are being deployed to minimize the loss of life and property. Sometimes the rescue team cannot reach many parts of disaster affected area due to the inability to search for the live person in the debris. In some situation, they themselves became the victim of the situation. To reduce losses of lives and for getting accurate information of the situation, a robotic system can be used and can be modified according to the needs of the situations.

Quality work has been done in the field of robotics to develop rescue robot. In last decade, different types of rescue robot are made for different type's works and situations. During September 11 disasters rescue robots were first really tested [1]. They were sent into the rubble to look for survivors and bodies. But since 2010, the numbers of incidents that are using robots and using them quickly are rising, with 2011 being a major year with robots at the Christchurch and Tohoku earthquakes. Robots have been used in 35 disasters internationally [2].

There are many types of rescue robots used in this field. Some of them use sensors like ultrasonic sensor [3] or PIR sensor [4] [5] for detecting human in harsh condition and others use different kinds of camera like thermal and IR camera [5] or wide angle camera [6] for wide vision of the debris to find survivors. Some of the robot contain some extra sensors for detecting temperature, fire and bomb [3].

However, the authors try to develop a robot which can detect live human being by using Passive infrared (PIR) sensor and IP Camera. RF and joystick based controller gives smooth control for user. Besides that, ultrasonic sensor is used to avoid obstacles and gas sensor is used for excess gas detection in the affected area. In this paper, we present the system block diagram in Section II. Section III present and describe the system flowchart. Section IV describes about the physical implementation of the system. Finally, conclusion and future improvement are described in Section V.

## II. SYSTEM BLOCK DIAGRAM

### A. Block Diagram

The system consists of a controller and a semi-autonomous robot. The controller shown in Fig. 1 consists of a joystick which is used to drive the robot in a controlled way. A potentiometer is also used to control the servo motor attached with the robot. The microcontroller on the controller processes data from the joystick and potentiometer and sends the data through a Transceiver. Besides that, the controller receives a signal from the robot about human detection through an RF transceiver which turns on a buzzer connected with it. LPG or CO level detection is indicated by an LED connected with a microcontroller output pin. The controller circuit diagram is shown in Fig. 2.

Fig. 3 shows the block diagram and Fig. 4 shows the circuit diagram of a semi-autonomous robot. The semi-autonomous robot has PIR and gas sensors to detect human presence and excessive LPG or Carbon Monoxide (CO) in the air of the collapsed building respectively. The robot detects and sends the sensor values to the controller for further processing. The robot is a four-wheel control robo-car which can be controlled using joystick commands from the controller. An RF transceiver module is used to receive control data to the microcontroller to drive the car. In addition, an ultrasonic sensor is used to detect obstacles and for auto navigation if needed. A servo motor is integrated in the robot to drive the camera of the robo-car, which is controlled by the analog switch of the controller. The microcontroller receives control data through an RF transceiver and drives the servo motor accordingly. An IP camera is also used for observing from a computer terminal and finding survivors of the disaster-affected area.

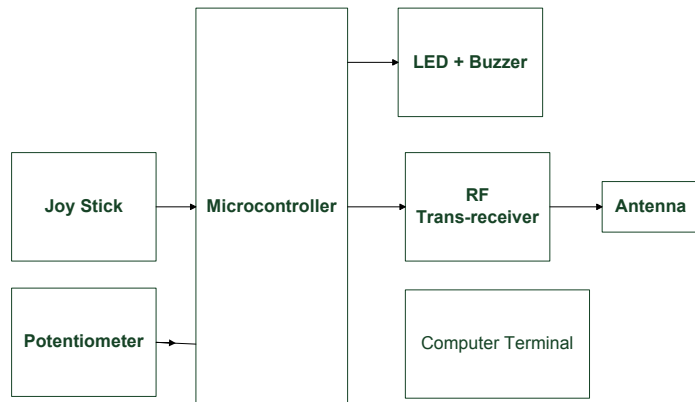


Fig. 1: Block diagram of controller of Robot

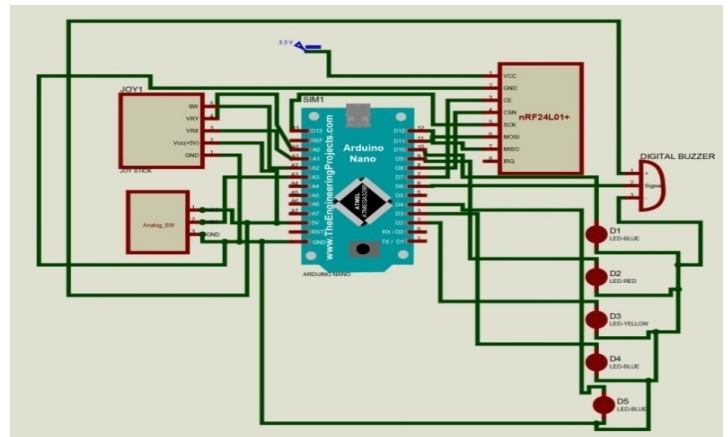


Fig. 2: Circuit Diagram of Controller

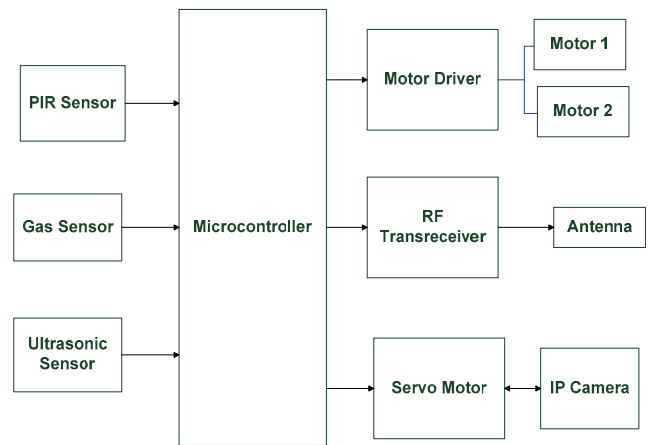


Fig. 3: Block diagram of Robot with different sensor

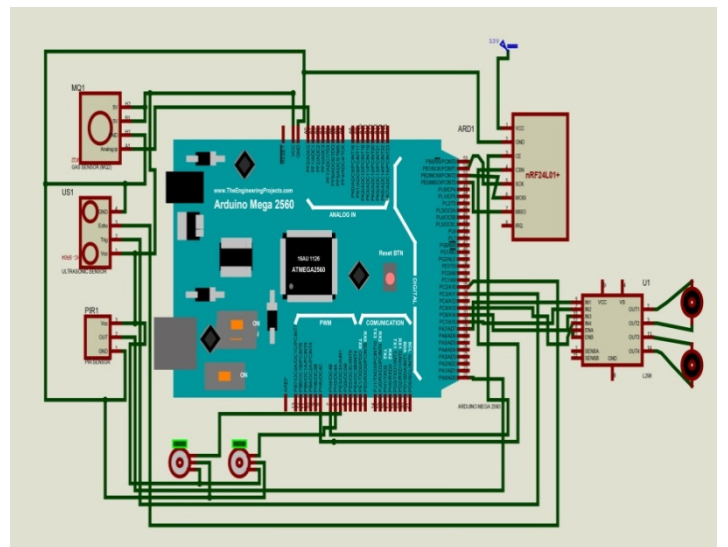


Fig. 4: Circuit Diagram of Robot

## B. System Operation

Human body radiates infrared waves with wavelengths of 8 to 12 micrometers [2]. When the PIR Sensor detects any signal, it sends the response to the rescue team through the RF transceivers. The IP camera in the Robot is used to observe the situation from a dedicated Computer or mobile terminal to help rescue team to find survivors in the disaster effected area. The IP camera is only turn on after human's presence detection by PIR sensors. It will reduce power consumption of the robotic system. The IP camera video feed can be send via WIFI technology or Cellular data. The IP camera on the robot can be rotated 360° by a servo for getting 360° vision of the disaster affected area. The robot is controlled by joystick and RF module attach with the controller. Besides that, ultrasonic sensor is integrated in the robot to detect obstacles on robotic movement. Moreover, the robot has also incorporated gas sensor to detect any major gas leak in the building and it can also detect the carbon monoxide level in the building. The data is send to the rescue team through RF transceivers for different safety measures.

## III. SYSTEM FLOWCHART

Fig.5 shows the flow chart of the developed system. First, the robo-car will check for navigation instruction from the controller. The position of the joystick will determine the driving path of the robo-car which will send through RF transceiver. Depending on the position of joystick, the robo-car can move five different directions "Forward", "Backward", "Right", "Left", "Stop". After that, it will check PIR and gas sensor value. The output of PIR sensor is digital and it will send to controller terminal using RF transceiver. Human presence will be detected by PIR sensor if the value of the sensor is high. After human presence detection by PIR sensor, IP camera will be checked for confirmation. The location and information about the person will send to the recue team after confirmation of detection. After that, PIR sensor will search again for human presence. In parallel with PIR sensor, Gas level will be detected by gas sensor. The gas sensor is an analog gas sensor. The data of sensors will be transmitted by the transceiver to controller for processing the data. Led will keep blinking if LPG and CO level is higher in the air

## IV. HARDWARE IMPLIMENTATION

The robot has two sections one is controller and another is the robot itself. The microcontroller is programmed using programming language C and ARDUINO IDE. ARDUINO IDE has many features which makes it easy to program and compile any arduino based program.

The controller has a microcontroller, a joystick, a buzzer, five LEDs and a RF transceivers module which are aliened according

to Fig.2. Fig.6 shows the physical appearance of the controller. Besides that, there is a computer terminal shown in Fig.7 in the controller section to watch the video feed from the robot. The robot has a PIR sensor, an ultrasonic sensor, a gas sensor, four dc motor, a dc motor driver, a RF

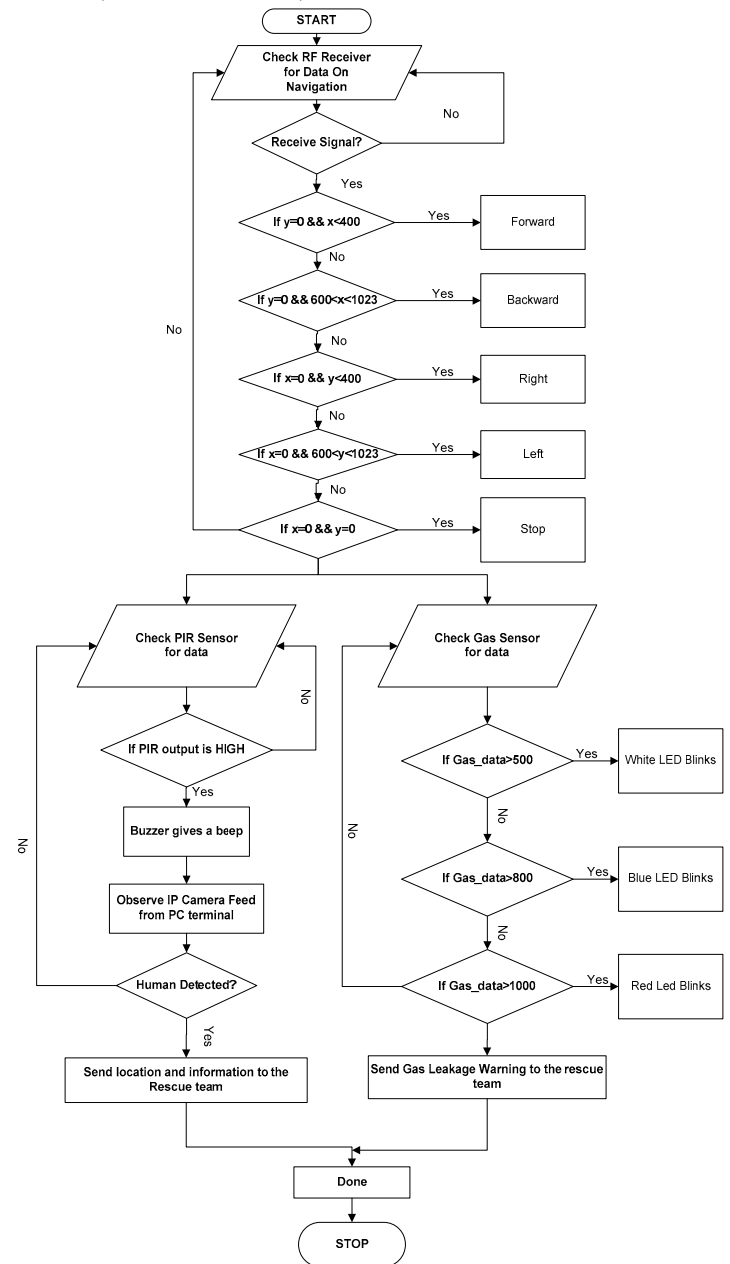


Fig.5: Flowchart of the system

transceiver and an IP camera. The robot is assembled according to the circuit diagram shown in Fig.4. The robot is assembled by adding individual module with the breadboard. All the components except IP camera is interfaced with the microcontroller. The IP camera is attached with a servo motor to

control a movement of 360 degree. Fig.8 shows the physical appearance of the robot.

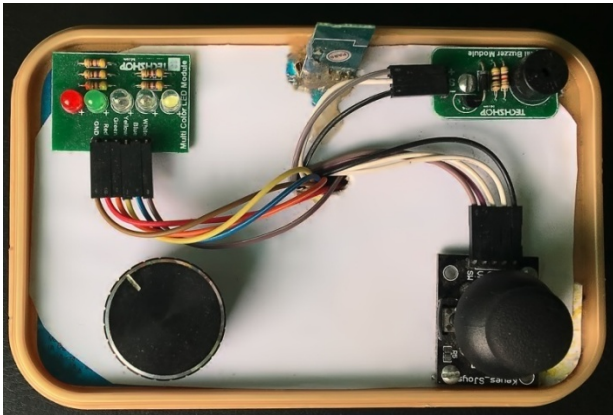


Fig.6: Hardware implementation of Controller of the Robot

the system is well functioning and can easily navigate through narrow path.

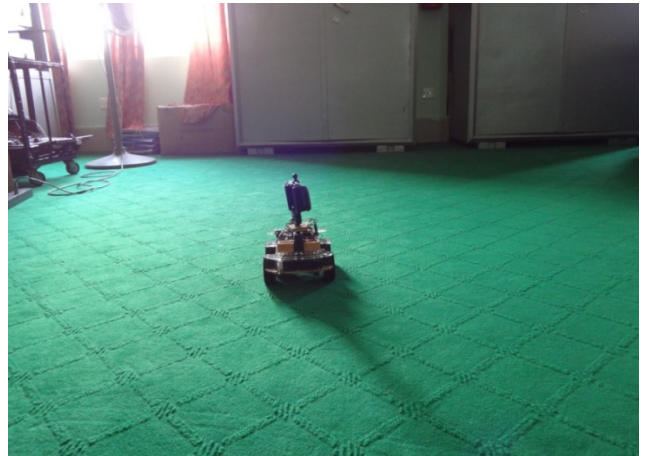


Fig.9: Navigating and searching for human in a room

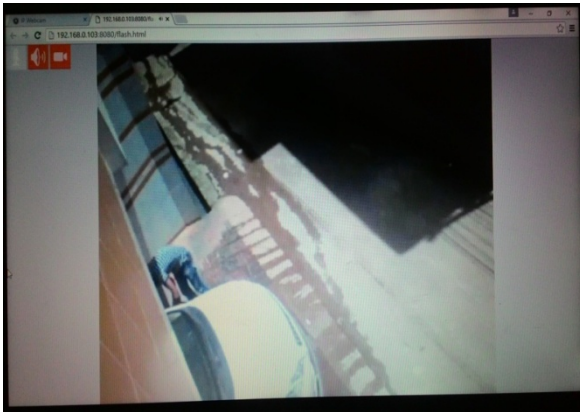


Fig. 7: Computer Terminal for Observing IP camera Video feed



Fig.10: Navigating through narrow path inside a room

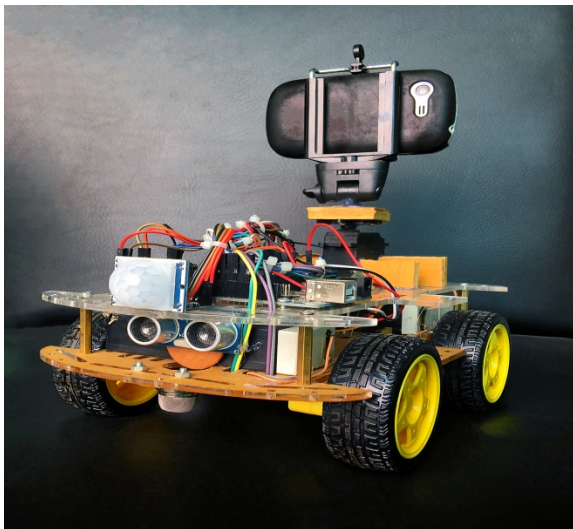


Fig.8: Hardware implementation of Robot

The system is tested for confirming the basic functions and ability of the robot. Those experiments are performed in a realistic training scenario. From Fig.9 and Fig.10, it is clear that

## V. CONCLUSION

The goal of this paper is to provide a low cost human detection robot for developing countries rescue mission in extreme situation. The developed robot is joystick control which will facilitate user to drive the system easily. RF module is used for data transfer to make the system reliable inside the disaster area. Though there are many Urban Search and Rescue (USAR) rescue robot available with many sensors and features but they are very costly. The sensors used in this project are cheap and easily available and reliable. The authors developed a system with two level of human sensing in order to reduce power consumption and get higher efficiency in rescue operation. The first level is a PIR sensor which detect human by their radiated infrared wave and second level is an IP camera to confirm the existence of human in disaster affected area. Because of the two levels human detection system the system is reliable for rescue missions.

## REFERENCES

- [1] <http://spectrum.ieee.org/automaton/robotics/industrial-robots/japan-earthquake-robots-help-search-for-survivors>
- [2] <http://crasar.org/2013/09/11/september-11-11-years-after-the-first-use-of-rescue-robots/>
- [3] S. Bhatia ,Raj Kumar Goel and N. Kumar “Alive human body detection system using an autonomous mobile rescue robot” India Conference (INDICON), December 2011.
- [4] Shuddha Chowdhur ,Mahmud Rafiq “A Proposal of User Friendly Alive Human Detection Robot to Tackle Crisis Situation” 12th International Conference on Control, Automation and Systems, Oct. 17-21, 2012 in ICC, Jeju Island, Korea.
- [5] Burion, Steve (2004), Casper, J. (2002), Amerada, Yams, Igarashit, & Matsunos, (2004) and Cappello, C., etal (2005) “Human Detection for Robotic Urban Search and Rescue” Carnegie Mellon University, Institute of Production Robotique (IPR) LSRO2 –VRAI-Group, Microtechnique, February 2004.
- [6] Raymond Sheh and David Mees “Human-System Interaction for Bomb Squad Applications: Preliminary Experiments with Low Cost Cameras in Real World Deployment” IEEE International Symposium on Safety, Security, and Rescue Robotics (SSRR),18-20 Oct. 2015.
- [7] Carlos Marques, Pedro Lima, Rodrigo Ventura “Semi autonomous robot for rescue operations” Proceedings of the 2006 IEEE/RSJ International Conference on Intelligent Robots and Systems, October 9 - 15, 2006, Beijing, China.

# Analysis of Charge-Shared Matchline Sensing Schemes and Current Race Scheme in High-Speed Ternary Content Addressable Memory (TCAM)

Raqqib Bin Kadir, Ahmed Selim Anwar and Muntasim-Ul-Haque  
Department of Electrical and Electronic Engineering,  
Islamic University of Technology,  
Board Bazar, Gazipur 1704, Bangladesh.

**Abstract**—Due to emerging of hi-speed communication larger TCAMs with higher speed is needed. A comparative analysis of different Matchline sensing schemes in high speed Ternary content addressable memory (TCAM) is presented in this paper. With the conventional current race scheme, two different methods of charge sharing matchline sensing schemes are being analyzed. The power is distributed along the matchline by dividing it and sharing charge. This two charge shared schemes also improve search time and voltage margin. Simulations are performed using 180nm 1.8V CMOS logic in HSPICE.

**Keywords**—content-addressable memory; charge sharing; energy consumption; search time; sensing scheme; current race, voltage margin

## I. INTRODUCTION

**CONTENT-ADDRESSABLE memory (CAM)** is a high speed memory which allows an input search data to be searched in entire memory and return the address of the data in a single clock cycle [1]. For its impeccable search speed, it is widely used in network router where high speed data forwarding is necessary [2]. An ordinary binary CAM can perform searching operation but Ternary Content Addressable Memory (TCAM) has the advantage of having don't care bits which makes the search operation more efficient specially while longest-prefix-match searches in routing tables[3]–[4]. Due to the rapid growth of data transfers the word sizes are getting larger which in turns reduces the search time because of larger matchline capacitances and also increased amount of matchline sensing amplifiers between the matchlines are increasing the power consumption to greater extent. Therefore, low-energy high-performance designs are needed, that improve the search speed of TCAMs without increasing their power consumption. Several methods [5]–[8] have been developed to reduce the power consumption in TCAMs. However in all those methods power in the matchline is distributed uniformly independent of match or mismatch.

In this paper, we divide the matchline into segments in two different ways rather distribute charge uniformly so that the charge can be shared by the matchlines from segments and

then we compare performance with traditional current race scheme.

## II. TCAM BASICS

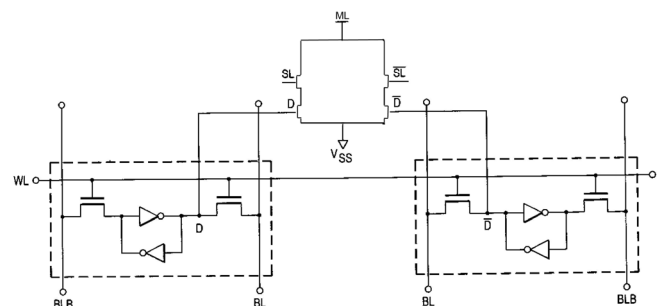


Fig. 1. TCAM cell

A typical TCAM cell consists of two SRAMs, where the data are stored and read while comparing with the searched data. The core cells may be different depending on number of transistors and performance priorities. Typically, core cells available are 9-T, 10-T and 16-T structures [9]. The matchline structures can be of different variants. [4]. The READ and WRITE operation are carried out using the Bit Lines (BLs) and Word Lines (WL). The data to be searched are supplied to the Search Lines (SLs) and the data word is connected to the Match Line (ML). Therefore, when there is a match, the Match line (ML) goes HIGH. Otherwise, the ML is pulled down to the ground. The HIGH is sensed by the Match Line Sensing Amplifiers (MLSAs). The MLSAs can be different according to the scheme chosen for the operation. For our simulation purpose we have used 10-T NAND type structure.

## III. CURRENT-RACE SCHEME

Current Race (CR) Scheme is one of the most used match line sensing schemes. It was introduced to reduce the amount of power used by Match - Line (ML). It is used to get better performance over the usual pre-charge high scheme. This

scheme is considered as a separate class of sensing scheme, nowadays. CR is used widely since it is a pre-charge low scheme. It pre-discharges all the MLs to low, not the other way around, e.g. charging them to high. All the MLs are charged to high while MLs are being evaluated. We use NOR cells, and for that, when there is match, the matched MLs are charged up quickly to high voltage, and when there is a mismatch, the mismatched MLs have low voltage as there is no discharging paths. Fig. 2 shows the CR scheme.

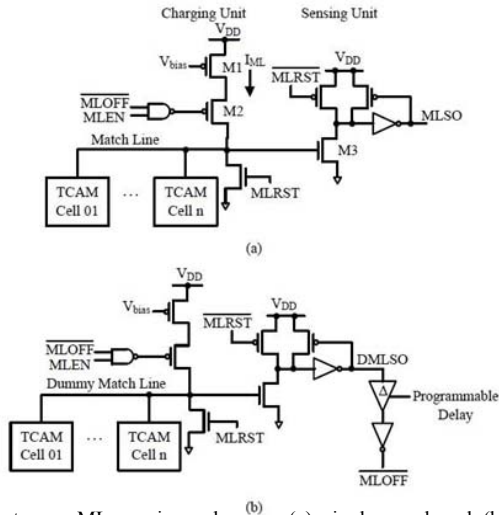


Fig. 2. Current race ML sensing scheme - (a) single word and (b) using dummy (replica) word

Match-Line Sensing Amplifiers (MLSA) have two units: the charging unit and the sensing unit. We set any voltage of ML ( $V_{ML}$ ) and outputs (MLSOs and DMLSO) by using MLRST. Then the transistor M2 is turned on by enabling MLEN signal which causes  $I_{ML}$  current flowing. The Match-Line capacitance ( $C_{ML}$ ) starts charging. If the word matches, then the ML gets charged up to the threshold voltage of M3 transistor which makes it turn on. Thus, MLSO becomes high. Otherwise If the word miss matches then M3 remains off and MLSO remains null. The dummy word never miss matches and so MLSA always gives high output. MLOFF turns off the M2 transistors in all words. DMLSO signal is created by delaying and inverting MLOFF. By turning off the M2 transistors in all word segments, unnecessary charging is stopped and so power consumption of the MLs remains low. The dummy word also minimizes the effects of process variations since it is situated close to the usual words and process variations are same as those words. When the dummy word finds the match, the programmable delay DMLSO confirms that all the MLs can get sufficient amount of time to get charged up until it reaches threshold voltage of M3 transistors.  $V_{bias}$  controls  $I_{ML}$  that controls the speed and also energy consumption of detection process. Parasitic capacitance ( $C_{ML}$ ) of MLs depends on data stored and also search data. As different cells have different stored data so  $C_{ML}$  will vary from ML to ML. As bits to be searched are same along a column,  $C_{ML}$  is same for all MLs in a search. This ensures precise matching between MLs and reduces sensing error which is caused by variation of capacitance.

#### IV. CHARGE SHARED MATCH LINE SENSING SCHEME WITH 2 BLOCKS (FOUR SEGMENTATION)

In this technique the ML is divided into 4 segments. It precharges two segments (segment 1 & 4) to  $V_{DD}$  while in operation. Signal CS is kept low so that the charge is not shared. In the 2nd phase, SLs are provided with search data, so, CS gates are made open. If the two segments in a block fully matches, it keeps its voltage; otherwise mismatch causes the ML voltages to discharge to ground. The match sensor block combines the result of two blocks and give away the final match result. The main advantage is that the voltage remaining in the previous cycle has the opportunity to be reused in this technique. Therefore, it reduces power dissipation while retaining its speed.

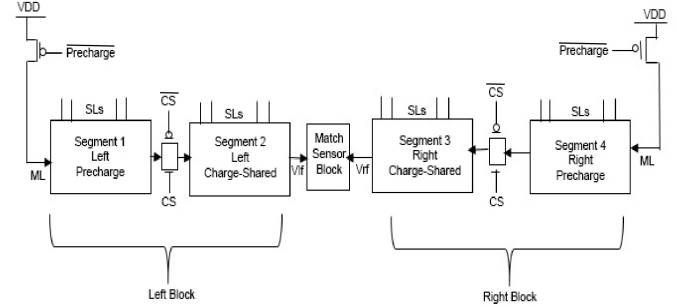


Fig. 3. Charge shared ML sensing proposed scheme.

#### V. CHARGE SHARED MATCHLINE SENSING SCHEME WITH SELECTIVE PRECHARGE AND REPLICA CONTROL

In this scheme two ML segments are used, where ML segment 1 is greater than ML segment 2. All the MLs and MLSA outputs discharge to the ground before starting the search operation. After starting the search operation the MLEN signal starts charging and match with the search keys. If only there is a match, ML segment 1 enables the sensing unit to produce high MLSO1. So the second segment can get charged up by sharing charge from transistor M1 by the pass transistor M2. Segment 2 is then compared with the remaining portion of search keys. If there is a match, then output logic will be high and in case there is mismatch the output voltage will gets low.

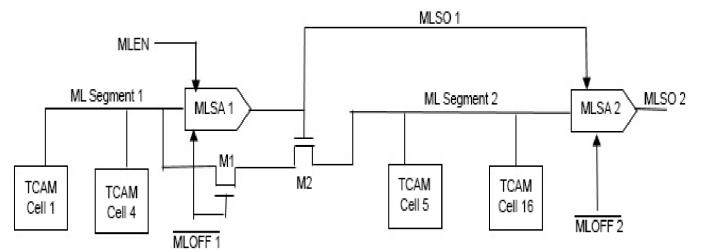


Fig. 4. ML sensing scheme using charge sharing one word of TCAM array.

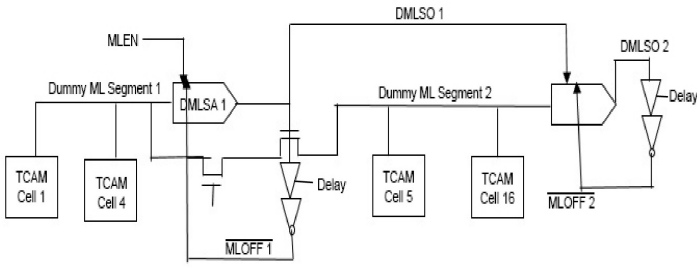


Fig. 5. ML sensing method using charge shared between dummy words

In case of dummy words, they are always matched due to local masking. When DMLSO1 becomes high as they are matched, the charging of 1<sup>st</sup> segments are stopped by MLOFF1. This makes the charge sharing between the two segments stop. This scheme is actually a combination of charge sharing and current race techniques using selective precharge.

## VI. SIMULATION RESULTS AND ANALYSIS

The simulation presented here are done each with 32 bit 16x16 array of TCAM and the graphs were viewed in COSMOSCOPE. Our main objective was to visualize the search time that is the delay between the initializing signal (Precharge or Matchline reset signal) and output of matchline sensing amplifier. We also gained voltage margin (difference in 1bit mismatching maximum voltage and crossing of matchline result with matched matchline voltage) for comparing overall performance.

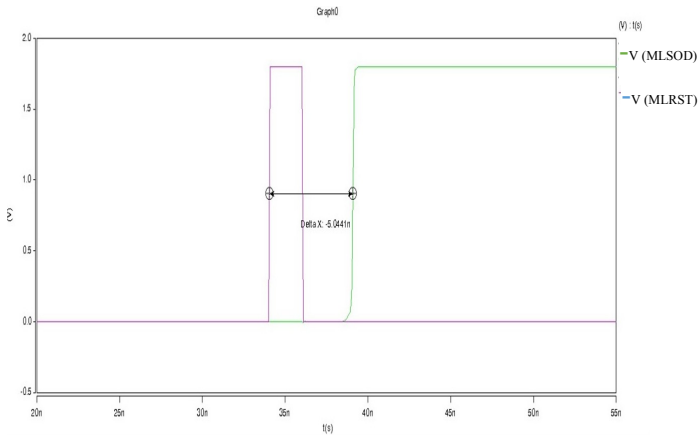


Fig. 6. Search time for current race scheme.

Fig. 6 shows the search time for current race scheme where we view the difference (5.0441 ns) between the initial MLRST signal and final output DMLSO signal. In case of voltage margin (Fig.6) we find the difference between maximum voltage of the matchline  $V_{ML}=0.030595V$  and crossing ( $V=1.095V$ ) of output matchline voltage (DMLSO) with the mismatched voltage. Therefore the voltage margin is  $(1.095-0.030595)=1.64405V$

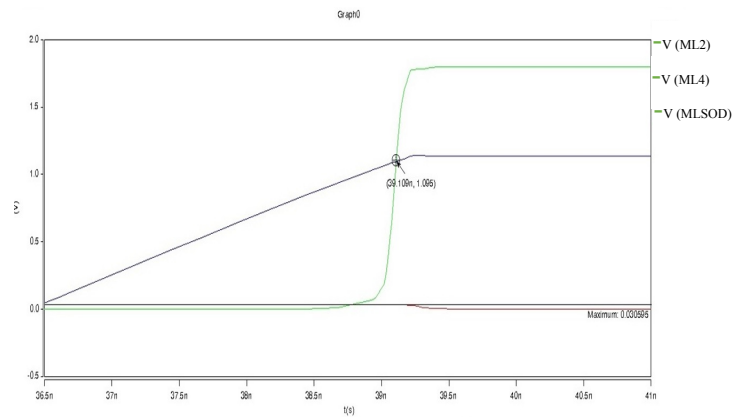


Fig. 7. Voltage margin for current race scheme.

For charge shared match line sensing scheme with 4 segments (Fig.7) search time is difference between precharge (PREB) signal and final match result.

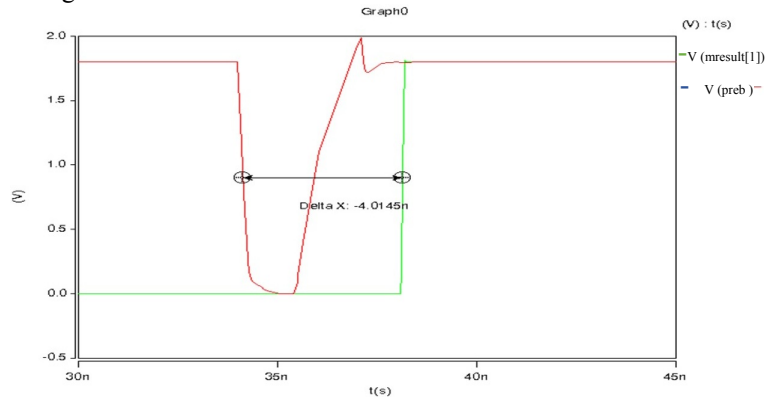


Fig. 8. Search time for charge shared matchline sensing scheme with 4 segmentation.

For measuring voltage margin we have considered two cases depending on mismatch occurring in different blocks. Fig.8 shows voltage margin for mismatch in left block while Fig.9 depicts mismatch in right block. In both cases we measured the difference between maximum voltage and crossing of final output with mismatched ML voltage. For mismatch in left block voltage margin (0.25157 V) is lesser than voltage margin (0.76002 V) due to mismatch in right block because of ML capacitance.

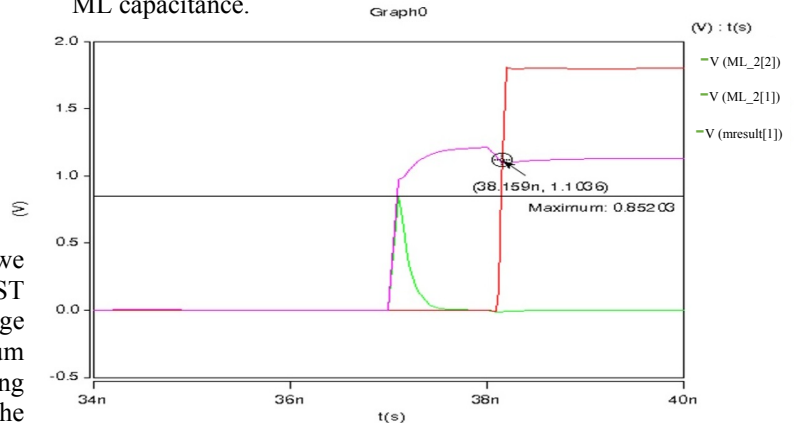


Fig. 9. Voltage margin for charge shared matchline sensing scheme with 4 segmentation (mismatch in left block).



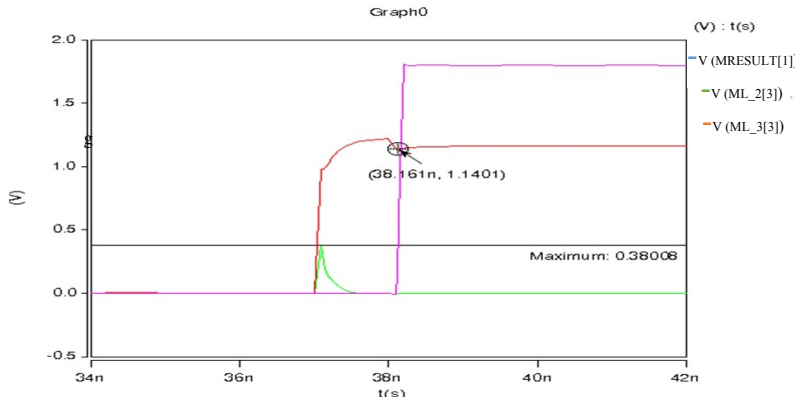


Fig. 10. Voltage margin for charge shared matchline sensing scheme with 4 segmentation (mismatch in left block).

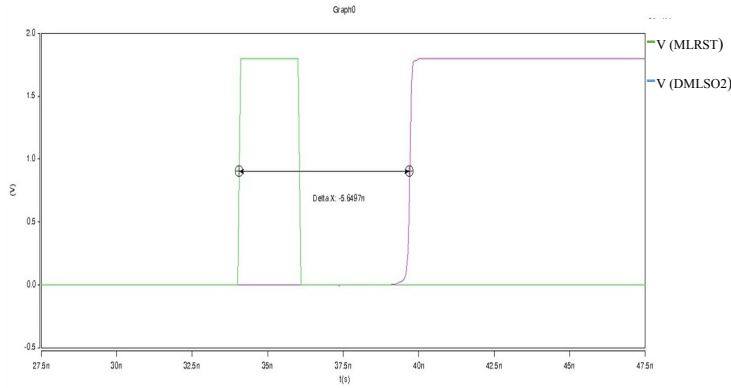


Fig. 11. Search time for charge shared matchline sensing scheme with selective precharge and replica control.

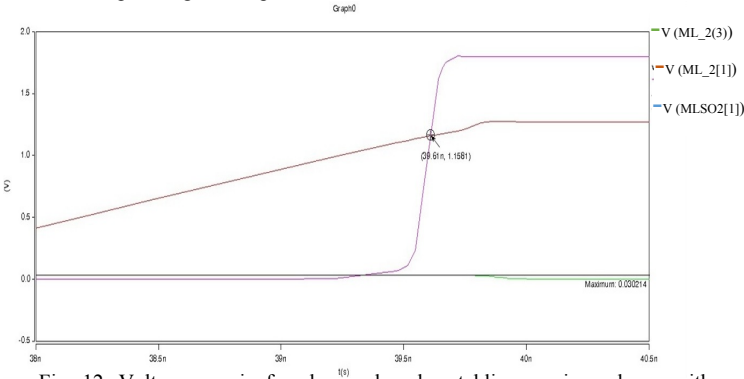


Fig. 12. Voltage margin for charge shared matchline sensing scheme with selective precharge and replica control (mismatch in 1st segment).

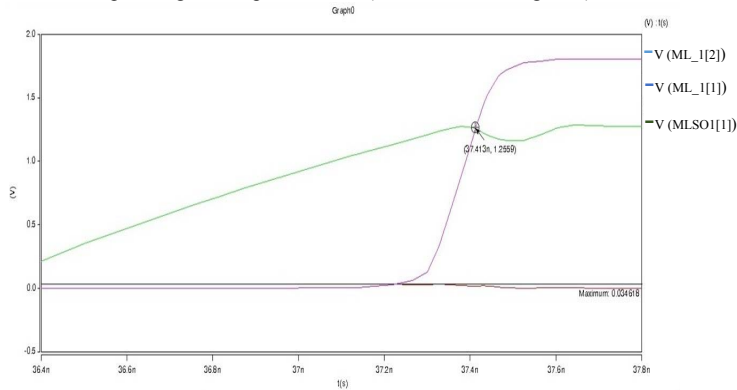


Fig. 13. Voltage margin for charge shared matchline sensing scheme with selective precharge and replica control (mismatch in 2nd segment).

For measuring voltage margin we considered similar cases as previous scheme. If there is mismatch in 1<sup>st</sup> segment, voltage margin nothing but the difference between maximum voltage of matched ML and crossing of matchline sensing amplifier's output with mismatched ML (Fig.11). In case of mismatch in 2<sup>nd</sup> segment (Fig.12) voltage margin is calculated same as before but the matchline sensing amplifier will be different in this case

TABLE I  
PERFORMANCE COMPARISON OF DIFFERENT MATCHLINE SENSING SCHEMES FROM SIMULATION RESULTS

Current Race Matchline Sensing Scheme		Charged Shared Matchline Sensing Scheme			
Search time	5.0441	Segmentation into 2 Blocks (4 Segments)		Selective Precharge and Replica Control	
		4.0145		5.6497	
Voltage margin	1.064405	Mismatch in Left Block	Mismatch in Right Block	Mismatch in 1st Segment	Mismatch in 2nd Segment
		0.25157	0.76002	1.127786	1.2212

## VII. CONCLUSION

The matchline (ML) consumes most of the power while searching. To decrease the amount of power consumption, we have segmented the ML in two different ways. The main advantage of Charge shared matchline sensing scheme with 4 segments is that it divides the ML in 4 parts. So any charge remaining in most recent search can be reused to save power and also as we see the search time is considerably low than other schemes. While in charge shared method with selective precharge and Replica control scheme the performance is degraded to some extent from segmented schemes but it reduces power consumption to a great extent [10].

## REFERENCES

- [1] L. Chisvin and R. J. Duckworth, "Content-addressable and associative memory: alternatives to the ubiquitous RAM," *IEEE Computer*, vol. 22, no.7, pp. 51–64, Jul. 1989.
- [2] H. J. Chao, "Next generation routers," in *Proc. IEEE*, Sep. 2002, vol. 90, no. 9, pp. 1518–1558.
- [3] M. Kobayashi, T. Murase, and A. Kuriyama, "A longest prefix match search engine for multi-gigabit IP processing," in *Proc. IEEE Int. Conf. Communications*, vol. 3, June 2000, pp. 1360–1364.
- [4] K. Pagiamtzis, A. Sheikholeslami, "Content-addressable memory (CAM) circuits and architectures: A tutorial and survey," in *IEEE JOURNAL OF SOLID-STATE CIRCUITS*, VOL. 41, NO. 3, pp. 712–727, March 2006
- [5] H. Miyatake, M. Tanaka, and Y. Mori, "A design for high-speed lowpower CMOS fully parallel content-addressable memory macros," *IEEE J. Solid-State Circuits*, vol. 36, pp. 956–968, June 2001.
- [6] I. Arsovski, T. Chandler, and A. Sheikholeslami, "A ternary content addressable memory (TCAM) based on 4T static storage and including a current-race sensing scheme," *IEEE J. Solid-State Circuits*, vol. 38, pp. 155–158, Jan. 2003.
- [7] G. Thirugnanam, N. Vijaykrishnan, and M. J. Irwin, "A novel low power CAM design," in *ASIC/SOC Conf. Proc.*, 2001, pp. 198–202.
- [8] Y. L. Hsiao, D. H. Wang, and C. W. Jen, "Power modeling and low-power design of content addressable memories," in *Proc. IEEE Int. Symp. Circuits and Systems*, vol. 4, 2001, pp. 926–929.
- [9] K. J. Schultz, "Content-addressable memory core cells: a survey," *Integration, VLSI J.*, vol. 23, no. 2, pp. 171–188, Nov. 1997.
- [10] I. Nitin Mohan, and Manoj Sachdev, "Low-Capacitance and Charge-Shared Match Lines for Low-Energy High-Performance TCAM," *IEEE J. Solid-State Circuits*, vol. 42, pp.2054–2060, sept. 2007.

# Switching Signal Reduction of Load Aggregator with Optimal Dispatch of Electric Vehicle Performing V2G Regulation Service

M. Shafiul Alam<sup>1\*</sup>, Md Shafiullah<sup>2</sup>, Md Juel Rana<sup>3</sup>, M. S. Javaid<sup>4</sup>, Usama Bin Irshad<sup>5</sup> and Muhammad Athar Uddin<sup>6</sup>

<sup>1-5</sup>Dept. of EE, King Fahd University of Petroleum and Minerals Dhahran, Saudi Arabia

<sup>6</sup>Dept. of EEE, International Islamic University Chittagong, Bangladesh

\*shafiul@kfupm.edu.sa

**Abstract**—Environmental concerns over the production of greenhouse gas have led to the development of environmental friendly transportation such as electric vehicle (EV). As the number of EVs is increasing day by day, it will have a great impact on grid operation and electricity market. Significant amount of EV charging during peak hour will cause branch congestions and low voltage. Moreover, high penetration of EVs plays an important role in altering electricity price. Thus, optimal scheduling of EVs charging is inevitable from the perspective of both system reliability and market. Load aggregators can combine the capacities of many EVs to participate in wholesale energy market. In this paper, optimal dispatch algorithm of EVs is developed and tested on a system consisting 1000 EVs. The advantage of the algorithm is that it requires less number of communication signals and less expensive infrastructure. EVs are turned on and turned off in binary fashion based on priority to follow the regulation signal.

**Index Terms**— Dispatch algorithm; Electric vehicle; Greenhouse gas; Load aggregator; Regulation up; Regulation down; Switching signal.

## I. INTRODUCTION

In many recent works, several techniques have been proposed for scheduling EVs. In [1], discrete dispatch algorithm for EVs has been proposed to perform frequency regulation. In this work, regulation signal is discretized into increments that can be met by turning on and off of different EVs based on priority. Coordination algorithm for managing the EVs charging has been proposed in [2] and compared with an uncoordinated strategy. Heuristic technique dispatches EVs at each time interval separately and optimization technique dispatches EVs at all the time intervals. Controlling load with Plug-in Hybrid Electric Vehicle (PHEVs) can solve peak charging load demand due to large scale PHEVs charging as well as PHEV can be treated as mobile energy storage device which can provide ancillary services such as regulation, load shifting, emergency security, and spinning reserve with their optimal charging strategies [3-4]. An algorithm for unidirectional regulation has been developed

and aggregator profit maximizing set point selection has been formulated with constraints that are analogous to conditions in the smart charging algorithms [4]. A new algorithm for economic dispatch of plug-in electric vehicles (PEVs) is proposed in [5] considering uncertainties both in PEV and wind power. The algorithm is based on the integration of interior point method and particle swarm optimization (PSO). Generation cost of wind power and V2G power is derived analytically. The authors assume that each type of PEVs has specific charging period and it follows uniform charging pattern within that specified time. The main drawback of the proposed algorithm is that it will give uncertain profit if the mentioned assumptions do not hold. Y. Weifeng *et. al.* [6] have presented a hierarchical and zonal architecture for dispatching PEVs. The authors establish upper-level and lower-level model in their decomposition approach. The goal of upper-level decomposition is to minimize system operation cost through proper dispatch of generators and PEVs while the objective of the lower-level is to strictly follow the dispatching instructions from the upper-level through designing of appropriate charging and discharging strategies of each PEVs for the specified period. Risk of load mismatch between forecast and actual EVs load and charging cost reduction algorithm have been proposed in [7]. Non-convex of risk-aware day-ahead has been converted to convex one by using hidden convex structure which can be remodeled as two state stochastic linear program. Integration of PEVs and renewable energy resources (REV) has been studied [8] for energy cost saving and emission reduction through smart vehicle charges strategy. Simulation has been performed with real Spanish power system with a detailed hydro-thermal unit commitment (UC) model for energy and reserve. In [9], X. Xiaomin and S. Ramteen presented decentralized PEVs charging control. The technique conveys price and quantity to the load aggregator and compares to price only method and it shows superiority over price only scheme. Moreover, this method does not depend on regularization term to warrant convergence. The drawback of the proposed technique is that it is not as easy implementable as centralized technique. A multilevel architecture for bidirectional vehicle to grid regulation is proposed through appropriate

coordination of charging and discharging of electric vehicle [10]. To guarantee adequate charging of EVs, scheduling problem is formulated as convex optimization problem. The drawback is that proposed techniques does not consider centralized algorithm [11].

Continuous switching of load has great negative impact on system stability [12-13]. However, high penetration levels of renewable energy sources and microgrid flexibility offer more opportunities for the interaction between EVs and microgrid and increase system stability. EVs and battery swapping station (BSS) can mitigate load variability and improve microgrid economics also system reliability can be improved utilizing the advantage of V2G technology [14]–[18] through proper optimization approach in the day-ahead energy market. A couple of literatures [19]-[22] discussed promising strategies for energy management through optimized operation of EVs considering the impact of EVs’ deep penetration on the electric grid with utilization of price-incentive model.

Section II provides a brief description regulation service that can be provided by EVs. Dispatch algorithm for EVs for switching signal reduction is presented in Section III. Simulation result and discussion is presented in section IV. Section V presents the conclusion of this work. References are included at the end of this paper.

## II. REGULATION SERVICE

Energy and ancillary services from an electric vehicle (EV) to the grid is an important service to control the frequency of the system. With variation of load in the system frequency goes up and down continuously. This frequency can be controlled by controlling generation. Another mean of controlling frequency is demand response. Load aggregator can combine the capacity of many EVs to provide regulation service of to the system. Numerous studies have revealed that frequency regulation is the utmost valued facility that can be provided by an EV.

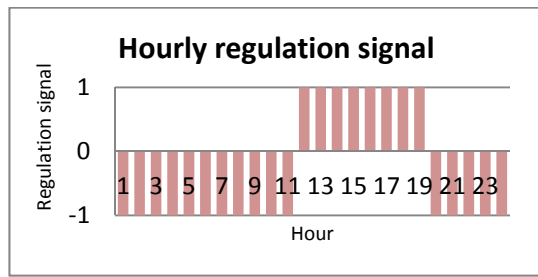


Fig. 1 Typical hourly regulation signal for 24 hours

Fig. 1 shows a typical regulation signal form the system operator. To follow this regulation signal, load aggregator need to turn on and turn off the electric vehicle. When regulation up signal is passed from the system operator, some EVs are turned off by the system operator to provide regulation service. On the

other hand, when regulation signal is negative, load aggregator turns on more EVs in addition to the existing EVs to provide frequency regulation to the system.

## III. OPTIMAL DISPATCH ALGORITHM

Load aggregator combines the preferred operating point (POP) of all EVs and then provides regulation service to the system by growing and decaying their charging around POP [16]. One major problem with such dispatch algorithm is that dispatch signal need to be directed to the all EVs to follow regulation signal and eventually it increases the number of signal. The number of signal can be reduced by turning on and off EVs in a binary fashion. This can be achieved by discrete dispatch algorithm as described in the following steps.

**Step1:** Calculation of POP and expected energy

**Step2:** Computation of percentage dispatch and percentage error of each dispatch.

**Step3:** Priority based “turn on” list and “turn off” list preparation to meet aggregated POP

**Step4:** Finding number of EVs (NEV) to track regulation signal

**Step5:** Calculation of difference of EV (DEV) between “turn on” list and NEV

**Step6:** If DEV is positive, transfer DEV from the lowermost of ‘turn off’ to the lowermost of ‘turn on’ list. If DEV is negative, move DEV from the upper of ‘turn on’ list to the upper of ‘turn off’ list.

**Step7:** Stop, if scheduling period is over. Otherwise, go to step4.

To test the above algorithm load data has been collected from ISO New England market. The algorithm starts with the calculation of POP of all EVs. POP can be calculated based on load, price, and maximum regulation participation. In this work, load based POP calculation has been used which is given as follows.

$$POP_i(t) = \frac{Mx_L - P(t)}{Mx_L - Mn_L} MP_i$$

Where, P(t) is the load at time t.

MxL is the maximum load over the given period.

MnL is the minimum load over the given period.

MP<sub>i</sub> is the maximum power drawn by an EV when it is turn on.

Expected energy at period t is calculated using following equation.

$$ExE_i = POP_i(t) - RegUP_i(t) * Ex_U + RegDOWN_i(t) * Ex_D$$

Where, RegUP<sub>i</sub>(t) is the regulation up capability of i<sup>th</sup> EV at

at period  $t$ .

$RegDOWN_i(t)$  is the regulation down capability of  $i^{th}$  EV at period  $t$ .

$Ex_U$  is the anticipated up dispatch

$Ex_D$  is the anticipated down dispatch

From the expected energy, percentage dispatch of each EV is calculated from the following equation.

$$DispatPer_i = \frac{\text{Expected Energy of } i\text{th EV at period } t}{\text{Total Energy of all EVs for the whole period}}$$

Then percentage error for each EV is calculated and based on error, urgency based turn on as well as turn off list is prepared so as to decrease the fast changing of the EVs while they are connected for charging.

Then, the regulation signal provided by the system operator is added to POP to get energy which is shown in the following equation.

$$Ener_R(t) = POP(t) + RS(t)$$

Finally, the number of electric vehicles (EVs) to track the regulation signal is calculated from the following equation.

$$Num_{EV} = Ener_R(t)/MP$$

After calculating the number of necessary EVs, it is subtracted from the number of turn off list. If the result is negative number (-N), then N number of EVs from the upper of turn on list is relocated to the upper of turn off list. On the other hand, if result in positive number (N), then N number of EVs from the end of turn off list is moved to end of turn on list.

#### IV. RESULT AND DISCUSSION

The algorithm has been coded in MATLAB. To test the algorithm following regulation signal has been considered over a 24 hour period.

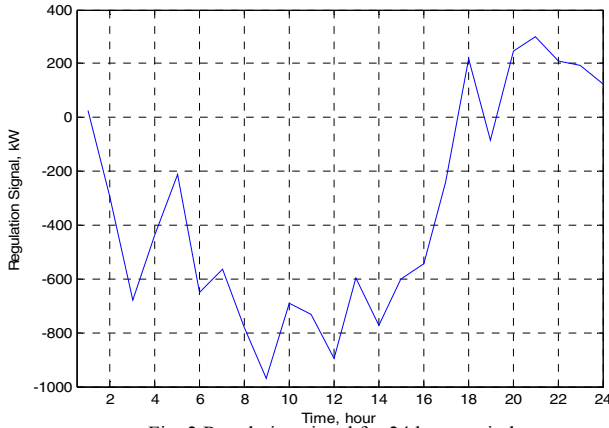


Fig. 2 Regulation signal for 24 hour period

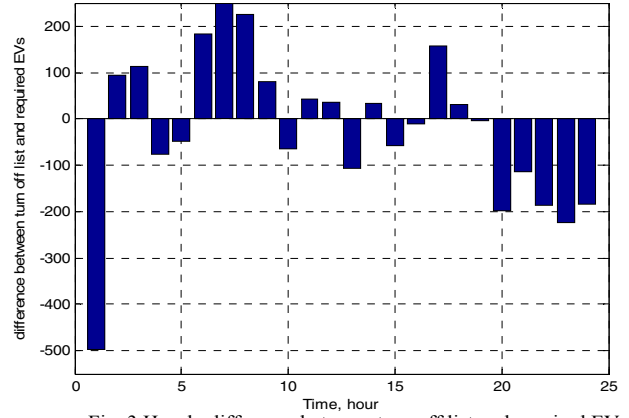


Fig. 3 Hourly difference between turn off list and required EVs.

Based on the difference between turn off list and the number of required EVs to track regulation signal, EVs are turned on or turned off as shown in Fig. 3.

Turn on and off states of EV1 and EV2 are shown in Fig. 4 and 5 respectively. In Fig. 4, we see that only 10 switching signals are required over a 24 hour period for EV1. On the other hand, incremental dispatch algorithm requires 24 signals. Thus, discrete dispatch algorithm reduces the number of switching signal for each new regulation signal.

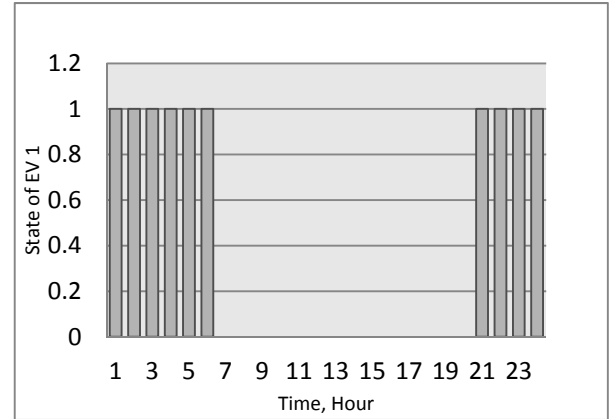


Fig. 4 Turn on and turn off states of EV 1 for 24 Hours

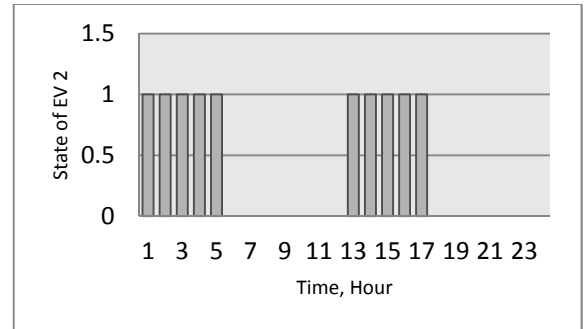


Fig. 5 Turn on and turn off states of EV 2 for 24 Hours

From table I, total number of switching signal required for discrete dispatch algorithm is 3066; this number increases to 24000 for incremental dispatch algorithm.

TABLE I: SUMMARY OF OFF AND ON LIST OVER 24 HOUR PERIOD

Difference between turn off list and required EVs	Number of EVs in turn off list	Number of EVs in turn on list
-498	998	2
95	903	97
112	791	209
-77	868	132
-49	917	83
183	734	266
297	437	563
226	211	789
81	130	870
-64	194	806
42	152	848
37	115	885
-107	222	778
33	189	811
-58	247	753
-10	257	743
158	99	901
32	67	933
-3	70	930
-197	267	733
-114	381	619
-186	567	433
-224	791	209
-183	974	26

## V. CONCLUSION

In this work, discrete dispatch algorithm for EVs has been tested. Algorithm has been coded in MATLAB. EVs are turned on and turned off in binary fashion for each new regulation signal to provide regulation service to the electric grid. Simulation has been performed for 24 hours for a system consisting 1000 EVs. It has been shown that this algorithm reduces the number of switching signal compared to incremental dispatch algorithm. In discrete algorithm, switching signal is sent to those EVs which are going to change state; whereas in incremental dispatch all EVs require switching signal to increase or decrease their charging or discharging around POPs.

## REFERENCES

[1] E. Sortomme and K. Cheung, "Intelligent dispatch of electric vehicles performing vehicle-to-grid regulation," *IEEE International Electric Vehicle Conference*. Greenville, SC, pp. 1–6, 2012.

[2] R. J. Bessa, N. Lima, and M. A. Matos, "Management Algorithms for an EV Aggregator" *8th Mediterranean Conference on Power Generation, Transmission, Distribution and Energy Conversion*, Cagliari, Italy, pp. 1–6, 2012.

[3] S. Han, S. Han and K. Sezaki, "Development of an optimal vehicle-to-grid aggregator for frequency regulation," *IEEE Trans. Smart Grid*, vol. 1, no. 1, pp. 65-72, Jun. 2010.

[4] E. Sortomme and M. A. El-Sharkawi, "Optimal charging strategies for unidirectional vehicle-to-grid," *IEEE Trans. Smart Grid*, vol. 2, no. 1, pp. 131-138, Mar. 2011.

[5] J. Zhao, F. Wen, and Z. Y. Dong, "Optimal dispatch of electric vehicles and wind power using enhanced particle swarm optimization," *IEEE Trans. Ind. Inf.*, vol. 8, no. 4, pp. 889–899, Nov. 2012.

[6] Y. Weifeng, Z. Junhua, W. Fushuan, X. Yusheng, and G. Ledwich, "A Hierarchical Decomposition Approach for Coordinated Dispatch of Plug-in Electric Vehicles," *Power Systems*, IEEE Transactions on, vol. 28, pp. 2768-2778, 2013

[7] L. Yang, J. Zhang, and D. Qian, "Risk-aware Day-ahead Scheduling and Real-time Dispatch for Plug-in Electric Vehicles," *IEEE Global Communications Conference (GLOBECOM)*, Anaheim, CA, Dec. 2012.

[8] J. Villar, C.A. Diaz, P. Gonzalez, F.A Campos, "Wind and solar integration with plug-in electric vehicles smart charging strategies," *IEEE 11th International Conference on the European Energy Market (EEM)*, Krakow, Poland, May 2014.

[9] X. Xiaomin and S. Ramteen, "Using Price-Based Signals to Control Plug-in Electric Vehicle Fleet Charging," *IEEE Trans. Smart Grid*, vol. 5, no. 3, pp. 1451-1464, May. 2014.

[10] L. Junhao, L. Ka-Cheong ; O. K. L. Victor, "Online scheduling for vehicle-to-grid regulation service," *IEEE International Conference on Smart Grid Communications (SmartGridComm)*, Vancouver, BC, 21-24 October, 2013

[11] Q. Kang, J. Wang, M. Zhou A. C. Ammari, "Centralized Charging Strategy and Scheduling Algorithm for Electric Vehicles Under a Battery Swapping Scenario," *IEEE Trans. on Intelligent Transportation Systems*, Vol. 17, No. 3, March 2016

[12] M. S. Alam , A. H. Chowdhury, "Power System Load Switching Monitoring Using Wavelet Transform Based Multiresolution Signal Decomposition," *6th International Conference on Electrical and Computer Engineering*, Dhaka, Bangladesh, December 2010.

[13] M. J. Rana, M. S. Alam, M. S. Islam, "Continuous Wavelet Transform Based Analysis of Low Frequency Oscillation in Power System," *3rd International Conference on Advances in Electrical Engineering*, Dhaka, Bangladesh, 17-19 December, 2015.

[14] D. Dallinger, D. Krampe, and M. Wietschel, "Vehicle-to-grid regulation reserves based on a dynamic simulation of mobility behavior," *IEEE Trans. Smart Grid*, vol. 2, no. 2, pp. 302–313, Jun. 2011

[15] E. Sortomme and M. A. El-Sharkawi, "Optimal scheduling of vehicle-to-grid energy and ancillary services," *IEEE Trans. Smart Grid*, vol. 3, No. 1, pp. 351–359, Mar. 2012.

[16] R. J. Bessa, M. A. Matos, F. J. Soares, and J. A. P. Lopes, "Optimized bidding of a EV aggregation agent in the electricity market," *IEEE Trans. Smart Grid*, vol. 3, no. 1, pp. 443–452, Mar. 2012.

[17] W. Su, H. Rahimi-Eichi, W. Zeng, and M. Chow, "A survey on the electrification of transportation in a smart grid environment," *IEEE Trans. Ind. Inf.*, vol. 8, no. 1, pp. 1–10, Feb. 2012.

[18] Y. Ma, T. Houghton, A. Cruden, and D. Infield, "Modeling the benefits of vehicle-to-grid technology to a power system," *IEEE Trans. Power Syst.*, vol. 27, no. 2, pp. 1012–1020, May 2012.

[19] M. Shafiullah and A. T. Al-Awami, "Maximizing the profit of a load aggregator by optimal scheduling of day ahead load with EVs," *2015 IEEE International Conference on Industrial Technology (ICIT)*. IEEE, pp. 1342–1347, Mar-2015.

[20] Y. Xu, L. Xie, and C. Singh, "Optimal scheduling and operation of load aggregators with electric energy storage facing price and demand uncertainties," *2011 North American Power Symposium*. IEEE, pp. 1–7, Aug-2011.

[21] M. Shafiullah, A. T. Al-Awami, and I. M. ElAmin, "Profit maximization planning of a Load Aggregator using Electric Vehicles through optimal scheduling of day ahead load," *2015 18th International Conference on Intelligent System Application to Power Systems (ISAP)*. IEEE, pp. 1–6, Sep-2015.

[22] J. Zhao, F. Wen, and Z. Y. Dong, "The Energy Management and Optimized Operation of Electric Vehicles Based on Microgrid," *IEEE Trans. Ind. Inf.*, vol. 8, no. 4, pp. 889–899, Nov. 2012.

# Optimal Placement of Phasor Measurement Units for Transmission Grid Observability

Md Shafiullah\*, Md Juel Rana, Md Shafiul Alam

Electrical Engineering Department  
King Fahd University of Petroleum & Minerals  
Dhahran, Saudi Arabia  
\*shafiullah@kfupm.edu.sa

Muhammad Athar Uddin

Department of Electrical & Electronic Engineering  
International Islamic University Chittagong  
Chittagong, Bangladesh  
mau\_iuc@yahoo.com

**Abstract**—Phasor Measurement Unit (PMU) provides both magnitude and phase information of current and voltage signals with appropriate time stamp which is very useful in controlling power system networks in real time. Consequently, PMU is considered as one of the most significant measurement devices for complete observability of the future electricity grids. But placing PMU in every bus of the network is not economically viable. This paper aims to place PMUs in different buses of electric network to ensure full network observability employing five evolutionary, colony and swarm optimization algorithms namely backtracking search algorithm (BSA), differential evolution (DE), artificial bee colony (ABC), particle swarm optimization (PSO) and invasive weed optimization (IWO). The proposed algorithms have been tested on IEEE 14-bus, 30-bus, 39-bus and 57-bus test networks. The obtained results illustrate the compatibility of the proposed schemes in compared to each other as well as in compared to available techniques in literatures.

**Keywords**— Artificial Bee Colony (ABC); Backtracking Search Algorithm (BSA); Differential Evolution (DE); Invasive Weed Optimization (IWO); Optimal PMU Placement(OPP); Particle Swarm Optimization (PSO); Phasor Measurement Unit (PMU); Power System Observability.

## I. INTRODUCTION

Due to the ever increasing demand of electricity and highly competitive electricity market conditions, the modern power system network operates to their maximum capacity; thus susceptible to instability which reduces the reliability. Therefore, it is of utmost importance to estimate the health of the power system through accurate measurements and taking control actions accordingly to prevent blackouts. State estimation is an efficient means in determining the real time states of a power system network[1]. Before the advent of time synchronized measurement technology the state estimation was dependent on traditional measurement systems. The supremacy of PMU measurement system over traditional schemes lies in its ability to provide time synchronized voltage and current measurement with an accuracy of less than  $1\mu\text{s}$  with the help of advanced global positioning systems (GPS) [2]. When PMU is installed on a bus it measures the current phasors of all branches connected to that bus and voltage phasor of that bus. From the measured branch current phasors and branch parameters voltage phasor of adjacent buses can also be computed [3]. The power system is said to be observable when all the system states are observable directly or indirectly. By placing PMU on all buses

the system can be made directly observable. However, it is neither economically viable because of higher cost of PMUs nor possible due to lack of communication facilities in some substations [4]. This situation creates the optimal PMU placement (OPP) problem which can be defined as the placement of lowest number of PMUs without compromising the full observability. Minimum number of PMUs in the system enhances the capability of the state estimators to extract the bad data even in the situation of measurement loss [5].

In order to solve the OPP problem various mathematical and heuristic algorithms have been reported in the literatures. Integer programming has been employed for OPP in [6], numerical methods has been used in [7] for optimal placement of PMUs. In [8] Binary search algorithm was used considering single line outage. The heuristic algorithms are widely used in solving power system optimization problems [9], [10]. The application of these approaches in solving OPP problem can not only examine the observability but also capable of overcoming some drawbacks of conventional techniques like branch outage or PMU failure [11]. The heuristic algorithm employed to realize OPP problem are genetic algorithm [12], simulated annealing [13], binary integer linear programming [14], Convex Programming [15], Tabu search [16], bacterial foraging algorithm [17].

This paper aims to compare five different heuristic and swarm optimization algorithms namely invasive weed optimization (IWO), backtracking search algorithm (BSA), artificial bee colony (ABC), differential evolution (DE) and particle swarm optimization (PSO) to obtain the system observability by installing minimum number of PMUs. The effectiveness of the algorithms has been tested on different IEEE standard test transmission networks.

## II. PHASOR MEASUREMENT UNITS

Phasor measurement unit provides the magnitude and phase angle of alternating voltage or current in the power system. While extracting magnitude and phase information basic PMU assumes pure sinusoidal waveform of alternating current (AC) signals with constant frequency. The instantaneous AC signal is written as  $x(t)$ .

$$x(t) = |X_m| \sin(\omega t + \theta) \quad (1)$$

Where,  $|X_m|$  and  $\theta$  represent the magnitude and phase of the signal respectively. In phasor form the above signal is represented as follows:

$$\vec{X} = |\vec{X}|e^{j\theta}; \text{ Where, } |\vec{X}| = \frac{V_m}{\sqrt{2}} \quad (2)$$

In order to calculate the phase value of a signal at a certain power system bus k the measurement unit must possess the capability for precise measurement of zero crossing instant ( $t_{zck}$ ) of AC signal as well as its reference time ( $T_{zcref}$ ) [18]. The phase value of the signal with frequency  $f$ Hz is then calculated in degree as:

$$\theta_k = 360^\circ f(t_{zck} - T_{zcref}) \quad (3)$$

Thanks to the high speed electronics and GPS which enables the precise measurement of zero crossing time as well as common time reference for PMU. The schematic of a basic phasor measurement unit is shown in Fig.1.

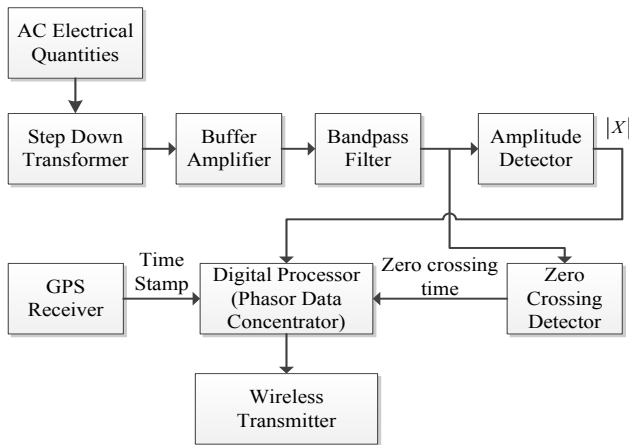


Fig.1 Schematic of PMU

The buffer amplifier along with the step down transformer is used to scale down the electrical signal as well as provide electrical isolation. All unwanted signals from the measured waveform of the signal are blocked by the band pass filter. Amplitude and zero crossing detectors provide the required information to determine the phase and magnitude of the signal. This information and the time stamp from the GPS are further processed at the phasor data concentrator to generate accurate magnitude and phase angle of the signal. Then the data are sent through wireless transmitter to system operator/central controller.

### III. OPP PROBLEM FORMULATION

It is essential to have an efficient methodology which will determine minimum number of PMUs and their optimal location to make the system completely observable. For an  $N$ -bus power system the OPP problem can be formulated as follows:

$$\begin{aligned} & \text{Min } F(x) \\ & F(x) = \sum_{i=1}^N C_i n_{ij} + \sum_{i=1}^N W_i u_{ij} \end{aligned} \quad (4)$$

Where,  $C_j$  is the cost for installing a PMU,  $n_{ij}$  represent binary bit for PMU installation at bus  $i$ ,  $W_i$  is the penalty factor if the bus  $i$  is not observable and  $u_j$  is the binary bit to indicate bus unobservability at bus  $i$ .

Three topological observability rules have been considered for network observability analysis [5]: (i) If a PMU is installed on a bus, current phasors of all branches connected to that bus and voltage phasor of that bus are known. (ii) If voltage phasors of both ends of a branch are known then the current phasor of that branch can be obtained directly using ohm's law. (iii) If all the current phasors of the branches connected to a bus are known except one then the unknown one can be determined using Kirchhoff's current law.

### IV. PROPOSED TECHNIQUES

In this paper, five well known evolutionary and swarm optimization techniques (OT) namely invasive weed optimization (IWO), backtracking search algorithm (BSA), artificial bee colony (ABC), differential evolution (DE) and particle swarm optimization (PSO) have been employed to solve OPP problem. Evolutionary algorithms (EA) work on the principle of natural biological evolution. In order to achieve better solutions EA operates on the potential populations of solutions based on the principle of survival of the fittest. The optimization starts with the randomly chosen initial population of solutions and at each generation new set of populations are generated according to their fitness in the associated problem domain. This process causes the evolution of individuals having better characteristics than their previous generation. Thus improved approximation of the solutions is obtained. The flow chart of the EA is shown in Fig. 2. The target here is to find the strategic bus location for PMUs which will minimize the objective function formulated in equation (3). The rest part of this section briefly describes the used optimization techniques.

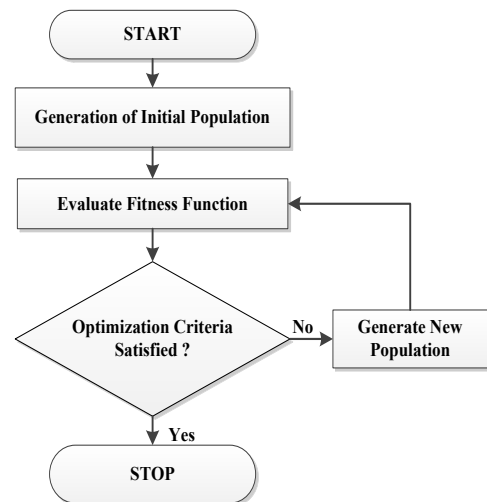


Fig.2 Flow Chart of Evolutionary Algorithm

#### A. Backtracking Search Algorithm (BSA)

BSA is a population based higher level iterative evolutionary algorithm for combinatorial optimization problems. Pinar Civicioglu proposed the algorithm in its present form in 2013 by optimizing benchmark mathematical problems[19].

Initialization of population, selection-I, mutation, crossover and selection-II are the major steps of BSA. Though BSA has huge similarity with famous optimization algorithm like GA, DE but the mutation and crossover and boundary control mechanisms are different. Details about BSA can be found in [20], [21].

### B. Differential Evolution (DE)

It is an effective optimization technique for realizing all kinds of non-linear as well as multimodal functions. It was first presented by Rainer Storn and Kenneth Price in 1995. The main operators used by this method are initialization of population, mutation, crossover and selection. Strength of this optimization method lies in its fast convergence, parallel computation and easy usage [22]. Details about differential evolution can be found in [23], [24].

### C. Artificial Bee Colony (ABC)

ABC is basically based on unique behavior of honey bees in searching nectar and transferring the information of availability of honey resources via waggle dance. The main parts of the algorithm are food resources, employed as well as unemployed foragers. The deciding factors for recruitment of nectar source by the bees depend on the direction, distance and quality of nectar resources. This method is capable of solving unimodal and multi-modal numerical optimization problems [25], [26].

### D. Invasive Weed Optimization (IWO)

IWO is a bio-inspired stochastic optimization algorithm that mimics the natural actions of weeds in finding and settling appropriate and better places for growth and reproduction. Compared to other evolutionary algorithm IWO has its distinctive features of reproduction, spatial dispersal and competitive exclusion [27], [28].

### E. Particle Swarm Optimization (PSO)

PSO is a population based technique which is based on social behavior of bird flocking. The particle denotes the individual hovered through multidimensional search space. The optimum location of an individual particle is achieved by the best solution generated by itself and its neighboring particles. Each particle moves with an primary location and velocity where velocities are bounded by the overflowing forbiddance and for not flying in the unusable fields [28], [29].

## V. SIMULATION RESULTS AND DISCUSSIONS

The proposed techniques have been applied in IEEE-14, 30, 39 and 57 bus networks. Full observability of the network under normal operating condition has been considered for the simulation. The techniques have been developed in the MATLAB programming environment. Fig. 3 shows the one-line diagram of IEEE standard 14-bus test network for better understanding of the OPP problem. Optimal locations and number of PMUs required for full system observability of IEEE-14 bus system is presented in Table I for normal operating condition without any contingency. Although different algorithm provides different optimum locations after solving the OPP problem but all the algorithm give same

number of PMUs for full observability of the system which is same as the existing results presented in [3].

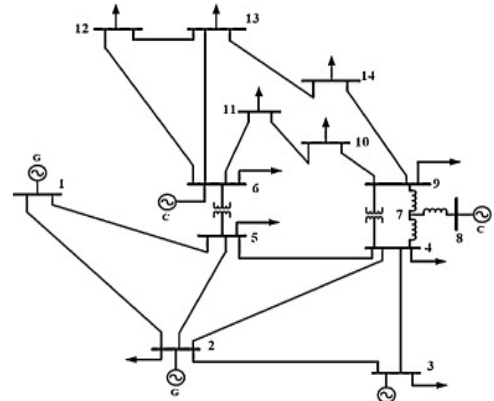


Fig. 3 IEEE-14 bus test system

Table I: IEEE-14 Bus Network

Techniques	Buses to Place PMU	Number of PMUs
BSA	2,6,7, 9	4
DE	2,7, 11, 13	4
ABC	2, 8, 10,13	4
IWO	2,7, 11, 13	4
PSO	2, 8, 10, 13	4
[3]	2,6,7, 9	4
[14]	2,6,7,9	4

Table II: IEEE-30 Bus Network

Techniques	Buses to Place PMU	Number of PMUs
BSA	3,5,8,10,11,12,15,18,25,27	10
DE	3,5,6,9,10,12,18,24,25,30	10
ABC	2,4,6,9,10,12,18,24,26,27	10
IWO	3,5,8,10, 11,12,19,24,25,29	10
PSO	1,6,7,10,11,12,19,24,25,30	10
[3]	2,3,6,9,10,12,15,19,25,27	10
[14]	1,7,9,10,12,18,24,25,27,28	10

Table III: IEEE-39 Bus Network

Techniques	Buses to Place PMU	Number of PMUs
BSA	2,6,9,13,14,17,19,20,22,23,29,32,37	13
DE	2,6,9,10,12,14,17,19,22,23,29,34,37	13
ABC	2,6,9,10,12,14,17,19,22,23,25,29,34	13
IWO	2,6,9,10,12,14,17,19,20,22,23,25,29	13
PSO	2,6,9,10,12,14,17,19,22,23,25,29,34	13
[3]	2,6,9,10,12,14,17,19,20,22,23,25,29	13
[15]	2,6,9,10,13,14,17,19,20,22,23,25,29	13

Table IV: IEEE-57 Bus Network

Techniques	Buses to Place PMU	Number of PMUs
BSA	2,6,12,15,19,22,26,29,30,32,36,38,39,41,47,50,54	17
DE	1,4,9,10,20,23,25,26,29,32,36,38,41,45,46,49,53,57	17
ABC	1,4,9,19,22,25,26,29,32,36,38,41,45,46,50,53,57	17
IWO	1,4,9,19,22,25,26,29,32,36,38,41,45,46,50,53,57	17
PSO	2,6,12,15,19,22,26,29,30,32,36,38,39,41,47,50,54	17
[3]	1,4,9,20,24,27,29,30,32,36,38,39,41,45,46,51,54	17
[14]	1,4,6,10,20,23,25,27,29,32,36,39,41,45,46,49,54	17

The optimization techniques have also been applied to solve OPP problem for IEEE-30 bus test system and the results



obtained is presented in Table II. In this case the optimum number of PMUs required for system observability is 10 which matches with the results of [3] and all the algorithms give almost same optimum locations with identical number of PMUs. For IEEE-39 bus system the optimum number of PMUs is 13 as shown in Table III. Similarly, for IEEE-57 bus the optimum PMU numbers are 17 and locations for different optimization techniques are summarized in Table IV.

## VI. CONCLUSIONS

This paper employs five evolutionary, colony and swarm optimization algorithms such as backtracking search algorithm (BSA), differential evolution (DE), artificial bee colony (ABC), invasive weed optimization (IWO) and particle swarm optimization (PSO) in order to make observable different power system networks. Though all the techniques do not end up with same bus numbers but give same number of PMUs to be installed for complete observability. Additionally, the available literatures also give exactly same number of PMUs are required to make the specified power networks to be observable. Furthermore, from the obtained results it could be concluded that the proposed techniques are capable enough to come up with satisfactory solutions for big or small networks.

## REFERENCES

- [1] A. G. Phadke, "Synchronized phasor measurements in power systems," *IEEE Comput. Appl. Power*, vol. 6, no. 2, Apr. 1993.
- [2] J. Bertsch, C. Camal, D. Karlson, and J. McDaniel, "Wide-Area Protection and Power System Utilization," *Proc. IEEE*, vol. 93, no. 5, pp. 997–1003, May 2005.
- [3] B. K. Saha Roy, A. K. Sinha, and A. K. Pradhan, "An optimal PMU placement technique for power system observability," *Int. J. Electr. Power Energy Syst.*, vol. 42, no. 1, pp. 71–77, Nov. 2012.
- [4] F. Aminifar, C. Lucas, A. Khodaei, and M. Fotuhi-Firuzabad, "Optimal Placement of Phasor Measurement Units Using Immunity Genetic Algorithm," *IEEE Trans. Power Deliv.*, vol. 24, no. 3, pp. 1014–1020, Jul. 2009.
- [5] S. A. Taher, H. Mahmoodi, and H. Aghaamouei, "Optimal PMU location in power systems using MICA," *Alex. Engr. J.*, Dec. 2015.
- [6] A. Abur, "Observability analysis and measurement placement for systems with PMUs," *IEEE PES Power Systems Conference and Exposition, 2004*. IEEE, pp. 1472–1475, 2004.
- [7] A. Abur, "Improved bad data processing via strategic placement of PMUs," *IEEE Power Engineering Society General Meeting, 2005*. IEEE, pp. 2759–2763, 2005.
- [8] S. Chakrabarti and E. Kyriakides, "Optimal Placement of Phasor Measurement Units for Power System Observability," *IEEE Trans. Power Syst.*, vol. 23, no. 3, pp. 1433–1440, Aug. 2008.
- [9] M. Shafiqullah, M. S. Alam, M. I. Hossain, and M. N. Hasan, "Transient performance improvement of power system by optimal design of SVC controller employing genetic algorithm," *8th International Conference on Electrical and Computer Engineering*. IEEE, pp. 540–543, Dec-2014.
- [10] M. S. Alam, M. Shafiqullah, M. I. Hossain, and M. N. Hasan, "Enhancement of power system damping employing TCSC with genetic algorithm based controller design," *International Conference on Electrical Engineering and Information Communication Tech. (ICEEICT)*. IEEE, pp. 1–5, May-2015.
- [11] M. Nazari-Heris and B. Mohammadi-Ivatloo, "Application of heuristic algorithms to optimal PMU placement in electric power systems: An updated review," *Renew. Sustain. Energy Rev.*, vol. 50, pp. 214–228, Oct. 2015.
- [12] P. P. Bedekar, S. R. Bhide, and V. S. Kale, "Optimum PMU placement considering one Line/ One PMU outage and maximum redundancy using genetic algorithm," *The 8th Electrical Engineering/ Electronics, Computer, Telecommunications and Information Technology (ECTI) Association of Thailand - Conference 2011*. IEEE, pp. 688–691, May-2011.
- [13] R. F. Nuqui and A. G. Phadke, "Phasor Measurement Unit Placement Techniques for Complete and Incomplete Observability," *IEEE Trans. Power Deliv.*, vol. 20, no. 4, pp. 2381–2388, Oct. 2005.
- [14] S. Billakanti and C. Venkaiah, "An effective binary integer linear programmed approach for optimal placement of PMUs in power systems," *Smart Electr. Grid (ISEG), 2014 Int. Conf.*, pp. 1–8, 2014.
- [15] S. Akhlaghi, "Optimal PMU placement considering contingency-constraints for power system observability and measurement redundancy," *2016 IEEE Power and Energy Conference at Illinois (PECI)*. IEEE, pp. 1–7, Feb-2016.
- [16] G. N. Korres, P. S. Georgilakis, N. C. Koutsoukis, and N. M. Manousakis, "Numerical observability method for optimal phasor measurement units placement using recursive Tabu search method," *IET Gener. Transm. Distrib.*, vol. 7, no. 4, pp. 347–356, Apr. 2013.
- [17] K. Mazlumi and H. Vahedi, "Optimal placement of PMUs in power systems based on bacterial foraging algorithm," *18th Iranian Conference on Electrical Eng.* IEEE, pp. 885–888, May-2010.
- [18] A. S. Deese, T. Nugent, and S. Coppi, "A comparative study of optimal PMU placement algorithms for cost minimization," *2014 IEEE PES General Meeting*. IEEE, pp. 1–5, Jul-2014.
- [19] P. Civicioglu, "Backtracking Search Optimization Algorithm for numerical optimization problems," *Appl. Math. Comput.*, vol. 219, no. 15, pp. 8121–8144, Apr. 2013.
- [20] M. S. Shahriar, M. Shafiqullah, M. A. Asif, M. M. Hasan, and M. Rafiqzaman, "Design of multi-objective UPFC employing backtracking search algorithm for enhancement of power system stability," *18th International Conference on Computer and Information Technology (ICCIT)*. IEEE, pp. 323–328, 2015.
- [21] M. Shafiqullah, M. A. Abido, and L. S. Coelho, "Design of robust PSS in multimachine power systems using backtracking search algorithm," *2015 18th International Conference on Intelligent System Application to Power Systems (ISAP), Proceedings of the Conference on*. pp. 1–6, Sep-2015.
- [22] R. Storn and K. Price, "Differential Evolution – A Simple and Efficient Heuristic for global Optimization over Continuous Spaces," *J. Glob. Optim.*, vol. 11, no. 4, pp. 341–359, 1997.
- [23] M. Ijaz, M. Shafiqullah, and M. A. Abido, "Classification of power quality disturbances using Wavelet Transform and Optimized ANN," *2015 18th International Conference on Intelligent System Application to Power Systems (ISAP), Proceedings of the Conference on*. IEEE, pp. 1–6, Sep-2015.
- [24] M. A. Zamee, K. K. Islam, A. Ahmed, and K. R. Zafreen, "Differential evolution algorithm based load frequency control in a two-area conventional and renewable energy based nonlinear power system," *4th International Conference on the Development in the Renewable Energy Technology*. IEEE, pp. 1–6, Jan-2016.
- [25] D. Karaboga and B. Basturk, "On the performance of artificial bee colony (ABC) algorithm," *Appl. Soft Comput.*, vol. 8, no. 1, pp. 687–697, Jan. 2008.
- [26] A. H. M. A. Rahim and M. A. Ali, "Tuning of PID SSSC controller using artificial bee colony optimization technique," *2014 IEEE 11th International Multi-Conference on Systems, Signals & Devices (SSD14)*. IEEE, pp. 1–6, Feb-2014.
- [27] A. R. Mehrabian and C. Lucas, "A novel numerical optimization algorithm inspired from weed colonization," *Ecol. Inform.*, vol. 1, no. 4, pp. 355–366, Dec. 2006.
- [28] M. S. Shahriar, M. Shafiqullah, M. Asif, Afzal, M. M. Hasan, and A. Ishaque, "Comparison of Invasive Weed Optimization (IWO) and Particle Swarm Optimization (PSO) in Improving Power System Stability by UPFC Controller Employing a Multi-Objective Approach," in *1st International Conference on Advanced Information and Communication Technology*, 2016.
- [29] R. Eberhart and J. Kennedy, "A new optimizer using particle swarm theory," *MHS'95. Proceedings of the Sixth International Symposium on Micro Machine and Human Science*. IEEE, pp. 39–43, 1995.

# Effect of Higher Carrier Injection Rate on Charge Transport and Recombination In Mixed-Host Organic Light Emitting Diode

Riku Chowdhury<sup>1\*</sup>, Md. Rashedul Haq<sup>2</sup>, Md. Sarwar Uddin Chowdhury<sup>3</sup>, Sharmin Afrose<sup>4</sup> and Sukanta Paul<sup>5</sup>

<sup>1,2,4</sup>Department of Electrical & Electronic Engineering, Faculty of Science, Engineering and Technology  
University of Science and Technology Chittagong (USTC), Chittagong-4202, Bangladesh

<sup>3</sup>Department of Electrical & Electronic Engineering,  
Chittagong University of Engineering and Technology (CUET), Chittagong-4349, Bangladesh

<sup>5</sup>Department of Computer Science & Engineering  
Chittagong University of Engineering and Technology (CUET), Chittagong-4349, Bangladesh

<sup>1</sup>\*eeriku@gmail.com, <sup>2</sup>rasahaq\_17@yahoo.com, <sup>3</sup>sarwarcuete@gmail.com, <sup>4</sup>sharminafrose99@gmail.com, and  
<sup>5</sup>skpaulustc@gmail.com

**Abstract**— The effect of anode surface modification on performance of uniformly mixed-host (MH) emissive layer (EML) based organic light emitting diode (OLED) has been investigated by the numerical simulation. Indium Tin Oxide (ITO) used as anode in the device. Due to proposed surface modification technique of ITO, the energy barrier at anode/organic layer interface is reduced which consummately enhanced the hole injection rate that leads to balance of carriers transportation and recombination in the EML. Through the numerical simulation, the electrical characteristics and internal device physics of uniform MH-OLED have been analyzed quantitatively. Calculated current balance factor which is related to the external quantum efficiency also confirmed the efficiency enhancement of MH-OLED by the proposed ITO work function modification technique.

**Keywords**— indium tin oxide (ITO) modification; hole injection; numerical simulation; carrier recombination; current balance factor.

## I. INTRODUCTION

As a next generation display technology, organic light emitting diodes (OLEDs) has been drawn enormous attention over other displays, like CRT, LCD etc. due to simple fabrication process, wide viewing angle, very fast switching time ( $<1\mu\text{s}$ ), broad operating temperature range ( $-46\text{ }^\circ\text{C}$  to  $70\text{ }^\circ\text{C}$ ) and low turn-on voltage [1]. The first OLED consisting of bi-layer organic materials was fabricated by Tang and Vanslyke in 1987 [2]. Since then, number of research works have been carried out to improve the device performance over the conventional bi-layer OLED via organic materials improvement and development of the layer architecture and composition [3].

In order to improve the conventional heterojunction (HJ) OLED performance and reliability, a mixed-host structure had been introduced where hole transport material (HTM) and electron transport material (ETM) mixed uniformly as the host material in the single emissive layer (EML) [4]. The interface

of hole transport layer (HTL) and electron transport layer (ETL) which formed in HJ structure, can be eliminated by mixing these two transport materials. About 6 times heightening of operation lifetime had been achieved from this MH structure as compared to the conventional HJ-OLED [4].

Current OLEDs research topics being reported were more on charge balance or confinement for better recombination [4-7] and replacement of ITO or its surface modification [8-9] to improve the device performance as well as operation life time. In OLEDs, the physical process involved in charge injection at an electrode/molecule interface has a crucial role. The energy barrier at this interface dictates the functionality of OLEDs. It was recently discovered that the surface work function of metal oxide electrodes is one of the most important parameters in determining the interfacial barrier [3, 9]. Owing to its unique combination of good electrical conductivity and excellent optical transmission properties, tin-doped indium oxide (ITO) has been well developed in industry as electrode which is widely used in opto-electronics devices ranging from solar cells to OLEDs [10-11]. But the potential barrier between ITO and the organic layer severely limits the efficiency of hole-injection. The treatment of the ITO surface to reduce the interfacial energy barrier usually has a strong influence on the performance of the OLED device. A recent breakthrough in boosting the ITO surface work function by  $\text{O}_2$  and  $\text{Cl}_2$  plasma treatment [9], post annealing treatments, adding buffer layer [8] and UV-ozone treatments [12] have been reported. A simple way, the soaking of ITO in different concentrations of Cesium Fluoride (CsF) solution and subsequent UV-ozone treatment to modify the ITO surface work function has been demonstrated by H.-W. Lu et al [3]. In that work, ITO surface modification technique using CsF solution qualitatively applied to analysis the performance of conventional HJ structure.

As a simple and better performed device over HJ structure, a modified uniform MH structure has been proposed in this work to further improvement of MH-OLED performance and

operation life time. The proposed MH structure is: ITO (modified with various CsF solutions) / NPB : Alq<sub>3</sub> (3:2) (100 nm) / LiF/Al. The feasibility of this proposed MH structure has been analyzed from the simulated current density- luminance - voltage (J-L-V) characteristic and efficiency curves. After that, the effect of ITO surface modification (using different concentrations of CsF solutions) to increase the hole injection efficiency has been explained in terms of distribution of carrier concentration, current density, electric field and carriers recombination.

By the systematic study of the MH-OLED performance, it is possible to qualitatively explain some effects on J-L-V characteristic and efficiency. But, without numerical simulation, it is difficult to explain these effects quantitatively [12]. Numerical simulation is more viable to get any analytical results directly from the OLEDs where complicated working process and several interfaces are involved. Therefore, this work led by numerical simulation which treated as powerful method to retrieve detailed information such as the charge carrier injection, distribution of electric field and recombination those are difficult to measure directly through experiments, investigated the underlying device mechanism and their amplitude which can affect the device performance.

## II. ELECTRICAL MODEL

To analysis the effect of ITO work function modification on the underlying physics and performance of MH-OLED, drift-diffusion electrical model has been implemented using a numerical simulator called ‘SETFOS’ (Semiconducting Thin Film Optics Simulation Software). Poisson equation and continuity equation as presented in “(1),” and “(2),” correspondingly considered in that electrical model to solve the electric field distribution and time evaluation of the system.

$$\frac{dE}{dx} = \frac{q}{\epsilon\epsilon_0} (p - n) \quad (1)$$

$$\frac{dn}{dt} = \frac{dJ_n}{qdx} - R - T \quad (2)$$

where,  $E$  is the electric field inside the OLED,  $q$  the elementary charge,  $\epsilon$  the dielectric permittivity of the organic materials,  $\epsilon_0$  the dielectric constant,  $p$  and  $n$  are the hole density and the electron density respectively,  $J_n$  the electron current density,  $R$  the recombination rate and  $T$  the trapping rate for free carriers. The carrier density distribution can be obtained by solving the drift and diffusion equation based on the Langevin recombination ( $R$ ) process those are calculated using “(3),” and “(4),” respectively. The conventional electric field dependent ‘Poole-Frenkel mobility (PFM)’ model as expressed in “(5),” applied for carrier mobility calculation in the device. The current balance factor (CBF) ( $b$ ) in “(6),” used to measure the device quantum efficiency [14] which is defined as the recombination current with the total current density.

$$J_n = qp\mu_n E + qD_n \frac{dn}{dx} \quad (3)$$

$$R = \frac{q}{\epsilon\epsilon_0} (\mu_p + \mu_n) \quad (4)$$

$$\mu(E) = \mu_0 \exp(\gamma^* \sqrt{E}) \quad (5)$$

$$b = \frac{\int_0^L qR(x)dx}{J_T} \quad (6)$$

Here,  $\mu_p$  and  $\mu_n$  are the hole and electron mobility respectively,  $D_n$  the diffusion constant,  $\mu(E)$  is the charge carrier mobility under electric field ( $E$ ),  $\mu_0$  is the mobility under zero electric field,  $\gamma$  is the Poole-Frenkel field dependent factor,  $J_T$  is the total current density and  $L$  is the total device thickness.

## III. DEVICE STRUCTURE AND INPUT PRAMETERS FOR SIMULATION

Three uniform MH-OLED structures, namely  $S_0$ ,  $S_1$  and  $S_2$  are presented in “Fig. 1,” where NPB (HTM) and Alq<sub>3</sub> (ETM) mixed with a uniform ratio of 3:2 (NPB:Alq<sub>3</sub>). The used HOMO and LUMO levels of MH material are 5.4 eV and 3.1 eV [7] and the work function of LiF/Al is 3.0 eV [3] in simulation. The work function of ITO is 4.78 eV, 4.95 eV and 5.11 eV used in simulation for device  $S_0$  (unmodified ITO), device  $S_1$  (ITO modified by 1 wt% CsF solution) and device  $S_2$  (ITO modified by 10 wt% CsF solution) respectively [3]. Considering the unmodified work function based ITO as reference, the effects of proposed ITO work function modification technique using different concentrations of CsF solutions on uniform MH-OLED performance have been analyzed in the next section in terms of hole injection density, carrier recombination rates and current balance factor.

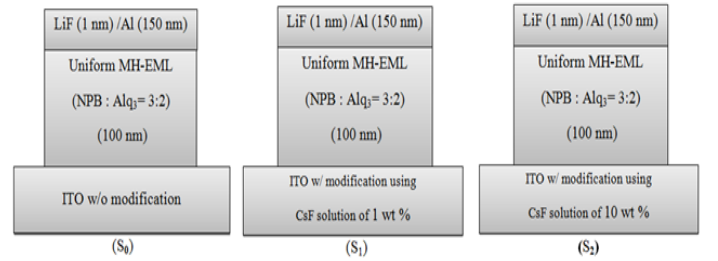


Fig. 1. W/ and W/O Modified ITO based MH-OLEDs

## IV. RESULTS AND DISCUSSIONS

### A. J-L-V Characteristics and Efficiencies

Figure 2 shows the current density-voltage-luminance (J-V-L) characteristic curve of three MH-OLEDs. 1 wt% and 10 wt% solutions of CsF improved the work function of ITO from normal value of 4.78 eV to 4.95 eV and 5.11 eV respectively. These work function improvement of ITO increased the hole injection rate by which the J-L-V curves influenced significantly. At a constant operating voltage of 8 V (Fig. 2(a)), the current density three MH-OLEDs of  $S_0$ ,  $S_1$  and  $S_2$  are 490 mA/cm<sup>2</sup>, 925 mA/cm<sup>2</sup> and 1480 mA/cm<sup>2</sup> correspondingly. In contrast, the luminescences of device  $S_0$ ,  $S_1$  and  $S_2$  shows the same trend as that of current density with

the same operating voltage, which indicates that high luminescence from a device can be obtained with high current density. 10 wt% CsF solution based MH-OLED shows the highest current density and luminance due to higher hole injection rate which also result of higher efficiency as evidence as presented in Fig. 2(b). The improved values of electroluminescence (EL) efficiency,  $\gamma$  of modified ITO based MH-OLEDs by 1 wt% and 10 wt% CsF solutions are 1.91 cd/A and 2.43 cd/A over without ITO modification based OLED where the value of EL efficiency is 1.40 cd/A. These significant performance improvements of uniform MH-OLED using ITO surface modification by CsF solutions can be visualized and explained from the carrier distribution and recombination profiles.

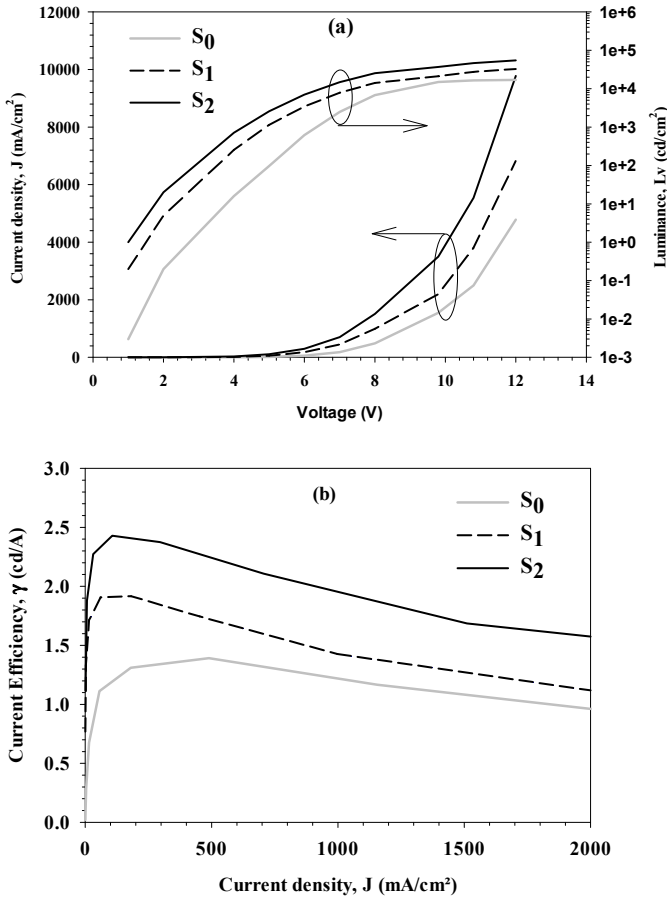


Fig. 2. (a) Current density-Luminance-Voltage and (b) Electroluminescence Efficiency vs Current density curves for unmodified and modified ITO based MH-OLEDs.

### B. Effects of ITO surface modification on carrier injection, transport and recombination

From the carrier concentration profile as shown in Fig. 3 (a), it is observed that at operation voltage of 8 V, the concentration of hole at anode/EML interface are increased around 1 and 1.7 orders due to ITO surface modification by 1 wt% and 10 wt% CsF solutions respectively, where the interfacial energy barrier between ITO (4.95 eV and 5.11 eV) and EML (HUMO=5.4 eV) reduced from 0.62 eV (in unmodified condition (4.78 eV)) to 0.45 eV, and 0.29 eV

correspondingly. Therefore, these significant reduction of interfacial energy barrier improved the hole current density at the ITO/EML interface (Fig. 3(b)) around 1.5 and 1.8 times which linked to increase the total current density (Fig. 2(a)) of the modified ITO based MH-OLEDs over unmodified ITO based MH-OLED. Furthermore, the electric field distribution along the EML as shown in Fig. 3(c) increased steadily from anode/EML interface due to this proposed CsF solution based ITO surface modification technique which harmoniously influenced the recombination rate at the EML.

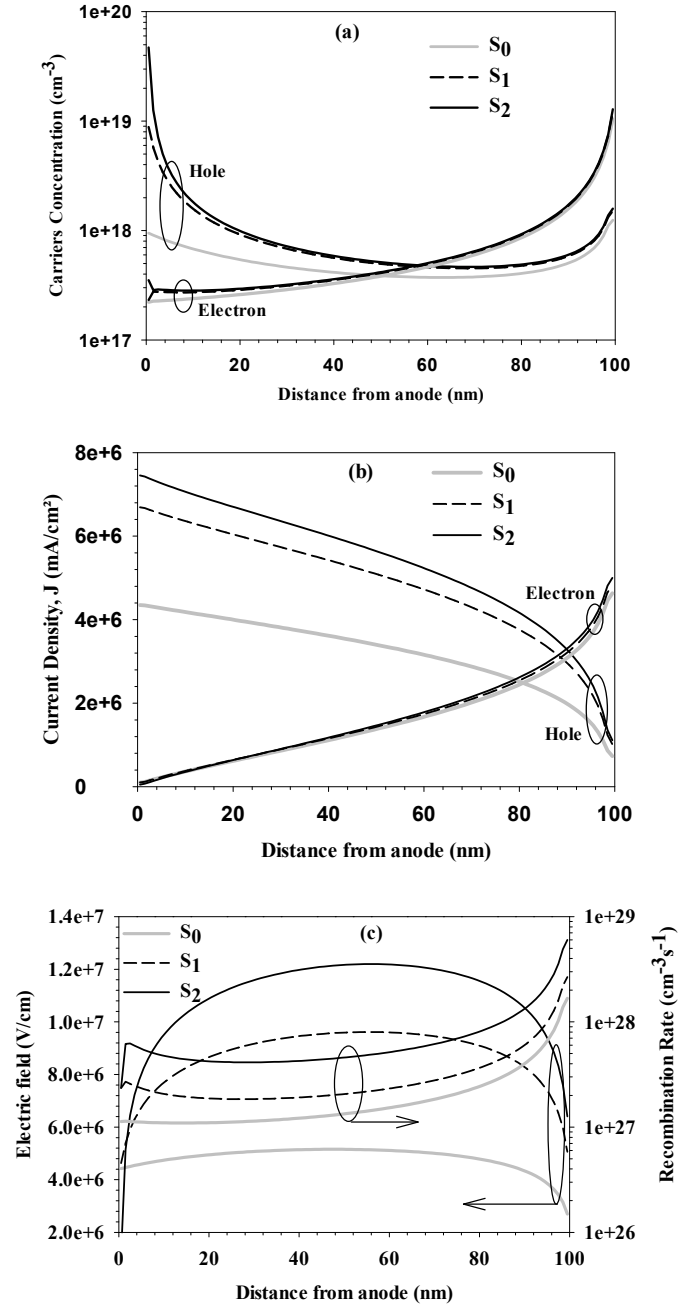


Fig. 3. Effect of hole injection rate (using treated ITO) on (a) Carriers density profile, (b) Current density (for hole and electron) and (c) Electric field and Carrier recombination zone in the EML at 8V with respect to untreated ITO based MH-OLEDs.

Fig. 4 presents the highest calculated values of current balance factor (using equation “(6),”) of modified ITO based MH-OLEDs with 1 wt% ( $b=0.77$ ) and 10 wt% ( $b=0.83$ ) CsF solutions. The CBF of MH-OLEDs based on ITO surface modification reached steady state position before unmodified ITO based MH-OLED which CBF is 0.71.

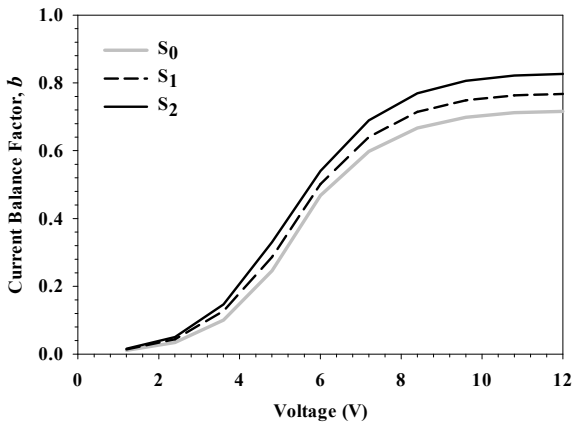


Fig. 4. Ameliorant of Current Balance Factor due to higher hole injection rate (treated ITO) over lower hole injection rate (untreated ITO) based MH-OLEDs at different operating voltage.

### C. Discussions

Through this numerical simulation, the influence of CsF solution on ITO work function modification and device performance have been explained from the hole current density, recombination rate and current balance factor. Due to the ITO surface modification by ITO soaking in 1 wt% and 10 wt% CsF solutions, the energy barrier at anode/emissive layer interface reduced by 0.17 eV and 0.33 eV respectively from the original value (0.62 eV) which ultimately boost up the hole injection efficiency through that interfacial region. Therefore, electroluminescence efficiencies of treated ITO based devices are improved by 1.36 and 1.73 times. Around 1.2 times improvement (with 10 wt% CsF solution) in current balance factor over normal condition also confirmed the improvement of device external quantum efficiency which is related to device life time.

### V. CONCLUSIONS

The effects of proposed CsF solution based ITO surface modification technique on uniform MH-OLED performance have been analyzed from the ‘SETFOS’ based numerical simulation results. Due to ITO surface modification with 10 wt% CsF solution, the energy barrier for hole injection reduced by about 2.37 times (from 0.69 eV to 0.29 eV) which significantly increased hole injection rate at anode/EML interface. Therefore, EL. efficiency is increased around 1.73 times. The value of current balance factor is also improved from 0.71 to 0.83 which is proportional to the experimental quantum efficiency. Sooth to say, the quantitative results of modified ITO based uniform MH-OLEDs performances those are obtained from the numerical simulation results, have proved the experimental feasibility of this proposed uniform

MH structure to improve the device performance and operation life time.

### REFERENCES

- [1] N. C. Erickson and R. J. Holmes, “Highly efficient, single-layer organic light-emitting devices based on a graded-composition emissive layer,” *Appl. Phys. Lett.*, vol. 97, no. 8, p. 083308, 2010.
- [2] C. W. Tang and S. a. VanSlyke, “Organic electroluminescent diodes,” *Appl. Phys. Lett.*, vol. 51, no. 12, p. 913, 1987.
- [3] H.-W. Lu, C.-W. Huang, P.-C. Kao, S.-Y. Chu, and Y.-D. Juang, “Effects of ITO Electrode Modification Using CsF Solution on Performance of Organic Light-Emitting Diodes,” *ECS J. Solid State Sci. Technol.*, vol. 4, no. 3, p. R54–R59, Jan. 2015.
- [4] D. Ma, C. S. Lee, S. T. Lee, and L. S. Hung, “Improved efficiency by a graded emissive region in organic light-emitting diodes,” *Appl. Phys. Lett.*, vol. 80, no. 19, p. 3641, 2002.
- [5] C.-H. Hsiao, Y.-H. Chen, T.-C. Lin, C.-C. Hsiao, and J.-H. Lee, “Recombination zone in mixed-host organic light-emitting devices,” *Appl. Phys. Lett.*, vol. 89, no. 16, p. 163511, 2006.
- [6] R. Chowdhury, T.S. Ong, Y.Y. Kee, S.S. Yap, T.Y. Tou, “Numerical and experimental studies of mixed-host organic light emitting diodes,” *Curr. Appl. Phys.* vol.15, no.11, p. 1472–77, 2015.
- [7] C. Riku, Y. Y. Kee, T. S. Ong, S. S. Yap, and T. Y. Tou, “Simulation of mixed-host emitting layer based organic light emitting diodes,” in *AIP Conference Proceeding*, vol. 1657, no. 1, p. 070002, 2015.
- [8] H. Wang, K. P. Klubek, and C. W. Tang, “Current efficiency in organic light-emitting diodes with a hole-injection layer,” *Appl. Phys. Lett.*, vol. 93, no. 9, p. 093306, 2008.
- [9] X. A. Cao and Y. Q. Zhang, “Performance enhancement of organic light-emitting diodes by chlorine plasma treatment of indium tin oxide,” *Appl. Phys. Lett.*, vol. 100, no. 18, p. 183304, May 2012.
- [10] Baldo, M. A., Thompson, M. E. & Forrest, S. R., “High-efficiency fluorescent organic light-emitting devices using a phosphorescent sensitizer,” *Nature*, vol. 403, p. 750–753, 2000.
- [11] Helander, M. G., Wang, Z. B., Qiu, J., Greiner, M. T., Puzzo, D. P., Liu, Z. W. & Lu, Z. H., “Chlorinated indium tin oxide electrodes with high work function for organic device compatibility,” *Science*, vol. 332, p. 944–947, 2011.
- [12] P.-R. Huang, Y. He, C. Cao, and Z.-H. Lu, “The origin of the high work function of chlorinated indium tin oxide,” *NPG Asia Mater.*, vol. 5, no. 8, p. e57, Aug. 2013.
- [13] E. Knapp and B. Ruhstaller, “Numerical analysis of steady-state and transient charge transport in organic semiconductor devices,” *Opt. Quantum Electron.*, vol. 42, no. 11–13, p. 667–677, Feb. 2011
- [14] J. C. Scott, S. Karg, and S. A. Carter, “Bipolar charge and current distributions in organic light-emitting diodes,” *J. Appl. Phys.*, vol. 82, no. 3, p. 1454, Aug. 1997.

# Solid State Lighting, A solution for Power Crisis in Bangladesh

K. M. Ahsan-uz-Zaman<sup>1</sup>, Kafi Mohammad Ullah<sup>2</sup>, Md. Shaidul Kabir Milon<sup>3</sup>, A S M Sayam<sup>4</sup>, Abdul Wahed<sup>5</sup>  
<sup>1,2,3,4</sup>Dept. of EEE, Mymensingh Engineering College (University of Dhaka), Mymensingh  
<sup>5</sup>Faculty, Dept. of EEE, Mymensingh Engineering College (University of Dhaka), Mymensingh  
<sup>1</sup>k.m.ahsanuzzaman@gmail.com

**Abstract**—Electricity is the most usable form of energy. For a developing country like Bangladesh, electricity plays an important factor. Due to increasing population and rapid industrial growth, the country lags behind than its rising demand of electric power supply. Power generation in Bangladesh is mostly dependent on natural gas, coal and fossil fuel which are also responsible for carbon emission. Alternative measures should be taken to resolve this power crisis. If the present power consumption can be reduced using smart energy efficient appliances then it would be possible to meet up the demand of the consumers with the present production capacity. Lighting is responsible for a gentle amount of energy consumption over the year. In this paper we discussed about using smart technologies like Solid State Lighting in terms of reducing energy consumption on lighting sector. Light emitting diode (LED) based solid state lighting technology have potential to exceed the efficiency of conventional lamp based lighting systems. LED offers better quality in lighting, have much longer lifespan and comparatively better on durability with only drawback of initial high pricing. In terms of much longer lifespan, this initial cost is not much accountable. This paper represents the features and efficiency of solid state lighting as well as comparison among conventional lighting and LEDs.

**Keywords**—solid state light; power crisis; energy efficient technology; LED

## I. INTRODUCTION

A universal trend towards the progressive development of an environmentally sustainable society has brought about a substantial demand for innovative, energy-efficient technology. Being a developing country Bangladesh is not much capable of utilizing renewable resources in terms of energy generation. Power sector of this country is much dependent on natural gas and fossil fuels. If the power consumption can be reduced somehow, this power crisis can be resolved gradually. Lighting is responsible for a large amount of energy consumption over the country. This research is focused on reducing the energy consumption on lighting sector. Reducing cost on lightening can be one of the solutions for energy crisis. This will also make the way for achieving the global goal of energy efficient technology implementation. Switching from provisional lighting systems to smart energy efficient lighting technology offers various advantages over energy efficiency and reducing cost for general usage. There are three major light source and their principles are much different.

Incandescence bulb - A tungsten filament is heated by electric current until it glows and emits light.

Fluorescent lamp – An electric arc excites mercury atoms which emits UV radiation. This radiation strikes the phosphor coating placed inside a glass tube. Then the UV rays are converted into visible light.

Solid state light – SSL is a kind of light emitting diode which are made of semiconductors.

Light emitting diode (LED) based solid state lighting system is the most promising energy saving solution for lighting applications. It have the potential of exceeding the conventional lighting systems in terms of advantages and features. However, replacing traditional lighting elements with LED can reduce the energy consumption in lighting sector at a significant scale. LED offers much longer lifetime than conventional lighting sources [1], as shown on the figure 1,

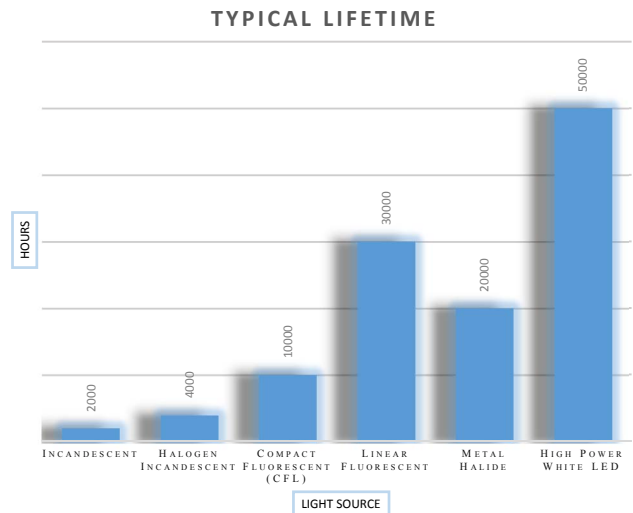


Fig. 1. Lifetime of various light source.

## II. SOLID STATE LIGHTING

Solid-state lighting technology is actually based on Light Emitting Diode (LED). This lightening device is made of semiconductors and use electricity as power. It consists of a chip of semiconducting material treated to create a p-n (positive-negative) junction. Impurities are doped on the p-n junction. A Substrate is attached to the semiconducting diode to support the die, this contacts to applied power. A heat sink and a lens is also being installed on the LED chip. The lens controls light

distribution characteristics of the mechanism. The whole package is covered by an outer casing.

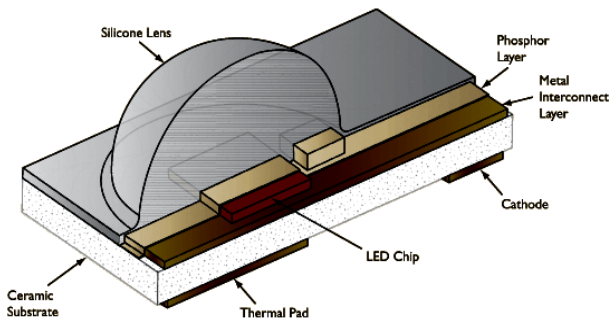


Fig. 2. Framework of a LED.

When the LED gets powered by electricity, electrons from the cathode (n-side) start to flow towards the anode (p-side). When the electrons and electron holes recombine, their electrical charges are cancelled out but the energy held by the electron is released instantly. This energy is released in form of electromagnetic waves and expelled as light.

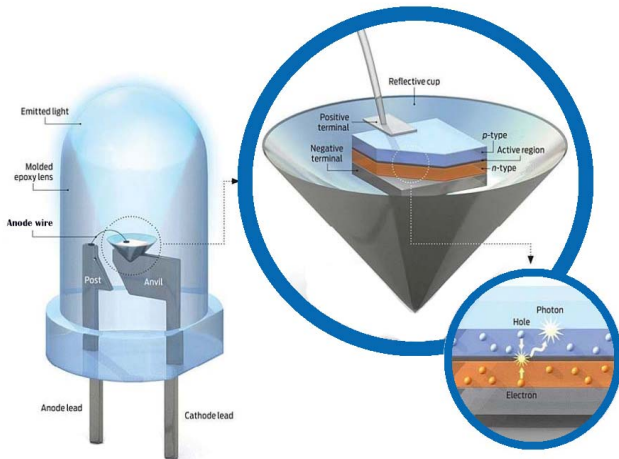


Fig. 3. Structure of a LED.

The wavelength of the light emitted by a LED depends upon the material used to construct the diode. Rather than the silicon and germanium used in normal diodes, compound semiconductors as like GaAs, AlGaInP, InGaN. Red LED is made of Aluminum Gallium Arsenide (AlGaAs). Green LED is based on Aluminum Gallium Phosphide (AlGaP) and Blue LED is from Indium Gallium Nitride (InGaN) [2]. White light is created by combining the light from red, green, and blue (RGB) LEDs or by coating a Blue LED with yellow phosphor. These white LEDs can be used as a replacement for conventional incandescent and CFL lighting.

### III. COMPARISON AMONG LIGHTING SOURCES

Light is a member of large family called Electromagnetic Radiation (EMR). From 380 to 750 Nm in wavelength is considered as visible light. Among the other lighting sources

LED based Solid State Lighting has much more efficiency [3]. Comparison among the light sources in terms of efficiency is shown in Table I,

TABLE I. EFFICIENCY OF LIGHT SOURCE

Light Source	Typical Efficacy (Lumens/Watt)
Incandescent	15-25
Metal Halide	80-105
High Pressure Sodium	70-110
Compact Fluorescent (CFL)	40-70
Light Emitting Diode (LED)	60-140

LED offers more durable features and advantages rather than traditional lighting systems. LED bulbs are also free from producing hazardous materials like mercury. Different features of incandescent, CFL and LED light are described in Table II,

TABLE II. FEATURES OF INCANDESCENT, CFL & LED LIGHTS

Features	Incandescent	CFL	LED
Durability	Fragile	Fragile	Durable
Instant turn on	Yes	Slight Delay	Yes
Sensitivity to Temperature	No	Yes	No
Sensitivity to Humidity	Some	Yes	No
Heat Emitted	89.68 kJ/hour	31.65 kJ/hour	3.59 kJ/hour
Hazardous Materials	None	5 mg mercury/bulb	None
Frequent on/off Cycling	Some Effect	Shortens Lifespan	No Effect

### IV. EFFICIENCY OF LED

The prospect of improving lighting technology has come up with recent advancement in terms of Solid State Lighting (SSL). These LED based SSL technology offers huge advantage when compared to fluorescent or incandescent lights in many aspects. Solid-state lighting (SSL) will mean greener homes and businesses that use substantially less electricity, making them less dependent on fossil fuels [5]. Solid State Lighting system is introducing superior features to users including,

- Low power consumption
- Ultra-long source life
- No UV or IR radiation
- No mercury content

Light Emitting Diodes (LEDs) are comparatively better than traditional incandescent and CFL light bulbs in account of efficiency. Power conversion efficiency is defined as the ratio of emitted optical power ( $P_o$ ) to the applied electrical power,

$$\eta_c = \frac{P_o}{iV} = \eta_{ext} \frac{h\nu}{eV}$$

Where  $V$  is the voltage drop across the device and  $i$  is the supplied electricity.

LEDs have up to 53% efficiency on electrical power conversion [4]. Table III shows the comparison of luminous efficiency among the light sources.

TABLE III. COMPARISON OF WATT EQUIVALENT TO LIGHT OUTPUT AMONG THE SOURCES

Light Output (Lumens)	Incandescent (Watts)	CFL (Watts)	LED (Watts)
450	40	9-13	4-5
800	60	13-15	6-8
1100	75	18-25	9-13
1600	100	23-30	16-20

For about 1500 lumen of light output over 10 years considering 10 hours burning per day,

Traditional incandescent light required = 100W

Purchase price of the bulb = 40 BDT

Typical lifespan of the bulb = 8000 hours

Bulb required over the time period = 40 unit

Traditional electricity cost = 6 BDT/kilowatt-hour

Total power consumption over the time period,

$$N = \frac{PT}{1000} = \frac{100 \times 365 \times 10}{1000} \text{ kWh} = 365 \text{ kWh}$$

Cost of electricity =  $365 \times 6 = 2190$  BDT

Total expense =  $40 \times 40 + 2190$  BDT = 3790 BDT

Compact fluorescent light (CFL) required = 23W

Purchase price of the bulb = 300 BDT

Typical lifespan of the bulb = 10000 hours

Bulb required over the time period = 2 unit

Traditional electricity cost = 6 BDT/kilowatt-hour

Total power consumption over the time period,

$$N = \frac{PT}{1000} = \frac{23 \times 365 \times 10}{1000} \text{ kWh} = 83.95 \text{ kWh}$$

Cost of electricity =  $83.95 \times 6 = 503$  BDT

Total expense =  $2 \times 300 + 503$  BDT = 1103 BDT

Light emitting diode (LED) required = 12W

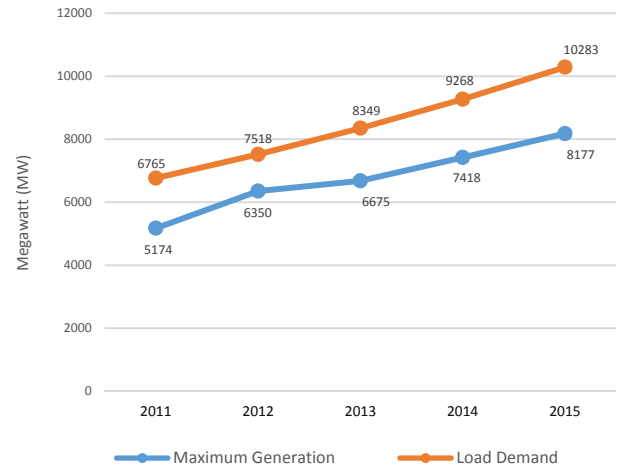


Fig. 4. Electricity generation vs demand in recent years.

Purchase price of the bulb = 620 BDT

Typical lifespan of the bulb = 50000 hours

Bulb required over the time period = 1 unit

Traditional electricity cost = 6 BDT/kilowatt-hour

Total power consumption over the time period,

$$N = \frac{PT}{1000} = \frac{12 \times 365 \times 10}{1000} \text{ kWh} = 43.80 \text{ kWh}$$

Cost of electricity =  $43.8 \times 6 = 262.80$  BDT

Total expense =  $1 \times 620 + 262.80$  BDT = 882.80 BDT

With having only drawback of initial high cost, LED is still much more efficient for longtime usage. Alongside 3790 BDT for incandescent bulb and 1103 BDT for CFL, LED will only cost about 883 BDT in terms of 10 years usage for a single bulb as shown in the calculations above.

## V. POWER SECTOR SCENARIO OF BANGLADESH

Electricity is the main source of power for country's most of the economic, social and cultural activities. But our electricity sector is now in a sickbed. The energy infrastructure is quite small, insufficient and poorly managed. Total power demand exceeds the power generation capacity limit by a large number every year [6][7]. This situation resulting in load shedding throughout the entire country. Problems in the Bangladesh's electric power sector include corruption in administration, high system losses, low plant efficiencies, erratic power supply, electricity theft, blackouts, and shortages of funds for power plant maintenance [8]. Bangladesh Government has taken several attempts to balance the situation. In the Power System Master Plan (PSMP) -2010 demand forecast was made based on 7 % GDP growth rate. The electricity development is required to be accelerated to increase access and attain economic development. The desirable economic growth rate would be about 7% p.a [9]. Despite of all these measures taken, this country still lacks in electric power sector as shown in figure 4.



## VII. SSL IN TERMS OF POWER CRISIS IN BANGLADESH

Solid state lighting have potential to reduce the cost of lighting in about one third in Bangladesh [10]. Solid state lighting also offers comparatively long lifetime and also reduce carbon emission. The main reason of LED based solid state lighting is not much used in Bangladesh is the unawareness about the feasible benefits and features that LED offers.

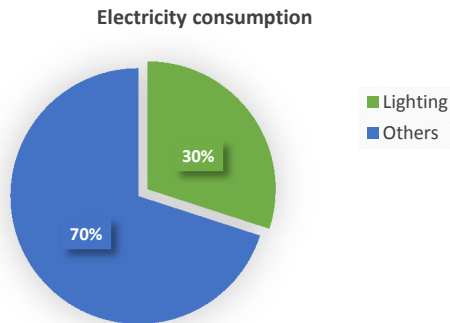


Fig. 5. Electricity consumption in different sectors.

As shown in the figure above, about 30 percent of the total energy consumption is for lighting purpose [10]. Two third of this lighting is by incandescent lights and other one third is by CFL across the country. LED generally consume 80% less power than incandescent lamp and 50% of CFL [11]. So replacing incandescent and CFL light sources with LED can save big amount of energy over the year. The power crisis in Bangladesh is rapidly increasing resulting large amount of load shedding over the year.

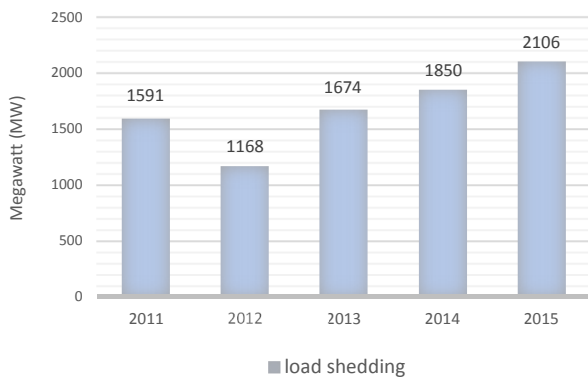


Fig. 6. Load shedding in last five years.

From the data shown in the figure 4, we can mathematically calculate the energy saving per year by replacing incandescent and CFL bulbs with light emitting diodes.

For the year of 2015,

Total demand of electricity = 10283 MW

Total generation over the year = 8177 MW

Load shedding = 2106 MW

Consumption over lighting purpose = 30% of 10283 MW = 3084.9 MW

Consumption by incandescent light = 2/3 of 3084.9 MW = 2056.6 MW

Consumption by CLF = 1/3 of 3084.9 MW = 1028.3 MW

If incandescent sources are replaced by LED,

Energy saving over the year = 80% of 2056.6 MW = 1645.28 MW

Again, if CFL light bulbs are replaced by LED,

Energy saving over the year = 50% of 1028.3 MW = 514.15 MW

From above calculations, if conventional incandescent and CFL lights are replaced by LED then total saving from the lighting sector is about 2159.43 MW. Which clearly exceeds the annual load shedding across the country.

## VIII. CONCLUSION

Replacing conventional lighting sources with LEDs can reduce the power consumption by a large amount in Bangladesh. With only drawback of initial high cost LED offers superior advantages in terms of efficiency and durability [12]. In this paper, calculation and statistics have shown that replacing incandescent and CFL bulbs with LED can resolve the power crisis over the country. Along with being efficient, LED will also take the country one step forward towards achieving the global goal of implementing ecofriendly smart technologies.

## REFERENCES

- [1] Department of Energy US (DOE), "Lifetime of White LEDs," PNNL-SA-50957, September 2009
- [2] Dronacharya College of Engineering, "LED Principle & Structure," Electronics and Communication Engineering department report.
- [3] STATELINE Eco Electric Corp., LED Watt Conversion & Light Replacement Guide.
- [4] Philips, "All in 1 LED Lighting Solutions Guide". PhilipsLumileds.com. 2012-10-04. p. 15.
- [5] Shigeru Suehero, Yoshiaki Shibata, "Electricity Saving Potential and Cost & Benefit of LED Lighting in Japan," IEEJ, July 2011.
- [6] Bangladesh Power Development Board, [http://www.bpdb.gov.bd/bpdb/index.php?option=com\\_content&view=article&id=20&Itemid=18](http://www.bpdb.gov.bd/bpdb/index.php?option=com_content&view=article&id=20&Itemid=18).
- [7] Finance Division, Ministry of Finance Government of People's Republic of Bangladesh, Power and Energy Sector Road Map: An update'2011, [www.mof.gov.bd/en/budget/11\\_12/power/power\\_energy\\_en.pdf](http://www.mof.gov.bd/en/budget/11_12/power/power_energy_en.pdf).
- [8] Mohammad Asadul Haquea and Jalalur Rahman, — Power Crisis and Solution in Bangladesh | Bangladesh J. Sci. Ind. Res.
- [9] Bangladesh Power Development Board, [http://www.bpdb.gov.bd/bpdb/index.php?option=com\\_content&view=article&id=12&Itemid=126](http://www.bpdb.gov.bd/bpdb/index.php?option=com_content&view=article&id=12&Itemid=126).
- [10] Energypac Bangladesh, "Bangladesh Case Studies on Energy Efficient Lighting", <http://energypacelectronics.com>.
- [11] Leotek Electronics USA Corp, A Municipal Guide for Converting to LED Street Lighting. V7-101613. [www.leotek.com](http://www.leotek.com).
- [12] E. Fred Schubert, "Light Emitting Diodes, second edition," ISBN: 0521865387, Cambridge University Press, Cambridge UK.

# Design of N-Segmented Display system for Bengali vowels

Saif Hannan<sup>1</sup>, Ahasan Ullah Shohag<sup>2</sup>

<sup>1,2</sup>Department of Electronic and Telecommunication Engineering  
International Islamic University Chittagong, Bangladesh.

Corresponding e-mail: [saifhannan@yahoo.com](mailto:saifhannan@yahoo.com)

## Abstract

Different segmented display systems have been proposed for representing Bangla and English alphabets and numerals in past few years. In order to distinguish Bengali Vowels in precise form, they must be represented with their unavoidable curved shapes. Accurate recognition of Vowels is difficult due to their complex shapes. In this paper, we tried to represent a total of 11 Bangla vowels in simpler and accurate look. To improve their accuracy, we have proposed a 58-segmented display. And we derived a very simple, scientific logic to find segments out of matrix display. We have introduced a 4-bit input line to represent all the Bengali Vowels, analyzed all the 58-segments against each and every Vowel, and designed the suitable circuit for each of the 58 segments.

**Keywords:** Segments, Truth table, Expressions, 4-bit input line, Points.

## I. INTRODUCTION

In order to represent Bangla vowels in an n segmented display, it is not possible to avoid both strokes and curves. For ingeniousness, we have to use least number of segments as possible, as well as obviate the co-existence of both curves and strokes. Curved segments will be expensive. So, envisaging accuracy, simplicity and efficiency, following purposes are followed: to represent all the Bengali vowels using least number of segments as possible, to improve their accuracy, to avoid segment overlapping and to alleviate the necessity of representing curved shapes using curved segments. For representing Bengali vowels, many types of segmented displays were developed. In order to obtain minimum segmentation using above mentioned points, we have to allow adequate space for drawing shapes for all vowels, place all the vowels on the same model and point out the similarities and dissimilarities.

Among different technologies to build the IC, we prefer CMOS technology for this work to implement, because CMOS technology has low power consumption and scalable high noise immunity [1] and CMOS circuits are much cheaper in comparison to other technologies [2].

## II. DESIGN METHOD

As matrix display represents nice outlook, we have tried to find the segments over matrix display. At the beginning, we

drew the shapes for all Bengali vowels on a  $30 \times 30$  matrix, keeping both similarities and dissimilarities among vowels; i.e., we have chosen the appropriate and minimum number of segments to represent different curves. Our  $30 \times 30$  matrix whose cells are indexed from 1 to 900 and those are known as points. We drew the curves with distinct shapes without causing partition [3].

### A. Segments

By the term 'Segment', we mean here a set or group of points that can be switched at a time [3]. To represent the shape of a particular vowel on the matrix, we need to split the shape of the vowel into several pieces and find out the points on the matrix for each piece. Then for all the vowels, we find all the pieces and superimpose them for similarities.

The common and similar pieces are separated from dissimilar pieces and then we have taken as minimum number of pieces as possible to identify them as segments.

### B. Points to represent segments

Using *Find\_Segment algorithm* we found that, a total of 58 segments were required to cover all the points that were possessed by all vowels drawn over the  $30 \times 30$  matrix. The segments were named from  $S_0$  to  $S_{57}$ . The points that were needed to represent the segments are summarized in Table I.

**Table I: Points needed to represent Segments**

Segments	Points Needed
$S_0$	212, 213, 214, 215, 216, 217, 218, 219, 220, 221, 222, 223, 224, 225, 226, 227, 228, 229, 230, 231, 232, 233, 235, 236, 237, 238, 239
$S_1$	234
$S_2$	282, 311, 315, 340, 346, 377, 469, 529, 588, 646, 652, 681, 731, 732, 733
$S_3$	353, 383, 413, 443, 473, 503, 533, 563, 593, 623, 653, 683, 713, 743, 773, 803, 833
$S_4$	371
$S_5$	283
$S_6$	284
$S_7$	408
$S_8$	439

S <sub>9</sub>	499
S <sub>10</sub>	559
S <sub>11</sub>	617
S <sub>12</sub>	704
S <sub>13</sub>	730
S <sub>14</sub>	590
S <sub>15</sub>	621
S <sub>16</sub>	266, 326, 356, 386, 446, 476, 506, 536, 566, 596, 626, 656, 686, 716, 746, 776, 806, 836
S <sub>17</sub>	296
S <sub>18</sub>	416
S <sub>19</sub>	41, 70, 100, 131, 132, 133, 134, 135, 136, 137, 168, 198
S <sub>20</sub>	368, 337, 308, 279, 280, 281, 312, 374, 405, 435, 494, 523, 552, 581, 608, 609
S <sub>21</sub>	343
S <sub>22</sub>	465
S <sub>23</sub>	610
S <sub>24</sub>	641
S <sub>25</sub>	672
S <sub>26</sub>	703
S <sub>27</sub>	734, 765, 796, 827, 828
S <sub>28</sub>	436
S <sub>29</sub>	407
S <sub>30</sub>	378, 350, 381, 410, 468, 497, 526, 556
S <sub>31</sub>	349
S <sub>32</sub>	351
S <sub>33</sub>	586
S <sub>34</sub>	678
S <sub>35</sub>	740
S <sub>36</sub>	771
S <sub>37</sub>	253, 373, 403, 434, 501, 531, 561, 619, 677, 735, 764, 763, 762
S <sub>38</sub>	313
S <sub>39</sub>	470
S <sub>40</sub>	706
S <sub>41</sub>	761
S <sub>42</sub>	483, 513, 544, 575, 606, 637, 668, 699
S <sub>43</sub>	572, 603, 634, 665, 696, 727, 758, 759, 760
S <sub>44</sub>	263, 293, 332
S <sub>45</sub>	624, 654, 685, 715
S <sub>46</sub>	322
S <sub>47</sub>	380
S <sub>48</sub>	254, 285, 288, 317, 409, 438, 467, 496, 525, 555,
S <sub>49</sub>	679
S <sub>50</sub>	772
S <sub>51</sub>	316
S <sub>52</sub>	259, 260, 291
S <sub>53</sub>	376, 345, 258, 709, 708, 707, 705, 456, 486, 517, 548, 579
S <sub>54</sub>	444, 445, 327, 357, 387, 265, 108, 139, 170, 171, 172, 201

S <sub>55</sub>	462, 461, 430, 400, 342, 255, 256, 318, 441, 471, 528, 527, 651, 681, 739, 768, 797, 826, 825, 824, 823, 792
S <sub>56</sub>	287
S <sub>57</sub>	442

### C. Segments to Represent each Alphabet

We required a total of 58-Segments to take all the points that were possessed by any vowels over a 30x30 matrix. The Segments that needed to represent the Vowels are summarized in Table II.

**Table II: Bengali Vowel versus 58-Segments**

Bengali vowels	Segment needed to be activated
A	S <sub>0</sub> , S <sub>1</sub> , S <sub>2</sub> , S <sub>3</sub> , S <sub>4</sub> , S <sub>5</sub> , S <sub>6</sub> , S <sub>7</sub> , S <sub>8</sub> , S <sub>9</sub> , S <sub>10</sub> , S <sub>11</sub> , S <sub>12</sub> , S <sub>13</sub> , S <sub>14</sub> , S <sub>15</sub> , S <sub>42</sub> , S <sub>44</sub> = <b>18</b>
Av	S <sub>0</sub> , S <sub>1</sub> , S <sub>2</sub> , S <sub>3</sub> , S <sub>4</sub> , S <sub>5</sub> , S <sub>6</sub> , S <sub>7</sub> , S <sub>8</sub> , S <sub>9</sub> , S <sub>10</sub> , S <sub>11</sub> , S <sub>12</sub> , S <sub>13</sub> , S <sub>14</sub> , S <sub>15</sub> , S <sub>16</sub> , S <sub>17</sub> , S <sub>18</sub> , S <sub>42</sub> , S <sub>44</sub> = <b>21</b>
B	S <sub>0</sub> , S <sub>1</sub> , S <sub>19</sub> , S <sub>20</sub> , S <sub>21</sub> , S <sub>22</sub> , S <sub>23</sub> , S <sub>24</sub> , S <sub>25</sub> , S <sub>26</sub> , S <sub>27</sub> = <b>11</b>
C	S <sub>0</sub> , S <sub>1</sub> , S <sub>8</sub> , S <sub>11</sub> , S <sub>19</sub> , S <sub>20</sub> , S <sub>21</sub> , S <sub>22</sub> , S <sub>23</sub> , S <sub>28</sub> , S <sub>29</sub> , S <sub>30</sub> , S <sub>31</sub> , S <sub>32</sub> , S <sub>33</sub> , S <sub>34</sub> , S <sub>35</sub> , S <sub>36</sub> , S <sub>49</sub> = <b>19</b>
D	S <sub>0</sub> , S <sub>1</sub> , S <sub>5</sub> , S <sub>7</sub> , S <sub>8</sub> , S <sub>13</sub> , S <sub>14</sub> , S <sub>19</sub> , S <sub>21</sub> , S <sub>22</sub> , S <sub>28</sub> , S <sub>29</sub> , S <sub>34</sub> , S <sub>37</sub> , S <sub>38</sub> , S <sub>39</sub> , S <sub>40</sub> , S <sub>41</sub> , S <sub>42</sub> = <b>19</b>
E	S <sub>0</sub> , S <sub>1</sub> , S <sub>5</sub> , S <sub>7</sub> , S <sub>8</sub> , S <sub>13</sub> , S <sub>14</sub> , S <sub>19</sub> , S <sub>21</sub> , S <sub>22</sub> , S <sub>28</sub> , S <sub>29</sub> , S <sub>34</sub> , S <sub>37</sub> , S <sub>38</sub> , S <sub>39</sub> , S <sub>40</sub> , S <sub>41</sub> , S <sub>42</sub> , S <sub>43</sub> = <b>20</b>
F	S <sub>3</sub> , S <sub>11</sub> , S <sub>16</sub> , S <sub>17</sub> , S <sub>18</sub> , S <sub>32</sub> , S <sub>33</sub> , S <sub>34</sub> , S <sub>35</sub> , S <sub>44</sub> , S <sub>45</sub> , S <sub>46</sub> , S <sub>47</sub> , S <sub>48</sub> , S <sub>49</sub> , S <sub>50</sub> , S <sub>51</sub> , S <sub>52</sub> = <b>18</b>
G	S <sub>3</sub> , S <sub>12</sub> , S <sub>23</sub> , S <sub>24</sub> , S <sub>25</sub> , S <sub>26</sub> , S <sub>35</sub> , S <sub>36</sub> , S <sub>40</sub> , S <sub>46</sub> , S <sub>50</sub> , S <sub>51</sub> , S <sub>52</sub> , S <sub>53</sub> , S <sub>56</sub> = <b>15</b>
H	S <sub>1</sub> , S <sub>3</sub> , S <sub>12</sub> , S <sub>17</sub> , S <sub>18</sub> , S <sub>23</sub> , S <sub>24</sub> , S <sub>25</sub> , S <sub>26</sub> , S <sub>35</sub> , S <sub>36</sub> , S <sub>40</sub> , S <sub>46</sub> , S <sub>50</sub> , S <sub>51</sub> , S <sub>52</sub> , S <sub>53</sub> , S <sub>54</sub> , S <sub>56</sub> = <b>19</b>
I	S <sub>4</sub> , S <sub>6</sub> , S <sub>9</sub> , S <sub>10</sub> , S <sub>13</sub> , S <sub>14</sub> , S <sub>15</sub> , S <sub>31</sub> , S <sub>35</sub> , S <sub>38</sub> , S <sub>39</sub> , S <sub>41</sub> , S <sub>42</sub> , S <sub>47</sub> , S <sub>55</sub> , S <sub>56</sub> = <b>16</b>
J	S <sub>1</sub> , S <sub>4</sub> , S <sub>6</sub> , S <sub>9</sub> , S <sub>10</sub> , S <sub>13</sub> , S <sub>14</sub> , S <sub>15</sub> , S <sub>17</sub> , S <sub>18</sub> , S <sub>31</sub> , S <sub>35</sub> , S <sub>38</sub> , S <sub>41</sub> , S <sub>47</sub> , S <sub>39</sub> , S <sub>41</sub> , S <sub>42</sub> , S <sub>54</sub> , S <sub>55</sub> , S <sub>56</sub> , S <sub>57</sub> = <b>21</b>

### III. ARCHITRCTURE PROPOSAL

We got the desired architecture by using Find\_Segments algorithm, which is imprinted in Figure.1. For design simplicity, we have used bar type segments most. Matrix points that make up a curved shape, are considered as detached points connected together to form a segment. A pictorial view of all characters is shown in figure 2.

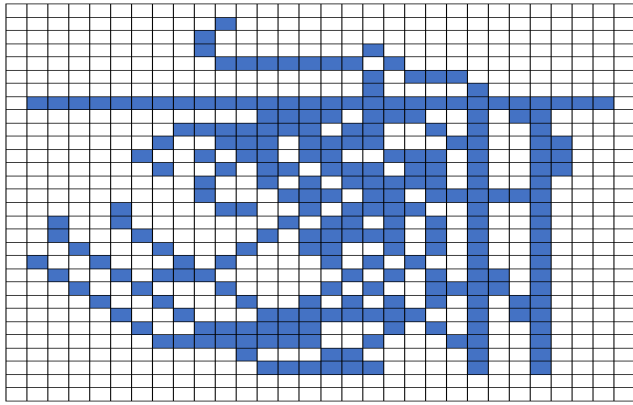
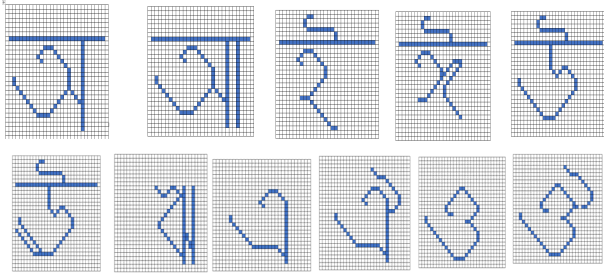


Figure 1: Proposed Model of 58-Segmented display for Bengali Vowels.



(a)



(b)

Figure 2: Overview of all vowels (a) proposed 58-segmented system and (b) 49-segment display [4]

#### IV. PERFORMANCE

From Fig.2 (b), the difference between the proposed and previous architecture [4] becomes apparent. For all vowels, the newly proposed design is better. Moreover, they [4] are incapable to depict the real curved shapes of Bangla vowels. So, our proposed design wins the extent in all aspects, at the cost of a few more segments.

#### V. CIRCUIT DESIGN

##### A. Truth table

The truth table was derived as shown in Table III. Simplified expression for each segment was found from this truth table by K-map. We have derived appropriate logic circuits to display each and every Bengali Vowels. We also have assumed that 'A' has a 4-bits code 0000; 'Av' has a 4-bits code 0001, and so on [5].

Table III: Truth table

A	0	0	0	0	0	0	0	1	1	1	
B	0	0	0	0	1	1	1	1	0	0	0
C	0	0	1	1	0	0	1	1	0	0	1
D	0	1	0	1	0	1	0	1	0	1	0
S <sub>0</sub>	1	1	1	1	1	1	0	0	0	0	0
S <sub>1</sub>	1	1	1	1	1	1	0	0	1	0	1
S <sub>2</sub>	1	1	0	0	0	0	0	0	0	0	0
S <sub>3</sub>	1	1	0	0	0	0	1	1	1	0	0
S <sub>4</sub>	1	1	0	0	0	0	0	0	0	1	1
S <sub>5</sub>	1	1	0	0	1	1	0	0	0	0	0
S <sub>6</sub>	1	1	0	0	0	0	0	0	0	1	1
S <sub>7</sub>	1	1	0	0	1	1	0	0	0	0	0
S <sub>8</sub>	1	1	0	1	1	1	0	0	0	0	0
S <sub>9</sub>	1	1	0	0	0	0	0	0	0	1	1
S <sub>10</sub>	1	1	0	0	0	0	0	0	0	1	1
S <sub>11</sub>	1	1	0	1	0	0	1	0	0	0	0
S <sub>12</sub>	1	1	0	0	0	0	0	1	1	0	0
S <sub>13</sub>	1	1	0	0	1	1	0	0	0	1	1
S <sub>14</sub>	1	1	0	0	1	1	0	0	0	1	1
S <sub>15</sub>	1	1	0	0	0	0	0	0	0	1	1
S <sub>16</sub>	0	1	0	0	0	0	1	0	0	0	0
S <sub>17</sub>	0	1	0	0	0	0	1	0	1	0	1
S <sub>18</sub>	0	1	0	0	0	0	1	0	1	0	1
S <sub>19</sub>	0	0	1	1	1	1	0	0	0	0	0
S <sub>20</sub>	0	0	1	1	0	0	0	0	0	0	0
S <sub>21</sub>	0	0	1	1	1	1	0	0	0	0	0
S <sub>22</sub>	0	0	1	1	1	1	0	0	0	0	0
S <sub>23</sub>	0	0	1	1	0	0	0	1	1	0	0
S <sub>24</sub>	0	0	1	0	0	0	0	1	1	0	0
S <sub>25</sub>	0	0	1	0	0	0	0	1	1	0	0
S <sub>26</sub>	0	0	1	0	0	0	0	1	1	0	0
S <sub>27</sub>	0	0	1	0	0	0	0	0	0	0	0
S <sub>28</sub>	0	0	0	1	1	1	0	0	0	0	0
S <sub>29</sub>	0	0	0	1	1	1	0	0	0	0	0
S <sub>30</sub>	0	0	0	1	0	0	0	0	0	0	0
S <sub>31</sub>	0	0	0	1	0	0	0	0	0	1	1
S <sub>32</sub>	0	0	0	1	0	0	1	0	0	0	0
S <sub>33</sub>	0	0	0	1	0	0	1	0	0	0	0
S <sub>34</sub>	0	0	0	1	1	1	1	0	0	0	0
S <sub>35</sub>	0	0	0	1	0	0	1	1	1	1	1
S <sub>36</sub>	0	0	0	1	0	0	0	1	1	0	0
S <sub>37</sub>	0	0	0	0	1	1	0	0	0	0	0
S <sub>38</sub>	0	0	0	0	1	1	0	0	0	1	1
S <sub>39</sub>	0	0	0	0	1	1	0	0	0	1	1
S <sub>40</sub>	0	0	0	0	1	1	0	1	1	0	0
S <sub>41</sub>	0	0	0	0	1	1	0	0	0	1	1
S <sub>42</sub>	1	1	0	0	1	1	0	0	0	1	1
S <sub>43</sub>	0	0	0	0	0	1	0	0	0	0	0
S <sub>44</sub>	1	1	0	0	0	0	1	0	0	0	0
S <sub>45</sub>	0	0	0	0	0	0	1	0	0	0	0
S <sub>46</sub>	0	0	0	0	0	0	1	1	1	0	0
S <sub>47</sub>	0	0	0	0	0	0	1	0	0	1	1
S <sub>48</sub>	0	0	0	0	0	0	1	0	0	0	0
S <sub>49</sub>	0	0	0	1	0	0	1	0	0	0	0
S <sub>50</sub>	0	0	0	0	0	0	1	1	1	0	0
S <sub>51</sub>	0	0	0	0	0	0	1	1	1	0	0
S <sub>52</sub>	0	0	0	0	0	0	1	1	1	0	0
S <sub>53</sub>	0	0	0	0	0	0	0	1	1	0	0

S <sub>54</sub>	0	0	0	0	0	0	0	0	0	1	0	1
S <sub>55</sub>	0	0	0	0	0	0	0	0	0	0	1	1
S <sub>56</sub>	0	0	0	0	0	0	0	1	1	1	1	1
S <sub>57</sub>	0	0	0	0	0	0	0	0	0	0	0	1

## B. Simplified Expression

We first constructed the combination vector for each Vowel. It shows which segments are needed to represent each Vowel. Then from the truth table the expression for each segment is derived.

$$\begin{aligned}
S_0 &= A'B' + A'BC' & S_1 &= A'B' + ABC' + AB'D' & S_2 &= A'B'C' \\
S_3 &= A'B'C' + A'BC + AB'C'D' \\
S_4 &= A'B'C' + AB'C'D + AB'CD' & S_5 &= A'C' \\
S_6 &= A'B'C' + AB'C'D + AB'CD' & S_7 &= A'C' \\
S_8 &= A'C' + A'B'CD & S_9 &= A'B'C' + AB'C'D + AB'CD' \\
S_{10} &= A'B'C' + AB'C'D + AB'CD' \\
S_{11} &= A'B'C' + A'B'CD + A'BCD' \\
S_{12} &= A'B'C' + A'BCD + AB'C'D' \\
S_{13} &= A'C' + AB'C'D + AB'CD' & S_{14} &= AC' + AB'C'D + AB'CD' \\
S_{15} &= A'B'C' + AB'C'D + AB'CD' & S_{16} &= A'B'C'D + A'BCD' \\
S_{17} &= A'B'C'D + A'BCD' + AB'D' \\
S_{18} &= A'B'C'D + A'BCD' + AB'D' & S_{19} &= A'B'C + A'BC' \\
S_{20} &= A'B'C & S_{21} &= A'B'C + A'BC' & S_{22} &= A'B'C + A'BC' \\
S_{23} &= A'B'C + A'BCD + AB'C'D' \\
S_{24} &= A'B'CD' + A'BCD + AB'C'D' \\
S_{25} &= A'B'CD' + A'BCD + AB'C'D' \\
S_{26} &= A'B'CD' + A'BCD + AB'C'D' \\
S_{27} &= A'B'CD' & S_{28} &= A'B'CD + A'BC' & S_{29} &= A'B'CD + A'BC' \\
S_{30} &= A'B'CD & S_{31} &= A'B'CD + AB'C'D + AB'CD' \\
S_{32} &= A'B'CD + A'BCD' & S_{33} &= A'B'CD + A'BCD' \\
S_{34} &= A'B'CD + A'BC' + A'BCD' \\
S_{35} &= A'B'CD + A'BC + AB'C' + AB'CD' \\
S_{36} &= A'CD + AB'C'D' & S_{37} &= A'BC' \\
S_{38} &= A'BC' + AB'C'D + AB'CD' \\
S_{39} &= A'BC' + AB'C'D + AB'CD' \\
S_{40} &= A'BC' + A'BCD + AB'C'D' \\
S_{41} &= A'BC' + AB'C'D + AB'CD' \\
S_{42} &= A'C' + AB'C'D + AB'CD' & S_{43} &= A'BC'D \\
S_{44} &= A'B'C' + A'BCD' & S_{45} &= A'BCD' \\
S_{46} &= A'BC + AB'C'D' & S_{47} &= A'BCD' + AB'C'D + AB'CD' \\
S_{48} &= A'BCD' & S_{49} &= A'B'CD + A'BCD' \\
S_{50} &= A'BC + AB'C'D' & S_{51} &= A'BC + AB'C'D' \\
S_{52} &= A'BC + AB'C'D' & S_{53} &= A'BCD + AB'C'D' \\
S_{54} &= AB'D' & S_{55} &= AB'C'D + AB'CD' \\
S_{56} &= A'BCD + AB'C' + AB'CD' & S_{57} &= AB'CD'
\end{aligned}$$

## C. Implementation

There are 11 Alphabets in Bangla vowels. For this we needed 11 output signals. To get 11 signals, it is required to have 4 signals as input lines. By using these lines, we can specify our desired output signal as binary value. The logic circuit for the 1<sup>st</sup> segment of display is shown below. All the 58 segments would be designed accordingly. Here, only AND, OR and NOT gates are used. In this design process we have taken the assistance from **DSCH** and **Micro wind** software. The cost was not estimated for implementing the system, as the work was just a proposal and hence no experiment was done.

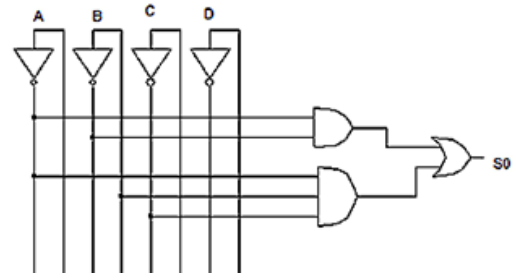


Figure 3: Sample Circuit Implementation.

## VI. DISCUSSION AND CONCLUSION

The distinction between the proposed and previous architecture [4, 5, 6, and 7] becomes clear. For all vowels, the newly proposed design is better. Since our designed circuit is little bit complex, we can reduce the complexity of the circuit through k-map analysis. If, we can reduce the number of required segment, it will respond faster. In future work, we can make it capable to implement the joint Bangla Alphabets, try to increase the number of characters in same display and can reduce the complexity.

Our designed architecture helps to find segments for characters and symbols used in Bangla language by matrix display. The output is quite nice, though the characters are in segmented form. It may be interfaced with any Computer or may be used on **calculators, ATM, Ticket Counter, and Toll Plaza** where users are friendly with Bangla language.

## REFERENCES

- [1] S.H.Teen, L.L.Lim and J.H. Lim; "IC Layout Design of Decoder Using Electric VLSI Design System", International Journal of Electronics and Electrical Engineering Vol. 3, No. 1, February, 2015.
- [2] R.Behzad, "Design of analog CMOS integrated circuits", McGraw-Hill Higher Education, New York, 2001
- [3] Tanzin Rahman, Tanvir Khan, Sarder Saadat Ahmed, Chandan Kumar Karmakar 'N-Segmented Display of Bangla Numerals' in proceedings of 8<sup>th</sup> international conference on computer and information Technology (ICCIT), Dhaka, Bangladesh, 2005.
- [4] Salahuddin Mohammad Masum, Sarwar Morshedul Haque, Swapon Chandra Dash, Kazi Faisal Kabir 'Segmented Display System for Bengali Alphabets'. Faculty of Science & Information Technology, Daffodil International University, Dhaka 1207, Bangladesh.
- [5] Islam, A.K.M.N., Mahmud, S.M.M., Shahrier, N., & Sattar, M.A. (2003); "Designing 17-segment Display for Bangla Vowels", 6th ICCIT 2003, Jahangirnagar University, PP. 283-286, December 19-21.
- [6] MASUM, S.M. & AL-MAMUN, M.A. (2005); "Designing 14-Segment Display for Bengali Vowels", Asian Journal of Information Technology, Grace Publications Network, Vol. 4 No. 2, PP. 178-184.
- [7] Mohammad Osiur Rahman, Mohammad Aktaruzzaman Khan, "Display Unit for Bangla Characters" ISSN 1813-7733 Vol. - 4, December 2007 Published in April 2008 (p 71-86).

# A Comparative Analysis Among PWM Control Z-source Inverter with Conventional PWM Inverter for Induction Motor Drive

Md. Khurshedul Islam\*, Md. Mustafa Zaved, Air Mohammad Siddiky, Khandakar Abdulla Al Mamun  
Department of Electrical & Electronic Engineering  
International Islamic University Chittagong (IIUC)  
Chittagong, Bangladesh  
khurshedeiiuc@gmail.com\*, mustafaxaved@gmail.com and armaneeiiuc@yahoo.com

**Abstract-**The uses of induction motor is ever-growing day by day because of its superiority and high efficiency over dc machine. So for wide range of use in the industry, this machine requires an efficient driver circuitry arrangement. Currently conventional Voltage Source Inverter (VSI) or Current Source Inverter (CSI) is dealing as key part in the field of induction motor driver circuit. These converters fail to perform at our desire level due to some crucial drawbacks like they can perform as either buck or boost operation and they contain considerable amount of harmonics as well as EMI noise. So we are trying to replace these traditional inverters by PWM control Z-Source Inverter (ZSI) which offers buck-boost operation capability by utilizing shoot through state and provides less EMI noise. This paper presents a comparative study among these three inverters. Firstly three MATLAB simulation model of Induction motor driver by using VSI, CSI and ZSI (having almost same environment) have arranged. Then some important motor characteristics such as rotor speed, electromagnetic torque, rotor current and stator current have observed for three system models at various loading conditions. The model using Z-source inverter exhibits efficient performance in all cases compared to the other models.

**Keywords-** PWM, Z-Source Inverter, Conventional Inverter, Shoot Through, Buck-boost.

## I. INTRODUCTION

In the previous decades the dc motors were extensively used for the industrial purposes due to the decoupled torque and flux that can be obtained by controlling field and armature current respectively [1]. Though the dc motor provides high starting torque, it has a number of drawbacks such as it requires high maintenance and not suitable for hazardous environment [2].

But in this decade the induction motor has taken the place of work horse in industry instead of dc motors because its robustness, less maintenance, high efficiency and low cost [3]. At past induction motors were mainly used for essentially constant speed applications as there was unavailability of variable frequency voltage supply. But with the advancement of the power electronics, it has made possible to supply variable frequency voltage, thus increase the use of induction motor in variable speed drive applications.

There are basically two ways to get voltage at variable frequency for the induction motor drives. One is cycloconverter and another is three phase inverter. The cycloconverter is widely used in very large power application such as locomotives and cement mills where the frequency requirement is one half or one third of line frequency. On the other hand, three phase inverters are very suitable for small and medium application [4]. The pulse width modulation (PWM) is the most efficient method used to varying both the voltage and frequency within a three phase inverter. In this method, a fixed dc input voltage is applied to the inverter and a controlled ac output voltage is obtained by adjusting the on and off periods of the inverter components [5].

## II. CONVENTIONAL PWM INVERTERS FOR MOTOR DRIVE

There are basically two types of conventional inverter for the motor drive on the basis of input power supply. Those are a) Current source inverter (CSI) and b) Voltage source inverter (VSI).

### a. Conventional Current Source Inverter:

The current source inverter is that one, in which the source and therefore the load current is predetermined and the load impedance decide the output voltage [6]. The supply current cannot change rapidly and the magnitude of the load current is controlled by varying input dc voltage to the large inductance, hence inverter response to the changing load is slow.

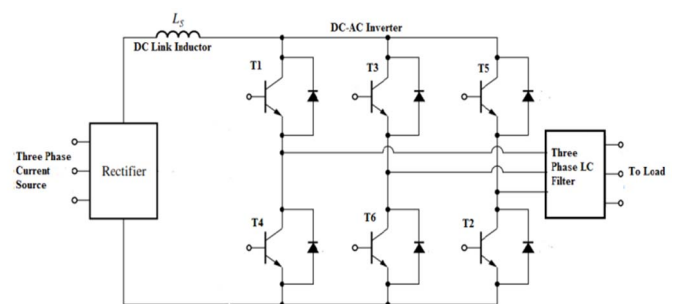


Fig. 1. Basic circuit diagram of conventional CSI.

Figure 1 shows the basic circuit diagram of conventional current source inverter. A three phase ac current source is fed

to the rectifier circuit in order to convert three phase ac current into dc current. Then the rectified dc current is fed to the three phase semiconductor switch based inverter through a dc link inductor. After that the output voltage from inverter is fed to a three phase LC filter in order to obtain sinusoidal three phase output voltage.

The current source inverter for motor drives have some conceptual limitations such as, they usually perform as a buck converter so additional power conversion stage is required to maintain required power, which increases the system cost, their output response is very slow and output voltage contains more harmonics and EMI noise[7].

*b. Conventional Voltage Source Inverter:*

A voltage source inverter is an arrangement where input voltage is constant and output voltage is independent of nature of the load.

But the output current waveform as well as magnitude depends upon nature of load impedance [8]. Three phase voltage source inverters are more common for providing adjustable frequency power to industrial application as compared to single phase inverters. The voltage source inverter takes dc supply from a battery or more usually from a 3-φ bridge rectifier [9].

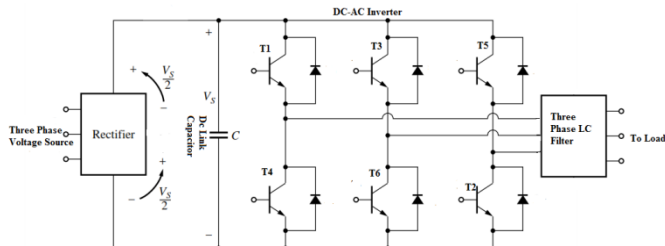


Fig. 2. Basic Circuit Diagram of Conventional VSI.

Figure 2 shows a basic circuit diagram of conventional voltage source inverter. The rectified dc voltage from the rectifier section is fed to the three phase bridge inverter through a dc link capacitor. Then the output voltage from the three phase inverter is fed to the three phase LC filter in order to obtain sinusoidal output voltage,

The voltage source inverter drives also have some crucial drawback such as, they worked as a buck converter and required additional circuitry to get desired output voltage which further introduce a considerable amount of harmonics and EMI noise [10].

**III. Z-SOURCE INVERTER:**

In order to overcome the limitations of conventional inverter, researchers have concentrated to an efficient inverter system called Z-source inverter. The input power of the Z-source either be current or voltage source [11].

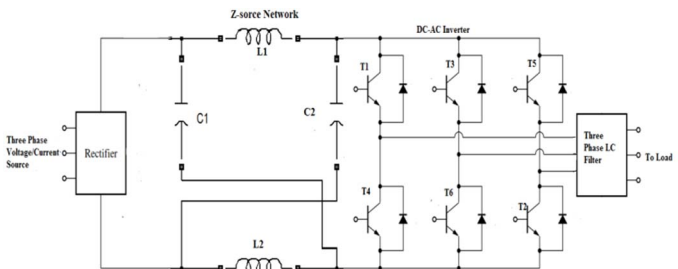


Fig.3. Basic Circuit Diagram of Z-source Inverter

Figure 3 shows the basic circuit diagram of Z-source inverter. From the circuit, it has been seen that the Z-source inverter utilizes an impedance network consists of two inductors and two capacitors of same values between the dc source and three phase inverter [12].

The impedance network also known as Z-source network, utilizes shoot through state to boost the dc voltage by gating on both the upper and lower switches of the same phase leg [13]. The shoot through state does not affect the PWM control of the inverter as it equivalently produce the same zero voltage to the load terminal but to achieve the high output voltage, it is required to increase the shoot through duty ratio[14]. The Z-source inverter offers some efficient feature such as it can operate by voltage source or current source, it contains fewer amounts of harmonics and EMI noise as compared to the conventional inverters and it provides buck-boost capability by utilizing shoot through state [15].

**III. Simulation and results**

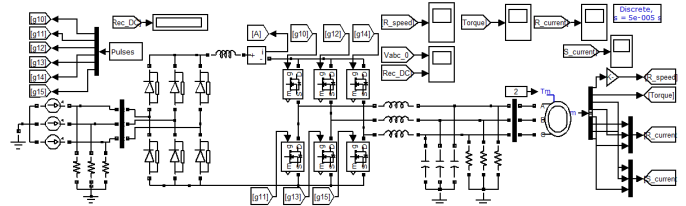


Fig. 4. Simulation circuit arrangement of CSI for Motor Drive.

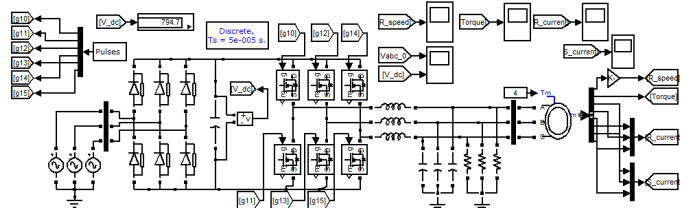


Fig.5. Simulation circuit arrangement of VSI for Motor Drive.

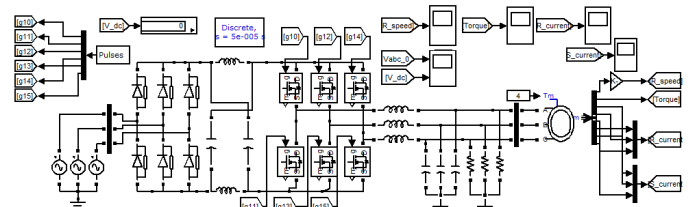


Fig. 6. Simulation circuit arrangement of ZSI for Motor Drive.

*a. Comparison of Rotor Speed:*

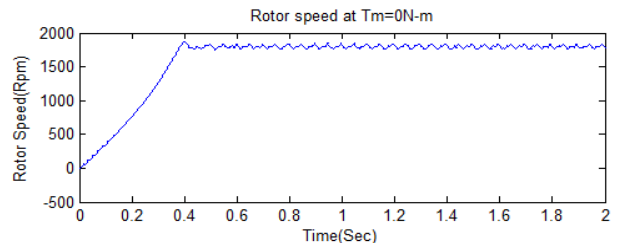


Fig. 7. Rotor Speed of CSI Fed IM at Tm=0N-m.

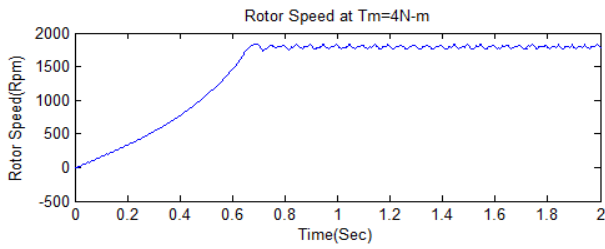


Fig. 8. Rotor Speed of CSI Fed IM at  $T_m=4N\text{-m}$ .

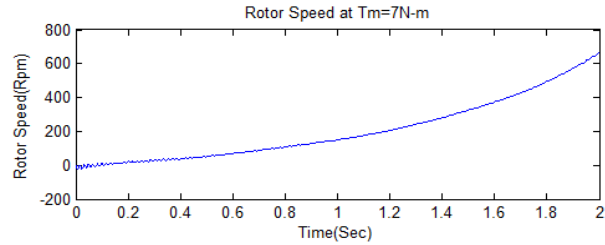


Fig. 9. Rotor Speed of CSI Fed IM at  $T_m=7N\text{-m}$ .

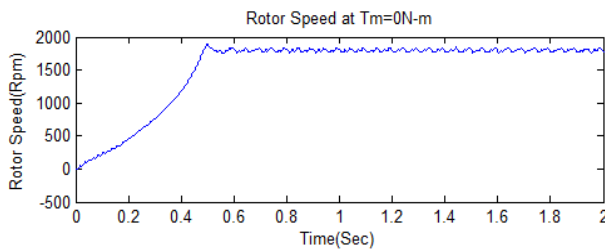


Fig. 10. Rotor Speed of VSI Fed IM at  $T_m=0N\text{-m}$ .

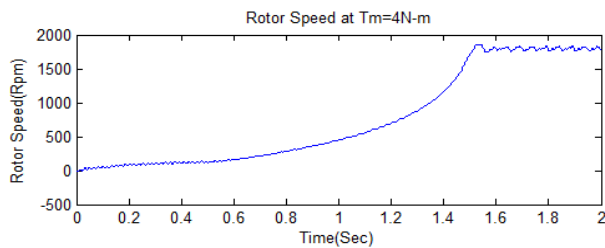


Fig. 11. Rotor Speed of VSI Fed IM at  $T_m=4N\text{-m}$ .

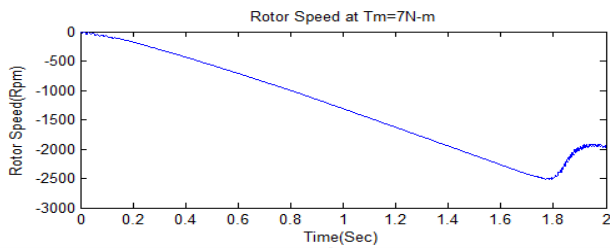


Fig. 12. Rotor Speed of VSI Fed IM at  $T_m=7N\text{-m}$ .

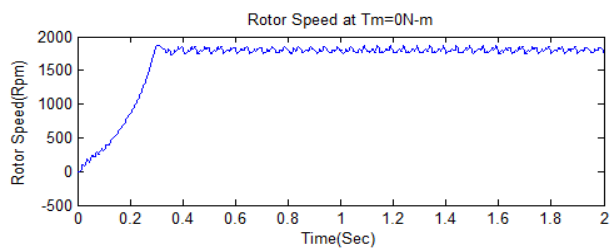


Fig. 13. Rotor Speed of ZSI Fed IM at  $T_m=0N\text{-m}$ .

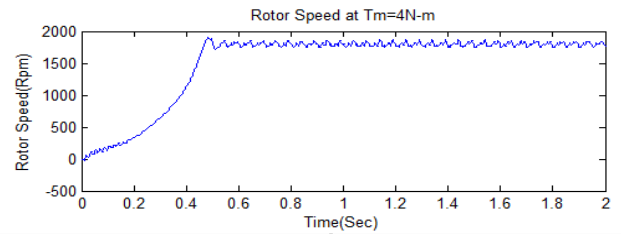


Fig. 14. Rotor Speed of ZSI Fed IM at  $T_m=4N\text{-m}$ .

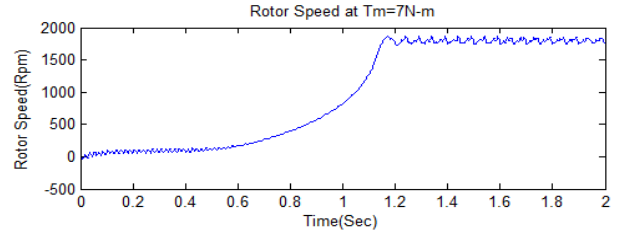


Fig. 15. Rotor Speed of ZSI Fed IM at  $T_m=7N\text{-m}$ .

Table. I: Comparison of rotor speed settling time at different torque

Drive	Settling time(Sec) at $T_m=0N\text{-m}$	Settling time(Sec) at $T_m=4N\text{-m}$	Settling time(Sec) at $T_m=7N\text{-m}$
CSI	0.4	0.68	$t > 2$
VSI	0.48	1.57	failed
ZSI	0.29	0.47	1.18

Table-I shows that, the ZSI fed IM attains steady state speed condition earlier than CSI and VSI fed induction motor. It has also shown that, ZSI fed IM can run at higher load condition than the CSI and VSI fed IM.

*b. Comparison of Electromagnetic Torque:*

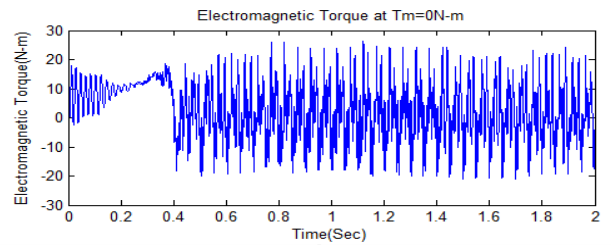


Fig. 16. Electromagnetic Torque of CSI Fed IM at  $T_m=0N\text{-m}$ .

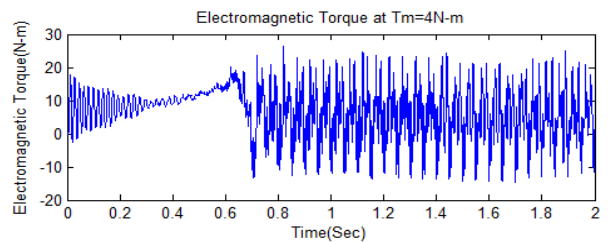


Fig. 17. Electromagnetic Torque of CSI Fed IM at  $T_m=4N\text{-m}$ .



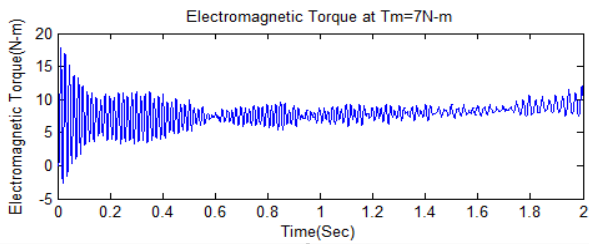


Fig. 18. Electromagnetic Torque of CSI Fed IM at  $T_m=7N\text{-m}$ .

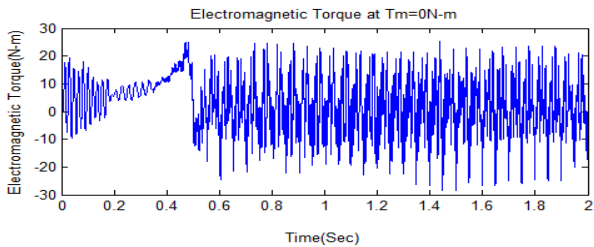


Fig. 19. Electromagnetic Torque of VSI Fed IM at  $T_m=0N\text{-m}$ .

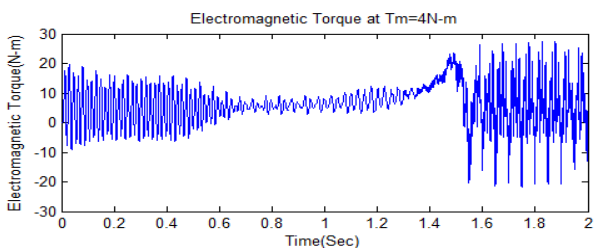


Fig. 20. Electromagnetic Torque of VSI Fed IM at  $T_m=4N\text{-m}$ .

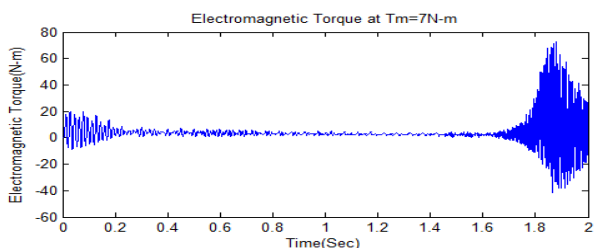


Fig. 21. Electromagnetic Torque of VSI Fed IM at  $T_m=7N\text{-m}$ .

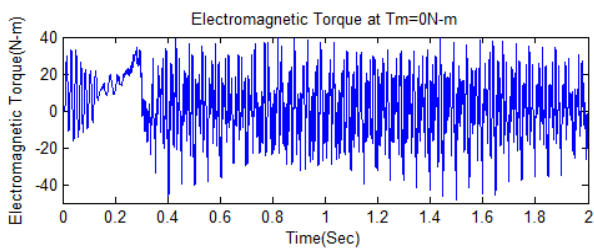


Fig. 22. Electromagnetic Torque of ZSI Fed IM at  $T_m=0N\text{-m}$ .

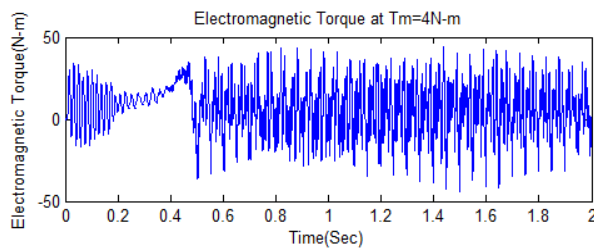


Fig. 23. Electromagnetic Torque of ZSI Fed IM at  $T_m=4N\text{-m}$ .

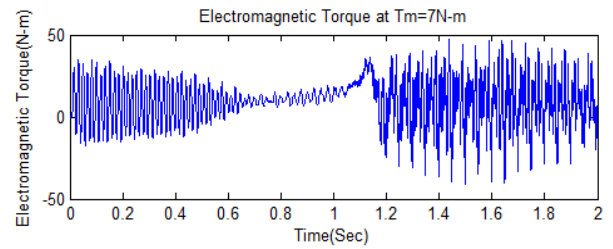


Fig. 24. Electromagnetic Torque of ZSI Fed IM at  $T_m=7N\text{-m}$ .

The Figures 16 to 24 shows the electromagnetic torque of CSI, VSI and ZSI fed IM respectively. From those figures it has been clear that ZSI fed IM attains load torque quicker than CSI and VSI fed.

*c. Comparison of Rotor Current:*

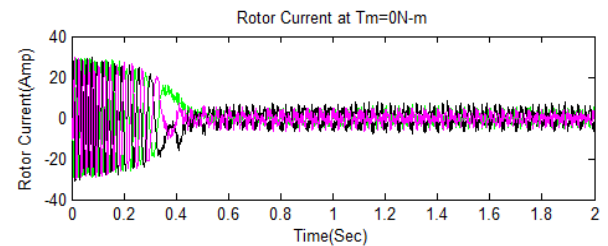


Fig. 25. Rotor Current of CSI Fed IM at  $T_m=0N\text{-m}$ .

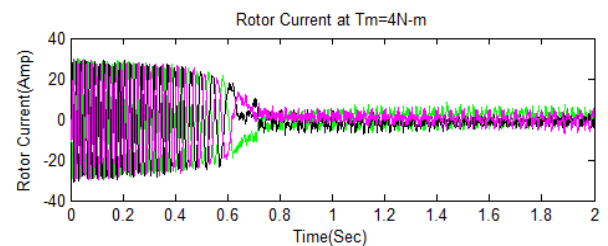


Fig. 26. Rotor Current of CSI Fed IM at  $T_m=4N\text{-m}$ .

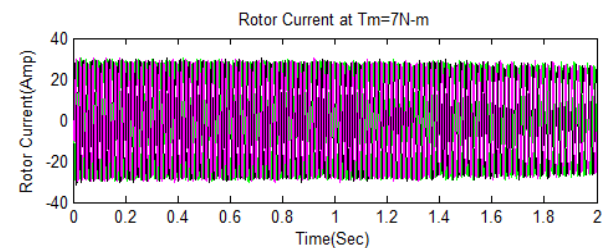


Fig. 27. Rotor Current of CSI Fed IM at  $T_m=7N\text{-m}$ .

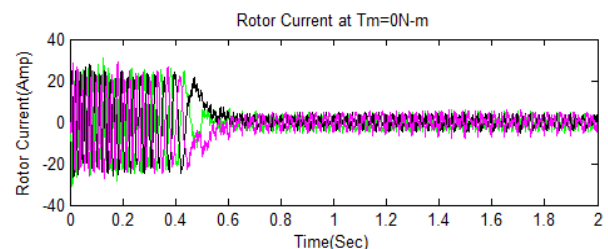


Fig. 28. Rotor Current of VSI Fed IM at  $T_m=0N\text{-m}$ .

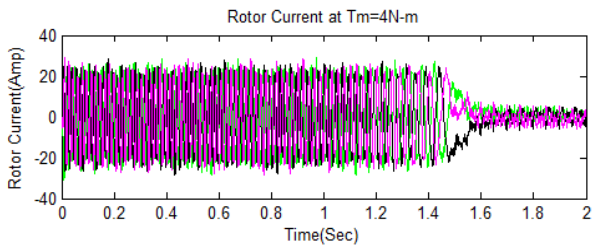


Fig. 29. Rotor Current of VSI Fed IM at  $T_m=4N\text{-m}$ .

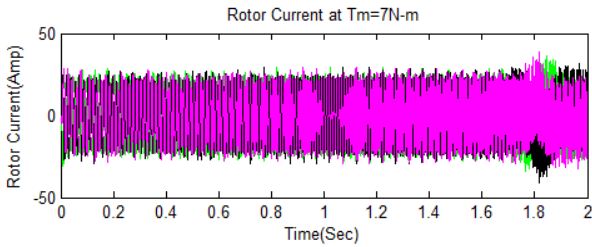


Fig. 30. Rotor Current of VSI Fed IM at  $T_m=7N\text{-m}$ .

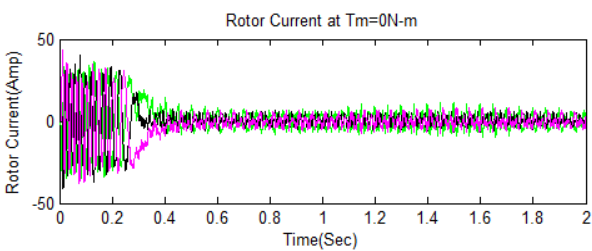


Fig. 31. Rotor Current of ZSI Fed IM at  $T_m=0N\text{-m}$ .

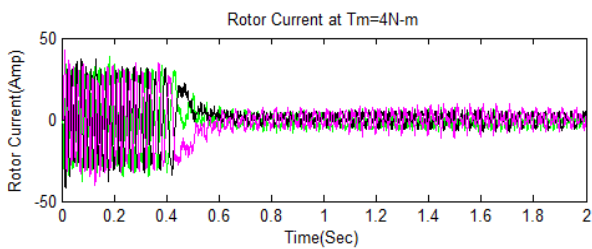


Fig. 32. Rotor Current of ZSI Fed IM at  $T_m=4N\text{-m}$ .

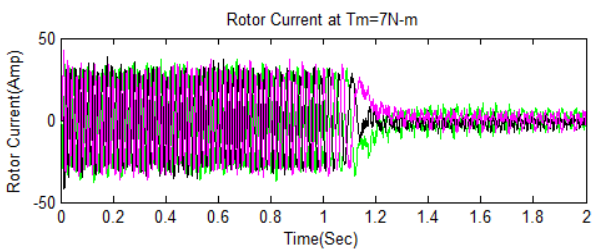


Fig. 33. Rotor Current of ZSI Fed IM at  $T_m=7N\text{-m}$ .

The Figures 25 to 33 show the rotor current of CSI, VSI and ZSI fed IM at different torque condition respectively. From those figures it has been seen that the settling time of ZSI fed IM rotor current is quicker than the CSI and VSI fed IM rotor currents. The rotor current of ZSI fed IM also contains fewer ripples than the rotor currents of CSI and VSI fed IM.

d. Comparison of Stator Current

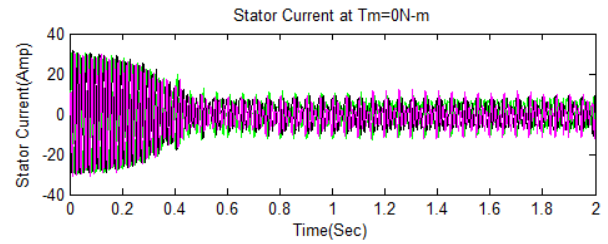


Fig. 34. Stator Current of CSI Fed IM at  $T_m=0N\text{-m}$ .

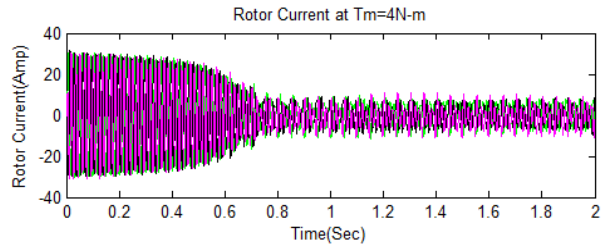


Fig. 35. Stator Current of CSI Fed IM at  $T_m=4N\text{-m}$ .

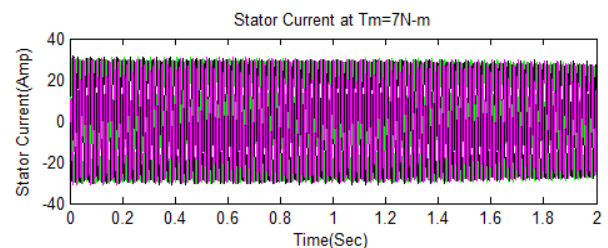


Fig. 36. Stator Current of CSI Fed IM at  $T_m=7N\text{-m}$ .

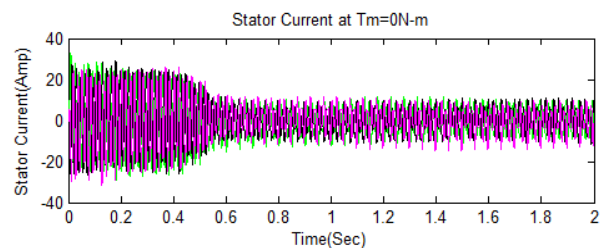


Fig. 37. Stator Current of VSI Fed IM at  $T_m=0N\text{-m}$ .

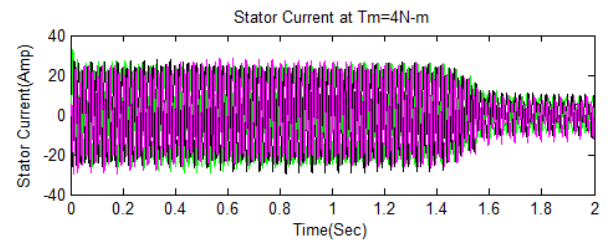


Fig. 38. Stator Current of VSI Fed IM at  $T_m=4N\text{-m}$ .

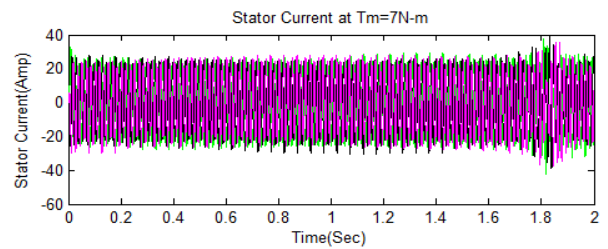


Fig. 39. Stator Current of VSI Fed IM at  $T_m=7N\text{-m}$ .

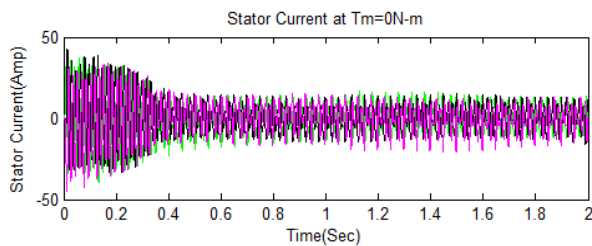


Fig. 40. Stator Current of ZSI Fed IM at  $T_m=0N\text{-m}$ .

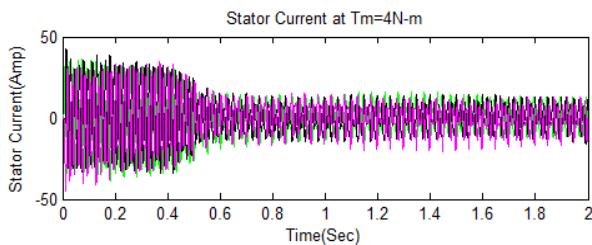


Fig. 41. Stator Current of ZSI Fed IM at  $T_m=4N\text{-m}$ .

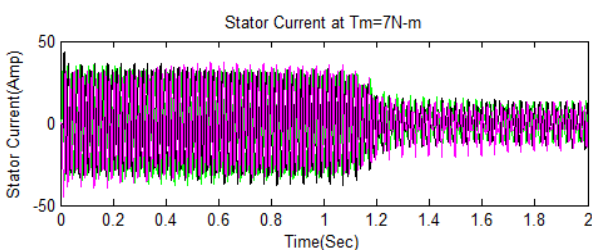


Fig. 42. Stator Current of ZSI Fed IM at  $T_m=7N\text{-m}$ .

The Figures 34 to 42 shows the stator currents of CSI, VSI and ZSI fed IM at different torque respectively. The settling time of stator current of ZSI fed IM decreases as compared to the stator currents of CSI and VSI fed IM.

#### CONCULATION

This paper presents the comparative study of PWM control Z-source inverter for motor drive with conventional inverters for motor drive by using MATLAB Simulink simulation. Various performance of induction motor such as rotor speed, electromagnetic torque, rotor current and stator current has been analyzed at different torque conditions. It has been prove that the induction motor fed with Z-source inverter provides quick operation, fewer harmonic, reduces the settling time of rotor and stator currents as compared to CSI and VSI fed IM.

#### REFERANCES:

[1]Atul Kushwaha, Mohd Arif Khan, Atif Iqbal, Zakir Husain. Z- Source Inverter Simulation and Harmonic Study. *Global Journal of Advanced Engineering Technologies*. 2012; 1(1).  
 [2]Bindeshwar Singh, SP Singh, J Singh, Mohd Naim. Performance evaluation of three phase induction motor drive fed from z-source inverter. *International Journal on Computer Science and Engineering (JCSE)*. 2011; 3(3).  
 [3]Jaswant Singh. Transient Analysis of Z-Source Inverter Fed Three-Phase Induction Motor Drive by Using PWM Technique. *International Electrical Engineering Journal (IEEJ)*. 2013; 4(1): 856-863.

[4]Fang Zheng Peng, Alan Joseph, Miaosen Shen. Z source inverter for motor drives. *IEEE transactions on power electronics*. 2005; 20(4).  
 [5]D Amudhavall, L Narendran. Improved Z Source Inverter for Speed Control of an Induction Motor. *International Journal of Advanced Research in Electrical, Electronics and Instrumentation Engineering*. 2013; 2(4).  
 [6]Sweeka Meshram, Ganga Agnihotri, Sushma Gupta. An Efficient Z-Source Inverter based Solar Power Generation System Fed IM. *International Journal of Scientific & Engineering Research*. 2013; 4(1).  
 [7]P Elangovan, C Kumar, V Suresh. Space Vector Modulation based Speed Control of Induction Motor Fed by Z-Source Inverter using PI controller. *The International Journal of Engineering and Science (IJES)*. 2013; 2(2): 130137.  
 [8]Fang Zheng Peng. Senior Member. IEEE Z-Source Inverter, *IEEE transactions on industry applications*. 2003; 39(2).  
 [9]Omar Ellabban, Joeri Van Mierlo, Philippe Lataire. Experimental Study of the Shoot-Through Boost Control Methods for the Z-Source Inverter. *EPE Journal*. 2011; 21(2).  
 [10]Santosh Sonar, Tanmoy Maity. A Single phase to Three Phase Buck-Boost Converter cum Voltage Regulator suitable for Wind Power. *Energy and Power*. 2012; 2(3): 33-38 doi: 10.5923/j.ep.20120203.02  
 [11]S Nagaraja Rao, BM Manjunatha, VV Ramana Reddy. Shoot through PWM control Strategies for three Level Z-source Inverter. *International Journal of Systems, Algorithms & Applications*. 2012; 2(ICRAET12).  
 [12]CS Sharma, Tali Nagwani. Simulation and Analysis of PWM Inverter Fed Induction Motor Drive. *International Journal of Science, Engineering and Technology Research (IJSETR)*. 2013; 2(2).  
 [13]Aadyasha Patel1, A Mirunalini. Renewable Energy using Z-Source for High Power Applications. *IJREAT International Journal of Research in Engineering & Advanced Technology*. 2013; 1(1).  
 [14]Ibrahim K Al-Abbas. Reduced Order Models of a Current Source Inverter Induction Motor Drive. *American J. of Engineering and Applied Sciences*. 2009; 2(1): 39-43.  
 [15]Nisha kcr, TN Basavaraj. Implementation of impedance source inverter system for photovoltaic applications. *International Journal of Power System Operation and Energy Management ISSN (PRINT): 2(1): 2231-4407*.

# Optoelectronic Performance of Vertical Cavity Surface Emitting InGaAs/InP QW Laser in non-conventional orientation

Sourav Roy<sup>1,2,\*</sup>, Md. Imtiaz Kabir<sup>1</sup>, K.M Abdullah Al-Mamun<sup>1</sup>

<sup>1</sup>Department of Electrical and Electronic Engineering, JUST, Jessore-7408, Bangladesh

<sup>2</sup>Department of Electrical and Electronic Engineering, KUET, Khulna-9203, Bangladesh

\*E-mail: souravroy2k9@gmail.com

**Abstract**—Here, the optoelectronic performance of lattice matched InGaAs/InP vertical cavity surface emitting LASER is numerically simulated using MATLAB in (100), (110), (111), (113) and (131) crystal orientation by solving an eight-band  $k,p$  Hamiltonian using finite difference scheme including spin-orbit coupling. Tensor plane rotation formulae is applied to change the wave-vector  $k$  and Hamiltonian from orthodox (100) plane orientation. It is shown that there is a notable interrelationship between optical emission spectra and crystal plane orientations. The highest and lowest gains are estimated in (111) and (100) orientations with their respective peak emission wavelengths of 1770nm and 1680 nm at the carrier injection density of  $2.5 \times 10^{18} \text{ cm}^{-3}$ . The outcome of this paper would be a stimulus to design ultra-speed optoelectronic devices with performance amelioration by using non-100 oriented epitaxial layers.

**Keywords**—VCSEL; Lattice matching;  $k,p$  method; Crystal orientation; Optical gain

## I. INTRODUCTION

Time division multiplexing (TDM) systems operating beyond 40 Gbit/s, combined with wavelength division multiplexing (WDM), promise auspicious solutions for over-Tbit/s systems due to elevation in lightwave communications technology and the research interest is now towards 100-Gbit/s-class architecture. One of the major barricade in realizing such ultrahigh speed TDM design is the upgradation of ultrahigh speed electronic ICs [1]. Vertical cavity surface emitting laser (VCSEL) first revealed in 1992 (optical pumping) and 1993 (electrical pumping) at Sandia National Laboratories and Chiao Tung University in Taiwan [2-3] is a strong contender for high power laser source. The larger output aperture of VCSELs produces a lower divergence angle of the output beam, and makes possible high coupling efficiency with optical fibers. Mirrors having high reflectivity, in contrast to most edge-emitting lasers, reduce the threshold current of VCSELs, resulting in low power consumption. The oldest and probably the most utilized hetero-structure laser technique is AlGaAs/GaAs QW. However, the InP-based lattice matched systems InP/In<sub>0.53</sub>Ga<sub>0.47</sub>As, came into attention not only because of its material affinity with the optical devices, but also due to its superior drift-diffusion properties with respect to the AlGaAs QW systems. At the InP/InGaAs interface, the higher valence band discontinuity as compared to that in the conduction band ( $\Delta E_C = 0.25\text{eV}$  and  $\Delta E_V = 0.34\text{eV}$ ) provides a high injection efficiency. Moreover, the typical electron mobility is about double that of GaAs and the ohmic contact resistance to n-InGaAs is lower than GaAs due to the lower Schottky barrier height and higher saturation doping density of donors. The emission wavelength from this laser system ranges from 1.2 to 1.7  $\mu\text{m}$  which covers low dispersion

and minimum attenuation region in present-day optic-fiber communication (OFC) [4].

Recently, it has become established that energy band dispersion profile of III-V materials is strongly interrelated with crystal orientations. While better crystalline film quality is achieved for (100) oriented growth of QWs, the internal quantum efficiency reduces with increasing wavelength, resulting partially from the decreased oscillator strength due to the field injected separation of electrons and holes [5]. Performance amelioration in optoelectronic devices can be realized in nonconventional orientation having favorable band structure due to anisotropy of the topmost bulk valence band and minimum interaction between hole sub-bands. Advanced film preparation techniques such as molecular beam epitaxy (MBE) and metal-organic chemical vapor deposition (MOCVD) enables the growth of non-(100)-orientated crystal structure [6-7]. In our previous works, the influence of crystal orientation on different optoelectronic properties of InGaAs/GaAs QW has been studied [8]. There are few reports on orientation-dependent growth of InGaAs/InP QW [9-10]. However, to best of our knowledge, the optical emission profile of InP based laser in non-conventional orientation and its possible application in 1.55  $\mu\text{m}$  OFC is unavailable.

Throughout this paper, the optical properties of lattice matched ZB InP/In<sub>0.53</sub>Ga<sub>0.47</sub>As VCSEL laser have been demonstrated by using the 8\*8  $k,p$  matrix for (100), (110), (111), (113) and (131) crystal orientations. Here, 10 nm quantum well is sandwiched between 7 nm barrier layers. To reveal the optoelectronic properties in (hkl) crystal orientations, plane transformation matrixes are used to modify the wave vector and Hamiltonian matrix from orthodox (100) crystal orientation. The wave functions and Eigen energies of the proposed architecture are evaluated using the numerical finite difference method. The emission profile is anticipated using the energy dispersion profile and wave functions.

The description of this paper is designed as follows: the theoretical formula to calculate optical properties of the InGaAs/InP QW are mentioned in section 2. Results and discussions on the energy band structure and optical emission spectra are illustrated in section 3. Finally, a summary is depicted in section 4.

## II. THEORY

### A. LASER Structure:

In Laser structure of Fig. 1, a 10nm In<sub>0.53</sub>Ga<sub>0.47</sub>As active layer is sandwiched between 7nm InP barrier layers and high band gap GaInAsP is used as cladding layer. Two Al<sub>0.05</sub>Ga<sub>0.42</sub>In<sub>0.53</sub>As/ InP DBRs of mean reflectivity 99.5% are also used as mirrors. All the layers are grown on GaAs

substrate. In non-orthodox (hkl)-orientated laser structure; the h, k and l parameters in the active region is changed.

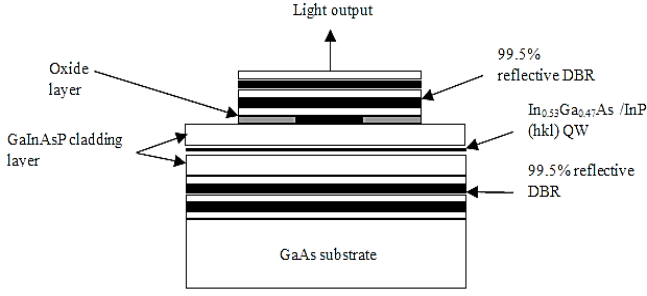


Fig. 1: Structure of lattice matched InGaAs/InP VCSEL

### B. The $k \cdot p$ Method of Band-Structure Calculation near $\Gamma$ -point:

The electronic energy band profile is solved in the envelope approximation using an eight-band  $\mathbf{k} \cdot \mathbf{p}$  Hamiltonian. The modified Kane  $8 \times 8$  Hamiltonian matrix can be given by [11]:

$$H\psi_h(z) = E\psi_h \quad (1)$$

The components of resultant Hamiltonian matrix  $H=H_0$  are:

$$H_0 = \begin{pmatrix} A & 0 & V^* & 0 & \sqrt{3}V & -\sqrt{2}U & -U & \sqrt{2}V^* \\ 0 & A & -\sqrt{2}U & -\sqrt{3}V^* & 0 & -V & \sqrt{2}V & U \\ V & -\sqrt{2}U & -P+Q & -S^* & R & 0 & \sqrt{\frac{3}{2}}S & -\sqrt{2}Q \\ 0 & -\sqrt{3}V & -S & -P-Q & 0 & R & -\sqrt{2}R & \frac{1}{\sqrt{2}}S \\ \sqrt{3}V^* & 0 & R^* & S & -P+Q & S^* & \frac{1}{\sqrt{2}}S^* & \sqrt{2}R^* \\ -\sqrt{2}U & -V^* & 0 & R^* & S & -P+Q & \sqrt{2}Q & \sqrt{\frac{3}{2}}S^* \\ -U & \sqrt{2}V^* & \sqrt{\frac{3}{2}}S^* & -\sqrt{2}R^* & \frac{1}{\sqrt{2}}S & \sqrt{2}Q & -P-\Delta & 0 \\ \sqrt{2}V & U & -\sqrt{2}Q & \frac{1}{\sqrt{2}}S^* & \sqrt{2}R & \sqrt{\frac{3}{2}}S & 0 & -P-\Delta \end{pmatrix} \quad (2)$$

$$\Psi_h(z) = \begin{bmatrix} \Phi_{1/2,1/2}(z) \\ \Phi_{1/2,-1/2}(z) \\ \Phi_{3/2,1/2}(z) \\ \Phi_{3/2,-1/2}(z) \\ \Phi_{3/2,3/2}(z) \\ \Phi_{3/2,-3/2}(z) \\ \Phi_{1/2,1/2}(z) \\ \Phi_{1/2,-1/2}(z) \end{bmatrix} = \begin{bmatrix} g^{(1)}(z) \\ g^{(2)}(z) \\ g^{(3)}(z) \\ g^{(4)}(z) \\ g^{(5)}(z) \\ g^{(6)}(z) \\ g^{(7)}(z) \\ g^{(8)}(z) \end{bmatrix} \quad (3)$$

Where,  $\phi_{j,m_j}$  or  $g^{(j)}$  is the conduction and valence band wave function component and  $E$  is the energy of conduction band and three valence bands. The atomic Bloch states shown in Table I are Eigen states of the Hamiltonian  $H_0$ .  $\Gamma_6$  corresponds to the conduction band,  $\Gamma_8$  denotes the heavy-hole ( $m_j = \pm 3/2$ ) and  $\Gamma_8$  ( $m_j = \pm 1/2$ ) the light-hole band.  $\Gamma_7$  is known as split-off band.

Table I: The atomic basis states at  $\Gamma$  point

$u_i$	$ j, m_j\rangle$	$\Psi_{j, m_j}$	$E_i(k=0)$	
$u_1$	$1/2, 1/2$	$i s\rangle$	0	$\Gamma_6$
$u_3$	$3/2, 1/2$	$-\sqrt{(2/3)} Z\rangle + \sqrt{(1/6)} X+iY\rangle$	$-E_0$	$\Gamma_8$
$u_5$	$3/2, 3/2$	$1/\sqrt{2} X+iY\rangle$	$-E_0$	$\Gamma_8$
$u_7$	$1/2, 1/2$	$\sqrt{(1/3)} Z\rangle + \sqrt{(1/3)} X+iY\rangle$	$-E_0-\Delta$	$\Gamma_7$
$u_2$	$1/2, -1/2$	$i s\rangle$	0	$\Gamma_6$
$u_4$	$3/2, -1/2$	$-\sqrt{(2/3)} Z\rangle - \sqrt{(1/6)} X-iY\rangle$	$-E_0$	$\Gamma_8$
$u_6$	$3/2, -3/2$	$1/\sqrt{2} X-iY\rangle$	$-E_0$	$\Gamma_8$
$u_8$	$1/2, -1/2$	$\sqrt{(1/3)} Z\rangle - \sqrt{(1/3)} X-iY\rangle$	$-E_0-\Delta$	$\Gamma_7$

The matrix elements are:

$$A = E_c - \frac{\hbar^2}{2m_0} (k_x^2 + k_y^2 + k_z^2) \quad (4)$$

$$P = -E_v - \gamma_1 \frac{\hbar^2}{2m_0} (k_x^2 + k_y^2 + k_z^2) \quad (5)$$

$$Q = -\gamma_2 \frac{\hbar^2}{2m_0} (k_x^2 + k_y^2 + k_z^2) \quad (6)$$

$$R = \sqrt{3} \frac{\hbar^2}{2m_0} [\gamma_2 (k_x^2 - k_y^2) - 2i\gamma_3 k_x k_y] \quad (7)$$

$$S = -\sqrt{3} \gamma_3 \frac{\hbar^2}{2m_0} k_z (k_x - ik_y) \quad (8)$$

$$U = \frac{-i}{\sqrt{3}} P_0 k_z \quad (9)$$

$$V = \frac{-i}{\sqrt{6}} P_0 (k_x - ik_y) \quad (10)$$

$P_0$  is the coupling between the conduction and valence bands,  $E_c$  and  $E_v$  are the (unstrained) conduction and valence band energies respectively,  $\Delta$  is the spin orbit splitting and  $\gamma_i$ 's are modified Luttinger parameters. The energy dispersion profile along (100) orientation is shown as a function of  $k$  for the 8-band  $k \cdot p$  theory by diagonalizing the Hamiltonian using numerical finite difference scheme.

### C. Crystal orientation dependent wave vector

If the active channel is grown on (hkl) crystal orientation, the wave vectors on (100) crystal can be anticipated by the following expression [12]:

$$\begin{pmatrix} k_1 \\ k_2 \\ k_3 \end{pmatrix} = O_R \begin{pmatrix} k_x \\ k_y \\ k_z \end{pmatrix} \quad (11)$$

The expression of the rotation matrix is as follows [13]:

$$O_R = \begin{pmatrix} \cos\theta \cos\phi & -\sin\phi & \sin\theta \cos\phi \\ \cos\theta \sin\phi & \cos\phi & \sin\theta \sin\phi \\ -\sin\theta & 0 & \cos\theta \end{pmatrix}$$

Where,  $\theta = \tan^{-1} \left( \frac{\sqrt{h^2 + k^2}}{l} \right)$  and  $\phi = \tan^{-1} (k/h)$

Applying the wave vector in the (100) crystal orientation, the Hamiltonian matrix for (100) crystal orientation can be calculated according to eq. 2. Then the Hamiltonian matrix in (hkl) orientation can be counted by the simple equation:

$$H^{hkl} = U H^{(100)} U^* \quad (12)$$

Where,  $U = R(\theta)R(\phi)$

In this formulae,  $R(\theta)$  and  $R(\phi)$  are denoted as rotations which transform the (100) orientated valence band Hamiltonian to arbitrary crystal orientated Hamiltonian matrix. The argument of  $R(\theta)$  and  $R(\phi)$  can be defined by:

$$R(\theta) = \begin{pmatrix} \alpha^2 & -\sqrt{3}\alpha\zeta & \sqrt{3}\alpha\zeta^2 & \zeta^3 \\ \sqrt{3}\alpha\zeta & \alpha^3 - 2\alpha\zeta^2 & -2\alpha^2\zeta + \zeta^3 & \sqrt{3}\alpha\zeta^2 \\ \sqrt{3}\alpha\zeta^2 & 2\alpha^2\zeta - \zeta^3 & \alpha^3 - 2\alpha^2\zeta & -\sqrt{3}\alpha\zeta \\ \zeta^3 & \sqrt{3}\alpha\zeta^2 & \sqrt{3}\alpha\zeta & \alpha^3 \end{pmatrix} \quad (13)$$

$$\alpha = \cos \frac{\theta}{2} \quad \text{and} \quad \zeta = -\sin \frac{\theta}{2}$$

$$R(\phi) = \begin{pmatrix} e^{i(3/2)\phi} & 0 & 0 & 0 \\ 0 & e^{i(1/2)\phi} & 0 & 0 \\ 0 & 0 & e^{-i(1/2)\phi} & 0 \\ 0 & 0 & 0 & e^{-i(3/2)\phi} \end{pmatrix} \quad (14)$$

### D. Optical Gain

The optical gain as a function of energy for quantum well structure can be approximated by [14]:

$$g(E) = \frac{2q^2 \hbar}{n \epsilon_0 c m_0^2 L E} \times \sum_{n, m} \int_0^\infty \frac{k_i M_{nm}(k_i) \Gamma / (2\pi)}{(E_{cn}(k_i) - E_{kpm}(k_i) - E)^2 + (\Gamma / 2\pi)^2} (f_c^n - f_v^m) dk_i \quad (15)$$

Here,  $q$  is denoted as free electron charge,  $\hbar$  as reduced Planck constant,  $n$  as the index of refraction,  $\epsilon_0$  as free space dielectric constant,  $c$  as speed of light,  $E$  as photon energy,  $E_{cn}$  as the  $n^{\text{th}}$  conduction sub-bands,  $E_{kpm}$  as the  $m^{\text{th}}$  valence

sub-bands, and  $M_{nm}$  as the momentum matrix element in strained quantum well architecture.  $\Gamma = \frac{\hbar}{\tau}$ ;  $\tau$  is the photon relaxation time.  $F_c$ ,  $F_v$  are the Fermi levels of conduction and valence band. The momentum matrix element for transition can be written as:

$$M_{nm}(k_t) = \frac{3}{4} \left[ \langle \Psi_{n(k_t=0)} | g_m^{(1)} \rangle^2 + \frac{1}{3} \langle \Psi_{n(k_t=0)} | g_m^{(2)} \rangle^2 \right] M_b^2$$

### III. RESULTS AND DISCUSSIONS

Following the k.p method formula given in Section 2, the optical properties of lattice matched 10 nm ZB InP/In<sub>0.53</sub>Ga<sub>0.47</sub>As QW VCSEL structure at the  $\Gamma$ -point have been studied. The simulation is carried out in MATLAB environment at room temperature. The valence band dispersion curves obtained in (100), (110), (111), (113) and (131) crystal orientations for the first Brillouin zone have been shown in Fig. 2 (a)-(e) where HH, LH and SH indicate heavy hole, light hole and spin-orbit split off hole bands. To compare the orientation dependent energies, the figures are plotted as a function of wave vector in the same scale. It has been observed, for values of  $k \neq 0$  (wave vector in the plain direction), the increasing conduction and spin-orbit split off band coupling offer strong anisotropy of the topmost valence band structure at (110) and (111) orientation. Lasing action occurs due to the allowed transition from conduction band (C) to HH. Other transitions such as intra-subbands transitions are forbidden because it reduces the gain of the laser. Among the intra-subbands, transition probability is highest between HH and LH, which is reduced when the energy separation between them is higher. For (111) orientation, larger energy spacing between HH and LH has been observed causing the variation of electron and hole mass  $m^*$ , which changes the topmost curvature of valence sub-bands as well as emission profile. In order to explain the wavelength dependence of peak emission wavelength the energy separation between the C-HH and HH-LH bands is estimated from the energy band dispersion profiles and listed in table II. It is found that the energy separation between conduction band minima and valence band maxima changes with crystal plane orientations. It can be seen from the table that the intraband mixing effect is minimum for this laser along (111) orientation. With the easy MOVPE growth, the fabrication of (110) oriented VCSEL has strong possibility. The orientation dependent peak gain can be

$$\langle \Psi_{n(k_t=0)} | g_m^{(1)} \rangle = \int_{-\infty}^{\infty} \Psi_{n(k_t=0)}(z) g_m^{(1)}(z) dz$$

$M_b$  is the bulk average crystal momentum matrix that can be noted by ( $E_g$ =band gap and  $\Delta$ =split-off band separation):

$$M_b = \left( \frac{m_0}{m_e} - 1 \right) \frac{m_0 E_g (E_g + \Delta)}{6(E_g + \frac{2}{3}\Delta)} \quad (16)$$

revealed by the momentum matrix elements that depend on the overlapping wave functions of electrons and holes. It is observed from fig. 3 that transition probability is maximum in (111) orientation and least in (113) and (131) orientations. The lowest band gap and minimum intraband interaction is responsible for the improved result along (111). Here we have calculated the optical gain spectra in different crystal orientations using Eq. (15) and shown in Fig. 4 and the approximated gains is found to be 3700, 4650, 4800, 4200 and 3990  $\text{cm}^{-1}$  in (100), (110), (111), (113), and (131) orientations, respectively. Here highest gain is observed in (111) crystal orientation and lowest gain is in (100) orientation. The highest gain in (111) crystal orientation is obtained due to the small band mixing effect and greater transition probability. For this similar issue, minimum gain is observed in (100) crystal orientation. The peak emission wavelength are found to be 1.68, 1.55, 1.77, 1.58 and 1.75  $\mu\text{m}$  for (100), (110), (111), (113) and (131) crystal orientations.

That demonstrates peak emission spectra ( $\lambda$ ) can be tuned from 1680 nm to 1770 nm with the change in plane orientation from (100) to (111). The cause of tuning  $\lambda$  is due to the energy gap between C and HH bands. Moreover, an interesting phenomenon is observed in (111) as the C-HH band gap is 0.794 eV which indicates the lasing emission wavelength of 1.55  $\mu\text{m}$  that covers minimum chromatic dispersion range of OFC. The crystal orientation-dependent differential gain is calculated and shown in fig.5. The maximum differential gains are obtained when the injected carrier densities  $2.75 \times 10^{18} \text{cm}^{-3}$  and  $3.0 \times 10^{18} \text{cm}^{-3}$  in (111) and (113) crystal orientations. For (100), (110), and (131) crystal orientations, the maximum differential gains are evaluated when the injection carrier density is  $3.25 \times 10^{18} \text{cm}^{-3}$ .

So, it is quite visible that (111)-oriented vertical cavity surface emitting InGaAs/InP Laser system leads to have high performance. Also, in (110) oriented growth, the laser emits at 1550nm.

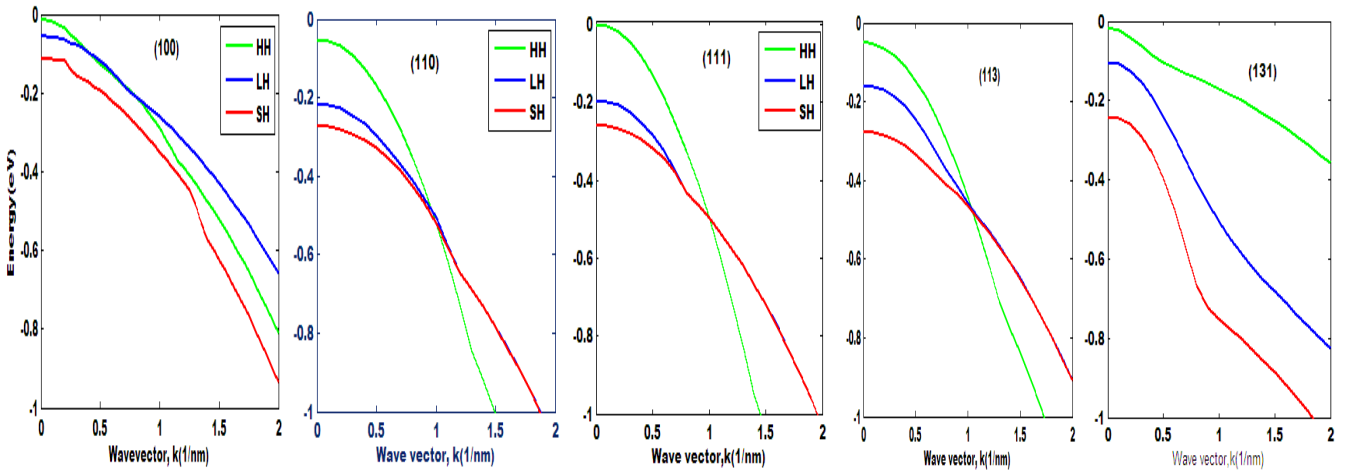


Fig. 2: Valence band dispersion profile of (a) 100 (b) 110 (c) 111 (d) 113 and (e) 131-oriented InGaAs/InP Laser.

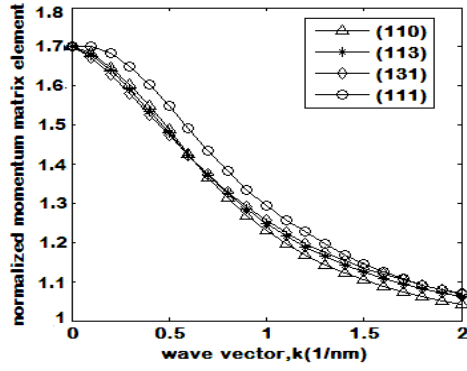


Fig 3. Momentum matrix element in different crystal orientations

Table I. Orientation dependent energy separation

Crystal orientation	C-HH (eV)	HH-LH (eV)
(100)	0.738	0.03
(110)	0.794	0.17
(111)	0.702	0.20
(113)	0.782	0.10
(131)	0.714	0.07

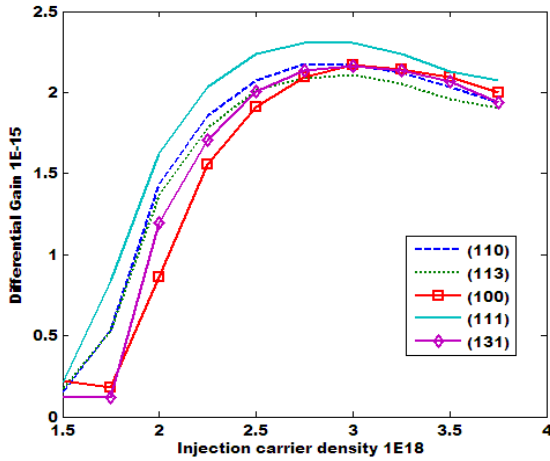


Fig 5: Differential gain in different orientation

#### IV. CONCLUSION

To summarize, the influence of crystal orientation on optical properties of Lattice matched zinc-blend InGaAs/InP QW VCSEL are demonstrated at the  $\Gamma$ -point by practicing the eight band  $k.p$  method including spin orbit coupling. The theoretical results depict the exclusive variation of conduction and valence band energy band dispersion profile with crystallographic direction. Due to minimum interaction from distant band, larger splitting between heavy hole and light hole band is observed in (111) orientation. As the maximum value of momentum matrix element is also evaluated in this orientation, the maximum optical gain is found to be  $4800 \text{ cm}^{-1}$ . Peak emission wavelength can be tuned from 1680 to 1770 nm with the

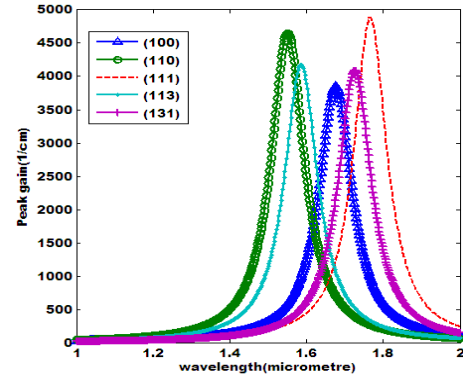


Fig. 4: Orientation dependent optical emission profile

tuning in crystal orientation from (100) to (111). This result regards that (111) and (110)-oriented InGaAs/InP QW VCSEL Laser is a highly potential material for the fabrication of high speed optoelectronic devices in the minimum dispersion range for optical fiber communication.

#### REFERENCES

- [1] T.Enoki, E.Sano & T.Ishibashi, "Prospects of InP-based IC technologies for 100-Gbit/S -class lightwave communication systems," International Journal of High Speed Electronics and Systems, Vol. 11, No. 1 (2001) pp. 137-158.
- [2] R. P. Schneider and J. A. Lott, "Cavity design for improved electrical injection in InAlGaP/AlGaAs visible (639-661 nm) vertical-cavity surface-emitting laser diodes," Applied Physics Letters, vol. 63, no. 7, pp. 917-919, Sep. 1993.
- [3] K.F. Huang, K. Tai, C.C. Wu and J.D. Wynn, "Continuous wave visible InGaP/InGaAlP quantum-well surface-emitting laser diodes," IEEE Trans. Electron Devices, vol. 40, no. 11, pp. 613-614, Nov. 1993.
- [4] Temkin et al., InGaAs/InP graded index quantum well lasers with nearly ideal static characteristics, Applied Physics Letters 56, 1222 (1990).
- [5] M. Phon, Y. Chung, W.I. Wang, Orientation dependence of valence subband structures in GaAs-Ga<sub>x</sub>Al<sub>x</sub>As quantum well structures, Appl. Phys. 64 (1988) pp. 4609-4613.
- [6] D.A. Woolf et al., The homoepitaxial growth of non-axis GaAs (111)A, (111)B and(201) compared with GaAs(100): doping and growth temperature studies, J. Cryst. Growth 127 (2002) 913-917.
- [7] R. Notzel, K.H. Ploog, Man-made low-dimensional solids: new challenges in microstructure material science, Int. J. Mod. Phys. B7 (1993), pp. 2743-2778.
- [8] Sourav Roy, Nazmus Sakib, Utpal Bhowmik and Md. Rafiqul Islam, "Piezoelectric field-dependent optical properties of InGaAs/GaAs quantum well architecture in arbitrary crystal orientation", 17<sup>th</sup> International Conference on Computer and Information Technology (ICIT), 2014, Dhaka, Bangladesh.
- [9] Bakin et al., "Simulation of the orientation-dependent growth of InGaAs/InP by MOVPE, Journal of Applied Physics 76, 4906 (1994).
- [10] G. Zwinge, H.H. Wehmann, A. Schlachetzki, and C. C. Hsu, "Orientation-dependent growth of InGaAs/InP for applications in laserdiode arrays", Journal of Applied Physics 74, 5516 (1993).
- [11] Craig Pryor, Eight-band calculations of strained InAs/GaAs quantum dots compared with one, four, and six-band approximations, Physical Review B, 03/1998.
- [12] M.M. Hasan, et al., Crystallographic orientation-dependent optical properties of GaInSb mid-infrared quantum well laser, Optik - Int. J. Light Electron Opt. (2011), doi:10.1016/j.jleleo.2011.09.021
- [13] Dragica Vasileska, Tutorial for semiconductor band structure calculation, Arizona State University, Tempe, AZ
- [14] A. Niwa, T. Ohtoshi, T. Kuroda, Orientation dependence of optical properties in long wavelength strained quantum-well lasers, IEEE J. Selected Top. Quantum Electron. 1 (1995) 211- 217.

# Predicting the Popularity of Online News from Content Metadata

Md. Tafueeq Uddin, Muhammed Jamshed Alam Patwary, Tanveer Ahsan, Mohammed Shamsul Alam

Department of Computer Science and Engineering, International Islamic University Chittagong, Bangladesh  
mohamed.taufeeq.uddin@gmail.com

**Abstract**—Popularity prediction of online news aims to predict the future popularity of news article prior to its publication estimating the number of shares, likes, and comments. Yet, popularity prediction is a challenging task due to various issues including difficulty to measure the quality of content and relevance of content to users; prediction difficulty of complex online interactions and information cascades; inaccessibility of context outside the web; local and geographic conditions; social network properties. This paper focuses on popularity prediction of online news by predicting whether users share an article or not, and how many users share the news adopting before publication approach. This paper proposes the gradient boosting machine for popularity prediction using features that are known before publication of articles. The proposed model shows around 1.8% improvement over previously applied techniques on a benchmark dataset. This model also indicates that features extracted from articles keywords, publication day, and the data channel are highly influential for popularity prediction.

**Keywords**—Social Media Contents, Popularity Prediction, Before Publication Approach, Machine Learning, Text Mining

## I. INTRODUCTION

The consumption of online news accelerates day by day due to the widespread adoption of smartphones and the rise of social networks. Note that online news content comprises of numerous key properties. For instance, it is easily produced and small in size; its lifespan is short and the cost is low. Such properties make news content more effective to be consumed on social sharing platforms. More interestingly, this type of content can capture the attention of a significant amount of Internet users within a short period of time. As a consequence, researchers focus on the analysis of online news content such as predicting the popularity of news articles, demonstrating the decay of interest over time to understand the world of online news since it has so many practical implications [1].

The prediction of the popularity of online news content has remarkable practical values in many fields. For example, by utilizing the advantages of popularity prediction, news organization [2] can gain a better understanding of different types of online news consumption of users. As a result, the news organization can deliver more relevant and engaging content in a proactive manner as well as the organization can allocate resources more wisely to develop stories over their life cycle. Furthermore, prediction of news content is also beneficial for trend forecasting, understanding the collective

human behavior, advertisers to propose more profitable monetization techniques, and readers to filter the huge amount of information quickly and efficiently [1] [3].

The notion of popularity is often expressed by investigating the number of interactions in the web and social networks, for example, click-through rate, number of shares, likes, and retweets. Tatar et al. [4] demonstrated two types of popularity prediction techniques that are **after publication**: more common technique, which uses features capturing the attention that one content receives after its publication. Higher prediction results are expected in after publication technique since utilization of information about the received attention makes the prediction task easier [1] [5] [6] [7]; **before publication**: relatively challenging and effective technique. This technique uses only content metadata features that are known prior to the publication of contents instead of using features related to the attention that one content receives after contents release. Although the expected prediction accuracy is comparatively low in before publication method as we are using only metadata features rather than original news content [8], the prediction is more desirable as far as it fosters the possibility of decision making to customize the content before the release of content [9]. In this work, we model popularity prediction problem in before publication technique.

Although popularity prediction of web content has tremendous impacts in many areas, popularity prediction task still faces a bunch of major challenges [4] [9]. First, different factors make prediction difficult, for example, the quality of content or relevance of content to users can influence contents popularity. Second, the relationship between events in the real world and content itself are not only difficult to capture but also hard to further feed into the prediction engine. Third, prediction of complex social interactions and information cascades at the microscopic level are extremely challenging. Fourth, the prediction might also be difficult because of the inaccessible content like context outside the web, local and geographical conditions, and situations which influence the population. Last but not least, the prediction may also be hard based on the network properties e.g. the structure of the networks, and the interplay between different layers of the web.

Previously, researchers try to estimate the popularity by predicting whether or not someone shares the news. However, this approach is less informative since we can only identify



users share the news rather than how many users share the news. Hence, this paper proposes an extension to the previous popularity prediction models by predicting the number of shares of news using a novel ensemble learning algorithm, namely gradient boosting machine (GBM) [10] in **before publication** setting. In this work, we use a heterogeneous set of metadata features that are known prior to the publication of the article to train the proposed GBM, where the goal is not only to predict whether users share an article or not but also to predict how many users shares the article. Hence, GBM is the ensemble of multiple weak learners or decision trees in which each successive decision trees are built from the prediction residual of the preceding decision trees to form a final highly accurate prediction model. The final prediction model guarantees that it performs much better than the individual performance of each decision tree. Note that the proposed GBM comprises of several good qualities including high popularity prediction accuracy, competitive computational performance both in training and prediction steps, and capability to handle large training dataset.

## II. RELATED WORK

Over the last couple of years, researchers conducted several web mining and machine learning studies regarding web content analysis. For instance, Tatar et al. [4] analyzed different types of web content such as online videos, online news and social networking sites. They also reviewed different web content popularity prediction models including both classification and regression models. They further presented *good predictive features such as characteristics of content creators, textual features, and sentiment analysis, and revealed influential factors toward web content popularity*. Gao et al. [3] investigated the arrival process of retweets as well as user activity variation on the retweeting dynamics. They predicted the popularity by modeling the retweeting dynamics using extended reinforced Poisson process model with time mapping process. They, in addition, reduced the effect of user activity variation introducing the Weibo time notation as well as integrating a time mapping process into the proposed model. Castillo et al. [2] provided a qualitative and quantitative analysis of the life cycle of articles' stories demonstrating the interplay between site visitation patterns and social media reactions to articles. Furthermore, they modeled overall traffic of articles by observing social media reactions or attention profile such as *decreasing, steady, increasing, and rebounding*.

*After publication method* is highly popular in popularity prediction research. For instance, Tatar et al. [1] ranked news articles by predicting *user comments* using the linear model on a logarithmic scale and constant scaling model in after publication setting. They outlined that *popularity prediction methods are the good alternative for automatic online news ranking*. Lee et al. [5] inferred the likelihood of the popularity of online content for survival analysis applying Cox proportional hazard regression. They used a set of observable explanatory factors to model and to predict objective metric such as threads lifetime and the number of comments. Petrovic et al. [11] predicted

message propagation in twitter using passive-aggressive (PA) learning algorithm in time-sensitive approach. They extracted features related to the author and text of the tweets and various statistics of the tweet itself. Their findings suggested that *automatic retweets prediction performance of PA is as good as prediction performance of humans*. Szabo and Huberman [6] predicted the long-term dynamics of individual submissions e.g. number of views for Youtube videos and the number of votes for Digg stories from early measurements of access of users. They highlighted that Digg stories outdated shortly while Youtube videos were found popular for a long time after their initial submission to the portal.

However, there are only a few studies which followed the challenging *before publication approach* like this study. For example Bandari et al. [9] constructed features from the content of the news articles and its source of publication that were available prior to contents release. They considered four characteristics of the articles: *news source, the category of news, the subjectivity of the language, and named entities mentioned in the articles*. They reported that ranges of popularity on social media could possibly be predicted with 84% accuracy using the bagging technique. Arapakis et al. [12] pointed out that *news popularity prediction at cold start is still an open challenge*. They predicted tweet counts and page views using features related to time, news source, genre, Wikipedia, web search and twitter. In their findings, they reported that *the imbalanced class distribution drove the prediction models to bias toward the unpopular articles that concluded the predictions not useful in realistic scenarios*. Fernandes et al. [8] proposed proactive intelligent decision support system for online news articles that predicted whether user shares articles or not analyzing features known before publication such as keywords, digital media content, and earlier popularity of news referenced in articles. They achieved 73% popularity prediction accuracy on Mashable news dataset via random forests algorithm adopting rolling windows evaluation strategy.

## III. GBM FOR NEWS POPULARITY PREDICTION

The goal of this work is to predict whether a news article may share or not by users as well as the total count of shares in the realistic setting using GBM algorithm in both classification and regression settings. In training step of this approach, heterogeneous set of metadata features extracted from articles is fed to GBM to build the desired prediction model. The trained GBM model is then used in prediction step to carry out popularity prediction task. The rest of this section covers a brief description of the key idea, and regularization techniques of GBM for classification and regression.

### A. Key Idea

GBM [13] is an ensemble learning algorithm that is the combination of gradient-based optimization and boosting. GBM produces strong prediction model by combining multiple weak prediction models in which weak models are created by sequentially applying to the incrementally changed dataset.

Optimization based on the gradient in GBM utilize the gradient computations to minimize the cost function of a model with respect to training dataset while boosting additively gathers an ensemble of weak models to build the prediction model for popularity prediction challenge. In short, the main idea beneath GBM is to build a series of simple and probably inaccurate decision trees or weak models successively from the prediction residuals of the preceding decision trees and combine them to construct a final highly accurate prediction model.

### B. Regularization

Generalization capability of GBM is one of the crucial concern [14]. A number of parameters can contribute towards reducing the effects of overfitting by controlling learning rate and/or by introducing randomness into GBM. For instance, the smaller values of learning rate  $v$  such as  $v \leq 0.1$  can generally ensure better generalization and performance on the test dataset. Overfitting can also be eliminated by fitting weak models on a subsample or constant fraction e.g.  $0.5 \leq fraction \leq 0.8$  of the training dataset at random with no replacement. Furthermore, to reflect generalization, we can use a large number of trees or the boosting iteration  $M$ , and control  $J$ , by picking the value of  $J$  in between 4 and 8.

## IV. MASHABLE NEWS DATASET

Online news popularity prediction (**Mashable news**) dataset [8] is publicly available at <http://archive.ics.uci.edu/ml/datasets/Online+News+Popularity>, which aims to predict the future popularity of news articles using information that are known before the release of news articles. Mashable news dataset consists of 58 heterogeneous features about the associated statistics of the original news articles released by Mashable ([www.mashable.com](http://www.mashable.com)) during a two years period from January 7, 2013 to January 7, 2015. Fernandes et al. crawled news articles from Mashable website, and then they discarded special occasion and very recent articles e.g.  $< 3$  weeks from the crawled articles.

More precisely, they extracted 47 features from HTML code and classified them into 4 different categories such as *number*, *ratio*, *bool*, and *nominal*. The unbounded numeric features like the number of words in the article were scaled by logarithmic transformation as well as they transformed the nominal features with the common *1-of-C* encoding. They also extracted the statistical summary of the number of shares of all Mashable links cited in articles that were known before the release of articles. Three types of keywords such as worst, average and best were captured by ranking all articles keyword average shares that were also known before release.

Additionally, they extracted a bunch of natural language processing features such as closeness to top latent Dirichlet allocation (LDA) [15] topics, title subjectivity, the rate of positive and negative words and title sentiment polarity by using LDA to compute relevant topics as well as to measure the closeness of current article to the previously computed topics. Sentiment polarity and subjectivity scores were also computed by applying the pattern web mining module [16].

## V. EXPERIMENTS AND RESULTS

The proposed GBM prediction model was evaluated on Mashable news dataset using *5-fold* cross-validation strategy. To benchmark the proposed GBM against previously applied algorithm, namely random forests, we also reproduced random forests (**RF**) from reference [8] adopting 5-fold cross validation. Each of the experiments was run for 20 times with different random seeds, and then we averaged over 20 different experimental runs to achieve the final results. For predicting whether users share a news article or not, we modeled the popularity prediction problem as binary classification problem that is *Popular vs. Unpopular*. In the case of binary classification, receiver operating characteristics (ROC) curve was produced to demonstrate the performance of the models. Note that ROC is created by plotting sensitivity against one minus specificity i.e.  $1 - specificity$  at numerous threshold values. The larger value of the performance metric area under the ROC curve (**AUC**) indicates the higher popularity prediction accuracy.

As mentioned earlier, the experimental set up was binary classification problem in which the goal was to classify whether an article was popular or unpopular by predicting whether users share that article or not. We defined the popularity of an article based on a decision threshold  $D$ . For instance, when an article is shared more than 1400 times e.g.  $D \geq 1400$ , we labeled the article as *Popular*; otherwise, we labeled the article as *Unpopular* as suggested in [8]. We considered AUC as the primary evaluation metric as far as AUC is the most suitable metric as AUC is independent of the threshold value as well as AUC calculates discrimination power of the models very efficiently.

On the other hand, we modeled the popularity prediction problem as regression problem during the estimation of popularity via predicting the number of shares of the news article by users. Note that we took the logarithm of the original number of shares of news to use as the prediction label to train and test using GBM and RF regressors. During performance evaluation of the regression models, we evaluated the models by measuring the mean absolute percentage error between the predicted shares and logarithm of the original number of shares (**MAPE\_LOG**), and between the exponents of predicted shares and the original number of shares (**MAPE**).

For training and validating the proposed GBM, we set *logistic regression*, and *linear regression* as objective functions during binary classification and regression, respectively, the value of the learning rate  $v = 0.001$  to reflect better generalization, the size of the tree  $J = 8$ , and subsample size *fraction* = 0.8. Finally, the number of boosting iteration  $M$  was selected using 5-fold validation approach. Figure 2 shows the performance of RF and GBM classifiers. Notice that the best AUC value obtained on Mashable news dataset was **74.5%** using GBM. It can be seen that GBM performed **1.8%** better than widely used machine learning algorithm RF which generated previous benchmark results on Mashable news dataset. Although the obtained result was around **74-75%** discrimination level which was far away from being

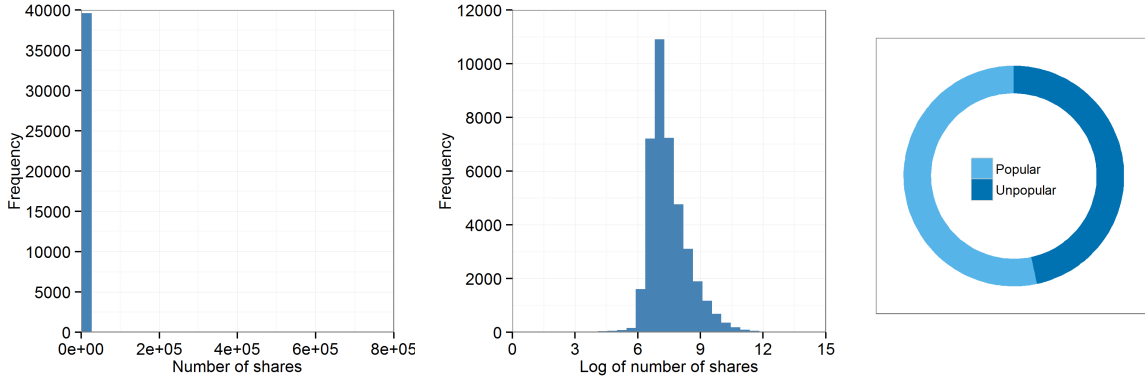


Fig. 1. From left to right, distribution of the popularity prediction label e.g. original number of shares, the logarithms of the number of shares, and proportion of the popular and unpopular article classes of Mashable news dataset

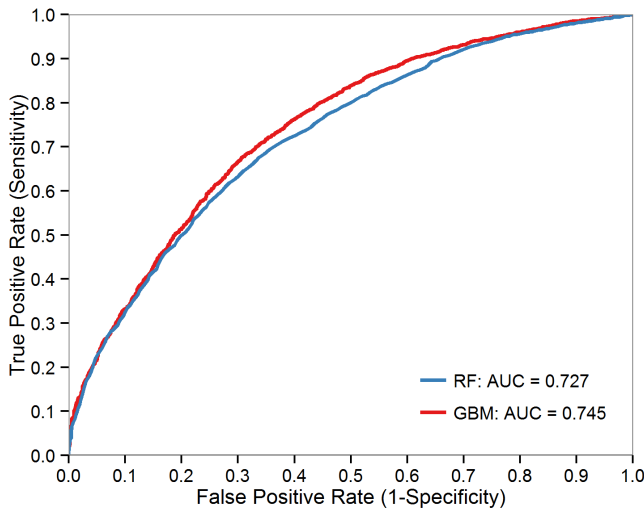


Fig. 2. Comparison of the AUC produced from RF and GBM

TABLE I  
PREDICTION BENCHMARK OF NUMBER OF SHARES OF NEWS ARTICLES. THIS TABLE DISPLAYS MAPE\_LOG, MAPE, AND THEIR STANDARD DEVIATION (SD) RESULTED FROM RF AND GBM APPLYING ON MASHABLE NEWS DATASET

Model	MAPE_LOG	MAPE_LOG SD	MAPE	MAPE SD
RF	8.39 %	0.0083	73.41 %	0.0986
GBM	<b>8.11 %</b>	0.0073	<b>69.42 %</b>	0.0989

perfect, performance was still interesting since we only fed metadata features for prediction task following before publication technique. As we obtain this prediction results using some meta features or statistical features before publication of the news, we can, therefore, feed this results for further modification of the articles.

Table I shows the performance of RF and GBM during the prediction of the count of shares of articles. From Table I, it can be indicated that GBM was better than RF since MAPE\_LOG and MAPE generated from GBM were 8.11%

and 69.42%, respectively, that were relatively smaller than the MAPE\_LOG and MAPE generated from RF.

GBM uses *gain* [17] to estimate the contribution of each feature to the prediction model. GBM takes each gain of each feature of each tree and computes mean per feature to provide a vision of the entire prediction model. We measured the relative importance scores of features using GBM for both predicting popularity and number of shares of news for which we trained GBM using 35679 news articles. Figure 3 highlights the relative importance scores or  $Gain * 100$  of the top 20 features; x-axis represents the relative feature importance scores and y-axis represents the 20 features from Mashable news dataset. In can be observed from Figure 3 that features related to the summary statistics of contents keywords, the summary statistics of the number of the shares of the referenced articles, tokens, links, data channel types whether it is entertainment or technology channels, and publication day had strong significance for predicting popularity and number of shares of online news. Moreover, natural language processing features such as closeness of target article to different LDA topics e.g. 0, 1, 2, rate of positive and negative words, text subjectivity, and global sentiment polarity encapsulated high discrimination power towards popularity prediction.

## VI. CONCLUSION AND FUTURE WORK

This paper introduces and implements GBM to tackle the challenge of classifying popular news articles from unpopular articles by measuring the count of shares in before publication approach. Our findings suggest that GBM is able to predict popularity with a decent prediction rate using only statistical features associated with original news articles without using the original content of news articles or after publication attention. GBM also outlined discriminative and useful metadata features such as the statistical summary of keywords, the earlier popularity of articles referenced in articles, natural language processing features, and publication time. Future work will include, first, the exploration of more advanced features regarding content like trend analysis. Second, the evaluation of the prediction model on more complex and

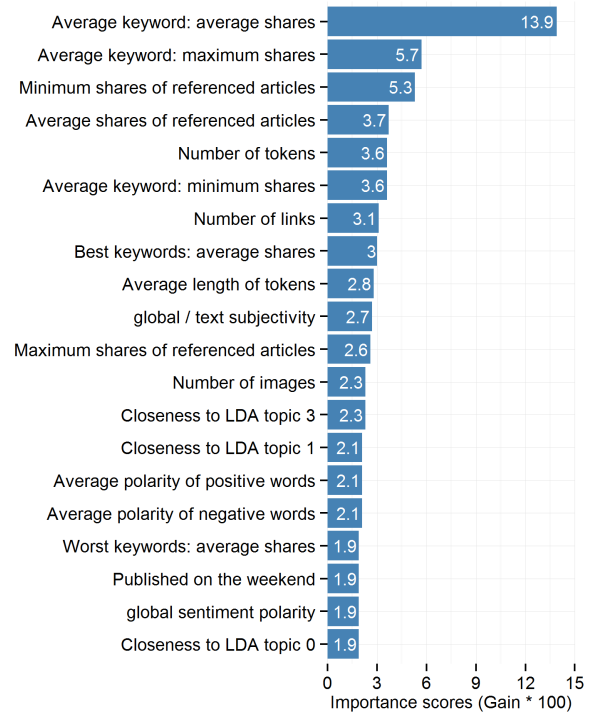
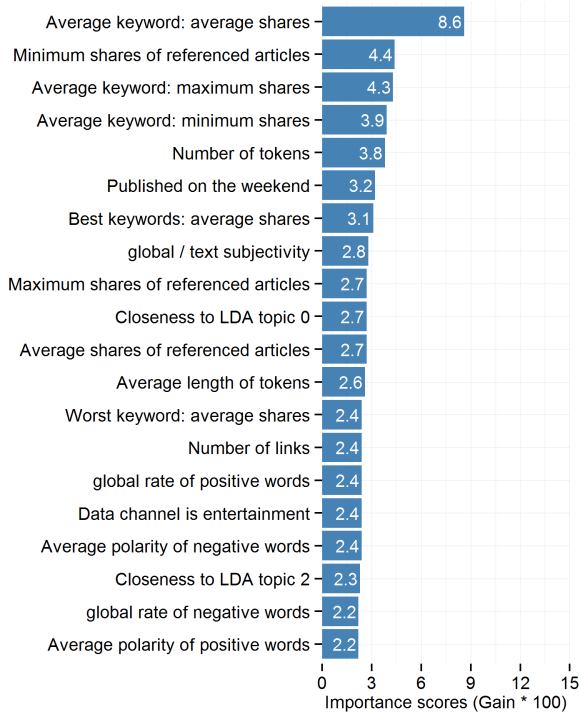


Fig. 3. Top 20 features based on the importance scores of features, measured via GBM, for predicting the, from left to right, popularity of online news, and number of shares of online news

more unbalanced popularity prediction datasets. Third, the comparison of the model with many other state-of-the-art techniques.

#### REFERENCES

- [1] A. Tatar, P. Antoniadis, M. Amorim, and S. Fdida, "From popularity prediction to ranking online news," *Social Network Analysis and Mining*, vol. 4, no. 1, 2014. [Online]. Available: <http://dx.doi.org/10.1007/s13278-014-0174-8>
- [2] C. Castillo, M. El-Haddad, J. Pfeffer, and M. Stempeck, "Characterizing the life cycle of online news stories using social media reactions," in *Proceedings of the 17th ACM Conference on Computer Supported Cooperative Work & #38; Social Computing*, ser. CSCW '14. New York, NY, USA: ACM, 2014, pp. 211–223. [Online]. Available: <http://doi.acm.org/10.1145/2531602.2531623>
- [3] S. Gao, J. Ma, and Z. Chen, "Modeling and predicting retweeting dynamics on microblogging platforms," in *Proceedings of the Eighth ACM International Conference on Web Search and Data Mining*, ser. WSDM '15. New York, NY, USA: ACM, 2015, pp. 107–116. [Online]. Available: <http://doi.acm.org/10.1145/2684822.2685303>
- [4] A. Tatar, M. de Amorim, S. Fdida, and P. Antoniadis, "A survey on predicting the popularity of web content," *Journal of Internet Services and Applications*, vol. 5, no. 1, 2014. [Online]. Available: <http://dx.doi.org/10.1186/s13174-014-0008-y>
- [5] J. G. Lee, S. Moon, and K. Salamatian, "Modeling and predicting the popularity of online contents with cox proportional hazard regression model," *Neurocomputing*, vol. 76, no. 1, pp. 134–145, 2012.
- [6] G. Szabo and B. A. Huberman, "Predicting the popularity of online content," *Communications of the ACM*, vol. 53, no. 8, pp. 80–88, 2010.
- [7] M. Ahmed, S. Spagna, F. Huici, and S. Niccolini, "A peek into the future: Predicting the evolution of popularity in user generated content," in *Proceedings of the Sixth ACM International Conference on Web Search and Data Mining*, ser. WSDM '13. New York, NY, USA: ACM, 2013, pp. 607–616.
- [8] K. Fernandes, P. Vinagre, and P. Cortez, *Progress in Artificial Intelligence: 17th Portuguese Conference on Artificial Intelligence, EPIA 2015, Coimbra, Portugal, September 8-11, 2015. Proceedings*. Cham: Springer International Publishing, 2015, ch. A Proactive Intelligent Decision Support System for Predicting the Popularity of Online News, pp. 535–546.
- [9] R. Bandari, S. Asur, and B. A. Huberman, "The pulse of news in social media: Forecasting popularity," *CoRR*, vol. abs/1202.0332, 2012. [Online]. Available: <http://dblp.uni-trier.de/db/journals/corr/corr1202.html#abs-1202-0332>
- [10] J. H. Friedman, "Greedy function approximation: A gradient boosting machine," *Annals of Statistics*, vol. 29, pp. 1189–1232, 2000.
- [11] S. Petrovic, M. Osborne, and V. Lavrenko, "Rt to win! predicting message propagation in twitter," in *JCWSM*, L. A. Adamic, R. A. Baeza-Yates, and S. Counts, Eds. The AAAI Press, 2011. [Online]. Available: <http://dblp.uni-trier.de/db/conf/icwsm/icwsm2011.html#PetrovicOL11>
- [12] I. Arapakis, B. Cambazoglu, and M. Lalmas, "On the feasibility of predicting news popularity at cold start," in *Social Informatics*, ser. Lecture Notes in Computer Science, L. Aiello and D. McFarland, Eds. Springer International Publishing, 2014, vol. 8851, pp. 290–299. [Online]. Available: [http://dx.doi.org/10.1007/978-3-319-13734-6\\_21](http://dx.doi.org/10.1007/978-3-319-13734-6_21)
- [13] M. M. Cliff Click, Jessica Lanford and V. Parmar, "Gradient boosted models with h2o's r package," February 2015: Second Edition, published by H2O.ai, Inc. 2307 Leghorn Street Mountain View, CA 94043, Inc. Available: <https://leanpub.com/gbm/read>. [Online]. Available: <https://leanpub.com/gbm/read>
- [14] "Gradient boosting," wikipedia, Wikimedia Foundation, Inc. , Web. Last Accessed: 26 August 2015. [Online]. Available: [https://en.wikipedia.org/wiki/gradient\\_boosting](https://en.wikipedia.org/wiki/gradient_boosting)
- [15] D. M. Blei, A. Y. Ng, and M. I. Jordan, "Latent dirichlet allocation," *the Journal of machine Learning research*, vol. 3, pp. 993–1022, 2003.
- [16] T. De Smedt, L. Nijs, and W. Daelemans, "Creative web services with pattern," in *Proceedings of the Fifth International Conference on Computational Creativity*. Citeseer, 2014.
- [17] tianqi chen, kailong chen, and tong he, "Xgboost," 2015, <http://mloss.org/software/view/543/>.

# Combining a Rule-based Classifier with Weakly Supervised Learning for Twitter Sentiment Analysis

Umme Aymun Siddiqua\*, Tanveer Ahsan\*, and Abu Nowshed Chy†

Department of Computer Science & Engineering

\*International Islamic University Chittagong

Chittagong-4314, Bangladesh

†Toyohashi University of Technology

Toyohashi, Aichi, Japan

aymun@kdml.org, tanveer.ahsan@gmail.com, and nowshed@kde.cs.tut.ac.jp

**Abstract**—Microblog, especially Twitter, have become an integral part of our daily life, where millions of user sharing their thoughts daily because of its short length characteristics and simple manner of expression. Monitoring and analyzing sentiments from such massive amount of twitter posts provide enormous opportunities for companies and other organizations to learn about what user think and feel about their products and services. But the ever-growing unstructured and informal user-generated posts in twitter demands sentiment analysis tools that can perform well with minimum supervision. In this paper, we propose an approach for sentiment analysis on twitter, where we combine a rule-based classifier with weakly supervised Naive-Bayes classifier. To classify the tweets sentiment, we introduce a set of rules for the rule-based classifier based on the occurrences of emoticons and sentiment-bearing words, whereas several sentiment lexicons are applied to train the Naive-Bayes classifier. We conducted our experiments based on the Stanford sentiment140 dataset. Experimental results demonstrate the effectiveness of our method over the baseline in terms of recall, precision,  $F_1$  score, and accuracy.

**Keywords:** Microblogs, sentiment analysis, sentiment classification, twitter, sentiment lexicons, emoticons.

## I. INTRODUCTION

Nowadays, microblog websites play an important role in maintaining social relationships as well as act as a valuable information source. Every day lots of users utilizing microblog sites for expressing their views, opinions, experiences, and feelings about specific topics or entities. Among several microblog sites, Twitter<sup>1</sup> is now the most popular, where millions of users spread millions of tweets (posts on twitter) on a daily basis. As these tons of tweets reflect people's opinions and attitudes, sentiment analysis in twitter has made a hit with a lot of complaisance. Monitoring and analyzing tweets sentiment from twitter provide enormous opportunities for the public and private sectors as well as individual users. For example, people are eager to know the feelings of others about Apple's new product "iPhone 7" and it will provide great convenience for them if the opinions are extracted from massive tweets. As the reputation of a certain product is highly affected by the people's opinions posted in twitter, companies are now monitoring and detecting public opinions from twitter to estimate the extent of product acceptance and to determine the strategies for improving product quality. Fans of famous personalities are always fascinated about what is going on with their favorite person and the reaction from other people. Moreover, there is a strong correlation between the users' posts on twitter and

the outcomes of political elections. Both voters and political parties are increasingly seeking ways to get an overview of the support and opposition candidates before the elections [1]. Therefore, a comprehensive sentiment analysis in twitter will provide an effective solution to address these scenarios. In this paper, we have proposed a method for sentiment analysis on twitter. To classify the tweets sentiment either positive or negative, we combine a rule-based classifier with weakly supervised Naive-Bayes classifier. Our rule-based classifier is based on the occurrences of emoticons and sentiment-bearing words, whereas several sentiment lexicons are used to train the Naive-Bayes classifier. Experimental results with Stanford sentiment140 dataset showed that our method improves the sentiment classification performance.

The main contributions of this paper include: (1) We propose a rule-based classifier based on the occurrences of emoticons and sentiment-bearing words and combine it with the weakly-supervised classifier. (2) We investigate the impact of utilizing sentiment lexicons for training the supervised Naive-Bayes classifier instead of the large training dataset. For this, we separately train our own developed Naive-Bayes classifier by using the ensemble of sentiment lexicons and sentiment140 dataset to compare the performances.

The rest of the paper is structured as follows: **Section II** describes the state-of-the-art of sentiment analysis task while our proposed framework is described in detail in **Section III**. Next, in **Section IV**, the experimental setup and results are discussed to show the effectiveness of our proposed method. Finally, some concluded remarks and future directions of our work described in **Section V**.

## II. RELATED WORK

Sentiment analysis in a microblogging environment, such as twitter is one of the state of the art research tasks in information retrieval domain, where the major goal is to classify the polarity of a tweet sentiment either positive, negative or neutral based on its contents. Usually sentiment analysis tasks conducted into different levels of graininess, including word level, a phrase or sentence level, document level, and feature level [2]. Prior works on twitter sentiment analysis mostly based on the noisy labels or distant supervision, for example, considering emoticons to decide the tweets sentiment, to train the supervised classifiers, and so on [3][4]. After that, several researchers explore feature engineering along with the combination of machine learning methods like Naive-Bayes (NB), Support Vector Machine (SVM), Maximum Entropy (Max Ent.) etc. to improve the classification performance [5].

<sup>1</sup><https://twitter.com>

Since it is very costly to obtain sentiment labels for large training data and expressions in twitter are unstructured, informal, and fast-evolving, some researcher introduced the unsupervised methods based on lexicons [6] as well as the combination of lexicons and emotional signals [7]. Along with this direction, current studies showed that results of twitter sentiment analysis is widely used in various social applications, including trend identification of political elections [8], natural disaster management [9], etc.

### III. PROPOSED FRAMEWORK

In this section, we describe the details of our proposed framework. The goal of our proposed sentiment classification task is to assign positive or negative sentiment label to a tweet document based on its contents. The overview of our proposed sentiment analysis framework illustrated in Fig. 1.

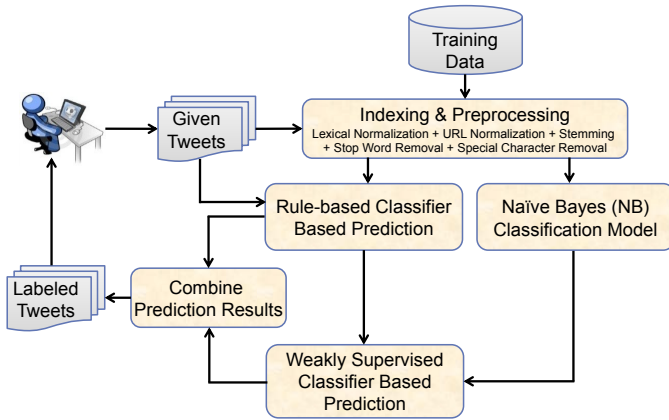


Fig. 1: Proposed sentiment analysis framework

At first, our system fetches the set of tweets from the user and indexed them for further processing. In the preprocessing stage, we perform the tokenization, lexical normalization, URL normalization, stemming, stop-word removal, and special character removal. Next, our proposed rule-based classifier is applied to classify the tweets sentiment as positive, negative or unknown. Tweets that are labeled as unknown are then considered as bag-of-words and classified by using weakly supervised Naive-Bayes (NB) classifier. Results of both rule-based classifier and weakly supervised classifier are then combined and set of labeled tweets return to the user.

#### A. Lexical Resources for Sentiment Analysis

For our sentiment analysis task, we construct a strong sentiment lexicon. A sentiment lexicon is a collection of sentiment words such as “affluent”, “brilliant”, “crime”, and “hate”, that are used to imply the positive or negative sentiments. We consider seven publicly available sentiment lexicons, including the Bing Liu lexicon [10], subjectivity clues from [11], EffectWordNet [12], WordStat Sentiment Dictionary<sup>2</sup>, NRC emotion lexicon [13], SentiStrength lexicon [14], and SentiWordnet [15]. We extract the positive and negative sentiment words separately from these lexicons, which are then used to count the sentiment-bearing words in our rule-based classifier. We also used these lexicons to train our weakly supervised Naive-Bayes classifier.

Like sentiment lexicon, we also construct an emoticon lexicon, as peoples are increasingly interested in using emoticons on twitter in order to express their feelings. For our emoticon lexicon, we combine four publicly available emoticon lists, including the SentiStrength emoticon lexicon [14], emoticon list from Wikipedia<sup>3</sup>, Sharpened-text based emoticons<sup>4</sup>, and DataGenetics<sup>5</sup> popular emoticons list in twitter.

#### B. Rule-based Classifier

In a rule-based classifier, a set of rules usually constructed to determine a certain combination of patterns, that are most likely to be related to the different classes. Each rule consists of two parts: the antecedent part and the consequent part. The antecedent part corresponds to a word pattern and the consequent part corresponds to a class label. We can define a rule as follows:

$$R_k : \text{if } x_1 \text{ is } A_{k1} \text{ and } \dots \text{ and } x_n \text{ is } A_{kn} \\ \text{then } \text{Class} = C_k, \quad k = 1, \dots, N$$

where  $R_k$  is a rule label,  $A_{k1}$  is an antecedent set,  $C_k$  is a consequent class,  $k$  is a rule index, and  $N$  is the total number of rules. Our unsupervised rule-based classifier casts the sentiment analysis problem as a multi-class classification problem and labeled each tweet as positive, negative or unknown. We define the following set of rules based on the emoticons and occurring of positive and negative sentiment-bearing words:

$$R_1 : \text{if } N_{PE} > 0 \text{ and } N_{NE} = 0 \text{ then, } \text{Class} = \text{Positive} \\ R_2 : \text{if } N_{NE} > 0 \text{ and } N_{PE} = 0 \text{ then, } \text{Class} = \text{Negative} \\ R_3 : \text{if } N_{PW} - N_{NW} > P \text{ then, } \text{Class} = \text{Positive} \\ R_4 : \text{if } N_{NW} - N_{PW} > P \text{ then, } \text{Class} = \text{Negative}$$

where  $N_{PE}$  is the number of positive emoticons,  $N_{NE}$  is the number of negative emoticons,  $N_{PW}$  is the number of positive words,  $N_{NW}$  is the number of negative words, and  $P$  is the positive integer. These rules are applied sequentially. If a tweet satisfies any of these rules, it is labeled with the corresponding class and the remaining rules are ignored. Whereas, tweets that do not satisfy any of these rules are labeled with unknown class. We use the original tweet for  $R_1$  and  $R_2$  rule, while performing the preprocessing described in section III-C1 for  $R_3$  and  $R_4$  rule.

#### C. Weakly Supervised Learning Approach

Weakly supervised sentiment classification uses the prior word polarity knowledge, where a small number of seed words with known polarity are used to infer the polarity of a target document. The weakly supervised learning process described in detail, as follows:

1) *Internal Preprocessing*: Internal data preprocessing step is initiated with tokenization, which is the process of forming tokens from an input stream of characters. As we are working on tweet documents, there are lots of emoticons and other special characters. But meaningful English words do not contain these characters. We remove these characters from tweet documents as well as removing the single-letter

<sup>3</sup>[https://en.wikipedia.org/wiki/List\\_of\\_emoticons](https://en.wikipedia.org/wiki/List_of_emoticons)

<sup>4</sup><http://www.sharpened.net/emoticons/>

<sup>5</sup><http://www.datagenetics.com/blog/october52012/index.html>

<sup>2</sup><http://provalisresearch.com/Download/WSD.zip>

word. Moreover, in sentiment classification task, stop-words play a negative role because they do not carry any sentiment information and may actually damage the performance of the classifier. For stop-word removal, we utilize the refined form of Indri’s standard stop-list<sup>6</sup>, because it contains some words that have sentiment information, such as like, thank, useful, downward, etc. So, we manually inspect the list and discard these words from the list. After performing stop-word removal, the remaining words are then stemmed by using Krovetz stemmer<sup>7</sup> to reduce the word variants to a common form.

*Lexical Normalization:* As tweets are informal user generated texts, it often contains non-standard word forms and some domain-specific entities. Some used non-standard word examples are: “thnx” instead of “thanks”, “plzzzzzz” instead of “please”, “happpppppy” instead of “happy”, etc. To normalize the non-standard words into their canonical forms, we utilize two publicly available lexical normalization dictionaries, collected from [16] and [17]. The first one contains 41,181 words and the second one contains 3,802 words. For URL normalization, we replace all the links present with just the word “URL”.

2) *Classification Model:* We make use of well-known Naive-Bayes (NB) classification model for our sentiment classification system. For a given tweet document, the Naive-Bayes (NB) classifier make use of the joint probabilities of words and categories to estimate the probabilities of categories. The assumption of word independence makes the computation of this classifier far more efficient than the exponential complexity of non-Naive-Bayesian approaches [18].

#### D. Combining the Classifiers

After developing our proposed rule-based classifier and training the Naive-Bayes classifier with sentiment lexicons described in section III-A, we combine them to classify the tweets sentiment. At first, our rule-based classifier is applied to classify the tweets sentiment as positive, negative or unknown. But, our goal is to classify the tweets sentiment only positive or negative class. That is why; for the tweets that are labeled as unknown by the rule-based classifier, we consider the predictions of weakly supervised Naive-Bayes classifier as the final labels.

### IV. EXPERIMENTS AND EVALUATION

#### A. Dataset Collection

For conducting our experiments, we used the Stanford Twitter Sentiment140 dataset [3]<sup>8</sup>. The training dataset has 1.6 million tweets with the equal number of positive and negative tweets, while the test set consists of 182 positive and 177 negative tweets, which were manually annotated. The test set was collected with specific queries arbitrarily chosen from different categories including products’ name, companies, people, etc. Table I presents the categories and the total number of corresponding tweets, positive tweets, and negative tweets. Each training and test tweet are composed of the tweet\_polarity, tweet\_id, date, query, screen\_name, and tweet\_text.

Table I: Categories for test set

Category	#Tweets	#Positive	#Negative
Company	119	33	86
Misc.	67	26	41
Person	65	48	17
Product	63	47	16
Movies	19	16	3
Location	18	4	14
Events	8	8	0
Total	359	182	177

#### B. Parameter Setting for Rule-based Classifier

To determine the optimal value of parameter  $P$  for the  $R3$  and  $R4$  rule in our rule-based classifier, we examine the accuracy of our  $Run4$  method (described in Section IV-C) for different values of  $P$ . Based on the result illustrated in Fig. 2, the parameter  $P$  is set to as 3.

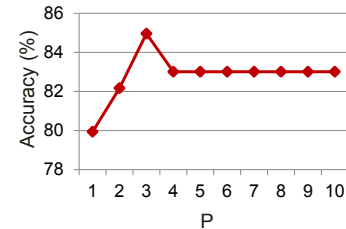


Fig. 2: Accuracy estimation for different values of  $P$

#### C. Results with Sentiment Classification

At first, we used the training dataset of 1.6 million tweets to train our own developed Naive-Bayes classifier using bag-of-words model for classifying the sentiment of the test set, which we considered as our baseline. To evaluate the performance, we considered four standard evaluation measures including recall, precision,  $F_1$  score, and accuracy.

Table II: Classification results (in %) on sentiment140 dataset

Method	Recall	Precision	$F_1$ Score	Accuracy
Baseline	63.19	80.99	70.99	73.82
Run1	80.77	81.67	81.22	81.06
Run2	89.56	74.43	81.30	79.11
Run3	85.16	82.45	83.78	83.29
Run4	<b>91.76</b>	81.07	<b>86.08</b>	<b>84.96</b>
SentiStrength [14]	80.77	79.46	80.11	81.70
Semantria <sup>9</sup>	70.88	<b>83.23</b>	76.56	78.10

The summarized results of our experiments and comparison with two known related systems (SentiStrength and Semantria) are presented in Table II. At first, we showed the classification performance based on the baseline. Then performance incorporating preprocessing with baseline method resulted in  $Run1$ . After that, we trained the Naive-Bayes classifier with several sentiment lexicons, which has resulted in  $Run2$ . Next, to improve the classification performance, we combined our rule-based classifier with the setup of  $Run1$  and  $Run2$ . Results of these experiments are articulated in  $Run3$  and  $Run4$  respectively. Results showed that both  $Run3$  and  $Run4$  outperform the baseline and  $Run1$  (baseline+preprocessing), which indicates the complementary importance of our proposed rule-based classifier. As we achieved the best result in terms of recall,  $F_1$  score, and accuracy at  $Run4$ , we can deduce that combining a rule-based classifier with weakly supervised Naive-Bayes classifier improves the sentiment classification performance.

<sup>6</sup><http://www.lemurproject.org/stopwords/stoplist.dft>

<sup>7</sup><http://sourceforge.net/p/lemur/wiki/KrovetzStemmer/>

<sup>8</sup><http://help.sentiment140.com/for-students>

<sup>9</sup><https://www.lexalytics.com/semantria>

We also evaluate the performance of our several runs by receiver operating characteristic (ROC) curve analysis. The method, which curve is closer to the  $y$ -axis than the other in ROC curve, is treated as the best. Fig. 3 illustrated that the curve of *Run4* method is closer to the  $y$ -axis that means it performs best i.e.; yielded the most desirable ratio between false positives and true positives.

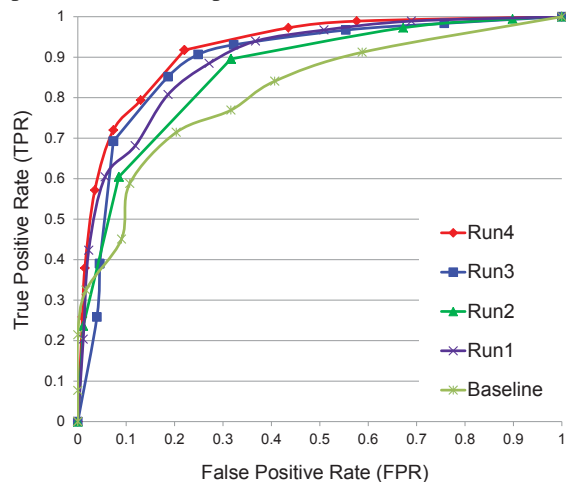


Fig. 3: Receiver operating characteristic (ROC) curve analysis

We also compare the category-wise performance of our proposed method (*Run4*) with baseline. Fig. 4 showed the category-wise comparative results. For 5 types of tweet categories, our proposed *Run4* outperforms the baseline significantly in terms of accuracy and for 2 types of categories, our system yielded similar results. This indicates the applicability of our proposed system for all types of tweets.

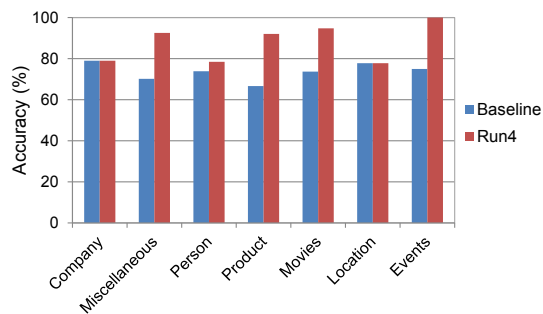


Fig. 4: Category-wise performance comparison

## V. CONCLUSION AND FUTURE DIRECTION

In this paper, we proposed an efficient and effective method for sentiment analysis on twitter. We introduced a rule-based classifier based on emoticons and sentiment-bearing words and combined it with our weakly supervised Naive-Bayes classifier to classify the tweets sentiment. To alleviate the construction of large annotated training dataset, we utilized several sentiment lexicons to train the Naive-Bayes classifier and found that it is effective rather than using large training dataset. Experimental results demonstrated that our proposed method achieved the significant improvements in sentiment analysis task.

In future, we have a plan to incorporate several rules based on complex semantics along with the ensemble of standard machine learning techniques to improve the classification efficacy. We also have a plan to consider the neutral sentiment class along with the positive and negative sentiment class.

## REFERENCES

- [1] X. Wang, F. Wei, X. Liu, M. Zhou, and M. Zhang, "Topic sentiment analysis in twitter: a graph-based hashtag sentiment classification approach," in *Proceedings of the 20th International Conference on Information & Knowledge Management*. ACM, 2011, pp. 1031–1040.
- [2] R. Feldman, "Techniques and applications for sentiment analysis," *Communications of the ACM (CACM)*, vol. 56, no. 4, pp. 82–89, 2013.
- [3] A. Go, R. Bhayani, and L. Huang, "Twitter sentiment classification using distant supervision," *CS224N Project Report, Stanford*, vol. 1, p. 12, 2009.
- [4] L. Barbosa and J. Feng, "Robust sentiment detection on twitter from biased and noisy data," in *Proceedings of the 23rd International Conference on Computational Linguistics (COLING): Posters*. Association for Computational Linguistics (ACL), 2010, pp. 36–44.
- [5] F. Bravo-Marquez, M. Mendoza, and B. Poblete, "Combining strengths, emotions and polarities for boosting twitter sentiment analysis," in *Proceedings of the 2nd International Workshop on Issues of Sentiment Discovery and Opinion Mining (WISDOM)*. ACM, 2013, p. 2.
- [6] G. Paltoglou and M. Thelwall, "Twitter, myspace, digg: Unsupervised sentiment analysis in social media," *ACM Transactions on Intelligent Systems and Technology (TIST)*, vol. 3, no. 4, p. 66, 2012.
- [7] X. Hu, J. Tang, H. Gao, and H. Liu, "Unsupervised sentiment analysis with emotional signals," in *Proceedings of the 22nd International Conference on World Wide Web (WWW)*. International World Wide Web Conferences Steering Committee, 2013, pp. 607–618.
- [8] O. Almatrafi, S. Parack, and B. Chavan, "Application of location-based sentiment analysis using twitter for identifying trends towards indian general elections 2014," in *Proceedings of the 9th International Conference on Ubiquitous Information Management and Communication (IMCOM)*. ACM, 2015, p. 41.
- [9] D. Buscaldi and I. Hernandez-Farias, "Sentiment analysis on microblogs for natural disasters management: a study on the 2014 genoa floodings," in *Proceedings of the 24th International Conference on World Wide Web (WWW) Companion*. International World Wide Web Conferences Steering Committee, 2015, pp. 1185–1188.
- [10] B. Liu, M. Hu, and J. Cheng, "Opinion observer: analyzing and comparing opinions on the web," in *Proceedings of the 14th International Conference on World Wide Web (WWW)*. ACM, 2005, pp. 342–351.
- [11] T. Wilson, J. Wiebe, and P. Hoffmann, "Recognizing contextual polarity in phrase-level sentiment analysis," in *Proceedings of the Conference on Human Language Technology and Empirical Methods in Natural Language Processing (HLT/EMNLP)*. Association for Computational Linguistics, 2005, pp. 347–354.
- [12] Y. Choi, L. Deng, and J. Wiebe, "Lexical acquisition for opinion inference: A sense-level lexicon of benefactive and malefactive events," in *Proceedings of the 5th Workshop on Computational Approaches to Subjectivity, Sentiment and Social Media Analysis (WASSA)*, 2014, pp. 107–112.
- [13] S. M. Mohammad and P. D. Turney, "Crowdsourcing a word–emotion association lexicon," *Computational Intelligence*, vol. 29, no. 3, pp. 436–465, 2013.
- [14] M. Thelwall, K. Buckley, and G. Paltoglou, "Sentiment strength detection for the social web," *Journal of the American Society for Information Science and Technology (JASIST)*, vol. 63, no. 1, pp. 163–173, 2012.
- [15] S. Baccianella, A. Esuli, and F. Sebastiani, "Sentiwordnet 3.0: An enhanced lexical resource for sentiment analysis and opinion mining," in *LREC*, vol. 10, 2010, pp. 2200–2204.
- [16] B. Han, P. Cook, and T. Baldwin, "Automatically constructing a normalisation dictionary for microblogs," in *Proceedings of the 2012 Joint Conference on Empirical Methods in Natural Language Processing and Computational Natural Language Learning (EMNLP-CoNLL)*. Association for Computational Linguistics (ACL), 2012, pp. 421–432.
- [17] F. Liu, F. Weng, and X. Jiang, "A broad-coverage normalization system for social media language," in *Proceedings of the 50th Annual Meeting of the Association for Computational Linguistics: Long Papers-Volume 1*. Association for Computational Linguistics, 2012, pp. 1035–1044.
- [18] A. N. Chy, M. H. Seddiqui, and S. Das, "Bangla news classification using naive bayes classifier," in *Proceedings of the 16th International Conference on Computer and Information Technology (ICCIT)*. IEEE, 2014, pp. 366–371.



# *Design and Simulation of an improved bandwidth V-slotted Patch Antenna for WiMAX*

*Nasimul Hyder Maruf  
Bhuyan*  
MSc in Radio  
Communication.  
Blekinge Tekniska  
Högskola. Karlskrona,  
Sweden.

*Mamun Ahmed*  
MSc in Signal Processing  
(BTH, Sweden).  
BSc in CSE  
(CUET, Bangladesh).

*Masoud Khazaei*  
MSc in Radio  
Communication.  
Blekinge Tekniska  
Högskola. Karlskrona,  
Sweden.

*Zoraze Ali*  
MSc in Radio  
Communication.  
Blekinge Tekniska  
Högskola. Karlskrona,  
Sweden.

**Abstract**— A conventional rectangular V-slotted patch antenna is commonly used for 2.4 GHz Wireless local area network (WLAN) applications. The microstrip patch antenna has the inherent characteristic of narrow bandwidth that limits the use of rectangular V-slotted patch antenna for broadband technologies, like world-wide interoperability for microwave access (WiMAX). In this paper, a corner truncated scheme is designed and simulation to improve the operational bandwidth of the subjected antenna to make it operational for WiMAX (2~6 GHz) applications. The simulation carried out it is shown that by truncating the corners of rectangular V-slotted patch antenna, results in enhanced operational bandwidth and better return loss for WiMAX.

**Keywords**— *Bandwidth, V-slotted Patch antenna, Wireless LAN, WiMAX.*

## I. INTRODUCTION

The air interface standard IEEE 802.16 which is commonly mentioned to world-wide interoperability for microwave access (WiMAX) is one of the most popular broadband wireless access technology. The operating frequency range of WiMAX 802.16 which is also known as 2~6 GHz portable wireless metropolitan area network (WMAN). The existing operation frequency of WiMAX systems are 2.4 GHz, 3.5 GHz and 5.2 GHz. The WiMAX technology has occupied all of the wireless communication area and developing this WiMAX system can be best achieved, which based on the ideal model of the WiMAX system [1].

A number of antennas have been proposed for WiMAX technology, but it requires efficient antennas at both ends (transmitter and receiver). These antennas are compact and working on the broadband multiple resonant frequency's. Microstrip patch antennas are conformable to planar and non-planar surfaces, diminutive profiled, easy and economical to construct using the advanced printed circuit technology. Besides these advantages of microstrip patch antenna it has a disadvantage of narrow bandwidth. Various methods have been proposed to enhance the bandwidth of microstrip patch antenna, which includes the use of thicker substrate, multiple resonators etc.

At the present time, there are some methods have been proposed to enhance the WiMAX bandwidth. The dual patch microstrip antenna was proposed to enhance the bandwidth by using a second patch antenna in front of the basic one. This is the stacking patches concept which gives the bandwidth enhancement by using the electromagnetic coupling [5]. The comprehensible bandwidth of microstrip antenna shown the approximately proportional to its volume [7]. Thicker substrates are used for enhancing bandwidth for the microstrip patch antenna, but it has several problems. The thicker substrate causes the radiation efficiency because its support the surface waves, which will deteriorate the radiation pattern and feeding problem technique of the antenna arrays. The higher order z-direction modes, which introducing the impedance of further distortions pattern and characteristics. In [6] a good feeding technique has been proposed for the electromagnetic coupling (instead of direct coupling) technique which is electrically thick microstrip antenna.

Symmetrical sharp V-slotted patch antenna has given the better return loss as compared to rectangular patch antenna [4]. This characteristic of V-slotted patch antenna enables the patch input impedance optimization to be made without moving the feed location. [4]. The limit of the patch antenna inherent characteristic is narrow bandwidth which is used for wireless broadband communication. By using the thicker substrate of the microstrip patch antenna is possible to increase the bandwidth [2]. But this technique arise has several problems of antennas feeding technique [2]. There is an effective method is corner truncated scheme is used to enhance the bandwidth for ultra-wideband (UWB) applications [3]. A monopolar V-shaped slot patch antenna has been proposed for car-to-car and WLAN communications which is vertical polarization [9]. By adding a shorting pin for enhancing the impedance bandwidth of V-shaped slot equilateral triangular patch antenna, which has two operating modes, i.e.,  $TM_{10}$ ,  $TM_{20}$ , operating frequency from 4.82 to 6.67 GHz and gain of around 5.0 dBi [9]. There are two types of feeding in microstrip patch antenna are non-contacting scheme is electromagnetic field coupling between the radiating patch and transfer power of microstrip line and the other method is contacting method which the RF power is directly to the radiating patch by using the connecting microstrip line.

In this paper, we design and simulation of an improved bandwidth V-slotted Patch Antenna for WiMAX which is operated for WLAN applications is used as a based model. It is proposed that by the use of the corner truncated patch scheme we can widen the operational bandwidth of the antenna and can achieve better performance in terms of return loss for WiMAX.

## II. PROBLEM STATEMENT

A V-slotted rectangular patch antenna has been used for WLAN applications widely. There is a need of adaptation, which can enhance the operational bandwidth of this antenna, so that it can be used for WiMAX applications.

The research problem is “how to enhance the operational bandwidth and return loss of V-slotted rectangular patch antenna to utilize it for WiMAX applications”?

This research problem can be resolved by cutting short the two opposite corners of V-slotted rectangular patch antenna to enhance the operational bandwidth and return loss.

The primary contribution of this project is to present a system for raising the operational bandwidth and return loss of the rectangular V-slotted patch antenna WiMAX. The execution and verification have been performed by utilizing a high frequency structure simulator (Ansoft HFSS).

## III. RESULT AND CALCULATION

To obtain the enhanced operational bandwidth and return loss for V-slotted rectangular patch antenna to resonate at WiMAX frequencies, the truncation of two opposite corners of the rectangular patch is proposed in this paper.

### A. Modeling

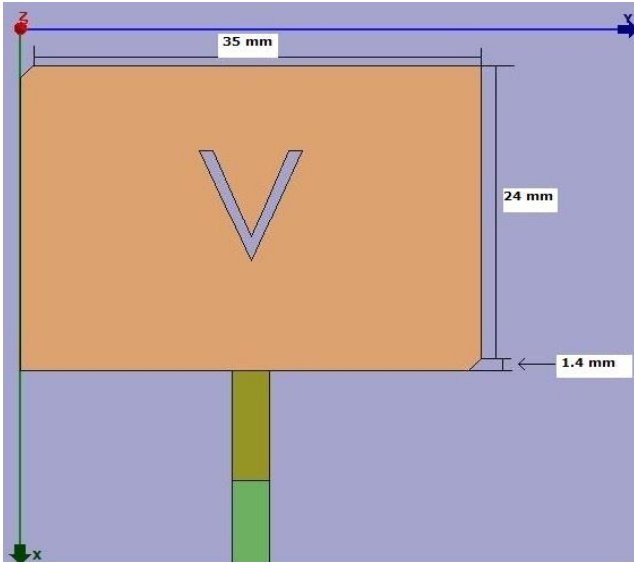


Fig. 1. Corner truncated V-slotted patch antenna.

The geometry of the proposed antenna is shown in Fig. 1 with various dimensions. The antenna is mounted on FR4 substrate having thickness 1.6 mm with relative permittivity of 4.7. Microstrip transmission line of (17x3) mm is used to obtain 50 Ω line. The length and width of the patch have been calculated with the help of general formulas for microstrip patch

antenna. By truncating the two opposite corners of the patch with equal length of 1.4142 mm, a good impedance match over the frequencies can be excited well. There is tolerance of ±0.0142 mm in truncation of corners in this model to remain on WiMAX frequencies and to avoid significant change in return loss and percentage bandwidth. The normal radiation of the microstrip patch antenna is on its surface. The H-Plane patterns is 0 and the E-Plane patterns are 90. The resonant frequency of microstrip patch antenna of 2.45, 3.5 and 4.65 GHz are described in [10].

### B. Resonance frequency

The dimensions of a single rectangular microstrip patch antenna is  $L \times W$ ,  $f_r$  is the lowest order resonant frequency which is accurately anticipated from the following equation [8],

$$f_r = \frac{c}{2(L+2\Delta L)\sqrt{\epsilon_{eff}}} \quad (1)$$

Hear,  $c$  is the speed of light.

$\Delta L$  is the line extension,

$\epsilon_{eff}$  is the effective dielectric constant.

$\epsilon_{eff}$  and  $\Delta L$  can be computed from the following relations,

$$\epsilon_{eff} = \frac{\epsilon_r + 1}{2} + \frac{\epsilon_r - 1}{2} \left( \frac{1}{\sqrt{1 + 10h/W}} \right) \quad (2)$$

And,

$$\Delta L = 0.412h \frac{(\epsilon_{eff} + 0.3) \left( \frac{W}{h} + 0.264 \right)}{(\epsilon_{eff} - 0.285) \left( \frac{W}{h} + 0.823 \right)} \quad (3)$$

### C. Implementation and verification

The proposed model is implemented on a high frequency structure simulator (Ansoft HFSS). Return loss and percentage bandwidth for V-slotted rectangular patch antenna without truncation as shown in Fig. 2 and corner truncated V-slotted rectangular patch antenna as shown in Fig. 1 have been analyzed.

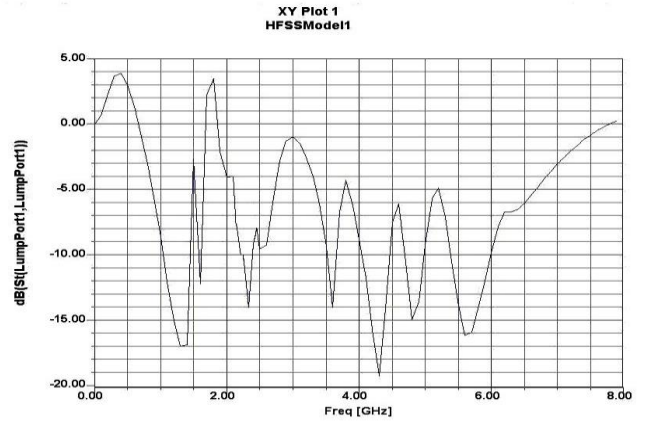


Fig. 2. Simulated return loss of v-slotted rectangular patch antenna without truncation.

TABLE I is the compiled data from Fig. 2 which shows the return loss and percentage bandwidth of V-slotted patch antenna centered on multiple frequencies.

TABLE I. RETURN LOSS AND PERCENTAGE BANDWIDTH FOR V-SLOTTED RECTANGULAR PATCH ANTENNA

Resonant frequency [GHz]	Return loss [dB]	Bandwidth [%]
2.4	-14.00	7.11
3.6	-13.90	3.88
4.3	-19.16	7.9
5.6	-16.05	10.35

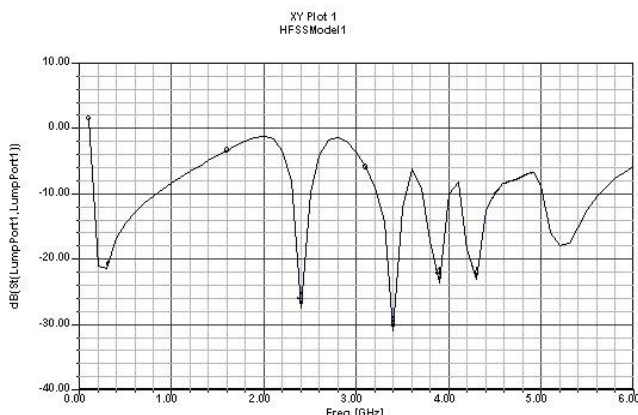


Fig. 3. Simulated return loss of v-slotted rectangular patch antenna with truncation.

TABLE II is compiled data from Fig. 3 which shows the enhanced return loss and percentage bandwidth of V-slotted patch antenna after truncating the corners.

TABLE II. RETURN LOSS AND PERCENTAGE BANDWIDTH FOR CORNER TRUNCATED V-SLOTTED RECTANGULAR PATCH ANTENNA

Resonant frequency [GHz]	Return loss [dB]	Bandwidth [%]
2.4	-27.39	8.33
3.4	-30.99	9.41
3.9	-20.60	7.18
4.3	-23.12	8.83

#### IV. CONCLUSION

The corner truncated scheme is an efficient technique to raise the operational bandwidth and return loss of V-slotted patch antenna for WiMAX. By cutting short the two opposite corners of the patch 1.18% of the bandwidth has been improved by 1.81 [dB] reduced return loss in WiMAX frequency of 5.2 GHz in comparison with the WiMAX frequency of 5.6 GHz. The antenna is proposed for capable of operating on multiple frequencies which are useful for Bluetooth, Wifi and CDMA 2000/1xEVDO (3G). Future work can be performed by varying the feed type of the antenna to proximity coupled feed or aperture coupled feed to achieve the enhance bandwidth and better return loss.

#### REFERENCES

- [1] N. H. Maruf Bhuyan, Jia Uddin, Monirul Hoque, Md. Ahasan Habib, "Performance Analysis of Wi-MAX: Modulation Scheme Versus Bit Error Rate", *International Journal of Electronics & Communication Technology (IJECT)*, VOL 3, ISSUE 4, VER. 2, Oct-Dec-2012.
- [2] A. A. Mohammad, H. Subhi, A. K. Ahmad, and S. M. Juma, "Bandwidth enhancement of stacked rectangular microstrip patch antenna," in *7th International Symposium on Antennas, Propagation & EM Theory*, Guilin, 2006, pp. 1-13.
- [3] K. Song, Y-z Yin, H-h Xie, S-l Zuo, and D. Xi, "A corner-truncated patch scheme of bandwidth enhancement for open slot antenna," in *2010 International Symposium on Signals Systems and Electronics*, China, 2010, vol. 2, pp. 1-3.
- [4] A. Sahadah, O. Hazila, H. Dayang, H. Nurbaya, A. Hasnah, "A study on performance of V-slot shapes on rectangular patch antenna," in *2010 International Conference on Computer and Communication Engineering*, Malaysia, 2010, pp. 1-6.
- [5] A. Hussien, "Microstrip backfier antenna", M.Sc. Thesis, College of Science, Al-Nahrain university (Formerly Saddam University), Baghdad, Iraq, 1995.
- [6] Z. N. Chen, M.Y.W.Chia, and C. L.Lim, "A stacked suspended plate antenna" *Microwave and Optical Technology Letters*, vol.37, no.5, pp 337-339, 2003.
- [7] E. C., S. A. Long and W. F. Richards, "An experimental investigation of electrically thick rectangular microstrip antennas," *IEEE Trans. Antennas Propagat.*, vol. AP-34, no. 6, pp 767-772, 1986.
- [8] J. R. James and P. S. Hall, "Handbook of microstrip antennas," *IEEE Electromagnetic Waves Series 28*, Peter Peregrinus Ltd, 1989.
- [9] H. Wong, K. K. So and X. Gao, "Bandwidth Enhancement of a Monopolar Patch Antenna With V-Shaped Slot for Car-to-Car and WLAN Communications," in *IEEE Transactions on Vehicular Technology*, vol. 65, no. 3, pp. 1130-1136, March 2016.
- [10] Pragati, S. L. Tripathi, S. R. Patre, S. Singh and S. P. Singh, "Triple-band microstrip patch antenna with improved gain," *2016 International Conference on Emerging Trends in Electrical Electronics & Sustainable Energy Systems (ICETEESES)*, Sultanpur, India, 2016, pp. 106-110.

# Design, Fabrication and Performance Evaluation of a Three Electrode ECG Recorder

Mehdi Hasan Chowdhury\*, Quazi Delwar Hossain, Pradipta Saha, Md. Mushfiqur Rahaman

Department of Electrical and Electronic Engineering  
Chittagong University of Engineering and Technology  
Chittagong, Bangladesh  
\*arnob\_eee@yahoo.com

**Abstract**—Frequent monitoring is required for chronically ill cardiac patients to ensure superior treatment. This paper presents a low-cost, novel wearable electrocardiogram (ECG) measuring unit for consistent use. In this study, the ECG signal is accumulated by a three electrode data acquisition system and measured by an integrated signal conditioning block AD8232. The analog signal from AD8232 is converted to digital data and recorded on a computer using unique software developed for this study. This automated software can store electronic records of the patients. These patient particulars can be forwarded to a proper medical support system if needed. To confirm the quality of ECG recorded by this prototype, clinical tests are conducted. The results of these assessments demonstrate the viability and efficacy of this system.

**Keywords**—biomedical measurement; electrocardiogram; ECG; EKG; AD8232; biopotential; signal processing; .net framework.

## I. INTRODUCTION

Cardiovascular Disease (CVD) is the prominent cause of death of older people across the globe. A study conducted by A.S. Go et al. in 2003 shows 11% of people between ages 20 to 40 have CVD, while 37% between 40 and 60, 71% of people between 60 and 80 and 85% of people over 80 have CVD [1]. Frequent monitoring of heart condition would allow for early detection of the CVD. The regular assessment would be also helpful for prescribing the right dose of medication. The electrical activity of the heart over a specified period is graphically recorded as Electrocardiogram (ECG). It is the most recognized non-invasive method for diagnosis of various cardiovascular diseases.

The clinical standard uses a 12-lead ECG for assessing heart health. In the typical representation, each lead corresponds to a specific vector of heart's electrical potential [2]. Although 12 lead ECG is standard, it is not always required. Detecting an arrhythmia, for example, only requires one ECG lead [3]. A three electrode configuration is used in this research that would allow a Lead I, Lead II or Lead III bipolar limb lead configuration to be selected. Finally Lead I configuration is chosen for the experimental purpose as its output signal is more amplified than the other two [4]. This configuration represents the electrical potential between the Left Arm (LA) electrode (positive) and Right Arm (RA) electrode (negative) while the ground electrode is placed on Right Leg (RL) of the physiological subject (human).

The aim of this study is to design a novel low power and portable ECG measurement unit for frequent use. The goal is to design a prototype which can generate a high-quality electrocardiogram that is comparable to the available commercial unit. Conventional ECG units allow electrocardiography to be performed in the hospitals, but miniaturization of machines has allowed ECG to be performed outside of clinical setup [5]. As portable electrocardiography saves time and costs, many scholars and research institutions have designed various kinds of portable ECG monitor devices, in order to record user's long-term ECG signals in daily activities. S. Suave Lobodzinski et al. presented a review paper discussing new devices for very long-term portable ECG monitoring which are attached directly to the skin [6]. A brief comparative study is presented in the later part of this paper to compare the newly designed prototype with the already existing ones.

This paper presents the design of a prototype system which utilizes a fully integrated signal conditioning block AD8232. The accumulated ECG data from bipolar limb configuration Lead I is uploaded to the computer through USB communication protocol using dedicated software specially designed for this research work. This software is designed not only to display the electrocardiogram on the computer monitor; it has also the capability of recording the ECG for further analysis. Thus, a chronic heart patient can frequently monitor and store his ECG on the computer. Then these particulars can be printed or electronically mailed to the cardiovascular specialist physicians for proper diagnosis of the disease.

## II. SYSTEM ARCHITECTURE

The challenge of this research is to develop a low-cost and low-power portable ECG monitoring unit.

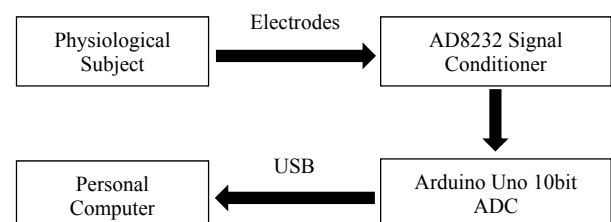


Fig.1. Operating principle in a simplified block diagram

Simplified block diagram of Fig.1 illustrates the basic operation of the proposed system. This scheme includes a three electrode ECG signal acquisition unit, an analog to digital converter and a Universal Serial Bus (USB) interface. The electrocardiogram will be displayed on a computer monitor using exclusive software developed for this research project.

In general, bio-potentials are weak signals and consequently it is susceptible to environmental noise sources. Therefore, an Analog Front End (AFE) is used to condition the acquired signal. Then a Digital Back End (DBE) is required for digitizing the conditioned analog signal and transmitting it using USB communication protocol. Software implementation will be discussed in the next section.

### A. Analog Front End

Analog Devices Incorporated (ADI) developed AD8232 as a fully integrated signal conditioning block which can extract, amplify and filter small bio-potentials such as ECG. Its design allows an ultra-low power analog-to-digital converter (ADC) to acquire the output signal proficiently. Therefore, it is selected to be the best fit for the purpose of this research project.

AD8232 has a specialized instrumentation amplifier (IA), an operational amplifier (A1), a right leg drive amplifier (A2) and a mid-supply reference buffer (A3) as shown in Fig.2. It is configured with a 0.5 Hz two-pole high pass filter followed by a 40 Hz two-pole low pass filter [7]. This helps to eliminate noises like 50 Hz power line interference and obtain an ECG waveform with minimal distortion.

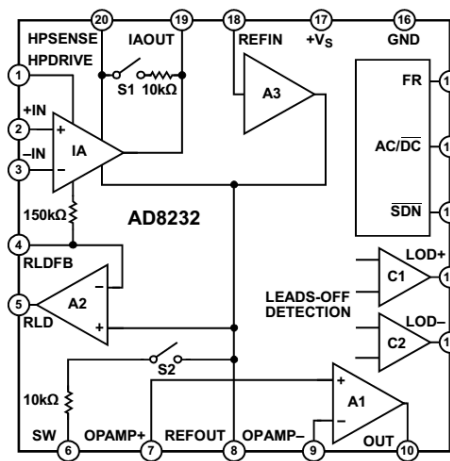


Fig.2. Functional block diagram of the AD8232 [7]

While using this chip as the Analog Front End of this prototype, data acquisition is possible via three electrodes. This is necessary for the Lead I ECG configuration. In this particular circuit arrangement, the Right Leg Drive (RLD) amplifier is employed for rejecting the common mode voltage, thus ensuring optimum common mode rejection of the system. The circuit connection for cardiac monitoring is illustrated in Fig. 3.

The op-amp stage is configured for a maximum system gain of 1100 [7] in this design. However, this gain level can be adjusted depending on the peak-to-peak input signal amplitude and ADC requirements.

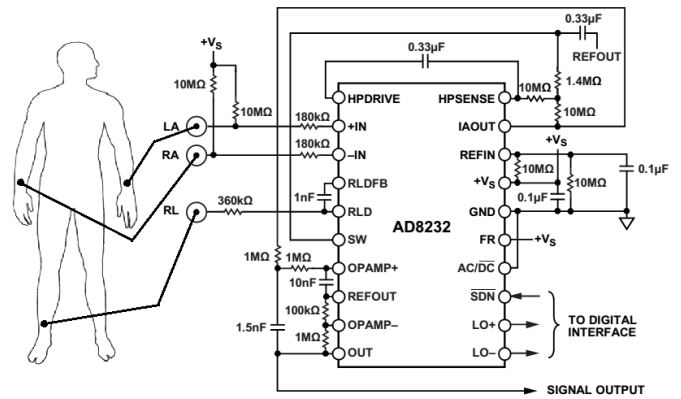


Fig.3. Circuit configuration of ECG waveform monitoring

### B. Digital Back End

ATmega328P is a low-power CMOS microcontroller [8] developed by Atmel Corporation. This chip is configured with integrated USB in Arduino Uno R3 development board which includes 32KB of flash memory and 2KB of RAM. This device is used as the Digital Back End of the prototype for converting the analog ECG signal from AD8232 to a digital signal with 100 Hz sampling frequency. The overall connection diagram between the AD8232 and Arduino Uno R3 is shown in Fig. 4.

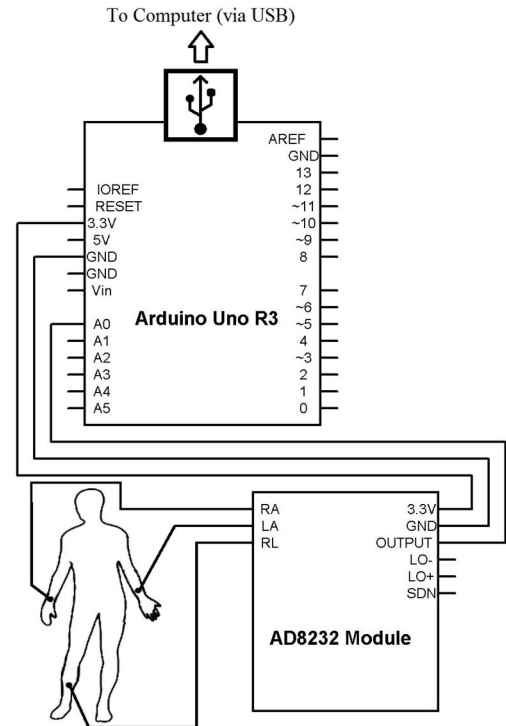


Fig.4. Connection between Analog Front End and Digital Back End

The ADC converts an analog input signal to a 10-bit digital value through successive approximation and it only takes 13 $\mu$ s to 260 $\mu$ s conversion time. ATmega328P offers ADC Noise Reduction mode [8]. While performing analog-to-digital conversion, it stops the CPU and all I/O modules (except asynchronous timer and ADC) to minimize switching noise during ADC conversions.

### III. SOFTWARE DESIGN

The accumulated digitalized ECG data from Arduino Uno R3 development board is transmitted to the computer through the USB communication protocol.

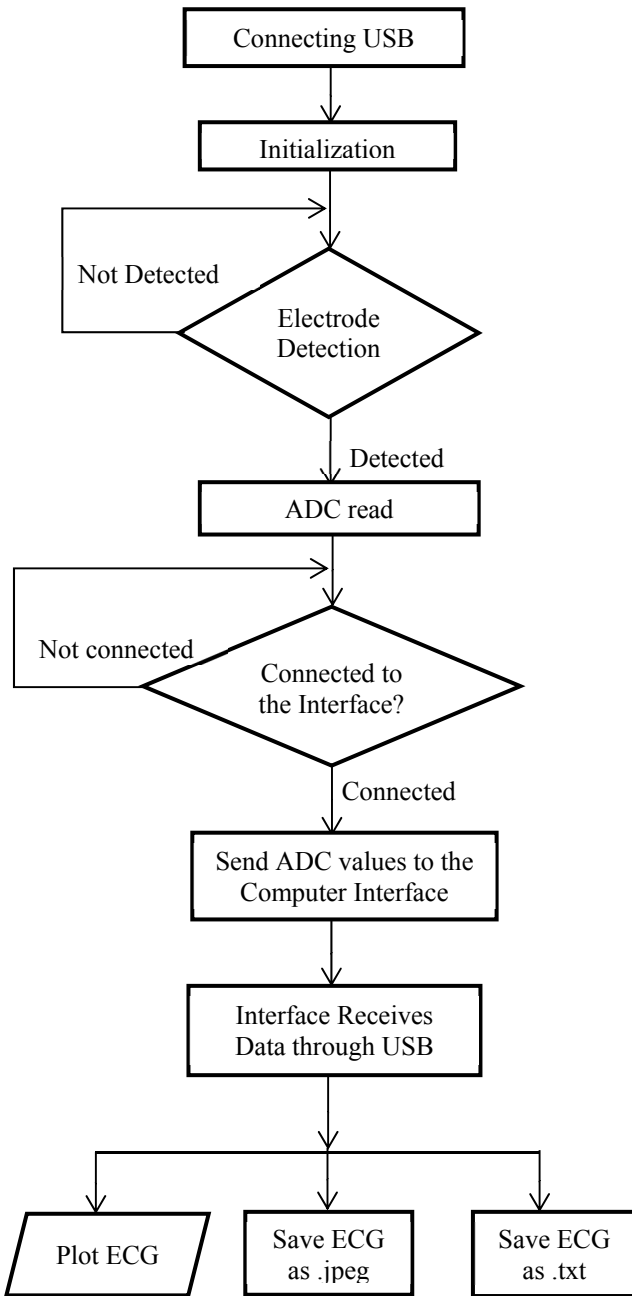


Fig.5. Flowchart of the algorithm

To view the electrocardiogram and store it for future analysis, dedicated software is specially designed. This computer interface has been developed using .net framework. It can view the real time curve and store it for further investigation. To use this software, the ECG device is needed to be connected to the computer through USB port and the user has to select the port address and connect the device. Then the software gets the ECG values through USB and plots the electrocardiogram. A flowchart is given in Fig. 5 showing the

program flow from the hardware end to the software end of the prototype.

The ECG waveforms from this software can be easily interpreted by any specialist physicians because these are exactly similar to traditional electrocardiogram reports. The user interface of this software is shown in Fig. 6.

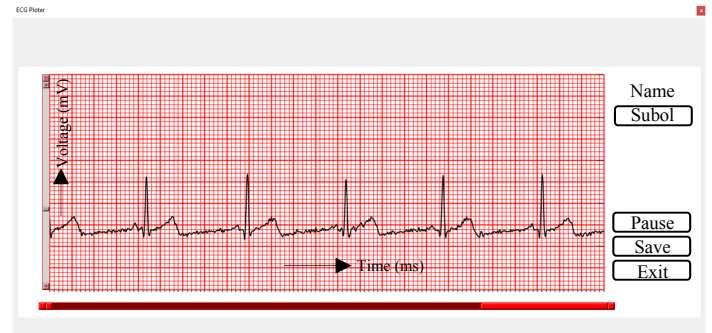


Fig.6. User interface of the software displaying an ECG waveform

For accurate medical diagnosis, this software also stores the received values as a .txt file and the graph as a.jpeg file, which can be printed or e-mailed to the cardiac experts.

### IV. CLINICAL TEST AND RESULT ANALYSIS

An intrinsic clinical study is designed and conducted to investigate the effectiveness of the implemented prototype. The study consisted of two conditions, using the newly developed prototype and using a device already commercially available (i.e. Biocare ECG-300G). The two ECG traces from Lead I configuration are graphically compared and mathematical correlation is calculated to find out the viability of the prototype.

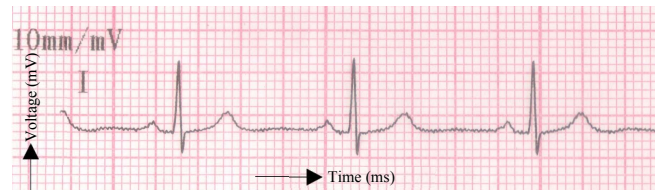


Fig.7. Electrocardiogram from Biocare ECG-300G

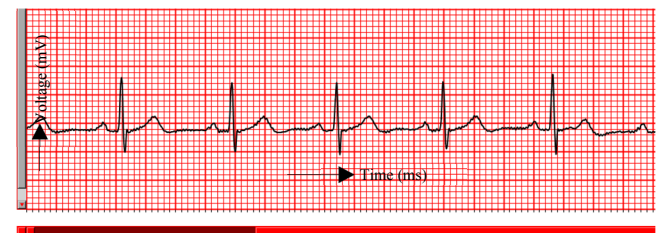


Fig.8. Electrocardiogram from the Implemented Prototype

The clinical test is performed on a 25 years old healthy test subject and the ECG data is acquired for both conditions, one after the other. Electrocardiogram from commercially available Biocare ECG-300G and implemented prototype is illustrated in Fig. 7 and Fig. 8 respectively.

The graphical comparison between these two done by superimposing these two ECG traces in Fig. 9 and it can be easily interpreted that these two electrocardiograms are visually

identical. P, QRS and T wave can be identified easily from the electrocardiogram form the newly developed prototype and it can be used for primary medical diagnosis.

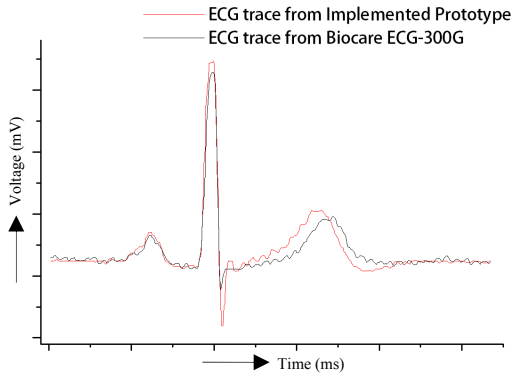


Fig.9. Superimposed ECG traces from Biocare ECG-300G and Prototype

Correlation is a statistic measure that indicates the degree to which two or more variables are linearly associated. Correlation coefficient ( $r$ ) can vary numerically between 0.0 and 1.0. The closer the correlation is to 1.0, the stronger the relationship between the two variables [9]. The formula for the correlation coefficient ( $r$ ) is:

$$r = \frac{1}{n-1} \left( \frac{\sum_X \sum_Y (X-\bar{X})(Y-\bar{Y})}{S_X S_Y} \right) \quad (1)$$

Here,  $n$  is the number of pairs of data;  $\bar{X}$  and  $\bar{Y}$  are the sample means of all the  $x$ -values and all the  $y$ -values, respectively; and  $S_X$  and  $S_Y$  are the sample standard deviations of all the  $x$ - and  $y$ -values, respectively. Equation (1) is used to compute the correlation between the two ECG traces of Fig. 9 and calculated value is found to be 0.964. Hence, it is evident that the two traces are following a similar path and it ensures the legitimacy of the implemented prototype.

Some electrical parameters are measured for the prototype circuit. These criteria are summarized in the Table 1.

TABLE I. SYSTEM PARAMETERS

Parameter	Value
Electrode Number	3
Operating Frequency	0.5 Hz - 40 Hz
Sampling Frequency	100 Hz
Drawing Current	1.64 mA
Operating Voltage	3.33 V
Power Consumption	5.46 mW

The developed prototype is uniquely designed for low-cost, low-power and ultra-portability. Table 2 shows the comparison of some of these properties between the prototype ECG monitoring system and some commercially available single lead ECG recorders. The features of commercially available ECG recorders are collected from a rigorous review study done by Dr. Grier [10]. From this comparative study, it is noticeable that cost of the developed prototype is the lowest among the

others. It is because of the low price of all the required components. Also, its size and weight ensure that this device can be conveniently used as a portable one.

TABLE II. COMPARATIVE STUDY

Device Name	Dimensions	Weight	Power Supply	Cost
AfibAlert	1.5×7.0×2.2cm	130 gm	2 × 1.5 V AAA	\$449
InstantCheck	12.3×7.8×2.3cm	140 gm	2 × 1.5 V AAA	\$800
MD100E	13.8×7.5×2.4 cm	100 gm	2× 1.5 V AA	\$259
PC-80	11.2×5.5×1.7 cm	100 gm	2 × 1.5 V AAA	\$200
ReadMyHeart	12.5×8.5×2.2 cm	130 gm	2 × 1.5 V AAA	\$200
Prototype	7.0×6.0×2.2 cm	80 gm	5 V USB supply	\$58

## V. FUTURE WORK AND CONCLUSION

The newly developed prototype is capable of transmitting data to a PC via wired USB communication protocol. However, wireless transmission can be done using radio frequency, Wi-Fi or Bluetooth communication. This device can use a cellular phone as the display unit. Thus, it can be used as a wireless wearable device. Nevertheless, the purpose of this research was to design a low-cost, low-power and portable ECG monitoring system. Goals of this study are largely met as this device costs less than \$60 and uses only 5.46 mW power. The preliminary clinical result suggests that the quality of resultant electrocardiogram of the implemented prototype is quite satisfactory. In future, this study can be expanded to measure other electrical biopotential signals.

## REFERENCES

- [1] A. S. Go et al. "Heart disease and stroke statistics-2013 update: a report from the American Heart Association", *Circulation*. 2013, doi: 10.1161/CIR.0b013e31828124ad, Epub, December 2012.
- [2] Robert P. Grant, "Clinical Electrocardiography", *Journal of Medical Education*, Volume 33 - Issue 3 - pp 242, March 1958.
- [3] Roger G. Mark, "Clinical electrocardiography and arrhythmias", Harvard-MIT Division of Health Sciences and Technology, 6.022J/2.792J/HST542J: Quantitative Physiology: Organ Transport Systems, 2004.
- [4] James W. Grier, "eHeart: an introduction to ECG/EKG", Department of Biological Sciences, North Dakota State University, Fargo, ND 58105-5517, 2008.
- [5] Roxy Senior and John Chambers, "Portable Echocardiography: A Review", *British Journal of Cardiology*, 2006, Vol. 13, No. 3, pp. 185-190.
- [6] S. Suave Lobodzinski1 and Michael M. Laks, "New devices for very long-term ECG monitoring", *Cardiology Journal*, 2012, Vol. 19, No. 2, pp. 210-214.
- [7] Analog Devices Incorporated, "Single-lead heart rate monitor front end", AD8232 datasheet, 2013.
- [8] Atmel Corporation, "8-bit AVR Microcontrollers", ATmega328/Pdatasheet, 2016.
- [9] Kenney, J. F. and Keeping, E. S. "Linear Regression and Correlation." Ch. 15 in *Mathematics of Statistics*, Pt. 1, 3rd ed. Princeton, NJ: Van Nostrand, pp. 252-285, 1962.
- [10] James W Grier, "Comparison and review of portable, handheld, 1-lead/channel ECG/EKG recorder", Ndsu.edu, 2016. [Online]. Available: <https://www.ndsu.edu/pubweb/~grier/Comparison-handheld-ECG-EKG.html>. [Accessed: 19- Jul- 2016].

# Selection of Better Strategy for Self Organized Data Aggregation Techniques using Evolutionary Game Theory

Md.Salehin Ferdous Kader<sup>1</sup>, Mir Muntasir Hossain<sup>2</sup>, Sanchita Ghose<sup>3</sup>, Kazi Rehnuma Zafreen<sup>4</sup>

<sup>1</sup>Department of Electrical and Electronic Engineering, Fareast International University, Bangladesh

<sup>2</sup>Department of Electrical and Electronic Engineering, Northern University Bangladesh, Bangladesh

<sup>3</sup>Department of Electrical and Electronic Engineering, Bangladesh University, Bangladesh

<sup>4</sup>Department of Electrical and Electronic Engineering, Bangladesh University, Bangladesh

E-mail: princemahin4@gmail.com<sup>1</sup>, mirmuntasir.eee@gmail.com<sup>2</sup>, sanchita\_xmr@yahoo.com<sup>3</sup>, rehnunazafreen@gmail.com<sup>4</sup>

**Abstract**— Self Organized Data Aggregation Technique applying Evolutionary Game Theory is one of the most effective methods to select the optimum strategy for Delay Tolerant Network (DTN). In DTN, reliable end-to-end data transfer is provided by custody transfer mechanism where special nodes (custodians) exchange information with custody following hop-by-hop manner. For multi cluster Delay Tolerant Network, message ferrying approach is considered here. Now, the strategy selection (to become an aggregator or sender) is considered as a game in Evolutionary Game Theory, where, each node will draw result after interaction. For strategy selection, Imitation Update Rule of Evolutionary Game Theory has been utilized. We will focus mainly on the Birth-Death and Death-Birth Update Rules of Evolutionary Game Theory and select the better Update rules among three update rules.

**Keywords**— Delay Tolerant Networks (DTNs), Evolutionary Game Theory, Self-Organized, Aggregators, Message ferry, Update Rules

## I. INTRODUCTION

Delay Tolerant Network [1-2] where, a *store-carry forward* [1] message conveyance and *custody transfer* [3] method is utilized, is considered useful where there is no end to end data connectivity and there is solid exchange of information (bundle) with custody following hop-by-hop manner. *Custodians* are the in between nodes which keep the custody bundles, and facing capacity clog for space congestion where they should decline to get any bundles from different nodes. Likewise, every battery fuelled node [10] should awaken when bundles are contained. Own bundles are produced by each custodian. Moreover, for preserving its energy and space it acts selfishly and denies the transfer requests of custody from other nodes. Gradually it increases with time for isolated networks. In such circumstance, a few mobile vehicles alluded to as *message ferries* [9-11], which have enough space and energy to convey the bundles to the targeted destination named as *sink node*, can take care of the capacity congestion issue by effectively going to the system and assemble bundles from the custodians and they must visit and accumulate bundles from the custodians for isolated clusters. Message ferry faces difficulties to visit all nodes in a specific timeframe. Making note of the difficulties, *Self-Organized Data Aggregation Technique* is developed [4]. By

the assistance of *Evolutionary Game Theoretic Methodology* [6-8], our arrangement can consequently choose a few exceptional custodians alluded as *aggregators*, which are naturally helpful and energetically contain custody bundles from other nodes called as senders. In this way, the bundles need to be gathered by the message ferry just from the aggregators. It should be noted that, every aggregator, which will get energy supply form message ferries [10], must be vigilant to get and seize the bundles until exchanging them to the message ferry [1-4], when every sender rises during the creation and transfer of the bundles [1-4]. As per our plan, strategy is selected properly by every node, i.e., sending or aggregating, considering upon neighbor's strategies which is modeled as a game in game theory [1-4].

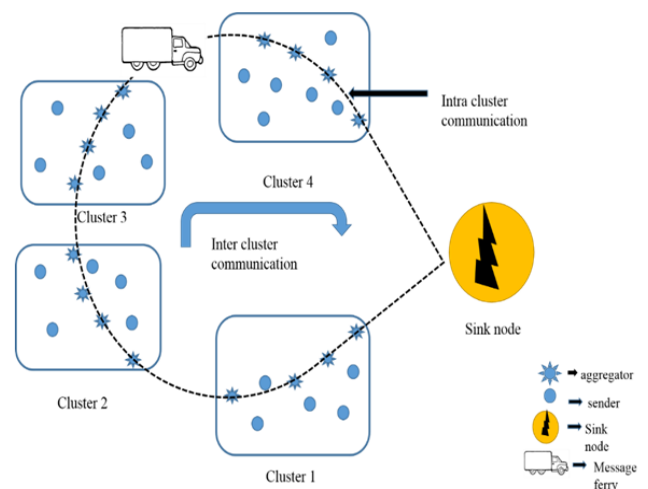


Fig. 1. Model Scenario: Message ferry visits a limited number of aggregators in each cluster and delivers collected bundles to sink node (Inter Cluster)

## II. SELF-ORGANIZED DATA AGGREGATION

Bundles are gathered by a predefined sink node from isolated clusters nodes exploiting message ferry which can be observed from Fig. 1. Every node inside a cluster straightforwardly can contact with the members of different cluster inside the transmission extend however can't contact to a sink node and/or different clusters because of prolonged



separations within the clusters. The inter-cluster connection is established by the message ferry and observes predetermined sets of aggregators inside every cluster.

This paper focused on the aggregation of bundle inside a cluster. The aggregation of bundle is directed throughout three stages: a) Aggregator selecting stage, b) Bundle aggregating stage, and c) Bundle collecting stage. At every node, these stages are rehashed and the reiteration unit is alluded to as round. Because of the absence of dependable connectivity within random nodes, accomplishing a unified regulation in DTNs is arduous. In this manner, the determination of aggregators ought to be executed decentralizedly. It decides either a sender or an aggregator through reciprocal interaction in light of its own advantage contingent upon the encompassing stipulations. As aggregators are constantly alert amid a round and senders just get up while producing and their bundles are transmitted, the loss of energy of every node is anticipated and it remains conscious relative to that time period.

TABLE I. ABSTRACT PAYOFF MATRIX

	<i>Node 2</i>	
	<i>Send</i>	<i>Aggregate</i>
<i>Node 1</i>		
<i>Sender</i>	<i>R, R</i>	<i>S, T</i>
<i>Aggregator</i>	<i>T, S</i>	<i>P, P</i>

TABLE II. PAYOFF MATRIX FOR NO RETRANSMISSION CASE

	<i>Node 2</i>	
	<i>Sender</i>	<i>Aggregator</i>
<i>Node 1</i>		
<i>Sender</i>	<i>-s, -s</i>	<i>-s, b-c</i>
<i>Aggregator</i>	<i>b-c, -s</i>	<i>-c, -c</i>

Let the *utilization of energy measurement be denoted as c* for aggregators and *s* for senders *per round*. Increment of *s* with *the time of retransmission* however *not in any way* surpasses *c*, i.e.,  $c - s > 0$ . The message ferry provides energy to every aggregator which is spoken by *b*. Naturally, *b* increases with the increment of aggregators.  $b > c$  ought to be fulfilled to maintain the nodes battery active. Between two adjacent nodes the interconnection is displayed as a game which is compiled as a payoff matrix. For every node have two main functions: Aggregator (aggregate) and sender (send). Four conceivable blends of the methodologies of the two nodes where every node gets diverse result from every strategically permutation. Table 1 represents the hypothetical payoff matrix where Tables 2 outline the payoff matrices for no-retransmission case.

The consequential payoffs for every amalgamation can be demonstrated by considering the supply of energy and energy utilization. In the event when both nodes choose to be aggregators, from the message ferry without any energy contribution greatest energy  $P=c$  is lost, since they do not have the capacity to gather an adequate amount of packs/bundles to

ask for the message ship to travel. With the combination to a sender, an aggregator gets the biggest energy  $T=b-c$ ; *c* is lost, however, *b* is acquired from the message ferry, while the littlest energy  $S=s$  is lost by the sender. Where both nodes choose to be as senders, two conceivable cases can occur contingent upon the presence of retransmission.

### III. METHODOLOGIES

#### A. Three different update rules of Evolutionary Game Theory:

- **Birth-Death update rule (BD):** A node (called mother node) is selected depending on its own payoff to update the strategy of randomly chosen neighbouring node (called offspring node). The new updated strategy of the offspring node is changed similar to the mother node (which implies mother node is giving birth of its strategy). While updating, the previous strategy of offspring is deleted (which implies the strategy of offspring node is death).
- **Death-Birth Update Rule (DB):** A node (here it is offspring node) is selected depending on its pay off to delete its own existing strategy (which implies offspring node is giving death of its existing strategy). The strategy of offspring node is renewed and made similar to the strategy of a selected node (mother node which gives birth of its strategy) which is chosen among neighbouring nodes depending on its payoff.
- **Imitation Update Rule (IM):** Each node analyses its own payoffs according to the strategies of its neighbours, as well as its own strategy, in the previous round. It then chooses between keeping its present strategy or imitating one of the neighbour's strategies proportional to payoffs.

### IV. MATHEMATICAL MODEL

Give *x* a chance to signify the proportion of the quantity of aggregators to the entire number of cluster members. It should be noted that  $1 - x$  denotes to the proportion of the quantity of senders. For the no retransmission case, we utilize Table 2.

#### Ratio of aggregators for the case of no retransmission:

Birth-Death:

$$x_{1(BD)} = \frac{b(k-1) - k(c-s)}{b(k-2)} \quad (1)$$

Death-Birth:

$$x_{1(DB)} = \frac{b(k^2 - k - 2) - k^2(c-s) + b}{b(k^2 - k - 2)} \quad (2)$$

Imitation:

$$x_{1(IM)} = \frac{b(k^2 + k - 3) - (c-s)(k^2 + 2k)}{b(k+3)(k-2)} \quad (3)$$

Equilibrium Conditions for three cases

Birth-Death:

$$\frac{k}{k-1} < \frac{b}{c-s} < k \quad (4)$$

Death-Birth:

$$\frac{k^2}{k^2-k-1} < \frac{b}{c-s} < k^2 \quad (5)$$

Imitation:

$$\frac{k^2+2k}{k^2+k-3} < \frac{b}{c-s} < \frac{k^2+2k}{3} \quad (6)$$

## V. NUMERICAL ANALYSIS

Four autonomous variables are considered,  $b$ ,  $c$ ,  $s$  and  $k$ , which influence  $x$ . To start with, for rearrangements, we expect that  $c-s=1$ . Note that this disentanglement does not lose all inclusive statement. Presently we will demonstrate some numerical investigation with perception and talk for selecting the better overhaul rules for the distinctive variables for the instance of no re-transmission.

### A. Degree ( $k$ ) vs. Intensive ( $b$ ) graph for no-retransmission:

Fig.2 shows the rapport between Degree and the choice of Intensive with the suprimum and infimum that satisfy Eq. (4), (5) and (6) for the case BD,DB and IM Update Rules respectively for case no-retransmission.

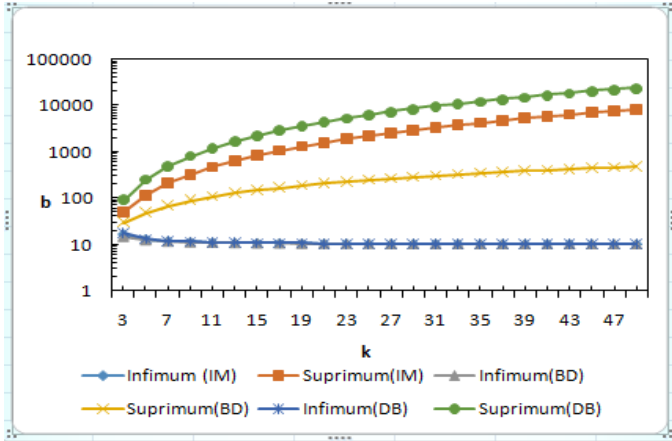


Fig. 2. Degree ( $k$ ) vs. intensive ( $b$ ) graph for three update rules for case no retransmission

**Observation:** All infimum have the same value of Intensive. For suprimum of each  $k$ , DB has the highest values of Intensive ( $b$ )

**Discussion:** Message ferry is supplying nearer same amount of energy to nodes to become aggregators.

**Better update rule for novel strategy selection:** BD, DB and IM update rules show the same characteristics.

### B. Degree ( $k$ ) vs. Modifier matrix ( $m$ ) graph for variable Intensive ( $b$ )

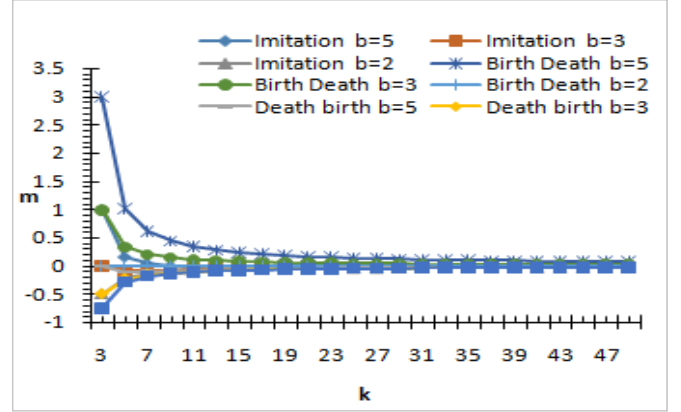


Fig. 3. Degree ( $k$ ) vs. Modifier matrix ( $m$ ) graph for three update rules for variable  $b$  for no-retransmission

**Observation:** For particular  $k$ , BD shows the highest value and DB shows the lowest value of modifier matrix.

**Discussion:** Nodes are more willingly preferred to be aggregators than senders. So, the Modifier Matrix converges largest value for BD Update Rule when  $k < 25$ . After  $k > 25$ , all graphs converges to zero.

**Better update rule for novel strategy selection:**

For  $k < 25$ , BD update rule is better. For  $k > 25$ , BD, DB and IM shows the same characteristics.

### C. Degree ( $k$ ) vs. Ratio of aggregators ( $x^*$ ) graph:

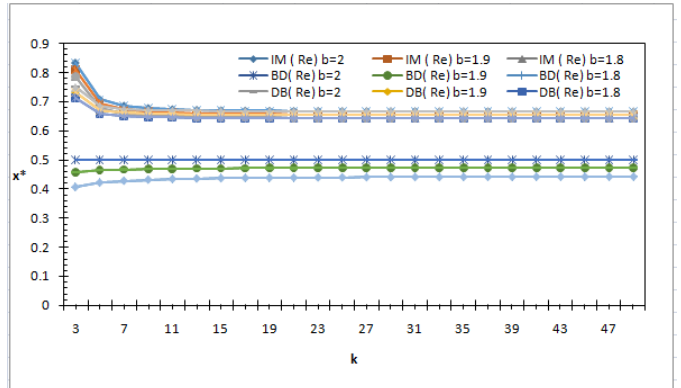


Fig. 4. Degree ( $k$ ) vs. Ratio of Aggregators ( $x^*$ ) graph for three update rules for variable  $b$  for the case no retransmission

**Observation:** For  $k < 10$ , BD has the lowest value of Ratio of Aggregators ( $x^*$ ). For  $k > 10$ , IM and DB has the nearer same values of the Ratio of Aggregators ( $x^*$ ).

**Discussion:** In IM update rule, the nodes have the highest intensity to be aggregators than senders and more co-operative in nature. So the Ratio of Aggregators ( $x^*$ ) are more than any other update rules for IM when  $k$  is small ( $k < 10$ ).

**Better update rule for novel strategy selection:** BD can be selected as better update rule.

#### D. Degree ( $k$ ) vs. Intensive ( $b$ ) for variable Ratio of Aggregators ( $x^*$ )

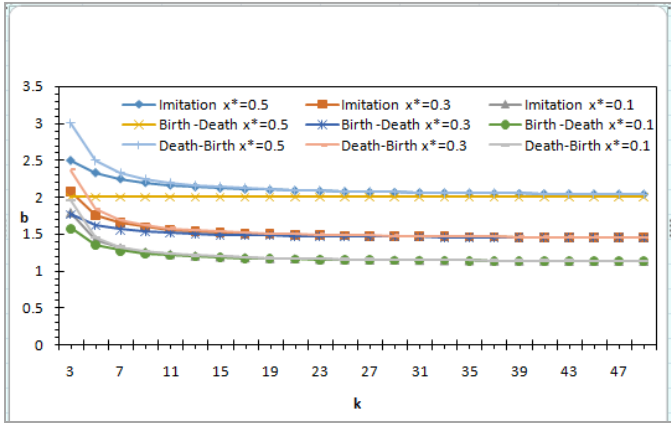


Fig. 5. Degree ( $k$ ) vs. Intensive ( $b$ ) graph for variable Ratio of Aggregators ( $x^*$ ) for the case no-retransmission

**Observation:** when  $k < 20$ , DB has the highest value of  $b$ . BD has the lowest value of  $b$  initially.

**Discussion:** Nodes are more co-operative in nature in BD. So message ferry needs to supply less energy to nodes to become aggregators.

**Better update rule for novel strategy selection:** When  $k < 20$ , BD as better update rule.

#### E. Degree ( $k$ ) vs. Intensive ( $b$ ) for variable $c$ and $s$

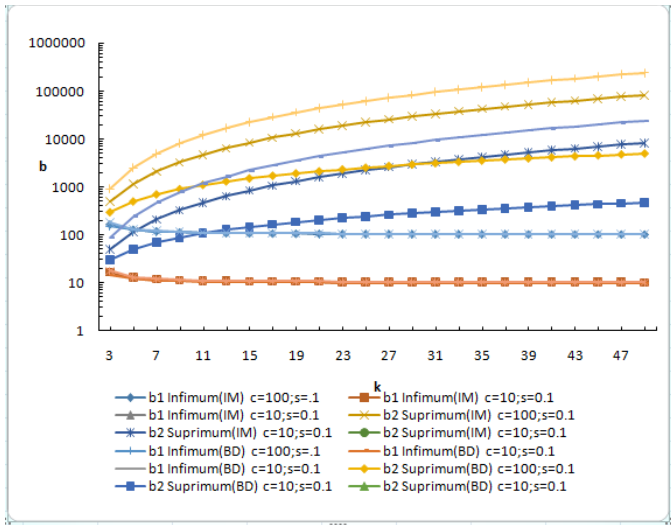


Fig. 6. Degree ( $k$ ) vs. Intensive ( $b$ ) graph for variable  $c$  and  $s$  for three cases for no retransmission

**Observation:** The infimum has almost the same value of three cases. For suprimum of each  $k$ , for higher  $c$ , DB has the largest value of intensive ( $b$ ).

**Discussion:** When more energy is lost by the senders, temptation  $b$  can be lesser to turn into an aggregator. Again when we increase the value of  $c$ , the graph shifts upwards, that directly indicates that  $b > c$ .

**Better update rule for novel strategy selection:** BD, DB and IM update rule have the same characteristics

## VI. CONCLUSION

This paper considered data aggregation in a cluster for ferry assisted multi-cluster DTNs. Nodes were considered characteristically selfish and non-agreeable in nature. Applying evolutionary game theory, the Self-Organized Data Aggregation plan in such a domain has been discussed. In this plan, the choice of aggregators is led throughout decentralized procedures by the assistance of strategic outcomes of evolutionary game theory. In this paper, Novel Strategy was selected for Ferry Assisted Multi Cluster DTNs for selection of aggregators for the case of no-retransmission. For this reason some mathematical calculations were introduced, performed numerical analysis. After that, Birth-Death (BD) Update Rule is selected as better update rule for selecting the strategy for selection of aggregators as it gives lowest number of Ratio of Aggregators among three update rules.

## References

- [1] K. Habibul Kabir, Masahiro Sasabe, and Tetsuya Takine, "Self-Organized Data Aggregation among Selfish Nodes in an Isolated Cluster," in Proceedings of the 1st Workshop on Bio-inspired Models and Technologies for Ambient Information Society (BioAmBIS 2010 workshop), Boston, MA, USA, December, 2010.
- [2] K. Habibul Kabir, Masahiro Sasabe, and Tetsuya Takine, "Evolutionary Game Theoretic Scheme for Stable and Resilient Data aggregation in DTNs," International Journal of Autonomous and Adaptive Communications Systems (IJAACS), 2013.
- [3] K. Habibul Kabir, Masahiro Sasabe, and Tetsuya Takine, "Evolutionary game theoretic approach to self-organized data aggregation in delay tolerant networks", IEICE Transactions on Communications, vol.E93-B, no.3, pp.490-500.
- [4] K. Habibul Kabir, Masahiro Sasabe, and Tetsuya Takine, "Design and Analysis of Self-Organized Data Aggregation Using Evolutionary Game Theory in Delay Tolerant Networks," in Proceedings of The Third IEEE WoWMoM Workshop on Autonomic and Opportunistic Communications, Kos, Greece, June, 2009
- [5] Cerf, V., Burtleigh, S., Hooke, A., Torgerson, L., Durst, R., Scott, K., Fall, K., Weiss, (2003) 'Delay tolerant network architecture', IETF RFC 4838 draft.
- [6] Fall, K. (2003) 'A delay-tolerant network architecture for challenged Internets'. Proceedings of ACM SIGCOMM 2003, pp.27-34.
- [7] K. Fall and W. Hong, "Custody transfer for reliable delivery in delay tolerant networks." Tech. report, in Delay Tolerant Networks, Intel Research, BerkeleyTR-03-030, 2003.
- [8] Guo, H., Li, J., Washington, A. N., Liu, C., Alfred, M., Goel, R. et al, "Performance Analysis of Homing Pigeon based Delay Tolerant Networks In: Military Communications Conference", 2007. MILCOM 2007. IEEE, pp. 1-7,2007.
- [9] Kevin, F, "A delay-tolerant network architecture for challenged internets," In: Proceedings of the 2003 conference on Applications, technologies, architectures, and protocols for computer communications Vol. 33, pp. 27-34. ACM 2003.
- [10] Tarek AlSkaif, Manel Guerrero Zapata, Boris Bellalta, "Game theory for energy efficiency in Wireless Sensor Networks", Journal of Network and Computer Applications: Volume 54 Issue C, August 2015 in Academic Press Ltd..
- [11] Hang Guo, Xingwei Wang, Hui Cheng, Min Huang, "A routing defense mechanism using evolutionary game theory for Delay Tolerant Networks", Elsevier Science Publishers B. V. in Applied Soft Computing: Volume 38 Issue C, January 2016.

# Effects of Buffer Size and Mobility Models on the Optimization of Number of Message Copies for Multi-Copy Routing Protocols in Scalable Delay-Tolerant Networks

Md. Sharif Hossen<sup>\*</sup>, Md. Tofael Ahmed<sup>\*</sup>, Muhammad Sajjadur Rahim<sup>†</sup>

<sup>\*</sup>Department of Information and Communication Technology, Comilla University, Comilla

<sup>†</sup>Department of Information and Communication Engineering, University of Rajshahi, Rajshahi  
Bangladesh

sharif5613@gmail.com, tofael\_ice\_ru@yahoo.com, sajid\_ice@ru.ac.bd

**Abstract**—In Delay-Tolerant Network (DTN), there exists a lack of direct path from source to destination, and it is also featured by extremely high bit error rate, unwanted delay, limited resource, etc. For such network, we have investigated the effects of buffer size and mobility models on the optimization of the number of message copies for multi-copy routing protocols such as Spray-and-Focus (SNF) and Spray-and-Wait (SNW). This investigation is essential for providing us with the insight on the number of message copies that would provide better delivery, lower latency and lower overhead considering the effects of buffer size and mobility models in scalable delay-tolerant networks. In this investigation, we have considered three performance metrics, namely delivery probability, average latency, and overhead ratio. Simulation is done using Opportunistic Network Environment (ONE) simulator, which is designed basically for evaluating the performance of DTN routing strategies. Here we have considered three mobility models, namely Shortest Path Map Based (SPMB) movement, Random Walk, and Random Direction. Simulation results show that for increasing buffer size and number of nodes on these considered mobility models for a particular value of number of message copies, indicated by  $L$ , SNF routing exhibits satisfactory performance, especially in the case of SPMB movement using only  $L = 2$  copies. Since our purpose is to provide a satisfactory performance, i.e., higher delivery, lower latency and lower overhead, SNW routing shows overall good performance using  $L = 10$  copies. Therefore, it would be a good optimization using Shortest Path Map Based movement model using  $L = 2$  copies for SNF routing, and  $L = 10$  copies for SNW in scalable DTN scenario, where there may be a high possibility of varying buffer size with number of mobile nodes.

**Keywords**—intermittently connected mobile networks; delay-tolerant networks; routing; opportunistic network environment simulator; buffer size; mobility models; average delay; delivery probability; overhead ratio

## I. INTRODUCTION AND RELATED WORKS

In Delay-Tolerant Networks (DTNs), there is no persistent route from source to destination due to scarce network resources and mobility models; this type of networks can be characterized by extremely high bit error rates, unwanted delays, fixed resources, etc. [1–2]. DTNs are also referred to as Intermittently Connected Mobile Networks (ICMNs) [3], which are featured by intermittent connectivity and temporarily

broken links [4]. It uses “store and forward” mechanism for providing the route of messages where a message is successively moved from the source to the next available node and stored in respective node’s buffer which is forwarded to other nodes with an aim to reach the destination [5–7]. DTNs have been extensively used in many areas including interplanetary networks [8], underwater networks [9], satellite communication [10], wildlife tracking sensor networks [6], military networks, and vehicular ad-hoc networks [11], etc.

In our previous work [22], we have investigated the optimization of number of message copies for two multi-copy routings, namely Spray-and-Wait (SNW) and Spray-and-Focus (SNF) with the variation of number of nodes. From the investigation, we have seen that SNF routing shows better performance using  $L = 2$  copies while for SNW it needs about  $L = 10$  copies. In the present work, we have included the impacts of varying buffer size and mobility models on their performance.

The rest of this paper is organized as follows: Section II describes the considered routings used in a scalable DTN. Section III includes the discussion of mobility models. Section IV introduces the simulation tool and setup. Section V discusses the simulation results. Section VI concludes this research work.

## II. INVESTIGATED ROUTINGS IN DTN

In this paper, we have considered two routings, Spray-and-Wait (SNW) [12], and Spray-and-Focus (SNF) [13].

SNW routing shows better performance than Epidemic [14], PRoPHET [15] as discussed in [16] by limiting the number of message copies. There are two versions, namely vanilla and binary. In case of vanilla, a single message is forwarded from source to the first  $L$  distinct nodes it encountered. On the other hand, in binary version source node containing  $L$  copies forwards  $L/2$  to the first node it encountered. Each node then forwards half of its copies to future nodes they meet having no copy in common. When a node has only a single copy, then it is in wait phase and tries to communicate directly to the destination.

In the focus phase of SNF routing, messages are not routed using direct transmission (i.e. forwarded only to their destination) [4, 17], rather copies can be forwarded to another

node having better probability to deliver them to the destination using a single-copy utility based routing.

### III. MOBILITY MODELS

In this research work, three mobility models, namely Random Walk (RW), Random Direction (RD), and Shortest Path Map Based (SPMB) movement have been used.

In RW, each node moves randomly towards a new node's location. Although random direction with speed is assigned to every node within a predefined range, nodes in a network are independent from each another [18]. Whenever a node reaches to the destination, a new direction is again assigned from predefined ranges.

In RD, a mobile node gets a movement degree randomly and moves in a particular direction until it touches the destination boundary of simulation area with a specified speed. When it travels to boundary area, it stops for a specified pause time before choosing a new direction to move again [19].

In SPMB movement, all nodes travel to a certain destination in the map and follow Dijkstra's shortest path algorithm [20] to discover the shortest path to the destination.

### IV. SIMULATION TOOL AND SETUP

In this section, we will discuss opportunistic network environment (ONE) simulator and simulation setting.

ONE [20–21] is an agent-based discrete event simulation engine, which is basically designed for evaluating the performance of DTN routing protocols. At each simulation step, ONE combines mobility modeling, inter node contacts, DTN routing, message handling and visualization in one package that provides a rich set of reporting and analyzing modules.

Simulation configuration for varying percentage of L copies in a scalable network is shown in table I. Two groups of nodes namely cars and pedestrians have been considered. Both groups have equal number of nodes.

TABLE I. SIMULATION ENVIRONMENT PARAMETERS

Parameters	Value	
Simulation Time	12 hours	
Number of Nodes	50, 100, 150, 200	
Pedestrians	Speed	0.5-1.5 m/s
	Group id	p
Cars	Speed	2.7-13.9 m/s
	Group id	c
Interface	Bluetooth Interface	
Transmit Speed	250 kbps	
Transmit Range	10 m	
Buffer Size	5, 10, 20, 30 MB	
Message Generation Rate	2, i.e., one message in 25-35 seconds	
Message TTL	300 minutes	
Mobility Models	SPMB, RW, RD	
Message Size	500 KB – 1 MB	
Number or Percentage of L Copies	2, 5, 10, 20	

### V. RESULTS AND DISCUSSION

In this investigation, we have used three mobility models and varied buffer size to achieve the optimum number of

message copies for the considered routing protocols in a scalable DTN scenario based on their performance.

#### A. Performance Analysis on Delivery Probability

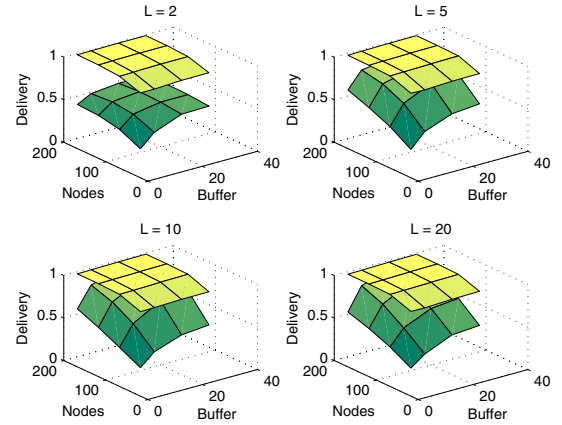


Fig. 1. Delivery probability with varying number of nodes and buffer size for L copies using shortest path map based movement mobility model

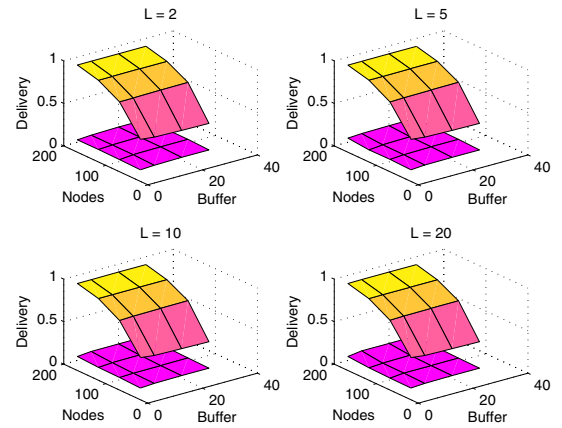


Fig. 2. Delivery probability with varying number of nodes and buffer size for L copies using random direction mobility model

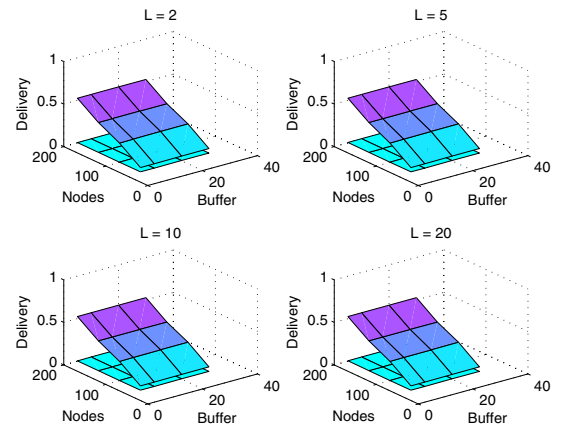


Fig. 3. Delivery probability with varying number of nodes and buffer size for L copies using random walk mobility model

Delivery probability is the ratio of the total number of messages delivered to the destination over the total number of messages created at the source. In the following figures, upper layer shows the performance of SNF routing and lower layer the SNW routing. We see that with increasing buffer size and number of nodes, delivery of SNF and SNW routings is better in case of SPMB movement than RD and RW. For clarification (considering only the highest value), SNF routing shows a delivery ratio 1 (approx.) in case of SPMB while for RD and RW, delivery ratios are less than 1 and 0.5, respectively. SNW routing shows approximately the same performance in RD and RW model. Hence, we see that SNF routing shows higher delivery when  $L = 2$ . On the other hand, in case of SNW routing, we see the better delivery for  $L = 10$ .

**B. Performance Analysis on Average Latency**

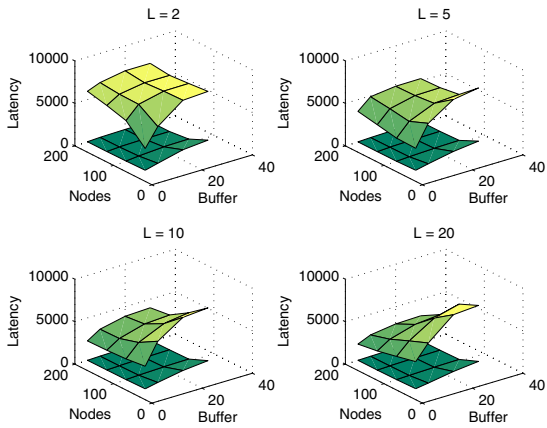


Fig. 4. Average latency with varying number of nodes and buffer size for L copies using shortest path map based movement mobility model

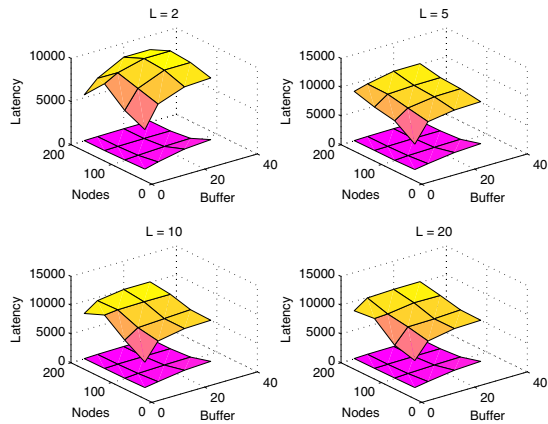


Fig. 5. Average latency with varying number of nodes and buffer size for L copies using random direction mobility model

Average latency is the measure of average time between messages generated and messages received to destination. In the following figures, upper layer shows the performance of SNW routing and lower layer the SNF. Average latency increases gradually in accordance with the increase of number of nodes and buffer size. Hence, in case of SNF routing, average latency is approximately same for varying L copies. For SNW routing,  $L = 10$  shows lower latency than  $L = 2$  and

$L = 5$ . Therefore, we can give a standard ( $L = 10$ ) with its higher delivery probability. That is, SNF routing gives lowest latency using only 2 copies but SNW requires 10 copies to obtain its optimization.

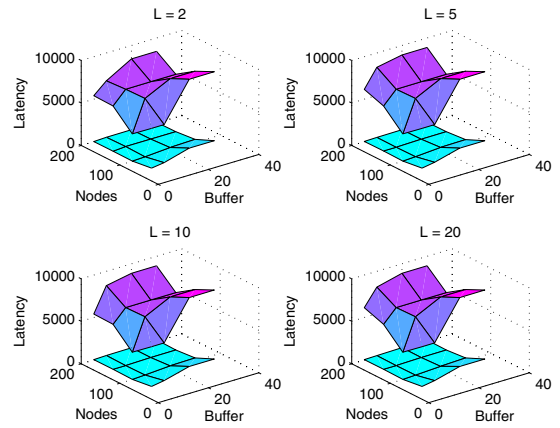


Fig. 6. Average latency with varying number of nodes and buffer size for L copies using random walk mobility model

**C. Performance Analysis on Overhead Ratio**

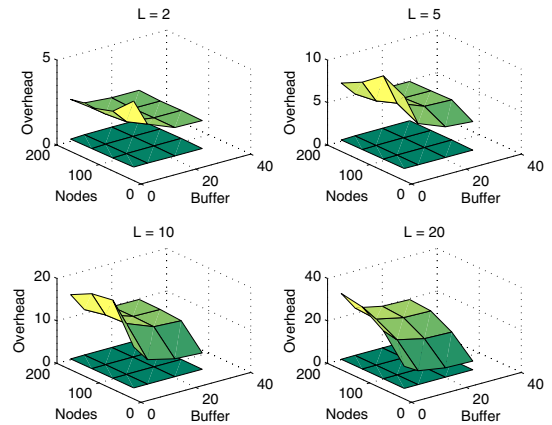


Fig. 7. Overhead ratio with varying number of nodes and buffer size for L copies using shortest path map based movement mobility model

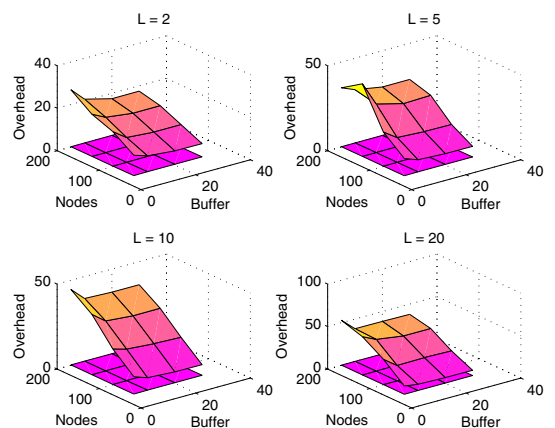


Fig. 8. Overhead ratio with varying number of nodes and buffer size for L copies using random direction mobility model

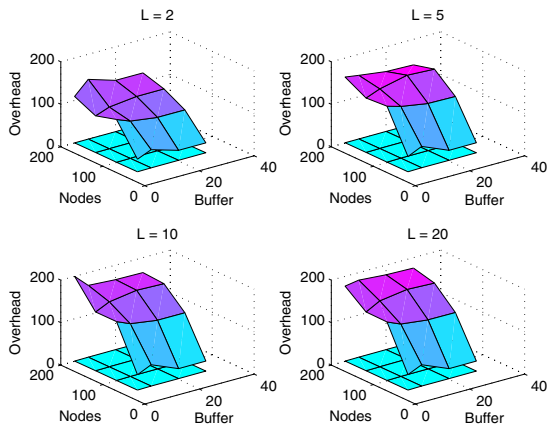


Fig. 9. Overhead ratio with varying number of nodes and buffer size for L copies using random walk mobility model

The overhead ratio defines how many redundant packets are relayed to deliver a single packet. It simply reflects the cost of transmission in a network. In the following figures, upper layer shows the performance of SNW routing and lower layer the SNF. With increase of number of nodes and buffer size we see that overhead ratio increases for SNW routing. Although SNW routing shows lower overhead for  $L = 2$  and  $L = 5$  than  $L = 10$  and  $20$ . We have considered  $L = 10$  as a standard considering its delivery probability. SNW shows lower overhead for  $L = 10$  compared to  $L = 20$ . On the other hand, SNF routing shows very low (approximately zero) overhead ratio for  $L = 2$  copies. So we can say that SNF routing shows lower overhead with only  $L = 2$  copies.

## VI. CONCLUSIONS

In this paper, we have investigated the effects of buffer size and mobility models, i.e. Shortest Path Map Based (SPMB) movement, Random Walk, and Random Direction, for optimizing the number of message copies for multi-copy routings such as Spray-and-Focus (SNF) and Spray-and-Wait (SNW) in a scalable delay-tolerant network. The investigation demonstrates that for increasing buffer size and number of nodes on these considered mobility models for a particular value of number of message copies, indicated by  $L$ , SNF routing exhibits the satisfactory performance using only  $L = 2$  copies, especially for SPMB. On the other hand, SNW routing shows overall good performance using  $L = 10$  copies. Hence, in comparison to SNW, SNF routing shows better results because of using the single-copy utility-based algorithm for enhancing the message delivery. Therefore, it will be a good optimization using Shortest Path Map Based movement model using  $L = 2$  copies for SNF routing, and  $L = 10$  copies for SNW in such scalable DTN scenario where there may be a high probability of having variable number of mobile nodes with varying buffer sizes.

## REFERENCES

[1] K. Fall, "A delay-tolerant network architecture for challenged internets," in Proc. of ACM SIGCOMM, Germany, Aug. 2003, pp. 27–34.  
 [2] S. Jain, K. Fall, and R. Patra, "Routing in a delay-tolerant network," in Proc. of ACM SIGCOMM, Portland, USA, Oct. 2004, pp. 145–157.

[3] L. Pelusi, A. Passarella, and M. Conti, "Opportunistic networking: data forwarding in disconnected mobile ad hoc networks," IEEE Comm. Mag., vol. 44, no. 11, pp. 134–141, Nov. 2006.  
 [4] Z. Zhang, "Routing in intermittently connected mobile ad hoc networks and delay tolerant networks: overview and challenges," IEEE Comm. Sur. and Tut., vol. 8, no. 1, pp. 24–37, Jan. 2006.  
 [5] J. Burgess, B. Gallagher, D. Jensen, and B. N. Levine, "Maxprop: routing for vehicle-based disruption-tolerant networks," in Proc. of IEEE INFOCOM, Barcelona, Spain, Apr. 2006, pp. 1–11.  
 [6] P. Juang, H. Oki, Y. Wang, M. Martonosi, L. S. Peh, and D. Rubenstein, "Energy-efficient computing for wildlife tracking: design tradeoffs and early experiences with zebraNet," in Proc. of ACM ASPLOS, San Jose, CA, USA, Dec. 2002, pp. 96–107.  
 [7] A. Chaintreau, P. Hui, J. Crowcroft, C. Diot, R. Gass, and J. Scott, "Impact of human mobility on opportunistic forwarding algorithms," IEEE Tran. on Mob. Com., vol. 6, no. 6, pp. 606–620, Jun. 2007.  
 [8] S. Burleigh, A. Hooke, L. Torgerson, K. Fall, V. Cerf, B. Durst, K. Scott, and H. Weiss, "Delay-tolerant networking: an approach to interplanetary internet," IEEE Comm. Mag., vol. 41, no. 6, pp. 128–136, Jun. 2003.  
 [9] J. Partan, J. Kurose, and B. N. Levine, "A survey of practical issues in underwater networks," in Proc. of ACM MobiCom, Los Angeles, California, USA, Sep. 2006, pp. 17–24.  
 [10] G. E. Prescott, S. A. Smith, and K. Moe, "Real-time information system technology challenges for NASA's earth science enterprise," in Proc. of the 20th IEEE Real-Time Sys. Sym., Phoenix, AZ, USA, Dec. 1999.  
 [11] J. Ott and D. Kutscher, "A disconnection-tolerant transport for drive-thru internet environments," in Proc. of IEEE INFOCOM, Miami, FL, USA, Mar. 2005, vol. 3, pp. 1849–1862.  
 [12] T. Spyropoulos, K. Psounis, and C. S. Raghavendra, "Spray and wait: an efficient routing scheme for intermittently connected mobile networks," in Proc. of ACM WDTN, Philadelphia, USA, Aug. 2005, pp. 252–259.  
 [13] T. Spyropoulos, K. Psounis, and C. S. Raghavendra, "Spray and focus: efficient mobility-assisted routing for heterogeneous and correlated mobility," in Proc. of IEEE PerCom, USA, Mar. 2007, pp. 79–85.  
 [14] A. Vahdat, and D. Becker, "Epidemic routing for partially connected ad hoc networks," Department of Computer Science, Duke University, Tech. Rep. CS-2000-06, Apr. 2000.  
 [15] A. Lindgren, A. Doria, and O. Scheln, "Probabilistic routing in intermittently connected networks," ACM Mob. Comput. Comm. Review, vol. 7, no. 3, pp. 19–20, Jul. 2003.  
 [16] M. S. Hossen and M. S. Rahim, "Performance analysis of delay-tolerant routing protocols in intermittently connected mobile Networks," in Proc. of Int. Conf. on Matls. Elec. & Info. Engg., Faculty of Engineering, University of Rajshahi, Rajshahi, Bangladesh, Jun. 2015.  
 [17] J. Leguay, T. Friedman, and V. Conan, "Evaluating Mobility Pattern Space Routing for DTNs," in Proc. of IEEE INFOCOM, Barcelona, Spain, Apr. 2006, pp. 1–10.  
 [18] H. Theus, T. Spyropoulos, and F. Legendre, "Putting contacts into context: mobility modeling beyond inter-contact times," in Proc. of ACM Int. Sym. Mob. Ad Hoc Net. and Com., Paris, France, May 2011.  
 [19] Royer, M. Elizabeth, P. Smith, and E. L. Moser, "An analysis of the optimum node density for ad hoc mobile networks," in Proc. of IEEE ICC, Helsinki, Finland, Jun. 2001, pp. 857–861.  
 [20] A. Keränen, J. Ott, and T. Kärkkäinen, "The ONE simulator for DTN protocol evaluation," in Proc. of Int. Conf. on Sim. Tools and Tech., Rome, Italy, Mar. 2009.  
 [21] Project page of the ONE simulator. [Online]. Available: <http://www.netlab.tkk.fi/tutkimus/dtn/theone> [Accessed Nov 2014].  
 [22] M. S. Hossen and M. S. Rahim, "On the optimization of number of message copies for multi-copy routing protocols in scalable delay-tolerant networks," in Proc. of Int. Conf. on Comp. Comm. Chem. Matls. & Elec. Engg., Faculty of Engineering, University of Rajshahi, Rajshahi, Bangladesh, Mar. 2016.

# Adopting Factors of Electronic Human Resource Management: Evidence from Bangladesh

Abdul Kadar Muhammad Masum

Associate Professor, Department of Business Administration, International Islamic University Chittagong, Bangladesh &

PhD Candidate, Department of Administrative Studies & Politics, University of Malaya, Malaysia  
akmmasum@yahoo.com

Mohammed Shamsul Alam

Associate Professor, Department of Computer Science & Engineering, International Islamic University Chittagong, Bangladesh  
alam\_cse@yahoo.com

Md. Golam Rabiul Alam

PhD Candidate, Department of Computer Science and Engineering,  
Kyung Hee University, South Korea  
robi@khu.ac.kr

Md. Abul Kalam Azad

PhD Candidate, Department of Applied Statistics,  
University of Malaya, Malaysia  
azadiiuc@gmail.com

**Abstract**— The incorporation of information technology (IT) instincts the legacy of human resource management (HRM) towards agile HRM. To achieve agility, this paper explores the factors or determinants inducing the organisation decisions to adopt electronic human resource management (e-HRM) in organisations of Bangladesh through structural equation modeling (SEM) of data science. To realize the influencing determinants, a research model was developed based on technology-organisation-environment (TOE) model. A total number of 320 respondents were participated from 48 organisations in Bangladesh using simple random sampling. The SEM results indicate that perceived compatibility, perceived cost, top management support, organisational culture, centralisation, IT vendor support, and government support have significant influence on management decision of e-HRM adoption. The applied implication of the findings and the scope of future studies are deliberated at the end of this paper.

**Keywords**—*electronic human resource management (e-HRM); Technology-Organisation-Environment (TOE); human resource information system (HRIS); influencing determinant*

## I. INTRODUCTION

Electronic human resource management (e-HRM) is a web based system that is developed to implement human resource (HR) policies, practices, and tactics to achieve the organisational goals [1]. Adopting e-HRM in organisation for agile management of human resources is an emerging trend in business, industrial and management domain. Generally, the greater part of e-HRM studies are on developed countries, while focuses on developing countries are scarce. However, comparatively a few studies have been examined on some developing countries, but there is an acute shortage of e-HRM research on South Asia, particularly in Bangladesh.

The prime objective of this study is detecting the most significant determinants of e-HRM adoption in the organisations of Bangladesh. Scholars have claimed that the weight of discovered determinants and the relative weight of every variable may change along with IT features and its setting. Also, researchers have exposed that the most results

of IT innovation research are consistently inconsistent [2]. Hence, for a specific setting (e.g., socio-cultural and socio-economic environment of Bangladesh), it is very important to comprehend the potential determinants that influence decision of e-HRM adoption in the organisations. Therefore, TOE framework [3] based research model is developed and the determinants influencing the management decisions are analysed through structural equation modeling (SEM) of data science to comprehend the most influential latent variables.

The remaining part of the paper is organised as follows. Section II describes the determinants of e-HRM adoption based on technological, organisational, and environmental (TOE) model. The research model and a series of testable hypotheses are presented in section III. Section IV includes the methodology of the study. The data analysis along with interpretation is in section V. A brief discussion on findings is provided in section VI, before concluding the paper in section VII.

## II. LITERATURE REVIEW

In this section, we scrutinised selected determinants for adopting e-HRM that occupied from IT innovation literature and theories.

The determinant ‘relative advantage’ is the trust of assured assistances in performance perfection, and savings in time and effort, costs reduction or in other means [1]. Researchers have revealed that the perceived advantage of e-HRM for HR department has a very positive association with the decision to adopt e-HRM in Singaporean firms [4]. However, Bian [5] has found insignificant influence of relative advantage on e-HRM adoption.

‘Perceived compatibility’ determinant is the degree to which the information system (IS) is supposed to be reliable with the potential users’ existing beliefs and earlier practices [2]. Teo, Lim et al. [4] have stated that compatibility of the IT has a strong impact on e-HRM implementation. However, some scholars have indicated that compatibility does not affect IT adoption [6-8].

‘Perceived complexity’ determinant is the degree to which an IS is supposed to be comparatively problematic to



understand and use [4]. Al-Dmour [9] has found that complexity is a significant determinant for e-HRM implementation in Jordan. Conversely, Bian [5] has revealed that perceived complexity is an insignificant determinant for e-HRM adoption decision in china's firms.

Researchers reported that IT is quickly adopted and implemented in an organisation if the perceived cost is less [10]. Ghobakhloo, Arias-Aranda [11] have revealed that cost is the only cause for non-adoption of e-SCM (electronic supply chain management). In contrast, the cost of EC (e-Commerce) adoption does not appear as a vital player in the adoption of EC by Korean SMEs [12].

The 'top management support' determinant is defined as the willingness of the senior executives of an organisation to allocate necessary resources for successful adoption of IT/IS project [2]. Scholars have reported that top management support is only important determinants among organisational determinants for adoption and diffusion of e-HRM [4]. On the contrary, some researchers argued that top management support is an insignificant determinant for e-HRM implementation [13].

The determinant 'organisational culture' comprises shared attitudes, customs and norms, beliefs and values [9]. Many scholars have highlighted the variable as a significant determinant for IS /IT adoption [14, 15]. In contrast with the said studies, organisational culture may be less of a vital differentiator between non-adopters and adopters of a new IS [16].

In decision-making, centralisation approach may diminish conflict among organisational units and foster IT adoption process [9]. Based on an extensive survey of North American firms, Ranganathan, Teo [17] have exposed that centralisation is a significant drivers of Web technology integration in the SCM function. On the other hand, Al-Dmour [9] has revealed that centralisation is not a vital determinant for e-HRM implementation in Jordanian firms.

'Industry pressure' determinant denotes to the degree of force that a firm senses from competitors within the industry [4]. Ghobakhloo, Arias-Aranda [11] have suggested that industry pressure is a cause of IT strategies in organisations. Some have researchers confront its significance in ITs adoption [4, 8].

'IT vendor' determinant denotes to suppliers of IT allied products and services to other companies [6]. Al-Dmour has [9] claimed that availability of IT suppliers and their support is the most significant determinant for adopting e-HRM. In contrary, Ahmadi et al. [6] did not found adequate proof that vendor support was important determinant for adopting IS applications in Malaysian hospitals.

The determinant 'government support' for IT adoption includes rules and regulations, tax incentives, national IT infrastructure, IT training and workshops and other activities [7]. Al-Dmour [9] has reported that government regulation and policy is a vital predictor to adopt e-HRM. However, some scholars have argued that the influence of government support for advanced information technology is insignificant [7, 19].

### III. CONCEPTUAL FRAMEWORK

A proposed conceptual model, based on TOE framework, of e-HRM adoption in organisations of Bangladesh is depicted in Fig.1. According to the TOE model, the potential influencing determinants are divided into organisational context, technological context, and environmental context. The conceptual model comprises of ten selected independent variables such as relative advantage [4, 5], perceived compatibility [6, 7], perceived complexity [4, 5], perceived cost [8, 11], top management support [6, 13], organisational culture [14, 15], centralisation [9, 17], industry pressure [5, 11], IT vendor support [6, 18], and Government support [7, 19] along with a dependent variable- e-HRM adoption.

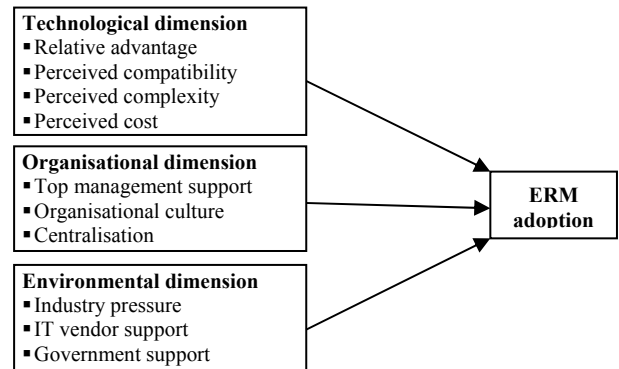


Fig. 1. Conceptual Framework of E-HRM Adoption

Therefore, the following hypotheses were described based on proposed research model:

- H1: Relative advantage significantly predicted e-HRM adoption.
- H2: Perceived compatibility significantly predicted e-HRM adoption.
- H3: Perceived complexity significantly predicted e-HRM adoption.
- H4: Perceived cost significantly predicted e-HRM adoption.
- H5: Top management support significantly predicted e-HRM adoption.
- H6: Organisational culture significantly predicted e-HRM adoption.
- H7: Centralisation significantly predicted e-HRM adoption.
- H8: Industry pressure significantly predicted e-HRM adoption.
- H9: IT vendor support significantly predicted e-HRM adoption.
- H10: Government support significantly predicted e-HRM adoption.

### IV. METHODOLOGY OF THE STUDY

Four hundred questionnaires were sent to IT experts and HR managers of sample organisations in Bangladesh. The valid questionnaires were 320, and the response rate was 80.0% applying non-probability sampling technique. For data collection, a pre-tested and close-ended questionnaire was used adapting seven-point Likert scale. The survey period was 3-months (January 2014 – March 2014). To analyse the collected data, descriptive statistics and Structural Equation Modeling (SEM) were used as statistical and data science tools. SEM analysis was employed with the 2-step methodology suggested by Hair, Black [20]. Initially, each latent variable was modeled as a separate measurement model. Finally, a structural model was analysed.

### V. DATA ANALYSIS AND FINDINGS

#### A. Sample Characteristics

A total sample of 48 firms from different sectors is considered in this paper. A 25% of these were from

education sector. The numbers of firms from the banking sector were 25.8%. However, 27.4% are manufacturing firms. The remaining 5.5% and 16.3% of the total firms were from logistics, transportation and telecommunication sector respectively. Refer to organisation size; there were 14 firms (29.17%) which have staff not more than 500. The quantity of companies with more than 500 employees is 70.83% (34 firms).

### B. Validity and Reliability Analysis

Two of the most widely accepted forms of validity are discriminant and convergent validity. In table I, Average shared squared variance (ASV) and maximum shared squared variance (MSV) for all the dimensions of the constructs of this study is less than average variance extracted (AVE). Hence, this provides enough evidence that all of the 11 constructs (both independent and dependent variables) used in this paper are distinct and thus discriminant validity is established [20].

TABLE I. CONSTRUCT VALIDITY

Construct	CR	AVE	MSV	ASV
Relative advantage	0.871	0.693	0.342	0.162
Perceived compatibility	0.873	0.634	0.507	0.253
Perceived complexity	0.877	0.640	0.487	0.273
Perceived cost	0.909	0.715	0.398	0.143
Top management support	0.900	0.643	0.315	0.179
Organisational culture	0.875	0.690	0.238	0.099
Centralisation	0.917	0.637	0.429	0.490
Industry pressure	0.878	0.645	0.296	0.158
IT vendor support	0.897	0.685	0.274	0.157
Government support	0.884	0.561	0.472	0.390
e-HRM adoption	0.923	0.635	0.469	0.404

Again, the composite reliability (CR) for all the dimensions of the constructs of this study is greater than AVE. Besides, the AVE for all the dimensions is greater than 0.5. Hence there is enough evidence that all the 10 constructs used in this study exhibit convergent validity. In addition to this, CR of all the dimensions in the measurement model is greater than 0.7 while factor loadings of all the items are above the cut-off point of 0.5. This provides enough confirmation of uni-dimensionality of the constructs of interest and reliability of the measures used in this paper [20].

### C. Results

TABLE II. SUMMARY OF MEASUREMENT MODEL VALIDATION OF LATENT CONSTRUCTS

Variables	CFI	RMSEA	CMIN/DF
Relative advantage	0.995	0.069	1.517
Perceived compatibility	1.000	0.000	0.701
Perceived complexity	1.000	0.010	1.012
Perceived cost	0.999	0.036	1.144
Top management support	0.997	0.042	1.191
Organisational culture	1.000	0.013	1.018
Centralisation	0.993	0.056	1.805
Industry pressure	1.000	0.021	1.049
IT vendor support	0.994	0.045	1.735
Government support	0.970	0.00	0.270
e-HRM adoption	0.991	0.058	1.376

The Table II shows the summary of results of measurement model validation of 11 constructs. Based on acceptable model fit standard, the CFI (Comparative Fit Index) value of all construct is greater than 0.9. The RMSEA

(Root Mean Square Error of Approximation) value of all construct is lower than 0.08. For Ratio Chi-Square/df, the desired level as low as 3 also achieved for all 11 constructs. Generally, these statistics have given evidence of a reasonably good fit of data [20].

The structural model shows the association between 10 independent variables and the dependent variable- e-HRM adoption. Based on the results of the SEM fit indices, the model presented an accepted fit (Table III).

TABLE III. MODEL FIT SUMMARY OF STRUCTURAL MODEL

	Observed Value	Acceptable Fit Standard
<i>Statistical Test:</i>		
CMIN (Chi-Square)	1694.879	
DF	1206	
CMIN/DF	1.405	Less than 3 and p < 0.01
<i>Fit Indices:</i>		
CFI	0.901	0.90 or larger
RMSEA	0.061	Less than 0.08

Among the 10 potential determinants, it was observed that there were significant relationship between 7 determinants and e-HRM adoption (Table IV). These 7 variables are perceived compatibility, perceived cost, top management support, organisational culture, centralisation, government support, and IT vendor support. So, 7 hypotheses were accepted among 10 hypotheses on the predictors of e-HRM adoption.

TABLE IV. SUMMARY OF STANDARDISED REGRESSION ANALYSIS

Relationship	Estimates	Decision
e-HRM adoption ← Relative advantage	0.245	Rejected H1
e-HRM adoption ← Perceived compatibility	0.062*	Accepted H2
e-HRM adoption ← Perceived complexity	0.103*	Rejected H3
e-HRM adoption ← Perceived cost	-0.166***	Accepted H4
e-HRM adoption ← Top management support	0.112***	Accepted H5
e-HRM adoption ← Organisational culture	0.162**	Accepted H6
e-HRM adoption ← Centralisation	0.042*	Accepted H7
e-HRM adoption ← Industry pressure	0.266	Rejected H8
e-HRM adoption ← IT vendor support	.0678**	Accepted H9
e-HRM adoption ← Government support	0.241	Accepted H10

\*P < 0.05 level, \*\*P < 0.01 level, \*\*\*P < 0.001 level of Significance

## VI. DISCUSSIONS

The results of the standardised regression analysis demonstrate that five variables – perceived compatibility, perceived cost, organisational culture, top management support, centralisation, IT vendor support, and government support, are significant variables that inducing e-HRM adoption in organisations of Bangladesh.

*Relative advantage* – The result shows that e-HRM adoption is not influenced by relative advantage. A possible explanation could be that organisations have realised the benefits of e-HRM, but there are others issues such as financial and infrastructural lacking that hinders to adopt the system. This result supports the study [5, 13] while rejects findings of [4, 9]. Hence, hypothesis 1 is not supported.

*Perceived compatibility* – It was found to have impact on management decision to adopt e-HRM. So, for strategic HRM practice, it requires the e-HRM to be compatible with the existing systems whinin the firms. This result complies

with state-of-the-art [4, 5, 11]. Hence, hypothesis 2 is supported.

*Perceived complexity* – Perceived complexity of e-HRM was not revealed to be a significant determinant for e-HRM adoption decision. A possible reason would be that practice with other systems available in the organisation may decrease the perceived complexity of e-HRM. The results are congruent with the past researches of Teo, Lim et al. [4] and Bian [5]. Therefore, hypothesis 3 is not supported.

*Perceived cost* – Perceived cost is identified as a significant determinant inducing the decision to adopt e-HRM. This result is consistent with Ghobakhloo, Arias-Aranda [12]. Hypothesis 4 is thus supported.

*Top management support* – This study finds that senior executives support is vital to overcome possible internal resistance to the adoption of e-HRM, which is also supported by [1, 4]. Thus hypothesis 5 is supported.

*Organisational culture* – In this study, organisational culture is the significant determinant for e-HRM adoption. This indicates that organisations that have strong organisational culture are more likely to adopt e-HRM. This result supports the study [23, 24] while rejects findings of [25]. Thus, hypothesis 6 is supported.

*Centralisation*– Centralisation is also identified as a significant determinant inducing the decision to adopt e-HRM. This result is consistent with earlier studies [9, 14]. Hypothesis 7 is thus supported.

*Industry pressure* –It was not revealed to be a significant determinant inducing the adoption of e-HRM that is similar to the findings of past studies [7, 15]. Thus, hypothesis 8 is not supported.

*IT vendor support* – It is identified as a significant determinant inducing the decision to adopt e-HRM. This finding is consistent with Al-Dmour [9] and Sophonthummapharn [18]. Hypothesis 9 is thus supported.

*Government support* – It is identified significant as a determinant inducing the decision to adopt e-HRM. The result is similar to Ahmadi, Nilashi [6] and Al-Dmour [9]. The result of the present study confronts the past studies [7, 19]. Hence, hypothesis 9 is supported.

## VII. CONCLUSION

The findings of this study suggested that perceived compatibility, perceived cost, top management support, organisational culture, centralisation, IT vendor support, and government support are the significant determinants to the adoption of e-HRM. However, the findings of this study also suggested that relative advantage, perceived complexity and industry pressure do not have any impact on the organisational adoption of e-HRM. The sample size of the study was chosen only 320. It is agreed that the bigger the sample is, the more representative the results are. We choose ten determinants to examine the decision of e-HRM adoption. The findings will be helping the HR managers to take decision on e-HRM adoption. In future research, researchers may incorporate other potential determinants that may affect the decision of e-HRM adoption.

## REFERENCES

- [1] Masum, A.K.M., Adoption Factors of Electronic Human Resource Management (e-HRM) in Banking Industry of Bangladesh. *Journal of Social Sciences*, 2015. 11(1): p. 1-14.
- [2] Masum, A.K. M., Kabir, M.J., and Chowdhury, M.M. (2015). Determinants that Influencing the Adoption of E-HRM: An Empirical Study on Bangladesh. *Asian Social Science*, 11(21), 117-124.
- [3] Tornatzky, L.G. and M. Fleischer, *Processes of technological innovation*. 1990, Lexington, Massachusetts: Lexington Books.
- [4] Teo, T.S., G.S. Lim, and S.A. Fedric, The adoption and diffusion of human resources information systems in Singapore. *Asia Pacific Journal of Human Resources*, 2007. 45(1): p. 44-62.
- [5] Bian, L., An Empirical Study on Factors that Influencing the Adoption of Electronic Human Resource Management (E-HRM) Among Firms in Northeast of China. 2012, University of Malaya.
- [6] Ahmadi, H., M. Nilashi, and O. Ibrahim, Organizational decision to adopt hospital information system: An empirical investigation in the case of Malaysian public hospitals. *International journal of medical informatics*, 2015. 84(3): p. 166-188.
- [7] Oliveira, T., M. Thomas, and M. Espadanal, Assessing the determinants of cloud computing adoption: An analysis of the manufacturing and services sectors. *Information & Management*, 2014. 51(5): p. 497-510.
- [8] Rahayu, R. and J. Day, Determinant Factors of E-commerce Adoption by SMEs in Developing Country: Evidence from Indonesia. *Procedia-Social and Behavioral Sciences*, 2015. 195: p. 142-150.
- [9] Al-Dmour, R.H., An integration model for identifying the determinants of the adoption and implementation level of HRIS applications and Its effectiveness in business organisations in Jordan in *Computer Science*. 2014, Brunel University London: UK.
- [10] Premkumar, G. and M. Roberts, Adoption of new information technologies in rural small businesses. *Omega*, 1999. 27(4): p. 467-484.
- [11] Ghobakhloo, M., D. Arias-Aranda, and J. Benitez-Amado, Adoption of e-commerce applications in SMEs. *Industrial Management & Data Systems*, 2011. 111(8): p. 1238-1269.
- [12] Jeon, B.N., K.S. Han, and M.J. Lee, Determining factors for the adoption of e-business: the case of SMEs in Korea. *Applied Economics*, 2006. 38(16): p. 1905-1916.
- [13] Al-Mobaideen, H., S. Allahawiah, and E. Basoni, Factors Influencing the Successful Adoption of Human Resource Information System: The Content of Aqaba Special Economic Zone Authority. *Intelligent Information Management*, 2013. 5(1): p. 1-9.
- [14] Panayotopoulou, L., M. Vakola, and E. Galanaki, E-HR adoption and the role of HRM: evidence from Greece. *Personnel Review*, 2007. 36(2): p. 277-294.
- [15] Jackson, S., Organizational culture and information systems adoption: A three-perspective approach. *Information and Organization*, 2011. 21(2): p. 57-83.
- [16] Teo, T.S., S. Lin, and K.-h. Lai, Adopters and non-adopters of e-procurement in Singapore: An empirical study. *Omega*, 2009. 37(5): p. 972-987.
- [17] Ranganathan, C., T.S. Teo, and J. Dhaliwal, Web-enabled supply chain management: Key antecedents and performance impacts. *International Journal of Information Management*, 2011. 31(6): p. 533-545.
- [18] Sophonthummapharn, K., The adoption of techno-relationship innovations: A framework for electronic customer relationship management. *Marketing Intelligence & Planning*, 2009. 27(3): p. 380-412.
- [19] Lian, J.-W., D.C. Yen, and Y.-T. Wang, An exploratory study to understand the critical factors affecting the decision to adopt cloud computing in Taiwan hospital. *International Journal of Information Management*, 2014. 34(1): p. 28-36.
- [20] Hair, J.F., W.C. Black, and B.J. Babin, *Multivariate Data Analysis: A Global Perspective*. 2010, London: Pearson Education.

# *Design of a low-cost lighting system for the rural areas of Bangladesh*

Mohammad Salman Yasin

Department of Naval Architecture and Marine Engineering,  
BUET, Dhaka, Bangladesh  
Email- ysalmancgt@gmail.com

Tanmoy Biswas

Department of Naval Architecture and Marine Engineering  
BUET, Dhaka, Bangladesh  
Email- tanmoy.biswas18@gmail.com

Mohammad Sharier Islam

Department of Naval Architecture and Marine Engineering  
BUET, Dhaka, Bangladesh  
Email-tonmoyahmed253@gmail.com

M. Saidur Rahman

Department of Electrical and Electronic Engineering  
BUET, Dhaka, Bangladesh  
Email-said.buet10@gmail.com

**Abstract**—This study was conducted to find a solution to solve the problem of deprivation of light present in the rural society of Bangladesh. More than 50percent of our rural population are deprived of electricity. This in turns results in absence of light in houses. A device was designed using bottles, Light Emitting Diode, solar panel and battery for an alternative lighting system. This device is not so costly and can be reproduced very easily. Different variations of this device was tested using a light meter (Model-LX 1102). A brief overview of this newly proposed lighting system is discussed in the study.

**Keywords**—*Light Emitting Diode; Solar energy; Rural society; Lighting;*

## I. INTRODUCTION

Bangladesh has a largely growing population and economic growth in South Asian subcontinent. There is a serious demand-supply gap of electricity in our country. Affordable energy for all has always been out of reach. Even today, Bangladesh is unable to provide ample production of energy. Meeting with the demand and supply of energy has been a hefty task for any government. The lighting is not taken seriously in many industrial countries and many developing countries. So, many don't even fathom passing their nights without proper lighting at flick of a switch. About 40% of the people in rural areas had access to the electricity in 2010[1]. Solar energy can be used to alleviate this problem. However, the usage of solar panel has its own demerits. The panel alone costs about 60Taka per watt capacity. Also the efficiency of locally available solar panels in Bangladesh is about 40 to 60 percent. Hence, even for the need of small amount of solar energy, installation becomes a problem. Thus, our research aims to decrease the load of energy necessary for lighting a household by designing an alternative lighting system.

Bangladesh is bestowed with plentiful supply of renewable energy sources. Bangladesh receives average daily solar radiation of 4-6.5 KWh/m<sup>2</sup> [2]. The average bright sunshine duration in Bangladesh in the dry season is about 7.6 hours a day and in the monsoon season it is about 4.6

hours [3]. Thus a system using LED, Photovoltaic cell and the refractory property of water, an alternative lighting system was designed. Using a light meter (Model- LX-1102) the light density at various distances were measured. Although the system generates a small amount of light, we hope to dramatically affect the lives of rural families who live with the deprivation of light [4].

## II. EXPERIMENTAL MODEL

Nine soda bottles (clear, plastic, 3 two liter bottles, 3 one liter bottles, 3 half liter bottles) were cleaned with cold water. The outside of the bottle were wiped. Then the bottles were filled with water. An amount 15grams of bleach were added to each bottle for sterilizing the water. These 15 grams of bleach were added not only to sterilize the bottles but also so that algae doesn't form within the bottle over the passage of time. The formation of algae would hinder the proper refraction of light from the bottle.

A standard nail and hammer was used to make a hole into the cap of the bottle. Then three sets of following LED were prepared: one 1W LED, two 1W LED and four 0.25W LED lights. The LED's were immersed into the water and the wire was brought out by the hole made before. The side of the hole were insulated using locally available adhesive. The prototypes were connected to a 3.6V 5000mA-h battery which was charged using a 5W solar panel. A switch was inserted within the circuit to control the light.

The light was measured using a light meter (Model- LX-1102) at various distances. All of the lights in the area or in surrounding area were turned off. The switch to control the LED turned on and the amount of Lux indicated on the light meter was recorded. Each design were tested for the comparison of data and the improvement of design.

## III. ARRAY DESIGN

In this study, the bottles can be arranged in a series connected grid. In this case the power necessary will be supplied by the use of a solar panel. The minimum capacity of the battery will need to be determined using the following

equation:

$$\text{Capacity} = \frac{p * t}{v} * 1000 \quad (1)$$

Where, p = Total power necessary for the array (Watt)

t = Time duration for giving light (Hour)

v = Voltage difference of the LED (Volt)

By calculating the total power and battery capacity, we can determine the necessary solar panel for our project. Power produced by any solar panel per day can be determined by the following equation:

$$\text{Minimum power of solar panel} = \frac{T * R}{1000} \quad (2)$$

Where, T = Average sunshine time (Hour)

R = Panel rating (Watt)

#### IV. RESULT

From the experiment, the light intensities regarding various distances were collected and stored for different designs. For this different sizes of bottles were used. These are shown as follows.

TABLE I. MEASUREMENT OF LIGHT INTENSITY WITHOUT BOTTLE

Distance (m)	Measured light without bottle for various sources (Lux)		
	One 1W LED	Two 1W LED	Four 0.25W LED
0.2	102.4	144	134.97
0.5	24.42	29.68	27.37
1.0	6.55	8.47	8.66
1.5	2.97	4.03	4.1
2.0	1.53	2.41	2.4

The light intensity of various LED for various vertical distances are shown in table 1. From Table 1, it can be observed that with the increase of distances from the bottle, the intensity of light drops.

The light density in flux at different vertical distances are shown one 1W LED configuration is shown in figure 1. According to figure 1, for 0.2m away from the bottle, the measured light intensity is 138.5, 48.3 and 32 Lux for the bottles of 0.5L, 1L and 2L respectively. And for 2m away from the bottle, the measured light intensity is 3.68, 0.33 and 0.98 Lux for the bottles of 0.5L, 1L and 2L respectively.

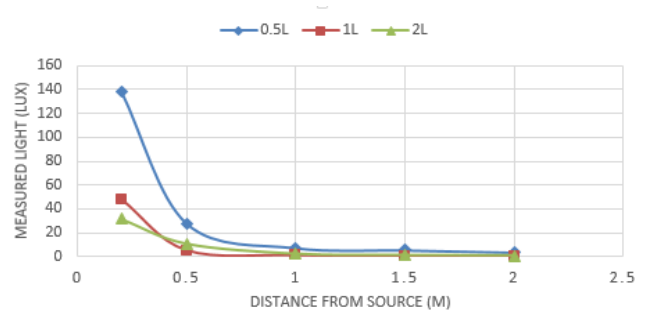


Fig.1 Measurement of light intensity for one 1W LED

The light density in flux at different vertical distances are shown two 1W LED configuration is shown in figure 2. According to figure 2, for 0.2m away from the bottle, the measured light intensity is 115.8, 60.88 and 55 Lux for the bottles of 0.5L, 1L and 2L respectively. And for 0.2m away from the bottle, the measured light intensity is 1.90, 0.68 and 0.62 Lux for the bottles of 0.5L, 1L and 2L respectively.

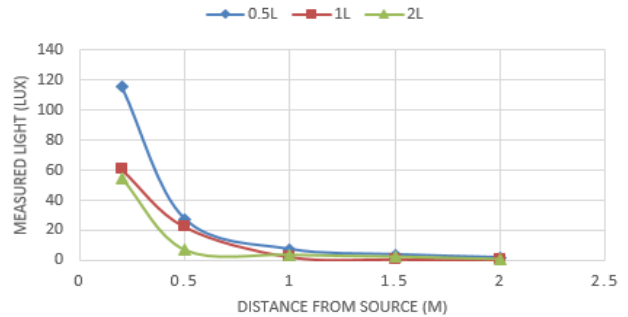


Fig.2 Measurement of light intensity for two 1W LED

The light density in flux at different vertical distances are shown four 0.25W LED configuration is shown in figure 3. According to figure 3, for 0.2m away from the bottle, the measured light intensity is 119.30, 58.85 and 46.5 Lux for the bottles of 0.5L, 1L and 2L respectively. And for 2m away from the bottle, the measured light intensity is 0.39, 0.36 and 0.22 Lux for the bottles of 0.5L, 1L and 2L respectively.

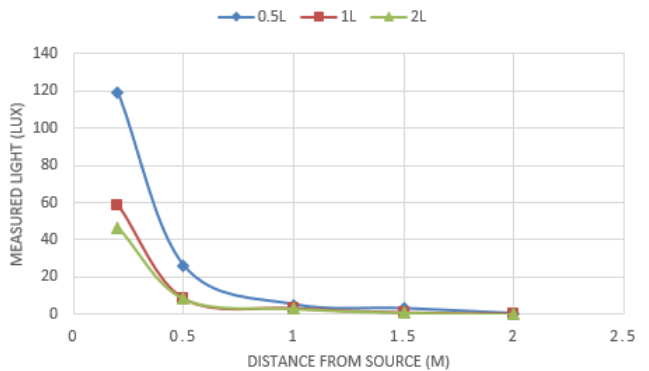


Fig.3 Measurement of light intensity for four 0.25W LED

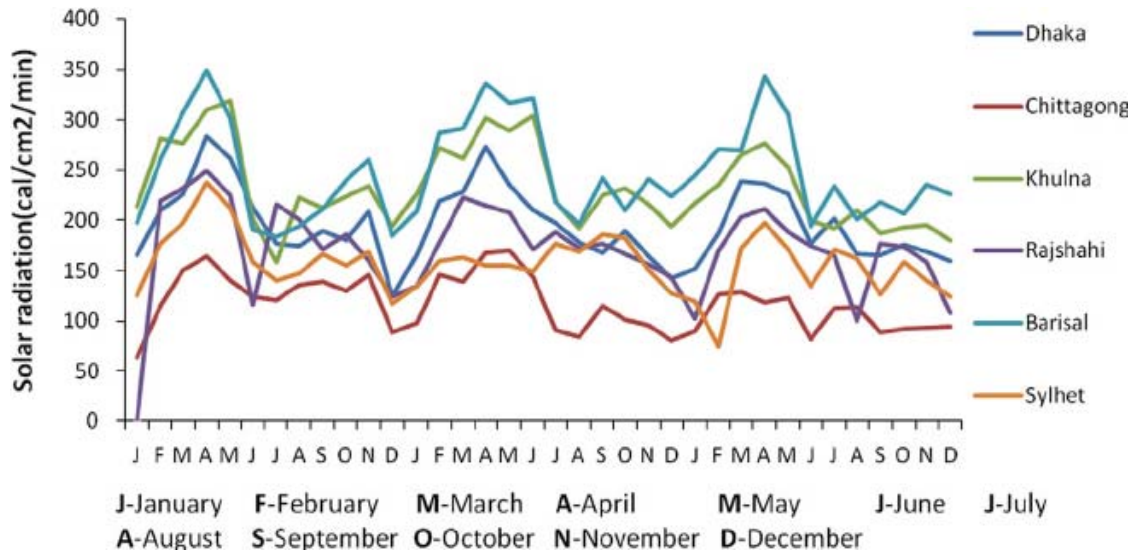


Fig.4 Solar radiation in various districts of Bangladesh [6]

The light density in flux at different vertical distances are shown above for four 0.25W LED. It can be seen that without bottle the measured lux amount is higher than with the bottle.

TABLE II. MEASUREMENT OF RADIAL DISTANCE FOR DIFFERENT LIGHT AND BOTTLE CONFIGURATION

Light Source	Measured highest distance for various bottles (cm)		
	0.5L	1L	2L
1W(1)	305	378	430
1W(2)	221	248	270
0.25W(4)	183	190	213

For different configuration of LED and bottles, the highest radial distance where the lux meter showed the value of 0.1Lux, was determined. From figure 1, 2 and 3, it can be determined that the intensity of light decreases with the increase of distance. It suggests that the bigger the bottle, the more area will be illuminated.

## V. ANALYSIS

The sun emits at a rate of  $3.8 \times 10^{23}$  KW per second and the solar radiation reaching the earth surface in a year is approximate to 3400000EJ (Exa-Joule) which is 7500 times worlds total annual primary energy consumption of 450EJ.[5] Bangladesh is endowed with plentiful supply of renewable source of energy. The average solar radiation in different parts of the country is shown in figure 4.

We have experimented nine different variation of light sources. From the data we can see that due to light diffraction, the intensity of light reduces for same distance. However, the energy of light is dissipated radially. As seen from the results, the use of smaller bottle and one high-powered LED can give the best solution to our problem.

## VI. CONCLUSION

More than 50% of the rural areas of Bangladesh are not connected to the national electricity grid. Their lives almost come to a standstill after sunset due to lack of energy. Our paper stands to use the abundant resources of solar energy of Bangladesh for illuminating the rural areas. This may not seem much, in the sense that much light intensity is not generated. But we hope that this would provide a significant change in the lifestyle of people where the electricity is yet to reach. To alleviate the problem of lighting, we have devised a system for the illumination of rural areas of Bangladesh. For our design, not much investment is necessary as parts used in our device comes from re-usable products. It can also be easily replaced. For our study, we suggest this system to be implemented in a medium scale. However, further research is required to optimize among costs, power and light intensity of the developed system.

## ACKNOWLEDGMENT

The authors would like to thank Dr. M.A.Basith for his support and the light meter.

## REFERENCES

- [1] (2016)Access to electricity(% of population)Data can be accessed at: <http://data.worldbank.org/indicator/EG.ELC.ACCS.ZS>
- [2] A.K.M.S.Islam, "Effective renewable energy in Bangladesh", in Renewable energy, vol 31, pp 677-688,2006.
- [3] S.H.Khan, T. Rahman, S. Hossain, "A Brief Study of the prospect of Solar energy in generation of electricity in Bangladesh." in Cyber Journals: Multidisciplinary Journals in Science and Technology, Journal of Selected Areas in Renewable and Sustainable Energy (JRSE), June Edition.
- [4] M.Alam, S. Mwakasonda, A. Rahman, E. Rovere, A. Simoes, H. Winkler, "Access and affordability of electricity in developing countries" in World Development, vol 39, pp 1037-1050, June 2011.

[5] Y.Kuang, Y. Zhang, B. Zhou, "A review of renewable energy utilization in island" in *Renewable and Sustainable Energy Reviews*, vol 59, pp 504–513, June 2016.

[6] F.Ahmed, Al-amin, A.Quasem, Hasanuzzaman, S. Rahman, "Alternative energy resources in Bangladesh and future prospects" in *Renewable and Sustainable Energy Reviews*, vol 25, pp 698–707, September 2016.

# Logical Clipper and De-clipper Technique to Reduce PAPR from OFDM Signal

Md. Salim Raza  
Department of EEE  
Hamdard University  
Bangladesh  
salim\_aece04@yahoo.com

Md. Mhedi Hasan  
Department of ICT  
Comilla University  
Bangladesh  
mhedi.iu@gmail.com

Md. Obidul Islam  
Department of EEE  
Hamdard University  
Bangladesh  
obidulapece@gmail.com

Md. Shahjahan Ali  
Department of APECE  
Islamic University  
Bangladesh  
jahanshah.iu@gmail.com

**Abstract**—Orthogonal frequency-division multiplexing (OFDM) is the most effective technique for high speed wireless communication systems. The key challenge of OFDM based transceiver is its large peak to average power ratio (PAPR) due to non-linearity effects of power amplifier at final stage of OFDM transmitter. In this work performance of OFDM system using logical clipper and de-clipper in the OFDM transmitter and receiver respectively has been studied. In the proposed method the clipped portion of the signal is transmitted as side information which is subsequently used by the receiver to reproduce the original signal. The whole system was simulated in MATLAB environment considering AWGN channel. It is observed that the proposed system can significantly reduce PAPR of OFDM signal.

**Keywords**—orthogonal frequency division multiplexing (OFDM); logical clipper; logical declipper; PAPR; complementary cumulative distribution function (CCDF).

## I. INTRODUCTION

For fourth and fifth generation (4G and 5G) wireless communication systems orthogonal frequency division multiplexing (OFDM) is one of the most attractive techniques [1-2]. It effectively combats the multipath fading channel, improves the bandwidth efficiency and increases system capacity to provide reliable transmission [2-3]. One inherent problem of OFDM is its large peak to average power ratio (PAPR) due to non-linearity of power amplifier, phase noise problems of local oscillator, frequency offset due to Doppler shift or difference between transmitter and receiver. This peak to average power (PAP) ratio can distort the signal if the transmitter contains nonlinear components such as power amplifiers (PAs) [4]. Spectral spreading, inter modulation and changing of signal constellation of the OFDM symbols are some effects of the nonlinearity. The PAPR in dB of OFDM symbol is defined as a ratio of the peak power and average power of OFDM signals [5]:

$$PAPR(dB) = 10 \log_{10} \frac{P_{peak}}{P_{av}} = 10 \log_{10} \frac{\max[|x_n|^2]}{E[|x_n|^2]} \quad (1)$$

where  $P_{peak}$  is the output peak power of OFDM signal and  $P_{av}$  is the average power of the signal.

In this research, we have used logical clipping and de-clipping method to reduce PAPR from OFDM signal.

## II. METHODOLOGY

### A. Clipping

The basic functional block diagram of clipping technique is shown in Fig. 1. Clipping is the simplest way to reduce the peak signal to the desired level [6-7]. But its main drawback is self-interference generated by clipping operation that distorts signal amplitude.

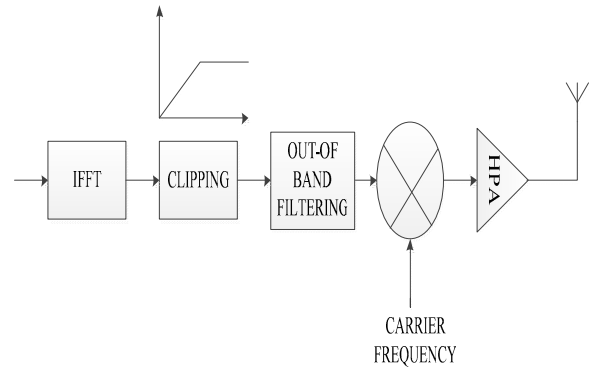


Fig. 1. OFDM transmitter including clipping scheme.

Due to this self-interference, clipping gives rise to re-growth of the high frequency components as a result spectral efficiency can be reduced. For overcoming such problems with clipping operation, several schemes have been developed. One such technique is the utilization of filtering to reduce or remove out-of-band radiation but it can also cause peak re-growth. Another technique is the iterative clipping and filtering that can reduce PAPR to the desired level, but this increases computational complexity [2, 7-9]. Peak windowing is a method to reduce the peak value by multiplying the correcting function by the original OFDM signal [7-8]. There



are several schemes for reducing problems at the receiver, which are inherently generated by clipping with filtering [10].

In the present study peak signals will be removed by signal processing steps only and no filter will be utilized.

### B. Proposed Logical Clipper

The model of the proposed Logical Clipper is shown in Fig. 2. This unit is placed after final stage of parallel to serial (P/S) converter of OFDM transmitter. P/S converter has added N discrete time OFDM signal after successful operation of IFFT/IDFT and cyclic prefix (CP) operation (N is the number of IFFT/IDFT points in that transmitter). As a result, it delivers discrete time OFDM signal with high PAPR. In this proposed technique, every N point discrete time domain OFDM signal is considered as a single segment that may pass through the first step of Logical Clipper known as comparator. This comparator will compare the amplitude of every segment of OFDM signal with the threshold value (VT). Where VT to be equal to the average value of OFDM signal. If amplitude of the signal is greater than VT then position & over threshold value counter (POTVC) will count the time domain position and over threshold value for every segment of OFDM signal. With the help of POTVC, the position & over threshold value selector (POTVS) will select the fixed number (two in this case) of time domain position corresponding over threshold value of every segment for clipping operation. After that, the

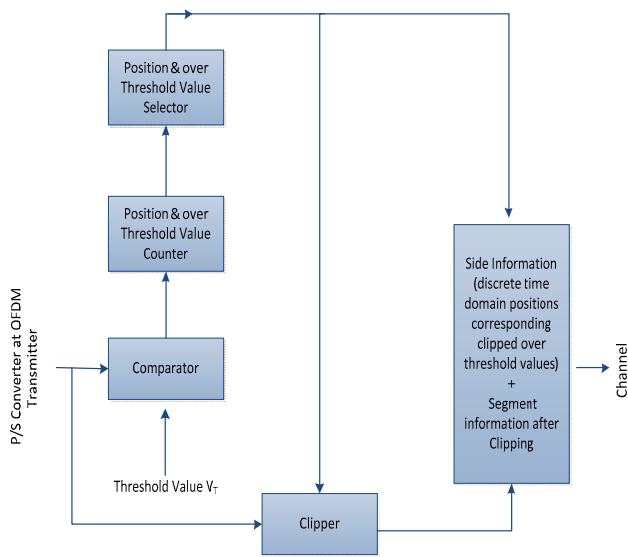


Fig. 2. Model of Logical Clipper at OFDM Transmitter.

clipper clips twice of the over threshold value from every segment of OFDM signal at selected position. Finally this portion of the signal is inserted as side information at the front of the corresponding

segment. In this technique length of every segment increases by the factor two because POTVS select only two positions.

Here goes a brief description of the main technical function of the logical clipper. For simplicity let us consider the case of single segment and also consider the value of  $V_T$  is  $V_x$ , the length of segment is L, time domain positions  $P_n$ ,  $P_{n+1}$  and  $P_{n+2}$  are containing the values  $V_x + 3\Delta V_x$ ,  $V_x + 2\Delta V_x$  and  $V_x + \Delta V_x$  respectively and rest of the position of that segment contains the values lower than  $V_x$ . Where n is a positive integer,  $0 \leq [n \pm \text{positive integer}] \leq L$  and  $\Delta V_x$  represents smallest unit value for the corresponding positions.

Therefore, POTVS will select the position  $P_n$  and  $P_{n+1}$  with over threshold value of  $3\Delta V_x$  ( $V_x + 3\Delta V_x - V_x$ ) and  $2\Delta V_x$  ( $V_x + 2\Delta V_x - V_x$ ) respectively. Finally, clipper clips the values  $2 \times 3\Delta V_x$  and  $2 \times 2\Delta V_x$  from corresponding selected positions  $P_n$  and  $P_{n+1}$  respectively. After clipping operation, the positions  $P_n$  and  $P_{n+1}$  of the segment contain the values  $V_x - 3\Delta V_x$  ( $V_x + 3\Delta V_x - 2 \times 3\Delta V_x$ ) and  $V_x - 2\Delta V_x$  ( $V_x + 2\Delta V_x - 2 \times 2\Delta V_x$ ) respectively and these positions are put in front of that segment. So segment length will be L+2.

### C. Proposed Logical De-clipper

The first block of the receiver for the proposed method is Logical De-clipper (Fig. 3.). Its working principle is just the reverse of Logical Clipper in OFDM transmitter. The first stage of Logical De-clipper, called position signal collector (PSC), removes time domain position signals (side information) that were placed in front of every segment at logical clipper in OFDM transmitter. Also PSC stores the side informations and subsequently passes these to Threshold Value Regenerator and Combiner. Clipped over Threshold Value Regenerator (CoTVR) compares VT with the value of every segment at selected position provided by PSC and identify the difference value at selected position. After that it multiplies the difference value by two and regenerate clipped over threshold corresponding time domain position for every segment of OFDM received signal. CoTVR, the final stage of Logical De-clipper (Combiner), adds clipped over threshold with every segment of discrete time OFDM signal at desired position. Thus the process generates original unclipped OFDM signal for further processing in OFDM receiver.

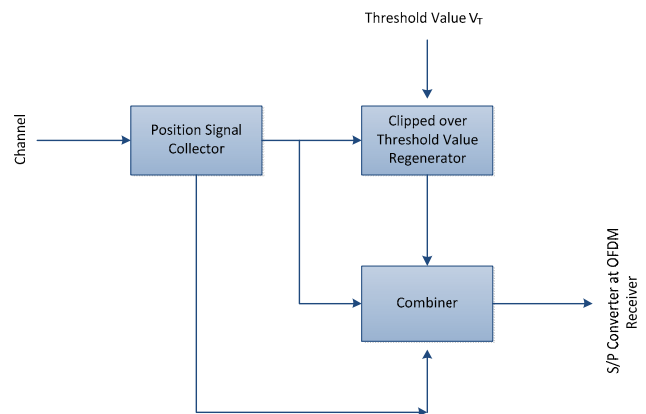


Fig. 3. Model of Logical De-clipper at OFDM Receiver.

### III. SIMULATION RESULT

In this research work, performance of Logical Clipper with OFDM transmitter and De-Clipper with OFDM receiver in reducing PAPR have been studied for different numbers of subcarriers and modulation schemes.

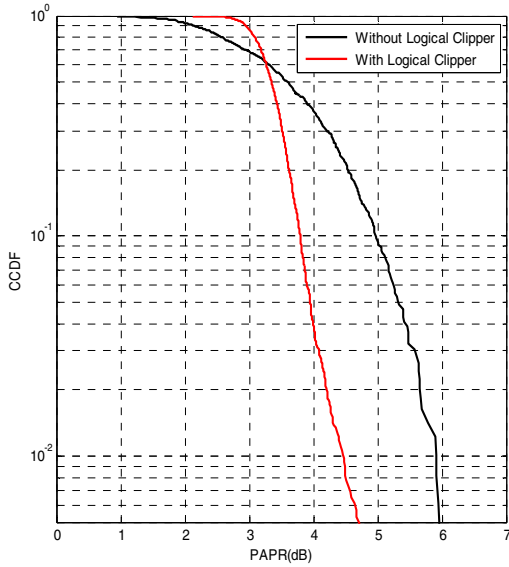


Fig. 4. CCDF Corresponding the PAPR for 64 Subcarriers and 4-QAM modulation scheme.

The whole process was simulated using MATLAB simulator. Here AWGN channel was used taking randomly generated data bits.

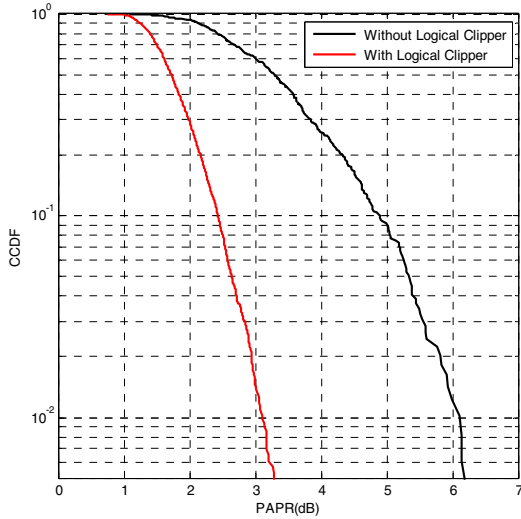


Fig. 5. CCDF Corresponding the PAPR for 32 Subcarriers and 4-QAM modulation scheme.

Fig. 4 shows the plot of complementary cumulative distribution function (CCDF) of PAPR of OFDM signal for 64 subcarrier and 4-QAM modulation scheme. From the figure it was observed that the value of PAPR of OFDM without applying Logical Clipper was 6.0dB and it was reduced by approximately 1.3dB when Logical Clipper was employed in transmitter.

Fig. 5 presents the plot of CCDF of PAPR of OFDM signal for 32 subcarriers and 4-QAM modulation scheme. In this case PAPR of OFDM signal without applying logical clipper was 6.2dB which was seen to reduce by approximately 3 dB after applying logical clipper in the transmitter.

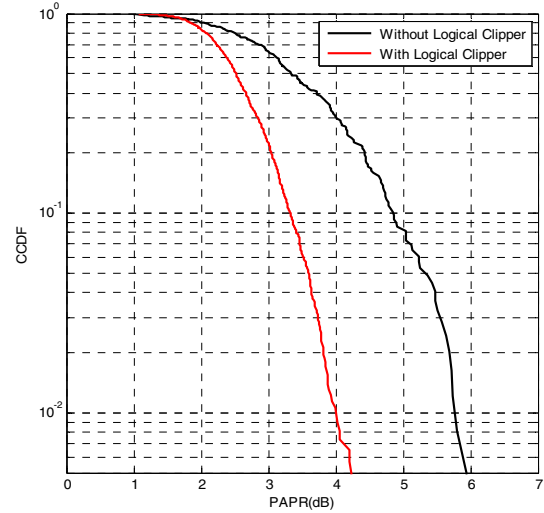


Fig. 6. CCDF Corresponding the PAPR for 64 Subcarriers and 16-QAM modulation scheme.

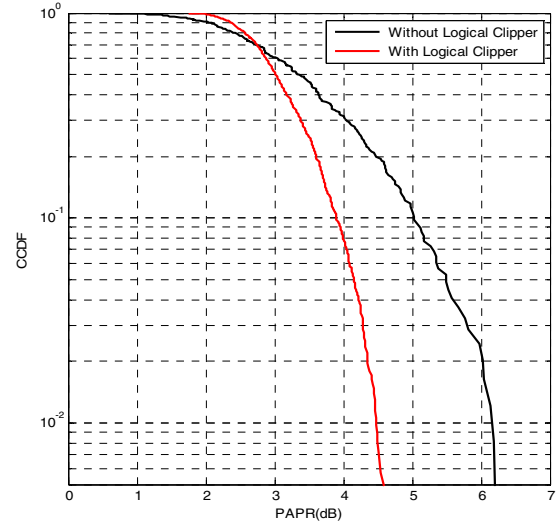


Fig. 7. CCDF Corresponding the PAPR for 32 Subcarriers and 16-QAM modulation scheme.

Fig. 6 shows the same type of plot for 64 subcarriers and 16-QAM modulation scheme. The PAPR of OFDM signal in this case was 5.9 dB without applying of clipper and was seen to reduce by approximately 1.7dB with logical clipper.

Fig. 7 gives the plot of CCDF of PAPR of OFDM signal for 32 subcarriers and 16-QAM modulation scheme. In this case PAPR was 6.2 dB without clipper and that was reduced to 1.6 dB with using clipper.

#### IV. CONCLUSION

In this study a technique named 'logical clipper and de-clipper' was applied to the OFDM system and its effect on the efficiency of OFDM transceiver in reducing PAPR from the signal was observed. The whole process was simulated using MATLAB simulator considering AWGN channel for communication. Performance of the OFDM system was evaluated by determining CCDF of PAPR from OFDM signal using 64 and 32 subcarriers and 4-QAM and 16-QAM modulation schemes respectively. From the obtained results it was seen that the proposed system performs well in reducing PAPR. Highest PAPR reduction was observed for 4-QAM modulation technique with 32 subcarriers.

#### References

- [1] Ramjee Prasad, "OFDM for Wireless Communications Systems", Artech House universal personal communications series, pp 149-179, 2004.
- [2] Md. Salim Raza, Md. Imran Hossain, Md. Khalid Hossain Jewel, Md Shahjahan Ali, " PAPR Reduction of OFDM Signal Using Sequential Phase Sequence SLM Based Transceiver without Side Information" I.J. Wireless and Microwave Technologies,, 1, 34-42, 2015.
- [3] [http://en.wikipedia.org/wiki/Orthogonal\\_frequency\\_division\\_multiplexing](http://en.wikipedia.org/wiki/Orthogonal_frequency_division_multiplexing).
- [4] M. Pauli and H. P. Kuchenbecker, "Minimization of the intermodulation distortion of a nonlinearly amplified OFDM signal", Wireless Pers. Commun., vol. 4, no. 1, pp. 93-101, Jan. 1997.
- [5] X. Wang, T.T. Tjhung, and C.S. Ng, "Reduction of peak-to average power ratio of OFDM system using a companding technique", IEEE Trans. on Broadcaststing, Vol.45, No. 3, pp. 303-307, Sep. 1999.
- [6] X. Li and L. J. Cimini Jr., "Effects of clipping and filtering on the performance of OFDM," IEEE Commun. Lett., vol. 2, no. 5. pp. 131-133, May 1998.
- [7] Wang Yi, Gulinfeng "An Investigation of Peak-to Average Power Reduction in MIMO-OFDM Systems" MSc Thesis, Blekinge Institute of Technology, Sweden, October 2009.
- [8] V. Vijayarangan, DR.(MRS) R. Sukanesh "An overview of techniques for reducing peak to average power ratio and its selection criteria for orthogonal frequency division multiplexing radio systems" Journal of Theoretical and Applied Information Technology, pp 25-36, 2009.
- [9] S. H. Han, J. H. Lee, "An overview of Peak-to-Average-Power Ratio reduction techniques for multi carrier transmission", IEEE Wireless Communication, pp.53-65, April 2005.
- [10] Sroy Abouty, Li Renfa, Zeng Fanzi and Fall Mangone, " A Novel Iterative Clipping and Filtering Technique for PAPR Reduction of OFDM Signals: System Using DCT/IDCT Transform", International Journal of Future Generation Communication and Networking Vol. 6, No. 1, February, 2013.

# Bio Inspired Cyber Security Architecture for Smart Grid

Muhammad Mostafa Amir Faisal

Dept. of Electronic and Telecommunications Engineering  
International Islamic University Chittagong  
Kumira, Chittagong, Bangladesh.

Muhammad Ariful Islam Chowdhury

Dept. of Electronic and Telecommunications Engineering  
International Islamic University Chittagong  
Kumira, Chittagong, Bangladesh.

**Abstract**— Smart grid is an advanced and intelligent form of conventional power grid with high fidelity power-flow control, self-healing, and energy reliability using advance computer and communication technologies. The idea of integrating power systems with complex computer communication has introduced serious cyber security concerns as it requires significant dependence on secured communication infrastructures. Because of the wide nature of smart grid, it is very risky to compromise any component of the grid which may lead to serious damage to the electrical infrastructure, energy theft and unnecessary expenditure. Studying various smart grid security architectures, efficient bio-inspired complete security architecture for smart grid is proposed in this work which can be easily implemented in the smart grid without changing any element of its infrastructure. Bio-inspired cyber security architecture for smart grid is developed with discussion on the core elements of the architecture. The threat detection is tested with simulation using popular KDDDump dataset and real time gas pipe line SCADA data.

**Keywords**—Cyber Security; Smart Grid; Cyber Security Architecture; Bio-inspired; KDDDump; SCADA security

## I. INTRODUCTION

The real motivation behind the development of this work is that the cyber security of smart grid is a very real issue and the failure to address the cyber security risk within the critical infrastructures may invite serious damage to the national and economic infrastructures. Unlike other infrastructures, compromising smart grid is a high risk and a life threatening issue. Possible threats include terrorism, government-sponsored attacks, energy theft etc. The Stuxnet attack on Iran's Nuclear plant is a great example cyber attack on critical infrastructure [1]. A smart grid consists of many sensors, valves and mechanical instruments which are controlled by PLC (programmable logic controller) / RTU (remote telemetry unit) and these components communicate with simple industrial network protocol like dnp3, Modbus etc [2] and common popular network protocol like Ethernet, 802.11 etc. These systems use common operating systems like windows, linux, mostly early and insecure versions of windows and other common vulnerable routing and switching devices [1]. Security is their last concern because most of the power or engineers are experts on control system, not security. So security experts and control system engineers are working together to solve this burning problem. An attempt has been made to solve the existing problems in this work. This easy to

implement cyber security architecture does not demand any alteration in the core infrastructure of current smart grid. The work was inspired from the amazing techniques followed by our body to fight different kinds of bacteria for securing smart grid from intruders, where intruders are analogous to bacteria and infrastructure to body.

## II. HACKING THE SMART GRID

### A. Approach

There are various approaches to compromise a smart grid. First and the easiest way to hack the smart grid is to compromise the Internet Service Providers and getting into LAN and then compromising based on the vulnerability of the Operating Systems, Routers, and Switches etc. This means that choosing perfect vendor is very important for securing smart grid infrastructure. The main scary thing is that every smart grid user is in local area network of the smart grid which is a great challenge here. When an intruder is in local area network of smart grid, he/they may apply DDOS attack or leverage common device specific and industrial protocol specific vulnerabilities. The intruder can also play with some other attack like MIMT (Man in the middle attack), HMI (Human Machine Interface) propping or they may use blended attacks combining various malwares like "Stuxnet" [3].

### B. Attack Vectors

Every component of a SCADA system can be a target for a person with malicious intent. But the main components, compromising which will do serious damage are smart meter, transformer, PLC, HMI, RTU, synchrophasors, recloser, sensors, coolers etc [4].

## III. PROPOSED SECURITY ARCHITECTURE FOR SMART GRID

A thorough study of different types of security architectures available show that most of the smart grid architectures were not built based on security consideration like NISTIR-7628, SGAM by EU M/490 and the SGCG [1]. On the other hand the 3x3 model by MacAfee [1] is a bit complex to implement in a complex structure system like smart grid. The proposed design, on the other hand, can be implement in any reference architecture of smart grid. The smart grid architecture model provided by CEN-CENELEC-ETSI Smart Grid Coordination Group [5] is used and

simplified for proposed smart grid security architecture. Simplified security model is shown in Figure – 1.

Like SGAM created by CENELEC, the domains is segmented in five categories. These are generation, transmission, distribution, distributed electrical resources (DER) and customer premises or Advance metering Infrastructure. We divided zones into five segments which are Field zone, Control Zone or Station, operation, enterprise, and market [5].

In this model, each of the elements can communicate with other with proper access. But the control zones should be very restricted to access from any remote zones like HAN (home area network), field zones, and enterprise and market network region. These networks should not be able to directly query or control the other critical infrastructure systems. If any consumer wants to know about any of his/her information which is stored in database management system in enterprise facility, then his/her query should not go through smart meter to AMI to AMI headend to Control Zone to Operation to Enterprise. He/she should generate query via internet to the financial or marketing department then marketing department will generate a safe query to the enterprise network.

The DNA like symbols represent Immune walls at different endpoints. Combining all the Immune walls, a complete Smart Grid Immune System (SGIS) is constructed. If Immune walls are implemented at the end points of any conventional or new smart grid reference architecture and an SGIS is built, it will enhance most of the security features very efficiently.

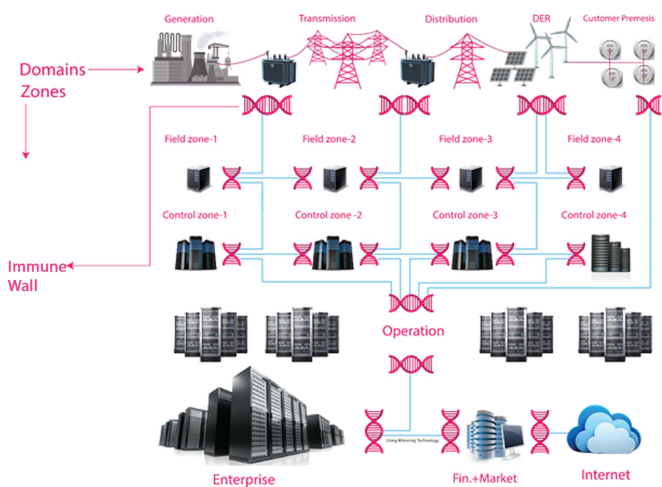


Fig. 1. Security architecture for smart grid. [Stock and images courtesy Freepic.com]

#### IV. SMART GRID IMMUNE SYSTEM (SSIS)

Smart grid immune system is the backbone of our architecture. While no one product or technology is certain to stop all attacks, when immune walls are used together in defense-in-depth posture across all areas of the Smart Grid, it is possible to greatly minimize the risk of a successful cyber-attack.

#### A. Why Bio-inspired?

Proposed SGSS is designed being inspired from human Immune System. Historically, immunity meant protection from disease and, more specifically, infectious disease. The cells and molecules responsible for immunity constitute the immune system, and their collective and coordinated response to the introduction of foreign substances is called the immune response [6].

Cardinal Feature of adaptive immune system: All humoral and cell-mediated immune responses to foreign antigens have a number of fundamental properties that reflect the properties of the lymphocytes that mediate these responses[6]. The main features of adaptive immune system are, (1) Specificity, (2) Diversity, (3) Clonal Expansion, (4) Specialization, (5) Contraction and Homeostasis and (6) Nonreactivity to self.

#### B. Features of Smart Grid Immune System

We have designed our smart grid immune system based on these 7 features of adaptive immune system. We have adjusted these features with necessary security requirements for protecting the critical infrastructure from any malicious attempt. The features of the smart grid immune system are describe below:

TABLE I.

Process	Details
Packet Filtering – Specificity	Specificity ensures that only the necessary connection will go through to the Immune wall. It will work as the advance packet filtering system.
Classification	Classify all the incoming connections as intrusion or normal connection based on signatures. It will work as a part of supervised learning based classification of intrusions.
Anomaly Detection– Diversity	Classify all the unknown incoming connections as anomaly or normal connections with anomaly detection technique. It will classify the connection based on unsupervised learning.
Synchronized intrusion and malware database– Cloning	Clone i.e update the latest detection signature with all Immune walls so that all immune wall can be ready to classify the new threat type. It will increase the ability to combat repeat attacks by the same intrusions or malware.
Self-healing and Incident response	Heal the effected system or block the exploit connection with predefined policies and the help of the administrator.

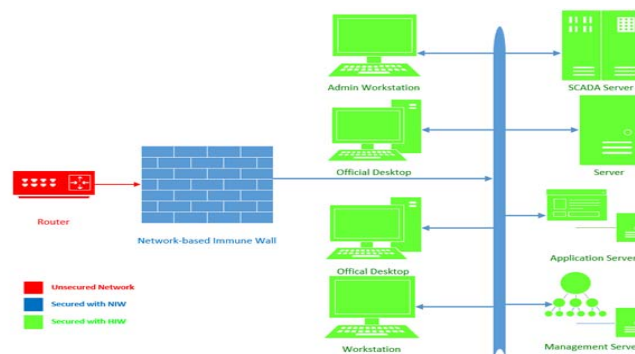


Fig. 2. Simplified structure of SGIS

### C. Structure of immune system

Smart grid itself is a very distributed and complex system. So, for increasing its security without creating any complexity, a security model is designed which can be implemented at any reference architecture. As shown in Fig. 2, without changing the reference architecture, two security systems are added to it. These are (1) Network-based Immune wall (NIW) i.e. Network-based unified threat management system and (2) Host-based Immune wall (HIW).

## V. STRUCTURE OF IMMUNE WALL

### A. Packet Filtering:

The most important task of the most conventional security mechanism “Firewall” is packet filtering. Firewall is a mechanism used to control and monitor traffic to and from a network for the purpose of protecting devices on the network. It compares the traffic passing through it to a predefined security criteria or policy[7]. Core elements of our packet filter are:

1) *Protocol filter*: The protocol filter should block any other connection using any protocol except SCADA protocol in a SCADA environment. So, the packets with industrial protocol like ModBus, FieldBus, ProfiBus, DNP3 etc. should pass the firewall. This will block majority of other unnecessary protocols like FTP, HTTP etc. where these protocols are not necessary.

2) *Port filter*: By restricting each defined connection to only the specific TCP or UDP port, the other 65,534 TCP/IP stacks are blocked. This port filtering system will block the large window of cyber-attack via malware or any port-specific exploits.

3) *Host filtering*: The major communication in SCADA system occurs by industrial protocols. Most of the contents of the packets are command and control requests from the specific devices like HMI, SCADA server, AMI headend etc. These devices have unique MAC addresses which do not change until the devices are replaced. As we know that most of the attacks are generated from unknown sources. So, this will shield the SCADA equipments from receiving any packet from most of the unknown source.

4) *Basic DDOS filtering*: A firewall can detect basic DDOS based intrusion by analyzing the bandwidth consumption by a single IP. With this rule it can reduce some of the DDOS based attacks.

### B. Classification and Diversity

Another security measure is still needed after implementing firewall, as a firewall is a dumb device which only follows the defined rules (except modern firewalls [8]). So in this part, an intelligent intrusion prevention system is introduced.

An intelligent intrusion detection system is essential for classifying dynamic attack vector. So in this part, a machine learning technique is implemented to detect most of the predictable and undefined attacks.

The first and foremost task of an intrusion detection system is to classify attack [9]. Classifying an intrusion based on previous training data is most difficult part to play for an intrusion detection system. To classify intrusions, different renowned learning algorithms are implemented. For learning the classifying ability of the learning algorithms, they are tested with different datasets. This helps to decide the algorithm that is best suited for classification and diversity.

1) *Testing with KDDcup99*: KDDCUP 99 dataset [10] is used for the first simulation that is carried out by data mining software named WEKA. A training set is chosen to train the classifier and the classifying ability of the classifier is tested by giving some test data. To classify attacks, some popular classifiers are used that are used by commercial intrusion detection. The classifiers were trained with 10% of the training data and 10% testing data. The data was cross checked into 4 folds, all of which give almost similar results.

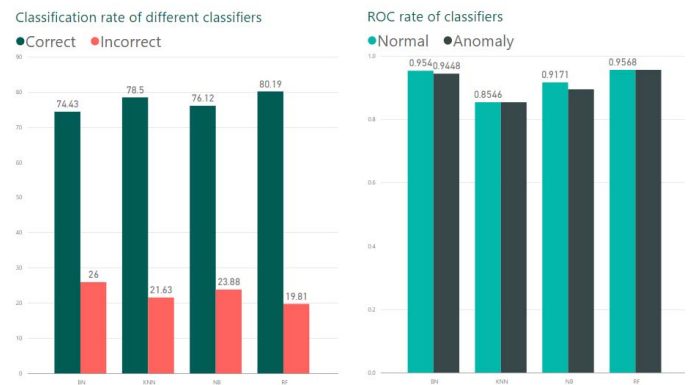


Fig. 3. Classification rate of different algorithms (Bayes Network, K-nearest neighbour, Naïve Bays and Random Forest).

So, according to classification rate and ROC curve, Random Forest has high correctly classified instances of 80% with having excellent ROC, KNN correctly classified 78% of the instances with having good ROC. As a result, Random Forest Algorithm is incorporated for classification and KNN for diversity. It has been seen that KNN is best for anomaly detection rather than random forest or bays algorithms.

2) *Testing with SCADA data*: Real time SCADA dataset created by Dr. Morris and Ian Turnipseed [11] is used for this part of testing. The dataset proposed and created for Ian’s research is a second iteration of a previous dataset from a gas pipeline system to fill the void in IDS research for SCADA applications. The first iteration of the dataset was created by Wei Gao [12]. Gao’s dataset was found to contain obvious patterns, which caused algorithms to appear to have extremely high detection rates, up to 100%. This data is now classified with elected Random Forest and K-nearest neighbor algorithm by using Weka in the same procedure. The result is highly impressive. Result shown in the Table II below. From this result, it can be said that the method looks promising. If the connections are filtered with Random Forest and then again filtered with KNN, then classification will be highly precise

TABLE II.

Algorithms	Correctly classified instances	Incorrectly classified instances	TP rate	FP rate	AUC
Random Forest	100%	0%	1	0	1
KNN	90%	10%	0.895	0.008	.944

C. Memory

Memory is the most important part in smart grid immune system. It consists all kinds of possible attacks and normal connection in a rule based or pcap form so that these can be compared with the incoming packet. Based on the data of the memory, the classifiers will classify a connection.

The memory could be based on sniffed data or rule. It can be created with TCP dump of collection of different types of normal network connections and attacks. Then the classifier will compare the incoming connections with the dataset. Based on classification, the classifier will label the data as normal or anomaly. The rule based database will work the same. The classifier will classify incoming connection by comparing with the rule based data. Then the classifier will classify the data by labeling it as normal or anomaly.

1) *Structure of Network based Immune Wall:* Network based immune wall is the most vital point of smart grid immune system. Each endpoint of smart grid should be secured with NIW (Network-based Immune Wall). It will protect the infrastructure from primary attacks. The flow chart of network based immune wall is shown in Fig. 4. If a NIW is implemented, then all incoming connections should go through this. At first, connection will go through the packet filter region “Specificity” and will be filtered through if it doesn’t meet the requirements the filters want to block. Then the filtered connection will again be classified by the random forest algorithm comparing with the database at the second phase “Classification”. Then if it classified with anomaly then the system will block the connection and report at the log. If the connection is classified as normal connection, then it has to go through the second phase “Diversity”. In this phase filtered data from random forest, will again be filtered and classified through the K-nearest neighbor algorithm. If it is classified as anomaly, system will block the connection and report the log, if not then system will pass the connection and report the log at SIEM (security information and event management).

2) *Structure of host based immune wall:* Host based immune wall is another important part of the smart grid immune system. The network based immune wall can protect the system from DDOS type attack. NIW can also protect the network infrastructure from various types of large attacks. But, a network based immune wall cannot protect the host from malware because the packages coming and going through this network are encrypted as the packets will only decrypt at the host system. NIW can protect the network from major attacks. But it cannot protect the hosts from specific

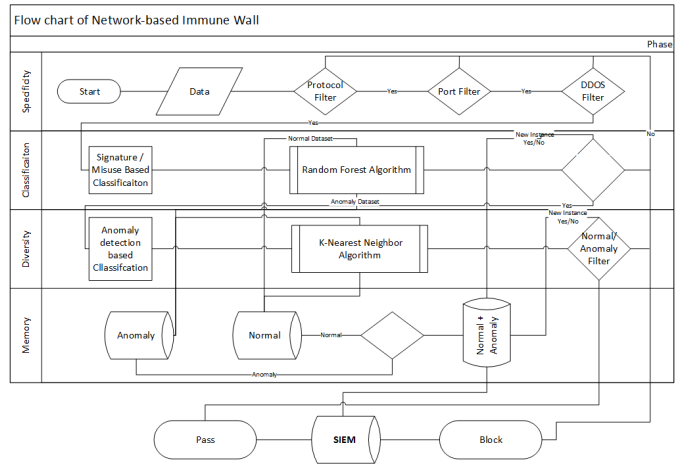


Fig. 4. Flow chart of NIW

attacks, where the use of host-based immune wall comes. Fig. 5 shows the flow chart of the entire host based immune wall. From the figure we can say that a host based immune wall is almost same as the network based immune wall. But there are few changes. It is most probable that a DDOS attack will occur at the endpoint end. If NIW detects the DDOS attack, then host can be safe. But the major threat of host network is device specific attack. That is why a MAC filtering system is added. Most of the threats that occur in SCADA system are device specific, i.e. the target is specifically for a HMI, RTU or for sensors created from the SCADA servers. If the SCADA servers and HMI are protected with HIW and specific MAC addresses are listed in the HIW that are usually communicate for command and control, then the command created from unknown MAC addresses will be declined. A NIW cannot inspect the packet elements because of the encryption but a HIW can inspect the packet because it lies in the host system. So an antivirus is included in the HIW so that it can protect the host from any kinds of malware like military grade malware, SCADA malware etc.

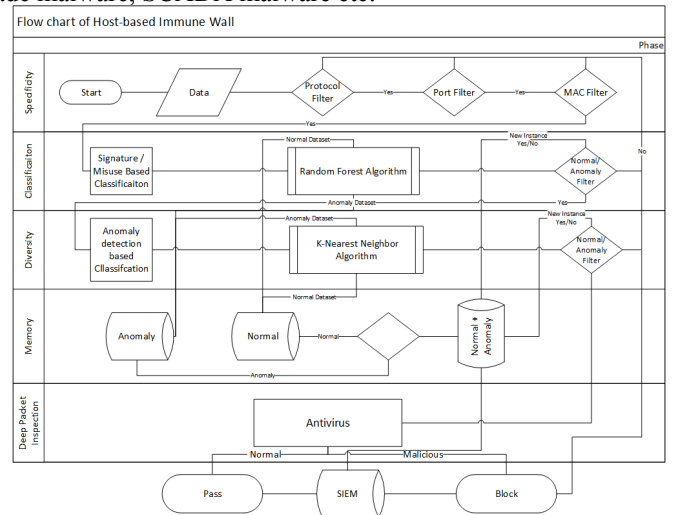


Fig. 5. Flow chart of HIW

## VI. CONCLUSION

In this research, a bio inspired security architecture for smart grid is proposed. The security system is explained in detail and it is shown that every element of the security architecture is crucial. The classification accuracy of the proposed system is also tested. The results show that the system is capable of detecting, with high accuracy, all SCADA intrusions, including injections, replays, and man-in-the-middle attacks. Moreover, the results show that the period of the learning phase plays an important role in improving the detection accuracy of the detection system. However, the detection accuracy of the system is still high even for a one-day learning period because it is basically designed to scale for SCADA systems applications. The advantages of the proposed method can be summarized as follows: (1) detects SCADA-specific attacks; (2) performs real-time detection; (3) shows high detection accuracy even with short learning periods; (4) low false positive (FP) rates; (5) packet filtering rules are added which can filter a huge amount of undesired data; (6) total security solution needed for a smart grid is covered; (7) It is a plug and play method. Just by implementing the NIW in the endpoint and installing the HIW in the host system, highest security can be ensured..

## ACKNOWLEDGMENT

First of all, we would like to convey our gratitude to the Almighty Allah (SWT), for giving us the right direction while attempting the task. The real spirit of achieving a goal is through the way of excellence and austere discipline.

We acknowledge with due respect the constant support and patience of our family members for completing this research.

## REFERENCES

- [1] Knapp, Eric D, and Raj Samani. *Applied Cyber Security And The Smart Grid*. Waltman, MA: Syngress, 2013. Print.
- [2] Knapp, Eric. *Industrial Network Security*. Waltham, MA: Syngress, 2011. Print.
- [3] Flick, Tony, and Justin Morehouse. *Securing the Smart Grid: Next Generation Power Grid Security*. Amsterdam: Syngress, 2011. Print.
- [4] Knapp, Eric D., and Raj Samani. "Hacking the Smart Grid." *Applied Cyber Security and the Smart Grid* (2013): 57-86. Web.
- [5] CEN, CENELEC, ETSI, SGCG report on reference architecture for the smart grid external version V2.0. SGSC Reference Architecture Working Group (RAWG); August, 2011.
- [6] Abbas, Abul K., Andrew H. Lichtman, and Shiv Pillai. *Cellular and Molecular Immunology*. Philadelphia, PA: Saunders Elsevier, 2011. Print.
- [7] Medhi, Deepankar, and Karthikeyan Ramasamy. "IP Packet Filtering and Classification." *Network Routing* (2007): 534-81. Web.
- [8] Turcanik, Michal. "Packet Filtering by Artificial Neural Network." *International Conference on Military Technologies (ICMT) 2015* (2015): n. pag. Web.
- [9] R. Bace and P. Mell, "Intrusion detection systems, NIST Technical Report 800-31," National Institute of Standards and Technology (NIST), 2001.
- [10] <http://kdd.ics.uci.edu/databases/kddcup99/kddcup99.html>
- [11] Morris, Thornton, Turnipseed. "Industrial Control System Simulation and Data Logging for Intrusion Detection System Research". Mississippi State University Starkville, MS, USA. Web.
- [12] Morris, Thomas, and Wei Gao. "Industrial Control System Traffic Data Sets for Intrusion Detection Research." *IFIP Advances in Information*

*and Communication Technology Critical Infrastructure Protection VIII* (2014): 65-78. Web.

- [13] N. S. A., "Defense in depth: A practical strategy for achieving information assurance in today's highly networked environments." Available at [http://www.nsa.gov/ia/\\_files/support/defenseindepth.pdf](http://www.nsa.gov/ia/_files/support/defenseindepth.pdf).
- [14] T. Bass and R. Robichaux, "Defense-in-depth revisited: Qualitative risk analysis methodology for complex network-centric operations," in *Military Communications Conference, 2001. MILCOM 2001. Communications for Network-Centric Operations: Creating the Information Force*. IEEE, vol. 1, pp. 64–70, 2001.



# GFCC-Based Robust Gender Detection

M. A. Islam

Electrical & Electronic Engineering, International Islamic University Chittagong, Chittagong, Bangladesh  
atiq.atrai@gmail.com

*Abstract— Gender classification technique is a part of the signal processing comprises with feature extraction and behavioural gender modelling. Fundamental frequency and pitch are mostly used as feature for gender detection due to their unique characteristics in voice source. In this study, Gammatone Frequency Cepstral Coefficient (GFCC)-based robust gender classification method has been presented. This study was accomplished using speech samples from a text-dependent data set. The prototype gender behavioural modelling was done using Gaussian mixture model (GMM) to obtain better performance and only clean signal was used to train the model. The performance of the proposed method was tested under both clean and contaminated conditions. The clean signal was contaminated using nine different noises at a range of signal-to-noise ratios (SNRs) from 0 dB to 10 dB. The obtained performance showed the proposed method was very robust against noise and the average performance at 0 dB SNR was almost 100% for female and 92% for male irrespective to noises. So, it could be said the proposed method performance was almost noise invariant.*

*Index Terms— Gender classification, GFCC, GMM, Modelling, Robustness.*

## I. INTRODUCTION

Gender classification is an important biometric technique in signal processing in which audio or video or both signals from both male and female are used to identify speaker gender. It is very important to distinguish speaker gender to enhance speaker as well as speech recognition, because separate acoustic behavioural model for male and female provides better performance. In addition, this technique is applied in sorting caller in telephoning, identifying a target speaker's sex among a number of speakers, and intelligibility of man-machine interfacing. Furthermore, the correct gender detection is one of the important criteria for speaker emotion detection.

The voice signal availability makes its application in signal processing very popular compare to fingerprint, face identity, and video signal applications. It is well known, the human voice source information (fundamental frequency) is unique for men and women, which is the basic key to distinguish gender. Moreover, vocal tract-oriented characteristics like formant frequency, amplitude, and bandwidth are also used in gender recognition [1].

The most crucial and important part in any classification technique is to extract hidden feature from the object. Similarly, in gender classification technique feature extraction from speech signal is the most essential stage. A number of studies have been carried on to achieve robust gender classification. Some of them are acoustic feature-based: fundamental frequency and pitch combination [2] is one of the prominent features. It is to be mentioned that the fundamental frequency plays crucial effect on pitch perception and mostly used in identification of speaker gender. The second group contains auditory feature in which feature extraction process is done following auditory peripheral system: auditory nerve (AN) model-based gender classification [4] one of them.

In signal processing, Mel-frequency Cepstral Coefficient (MFCC) is very well known which is designed following auditory peripheral system mechanism. MFCC-based gender classification performance degrades significantly under noisy conditions due to the application of Fast Fourier Transform (FFT) in feature extraction even worse than individual pitch-based performance [3]. To address non-linearity of auditory periphery system and obtain robust performance in gender detection, neurogram-based method has been introduced [4]. In clean, neurogram-based performance was almost 100% irrespective to gender. It was observed in [4], the neurogram-based method's performance was fluctuated quite a lot with the change of types of noise and degraded havoc at 0 dB signal-to-noise ratio (SNR). The combination of pitch and 10<sup>th</sup> order relative spectral perceptual linear predictive coefficients (RASTA-PLP) [5] provides robust performance in gender classification, but does not reflect non-linearities of the human auditory system. So, a method that reflects auditory periphery non-linearity and provides robust performance is necessary in gender classification technique.

A new method in gender detection including non-linearity of auditory system is presented in this study. An auditory peripheral property-based feature Gamma-tone Frequency Cepstral Coefficient (GFCC) [6] has been used to obtain robust gender classification. Motivated by the robust performance of the GFCC in speaker identification [6, 7] and speech recognition [8], it has been applied in gender classification. Moreover, the application of Gamma-tone filter and cubic operation in GFCC can capture physiological mechanism of the human auditory periphery system.

Once feature extraction is done; most crucial subject is to make gender behavioural model using latent information from extracted feature. In gender classification, gender prototype model is mostly implemented by using either statistical Gaussian mixture model (GMM) or one versus one (OVO) technique-based Support vector machine (SVM) [9]. SVM modelling provides comparable performance to GMM-based modelling in gender classification. The main drawback of SVM-based modelling is that, it requires all training samples at a time to create an object model which needs high configuration machine and also time consuming. Another disadvantage of SVM modelling is the selection of optimal values of cost and gamma variable. The SVM modelling, performance completely relies on the proper selection of these two parameters. On the other hand, GMM can estimate sufficient latent statistical variable from speech signals and needs a small number of mixture components.

In this study, the GMM modelling technique has been applied to create a gender behavioural model to obtain a fast gender detection system. The gender behavioural modelling was done using text-dependent clean speech signals. The performance of the proposed method was evaluated in clean and noisy conditions. Nine different noises were used to validate the proposed method extensively.

The rest of the part of this paper has been arranged as follows: the methodological description of feature extraction and gender modelling are given in section II. The obtained performance of the proposed method and robustness issues is described in section III. In section IV, the summarize form of this presented study is given.

## II. METHODOLOGY

The methodological procedure of the GFCC feature extraction is shown in Fig. 1. The gender detection process is shown in block diagram in Fig. 2. The assumption machine-based recognition is the features extraction in first step like auditory periphery system and second is to make decision based on stored information regarding testing object. So, the methodology section has two subsections: GFCC feature extraction and GMM-based behavioural modelling for further testing of the presented method's validity.

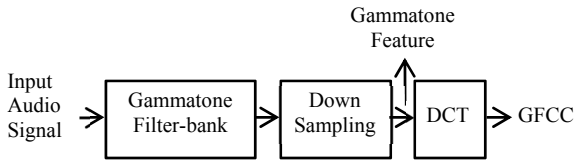


Fig. 1 GFCC feature extraction block diagram.

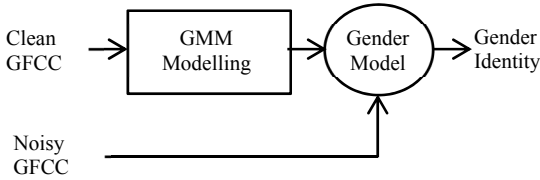


Fig. 2 The proposed gender detection method's block diagram using GFCC as a feature.

### A. GFCC-Feature Extraction

The Gamma-tone filter is more resemble with the human basilar membrane filter and can reflect psychological and physiological response of auditory cochlea filters. To simulate basilar membrane response, a fourth order Gamma-tone filter has been used. In human auditory system, there have 30000 neurons, which are connected selectively to basilar membrane filter. The basilar membrane is divided into a number of bands and each band is considered as a band pass filter. In this study, only 64 bands have been considered. Filter responses were simulated for centre frequency ranges from 50 Hz to 4 kHz considering the sampling frequency of input signal. So, the Gammatone filter response frequency remains same as it was for input signal.

Once the Gamma-tone time-frequency (T-F) responses were obtained it was down sampled to 100 Hz which is similar to 10 ms windowing technique application on T-F responses. A cubic root operation was applied to introduce cochlea non-linearity in GFCC features. This cubic root application reflects cochlea loudness compression property. The obtain feature is called Gammatone feature (GF). The GF has finer resolution at low frequencies compared to high frequencies. Moreover, the GF has better resolution than FFT-based linear time-frequency spectrogram resolution as shown in Fig. 2 in study [7]. Here is mentioned that, GF has 64 frequency channels which overlaps frequency information and correlates information. It is well known, too many correlation make worse behavioural prototype training model and

degrades the system performance. Furthermore, 64-dimension is larger compare to MFCC, neurogram or other conventional features for gender detection.

To reduce the size of Gammatone features discrete cosine transform (DCT) was applied. DCT also de-correlates data and restore spectral feature to instantaneous form.

$$f(i, j) = \sqrt{\frac{2}{M}} \cos\left(\frac{\pi}{2n} \cdot i \cdot (2j - 1)\right) \quad i, j = 1, 2, \dots, M \quad (1)$$

The content of DCT matrix F is  $f(i, j)$ , where n is the number of feature dimension. Here, M is 64. To obtain cepstral feature H from Gammatone feature G, DCT matrix F is multiplied by G.

$$H = D \times F \quad F = \{f(i, j) | i, j = 1, 2, \dots, M\} \quad (2)$$

The obtain feature is not exact cepstral feature because a log operation is required between first and second frequency analysis for the de-convolution purpose. The obtained feature name is given Gammatone frequency cepstral coefficient (GFCC). It was observed in this study, the most of energy of Gammatone features retain in 1<sup>st</sup> to 23<sup>rd</sup> coefficients after DCT application which is consistent with the finding of the study [7]. Moreover, 1<sup>st</sup> coefficient was more susceptible to noise. According to suggestion [7], only 2<sup>nd</sup> to 23<sup>rd</sup> order GFCC (22-dimensions) was kept for robust gender classification under noisy conditions. The detail GFCC feature extraction procedure can be found in [6].

There are two basic differences between GFCC and MFCC. MFCC uses triangular filter to capture basilar membrane responses, whereas GFCC uses Gammatone filter to do so. Second, GFCC uses cubic operation to reflect cochlea non-linear properties and MFCC uses log operation for the same purpose. It was found in [12], the combination of Gammatone filter and cubic operation on spectral feature in GFCC provides better performance than MFCC.

Once clean GFCC feature was extracted; it was forwarded to create GMM-based behavioural gender model. Noisy GFCC feature was used only to validate the propose method robustness.

### B. Gender Modelling

The most important in speech processing is to extract latent variable from the extracted feature from input signal. The performance accuracies of any system mostly depend on accurate modelling. GMM is mostly used in modelling for gender classification [2,4]. GMM follows Gaussian distribution (mean and deviation about the mean) of feature vectors. The main advantage of using GMM as classifier, it can represent each gender phonetic class distribution with few mixture components.

The GMM model is parameterized by mean vectors, covariance matrices and mixture weights from all mixture component densities. In this study, 128 GMM components were used to train the proposed method. It was observed that the application of diagonal covariance instead of full covariance de-correlated the off-diagonal covariance matrices elements and improved gender classification performances. GMM model male and female likelihood was computed as follows

$$P_g(x_t | \mu, \Sigma, \alpha) = \prod_{i=1}^N P_g(x_{ti} | \mu, \Sigma, \alpha) \quad (3)$$

Here,  $P_g$  is the gender probability score which indicates gender of testing sample's speaker. N is the total number of speakers and  $i=1, 2, 3, \dots, N$  are GMM mixture weight.  $x_{ti}$

is the individual speaker's training sample.  $A$  is the Gaussian density with mean  $\mu$  and covariance matrix  $\Sigma_i$ .

In testing stage, the testing sample from unknown gender was used to compare with gender trained model. The model which provided maximum likelihood probability score to that testing sample, that model indicated the gender of that testing sample. The probability density function was used to obtain maximum likelihood score of the testing sample's gender using following equation

$$X = \frac{1}{N} \sum_{i=1}^N P_g(x_{ti} | \mu, \Sigma \alpha) \quad (4)$$

If  $X_{\text{male}}$  (for any  $x_{ti}$ )  $>$   $X_{\text{female}}$  (for any  $x_{ti}$ ), it indicates the testing  $x_t$  is lied in male gender otherwise the gender is detected as female.

It was observed in this study, the application of logarithm in probability density function as it was applied in [4] increased the chance level of testing sample to be male. But, the overall performance was almost similar.

A 2 x 2 confusion matrix was created to provide the percentage accurate classification performance of the proposed method. Once, the target sample's gender was detected, a one was added corresponding gender in confusion matrix. Each instance of male and female gender testing was done independently.

### III. RESULT AND DISCUSSION

This section has two parts. Initially, the proposed system's experimental setup has been described and the obtain results and analytical study of the presented method has been described later.

#### A. Experimental Setup

In this study, a text-dependent dataset named Universiti Malaya (UM) is an asset of University of Malaya has been used. The speech samples were recorded at a sampling frequency of 8 kHz from 39 native Malay speakers. There have 25 males and 14 females. This dataset was mainly used in speaker identification [10] and has also been used in gender detection [4]. Each speaker was asked to utter 'University Malaya' for ten (10) times. 70% samples from each gender were used for GMM-based gender prototype modelling and rest 30% samples were used to test the performance of the system following [4]. So, total 223 samples were used to train the proposed method and 117 samples (75 samples from males and 42 samples from females) were used to test the validation of this study. The behavioural prototype gender model was made using clean GFCC feature. The proposed system was tested in clean and noisy conditions. The input clean signal was contaminated with nine different types of stationary and non-stationary noises. Noises were white Gaussian, pink, street, babble, train, restaurant, exhibition, speech shaped noise (SSN), and factory noise. The noises were added to clean signal for a range of SNRs from 0 dB to 10 dB at a step of 5 dB SNR. The noisy audio signal was used to extract noisy GFCC feature.

#### B. Results and Discussion

This section presents the performance evaluation of the proposed method using GFCC as a feature. The propose study performance was evaluated for five times for each SNR of each noise and average result was recorded. It is to be recalled, the presented study was tested under both clean and

noisy conditions. The gender classification performance of this study using text-dependent speech signal in clean condition is shown in the confusion matrix in TABLE I. It is seen from TABLE I result, the proposed method can detect male and female 100% in clean condition. The proposed method performance as shown in TABLE I indicates that the GFCC-based method can distinguish voice production sources faithfully and segregate male and female accurately. This robust performance could be due to the application of cubic root in GFCC and reflection of basilar membrane filter properties in Gammatone filter.

TABLE II shows the performance of the proposed method under noisy conditions. The results are explicated that the proposed method performances are almost noise invariant and robust to noises.

TABLE I  
THE CONFUSION MATRIX OF THE PROPOSED GENDER DETECTION METHOD IN CLEAN.

Gender	Male	Female	Accuracy (%)
Male	75	0	100
Female	0	42	100

TABLE II  
THE PROPOSED METHOD ROBUST GENDER DETECTION PERFORMANCE UNDER NOISY CONDITIONS USING NINE DIFFERENT NOISES FOR A RANGE OF SNRS.

Noise type	SNR	Male (%)	Female (%)	Overall (%)
White	10dB	97.33	100	98.67
	5dB	94.67	100	97.34
	0dB	74.67	97.62	86.14
Pink	10dB	100	100	100
	5dB	100	100	100
	0dB	96	100	98
Street	10dB	100	100	100
	5dB	96	100	98
	0dB	88	100	94
Babble	10dB	100	100	100
	5dB	100	100	100
	0dB	98.67	100	99.33
Train	10dB	100	100	100
	5dB	98.67	100	99.33
	0dB	96	100	98
Restaurant	10dB	100	100	100
	5dB	98.67	100	99.33
	0dB	97.33	100	98.67
Exhibition	10dB	100	100	100
	5dB	97.33	100	98.66
	0dB	78.67	100	89.34
SSN	10dB	100	100	100
	5dB	100	100	100
	0dB	100	97.62	98.81
Factory	10dB	100	100	100
	5dB	100	100	100
	0dB	98.67	100	99.34
Clean		100	100	100

The machine-based recognition is always subjected to additive noises and the system performance degrades with the increment of noise level. The performance of the proposed method was significantly dropped at 0 dB SNR for white Gaussian noise (which is considered as high frequency noise)

due to the inclusion of high frequencies information. It has been shown in [11]; the GFCC-based performance could improve under white Gaussian noise considering low frequency information. Besides this, the power spectral density of exhibition noise was used in this study was almost similar to white Gaussian noise and degraded the performance compared to other non-stationary noises. Otherwise, the proposed method performance was on average almost 100% for female and more than 92% for male irrespective of noises at 0 dB SNR. It is known that the fundamental frequencies of males and females are different and the study [5] showed the pitch level of females are higher than males which are distinguishing features. So, the finding of this study is the pitch information of audio signal helps to classify male and female accurately and GFCC feature can extract this from input audio signal.

Generally, the chance level of gender detection technique's performance is 50% i.e. either male or female. The study [4] performance was on average below 70% respective to noises at 0 dB SNR and showed results taking only 10 males and 10 females from UM dataset. This study showed result applying orthogonal polynomial on neurogram. A physiological auditory peripheral-based AN model was employed to compute neurogram. The best performance of the study [4] was shown for restaurant noise and has been compared with the presented study performance for same noise taking same number of speaker samples. The ENV neurogram-based performance has been copied in TABLE III from the study [4]. The comparison results are shown in TABLE III for a range of SNRs from 0 dB to 10 dB.

TABLE III  
COMPARISON OF THE PERFORMANCE OF THE PROPOSED METHOD A RELEVANT METHOD UNDER CLEAN AND RESTAURANT NOISE FOR 10 MALES AND 10 FEMALES.

SNR	Male (%)	Female (%)	Overall (%)
	GFCC/ENV	GFCC/ENV	GFCC/ENV
Clean	100/93.3	100/96.7	100/95
10 dB	100/96	100/74	100/85
5 dB	100/90	100/64	100/77
0 dB	100/83	100/50	100/67

The GFCC-based presented method performance contrasting to the neurogram-based study was more robust and also very robust to noises. So, it can be said based on this study result; the proposed method can successfully distinguish male and female voice production system as well as identity of gender. The study [12, 13] showed the speaker identification performance improves largely after loudness suppression using cubic operation. This could be said that the inclusion of cubic operation in GFCC provides robust gender detection performance in this study. Moreover, it was observed in this study that the exclusion of cubic operation in GFCC dropped gender detection performance to a remarkable level under noisy conditions.

#### IV. CONCLUSION

This study is an application of GFCC as a feature in gender detection. GFCC feature has been extracted following auditory peripheral mechanism using Gammatone filter to simulate cochlea filters responses. Twenty-two (22) dimensional GFCC features which contain most energy of 64-channels have been used in this study to capture latent information of gender distinguishing feature. GMM modelling

technique has been applied to make gender behavioural prototype model. The proposed method performance accuracy was 100% in quite condition. The proposed method performance was not reduced substantially with the increment of noise level which ensures the robustness of the proposed method. The performance of the proposed gender detection method was almost noise invariant and provided very robust score. The proposed method can also be studied for a large dataset like TIMIT and to dataset which contains different combination of language speeches to extensively validate this method.

#### ACKNOWLEDGEMENT

I would like to thanks anonymous reviewers for their valuable comments those have enhanced this paper quality.

#### REFERENCES

- [1] D. G. Childers, and Wu, K., "Gender recognition from speech. Part II: Fine analysis". The Journal of the Acoustical society of America, 90(4), 1991, pp.1841-1856.
- [2] S. Slomka and S. Sridharan, "Automatic gender identification optimized for language independence," in TENCON'97 Brisbane-Australia. Proceedings of IEEE TENCON'97. IEEE Region 10 Annual Conference. Speech and Image Technologies for Computing and Telecommunications. 1997, (Cat. No. 97CH36162).
- [3] G. Nisha Meenakshi and P. K. Ghosh, "Automatic gender classification using the mel frequency cepstrum of neutral and whispered speech: A comparative study," in Communications (NCC), 2015 Twenty First National Conference on, 2015, pp. 1-6.
- [4] Mamun, Nursadul, Wissam A. Jassim, and Muhammad SA Zilany. "Robust gender classification using neural responses from the model of the auditory system." Functional Electrical Stimulation Society Annual Conference (IFESS), 2014 IEEE 19<sup>th</sup> International. IEEE.
- [5] Y.-M. Zeng, Z.-Y. Wu, T. Falk, and W.-Y. Chan, "Robust GMM based gender classification using pitch and RASTA-PLP parameters of speech," International Conference on Machine Learning and Cybernetics, 2006, pp. 3376-3379.
- [6] Shao, Yang, Soundararajan Srinivasan, and DeLiang Wang. "Incorporating auditory feature uncertainties in robust speaker identification." IEEE International Conference on Acoustics, Speech and Signal Processing-2007, ICASSP'07. Vol. 4.
- [7] Zhao, Xiaojia, Yang Shao, and DeLiang Wang. "CASA-based robust speaker identification." IEEE Transactions on Audio, Speech, and Language Processing. 2012, pp. 1608-1616.
- [8] Shao, Yang, et al. "An auditory-based feature for robust speech recognition." IEEE International Conference on Acoustics, Speech and Signal Processing. 2009.
- [9] Burges, Christopher JC. "A tutorial on support vector machines for pattern recognition." Data mining and knowledge discovery. 1998, pp. 121-167.
- [10] M. Islam, M. Zilany, and A. Wissam, "Neural-Response-Based Text-Dependent Speaker Identification Under Noisy Conditions," in International Conference for Innovation in Biomedical Engineering and Life Sciences, 2016, pp. 11-14.
- [11] Islam, Md Atiqul, Wissam A. Jassim, Ng Siew Cheok, and Muhammad Shamsul Arefeen Zilany. "A Robust Speaker Identification System Using the Responses from a Model of the Auditory Periphery." PloS one 11, no. 7 (2016): e0158520.
- [12] Zhao, Xiaojia, and DeLiang Wang. "Analyzing noise robustness of MFCC and GFCC features in speaker identification." IEEE International Conference on Acoustics, Speech and Signal Processing, 2013, pp. 7204-7208.
- [13] Q. P. Li, "An auditory-based transform for audio signal processing," in Applications of Signal Processing to Audio and Acoustics, WASPAA'09. IEEE Workshop on, 2009, pp. 181-184.

# Frequency Domain Linear Prediction-Based Robust Text-Dependent Speaker Identification

M. A. Islam

Electrical & Electronic Engineering, International Islamic University Chittagong, Chittagong, Bangladesh  
atiq.atrai@gmail.com

**Abstract**— Speaker identification is a biometric technique of determining an unknown speaker's identity among a number of speakers using distinguish latent information of uttered speech. Crime investigation, security control, telephone banking and trading, and information reservation are some applications of this technique. Frequency Domain Linear Prediction (FDLP) is a time-frequency-based feature has been derived using 2-D autoregressive model. This feature was constructed from sub-bands short frame energies estimation. FDLP has been used in this study to propose a robust text-dependent speaker identification technique. The clean features were used to obtain speaker behavioural model. Support vector machine has been used to train the proposed method. This presented study was tested in both clean and noisy conditions to validate the method extensively. The proposed method got significant improved performance over all traditional methods performances in noisy conditions. The obtained performance was indicated; the proposed method was very robust to noises and showed consistent performance irrespective to noises.

**Index Terms**— *FDLP, Speaker Identification, Robust, SVM.*

## I. INTRODUCTION

The fundamental frequency, energy, pitch, and power are the hidden information carried by speech and unique characteristic for individual speaker. These features are varied from man to man due to the variation of physiology of voice production system. The uttered speech not only passes messages to listener but also provides information about gender identity, direction of the sound source, emotions, and talker identity. Ease availability and uniqueness of speech makes its application popular in speech processing.

Speaker identification is a part of speaker recognition. It is a biometric method which uses speaker voice signal to identify a target speaker by matching with a number of prototype speaker models [1]. Speaker identification is two types based on text: text-dependent and text-independent. In a text-dependent speaker identification system, recorded speech samples are aligned to a reference template from registered speakers. On the other side, speech is not limited to a specific length or sentence in a text-independent speaker identification system. This study presents a new approach to develop a robust text-dependent speaker identification system.

A significant number of studies and developments have been done to achieve robust performance on automatic speaker identification for more than four decades. The log operation-based Mel Frequency Cepstral Coefficients (MFCC) [2] and all pole system based Linear Prediction Cepstral Coefficients (LPCCs) [3] are most common feature in automatic speaker identification. LPCC is developed by following human voice production mechanism. On the other hand, MFCC is developed following the auditory peripheral physiology. LPCC features provide better performance in clean condition, but its performance drops significantly with the increment of noise level which causes substantial spectral distortion in the signal [4]. Similarly, Fast Fourier Transform (FFT)-based feature, MFCC, works better in matched condition but in noisy conditions; its performance declines to a remarkably low level [5]. Recently, Gammatone Frequency Cepstral Coefficient (GFCC) has been implemented following auditory peripheral mechanism to obtain robust score in speaker identification system but GFCC-based method's results were not substantially improved under noisy conditions [6]. To obtain robust speaker identification (SID) performance, Auditory Nerve (AN) model-based Neurogram [7] was used. Neurogram is a time-frequency-based synapse response but its extraction process from audio signal is complex and very time consuming. It was also provided comparatively poor performance under non-stationary noises [7].

It is well known, the speaker identification performance of Human listeners irrespective to noises is very robust. So, it is desirable to develop an automatic speaker identification system which performance will be comparable with human listening performance. The machine learning-based speaker identification performances degrade significantly when additive noise or distortion is added to clean signal. Hence, the goal of this study is to present a new method to achieve robust speaker identification performance.

In this study, 2-D autoregressive model-based FDLP [8] has been introduced for robust text-dependent speaker identification. The robust performance of FDLP-based text-independent speaker identification [8] motivates to explore its application in text-dependent speaker identification system. FDLP captures pitch information

from acoustic signal which enhance speaker identification performance.

In speaker identification system, Support Vector Machine (SVM) [9], Gaussian Mixture Model (GMM), and Gaussian Mixture Model-Universal Background Model (GMM-UBM) are employed to create speaker behavioural model. GMM and GMM-UBM provides almost similar performance and better in text-independent SID system. Sometimes, SID system's performance varies with the variation of modelling technique. In this study, SVM one versus rest (OVR) speaker modelling technique has been applied to provide robust text-

dependent SID performance. The proposed FDLP-based method was validated in both clean and noisy conditions. This study show, SVM speaker modelling provides better performance than the study [7] which was done based on GMM-UBM speaker modelling technique using same dataset.

The residual portion of the presented paper has been arranged in following structure: the methodological description of the proposed method has been given in section II, the evaluation and findings of the presented study is described in section III, and the summarize form of this study is given in conclusion section.

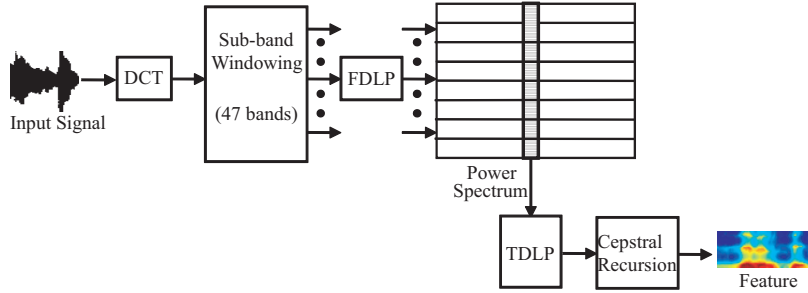


Fig. 1 Illustration of FDLP feature extraction schematic block diagram from an audio signal using 2-D autoregressive model.

## II. METHODOLOGY

Fig. 1 presents FDLP feature extraction process and Fig. 2 presents the block diagram of the proposed method. Initially, silence period of input signal was removed. In general, each speech utterance contains silence period which is essential to separate words and make sentences intelligible to listeners. In a machine-learning speaker identification system, the removal of silent period is necessary to make a better speaker model, because this part of speech portion does not carry any information and make similarities among speakers in speaker behavioural models. In this study, the silence period of input signals were removed using a standard algorithm called voice-activity-detector (VAD) available in the voice-box toolbox [10]. Silence period free signals were forwarded as input to extract features for robust SID performance.

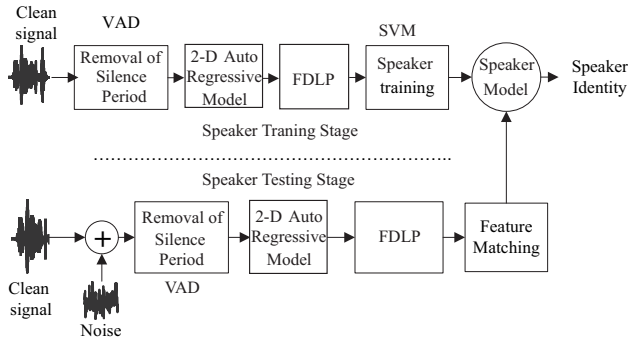


Fig. 2 The methodological block diagram of the proposed FDLP- based method for robust speaker identification.

### A. Feature Extraction

A 2-D auto-regressive model-based frequency domain coefficient was developed by Ganapathy et al. [8] applying all poles technique. This feature has been developed based on high-energy peaks estimation of audio signal in the time-frequency (T-F) unit. In this study, the FDLP extraction was done based on the 2-D autoregressive model following [8]. The procedure has several steps. The acoustic time-domain signal was transformed into frequency domain using the DCT. The frequency domain signal was windowed into 47 linear sub-bands with an upper limit of  $\sim 4$  kHz whereas lower limit was set to 0 Hz. Then the linear prediction system was applied to each sub-band to obtain the corresponding Hilbert envelope. A 25-ms length of window with an overlap of 40% between adjacent frames was used to compute 13 cepstral coefficients including the zero-order coefficient ( $C_0$ ). Delta and acceleration coefficients were also included. So, the total number of FDLP feature dimension was  $39 \times m$ . Here,  $m$  is the number of frames. The FDLP feature  $e$

### B. Existing baseline features

The presented FDLP-based method's results were compared to the results of the existing features such as the GFCC, MFCC, and Neurogram. The feature extraction procedures of the baseline features are given in the following subsections.

### *i. MFCC*

MFCC is a very common feature in automatic speaker recognition and also being used in speech recognition. This feature was computed from input signal using “rastamat toolbox” [11]. 40 bands of triangular filter with centre frequencies from 50 Hz to 4 kHz were used to extract MFCCs. A Hanning window having 25 ms length with 50 % overlap between adjacent windows was applied to extract MFCCs. The dimension of the obtained MFCCs was 13 per frame which is known as static coefficients. The dynamic and acceleration coefficients were also counted to obtain better performance. So, the dimension of MFCC was 39 in this study.

### *ii. GFCC*

GFCC feature extraction process was developed following auditory peripheral system. Gammatone filter-bank was used to reflect basilar membrane filter-bank responses. Because, the Gammatone filter is more similar to basilar membrane band filters according to the physiological observation. The filter centre frequencies were quasi logarithmically spaced from 50 Hz to 4 kHz. Unlike MFCC, Gammatone filter responses were down sampled to 100 Hz. This down sampling was same as 10ms windowing and reduced the dimension of the Gammatone features. A cubic root operation was then applied to compress loudness. GFCC extraction process is different in two ways from MFCC extraction method. Firstly, the application of Gammatone filter-bank instead of triangular filter to simulate basilar membrane response. Secondly, the cubic root operation instead of log operation on power spectrum. It was reported in [6] that most of the speaker-specific information remains in the lowest 23 GFCCs (among 64 bands) due to the compaction property of the DCT. Because the zeroth-order ( $C_0$ ) was mostly corrupted by noises, only the first 22 GFCCs (excluding  $C_0$ ) from each frame were used in this study.

### *iii. Neurogram*

Neurogram is the synapse responses were derived from an auditory peripheral-based model (AN model) responses. AN-model [12] is a useful simulation-based model for understanding physiological and mechanical mechanism of auditory system. Initially, the input signal was sampled to 100 kHz to adopt with requirement of the AN model and to replicate middle ear response meticulously. All input signals loudness was set at 70 dB. The Neurogram was constructed from the Synapse responses with a ranges of frequencies from 250 Hz to 1 kHz are spaced nonlinearly (using logarithmic space) into 12 bands of frequency called characteristics frequency (CF). The obtained synapse output of AN-model was windowed for 420 points with 50% overlap. This low resolution feature name was envelope (ENV) Neurogram. Only 12 bands i.e. low frequencies information was

chosen to provide robust performance in speaker identification. More detail about ENV Neurogram extraction can be found in [7].

### *C. Speaker Modelling*

SVM was used to make speaker behavioural model from the Matlab libsvm toolbox [13] to test the performance of the proposed method. There are two techniques in SVM modelling: one-versus-one (OVO) and one-versus-rest (OVR) classification technique. OVR speaker modelling technique has been applied in this presented work. SVM dimensional space is decided by the input feature vector. Seven (7) speech signals from each speaker were randomly chosen to create individual speaker prototype model and the rest samples were provided to test the identification score of the proposed method. It has been mentioned earlier the FDLP feature dimension was  $m \times 39$ , where  $m$  was the number of frame. On the other side, the MFCC-, GFCC-, and Neurogram- feature sizes were  $m \times 39$ ,  $m \times 22$ , and  $m \times 12$  respectively, where  $n$  was the number of frames of the speech signal.

Generally, the input features are normalized to zero (0) mean and one (1) standard deviation. This default normalizing procedure was applied in this study. Radial basis function (RBF) was applied as default to make speaker behavioural model. SVM speaker modelling was done setting cost ( $c$ ) and gamma ( $g$ ) function to 4 and 1 respectively. The testing samples were then used to obtain unknown speaker identity by comparing with each and every speaker model. The matched speaker model provided maximum probability score to the testing sample and speaker was identified.

## III. RESULTS AND EVALUATIONS

A text-dependent dataset has been used in this study. A simple text ‘University Malaya’ was spoken for 10 times by each of the 39 speakers. A comfortable sound-resisted booth was used to record uttered speech. The sampling rate of the recorded speech signals was 8 kHz. This database was designed for the application in text-dependent speaker recognition systems [7].

The proposed FDLP-based performances with other existing methods performances have been described in this section. The performance was tested in both clean and noisy conditions. The clean testing signals were contaminated with white Gaussian (stationary) noise, pink (slow-varying) noise, and street (non-stationary) noise for a range of SNRs -5 dB to 15 dB in steps of 5 dB to proof the robustness of this presented method.

The performance of the proposed method along with alternative methods has been illustrated in Fig. 3. It is well known, any system’s performances are reduced when noise level is increased. It is seen from Fig.3, the proposed method-based results are almost similar across different type of noises up to 5 dB SNR but dropped

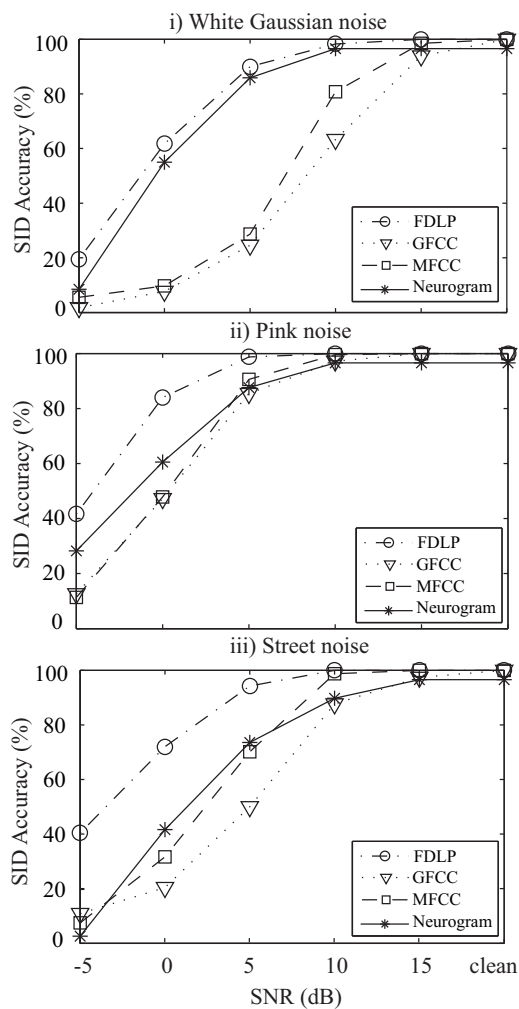


Fig. 3 Comparison of the proposed and substitutive methods performances using SVM speaker modelling. The speaker identification (SID) performance is shown for three different type of noises for SNRs -5 dB to 15 dB.

consecutively below that SNR level. It is also clear from Fig. 3, the FDLP-based method achieved the highest accuracy over existing methods performance irrespective to noises and SNR levels.

Furthermore, the Neurogram-based method's performance outperformed the other two existing methods performance, and was comparable to FDLP-based performance under white Gaussian noise. It is to be mentioned, the Neurogram was obtained considering only low frequencies information. The inclusion of low frequencies information provides better performance under noisy conditions [7]. Again, the proposed method showed a very consistent speaker identification accuracy across different types of noise.

It is to be noted that for SVM-based speaker modelling, MFCC-based method showed better identification results compared to those of GFCC-based system at all SNRs studied (could be due to the less number of support vectors in GFCC-based method). Another important point, the proposed method with low frequencies information (250 Hz to 1 kHz) provides improved performance compared to default system's performance which is studied in the study [7].

The performance shown in Fig. 3 implies that the proposed method was very robust to noises and can separate speakers successfully. The reason of the robustness could be the

application of all pole system i.e. linear prediction system in FDLP which can capture speaker distinguishing vocal production system information more accurately.

#### IV. CONCLUSION

A robust text-dependent speaker identification method has been presented in this paper based on a novel feature FDLP. This feature was derived from the all pole system using 2-D regressive model. The presented method's performances were tested in clean and noisy conditions. The introduced method's performance outperformed all alternative methods for all SNRs under noisy conditions and performance was comparable in clean. The proposed method also achieved a consistent pattern across different type of noises and provided very robust performance. This study results implicate that the proposed method can model human voice production system very accurately which is the cause of robustness of this presented method. The proposed method can also be applied in speech recognition, gender classification, and speaker recognition. The channel variation study could be an interesting topic for the proposed method.

#### ACKNOWLEDGEMENT

I would like to thanks to all anonymous reviewers for their helpful comments to make this study more acceptable.

#### REFERENCES

1. Togneri, R. and D. Pallella, *An overview of speaker identification: Accuracy and robustness issues*. Circuits and Systems Magazine, IEEE, 2011. **11**(2): p. 23-61.
2. Davis, S.B. and P. Mermelstein, *Comparison of parametric representations for monosyllabic word recognition in continuously spoken sentences*. Acoustics, Speech and Signal Processing, IEEE Transactions on, 1980. **28**(4): p. 357-366.
3. Makhoul, J., *Linear prediction: A tutorial review*. Proceedings of the IEEE, 1975. **63**(4): p. 561-580.
4. Li, Q., F.K. Soong, and O. Siohan. *A high-performance auditory feature for robust speech recognition*. in *Interspeech*. 2000.
5. Chi, T.-S., T.-H. Lin, and C.-C. Hsu, *Spectro-temporal modulation energy based mask for robust speaker identification*. The Journal of the Acoustical Society of America, 2012. **131**(5): p. EL368-EL374.
6. Zhao, Xiaojia, Yang Shao, and DeLiang Wang. "CASA-based robust speaker identification." *IEEE Transactions on Audio, Speech, and Language Processing* 20.5 (2012): 1608-1616.
7. Islam, Md Atiqul, Wissam A. Jassim, Ng Siew Cheok, and Muhammad Shamsul Arefeen Zilany. "A Robust Speaker Identification System Using the Responses from a Model of the Auditory Periphery." *PloS one* 11, no. 7 (2016): e0158520.
8. Ganapathy, S., S. Thomas, and H. Hermansky, *Feature extraction using 2-D autoregressive models for speaker recognition*. ISCA Speaker Odyssey, 2012.
9. Burges, Christopher JC. "A tutorial on support vector machines for pattern recognition." *Data mining and knowledge discovery* 2.2 (1998): 121-167.
10. Brookes M. Voicebox: Speech processing toolbox for matlab. Software, available [Mar 2011] from [www.ee.ic.ac.uk/hp/staff/dmb/voicebox/voicebox.html](http://www.ee.ic.ac.uk/hp/staff/dmb/voicebox/voicebox.html). 1997.
11. Ellis, D.P., *PLP and RASTA and MFCC and inversion in Matlab*. 2005.
12. Zilany, M.S., I.C. Bruce, and L.H. Carney, *Updated parameters and expanded simulation options for a model of the auditory periphery*. The Journal of the Acoustical Society of America, 2014. **135**(1): p. 283-286.
13. Chang C.-C. and C.-J. Lin, "LIBSVM: A Library for Support Vector Machines. *ACM Transactions on Intelligent Systems and Technology*, 2: 27: 1-27: 27, 2011," Software available at <http://www.csie.ntu.edu.tw/~cjlin/libsvm>, 2011.



# Automated Weather Event Analysis with Machine Learning

Nasimul Hasan<sup>1</sup>, Md. Taufeeq Uddin<sup>1</sup>, Nihad Karim Chowdhury<sup>2</sup>

<sup>1</sup> Department of Computer Science and Engineering, International Islamic University Chittagong, Bangladesh

<sup>2</sup> Department of Computer Science and Engineering, University of Chittagong, Bangladesh

nasimul\_hsn@yahoo.com, mohamed.taufeeq.uddin@gmail.com, nihadcu2@gmail.com

**Abstract**—Weather forecasting has numerous impacts in our daily life from cultivation to event planning. Previous weather forecasting models used the complicated blend of mathematical instruments which was insufficient in order to get higher classification rate. In contrast, simple analytical models are well-suited for weather forecasting tasks. In this work, we focus on the weather forecasting by means of classifying different weather events such as normal, rain, and fog by applying comprehensible C4.5 learning algorithm on weather and climate features. The C4.5 classifier classifies weather events by building the decision tree using information entropy from the set of training samples. We conducted experiments on LA weather history dataset; from evaluation results, it is revealed that C4.5 classifier classifies weather events with f-score of around 96.1%. This model also indicates that climate features such as rainfall, visibility, temperature, humidity, and wind speed are highly discriminative toward events classification.

**Keywords**—Weather Events, Forecasting, Machine Learning

## I. INTRODUCTION

The situation of weather plays a crucial role in almost every aspects of human life. Note that intelligent weather analysis techniques can help us to make efficient decisions that can lead us to save valuable lives, properties, and time. As a consequence, researchers focus on the automated analysis of weather and climate data such as forecasting rainfall, predicting air temperature to understand and to extract useful information. As modernization continued, prediction of weather events draws more attention. From the very beginning of civilization, people want to know the pattern of weather change. Discovering the weather pattern and forecasting weather has been a field of interest from the exploration of science and technology.

Weather forecasting involves foreseeing how the current situation with the air will change in which present climate conditions are taken by ground perceptions such as from boats, airplane, radiosondes, Doppler radar, and satellites. The collected data is then sent to meteorological focuses in which the information are gathered, analyzed, and made into an assortment of outlines, maps, and charts. Algorithms exchange a huge number of perceptions onto surface and upper air maps and draw the lines on the maps with assistance from meteorologists. Algorithms draw the maps as well as anticipate how the maps will look at some point later on. The

determination of climate condition using algorithms is outlined as numerical or computational climate forecasting [1].

Numerical or computational models for weather forecasting are the dynamic representations of the systems is being used in present days. These models discretize regions or bodies in a few measurements by separately utilizing estimated capacities to portray the behavior of the climatic variables of interest [2]. Nowadays, numerical or computational models are irreplaceable for atmosphere estimation. For instance, Bayesian networks [3] with time differed scaling features can be used to review whether there are factually noteworthy patterns in the climate information. In addition, Tae-wong [4] demonstrated a space-time model that displays the short time and geographical conditions of the day by day rain event.

Although there are several techniques available for weather forecasting, weather forecasting is actually a challenging task due to the complicated physics behind weather which depends on numerous features, and which is also boisterous and deterministically confusing natural event. Moreover, people produce numerous disasters, and change of climate or characteristics of climate such as air temperature, rainfall, dew point temperature, visibility, and humidity displays a strong role on the weather. Notice that several automated techniques including Artificial Neural Network (ANN), Support Vector Regressor (SVR), Genetic Algorithm (GA) were applied to forecast or model weather [5] [6] [7] [8], where ANN was the most commonly used technique that can forecast weather with decent performance rate.

In this paper, we apply comprehensible tree based learning algorithm, namely C4.5 [9] to classify the weather events as normal, rain, and fog using a set of 19 features e.g. minimum, maximum, and mean air temperature, dew point temperature, humidity, visibility, wind speed, sea level pressure, and total and highest rainfall that capture numerous information about climate and weather. Hence, C4.5 is a statistical classifier used to build a decision tree for classification in which C4.5 evaluates the goodness of a test using information theory-based formula choosing the test with the maximum amount of information from the set of examples. Note that the proposed C4.5 algorithm comprises of several good qualities including comprehensibility, pruning tree after construction, competitive computational performance both in training and prediction

steps, and capability to handle both continuous and discrete features, missing value features, and feature with different costs. In our experiments, we found that C4.5 classified three weather events e.g. normal, rain, and fog with f-score of **0.979**, **0.84**, and **0.845**, respectively, on LA weather history dataset [10]. To the best of our knowledge, this is the first time we apply C4.5 classifier for weather events classification task.

## II. RELATED WORK

Over the last few decades, researchers conducted a number of automated analyses on weather and climate data such as dew point temperature prediction using several Artificial Intelligence (AI) techniques from different sub-domains of AI including model output statistics, fuzzy logic, expert system, machine learning, and data mining. For instance, Chevalier et al. [11] trained SVR on small, and minimally pre-processed meteorological dataset to predict air temperature. Devi et al. [12] developed ANN based temperature forecasting model using real-time quantitative data about the current state of the atmosphere. Olaiya and Adeyemo [13] also investigated the performance of ANN and decision trees during the classification of maximum, minimum, and mean temperature, rainfall, evaporation, and wind speed on meteorological data gathered from Nigeria. Lin and Chen [8] designed typhoon rainfall forecasting model using ANN feeding eight typhoon characteristics and spatial rainfall information, where they found that excessive spatial rainfall information may not increase the generalization of the forecasting model. Mohammadi et al. [14] predicted the dew point temperature on the daily scale on different climate conditions applying extreme learning machine algorithm on five common climate-related features such as mean air temperature, relative humidity, atmospheric pressure, vapor pressure and horizontal global solar radiation.

As per our knowledge based on literature review, Awan and Awais's research [15] is the only similar study available in the literature that also attempted to predict weather events. In their research, they aimed to predict weather events based on fuzzy RBS method for Lahore, Pakistan. They used two different datasets of 365 examples with only 4 features, and 2500 examples with 17 features e.g. temperature, dew point, humidity, sea level, visibility, wind speed, respectively, for experimentation. They mentioned in their finding that fuzzy RBS method was sensitive to random sampling with replacement technique that was applied to produce training and test dataset. In contrary, we applied comprehensible tree-based machine learning algorithm for events classification for Los Angeles, California, the USA in which we used 5325 examples with 19 features extending the feature set to include rainfall information to build the weather events prediction model.

## III. LA WEATHER HISTORY DATASET

In this work, we used weather and climate data (LA weather history) [10] of 14 years from 2001 to 2015 of Los Angeles, California, USA, which is available at <http://www.wunderground.com/history/airport/KCQT/2015/1/1/CustomHistory.html>. LA weather history

dataset comprises of 19 weather and climate features, and weather events label that contains 3 different events or classes such as normal, rain, and fog. The comprised features of LA weather history dataset covers the following information [16] about weather and climate:

- **Temperature (°C)** has the impact in making the kind of precipitation that outcomes from the water vapor exchange in between the earth and air. LA weather history dataset contains three temperature features e.g. minimum, maximum, and mean temperature.
- **Dew point (°C)** determines the comfort level of feeling on a day that figures out if it will rain or snow. The saturation point is that temperature at that moisture (water vapor) within the air begins to condense. The hotter the air is, the more moisture it will hold. LA weather history dataset comprises three dew point features e.g. minimum, maximum, and mean dew points.
- **Humidity (%)** is just a consequence of the way that water exists at different rates in the water vapor in our climate. The surface temperature of the earth would be much cooler with no water vapor in the environment. LA weather history dataset includes three humidity features e.g. minimum, maximum, and mean humidities.
- **Sea level pressure (hPa)** is the air pressure at the sea level at the time of measuring at a given rise ashore. The station pressure adjusted to water level by considering that the temperature falls at a lapse rate of 6.5 thousand per kilometer within the fictive layer of air between the corresponding weather station and water level. LA weather history dataset contains three sea level pressure features e.g. minimum, maximum, and mean sea level pressure.
- **Visibility (m)** in meteorology is a measure of the distance at which an article or light can be obviously recognized. Visibility influences all types of movement including roads, sailing, and aviation. Meteorological visibility refers to the transparency of air in the dark, and it remains an equivalent as in daylight for a similar air. LA weather history dataset comprises three visibility features e.g. minimum, maximum, and mean visibilities.
- **Wind speed (km/h)** displays how quick the air is moving past a specific point. It gives a notion regarding the position of low and high-pressure territories. In the event that wind speed increases, it is a sign of fortification of pressure systems. It brings cool or hot air from the spot of root or from the spots through which they pass. LA weather history dataset includes three wind speed features e.g. minimum, maximum, and mean wind speed.
- **Rainfall (mm)** is an influential feature / predictor for weather forecasting that is a major component of climate that helps to continue ecosystem the way it should be. Cultivation depends mostly on rainfall and it is one of the richest sources of fresh water. LA weather history dataset contains two rainfall features e.g. maximum, and total rainfall.

#### IV. C4.5 FOR WEATHER EVENTS CLASSIFICATION

C4.5 [17] is a statistical classifier used to build a decision tree for classification. The key idea beneath C4.5 algorithm is that C4.5 creates decision trees using information entropy  $H$  from set of training samples e.g.  $S = s_1, s_2, \dots, s_n$  of pre-classified samples, where each sample  $s_i$  comprises of  $N$ -dimensional vector  $x_{1,i}, \dots, x_{N,i}$  in which  $x_j$  denotes feature of the sample and class in which  $s_i$  falls. At each node of the tree, C4.5 selects the feature that most effectively splits its set of samples into subsets using normalized information gain as splitting gain criteria. C4.5 makes a decision using the feature with highest information gain where information gain  $I_{Gain}$  is measured as follows.

$$I_{Gain}(Event, Feature) = H(Event) - H(Event|Feature) \quad (1)$$

where  $Event$  denotes weather event class, and  $Feature$  denotes available weather and climate features used in weather prediction model. Figure 1 shows a decision tree produced from C4.5 classifier on LA weather history dataset. The technical description of the C4.5 algorithm [18] is given in Algorithm 1.

---

#### Algorithm 1 C4.5 for weather events classification

---

- 1: Check for base cases
  - 2: **for** each feature  $f$  **do**
  - 3:   Compute normalized  $I_{Gain}$  ratio from splitting on  $f$
  - 4: **end for**
  - 5: Let  $f_{best}$  be the feature with maximum normalized  $I_{Gain}$
  - 6: Build decision node based on the splitting on  $f_{best}$
  - 7: Recurse on the sublists achieved via splits on  $f_{best}$ , and finally, include those node as children of node
  - 8: **return** decision trees
- 

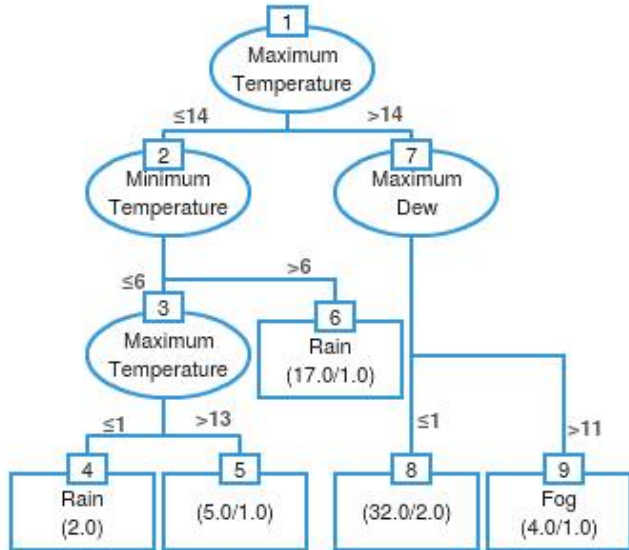


Fig. 1. An example decision tree generated by C4.5 classifier

#### V. EXPERIMENTS AND RESULTS

The proposed weather events classification model was evaluated on LA weather history dataset using J48, an open source implementation of C4.5 on Weka [19] data mining and machine learning tool, applying cross-fold validation e.g.  $5 - fold$ ,  $10 - fold$ ,  $20 - fold$ , and random splitting e.g.  $50\% - 50\%$ ,  $60\% - 40\%$ ,  $70\% - 30\%$  strategies. We benchmarked C4.5 classifier against classic learning algorithm naive Bayes, and displayed the comparison in Table I and II. Each of the experiments was run for 20 times with different random seeds, and the results were obtained by averaging over 20 different experimental runs. We produced accuracy, precision, recall, and f-score for each weather event class to demonstrate the performance of the models. The larger values of the performance metric accuracy, precision, recall, and f-score indicate the higher weather events classification performance.

Note that, we modeled the weather events prediction task as classification problem as we aimed to estimate the probable weather event using weather and climate features. Table I displays the performance of C4.5 and naive Bayes classifiers for multiple cross-fold validations and random splitting strategies, where Table II shows the performance of C4.5 and naive Bayes classifiers during the classification of three weather events e.g. normal, rain, and fog. From Table II, it can be indicated that C4.5 classifier was better than naive Bayes since C4.5 classified all three events with higher f-score than naive Bayes. More precisely, naive Bayes classified fog event with a low precision rate of 34.5%, and f-score rate of 49.9% that was extremely worst than the performance of C4.5 classifier. Another important point to note is that C4.5 basically confused fog and rain events with normal, and normal event with rain event, while naive Bayes widely confused fog event with both normal and rain events, and rain event with the normal event. According to the experimental results from Table II, we can outline that the proposed C4.5 classifier can efficiently classify each of the three weather events. Hence, C4.5 can be extensively utilized for weather event prediction or forecasting. In addition, C4.5 is extremely viable weather event classifier as the C4.5 classifier is comprehensible and interpretable, can deal with the over-fitting issue and may take care of persistent features.

The relative importance scores of weather and climate features in Table III were measured using C4.5 classifier with  $I_{Gain}$  ranking filter which investigate the relevance of a feature by measuring the  $I_{Gain}$  with respect to the weather event class. To measure the related importance score or rank of the available features, we trained the C4.5 classifier using LA weather history dataset with  $5 - fold$  cross validation method. It can be pointed out from feature importance measurements that total rainfall was more significant than maximum rainfall features. On the other hand, minimum visibility, and the high temperature had more influence than maximum or mean visibility, and minimum temperature, respectively. Furthermore, mean and minimum dew point features had an almost same

TABLE I  
WEATHER EVENTS CLASSIFICATION BENCHMARK. THIS TABLE DISPLAYS THE WEATHER EVENT CLASSIFICATION ACCURACY, GENERATED FROM NAIVE BAYES AND C4.5 ON LA WEATHER HISTORY DATASET

Models	Cross-fold validation					Random splitting				
	10-fold	20-fold	30-fold	40-fold	50-fold	50%-50%	60%-40%	70%-30%	80%-20%	90%-10%
Naive Bayes	0.9075	0.9069	0.9063	0.9067	0.9062	0.9161	0.9122	0.9075	0.9047	0.9188
C4.5	0.962	0.9626	0.9633	0.963	<b>0.9637</b>	0.946	0.949	0.9452	<b>0.9528</b>	0.9452

TABLE II  
WEATHER EVENTS CLASSIFICATION BENCHMARK. THIS TABLE DISPLAYS THE PRECISION, RECALL, F-SCORE, AND THEIR STANDARD DEVIATION (SD), FOR EACH WEATHER EVENT, GENERATED FROM NAIVE BAYES AND C4.5 ON LA WEATHER HISTORY DATASET. THE DISPLAYED RESULTS POINTS OUT THAT C4.5 CLASSIFIER IS COMPARATIVELY BETTER THAN NAIVE BAYES

Events	Naive Bayes						C4.5					
	Precision	Precision SD	Recall	Recall SD	F-score	F-score SD	Precision	Precision SD	Recall	Recall SD	F-score	F-score SD
Normal	<b>0.978</b>	0.00071	0.918	0.00141	0.947	0.00005	0.971	0.00003	<b>0.987</b>	0.00071	<b>0.979</b>	0.00002
Rain	0.733	0.00283	<b>0.824</b>	0.00283	0.776	0.00283	<b>0.874</b>	0.00212	0.809	0.00636	<b>0.84</b>	0.000283
Fog	0.345	0.00495	<b>0.906</b>	0.00495	0.499	0.00424	<b>0.98</b>	0.00002	0.742	0.00012	<b>0.845</b>	0.00005

level of importance, while high dew point feature comprised less importance than other two dew point features. Sea level features had less discriminative power towards classifying weather events in which minimum sea level feature contained more relevance than the maximum and mean sea level features.

TABLE III  
THIS TABLE DISPLAYS AVERAGE MERIT AND RANK OF EACH FEATURE OF LA WEATHER HISTORY DATASET, MEASURED VIA  $I_{GAIN}$  USING 5-FOLD CROSS VALIDATION STRATEGY

Feature	Average merit	Average rank
Total rainfall	0.39 ± 0.005	1 ± 0
Minimum visibility (Min vis)	0.226 ± 0.002	2 ± 0
Maximum temperature (Max temp)	0.139 ± 0.005	3 ± 0
Maximum humidity (Max hum)	0.089 ± 0.005	4.6 ± 0.8
Average visibility (Avg vis)	0.089 ± 0.001	4.6 ± 0.49
Average temperature (Avg temp)	0.084 ± 0.003	5.8 ± 0.4
Average humidity (Avg hum)	0.066 ± 0.003	7.4 ± 0.49
Average wind speed (Avg w speed)	0.064 ± 0.001	7.8 ± 0.75
Maximum rainfall (Max rainfall)	0.062 ± 0.003	8.8 ± 0.4
Minimum humidity (Min hum)	0.052 ± 0.005	10.8 ± 0.98
Average dew point (Avg dew)	0.05 ± 0.002	10.8 ± 0.75
Minimum dew point (Min dew)	0.048 ± 0.001	11.4 ± 0.49
Maximum wind speed (Max w speed)	0.044 ± 0.002	13.2 ± 0.4
Minimum temperature (Min temp)	0.044 ± 0.002	13.8 ± 0.4
Maximum dew point (Max dew)	0.034 ± 0.002	15 ± 0
Maximum visibility (Max vis)	0.028 ± 0.002	16 ± 0
Minimum sea pressure (Min sea pr)	0.019 ± 0.001	17.2 ± 0.4
Maximum sea pressure (Max sea pr)	0.018 ± 0.002	18.4 ± 0.49
Average sea pressure (Avg sea pr)	0.018 ± 0.001	18.4 ± 0.8

Figure 2 highlights the correlation among the weather and climate features analyzed in this study. The legend or the scale of figure 2 denotes the correlation scale, while X-axis and

Y-axis represent all available features. Recall that when the value of correlation between two features is 1, it indicates that there is a strong correlation between the two features, when the value of correlation between two features is -1, it indicates that there is a very weak correlation between the two features, and finally, when the correlation value between two features is 0 that indicates that there is no correlation between the two features. In our experimented feature set, there was strong correlation between air temperature and dew point, dew point and humidity, humidity, and temperature, temperature, and visibility, humidity and rainfall features. There is a significant correlation between wind speed and rainfall, visibility and humidity, humidity and wind speed, air temperature and rainfall features.

## VI. CONCLUSION AND FUTURE WORK

This paper we introduce C4.5 classifier in order to tackle the challenge of weather events classification such as normal, rain, and fog using weather and climate information. Our findings suggest that C4.5 classifier is able to predict different weather events with a very small error rate using a minimal number of weather and climate features. We also outline relevant and influential weather event features e.g. rainfall, visibility, temperature, wind speed, dew point computing their relative importance scores. In addition, feature correlation plot demonstrates that air temperature and dew point, dew point and humidity, humidity, and temperature, temperature, and visibility, humidity and rainfall are highly correlated. In our future work, we will include an extension of the weather event class to more complex events such as rain-fog, thunderstorm, rain-thunderstorm, tornado, rain-tornado, rain-thunderstorm-tornado, and fog-rain-thunderstorm. Next, the comparison of the proposed model with many other state-of-the-art techniques, and the validation of the proposed event

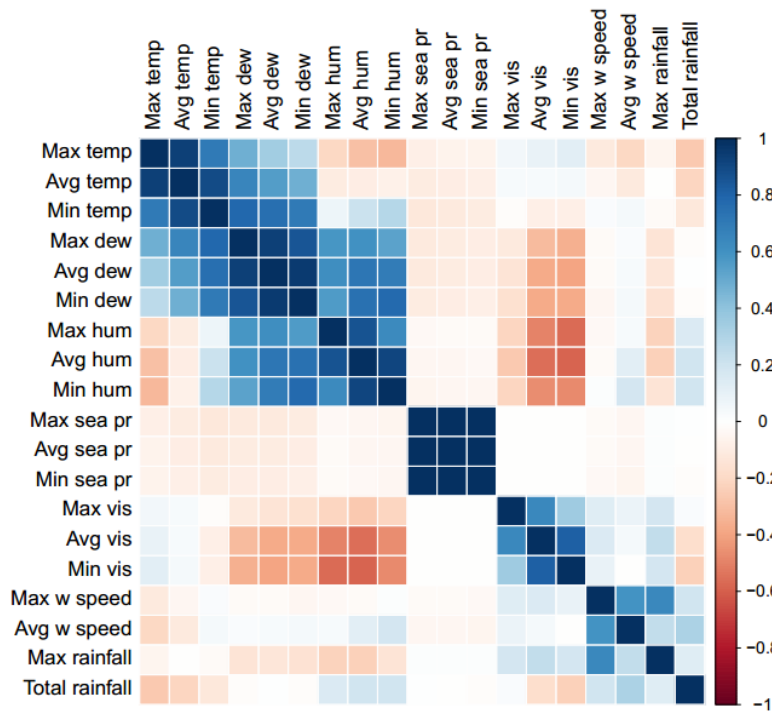


Fig. 2. Feature correlation plot of the investigated features on the LA weather history dataset

prediction model on more complex and unbalanced weather dataset with different climate conditions.

#### REFERENCES

- [1] F. Olaiya and A. B. Adeyemo, "Application of data mining techniques in weather prediction and climate change studies," *International Journal of Information Engineering and Electronic Business (IJIEEB)*, vol. 4.1, p. 51, 2012.
- [2] G. M. S.-Z. R. G.-G. De la Torre-Gea, Guillermo and E. Rico-García., "Bayesian networks for defining relationships among climate factors," *Int. J. Phys. Sci.*, vol. 6, no. 1, pp. 4412–4418.
- [3] C. H. Lima and U. Lall, "Spatial scaling in a changing climate: A hierarchical bayesian model for non-stationary multi-site annual maximum and monthly streamflow," *Journal of Hydrology*, vol. 383, no. 3, pp. 307–318, 2010.
- [4] T.-w. Kim, H. Ahn, G. Chung, and C. Yoo, "Stochastic multi-site generation of daily rainfall occurrence in south florida," *Stochastic Environmental Research and Risk Assessment*, vol. 22, no. 6, pp. 705–717, 2008.
- [5] J. Wu, L. Huang, and X. Pan, "A novel bayesian additive regression trees ensemble model based on linear regression and nonlinear regression for torrential rain forecasting," in *Computational Science and Optimization (CSO), 2010 Third International Joint Conference on*, vol. 2. IEEE, 2010, pp. 466–470.
- [6] A. Bautu and E. Bautu, "Meteorological data analysis and prediction by means of genetic programming," in *Proceedings of the 5th Workshop on Mathematical Modeling of Environmental and Life Sciences Problems Constanta, Romania*, 2006, pp. 35–42.
- [7] J. Wu and E. Chen, "A novel nonparametric regression ensemble for rainfall forecasting using particle swarm optimization technique coupled with artificial neural network," in *Advances in Neural Networks—ISNN 2009*. Springer, 2009, pp. 49–58.
- [8] G.-F. Lin and L.-H. Chen, "Application of an artificial neural network to typhoon rainfall forecasting," *Hydrological Processes*, vol. 19, no. 9, pp. 1825–1837, 2005.
- [9] J. R. Quinlan, *C4.5: Programs for Machine Learning*. San Francisco, CA, USA: Morgan Kaufmann Publishers Inc., 1993.
- [10] "La weather history dataset," Last Accessed: 23 January 2016. [Online]. Available: <http://www.wunderground.com/history/airport/KCQT/2015/1/1/CustomHistory.html>
- [11] R. F. Chevalier, G. Hoogenboom, R. W. McClendon, and J. A. Paz, "Support vector regression with reduced training sets for air temperature prediction: a comparison with artificial neural networks," *Neural Computing and Applications*, vol. 20, no. 1, pp. 151–159, 2011.
- [12] C. J. Devi, B. S. P. Reddy, K. V. Kumar, B. M. Reddy, and N. R. Nayak, "Ann approach for weather prediction using back propagation," *International Journal of Engineering Trends and Technology*, vol. 3, no. 1, 2012.
- [13] F. Olaiya and A. B. Adeyemo, "Application of data mining techniques in weather prediction and climate change studies," *International Journal of Information Engineering and Electronic Business (IJIEEB)*, vol. 4, no. 1, p. 51, 2012.
- [14] K. Mohammadi, S. Shamshirband, S. Motamedi, D. Petković, R. Hashim, and M. Gocic, "Extreme learning machine based prediction of daily dew point temperature," *Computers and Electronics in Agriculture*, vol. 117, pp. 214–225, 2015.
- [15] M. S. K. Awan and M. M. Awais, "Predicting weather events using fuzzy rule based system," *Applied Soft Computing*, vol. 11, no. 1, pp. 56–63, 2011.
- [16] G. De la Torre-Gea, G. M. Soto-Zarazúa, R. Guevara-González, and E. Rico-García, "Bayesian networks for defining relationships among climate factors," *Int. J. Phys. Sci.*, vol. 6, pp. 4412–4418, 2011.
- [17] X. Wu, V. Kumar, J. Ross Quinlan, J. Ghosh, Q. Yang, H. Motoda, G. J. McLachlan, A. Ng, B. Liu, P. S. Yu, Z.-H. Zhou, M. Steinbach, D. J. Hand, and D. Steinberg, "Top 10 algorithms in data mining," *Knowl. Inf. Syst.*, vol. 14, no. 1, pp. 1–37, Dec. 2007.
- [18] S. B. Kotsiantis, "Supervised machine learning: A review of classification techniques," in *Proceedings of the 2007 Conference on Emerging Artificial Intelligence Applications in Computer Engineering: Real World AI Systems with Applications in eHealth, HCI, Information Retrieval and Pervasive Technologies*. Amsterdam, The Netherlands, The Netherlands: IOS Press, 2007, pp. 3–24.
- [19] M. Hall, E. Frank, G. Holmes, B. Pfahringer, P. Reutemann, and I. H. Witten, "The weka data mining software: An update," *SIGKDD Explor. Newsl.*, vol. 11, no. 1, pp. 10–18, Nov. 2009. [Online]. Available: <http://doi.acm.org/10.1145/1656274.1656278>

# Bomb disposal Robot

## Discarding explosive through wireless controlled method

Abdul Kadir Bin Motaleb, Mohammad Busayeed  
Hoque

Dept. of Electrical & Electronic Engineering  
International Islamic University Chittagong (IIUC)  
Kumira, Chittagong, Bangladesh  
nabirctg@gmail.com, busayeed23@gmail.com

Md. Ahsanul Hoque

Dept. of Electrical & Electronic Engineering  
International Islamic University Chittagong (IIUC)  
Kumira, Chittagong, Bangladesh  
ahsan\_03@yahoo.com

**Abstract**— Bomb disposal robot has been developed by different experts around the world to make an affordable and safe device which will be useful for emergency rescue support. A 6 DOF articulated robotic arm mounted on a moveable base is been developed to help bomb disposal squad to dispose bomb safely from distance. The whole operation of the robot can be performed wirelessly from a computer. DC servo motor is used as actuator of the arm, and the servo is controlled by the PWM signal generated by microcontroller. This report is concerned with the mathematical modeling of a 6 DOF robotic arm along with the methodology of the entire prototype development. Architectural and circuitry development are separately deliberated. Lastly, the performance of the developed robot has been discussed.

**Keywords**—disposal, articulated, D-H parameter, kinematic, DOF

### I. INTRODUCTION

Human lives is becoming more dependent on robotics and the reason behind this is, robots can perform such daily activities with spectacular speed, precision and skill despite the level of difficulty. Robotics technology has already developed so much that, behavioral pattern of human being can be read by them and act according to fulfill that task while the person is not present there [1]. State of the art programming language is deployed on the robots and many advanced electronic devices are working along to increase efficiency in different activities performed by those robots instead of human [2].

Throughout the development in different field of robotics, life threatening task like disposing bomb has taken into consideration of research field. Two main aspects of development such robots like-disarmament of bomb with minor direct interaction of human to the bomb and saving crucial evidence of bomb material to trace technology, identifying the developer. Since different civil wars and recent terrorist attack around the world, it has become very risky to law enforcement department to disarm the bomb by hand. Those expert people who usually do this job, they also try to stay away as possible like other human being. A remote means is always required to observe and dispose the bomb. Therefore, robots are needed in many cases to aid the bomb disposal squads. This is the sole purpose of being involved to this project. A bomb disposal robot can save innumerable lives. It is faster, more maneuverable, better equipped with a

dexterity that could rival an explosive ordnance disposal technician operating in person.

### II. MODELING AND ARCHITECTURAL DEVELOPMENT

Mathematical modeling of any automated system is essential to realize & control and hence achieve the optimized output. Different parameters like manipulator, joint, end effector, actuator, controller, Degree of freedom (DOF) etc. has to be calculated to have optimal response of robot. Concurrently, the Denavit-Hartenberg parameters known as DH parameters have four parameters followed by specific convention to attach reference frames and spatial kinematic chain. The length of intersections between mutual joint is termed as Joint offset (b). Orthogonal projections and common normal angel to the joint axes symbolized as  $\theta$  called joint angle. The distance of common normal and axis called link length (a). Joint axes orthogonal projection to plane normal followed by common normal referred as twist angle ( $\alpha$ ) [7]. In this prototype, revolving joint referred as DH parameter joint variable and rest of the three parameters named link parameter are constant.

The prototype represented here has gone through mathematical modeling of different kinematics, preliminary structure analysis, software simulation of implemented circuit and finally hardware development [3,4,5]. In active part i.e. arm of the robot has five axis- one for the base, next bear/shoulder and last one elbow. All three were ensured to move the arm to the specific point and to feel the gripper action two minor axis incorporated like pitch & spin. Total six rotational joint considered in designs though in implementation it was taken to five because two joints that move the bear/shoulder rotate in unique direction. Fig.1 shows the preliminary design of axis and joints [6].

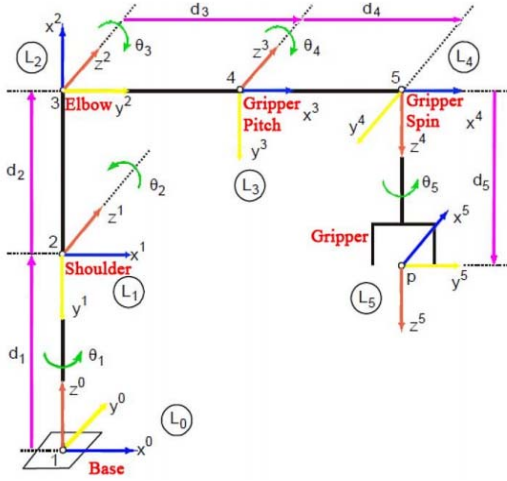


Fig. 1. Sample model for link axis & joints for prototype [8].

Let's take a look on the prototype manipulator where links are coupled by either rotational joints or prismatic joints. Here, base is named as link 0 and joint 1 connects base with link 1. Dimensional point of view like in fig. 2 shows  $i^{th}$  joint connected from  $i^{th}$  link to  $(i-1)$ . To evaluate the position and specific alignment of link  $i$  connection goes to adjacent link  $i-1$ . Overall, a system of frame written in Cartesian form like  $x_i y_i z_i$  is here to calculate all values. The arm parameter can be computed after a Cartesian frame  $x_i y_i z_i$  is assigned to the robot arm. Two parameters of the link  $i$  are the link length  $a_i$  and the twist angle  $\alpha_i$ . Two joint parameters are the joint angle  $\theta_i$  and the joint distance  $d_i$  as shown in Fig. 2.

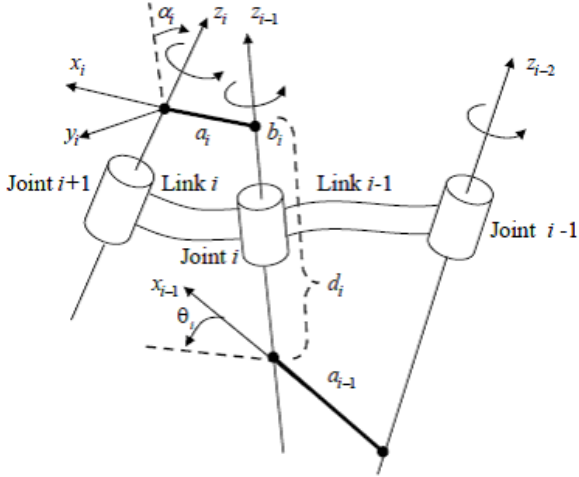


Fig. 2. D-H parameter frame of prototype [9].

To construct frame assignment a transformation matrix which is homogeneous is formed and hence, arm parameter calculated. Now, a frame like  $x_{i-1} y_{i-1} z_{i-1}$  to  $x_i y_i z_i$  can be found following these steps:

- i. Rotation of the frame  $x_{i-1} y_{i-1} z_{i-1}$  about the  $z_{i-1}$ .

$$\text{Rot}(z, \theta_i) = \begin{bmatrix} \cos \theta_i & -\sin \theta_i & 0 & 0 \\ \sin \theta_i & \cos \theta_i & 0 & 0 \\ 0 & 0 & 1 & 0 \\ 0 & 0 & 0 & 1 \end{bmatrix} \quad (1)$$

- ii. Translation of the frame  $x_{i-1} y_{i-1} z_{i-1}$  along the  $z_{i-1}$  axis by  $d_i$  units

$$\text{Trans}(z, d_i) = \begin{bmatrix} 1 & 0 & 0 & 0 \\ 0 & 1 & 0 & 0 \\ 0 & 0 & 1 & d_i \\ 0 & 0 & 0 & 1 \end{bmatrix} \quad (2)$$

- iii. Translation of the frame  $x_{i-1} y_{i-1} z_{i-1}$  along the  $x_i$  axis by  $a_i$  units

$$\text{Trans}(x, a_i) = \begin{bmatrix} 1 & 0 & 0 & a_i \\ 0 & 1 & 0 & 0 \\ 0 & 0 & 1 & 0 \\ 0 & 0 & 0 & 1 \end{bmatrix} \quad (3)$$

- iv. Translation of the frame  $x_{i-1} y_{i-1} z_{i-1}$  along the  $x_i$  axis by  $\alpha_i$  units

$$\text{Rot}(x, \alpha_i) = \begin{bmatrix} 1 & 0 & 0 & 0 \\ 0 & \cos \alpha_i & -\sin \alpha_i & 0 \\ 0 & \sin \alpha_i & \cos \alpha_i & 0 \\ 0 & 0 & 0 & 1 \end{bmatrix} \quad (4)$$

The transformation matrix for each joint can be calculated as:

$$H_{i-1}^i = \text{Rot}(z, \theta_i) \text{Trans}(z, d_i) \text{Trans}(x, a_i) \text{Rot}(x, \alpha_i)$$

D-H transformation matrix from the frame  $x_{i-1} y_{i-1} z_{i-1}$  to the frame  $x_i y_i z_i$  can be calculated by using post multiplication rule. The result is as follows:

$$H_{i-1}^i = \begin{bmatrix} \cos \theta_i & -\cos \theta_i \sin \alpha_i & \sin \theta_i \sin \alpha_i & a_i \cos \theta_i \\ \sin \theta_i & \cos \theta_i \sin \alpha_i & -\sin \theta_i \sin \alpha_i & a_i \sin \theta_i \\ 0 & \sin \alpha_i & \cos \alpha_i & d_i \\ 0 & 0 & 0 & 1 \end{bmatrix} \quad (5)$$

Frame movement & direction compare to base frame evaluated by the matrix:

$$H^n_0 = H^1_0 H^2_1 H^3_2 \dots H^n_{n-1} \quad (6)$$

The transformation matrix  $H^n_0$  can be expressed as follows:

$$H^n_0 = \begin{bmatrix} n & s & a & p \\ 0 & 0 & 0 & 1 \end{bmatrix} = \begin{bmatrix} n_x & s_x & a_x & p_x \\ n_y & s_y & a_y & p_y \\ n_z & s_z & a_z & p_z \\ 0 & 0 & 0 & 1 \end{bmatrix} \quad (7)$$

In this matrix, there are two vector's named approach vector and sliding vector signed as "a" & "s" respectively. Normal to those position a vector "n" and position vector "P" pointed to base from origin of frame [8].

#### A. Construction of the Kinematic Structure

The structure of the robot is built with combination of light weight steel plates and aluminum made servo brackets. Steel structure makes the prototype to carry out extra weight and make a balance of joints. At the bottom of the robot, arm is fastening so that if there is heavy weight or something then system can have an equilibrium position to work smoothly. Because, while grabbing a bomb and make necessary movement can make system out of balance. Servo motors was placed to do required shift with possible flexibility. The advantage of the servos is that they can be programmed to return to their initial position. A simple kinematic structure is shown in Fig.3.

**B. Hardware development**

The hardware is actually divide into two different segment, the transmitter section (see Fig. 4) and the receiver section (see Fig. 5). The transmitting section is adjacent to the computer, connected with pc using a USB cable. And the receiving section is into the robot vehicle. The transmitter panel is constructed with two microcontroller and a RF transmitter. And the receiving section, which is the core of the robot is consist two microcontroller, one de-multiplexer, one H-bridge DC motor driver and a RF receiver.

The USB interfacing of the transmitter board with computer is done by the PIC18F4550 microcontroller, which receives codes through USB buffer sent by the computer GUI application. This microcontroller then sends the code to other microcontroller which is PIC16f877 through I/O pin. The second microcontroller then convert the code to serial data from parallel data using its USART feature and pass the code the receiving end microcontroller through RF transmitter (see Fig. 4). The receiving-end micro controllers run by very low frequency crystal oscillator so that it can generate 50Hz PWM for the servo.

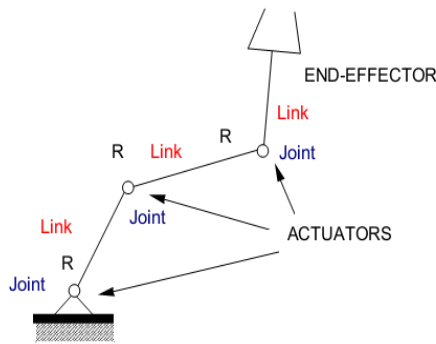


Fig.3. A kinematic structure with three revolute joints

So the transmitting end microcontroller has to run by same low value crystal oscillator so that it can make synchronous communication with the receiver. But for making USB communication with computer a microcontroller must have to run by a much higher than that crystal oscillator. Thus two different microcontrollers of two different frequencies have been used in transmitter board.

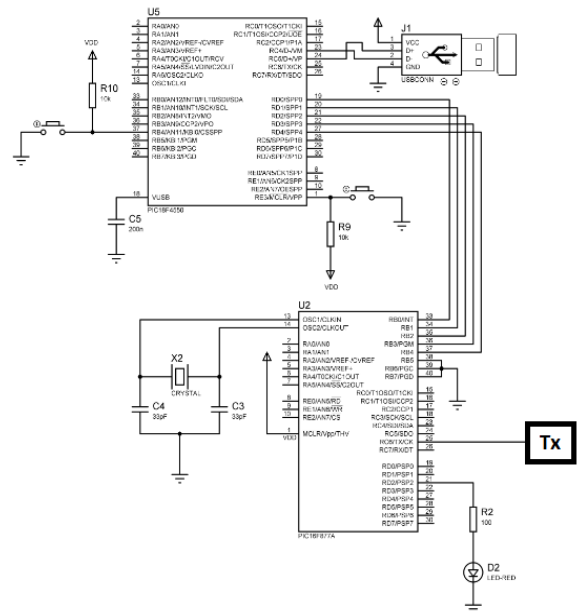


Fig.4. Circuit diagram of transmitting end.

The receiving end micro controller PIC16f877 convert the transmitted code to parallel data from serial data after receiving it through RF receiver. Each valid code has an assigned task to execute, such as driving the servo motor by increasing or decreasing the duty cycle of the PWM, or driving the dc motor.

The DC motors are driven by H-Bridge IC L293D which is controlled by the main microcontroller PIC16f877. And the Servo motors are directly controlled by PWM signal generated by microcontroller. Servo changes its shaft position with the change of the duty cycle of the PWM signal. So, two different codes is been sent from transmitter to receiver for each servo to rotate its shaft in either direction. One code causes the increment of the duty cycle, and other causes the decrement of the duty cycle of the PWM signal. Thus, there are total 12 different valid codes that can be sent from the transmitter to control all 6 servos of the arm. To move the base of the robot to forward, backward, left and right direction, 4 more unique codes is sent. The receiving unit will not react to any signal, unless any of these 16 codes is received.



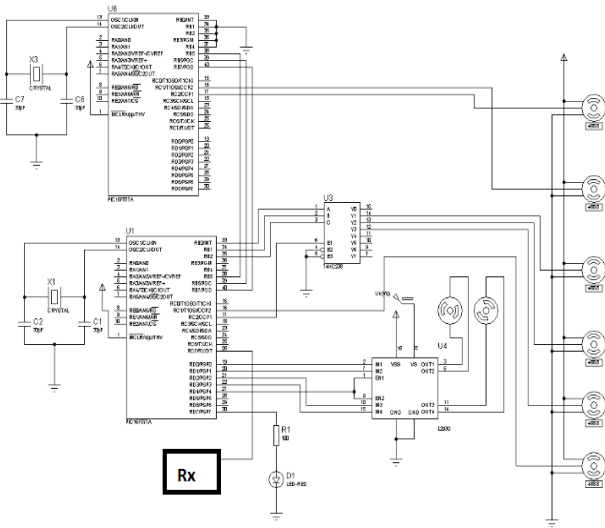


Fig.5. Circuit diagram of receiving end.

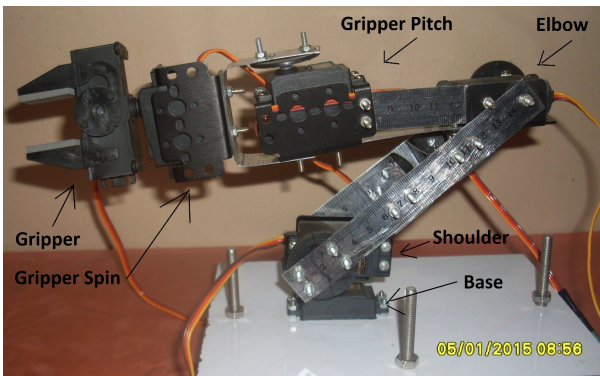


Fig.6. Implemented prototype receiving end.

Developed prototype of bomb disposal robot arm is shown in Fig. 6. The mechanical parts is designed by choosing aluminum because it strong and light material compare to other material. Aluminum is difficult to break due to its quality. On the other hand, Aluminum material also easily to find and the price is cheap. The power, torque and size of the servo motors can affect the dimensions.

### III. PERFORMANCE ANALYSIS

To analyze the disposal robot performance, ideal scenario is expected to anyone. That means, a simple bomb has to be placed within certain time limit and robot has to approach that spot, observe the wiring structure and dispose it before explosion. But here some parameter has been defined to analyze performance like-Target reaching: The ability of the end-effector of the arm to reach a specific point is not so precise but still satisfying. The reason behind it is the low resolution of generated PWM signal. As the increment or decrement gap of duty cycle of PWM is not so little, the servo shaft cannot move smoothly from 0 to 180 degree. Load lifting ability: The gripper of the arm can drag something and pull it up. From our calculation in chapter 3, we got that the excess torque available in shoulder is 5.45 kg-cm. Now since the arm is 25cm long, so the arm can lift an object of maximum 218g. Over that range, the servo used in shoulder starts to draw very

excessive current which may burn it. Arm Response at Various loads: The developed robotic arm has undergone a weight lifting test, where applied force on the end-effector was increasing by varying the weight of the object hold by the gripper. The state of the Arm is shown in Fig. 7.

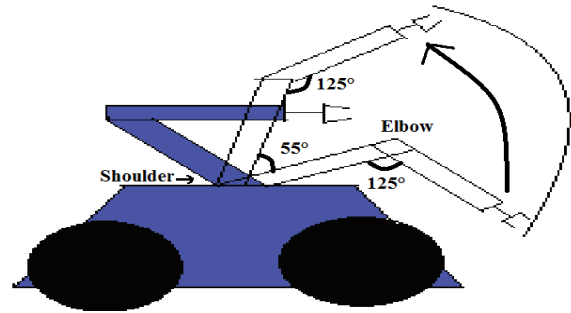


Fig.7. Weight lifting test arrangement.

The angle between shoulder link and elbow link was remaining fixed at 125°, while the shoulder link moved 55° up to complete a trajectory. The recorded value is shown in Table I. Here, worth to mention that the servos were powered by a 6V DC battery during the test. If the applied voltage reduced to 5V DC, then time required to complete that trajectory will be increase.

TABLE I. MEASURED VALUES OF THE WEIGHT LIFTING TEST.

Applied Weight on End-Effector (gram)	Time elapsed to move up 55° (mili sec.)	Total current consumption of the system (A)
0	850	0.693
25	850	0.709
55	900	0.793
80	1000	0.824
100	1150	0.855
140	1450	1.08
180	1750	1.29
210	2000	1.48
220(Dead Load)	Failed to lift	1.80

### IV. LIMITATION OF PROTOTYPE

As a prototype, this disposal robot shows bit of good performance in terms of signal transmission and reception, weight lifting, twisting over wide range of angle etc. Despite of these advantages there are few things need to mention as limitation of prototype-PWM Resolution: The PWM control signal of servo motor which is generated by 8-bit microcontroller PIC16f877 is of very low resolution. The servo motor used in this project rotates from 0 degree to 180 degree with the changing of the duty cycle of the PWM from 10% to 20%. But microcontroller can produce very few value of duty cycle between that ranges. As a result, servo cannot

rotate smoothly from 0 to 180 degree. It jumps from one position to other position with keeping gap of at least 8 degrees. If microcontroller of higher bit say 16 or 32 bit can be used then this problem will be compensated. Single channel communication: The transmitter can send only one command to the receiver at a time. So, two different movements of servo cannot be done at the same time. For example, if the shoulder of the starts to enlarge the all other joint will remain halt at that time.

#### V. CONCLUSION

Disposing a bomb quite a challenging job to military & law enforcement agency worldwide and that why bomb disposal robot demand will increase day by day. This prototype has few limitations in practical point of view, but improvement in design, dexterity, DOF can enhance the chance to implement in real life application.

#### REFERENCES

- [1] Lin, I. H., Liu, C. Y., Chen, L. C., "Evaluation of Human-Robot Arm Movement Imitation", Proceedings of 8th Asian Control Conference (ASCC), pp.287-292, 2011.
- [2] Nikku, S., "Introduction to Robotics" USA: John Wiley & Sons, 2011.
- [3] Manjunath, T. C., "Kinematic Modeling and Maneuvering of A 5-Axis Articulate Robot Arm", world academy of science, engineering and technology, pp.363-369, 2007.
- [4] Nones, Y. A., "Heterogeneous Modeling & Design of a Robot Arm Control System", Illinois Tech Robotics (ITR), pp.1-6, 2003.
- [5] Hpande, V. D.; George, P.M., "Kinematic Modelling and Analysis of 5 DOF Robotic Arm", International Journal of Robotics Research and Development (IJRRD), Vol.4, pp.17-24, 2014.
- [6] Park, I. D., Park, C., Do, H., Choi, T., Kyung, J., "Design and Analysis of Dual Arm Robot Using Dynamic Simulation" IEEE 10th International Conference on Ubiquitous Robots and Ambient Intelligence (URAI), pp. 681-682,2013
- [7]. A. Srikant, Y. Ravitnej, V. Sivaraviteja, V. Sreechand, "Kinematic Analysis and simulation of 6 D.O.F of robot for industrial Application", International Journal of Engineering & Science, Vol. 3, Issue 8, pp 1-4, September2013.
- [8]. A. Faravar, "Design, Implementation and Control of Robotic arm using PIC16F877A microcontroller," Masters dissertation, Dept. of Computer Engineering, Eastern Mediterranean University, Gazimağusa, North Cyprus,2014.
- [9]. M.R.B. Tarmizi, "Design and implementation of 6 DOF revolute robot using Fuzzy PID controller," Masters dissertation, Dept. of Electrical Engineering, Universiti Tun Hussein Onn Malaysia, Parit Raja, Johor, Malaysia,2014.

# Structural, Dielectric and Conductivity Studies of Ni-Cu-Cd Ferrite Nanoparticles

M. Arifuzzaman<sup>a,b,\*</sup>, M.J. Abden<sup>a</sup>

<sup>a</sup>Department of Electrical and Electronic Engineering  
International Islamic University Chittagong  
Chittagong-4314, Bangladesh

\*Corresponding author. *Email:* arifphy\_uzzaman@yahoo.com

S. K. Ahmed<sup>b</sup>, M. Belal Hossen<sup>b</sup>

<sup>b</sup>Department of Physics  
Chittagong University of Engineering and Technology  
Chittagong-4349, Bangladesh

**Abstract** - In this study, the nanoparticles (NPs) of  $\text{Ni}_{0.6}\text{Cu}_{0.1}\text{Cd}_{0.3}\text{Fe}_2\text{O}_4$  (NCCF) ferrite were successfully synthesized by sol-gel auto combusted process. The effects of temperature and size on the structural, dielectric and conductivity properties of NCCF ferrite nanoparticles were investigated. X-ray diffraction (XRD) analysis of the NPs annealed at 550 and 700 °C displayed the single phase cubic spinel structure with the particle size of 11 and 17 nm, respectively. The surface morphology of the annealed NCCF ferrite nanoparticles was studied by using Field emission scanning electron microscopy (FESEM). Dielectric constant of larger particles shows higher values at low frequency as well as lower dielectric loss tangent. ac conductivity shows conventional trend with size effects.

**Keywords**—Sol gel process, NCCF ferrite nanoparticles, dielectric properties, ac conductivity.

## I. INTRODUCTION

Nanocrystalline forms of ferrites are being considered as most significant materials in the scientific point of view owing to their wide range uses including high frequency devices and biomedical applications. Ferrite nanoparticle display better dielectric properties because of their size and surface effects which remarkably reduce the formation of Maxwell-Wagner interfacial polarization and dielectric loss tangent [1] and their properties can be defended by various things, such as preparation circumstances, heat treatment, microstructure, substituent or dopants and the synthesis techniques. Spinel ferrite nanoparticles have gained great attraction from researchers owing to their extensive applications in various sectors, like as microwave gripping equipments, aerial stick, computer elements, magnetic recording media, drug delivery, cancer cure, hyperthermia treatment and magnetic resonance imaging [2, 3]. Nickel based spinel ferrites are becoming the subject of interest mainly due to their high-frequency applications.

In comparison with bulk materials, ferrite nanoparticles display excellent physical, electric and dielectric properties. These nanoparticles are composed of low resistive grains alienated by high resistive grain boundaries and low resistive grain contribution decreases due to the increase of the volume ratio between grain and grain boundary. The dielectric behavior of ferrite particles are influenced significantly by this hetero-structure of the materials [4] and it is important to get low dielectric losses for the fabrication of high frequency devices. Although the magnetic properties of nickel based ferrites have already been explored, the electrical and dielectric

properties are rarely reported. The structural and electromagnetic properties of Cd containing Ni-ferrites were studied by Nath et al. [5]. Belavi et al. [6] also investigated  $\text{Ni}_{0.95-x}\text{Cd}_x\text{Cu}_{0.05}\text{Fe}_2\text{O}_4$  and reported that saturation magnetization ( $M_s$ ) increased with Cd substitution up to  $x = 0.3$ . Batoo et al. [7] synthesized single-phase  $\text{Ni}_{0.2}\text{Cd}_{0.3}\text{Fe}_{2.5-x}\text{Al}_x\text{O}_4$  nanoparticles successfully through sol-gel technique. To the best of author's knowledge, the size dependent electric and dielectric properties of NCCF ferrite nanoparticles were not explored earlier. Hence, the aim of the present work is to study the structural, dielectric and electric behaviors of NCCF ferrite nanoparticles for high frequency applications.

## II. MATERIALS AND METHOD

### A. Synthesis of NCCF Ferrite Nanoparticles

The  $\text{Ni}_{0.6}\text{Cu}_{0.1}\text{Cd}_{0.3}\text{Fe}_2\text{O}_4$  nanoparticles were synthesized by sol gel auto combusted technique. The stoichiometric mixtures of  $\text{Ni}(\text{NO}_3)_2 \cdot 6\text{H}_2\text{O}$ ,  $\text{Cu}(\text{NO}_3)_2 \cdot 3\text{H}_2\text{O}$ ,  $\text{Cd}(\text{NO}_3)_2 \cdot 4\text{H}_2\text{O}$ ,  $\text{Fe}(\text{NO}_3)_3 \cdot 9\text{H}_2\text{O}$  were dissolved into deionized water (DI) and a few drops of ethanol were added the mixtures to make homogeneous solution. A magnetic stirrer was used to stir the solution continuously at constant temperature of 70 °C until the gel was formed and required amount of liquid ammonia was used to maintain pH value of the mixtures fixed at 7. The resulted gel was then heated at 200 °C for 5 h and self-ignition occurred to burn out it into fluffy powder form. Afterwards, the fluffy powder was annealed at 500 and 700 °C for 5 h to eliminate any raw materials present in the composition and finally the NCCF ferrite nanoparticles of two different sizes were formed. The resultant powders were then ground to make them nanopowders and pressed into disc shaped without any binders. The both side of the discs was coated with silver paste to make them desired parallel plate capacitor geometry for characterizations. The synthesized samples were then used to study their structural, dielectric and ac conductivity properties.

### B. Characterization

The X-ray diffractometer (Philips X'Pert PRO XRD system) with  $\text{K}\alpha$  radiation ( $\lambda=0.154$  nm) was used to determine the phase of the prepared samples. To detect the diffracted X-rays, an electronic detector was placed on opposite side of the samples from the X-ray tube and X-ray data were recorded over a  $2\theta$  range of 15–60° using a step size 0.01° in units of counts/sec which were sent to the attached computer. The  $2\theta$  for each diffraction peak was then converted to d-spacing, using the Bragg's law;  $n\lambda = 2d\sin\theta$  and the lattice

parameter of the synthesized ferrite sample was calculated using the following equation

$$a = d_{hkl} \sqrt{(h^2 + k^2 + l^2)} \quad (1)$$

The morphology of NCCF ferrite nanoparticles was carried out by using FESEM (JEOL JSM-7600F, Japan). As the samples were non-conducting, a thin layer of platinum was coated using a sputter coater to get clear images. The average grain sizes of the samples were determined using the linear-intercept method from FESEM nanographs.

The complex dielectric constant was analyzed using Wayne Kerr Impedance Analyzer (6500B) by two probe method over frequency range 20 Hz to 15 MHz. The real part of di-electric constant is estimated by

$$\epsilon' = C_p t / \epsilon_0 A \quad (2)$$

where  $\epsilon_0$  is the permittivity of free space with value of  $8.854 \times 10^{-12}$  F/m,  $t$  is the thickness of the pellet,  $C_p$  is the capacitance of the pellet and  $A$  is the area of cross section of the pellet. The dielectric loss can be determined by imaginary part

$$\epsilon'' = \epsilon' \tan \delta \quad (3)$$

Here  $\tan \delta$  is the dielectric loss tangent.

The ac conductivity of the NPs is measured by the equation

$$\sigma_{ac} = \epsilon' \epsilon_0 \omega \tan \delta \quad (4)$$

where  $\omega$  is the angular frequency.

### III. RESULTS AND DISCUSSION

#### A. X-ray Diffraction Analysis

Fig. 1 shows XRD pattern of  $\text{Ni}_{0.6}\text{Cu}_{0.1}\text{Cd}_{0.3}\text{Fe}_2\text{O}_4$  ferrites annealed at both 550 and 700 °C using sol-gel method. The studied sample exhibits fundamental reflections coming from different crystal planes of (220), (311), (222), (400), (422), (511) and (440) with showing no secondary picks, thereby confirming the single phase cubic spinel structure of the composition. The well-defined diffraction peaks are observed

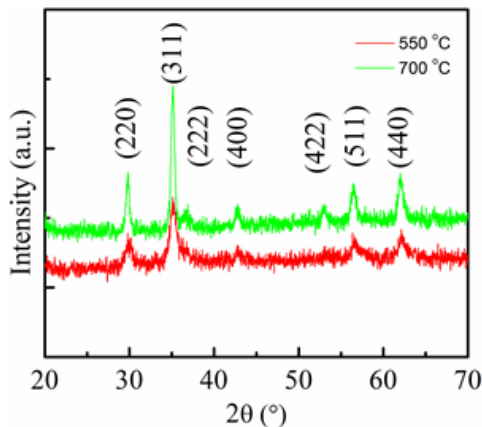


Fig. 1 XRD patterns of NCCF ferrite nanoparticles annealed at 550 and 700 °C, respectively.

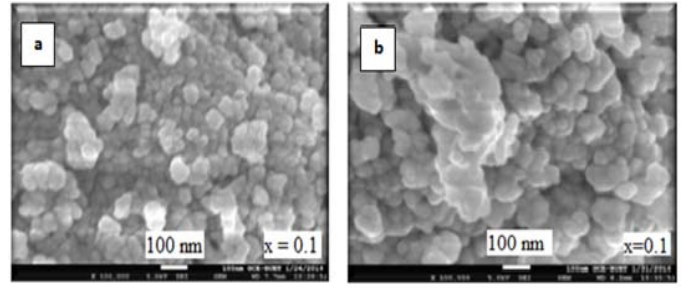


Fig. 2 FESEM nanographs of NCCF ferrite nanoparticles annealed at temperatures (a) 550 and (b) 700 °C, respectively.

in Fig. 1 and the peaks' position in XRD patterns match well with the literature value [8]. It is clearly visible that the diffraction peaks get sharper and wider nature at higher annealing temperature means that enhancing the crystallinity of ferrite nano powders. The narrow size distribution of the nanocrystalline ferrites is confirmed by broadness of the diffraction peaks. The most intense diffraction peak (3 1 1) of XRD patterns is used to estimate the average crystallite size of the ferrite composition using Scherrer formula [9]. The average crystallite size of NCCF ferrite nanoparticles annealed at 550 and 700 °C are 11 and 17 nm, respectively. The lattice constant was calculated using equation (1), where  $d_{hkl}$  is the observed inter-planar spacing for  $(h k l)$  planes and they were calculated from the diffraction peaks using Bragg's law. It can be observed that the lattice constant lies in the nano scale range i.e., 0.845 and 0.847 nm at 550 and 700 °C, respectively. The lattice constant is found to be increased a little bit with increasing the temperature, may be due to the structural stability factor of the crystal as well as the ionic radius variation of  $\text{Ni}^{2+}$  (0.0069 nm) and  $\text{Cu}^{2+}$  (0.072 nm).

#### B. Surface Morphology and Nanostructure

Fig. 2 shows the FESEM nanographs of the NPs annealed at temperatures 550 and 700 °C, respectively. From Fig. 2, it can be observed that the formation of spherical shaped grains separated by grain boundaries illustrating narrow size distribution. The average grain size values of ferrite nanoparticles annealed at 550 and 700 °C are 13 and 20 nm, which are very similar to the average crystallite sizes (11 and 17 nm) measured from XRD data. The particles' size increases a little bit with increasing temperature since thermal energy enhances the grain growth.

#### C. Dielectric Studies

The change in complex dielectric constant of NPs annealed at both 550 and 700 °C with frequency is illustrated in Fig. 3. It can be seen that both  $\epsilon'$  and  $\epsilon''$  exhibited usual dispersion behavior in the lower frequency region (20 Hz-1 kHz) whereas they decrease very slowly in the frequency domain (1 kHz-1 MHz) and thereafter they become almost frequency independent at both temperatures. The  $\epsilon'$  shows higher values slightly than that of  $\epsilon''$  which gives the indication of having low dielectric loss and it is crucial for selecting materials for fabricating devices. In the low frequency side, the dominance of  $\epsilon'$  is due to the contribution of interfacial polarization which is supported by Maxwell-Wagner's space charge polarization in accordance with Koop's phenomenological theory [10]. The

maximum values of dielectric constant are found at low frequencies because of availability of space charge polarization at the grain boundaries. The dielectric constant decrease very slowly after 10 kHz and become almost frequency independent beyond 1 MHz. This may be due to the fact that disappear of space charge polarization at higher frequencies i.e., the frequency of electron exchange between the ferrous and ferric ions cannot follow the alternating field. The effects of temperature also play a significant role for variation in dielectric values depending on space charge polarization. Hence, accommodation of charge carrier decreases which reduces the dielectric constant. The possible reasons for showing higher values of dielectric constant at lower frequency regime also include the predominance of  $Fe^{2+}$  ions, interfacial dislocation pile ups, oxygen vacancies, grain boundaries and defects [11].

The change in dielectric loss tangent ( $\tan\delta$ ) of NCCF nanoparticles at 550 and 700 °C with varying frequency is illustrated in Fig. 4. From this Fig. 4, it is apparent that the  $\tan\delta$  exhibited higher values in the lower frequency zone than that of high frequency zone exhibiting the peaking behavior. According to Rezlescu model, if the frequencies of hopping charge carriers exactly equal to the frequency of the applied frequency, a maximum in  $\tan\delta$  is appeared showing peaks. In both case the  $\tan\delta$  is found to be very low at higher frequencies and with increasing the size of NPs the  $\tan\delta$  goes down. This property makes them ideal for high frequency applications. The  $\tan\delta$  increases at low frequency region because of the phase lags between the applied field frequency and natural hopping frequency. The  $\tan\delta$  shows little lower values for larger size NPs synthesized at higher temperature due to hopping frequency cannot follow the applied field exactly and there exists the lag between them.

#### D. AC Conductivity Study

Fig. 5 shows the change in  $\sigma_{ac}$  with respect to the frequency ranging from 20 Hz to 15 MHz at room temperature. The  $\sigma_{ac}$  is found to be increased with frequency for both temperatures. The rate of hopping electrons between ferrous and ferric ions increases with increasing the applied frequency which ultimately increases the ac conductivity [10]. While the conductivity in higher frequency side is due to conduction through grains the  $\sigma_{ac}$  in the lower frequency domain is responsible for conduction through grain boundaries. The conduction mechanism occurs predominantly due to the grains contribution at higher frequencies.

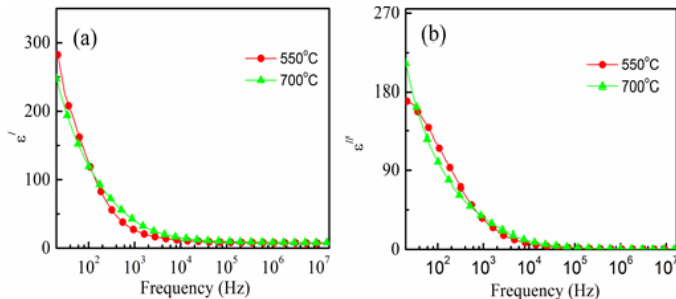


Fig. 3 Variation of (a)  $\epsilon'$  and (b)  $\epsilon''$  of NCCF ferrite nanoparticles annealed at 550 and 700 °C, respectively.

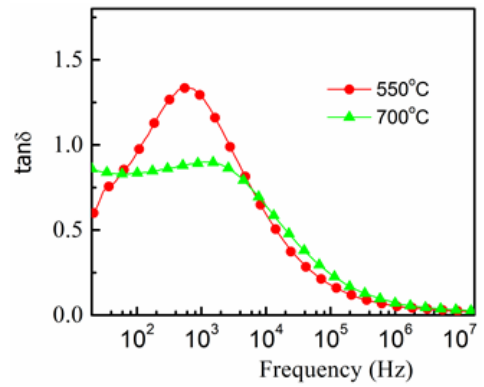


Fig. 4 Variation of  $\tan\delta$  in NCCF ferrite nanoparticles annealed at 550 and 700°C, respectively.

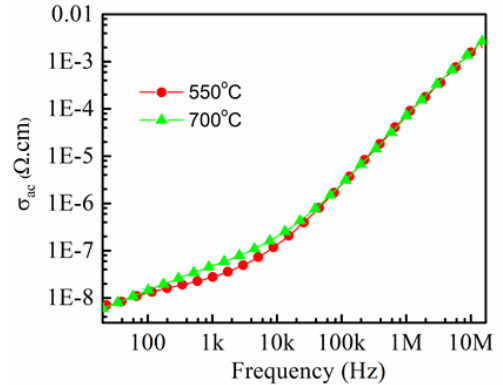


Fig. 5 Variation in ac conductivity of NCCF ferrite nanoparticles annealed at 550 and 700 °C, respectively

#### IV. CONCLUSIONS

The sol-gel auto combusted method was used for the synthesis of NCCF ferrite nanoparticles without adding any reagents. The particle size obtained from XRD analysis lies in the nano scale range of 11 and 17 nm with at 550 and 700 °C, respectively. The crystallite size increases slightly at higher annealing temperature. The increase trend of ac conductivity with applying frequency occurs due to the translation from a long range to the short range charge motion and the conduction takes place predominantly through the grains at higher frequencies. The dielectric loss and dielectric loss tangent values are found to be very low which makes the studied NCCF ferrite nanoparticles suitable for high frequency applications.

#### ACKNOWLEDGMENT

The present study was supported by CHSR, Chittagong University of Engineering and Technology (CUET), Chittagong-4349, Bangladesh. Two authors Md. Arifuzzaman and S.K. Ahmed would grateful to the Centre of Excellence in Nanomaterials research division, Department of Physics, CUET, Chittagong, Bangladesh.

#### REFERENCES

- [1] M. Guyot, DC and low frequency conductivity of Ni-ferrite and influence of microstructure, J. Magn. Magn. Mater., **15-18** (1980) 925-926.

- [2] D. Cruickshank, 1–2 GHz dielectrics and ferrites: overview and perspectives, *J. Eur. Ceram. Soc.*, **23** (2003) 2721-2726.
- [3] M.A. Ahmed, S.T. Bishay, The role of  $Dy^{3+}$  ions and sintering temperature on the magnetic characterization of Li-Co-Ferrite, *J. Magn. Mater.*, **279** (2004) 178-183.
- [4] V.K. Lakhani, B. Zhao, L. Wang, U.N. Trivedi, K.B. Modi, Negative magnetization, magnetic anisotropy and magnetic ordering studies on  $Al^{3+}$ -substituted copper ferrite, *J. Alloys. Compd.*, **509** (2011) 4861-4867.
- [5] S.K. Nath, K.H. Maria, S. Noor, S.S. Sikder, S.M. Hoque, M.A. Hakim, Magnetic ordering in Ni–Cd ferrite, *J. Magn. Mater.*, **324** (2012) 2116-2120.
- [6] P.B. Belavi, G.N. Chavan, B.K. Bammannavar, L.R. Naik and R.K. Kotnala, Magnetic properties of Cd substituted Ni-Cu ferrites, *AIP Conf. Proc.*, **1349** (2011) 1249-1250.
- [7] K.M. Bato, S. Kumar, C.G. Lee, Alimuddin, Influence of Al doping on electrical properties of Ni–Cd nano ferrites, *Curr. App. Phys.*, **9** (2009) 826-832.
- [8] M. Belal Hossen, A.K.M. Akther Hossain, Structural and dynamic electromagnetic properties of  $Ni_{0.27}Cu_{0.10}Zn_{0.63}Al_xFe_{2-x}O_4$ , *J. Magn. Mater.*, **387** (2015) 24-36.
- [9] R. Valenzuela, A sensitive method for the determination of the Curie temperature in ferrimagnets, *J. Mat. Sci.*, **15** (1980) 3173-3174.
- [10] C.G. Koops, On the dispersion of resistivity and dielectric constant of some semiconductors at audio frequencies, *Phys. Rev.*, **83** (1951) 121-124.
- [11] G. Mu, N. Chen, X. Pan, H. Shen, M. Gu, Preparation and microwave absorption properties of barium ferrite nanorods, *Mater. Lett.*, **62** (2008) 840-842.

# A Compact Patch Antenna for Ultrawideband Application

M. Tarikul Islam<sup>a</sup>, M. Samsuzzaman<sup>b</sup>

<sup>a,b</sup>Dept. of Computer and Communication Engineering  
Faculty of Computer Science and Engineering  
Email: <sup>a</sup>tarikulislam1994@gmail.com, <sup>b</sup>sobuz@pstu.ac.bd

M. M. Islam<sup>c</sup>, M.Z.Mahmmud<sup>d</sup>, M.T. Islam<sup>e</sup>

<sup>c</sup>Dept. of Software Engineering,  
Daffodil International University  
<sup>d,e</sup>Dept. of Electrical Electronic and Systems Engineering,  
Universiti Kebangsaan Malaysia, Malaysia  
Email: <sup>c</sup>mmoiislam@yahoo.com,  
zulfikerm@siswa.ukm.edu.my <sup>e</sup>titareq@gmail.com,

**Abstract**—A compact microstrip line fed tapered-shaped slotted ultra-wideband(UWB) antenna is presented. The new design is composed of a rectangular slotted patch with a compact size of  $21.44 \times 23.53 \text{ mm}^2$  and fed by microstrip transmission line of  $50 \Omega$ . The proposed antenna is simulated onto a less expensive FR4 substrate which has a height of 1.6 mm. There achieved a wider bandwidth of 8.51 GHz (3.49-12 GHz) with good impedance matching, constant gain, 5.76 dBi of maximum gain and stable radiation pattern results in the proposed antenna more appropriate for using UWB communication applications compared to existing antennas. The proposed antenna is designed and simulated in HFSS and CST Microwave Studio software to see the antenna performance.

**Keywords**—UWB;patch;slot; low cost;microstrip feed line.

## I. INTRODUCTION

Now-a-days ultra-wideband (UWB) technology with an operating frequency ranging from 3.1-10.6 GHz as low cost, low complexity, high gain, high data resolution, low interference, lightweight and easy to construct have turned it into various wireless communications applications. It must be electronically small in size and low cost without hampering its performance as well as high gain, stable radiation pattern, linear phase variation, low profile is also needed to satisfy the prerequisite for UWB applications. Designing a compact, high gain and cost effective UWB antenna is still a challenge to antenna designers and researchers in academia and industry. Planar antennas for ultra-wideband applications have already proposed by researchers. The most acceptable antenna for UWB applications is printed slot type antenna. Here a wide-slotted antenna has a broader bandwidth than narrow slotted antenna.

Since the Federal Communications Commission (FCC) declared unlicensed bandwidth of 3.1 to 10.6 GHz for radio communication in 2002 [1], antennas with ultra-wide bandwidth have been broadly researched and developed. In a UWB system, the antenna is one of the most effective passive element and attracted substantial research work in recent years. Among the challenges of designing a cost-effective, compact, smaller size, wide bandwidth and easy fabrication is a prerequisite for UWB applications [2-6]. In the last three decades, the printed microstrip slot antennas were significantly researched due to its various number of benefits including stable radiation pattern, low profile, high gain and easy inexpensive fabrication. Various printed wide-slot coplanar

waveguide (CPW) antennas have been stated [7, 8]. Besides, monopole slotted antennas have been testified to gain the characteristics of wide bandwidth [3]. The proposed microstrip antenna acquires the operating bandwidth of -10 dB which has the range of 3.49-12 GHz that covers UWB region. The proposed antenna size has been reduced and performance has been improved. To construct the UWB antennas with filtering characteristic, various number of methods have been proposed by designing numerous slots on either radiated patches or ground planes, like rectangular patch shaped [9], circular disk shape [10] Cross shaped [4] and Hexagonal-shaped [8] slot. The proposed antenna with a tapered-slotted ground plane and rectangular slotted patch which gives better bandwidth and gain than [11, 12]. As we know that the resonant frequency is shifted to lower frequency if the side slot width increases. As a result, we use a tapered slot ground for achieving better bandwidth. In recent times, for wideband applications, a printed wide-slot antenna is designed [13]. The proposed antenna is cost effective as FR4 is used as substrate material rather than expensive materials such as Rogers RT [14] and Shieldit Super [11].

A planar microstrip patch with tapered slotted ground plane structured antenna with a compact dimension of only  $21.44 \times 23.53 \text{ mm}^2$ , that is smaller than the antennas proposed in [2, 8, 11, 15], for the ultra-wideband application. After designing a tapered slot ground with the microstrip-fed rectangular slotted patch as a radiating element, this proposed antenna reached a wide bandwidth extending from 3.49 to 12 GHz.

## II. ANTENNA DESIGN AND STRUCTURE

Fig. 1 demonstrates the structure and configuration of the proposed microstrip patch antenna. Generally, Because of having only one resonance part the bandwidth of microstrip patch antenna is not wide in range. It can be possible to gain broad bandwidth if there are more than one resonant parts where each one operates independently. The proposed antenna contains a tapered-shaped slot scraped out of the ground plane with a rectangular slotted patch and a microstrip-fed-lined for radiation. The distance between the rectangular slotted patch and the ground plane ( $h$ ) defines the matching between slot antenna and the feed line. The patch is composed of the rectangular slot with different cuts  $l_n$ ,  $w_n$ ,  $w_p$ .

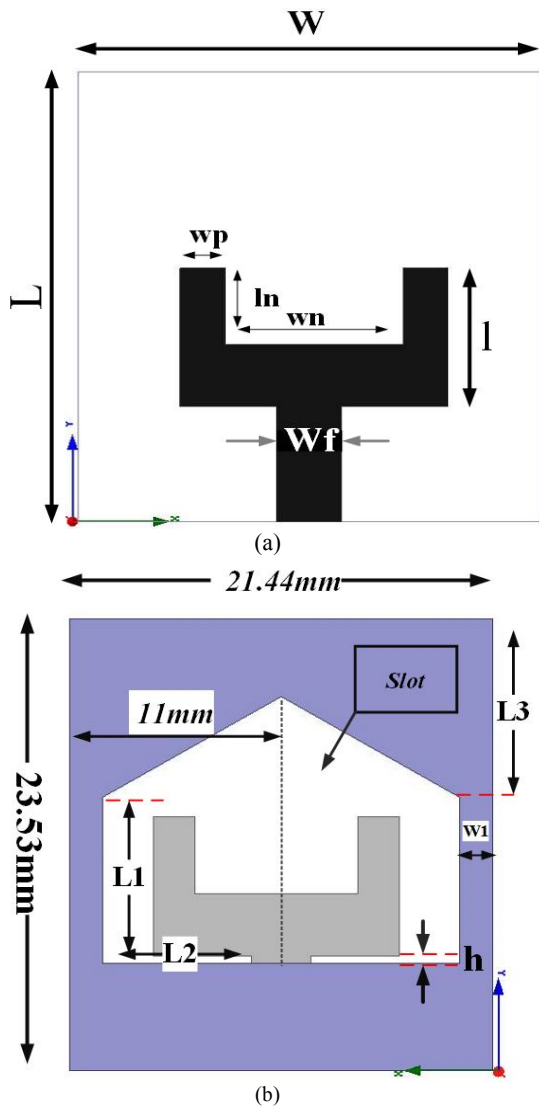


Fig. 1. The geometry of the proposed antenna. (a) Top view. (b) Bottom view.

By changing the value of  $l_n$ ,  $w_n$ , and  $w_p$  we can gain the ultra-wide bandwidth for the wideband application. Both the ground plane and the rectangular slotted patch are designed on a low-cost FR4 substrate which thickness is 1.6 mm, loss tangent 0.02 and relative permittivity of 4.6. The tapered slotted ground plane has a durable combination with the feeding construction. High gain, good range of bandwidth, and stable radiation patterns can be reached by choosing properly shaped slot at patch and ground plane. The entire dimensions of the proposed antenna are only  $21.44 \times 23.53 \text{ mm}^2$ , which is one of the smallest and cost effective UWB slotted antennas. The adjusted different constraints of proposed antenna are:  $W = 21.44 \text{ mm}$ ,  $L = 23.53 \text{ mm}$ ,  $l = 7.24 \text{ mm}$ ,  $w_p = 2.11 \text{ mm}$ ,  $l_n = 4 \text{ mm}$ ,  $w_f = 3 \text{ mm}$ ,  $L_1 = 8.66 \text{ mm}$ ,  $L_2 = 7.52 \text{ mm}$ ,  $L_3 = 9.30 \text{ mm}$ ,  $w_1 = 1.98 \text{ mm}$ ,  $h = 1.6 \text{ mm}$ .

### III. RESULTS AND DISCUSSION

The simulation of the proposed antenna was done with two simulation software called HFSS and CST. High-Frequency Structural Simulator (HFSS) based on finite element method and Computer Simulation Technology (CST) based on finite-difference-time-domain method. As a result, the graph value of the simulation may vary slightly for this two different working methods of the simulation software. The very first step of the design of the proposed antenna we have tested different patch shape to gain an ultra-wide bandwidth. We noticed that by improving the coupling between the rectangular slot and feed line and changing slot size and shape, good impedance matching can be achieved. Fig. 2 shows the different patch shape starting with proposed one. We have fed the rectangular slotted patch with a 50 Ohm transmission line. Here, the rectangular slotted patch element applied as the microstrip termination line which gives more wideband performance compared to the other ones. It is noticed that by using tapered ground slot structure, high-frequency performance can be enhanced, and a wider bandwidth can be achieved by using a tapered-shape slot coordinated with a rectangular slotted patch than with a circular, rectangular, elliptical or square-shaped slot. Fig. 3 defines the various simulated result of Reflection coefficient ( $s_{11}$ ) of different shapes of the patch in HFSS which can help us to choose the right shape of the patch for UWB application. Fig. 4 represents the reflection co-efficient ( $s_{11}$ ) of the proposed antenna with and without ground plane. We can see that by using tapered slot ground we are able to gain ultra wideband frequency band

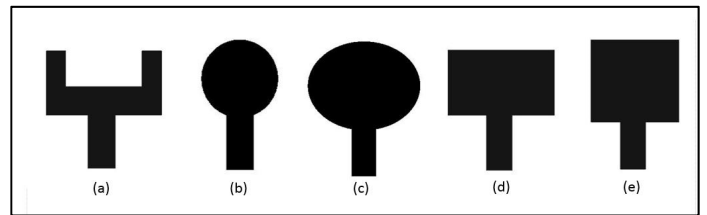


Fig. 2. Various patch structure: (a) rectangular slotted (proposed) (b) circular (c) elliptical (d) rectangular and (e) square shape.

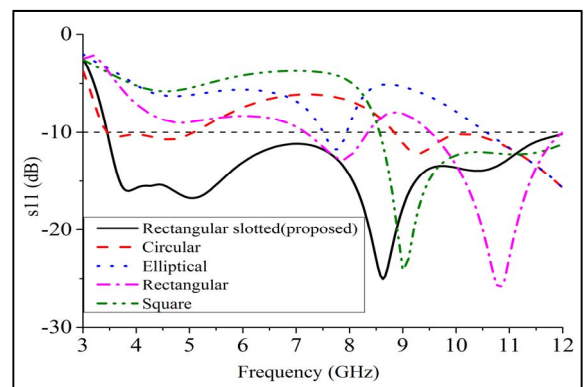


Fig. 3. Simulated  $s_{11}$  for dissimilar patch shapes.

Fig. 5 shows the VSWR result against frequency where the entire bandwidth (3.49 - 12 GHz) in  $VSWR \leq 2$  in HFSS and CST. Fig. 6 demonstrates the simulated reflection coefficient



against frequency for the proposed antenna in both HFSS and CST. We found that the proposed antenna shows a wide bandwidth performance from 3.49 to 12 GHz. Fig. 7 shows the simulated peak gain of the proposed antenna. It has an average 4.2 dBi peak gain. The maximum appreciated gain is 5.4 dBi at 7.9 GHz. The simulated radiation efficiency in HFSS and CST is displayed in Fig.8. We can see that the proposed antenna reached a maximum radiation efficiency of 98.3%. Fig. 9 indicates the proposed antenna's simulated radiation patterns of the two major planes specifically,  $-xz$  and  $-yz$  planes for three different operating frequencies of 3.5, 6.5, and 9.5 GHz. We can see that the radiation patterns are almost omnidirectional in the  $yz$ -plane at a low frequency of 3.5 GHz with low cross-polarization values.

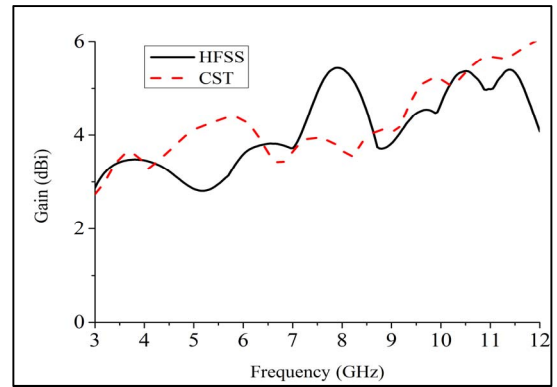


Fig. 7. Simulated Gain with HFSS and CST.

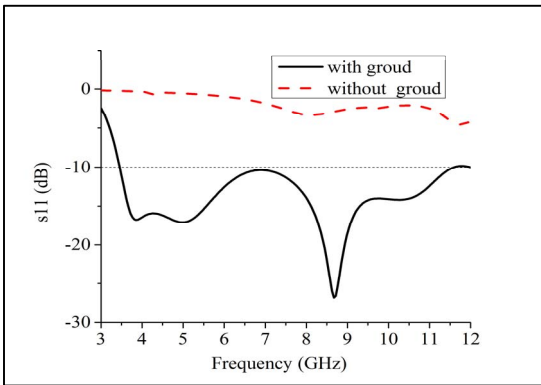


Fig. 4. Simulated  $s_{11}$  with and without ground.

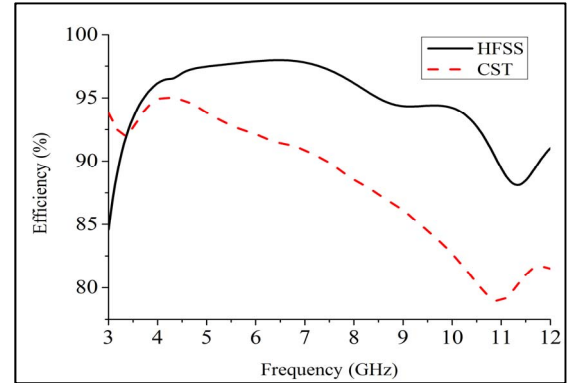


Fig. 8. Simulated Efficiency in HFSS and CST.

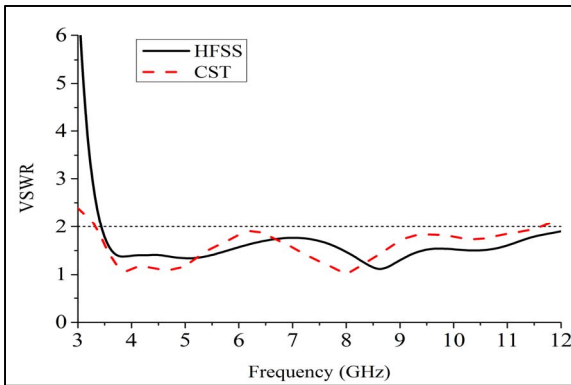


Fig. 5. Simulated VSWR in HFSS and CST.

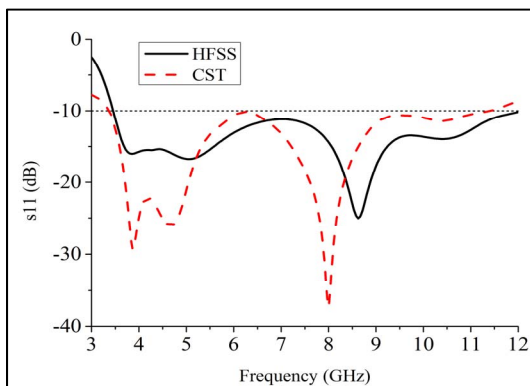


Fig. 6. Reflection coefficient ( $s_{11}$ ) of the proposed antenna with HFSS and CST.

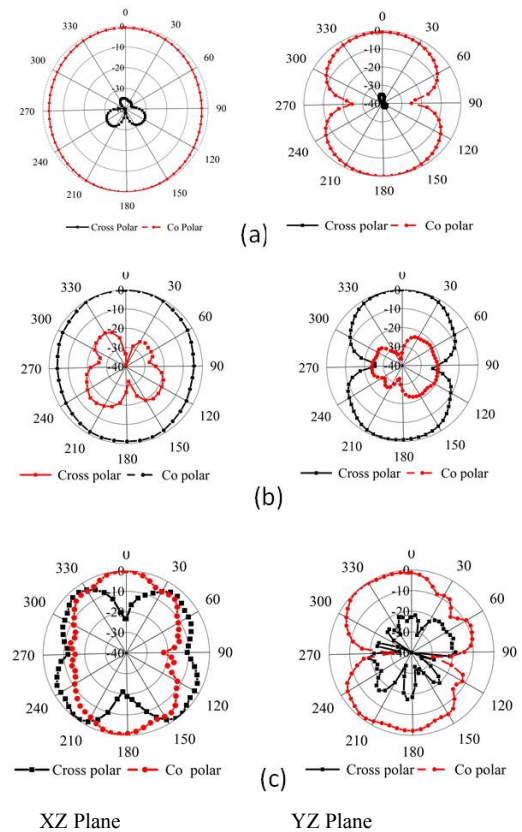


Fig. 9. Simulated radiation patterns at different frequencies. (a) 3.5 GHz; (b) 6.5 GHz (c) 9.5 GHz.

TABLE I. COMPARISON BETWEEN THE PROPOSED UWB ANTENNA WITH EXISTING ANTENNAS

Antennas	BW GHz (-10 dB)	Dimension Area (mm <sup>2</sup> )	FB(%)	Gain (dBi)
[2]	3.7 - 18	26 × 28	131.7	3.97
[6]	2.71 - 12.61	25 × 23	129.2	Not reported
[7]	3 - 11.2	22 × 24	115.5	3.6
[8]	3.3 - 20	27 × 23.5	143.3	5.11
[13]	3.2 - 20	31 × 31	144.8	5.1
[14]	2.6 - 12.3	39 × 40	130.2	5.52
Proposed	3.49 - 12	21.44 × 23.53	109.8	5.76

The radiation pattern is also omnidirectional in yz-plane at a medium frequency of 6.5 GHz. At 9.5 GHz, the radiation pattern is omnidirectional with both xy-plane and yz-plane. We can figure out that the radiation patterns are extraordinarily in stable condition during ultra-wideband. Table I shows the comparison between the proposed antenna and other existing UWB antennas. The considered parameters are antenna bandwidth, the size of the antenna and gain. The proposed antenna has shown decent performance in most of the conditions stated in Table I.

#### IV. CONCLUSION

The design and simulation of a compact rectangular slotted patch antenna with dimensions of 21.44 × 23.53 mm<sup>2</sup> have been presented. The proposed antenna covers a rectangular slot patch and a tapered-shape ground plane with a thickness of 1.6mm between them. The simulation indicates that the proposed antenna attains decent impedance matching constant-gain, excellent efficiency and stable omnidirectional radiation patterns with an impedance bandwidth of 109.8% (3.49 – 12 GHz) which covers the entire UWB band. The proposed antenna is quite simple in design and easy to fabricate for UWB applications with low manufacturing cost.

#### REFERENCES

[1] U. F. C. Commission, "FCC Revision of part 15 of the commission's rules regarding ultra-wideband transmission systems: First report and order," technical report, Feb2002.

[2] L. Liu, S. Cheung, R. Azim, and M. T. Islam, "A compact circular-ring antenna for ultra-wideband applications," *Microwave and Optical Technology Letters*, vol. 53, pp. 2283-2288, 2011.

[3] Y. Liu, K. Lau, Q. Xue, and C. Chan, "Experimental studies of printed wide-slot antenna for wide-band

applications," *IEEE Antennas and Wireless Propagation Letters*, vol. 3, pp. 273-275, 2004.

[4] Y. Jang, "Broadband cross-shaped microstrip-fed slot antenna," *Electronics Letters*, vol. 36, p. 1, 2000.

[5] M. Samsuzzaman and M. Islam, "A semicircular shaped super wideband patch antenna with high bandwidth dimension ratio," *Microwave and Optical Technology Letters*, vol. 57, pp. 445-452, 2015.

[6] M. Samsuzzaman and M. Islam, "Wideband hook-shaped circularly polarised antenna," *Electronics Letters*, vol. 50, pp. 1043-1045, 2014.

[7] S.-W. Qu, C. Ruan, and B.-Z. Wang, "Bandwidth enhancement of wide-slot antenna fed by CPW and microstrip line," *IEEE Antennas and Wireless Propagation Letters*, vol. 1, pp. 15-17, 2006.

[8] A. Gautam, R. Chandel, and B. Kr Kanaujia, "A CPW-fed hexagonal-shape monopole-like UWB antenna," *Microwave and Optical Technology Letters*, vol. 55, pp. 2582-2587, 2013.

[9] R. Azim, M. T. Islam, and N. Misran, "Compact tapered-shape slot antenna for UWB applications," *IEEE Antennas and Wireless Propagation Letters*, vol. 10, pp. 1190-1193, 2011.

[10] R. Azim, M. T. Islam, and N. Misran, "Printed circular disc compact planar antenna for UWB applications," *Telecommunication Systems*, vol. 52, pp. 1171-1177, 2013.

[11] P. B. Samal, P. J. Soh, and G. A. Vandenbosch, "A systematic design procedure for microstrip-based unidirectional UWB antennas," *Progress In Electromagnetics Research*, vol. 143, pp. 105-130, 2013.

[12] K. Kikuta and A. Hirose, "Compact Folded-Fin Tapered Slot Antenna for UWB Applications," *IEEE Antennas and Wireless Propagation Letters*, vol. 14, pp. 1192-1195, 2015.

[13] A. Dastranj, A. Imani, and M. Naser-Moghaddasi, "Printed wide-slot antenna for wideband applications," *IEEE Transactions on Antennas and Propagation*, vol. 56, pp. 3097-3102, 2008.

[14] M. Mahmud, S. Kibria, M. Samsuzzaman, N. Misran, and M. Islam, "A New High Performance Hibiscus Petal Pattern Monopole Antenna for UWB Applications," *Applied Computational Electromagnetics Society Journal*, vol. 31, 2016.

[15] R. Azim, M. T. Islam, and N. Misran, "Microstrip line-fed printed planar monopole antenna for UWB applications," *Arabian Journal for Science and Engineering*, vol. 38, pp. 2415-2422, 2013.

# Development of a telemedicine model with low cost portable tool kit for remote diagnosis of rural people in Bangladesh

Uzzal Kumar Prodhan  
Computer Science & Engineering Department  
Jatiya Kabi Kazi Nazrul Islam University  
Trishal, Maymensingh, Bangladesh  
uzzal\_bagerhat@yahoo.com

Mohammad Zahidur Rahman, Ahsin Abid, Mohtasim Bellah  
Computer Science & Engineering Department  
Jahangirnagar University  
Savar, Dhaka, Bangladesh

**Abstract** – In this paper we have developed a Telemedicine model with portable tool kit for remote patients to collect vital signs of patients which are used for Telemedicine services. This developed system is low cost, portable, and easily maintainable and can be integrated with any complex health system. We have used the GNU health where local doctors can communicate with a low cost terminal. Expert doctors can also take part through this terminal and deliver treatment to the patients. The patient's medical history is stored in GNU health database and accessed from the remote terminal. We have successfully designed the system and collected the patient's data. Through our developed android apps, the data will be stored in the staging server. From the staging server, any health system can collect the data and give the services to the rural people. Finally we can conclude that, Telemedicine service can be given effectively by using our portable tool kit in a cost effective manner which improves the quality and accessibility especially in rural areas.

**Keywords**—*telemedicine; gnu; ecg; spo2; glucometer*

## I. INTRODUCTION

Bangladesh is a small country with huge number of population. Most of the people in our country live in rural areas where health care facilities are poor. Most of the specialist doctors live in urban areas. In this scenario, healthcare facilities can be given to this huge number of populations through Telemedicine. Telemedicine is a promising cost- effective alternative method that has been shown to prevent deaths and improve functional recovery [1]. Telemedicine technologies have been proven to work, and are considered to be a viable option [2] in future healthcare delivery. Health professionals who used telemedicine in their work had more positive impression towards it [3]. According to Wootton, a successful telemedicine provides high quality care at low cost in comparison with an alternative such as regular care [4].

In Bangladesh, health service delivery in rural areas is extensively increased in absence of qualified human resources for health (HRH) [5]. In Bangladesh, the medical doctor to population ratio in urban areas is 1:1500, whereas the ratio is 1:15000 in rural areas [6]. Around 20% of physician positions and 22% of nurse positions at the sub-district or upazila health

complexes are vacant. The vacancy rate is even higher for the specialist positions (52%) at the upazila-level health complexes [7].

It was found that early diagnosis and treatment are vital to ensure sustainable medical treatment and enhance survival rates [8]. Alongside the potential to lower healthcare costs, telemedicine services have the strength to increase the accessibility and quality of care [9-10]. The main aim of this research is to develop a telemedicine model through a newly developed portable telemedicine tool kit which will be cost effective for our rural people.

## II. REVIEW OF LITERATURE

In order to carry out this research, related research articles are reviewed renowned journals, conferences, magazines, books and different sites. Most recent findings are analyzed in this section with their weaknesses and strengths.

A real-time heart monitoring system was developed by Priyanka Kakria, N. K. Tripathi, and Peerapong Kitipawang considering the cost, ease of application, accuracy, and data security [11]. In this paper, three types of wearable sensors are used to get heart rate, blood pressure, and body temperature from the patients. By using android phone, data were sent to the web server. Through the server, both doctors and patients are connected. Their developed system generates alarm and informs the doctor in case of emergency. The limitations of this research are to generate false alarm due to battery issues of sensors and smart phone.

M. Abo-Zahhad, Sabah M. Ahmed, and O. Elnahas proposed a system that can collect four different physiological signs of ECG, SPO<sub>2</sub>, temperature, and blood pressure. These signals are transferred to an intelligent data analysis scheme to diagnose abnormal pulses. The system has web-based interface for medical staff to observe immediate pulse signals for remote patient treatment [12].

The research was conducted by Meenu Singh and other's titled "Application of Handheld Tele-ECG for Health Care Delivery in Rural India" to identify heart conditions of the

rural people. Patient satisfaction was reported to be about 95% in this study [13].

Another study was conducted by Fang Zhao, Meng Li, Yi Qian and Joe Z. Tsien. They described a process to get blood volume pulse and respiratory wave from a single channel images captured by a video camera. This research enables a much needed low-cost means to protect sudden infant death syndrome in new born infants and detect stroke and heart attack in elderly population [14].

The authors Gregorio Lopez, Victor Custodio, and Jos Ignacio Moreno developed a system which monitors several physiological parameters, such as ECG, heart rate, body temperature, etc., and tracks the location of a group of patients within hospital. This paper depicts the system architecture, deployment and validation of results from both laboratory tests and a pilot scheme [15].

The researchers named Md. Nazmul Hossain and others developed a portable health clinic tool that was used for the rural people of Bangladesh in collaboration with Kyushu University, Japan. The project was running as pilot basis in two districts of Bangladesh. Patients and doctors are getting health services through a website [16].

### III. MATERIALS AND METHODS

This research was carried out through mainly four modules: Portable telemedicine tool kit module for collecting the vital information from patients through different sensors, communication module that is android apps to collect data from the portable tool to the server module, server module consists of staging server primarily used for storing the patient data from the android apps and GNU health server module to fetch data from staging server for future use and management. Remote health professionals connect to the GNU server for the delivery of healthcare services. The activity diagram of our proposed telemedicine model is shown in the following figure 1:

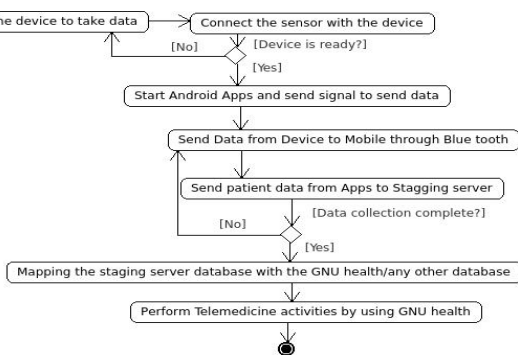


Fig. 1. The activity diagram of the telemedicine model

From the activity diagram we can understand the overall working procedure of the proposed telemedicine model. The activity diagram describes the starting to final activities of how the service is delivered through our proposed system.

Figure 2 shows the component diagram of the proposed telemedicine model. The major components of the diagram are

sensors, telemedicine tool kit, android phone, staging server, GNU health server database and client module.

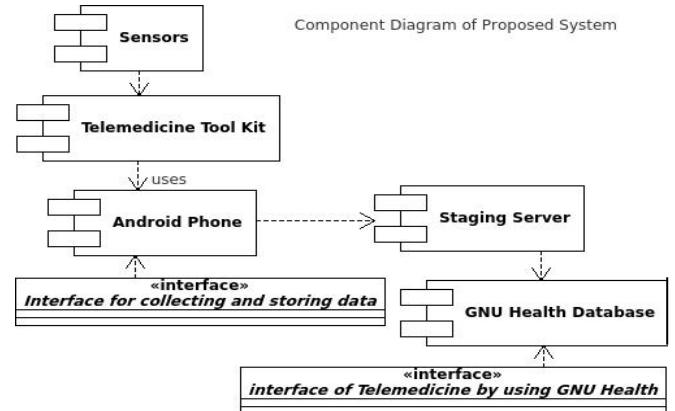


Fig. 2. The component diagram of proposed model

The deployment diagram is given in figure 3. The diagram consists of 1 to N number of remote telemedicine devices for collecting data from patients. Android phone is used to send data from the staging server. It is a repository of patient data. Our proposed system will fetch data from this server to GNU health server. After that a low cost client is made to connect to the GNU health server. The client is made of Raspberry pi, keyboard, mouse and monitor only.

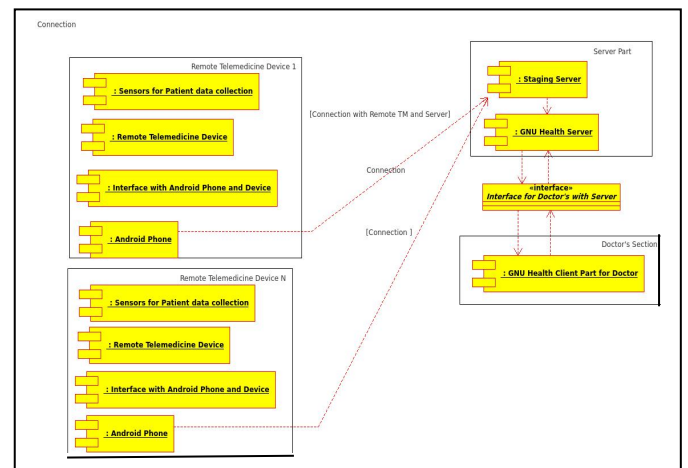


Fig. 3. Deployment diagram of proposed telemedicine model

The portable tool kit is composed of e-health sensor shield, sensors, arduino and Bluetooth module. After making proper connections with the sensors, the operating mechanisms are handled through code. After putting the sensors in the right position of the body, the data were collected from the kit through Bluetooth. By using the apps, we can send the data to the server.

The portable telemedicine tool kit arrangements are shown in the figure-4:



Fig. 4. Physical arrangement of portable tool kit

From figure 5, we can see that the SPO2 sensor sends data from the device. We can also format the data according to our desired format. The sensors are maintained through the command from the Android phone.

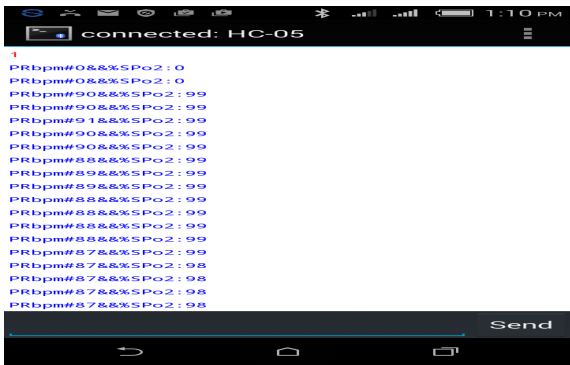


Fig. 5. Output from the SPO2 Sensor

#### IV. RESULTS

We have prepared the portable tool kit for collecting data through Bluetooth terminal to the app. We have installed GNU health server for storing the patient data. GNU health client module was implemented to connect remotely into the health system. The following sections show the results of different modules.

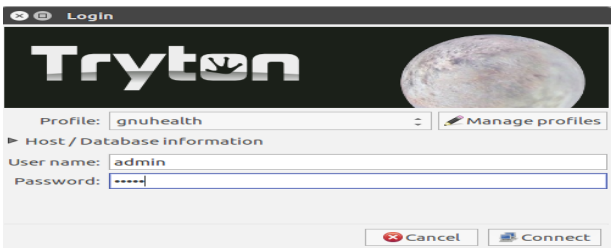


Fig. 6. GNU health client login window

Figure 6 shows the client login module. Client can use this section for connecting with the GNU health server. Remote health professionals use this module for telemedicine service. Valid user name and password is necessary to login the system and use the facilities of the health system.

The figure 7 shows the result of inserting the patient information into the system. At the time of registering a patient, an ID is assigned which is used in the system for different types of functions.

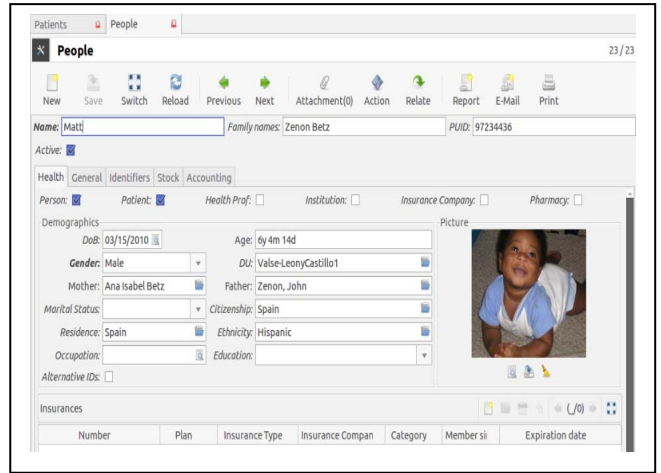


Fig. 7. GNU health patient information screen shot

Figure 8 depicts the prescription generated by expert doctors for different patients. Any patient can get his or her previous advices from the system easily. Doctors can also get the patient's history and treatment plan through this section. It is helpful for the doctors to make prescriptions of patients by investigating the patient's previous information.

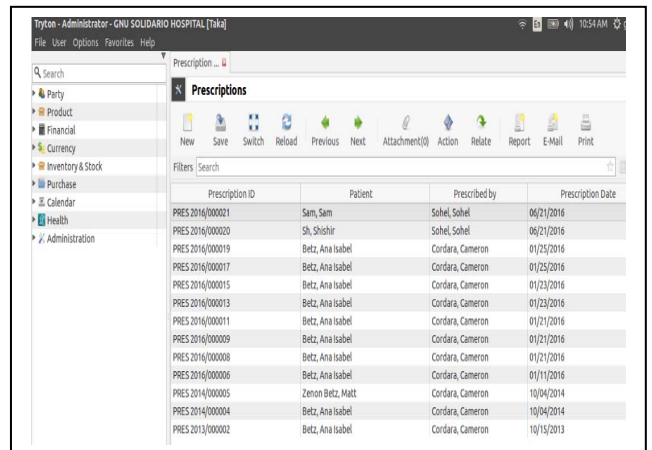


Fig. 8. Prescription of patient from the system

Figure 9 shows the lab test result generated by lab technician. Doctors send request for a lab test of a patient. The lab technician performs the test and inputs the values of the test in the prescribed format and saves it. Category wise lab test results are stored in the lab test result section. Doctors can easily search the patient lab test results from the system. The history of the results can be accessed and managed through terminal. After getting the lab result, doctors prepare the prescription of the patients.

ID	Test type	Patient	Date of the Analysis
TEST001	COMPLETE BLOOD COUNT	Betz, Ana Isabel	09/30/2013
TEST002	RENAL FUNCTION TEST	Zenon Betz, Matt	
TEST003	STOOL EXAMINATION	Zenon Betz, Matt	
TEST004	LIVER FUNCTION TEST	Zenon Betz, Matt	
TEST005	LIVER FUNCTION TEST	Zenon Betz, Matt	07/23/2014
TEST006	COMPLETE BLOOD COUNT	Betz, Ana Isabel	01/23/2016
TEST007	COMPLETE BLOOD COUNT	Carlos, Roberto	01/24/2016
TEST008	COMPLETE BLOOD COUNT	Betz, Ana Isabel	01/25/2016
TEST009	COMPLETE BLOOD COUNT	Betz, Ana Isabel	01/25/2016
TEST010	COMPLETE BLOOD COUNT	Sh, Shishir	06/08/2016
TEST011	COMPLETE BLOOD COUNT	Sh, Shishir	06/08/2016
TEST012	URINE ANALYSIS	Sam, Sam	06/25/2016

Fig. 9. Diagram of category wise lab test result

## V. DISCUSSION

In this paper, we have developed our portable telemedicine tool kit for collecting seven vital signs of patients. The sensors used in the tool kit are SPO2, airflow, temperature, blood pressure, body position, glucometer and ECG.

We have tested the GNU health server through client for our telemedicine application. Patients will not face any difficulties due to the change of his geographical positions. Our telemedicine model will provide the facilities to its users.

In order to make this model cost effective, we have created a low cost client module by using Raspberry pi 3, monitor, keyboard and mouse only. This arrangement can reduce the expense about half of the cost of a computer system. This GNU health client module is portable and can be easily installed at any remote locations.

Our proposed model is superior to other models because this model is composed of a customized tool kit capable of collecting the vital sign of patients in a cost effective manner. This model includes staging server facilities which can be shared by any health system for their patient's data. Patient data is stored centrally and accessed through remote locations. All the healthcare centers find the same format and structure of patient data and record. Our model facilitates the health services to the remote people.

## VI. CONCLUSION

Telemedicine is playing a vital role for giving the healthcare facilities to the poor people. We have implemented this telemedicine model to enhance the facilities of the services of telemedicine. Our developed portable telemedicine kit can collect seven vital signs of a patient in an automated manner. We have successfully collected the data from the kit to the server for permanent storage. From the GNU health, we have found that when any abnormalities are found from any test result for a patient, warning message is given to the test of the patients. Doctors can deliver the necessary treatment for the patient in the case of emergency. We have shown the low cost solution of telemedicine through a customized terminal. Health related services can be easily found and accessed through our developed model. Our proposed model can be used as a low cost standard model for the telemedicine services of rural people of Bangladesh.

## Acknowledgment

The authors would like to thank to Ahsan Uddin Department of IIT, Jahangirnagar University, Savar, Dhaka, Bangladesh for his valuable contribution on the implementation of GNU health. Authors also thank to the Ministry of Information and Communication Technology, Bangladesh for their financial support for the PhD fellowship.

## References

- [1] S. Scalvini, A. Giordano and F. Glisenti, "Telemedicine and the relationship between hospital and primary care," *Monaldi Archives for Chest Disease*, vol. 58, no. 2, pp. 132-134, 2002.
- [2] Doarn CR and Merrell RC, "A roadmap for telemedicine: barriers yet to overcome," *Telemedicine & e-Health*, vol. 14, issue. 9, pp. 861, 2008.
- [3] Vuononvirta T, Timonen M, Keinänen-Kiukaanniemi S, Timonen O, Ylitalo K, Kanste O and Taanila A, "The attitudes of multiprofessional teams to telehealth adoption in northern Finland health centres," *Journal of Telemedicine and Telecare*, vol. 15, no. 6, pp. 190-6, 2009.
- [4] Wootton R and Hebert MA, "What constitutes success in telehealth?," *Journal of Telemedicine and Telecare*, vol. 7, suppl. 2, pp. 3-7, 2001.
- [5] Ahmed SM, Evans TG, Standing H and Mahmud S, "Harnessing pluralism for better health in Bangladesh," *The Lancet*, vol. 382, no. 9906, pp. 1446-55, 2013.
- [6] Ahmed SM, Hossain MA, Raja Chowdhury A and Bhuiya A, "The health workforce crisis in Bangladesh: shortage, inappropriate skill-mix and inequitable distribution," *Human Resources for Health*, vol. 9, no. 1, pp. 3, 2011.
- [7] Health Bulletin 2015, Bangladesh. [online]. Link: <http://www.dghs.gov.bd/index.php/en/home/2281-health-bulletin-2015-is-now-online>
- [8] M. Schuster, M. Pints and M. Fiege, "Duration of mission time in prehospital emergency medicine: effects of emergency severity and physicians level of education," *Emergency Medicine Journal*, vol. 27, no. 10, pp. 398-403, 2010.
- [9] Dechant HK, Tohme WG, Mun SK, Hayes WS and Schulman KA, "Health systems evaluation of telemedicine: A staged approach," *Telmed J*, vol. 2, no. 4, pp. 303-312, 1996.
- [10] Car J, Huckvale K and Hermens H, "Telehealth for long term conditions," *BMJ*, vol. 344, 2012.
- [11] Priyanka Kakria, N. K. Tripathi and Peerapong Kitipawang, "A Real-Time Health Monitoring System for Remote Cardiac Patients Using Smartphone and Wearable Sensors," *International Journal of Telemedicine and Applications*, vol. 2015, 2015.
- [12] M. Abo-Zahhad, Sabah M. Ahmed and O. Elnahas, "A Wireless Emergency Telemedicine System for Patients Monitoring and Diagnosis," *International Journal of Telemedicine and Applications*, vol. 2014, 2014.
- [13] Meenu Singh, Amit Agarwal, Vineet Sinha, Rohit Manoj Kumar, Nishant Jaiswal, Ishita Jindal, Pankaj Pant and Munish Kumar, "Application of Handheld Tele-ECG for Health Care Delivery in Rural India," *International Journal of Telemedicine and Applications*, vol. 2014, 2014.
- [14] Fang Zhao, Meng Li, Yi Qian and Joe Z. Tsien, "Remote Measurements of Heart and Respiration Rates for Telemedicine," *PLOS ONE*, vol. 8, issue 10, 2013.
- [15] Gregorio Lopez, Victor Custodio and Jose Ignacia Moreno, "LOBIN: E-Textile and Wireless-Sensor- Network-Based Platform for Healthcare Monitoring in Future Hospital Environments," *IEEE Transactions on Information Technology in Biomedicine*, vol. 14, no. 6, 2010.
- [16] Md. Nazmul Hossain, Kazi Mozaher Hossein, Rajib Chakrabarty, Hiroshi Okajima, Hironobu Kitaoka and Ashir Ahmed, "Social adaptation of ICT based healthcare delivery systems in rural Bangladesh," *International Conference on Advanced Information and Communication Technology*, no. 1, 2016.

# Human Activity Recognition using Depth Body Part Histograms and Hidden Markov Models

Md. Zia Uddin

Department of Computer Education  
Sungkyunkwan University  
Seoul, Republic of Korea  
[ziauddin@skku.edu](mailto:ziauddin@skku.edu)

Jim Tørresen

Dept. of Informatics  
University of Oslo  
Oslo, Norway  
[jimtoer@ifi.uio.no](mailto:jimtoer@ifi.uio.no)

Tasked Jabid

Dept. of Computer Science and  
Engineering  
Sogang University  
Seoul, Republic of Korea

**Abstract**— This paper proposes a novel approach for human activity recognition based on body part histograms and Hidden Markov Models. From a depth video frame, body parts are segmented first using a trained random forest. Then, a histogram for each body part is combined to represent histogram features for a depth image. The depth video activity features are then applied on hidden Markov models for training and recognition. The proposed method was superior when compared with other conventional approaches.

**Keywords**—Depth Image, HMM, Histogram.

## I. INTRODUCTION

These days, Human Activity Recognition (HAR) from video sensors has been attracting immense number of researchers in different fields of image processing researches [1]. Traditionally, binary body shapes have been very much famous for activity recognition from video [1]-[3]. In [1], the authors showed Principal Component (PC)-based body shape features for human activity recognition where they obtained global body features in the video. As local body features can represent details of human activities in the video, local feature extraction such as Independent Component (IC) was tried in this regard [2]. In [2], the authors showed ICA can extract better features than PCA and hence can obtain better recognition results. Though binary shapes are common in HAR works, they have limitations such as binary information on body can never make differences between the near and distant body parts in the image and hence represent very flat distribution over body in the image. Depth representation of human body in the images can overcome this problem as pixels in the depth images are based on the distance to the camera [3]. Though depth shapes are better than binary ones but different body part detection and segmentation can represent human body information more properly which can help obtaining better activity features in the video for robust HAR.

Along with activity recognition, body part segmentation is getting enormous attentions from image processing researchers [4]-[8]. In [4], the authors adopted k-means-based body part segmentation. In [5], the authors focused on upper body for human pose estimation. In [6], the authors did manual-based body part segmentation to obtain human body joints for gait analysis and recognition.

In this work, we present a novel approach for HAR using

body part histograms and Hidden Markov Model (HMM). For training an activity, we segment the body parts first based on a trained random forest and then, histograms are generated for each body part which are augmented to represent a body shape histogram features. Thus, histogram features are calculated from each depth image of the activity videos. Then, the feature sequences from the activity videos are used to train each activity HMM. After training all HMMs for all activities, the histogram features from testing videos are applied on the trained activity HMMs to choose one of them for activity recognition.

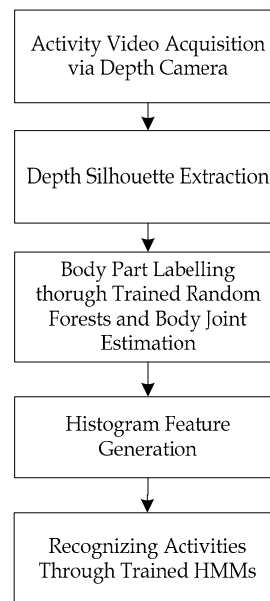


Fig. 1. The proposed HAR system

## II. METHODOLOGY

The proposed HAR system consists of depth image acquisition, segmentation of body parts, feature generation, and activity modeling as well as recognition using HMMs as depicted in Fig. 1. A depth camera is deployed for depth images acquisition of different human activities. Then, the body shape is extracted from the depth images based on background subtraction [9]. Fig.2 shows a sequence of depth

This work is partially supported by The Research Council of Norway as a part of the Multimodal Elderly Care systems (MECS) project, under grant agreement 247697.

body shapes from both hand waving and sitting activities respectively.

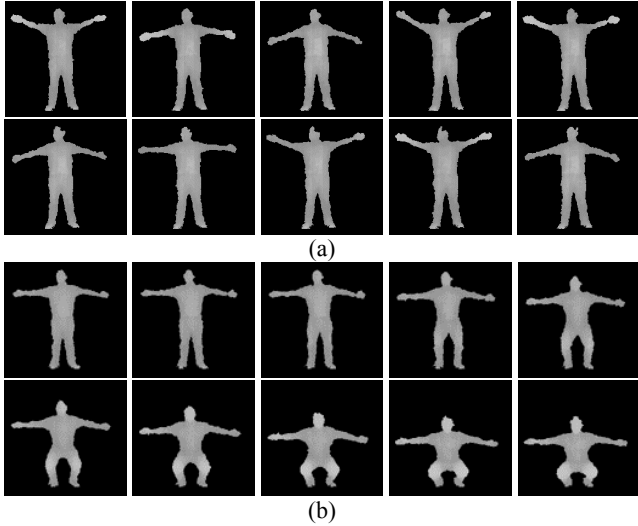


Fig. 2. Sequence of depth body silhouettes from (a) both hand waving and (b) sitting down.

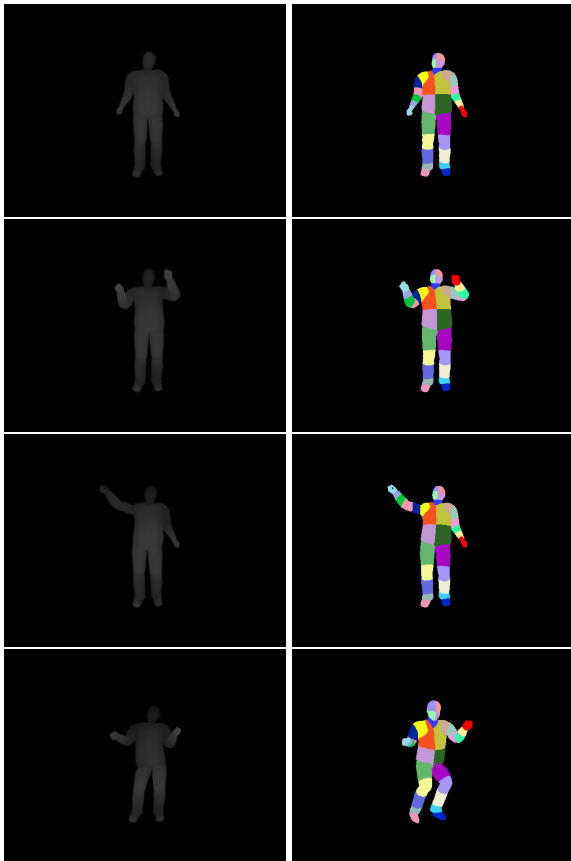


Fig. 3. Sample depth and body part segmented images from synthetic database created as a ground truth to build up random forest.

#### A. Body Part Segmentation and Feature Extraction

Random Forest (RF) is a reliable tool for multi-class classification analysis [10]. A forest is a collection of decision

trees  $T$  where each tree consists of nodes and leaves. To generate a RF, three decision trees are used in this work as more than three trees could not bring further improved recognition performance. Every single tree is trained with different pixels taken randomly from the training depth shapes and their corresponding body part labels. A synthetic database is applied where there are synthetic depth and segmented body part images. Fig. 3 shows some sample depth as well as segmented body part images from the synthetic database applied in this work where body parts are distinguished by different colors. Once RF is designed, the RF is used to segment 31 body parts from each depth image. Two thousand training sample pixels are applied randomly from each depth silhouette in the training database. The probabilities over 31 human body parts are computed at the leaf nodes in each tree. Final decision to segment each depth pixel for a body part is based on maximum voting result of all trees in the RFs. Fig. 4 shows sample activity body shapes obtained from depth camera and segmented body parts for both hand waving, right hand waving, sitting, left leg moving, and right leg moving activities after applying RF on the depth shape pixels.

Once the segmented depth body shape is obtained, histogram is calculated for each body part and then, all the body part histograms are augmented to represent features for that depth image. Thus, a depth image feature is presented by the histogram of the body part depth pixels where a bin  $h$  can be represented as

$$h = \sum_{x,y} \{I(x,y) = k\}, k = 0, 1, \dots, p-1 \quad (1)$$

where  $p$  is the number of the histogram bins and usually  $p$  is 256. Then, the histograms of the body parts are augmented for a depth shape  $A_i$  and are represented as

$$A_i = H_0 \parallel H_1 \parallel H_2 \parallel \dots \parallel H_{n-1} \quad (2)$$

where  $n$  is the number of body parts (31 in this work) and  $H$  represents the histogram of specific body part.

#### B. Activity Recognition

Vector quantization is very crucial step prior to apply HMM which symbolizes the features from every depth image from depth videos. There are basically two famous vector quantization methods for codebook generation in discrete HMMs: K-means [11] and the Linde, Buzo, and Gray (LBG)'s [12]. LBG is applied here to develop a codebook since LBG is a faster than K-means due its binary splitting of the clusters. When the codebook is obtained, the codebook vector indexes are used to represent symbols for discrete HMMs. To convert a feature vector to a discrete symbol, the feature vector is compared to all the codebook vectors followed by choosing the index number of the codebook vector as symbol which has least distance from the feature vector. Fig. 5 depicts the steps for codebook generation as well as symbol selection.



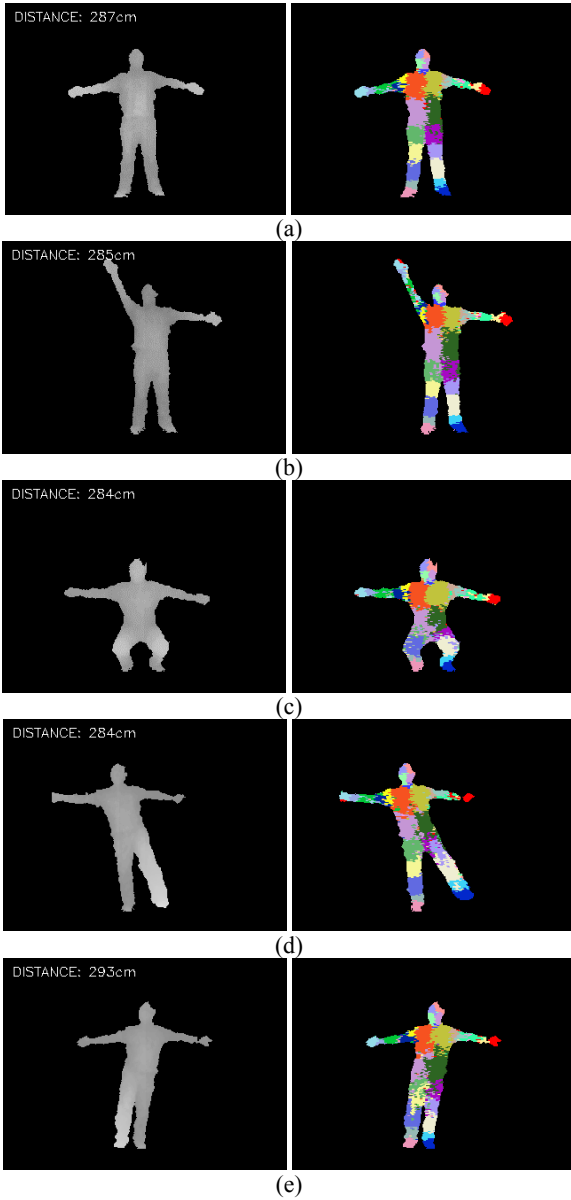


Fig. 4. A sample activity body silhouette obtained via depth camera and labeled body parts from (a) both hand waving, (b) right hand waving, (c) sitting, (d) left leg moving, and (e) right leg moving activity.

HMM is a very popular tool to model time-sequential events such human activities in video. HMM consists of a finite number of states where every state consists of transition probabilities to other states as well as observation probabilities of all the discrete symbols from every state. HMM has become very popular due its fast and efficient capability of decoding time sequential events [13]-[16]. In HAR from video, each activity represents a trained HMM [1]. Fig.6 shows an HMM for right leg waving activity.

To test a human activity in a depth activity video, the appropriate HMM is tried to find out. Thus, the discrete symbol sequence  $O$ , which is obtained from the testing depth video is applied on all trained activity HMMs  $M$  and one HMM is chosen as representative of human activity that represent the maximum likelihood as follows.

$$L = \arg \max_{k=1}^N (P(O | M_k)). \quad (3)$$

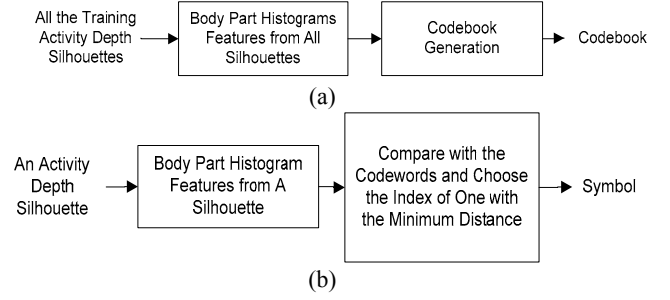


Fig. 5. Steps of (a) codebook generation and (b) symbol selection.

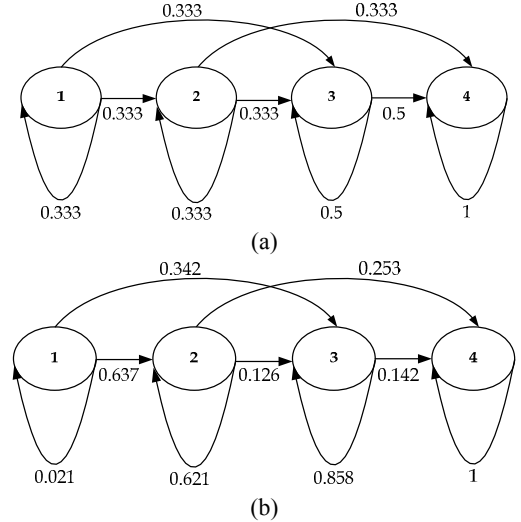


Fig. 6. A right leg waving HMM (a) before and (b) after training.

### III. EXPERIMENTAL RESULTS

A human activity database was built for training and recognition where there were six different activities. The activities are right leg moving, left leg moving, right hand waving, both hand waving, standing-up, and sitting-down. Ten videos from each activity were applied to build the training feature space where each video consisted of ten sequential depth images and hence, the training database contained a total of 600 depth images as well as segmented body shape images. Then, twenty five videos were applied to test every human activity which represented 150 activity videos in total for testing.

The HAR experiments were started with the conventional binary shape-based ones. Since the binary shapes represent very flat and limited color representations, the HAR system produced lowest recognition rates as shown in Table I where the highest average recognition rate for binary shape-based HAR was 77.33% using ICA approach. As ICA is considered to be better feature extractor than PCA, ICA was adopted for HAR on binary shapes and it showed better performance than PCA. Furthermore, as depth images can represent human activities better than binary ones in videos, depth shape-based HAR approaches were tried for better HAR results. Table II

shows the experimental results where it can be noticed that PCA and ICA on depth shapes showed better performance than PCA and ICA on binary shapes. Finally, the proposed body part histogram features-based HAR experiments were adopted where the proposed approach showed the maximum recognition rate (i.e., 94.67%) over all other approaches including both binary and depth shape-based approaches.

TABLE I. HAR EXPERIMENTAL ON BINARY SILHOUETTES RESULTS USING DIFFERENT APPROACHES.

Approach	Activity	Recognition Rate	Mean
PCA on Binary Silhouette-Based HAR	Right Leg Moving	68%	70.67
	Left Leg Moving	68	
	Right Hand Waving	76	
	Both Hand Waving	72	
	Sitting-Down	76	
	Standing-Up	64	
ICA on Binary Silhouette-Based HAR	Right Leg Moving	80	77.33
	Left Leg Moving	72	
	Right Hand Waving	80	
	Both Hand Waving	72	
	Sitting-Down	80	
	Standing-Up	80	

TABLE II. HAR EXPERIMENTAL RESULTS ON DEPTH SILHOUETTES USING DIFFERENT APPROACHES.

Approach	Activity	Recognition Rate	Mean
PCA on Depth Silhouette-Based HAR	Right Leg Moving	76%	76.67
	Left Leg Moving	76	
	Right Hand Waving	84	
	Both Hand Waving	80	
	Sitting-Down	72	
	Standing-Up	72	
ICA on Depth Silhouette-Based HAR	Right Leg Moving	88	87.33
	Left Leg Moving	84	
	Right Hand Waving	92	
	Both Hand Waving	88	
	Sitting-Down	84	
	Standing-Up	88	
Body Part Histograms on Depth Silhouette-Based HAR	Right Leg Moving	92	94.67
	Left Leg Moving	96	
	Right Hand Waving	96	
	Both Hand Waving	92	
	Sitting-Down	96	
	Standing-Up	96	

#### IV. CONCLUDING REMARKS

In this work, a novel work has been presented for depth video-based human activity recognition adopting robust body part histogram features and HMMs for activity modeling as well as recognition. The experimental results also indicate quite

significantly improved HAR performance using proposed approach than the traditional HAR approaches. The proposed approach could be tried in smart controlled environments for human activity analysis. In future, we plan to focus on more complex approaches for complex human activity recognition.

#### REFERENCES

- [1] M. Z. Uddin, D. H. Kim, J. T. Kim, and T.-S. Kim, "An Indoor Human Activity Recognition System for Smart Home Using Local Binary Pattern Features with Hidden Markov Models," *Indoor and Built Environment*, vol. 22, pp. 289-298, 2013.
- [2] A. Jalal, M. Z. Uddin, J. J. Lee, and T.-S. Kim, "Recognition of Human Home Activities via Depth Silhouettes and R Transformation for Smart Home," *Indoor and Building Environment*, vol. 21(1), pp. 184-190, 2012.
- [3] M. Z. Uddin, J.J. Lee, and T.-S. Kim, "Independent shape component-based human activity recognition via Hidden Markov Model," *Journal of Applied Intelligence*, pp. 193-206, 2010.
- [4] P. Simari, D. Nowrouzezahrai, E. Kalogerakis, and K. Singh, "Multi-objective shape segmentation and labeling," *Eurographics Symposium on Geometry Processing*, vol. 28, pp. 1415-1425, 2009.
- [5] V. Ferrari, M.-M. Jimenez, and A. Zisserman, "2D Human Pose Estimation in TV Shows," *Visual Motion Analysis, LNCS*, vol. 5604, pp. 128-147, 2009.
- [6] H. Lu, K. N. Plataniotis, and A. N. Venetsanopoulos, "A Full-Body Layered Deformable Model for Automatic Model-Based Gait Recognition," *EURASIP Journal on Advances in Signal Processing*, vol. 2008, pp. 1-13, 2008.
- [7] J. Wright, and G. Hua, "Implicit Elastic Matching with Random Projections for Pose-Variant face recognition," *IEEE conf. on Computer Vision and Pattern Recognition*, pp. 1502-1509, 2009.
- [8] A. Bosch, A. Zisserman, and X. Munoz, "Image classification using random forests and ferns," *IEEE Int. Conf. on Computer Vision*, pp. 1-8, 2007.
- [9] Microsoft Corporation, "Kinect for Xbox 360-Xbox.com", [Online]. Available: <http://www.xbox.com/en-GB/kinect/>, [2014, August 28].
- [10] V. Lepetit, and P. Fua, "Keypoint recognition using randomized trees," *IEEE Trans. on Pattern Analysis and Machine Intelligence*, vol. 28, pp. 1465-1479, 2006.
- [11] T. Kanungu, D. M. Mount, N. Netanyahu, C. Piatko, R. Silverman, and A. Y. Wu, "The analysis of a simple k-means clustering algorithm", *16th ACM Symposium On Computational Geometry*, pp. 101-109, 2000.
- [12] Y. Linde, A. Buzo, and R. Gray, "An algorithm for vector quantizer design", *IEEE Transaction on Communications*, vol. 28, no. 1, pp. 84-94, 1980.
- [13] M. Z. Uddin and M. M. Hassan, "A Depth Video-Based Facial Expression Recognition System Using Radon Transform, Generalized Discriminant Analysis, and Hidden Markov Model", *Multimedia Tools and Applications*, DOI: 10.1007/s11042-013-1793-1, 2013.
- [14] E. Baum and J. Eagon, "An inequality with applications to statistical estimation for probabilistic functions of markov processes and to a model for ecology", *American Mathematical Society Bulletin*, vol. 73, pp. 360-363, 1967.
- [15] R. Lawrence and A. Rabiner, "Tutorial on hidden markov models and selected applications in speech recognition", in *Proceedings of the IEEE*, vol. 77, No. 2, pp. 257-286, 1989.
- [16] H. Nishimura and M. Tsutsumi, "Off-line hand-written character recognition using integrated IDHMMs based on feature extraction filters", *Sixth International Conference on Document Analysis and Recognition*, pp. 417-421, 2001.
- [17] M. Z. Uddin and J. H. Kim, "An Efficient Facial Expression Recognition System Using LBP, GDA, and HMM from Depth Video", *KSIIT Transactions on Internet and Information Systems*, vol. 10, no.3, pp. 1390-1403, 2016.
- [18] M. Z. Uddin, "An Efficient Local Feature-Based Facial Expression Recognition System", *Arabian Journal for Science and Engineering*, vol. 39, no. 11, pp. 7885-7893, 2014.

# Financial Instability Analysis using ANN and Feature Selection Technique: Application to Stock Market Price Prediction

Risul Islam Rasel<sup>1</sup>, Nasrin Sultana<sup>2</sup>, Nasimul Hasan<sup>1</sup>

<sup>1</sup>Department of Computer Science and Engineering, International Islamic University Chittagong

<sup>2</sup>Department of Computer Science and Engineering, University of Chittagong

risul-islam@cse.iiuc.ac.bd<sup>1</sup>, nasrin\_cse@cu.ac.bd<sup>2</sup>, nasimul\_hsn@yahoo.com<sup>1</sup>

**Abstract**—Nowadays, Demand of forecasting stock market price is increasing at a higher rate than the ever before as more people are getting connected to the stock business. Many criteria play more or less strong inductive role over the stock market, the trend and price always keep changing here. So, it is challenging to predict exact price value. But some Data mining and Machine learning techniques can be implemented to do this challenging task to predict stock market price and trend. In this study, Artificial Neural Network (ANN) is used along with windowing operator; which is highly efficient for working with time series data for predicting stock market price and trend. This study is done on Wal-Mart Stores Inc. (WMT) a listed company of New York Stock Exchange. Five years historical dataset (2010-2015) is used to undertake the experiments of this study. According to the result of this study Artificial Neural Network (ANN) can produce a rational result with a small error.

## I. INTRODUCTION

The Stock market is a vital part of the economy of a nation. Money market plays a crucial role in the development of the business and trade of a nation that in the end influences the economy of the nation. This is the reason that the government, business organizations and even the national banks of a nation keep a close observation on the happenings of the share trading system. The share trading system is essential from both the business perspective and the financial analysis perspective. Thousands of people are getting involved in this potential business these days. It is a fundamental need for the people who are directly connected to the market to have an insight regarding the market trend [1] [2] [3]. So, forecasting stock price and market trend are getting more and more importance among the people. Stock market is basically a nonlinear, non-parametric, boisterous and deterministically disordered market [2] [3] [4]. The price and trend are frequently influenced by some critical and crucial factors; like liquid money, supply and the demand of goods, earnings of a company, the political situation etc. An Artificial Neural Network (ANN), generally called Neural Network (NN), is a scientific model or computational model that is propelled by the structure and features of natural neural systems. Artificial Neural Network (ANN) is widely used mostly in classification, regression, clustering,

anomaly detection etc. A neural framework contains an interconnected assembling of artificial neurons, and it forms data utilizing a connectionist way to deal with reckoning (the focal connectionist rule is that mental phenomena can be portrayed by interconnected systems of straightforward and regularly uniform units). As a rule; ANN is a versatile framework that progressions its structure in light of outside or inner data that courses through the system in the learning stage. Current neural systems are normally used to model complex connections between inputs and yields or to discover patterns in information [9]. YETIS, KAPLAN, and JAMSHIDI [5] showed in their research that Artificial Neural Network (ANN) can give an appreciative result with a very low error rate. Their model produced a result of 99 percent accuracy, where the best validation performance (MSE) was 37.12 which mean the error found in that model was less than 2%. Phua, P. K. H. Ming, W. Lin [8] combined ANN with Genetic Algorithm and predicted the stock price with 81% accuracy. In this study an approach of combining Artificial Neural Network with windowing operator which is very efficient for time series data prediction has been proposed. Three effective and highly efficient models, Model 1 for 1 day ahead prediction, Model 2 for 5 days ahead prediction and model 3 for 10 days ahead prediction is proposed here in this study. Comparison between some other novel algorithms like Support Vector Machine (SVM) and K-Nearest Neighbor (KNN) is shown in Table VII to understand the performance difference.

## II. METHODOLOGY

### A. Artificial Neural Network (ANN)

The goal of this study is to enhance the precision of day by day stock value forecasting of securities exchange by utilizing the neural network. An ANN has a few points of interest yet a standout amongst the most perceived of these is the way that it can really gain from watching information sets. Along these lines, ANN is utilized as an arbitrary capacity estimate instrument [11]. These sorts of devices gauge the most effective and perfect systems for touching base at arrangements while characterizing figuring capacities or disseminations. ANN takes information tests instead of whole information sets

to touch base at arrangements, which spares both time and money. ANNs are considered genuinely straightforward numerical models to improve existing information investigation innovations. ANNs have three layers that are interconnected. The primary layer comprises of data neurons. Those neurons send information on to the second layer, which thus sends the yield neurons to the third layer [12]. The study utilized three-layer (a hidden layer) perception model (a feed forward neural network) prepared with back propagation calculation. Authentic stock costs of distinctive organizations were taken from distributed stock information on the Web. The learning capacity or the initiation work that was utilized is sigmoid equation

$$f(x) = \frac{1}{(1 - e^{-fx})} \quad (1)$$

Neural Network gets various inputs (either from the unique information or from the yield of different neurons in the neural network). Every information comes through an association that has a quality (or weight); these weights relate to synaptic adequacy in an organic neuron. Every neuron additionally has solitary limit esteem. The weighted aggregate of the inputs is shaped, and the limit subtracted, to make the initiation out of the neuron (otherwise called the post-synaptic potential, or PSP, of the neuron). The activation signal is then passed through an activation function [6].

$$yk(x, \omega) = \sigma\left(\sum_{j=0}^M \omega_{kj}^{(2)} h\left(\sum_{i=0}^D \omega_{ji}^{(1)} xi\right)\right) \quad (2)$$

Here,  $yk$  is a set of output variables controlled by  $\omega$ , which is adjustable parameter. The parameter  $\omega_{ji}^{(1)}$  is the weights and  $\omega_{kj}^{(2)}$  is the biases. The superscript indicates the position of layer [6].

### B. Evaluation Processes MAPE:

Mean average percentage error (MAPE) is a measure of exactness of a system for developing fitted time arrangement values in insights, particularly in pattern estimation. It ordinarily communicates precision as a rate and is characterized by the technique [7].

$$MAPE = 100 \frac{\sum_{i=1}^n \left| \frac{A-P}{A} \right|}{n} \quad (3)$$

Here, A defines actual price, P defines the predicted price and n defines the number of days calculated.

### C. Evaluation Processes RMSE:

Root mean square error (RMSE) is a famous evaluation process to calculate the error rate of a regression model. Though, it can only be compared between models with errors calculated in same units.

$$RMSE = \sqrt{\frac{\sum_{i=1}^n (yt - \hat{y}t)^2}{n}} \quad (4)$$

Here,  $yt$  is the original value of a point for a given time period t, n is the total number of fitted points, and  $\hat{y}t$  is the fitted forecast value for the time period t.

## III. EXPERIMENT DESIGN

### A. Research Data

The proposed model can produce a rational result for almost every company. For a convenient study, a well-known company is considered here. The 5-year historical data (2010-2015) of Wal-Mart stores Inc., a listed company of New York Stock Exchange was considered for the experiment and evaluation in this study. The number of instances of the data set is 10805. Table 1 shows the attribute merit and rank measured by  $I_{GAIN}$  using 5 fold cross validation. In this study, the main aim was to predict the closing price of a Stock. For that purpose, three models are proposed here. They are 1 day ahead, 5 days ahead and 10 days ahead model. Five attributes; Date, Open price, Close price, High price and Low price are used in this study. The attribute 'Date' was chosen as id and the attribute 'Close price' as the label. The rest were kept as regular attributes. The dataset was divided into two parts. 80% of the data (2010-2014) were taken as training data and the rest 20% (2014-2015) as test data. Figure 1 shows the sample dataset for the year of 2015. Here the X axis denotes the price in BDT and the Y axis denotes the corresponding dates.

TABLE I  
ATTRIBUTE SELECTION 5 FOLD CROSS-VALIDATION, SEED: 1

Attribute	Average Merit	Average Rank
High	2.526 ± 0.003	1 ± 0
Open	2.503 ± 0.004	2 ± 0
Low	2.455 ± 0.003	3 ± 0
Volume	0.336 ± 0.006	4 ± 0

### B. Windowing Operator Analysis

The next process was the use of windowing operator to change time series data into generic data. Table II shows the windowing operator analysis for the result produced in this study. The parameter 'Windowing Size' denotes the size (Number of example for training) of the training window. The 'Step size' is the number step the window moves forward.

TABLE II  
WINDOWING OPERATOR ANALYSIS

Model	Windowing Size	Step Size	Training Window Width	Training Step Size	Testing Window Width
1 day ahead	3	1	2	1	2
5 day ahead	3	1	3	1	3
10 day ahead	3	1	3	1	3

### C. Neural Net Function Analysis

The learning stage begins with the application of Artificial Neural Network (ANN). For the best result, the function and the parameters of ANN were chosen carefully. Here,  $\alpha$  =learning rate and M=Momentum. Table III shows the function settings of Neural Net used in this study.

TABLE III  
NEURAL NET FUNCTION SETTINGS

Model	Training cycle	$\alpha$	M	Error Epsilon
1 day ahead	1300	0.3	0.2	1.0E-5
5 day ahead	1300	0.3	0.2	1.0E-5
10 day ahead	1300	0.3	0.2	1.0E-5

TABLE IV  
VALIDATION PROCESS PROPERTIES

Properties	1 day ahead	5 day ahead	10 day ahead
Training Window Width	2	2	1
Training Window Step	1	1	1
Test Window Width	2	2	1
Horizon	1	5	10
Cumulative Training	No	No	No

#### D. Model Setting and Analysis steps

The experimentation models are begun with data preprocessing steps to deliver inputs to ANN. For that, windowing technique, for example, rectangular windowing was utilized as data preprocessing strategies. Windowing operator changes the time series information into a universal dataset into the learning process [1] [2] [3]. In this study, the Artificial Neural Network (ANN) was utilized as a learning algorithm to understand the trend pattern from the dataset and to anticipate the stock cost as yield in view of that learning. This study is led in two stages, training stage, and testing stage. Steps from these two stages are given below:

1) Training stage

Step 1: Read the training data.

Step 2: Adjust Date.

Step 3: Apply windowing operator to transform the time series data into a generic dataset. This step will convert the last row of a windowing within the time series into a label or target variable. Last variable is treated as label.

Step 4: Perform a sliding windowing validation process of the produced label from windowing operator in order to feed them as inputs into ANN model.

Step 5: Select training cycles and special parameters of ANN (learning rate, momentum, error epsilon).

Step 6: Run the model and observe the performance (accuracy).

Step 7: If the accuracy is good than go to step 8 or go to step 4.(As the main motive of the study was to improve accuracy of Stock Price prediction, the best parameter combination should be set. So, if the result found in this step is not good enough; the whole process should be done from step 4 again) Step 8: Exit from the training stage and apply trained model to the testing dataset.

TABLE V  
NEURAL NETWORK MODEL

Hidden Layer 1	
Threshold: 0.185	
Node 1	0.665
Node 2	-0.561
Node 3	-0.539
Node 4	-1.005
Node 5	-0.532
Node 6	0.619
Node 7	0.652
Node 8	0.679

2) Testing stage

Step 1: Read the testing dataset.

Step 2: Apply the training model to test data

Step 3: Produce the predicted price and market trends

#### IV. EXPERIMENT RESULT

Table VI displays the predicted stock price by the proposed ANN models. All the three model predicted almost perfectly. Table VII shows the comparison of different algorithms on the same dataset for all three models.

TABLE VI  
RESULT FOR PROPOSED ANN MODEL

Date	Actual Price (USD)	Predicted Price		
		1 day ahead	5 day ahead	10 day ahead
13-01-15	89.30	89.44	87.90	91.71
07-11-14	78.76	77.63	77.72	78.08
29-07-14	75.44	75.00	76.43	77.59
04-06-14	77.12	76.26	76.96	77.53

##### A. Error Calculation (MAPE & RMSE)

The error is calculated between the actual price and the predicted price generated by the ANN model. Table VII shows the MAPE and RMSE for the models which were applied only on the testing data.

##### B. Graphical Representation of the Study

In this study, three different models are proposed for forecasting stock market price and trend. Different values for all the parameters were used to get the best result for each model. Figure 2, Figure 3 and Figure 4 shows the graphical representation of the difference between actual price and predicted price for 1 day, 5 day and 10 day prediction respectively.

#### V. CONCLUSION

##### A. Discussion

The motive of the study was to construct an effective and an efficient model to forecast stock price and stock market trend using Artificial Neural Network along with some

TABLE VII  
COMPARISON OF DIFFERENT ALGORITHMS

Dataset	Model	Horizon	ANN		SVM		KNN	
			MAPE	RMSE	MAPE	RMSE	MAPE	RMSE
Walmart Inc.	1 day ahead	1	<b>0.75</b>	<b>0.60</b>	2.57	1.90	2.71	2.28
	5 day ahead	5	3.28	2.73	0.41	0.33	3.40	2.82
	10 day ahead	10	<b>2.01</b>	1.59	2.07	1.56	4.47	3.70

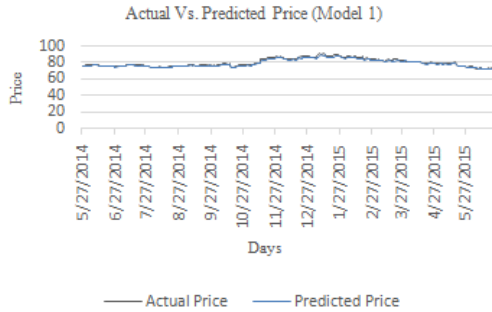


Fig. 1. Actual Price vs. Predicted Price, 1 day Model

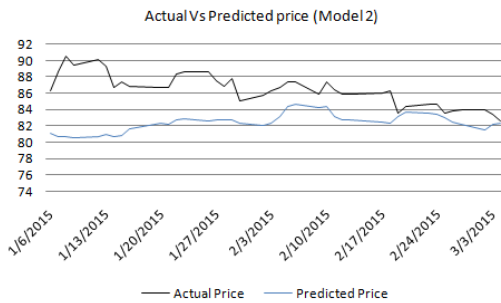


Fig. 2. Actual Price vs. Predicted Price, 5 day Model

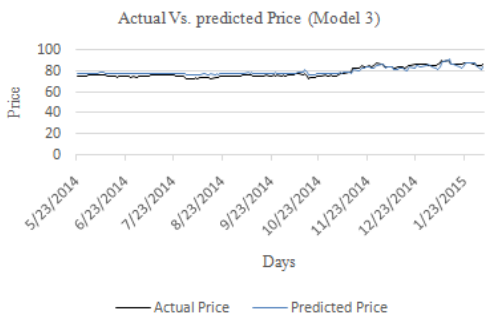


Fig. 3. Actual Price vs. Predicted Price, 10 day Model

special operators with meaningful selection of parameters of the operators. Two different evaluation processes, MAPE and RMSE were used to calculate the rate of error and the proposed models are capable of predict stock market price and trend with very little error. 1 day ahead model which predicts the

price of 1 day ahead market can predict the best among the three models. The proposed model can be used to predict stock price and trends instead of current techniques with low accuracy and thus it can help the business related people as well.

### B. Limitation and Future Work

Only Windowing operator was used in this study for data preprocessing step and the study was designed based on only the New York Stock Exchange. In future other data preprocessing techniques will be used. Some other algorithms will be applied to determine the best model and to upgrade prediction result. Different dataset from different stock markets will be applied in order to form a universal model for every market.

### REFERENCES

- [1] Meesad, Phayung, and Risul Islam Rasel. "Dhaka Stock Exchange Trend Analysis Using Support Vector Regression." The 9th International Conference on Computing and Information Technology (IC2IT2013): 9th-10th May 2013 King Mongkut's University of Technology North Bangkok. Vol. 209. Springer Science & Business Media, 2013.
- [2] Meesad, Phayung, and Risul Islam Rasel. "Predicting stock market price using support vector regression." Informatics, Electronics & Vision (ICIEV), 2013 International Conference on. IEEE, 2013.
- [3] Rasel, Risul Islam, Nasrin Sultana, and Phayung Meesad. "An efficient modelling approach for forecasting financial time series data using support vector regression and windowing operators." International Journal of Computational Intelligence Studies 4.2 (2015): 134-150.
- [4] Lu, Chi-Jie, et al. "Stock index prediction: A comparison of MARS, BPN and SVR in an emerging market." Industrial Engineering and Engineering Management, 2009. IEEM 2009. IEEE International Conference on. IEEE, 2009.
- [5] Yetis, Y.; Kaplan, H.; Jamshidi, M., "Stock market prediction by using artificial neural network," in World Automation Congress (WAC), 2014, vol., no., pp.718-722, 3-7 Aug. 2014
- [6] Ince, H., Trafalis, T.B.: Kernel Principal Component Analysis and Support Vector Machines for Stock Price Prediction, pp. 20532058 (2004)
- [7] Lucas, K., Lai, C., James, N., Liu, K.: Stock Forecasting Using Support Vector Machine. In: Proceedings of the Ninth International Conference on Machine Learning and Cybernetics, pp. 16071614 (2010).
- [8] Phua, P. K. H. Ming, W. Lin, "Neural Network With Genetic Algorithms For Stocks Prediction", Fifth Conferences of the Association of Asian-Pacific Operations Research Societies, Singapore, 5th-7th July, 2000
- [9] Yunus YETIS, Halid KAPLAN, Mo JAMSHIDI, Stock Market Prediction by Using Artificial Neural Network, In World Automation Congress, 2014
- [10] F.R.Eng.Lucas, K., Lai, C., James, N., Liu, K.: Stock Forecasting Using Support Vector Machine. In: Proceedings of the Ninth International Conference on Machine Learning and Cybernetics, pp. 16071614 (2010)
- [11] Chan, C. C., E. W. C. Lo, and Shen Weixiang. "The available capacity computation model based on artificial neural network for leadacid batteries in electric vehicles." Journal of Power Sources 87.1 (2000): 201-204.
- [12] Kim, Kyoung-jae, and Ingoo Han. "Genetic algorithms approach to feature discretization in artificial neural networks for the prediction of stock price index." Expert systems with Applications 19.2 (2000): 125-132.

# Implementation of 1xN Router Based on Mach-Zehnder Interferometer Electro-Optic Switch

Rabeya Khatun, A. Zahed Chowdhury

Department of Applied Physics, Electronics & Communication Engineering  
University of Chittagong  
Chittagong-4331, Bangladesh  
shompa.apece@gmail.com, zahed\_apece@cu.ac.bd

**Abstract**—Signal routers are novel photonic components that ensure communication between a large numbers of optical networks. In this paper we present the construction of 1xN router by using 2x2 Mach-Zehnder interferometer electro-optic switches operating at 1.55  $\mu\text{m}$ . The 2x2 Mach-Zehnder Interferometer (MZI) electro-optic switches in the routers are made by titanium diffused potassium niobate (Ti:KNbO<sub>3</sub>) and the results of the routers were compared with titanium diffused lithium niobate (Ti:LiNbO<sub>3</sub>) based routers to ease the choice of materials in implementing large networks. Enhanced performance of a single switch was evaluated at first to obtain reduced insertion loss, high extinction ratio & low excess loss. Then we implemented the 1x2, 1x4, 1x8 and 1x16 routers using that optimized switches. We can switch the input optical power to each of the output ports of the routers by the application of applied voltage at each second electrode of the MZI switches. The originality of this work is to introduce Ti:KNbO<sub>3</sub> waveguide in the design of signal router. The simulation is done and also outputs are calculated by using OptiBPM12.2 simulation software.

**Keywords**—Mach-Zehnder interferometer; Electro-optic switch; Insertion loss (IL); Signal router; Extinction ratio (ER).

## I. INTRODUCTION

Communication technology now-a-days includes a wide range of mediums, from internet to radio and to television to wireless signal providers. As a result communication technology is facing the problem of processing and distributing large amounts of information. Due to limited bandwidth, wireless communication is becoming more vulnerable to transmit such large data. Light frequency lies in the range of  $10^{13}$ - $10^{16}$  Hz [1], which is the key to the growth of optical communication as such large carrier frequency can easily be used in large and complex data transmission over a large optical network such as wavelength division multiplexing (WDM). Mach-Zehnder Interferometer (MZI) has become such a basic and essential component in WDM [2-6]. Electro-optic 2x2 MZI optical switch based on directional coupler requires high nonlinear materials i.e. InGaAs, GaAs-GaAlAs, LiNbO<sub>3</sub>, KNbO<sub>3</sub>, InP etc [7-11]. KNbO<sub>3</sub> and LiNbO<sub>3</sub> are in our interest because of their high electro-optic coefficient, speed of operation and lower switching loss & voltage [7, 12]. These switches have many applications such as signal router or multiplexer. Leick investigated on dispersion compensation of a 1x N passive optical router with

low loss, low crosstalk and a flat passband in 2002 [13]. K. Nara investigated a novel monolithically integrated 1x32 optical splitter/router for 1.31  $\mu\text{m}$ -band & 1.49  $\mu\text{m}$ -band in 2006 [14]. S. Kamei demonstrated a compact 50-GHz-spacing 64x64 ULCF-AWG router with low and uniform insertion losses of 5.4-6.8 dB and also demonstrated a 100-GHz-spacing 8x8 interconnected multiple-AWG router with a practical configuration, very low and uniform insertion losses of 2.3-3.4 dB and frequency deviations from the grid of less than plusmn6 GHz in 2009 [15]. I. H. White determined the electronic control and functionality requirement to enable full and practical operation of electro-optic switches in high performance networks to build optical routers which are able to switch on nanosecond timescales with more than  $16 \times 16$  ports in 2015 [16]. We have also found 1x4 and 1x8 signal routers based on 2x2 Ti:LiNbO<sub>3</sub> electro-optic MZI switch [17-18]. In our previous literature we presented the implementation of a 1x16 signal router using lithium niobate [19]. To overcome the problem of higher power requirement and loss in the above literature and to accommodate incredibly increasing no. of global subscriber, we implemented 1xN (1x2, 1x4, 1x8 and 1x16) signal router using both titanium diffused potassium niobate and titanium diffused lithium niobate based waveguide at 1.55  $\mu\text{m}$ . Finally an analysis on the effect of these two kinds of materials on such router configurations is shown by graphical representation. Section II shows the operating principle of a electro-optic switch, section III represents the construction and simulations of 1xN signal router and finally in section IV there is a conclusive study.

## II. BASICS OF ELECTRO-OPTIC SWITCH

Electro-optic effect is known as the change in the optical properties specifically in refractive index and absorption coefficient of a material with varying electric field. The change in the refractive index of the material is called pockels effect and the corresponding change is related to the change in the electric field in a proportional compartment. This electro-optic effect is the principle of MZI switch and router.

$$P_{out1} = \sin^2\left(\frac{\Delta\phi}{2}\right) \quad (1)$$

$$P_{out2} = \cos^2\left(\frac{\Delta\phi}{2}\right) \quad (2)$$

The outputs of the 2x2 MZI switch in Fig. 1 can be calculated by above equations [19]. When applied voltage is 0 V, phase change between the arms of MZI i.e.  $\Delta\phi$  becomes zero, so out 1 is zero, and out 2 becomes high. And for a particular switching voltage  $V_\pi$ ,  $\Delta\phi$  is  $\pi$ , so power is switched to out 1. To implement 1xN routers we have to cascade several no. of 2x2 switches and propagation of light is as same as that was for a single switch.

### III. CONSTRUCTION OF 1xN SIGNAL ROUTER

To design 1xN signal router we used titanium diffused potassium niobate waveguide with a width of 8.0  $\mu\text{m}$  along x axis. The strip of titanium with desired thickness is defined which should be heated on a Z-cut wafer of potassium niobate for several hours at a temperature lying in the range of a few thousands of Celsius during fabrication [7]. The structure of the switch is surrounded by the cladding of air. We started with a device length of 33000  $\mu\text{m}$  long and 100  $\mu\text{m}$  wide before optimization. In the 3D wafer properties the air is used as the coating material with a thickness of 2.0  $\mu\text{m}$  and we used substrate of potassium niobate with a thickness of 10  $\mu\text{m}$  & we set the values of electro-optic efficient and refractive index by using table I. To produce electro-optic effect we needed to introduce 3 electrodes, which were created on buffer layer with refractive index of 1.47 and 0.3  $\mu\text{m}$  thickness. The properties of buffer layer includes horizontal and vertical permittivity with a value of 4. Thickness of each electrode is set to 4.0  $\mu\text{m}$ . 1<sup>st</sup> and 3<sup>rd</sup> electrodes are defined with a width of 50  $\mu\text{m}$  and zero applied voltage. The 2<sup>nd</sup> electrode is set to a width of 26  $\mu\text{m}$  and voltage same as other electrodes. The separations d of 1-2 and 2-3 electrodes are set to 6  $\mu\text{m}$ . Table II presents the list of simulation parameters.

TABLE I. PARAMETERS OF POTASSIUM NIOBATE

Electro-Optic Coefficients $10^{-12}$ (m/V)				Refractive Index	
$r_{33}$	$r_{31}$	$r_{13}$	$r_{22}$	$n_o$	$n_e$
64	270	28	1.3	2.25	2.169

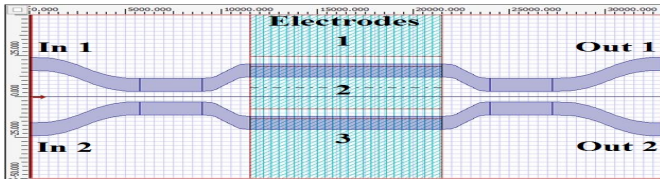


Fig. 1. 2x2 Mach-Zehnder electro-optic switch.

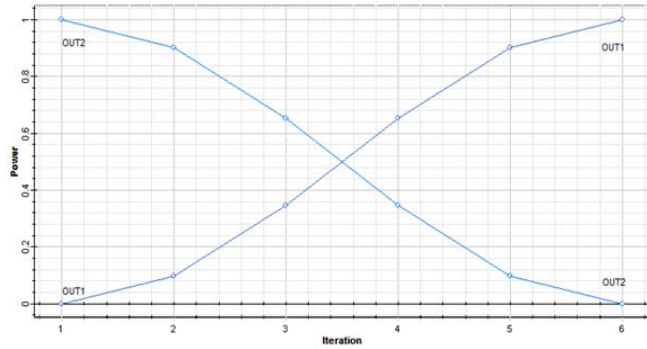


Fig. 2. Power in output waveguides.

TABLE II. SIMULATION PARAMETERS [11]

Parameters	Definitions
Reference index	Modal
Wavelength	1.55 $\mu\text{m}$
Mesh-number of points	500
Polarization	Transverse magnetic (TM)
BPM solver	Paraxial
Engine	Finite Difference
Propagation step	1.55
Scheme parameter	0.5
Boundary condition	Transparent Boundary Condition (TBC)

We evaluated the optimized value for the device parameters to obtain lowest insertion & excess loss and highest extinction ratio before constructing 1xN signal router. Optimization leads to an insertion loss of 0.00925 dB and extinction ratio of 32.157 dB and excess loss of 0.0066 dB for both cross state and bar state at 0.0825  $\mu\text{m}$  titanium strip thickness, 9900  $\mu\text{m}$  arm length, 8  $\mu\text{m}$  waveguide width, 32  $\mu\text{m}$  arm gap, 14.5  $\mu\text{m}$  gap in 3dB coupler gap [20]. The performance of this proposed structure is much better than Nazmi (2014) mentioned in ref [7] as we found reduction in insertion loss to 71.09% at 0 V & 64.56% at 4 V and extinction ratio also increases 9.38% at 0 V and 20.89% at 4 V [20]. Fig. 2 represents power in output waveguides. It can be ensured from Fig. 2 that the input power (optical) is switched completely from port 1 to port 2 in 6 iterations only by the application of applied voltage. 1xN routers using Ti:LiNbO<sub>3</sub> are implemented using the results of our previous literature in ref [11].

#### A. 1x2 Router

The switch described above is a 1x2 signal router. Layout and optical field propagation of 1x2 router are shown in Fig. 1 and Fig. 3. Dimensions of the device are, Length L= 32900  $\mu\text{m}$  and Width W= 100  $\mu\text{m}$ . Table II gives the simulation parameters for 1x2 router. Optical field propagation for both Ti:LiNbO<sub>3</sub> and Ti:KNbO<sub>3</sub> based router are same in look and Fig. 3 shows optical field propagation of Ti:KNbO<sub>3</sub> based 1x2 router. From Fig. 3 it is confirmed that input power at port 1 is switched to one of the two output ports at different time by varying the electrical input from 0 V to 8 V for Ti:LiNbO<sub>3</sub> based router and 0 V to 4 V for Ti:KNbO<sub>3</sub> based router. In this router there is only one control signal C<sub>1</sub> and different combinations of control signal are given at table III along with power calculated for both Ti:LiNbO<sub>3</sub> and Ti:KNbO<sub>3</sub> based router. From this table we can see that in case of insertion loss (I.L.), Ti:LiNbO<sub>3</sub> based router is better; but power requirement is double from that of Ti:KNbO<sub>3</sub> based router. In table III, 0 represents logic 0 i.e. 0 V for both type of router and 1 represents 8 V for Ti:LiNbO<sub>3</sub> based router & 4 V for Ti:KNbO<sub>3</sub> based router.

TABLE III. DIFFERENT COMBINATIONS OF CONTROL SIGNAL FOR 1x2 ROUTER

Output Port No.	C <sub>1</sub>	Ti:LiNbO <sub>3</sub> Based 1x2 Router [11]		Ti:KNbO <sub>3</sub> Based 1x2 Router	
		Power (mW)	I.L. (dB)	Power (mW)	I.L. (dB)
1	1	0.997974	0.00881	0.997872	0.00925
2	0	0.997974	0.00881	0.997872	0.00925



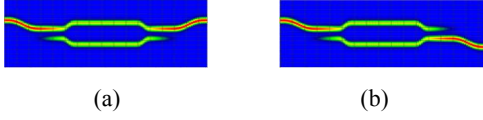


Fig. 3. Optical field propagation of 1x2 router at (a): Port 1, (b): Port 2.

### B. 1x4 Router

1x2 router is the basic building block of 1x4 router. We need three switches or in another word three 1x2 routers to implement 1x4 router. Simulation parameters are as same as table II. Fig. 4 and Fig. 5 show the layout and optical field propagation of the router. The dimensions of the device are, Length  $L= 98700 \mu\text{m}$  and Width  $W= 150 \mu\text{m}$ . Switches are marked as MZI 1, MZI 2 and MZI 3. Central electrodes of the switches are defined as control electrodes and are indicated as  $C_1$ ,  $C_2$  and  $C_3$ . Position of each control electrode is set to  $5.5 \mu\text{m}$  just above its corresponding axis. There are 4 output ports and to switch optical power to desired port it requires particular combination of control signals i.e.  $C_1$ ,  $C_2$  and  $C_3$ .

TABLE IV. DIFFERENT COMBINATIONS OF CONTROL SIGNAL FOR 1X4 ROUTER

Output Port No.	$C_1$	$C_2$	$C_3$
1	1	X	0
2	1	X	1
3	0	1	X
4	0	0	X

In table IV, X represents don't care condition. Don't care condition means that it does not matter whether the signal is on or off. If we want to get output at port 1 we have to set  $C_1$  high, then power will switch to MZI 3, with  $C_3$  low power will go to output port 1 and if  $C_3$  is high power will switch to output port 2. To switch power at port 3 and 4, we need to set  $C_1$  low. Power will switch to port 3 with  $C_2$  at 8 V for Ti:LiNbO<sub>3</sub> based router & 4 V for Ti:KNbO<sub>3</sub> based router and to port 4 with  $C_2$  at 0 V. As we implemented 1x4 router using both Ti:LiNbO<sub>3</sub> based switch & Ti:KNbO<sub>3</sub> based switch, so a comparative study between these two type of routers are given at table V. Comparing table III with table V, we can see that insertion loss (I.L.) is increased with the length of the device. Again loss is less in Ti:LiNbO<sub>3</sub> than Ti:KNbO<sub>3</sub> based router, but power requirement is double in Ti:LiNbO<sub>3</sub> based Router. If we compare our proposed router with the existing one as in ref [17], ours proposed one is better in smaller length and loss (indicated by black arrow) as shown in table VI.

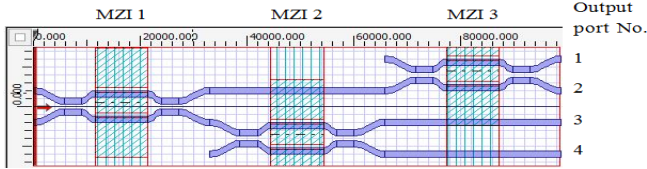


Fig. 4. Layout of 1x4 router.

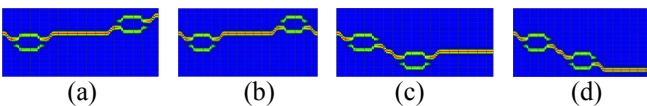
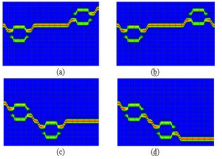
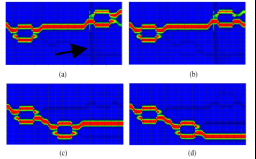


Fig. 5. Optical field propagation at (a) port 1, (b) port 2, (c) port 3, (d) port 4.

TABLE V. COMPARATIVE STUDY ON Ti:LiNbO<sub>3</sub> & Ti:KNbO<sub>3</sub> BASED 1X4 ROUTER

Output Port No.	Ti:LiNbO <sub>3</sub> Based Router		Ti:KNbO <sub>3</sub> Based Router	
	Power (mW)	I.L. (dB)	Power (mW)	I.L. (dB)
1	0.986207	0.060	0.967241	0.145
2	0.986207	0.060	0.967241	0.145
3	0.992529	0.033	0.973563	0.116
4	0.986207	0.060	0.973563	0.116

TABLE VI. COMPARATIVE STUDY ON PROPOSED 1X4 ROUTER

Specifications	Proposed 1x4 Router	Existing [17]
Length	98700 $\mu\text{m}$	99000 $\mu\text{m}$
Operating Wavelength	1.55 $\mu\text{m}$	1.3 $\mu\text{m}$
Switching Voltage	8 V for Ti:LiNbO <sub>3</sub> based switch and 4 V for Ti:KNbO <sub>3</sub>	6.75 V with Ti:LiNbO <sub>3</sub> based switch
Power Loss	Lower	Power leakage present
Optical Field Propagation		

### C. 1x8 Router

To design a 1x8 router it required 8 switches shown in Fig. 6, which gives the device dimensions of Length  $L= 197400 \mu\text{m}$  and Width  $W= 300 \mu\text{m}$ . Number of MZI switch could not be reduced as it will lead to the problem of overlapping of electrodes. As a result router would not function as it should be. Number of mesh point was changed to 1000. There are 8 control electrodes such as  $C_1$ ,  $C_2$ ,  $C_3$ ,  $C_4$ ,  $C_5$ ,  $C_6$ ,  $C_7$  and  $C_8$ .

TABLE VII. DIFFERENT COMBINATIONS OF CONTROL SIGNALS OF 1X8 ROUTER

Output Port No.	$C_1$	$C_2$	$C_3$	$C_4$	$C_5$	$C_6$	$C_7$	$C_8$
1	1	X	0	X	0	X	X	0
2	1	X	0	X	0	X	X	1
3	1	X	0	X	1	X	X	X
4	1	X	1	X	1	X	1	X
5	1	X	1	X	1	X	0	X
6	0	1	X	1	X	X	X	X
7	0	1	X	0	X	1	X	X
8	0	1	X	0	X	0	X	X

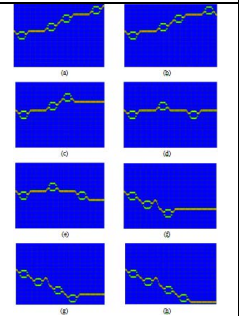
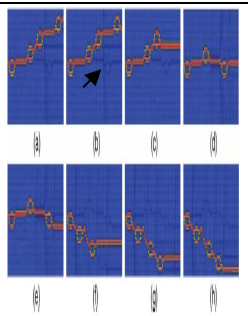
TABLE VIII. COMPARATIVE STUDY ON Ti:LiNbO<sub>3</sub> & Ti:KNbO<sub>3</sub> BASED 1X8 ROUTER

Output Port No.	Ti:LiNbO <sub>3</sub> BASED 1X8 ROUTER		Ti:KNbO <sub>3</sub> BASED 1X8 ROUTER	
	Power (mW)	I.L. (dB)	Power (mW)	I.L. (dB)
1	0.967241	0.145	0.96092	0.173
2	0.986207	0.060	0.967241	0.145
3	0.992529	0.033	0.973563	0.116
4	0.992529	0.033	0.973563	0.116
5	0.992529	0.033	0.973563	0.116
6	0.986207	0.060	0.973563	0.116
7	0.986207	0.060	0.967241	0.145
8	0.967241	0.145	0.96092	0.173

Effect of variation in power at these electrodes is given in table VII and table VIII includes corresponding power and

insertion loss for both Ti:LiNbO<sub>3</sub> & Ti:KNbO<sub>3</sub> based router. When C<sub>1</sub> is kept at high, power is switched to upper five ports and with C<sub>1</sub> at 0 V the lower ports can be switched. Optical power with C<sub>1</sub> high goes to MZI 3, which in turn switches power to MZI 5 if C<sub>3</sub> is at 0 V, then power goes to output port 1 while keeping C<sub>5</sub> and C<sub>8</sub> low. Similarly for each particular combination of these control voltage we can find each of the 8 ports at high state as shown in table VII. Fig. 7 shows optical power being switched to different output ports i.e. port 1 to port 8 at high state by the means of optical field propagation. Ti:LiNbO<sub>3</sub> and Ti:KNbO<sub>3</sub> based router show different performance at insertion loss and switching voltage as listed in table VIII. Again if we compare 1x8 router and 1x4 router, it is evident that power loss is function of length. It increases with the distance of the device. We compared our proposed 1x8 router with the existing one as in ref [18]; our proposed one is smaller in length and loss (arrow) as shown in table IX.

TABLE IX. COMPARATIVE STUDY ON PROPOSED 1X8 ROUTER

Specifications	Proposed 1x8 Router	Existing [18]
Length	197400 μm	200000 μm
Wavelength	1.55 μm	1.3 μm
Switching Voltage	8 V-Ti:LiNbO <sub>3</sub> and 4 V-Ti:KNbO <sub>3</sub>	6.75 V with Ti:LiNbO <sub>3</sub> based switch
Power Loss	Negligible	Power leakage present
Optical Field Propagation		

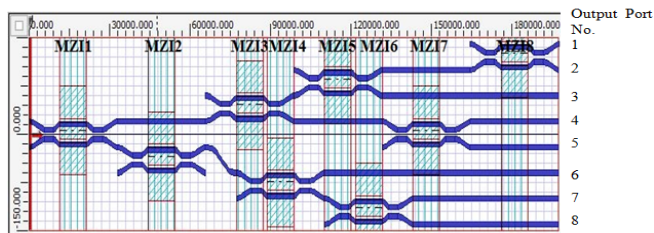


Fig. 6. Layout of 1x8 signal router.

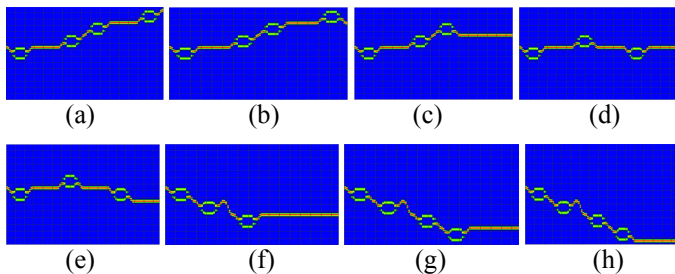


Fig. 7. Optical field propagation of 1x8 router at (a) port 1, (b) port 2, (c) port 3, (d) port 4, (e) port 5, (f) port 6, (g) port 7, (h) port 8.

#### D. 1x16 Router

For designing a 1x16 signal router, we needed 16 individual 2x2 MZI switches just like we needed in ref [19]. We could not minimize the number of switch, because if we minimize the number then we have to either increase the width of the router or electrodes will overlap each other. The router then will not function accurately. So device dimension is quite larger than 1x8 router and the length & width are,  $L = 307600 \mu\text{m}$ ,  $W = 700 \mu\text{m}$ . For simulation we had to set the no. of mesh point as 2000. Fig. 8 and Fig. 9 show the layout and optical field propagation of Ti:KNbO<sub>3</sub> based 1x16 router respectively. 16 switches are numbered as 1, 2, 3 and so on. We assumed the second electrode of each 2x2 MZI switch as control electrode and they are numbered as C<sub>1</sub>, C<sub>2</sub>, and C<sub>3</sub> and so on. Power at these control electrodes directs input optical power to one of the 16 output port in the signal router. Outputs are observed by OptiBPM software. Fig. 8 shows the 16 output ports of the device. If we want to switch power into one of these ports, then we will need particular combination of voltages across the central electrodes of these 16 MZI switches. Table X shows output at 16 different ports along with the variation of the control signal C<sub>1</sub>, C<sub>2</sub>, C<sub>3</sub>, C<sub>4</sub>, C<sub>5</sub>, C<sub>6</sub>, C<sub>7</sub>, C<sub>8</sub>, C<sub>9</sub>, C<sub>10</sub>, C<sub>11</sub>, C<sub>12</sub>, C<sub>13</sub>, C<sub>14</sub>, C<sub>15</sub> and C<sub>16</sub>. When upper 8 output ports are to be switched, we kept C<sub>1</sub> high and with C<sub>1</sub> low power will be switched to lower 8 output ports. If C<sub>1</sub> is high output goes to MZI 3, then C<sub>3</sub> is kept at 0 V and output goes to MZI 5, again with C<sub>5</sub> low power goes to MZI 9, with C<sub>9</sub> low power goes to MZI 11, consequently with C<sub>11</sub>, C<sub>13</sub>, C<sub>15</sub> low, power is switched to the output port 1. We can find high output at desired port for each of the combinations shown in table X. Table XI shows output powers at the 16 output ports of the router along with corresponding insertion loss for both Ti:LiNbO<sub>3</sub> and Ti:KNbO<sub>3</sub> based router.

If we consider a tradeoff between power requirement & loss factor, we can say that performance of the switch based on Ti:KNbO<sub>3</sub> is better than that of Ti:LiNbO<sub>3</sub>. But when implementing a large interconnecting network loss factor should be emphasized more because with the increment in distance power loss at output port can be high enough to produce error in transmission. We examined this relationship between length and loss by implementing several configurations of signal router as mentioned above. To understand the relationship between length i.e. propagation distance of light and insertion loss, we have drawn two curves. Fig. 10 and Fig. 11 represent length versus maximum and minimum loss obtain using the data of table III, V, VIII, and XI. Graphs are created by MATLAB software. From these figures we can observe clearly that loss is higher in Ti:KNbO<sub>3</sub>

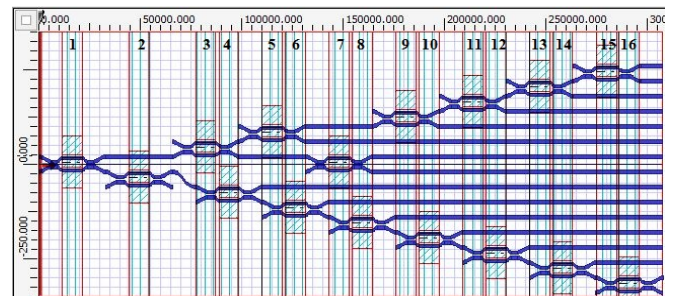


Fig. 8. Layout of 1x16 signal router.

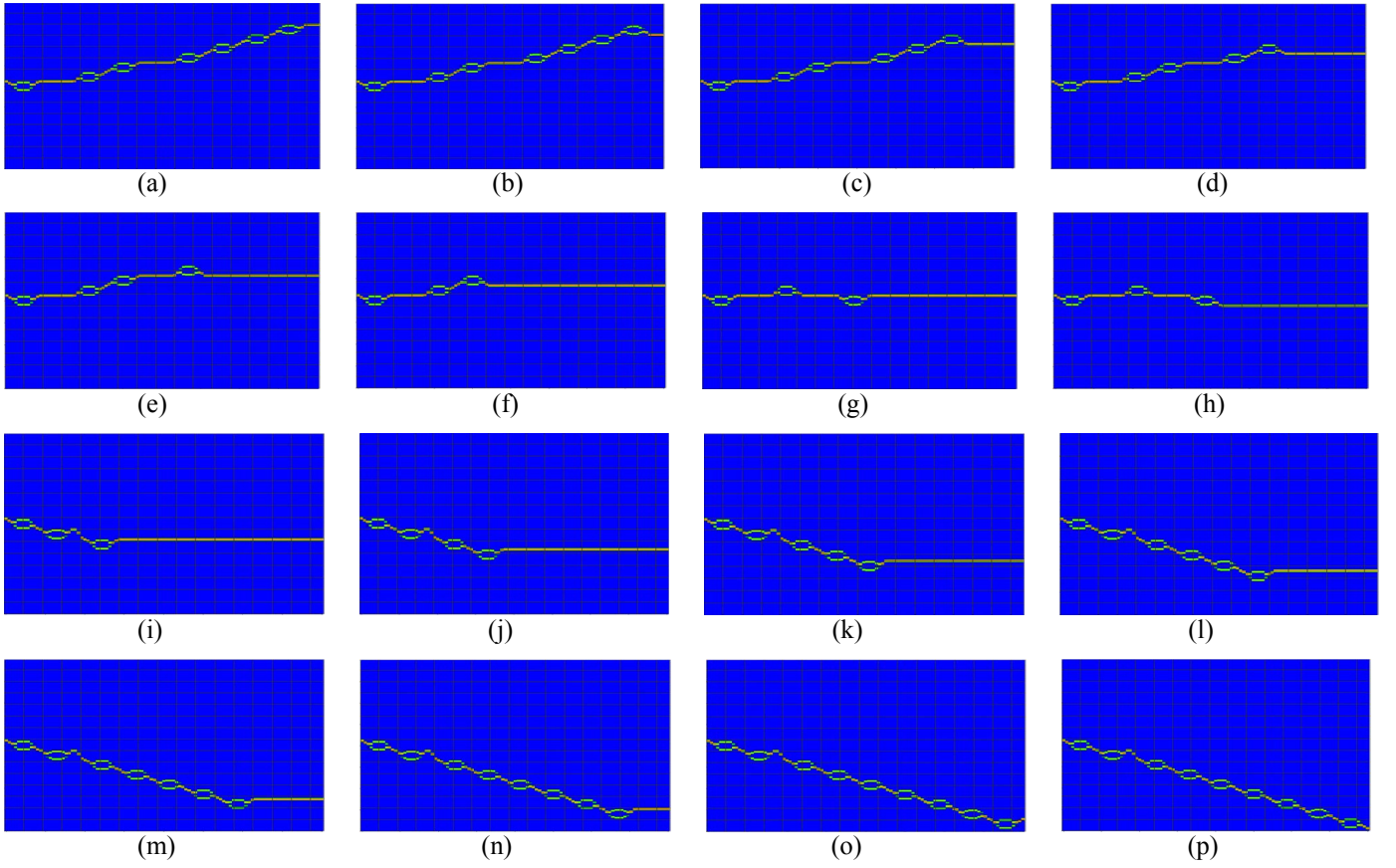


Fig. 9. Optical field propagation of 1x16 router at (a) port 1, (b) port 2, (c) port 3, (d) port 4, (e) port 5, (f) port 6, (g) port 7, (h) port 8, (i) port 9, (j) port 10, (k) port 11, (l) port 12, (m) port 13, (n) port 14, (o) port 15, (p) port 16.

TABLE X. DIFFERENT COMBINATIONS OF CONTROL SIGNALS FOR 1X16 ROUTER

Output Ports	C <sub>1</sub>	C <sub>2</sub>	C <sub>3</sub>	C <sub>4</sub>	C <sub>5</sub>	C <sub>6</sub>	C <sub>7</sub>	C <sub>8</sub>	C <sub>9</sub>	C <sub>10</sub>	C <sub>11</sub>	C <sub>12</sub>	C <sub>13</sub>	C <sub>14</sub>	C <sub>15</sub>	C <sub>16</sub>
1	1	X	0	X	0	X	X	X	0	X	0	X	0	X	0	X
2	1	X	0	X	0	X	X	X	0	X	0	X	0	X	1	X
3	1	X	0	X	0	X	X	X	0	X	0	X	1	X	X	X
4	1	X	0	X	0	X	X	X	0	X	1	X	X	X	X	X
5	1	X	0	X	0	X	X	X	1	X	X	X	X	X	X	X
6	1	X	0	X	1	X	X	X	X	X	X	X	X	X	X	X
7	1	X	1	X	X	X	1	X	X	X	X	X	X	X	X	X
8	1	X	1	X	X	X	0	X	X	X	X	X	X	X	X	X
9	0	1	X	1	X	X	X	X	X	X	X	X	X	X	X	X
10	0	1	X	0	X	1	X	X	X	X	X	X	X	X	X	X
11	0	1	X	0	X	0	X	1	X	X	X	X	X	X	X	X
12	0	1	X	0	X	0	X	0	X	1	X	X	X	X	X	X
13	0	1	X	0	X	0	X	0	X	0	X	1	X	X	X	X
14	0	1	X	0	X	0	X	0	X	0	X	0	X	1	X	X
15	0	1	X	0	X	0	X	0	X	0	X	0	X	0	X	1
16	0	1	X	0	X	0	X	0	X	0	X	0	X	0	X	0

based router. Since 2x2 MZI-EO switch is a basic building block in building large optical cross connect network (OXC) to provide interconnections between a large no. of optical network, so distance will get higher value with increasing no. of networks to connect. From our investigation, the solution is to use Ti:LiNbO<sub>3</sub> based switch in case of long communication to avoid larger loss which leads to error in received signal. But in case of smaller distance Ti:KNbO<sub>3</sub> will be appropriate.

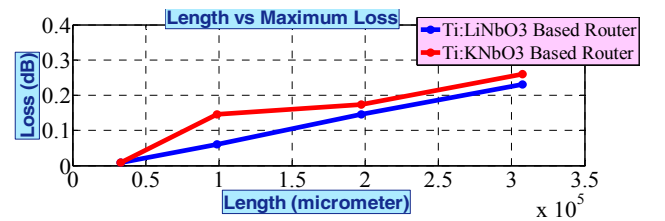


Fig. 10. Length (propagation distance of light) versus maximum loss curve.

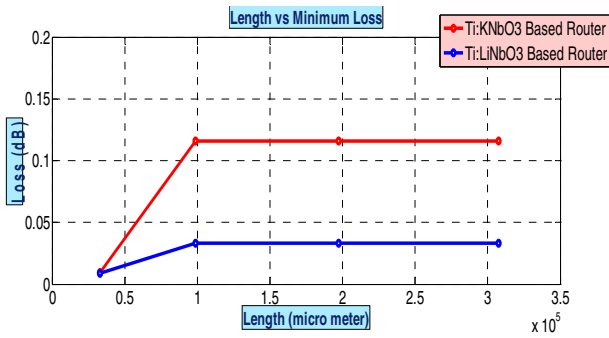


Fig. 11. Length ( propagation distance of light) versus minimum loss curve.

TABLE XI. COMPARATIVE STUDY ON Ti:LiNbO<sub>3</sub> & Ti:KNbO<sub>3</sub> BASED 1X16 ROUTER

Output Port No.	Ti:LiNbO <sub>3</sub> BASED 1X16 ROUTER		Ti:KNbO <sub>3</sub> BASED 1X16 ROUTER	
	Power (mW)	LL (dB)	Power (mW)	LL (dB)
1	0.954598	0.202	0.948276	0.231
2	0.96092	0.173	0.954598	0.202
3	0.96092	0.173	0.948276	0.231
4	0.967241	0.145	0.96092	0.173
5	0.967241	0.145	0.967241	0.145
6	0.986207	0.060	0.967241	0.145
7	0.992529	0.033	0.973563	0.116
8	0.992529	0.033	0.973563	0.116
9	0.992529	0.033	0.973563	0.116
10	0.986207	0.060	0.967241	0.145
11	0.986207	0.060	0.967241	0.145
12	0.967241	0.145	0.96092	0.173
13	0.96092	0.173	0.954598	0.202
14	0.954598	0.202	0.948276	0.231
15	0.948276	0.231	0.941954	0.260
16	0.948276	0.231	0.941954	0.260

#### IV. CONCLUSION

The design of 1xN signal router was presented in this paper. We designed 1x2, 1x4, 1x8 and 1x16 signal router using the optimized Ti:KNbO<sub>3</sub> based 2x2 MZI electro-optic switch. Variation in optical power at different ports by the application of control signal and their corresponding losses were shown and also compared with that of Ti:LiNbO<sub>3</sub> based routers. We got lower power loss in case of Ti:LiNbO<sub>3</sub> based routers than Ti:KNbO<sub>3</sub> based routers.

#### ACKNOWLEDGMENT

This work is provided with the support of Information and Communication Technology Division, Government of the People's Republic of Bangladesh by the ICT Fellowship 2015-2016.

#### REFERENCES

[1] Senior John M., "Optical Fiber Communications: Principles and Practice," Pearson Education Limited, 3<sup>rd</sup> edition, ISBN: 0-13-635426-2, pp. 4, 1 September 2009.

[2] G. Singh, "Design of 2x2 Optoelectronic Switch Based on MZI and Study the Effect of Electrode Switching Voltages," Journal of World Academy of Science, Engineering and Technology, vol. 39, pp. 401-407, 2008.

[3] D.J. Thomson, F.Y. Gardes, Sheng Liu, H. Porte, L. Zimmermann, J.M. Fedeli, Youfang Hu, M. Nedeljkovic, Xin Yang, P. Petropoulos, G.Z.

Mashanovich, "High Performance Mach-Zehnder Based Silicon Optical Modulators," IEEE Journal of Selected Topics in Quantum Electronics, vol. 19, issue 6, pp. 85 – 94, November-December 2013.

[4] Xianxin Jiang, Yangqing Chen, Fang Yu, Longhua Tang, Mingyu Li, Jian-Jun He, "High-sensitivity optical biosensor based on cascaded Mach-Zehnder interferometer and ring resonator using Vernier effect," Opt. Lett., vol. 39, issue 22, pp. 6363-6366, 2014.

[5] E.L. Wooten, R.L. Stone, E.W. Miles, E.M. Bradley, "Rapidly tunable narrowband wavelength filter using LiNbO<sub>3</sub> unbalanced Mach-Zehnder interferometers," Journal of Lightwave Technology, vol. 14, no. 11, pp. 2530-2536, November 1996.

[6] T. Mizuochi, T. Kitayama, K. Shimizu, K. Ito, "Interferometric crosstalk-free optical add/drop multiplexer using Mach-Zehnder based fiber gratings," Journal of Lightwave Technology, vol. 16, issue 2, pp. 265, 1998.

[7] Nazmi A. Mohammed, Huda S. Abo Elnasr, Moustafa H. Aly, "Analysis and design of an electro-optic 2 × 2 switch using Ti: KNbO<sub>3</sub> as a waveguide based on MZI at 1.3μm," Opt. Quant Electron (springer journal), vol. 46, pp. 295–304, 2014.

[8] M. P. Earnshaw, "8×8 Optical Switch Matrix Using Generalized Mach-Zehnder Interferometers," IEEE Photonics Technology Letters, vol. 15, no. 6, pp. 810-812, 2003.

[9] T. Sasaki, H. Sato, K. Nakatsuhara, T. Nakagami, "Demonstration of switching operation in a symmetric Mach-Zehnder interferometer switch using Si waveguide with a ferro-electric liquid crystal cladding," Conference on Lasers and Electro-Optics-Pacific Rim, pp. 1-2, 26-31 August 2007 .

[10] K. Suzuki, "High-Speed Optical 1×4 Switch Based on Generalized Mach-Zehnder Interferometer With Hybrid Configuration of Silica-Based PLC and Lithium Niobate Phase-Shifter Array," IEEE Photonics Technology Letters, vol. 19, no. 9, pp. 674-676, May 2007.

[11] Rabeya Khatun, Kazi Tanvir Ahmmed, A. Zahed Chowdhury, Raqibul Hossen, "Optimization of 2x2 MZI Electro-Optic Switch and Its Application as Logic Gate," 18th International Conference on Computer and Information Technology, pp. 294-299, December 2015.

[12] A.Z. Simoes, "Potassium niobate films prepared through polymeric precursor method," J. Mat. Lett., vol. 58, pp. 2537–2540, 2004.

[13] Leick L, Madsen CK., "Dispersion compensation of a 1x N passive optical router with low loss, a flat passband, and low cross talk," Opt Lett., vol. 27, no. 15, pp. 1318-20, 2002.

[14] K. Nara, N. Matsubara and H. Kawashima, "Monolithically integrated 1x32 optical splitter/router low loss ripple MZI-based WDM filter and low loss Y-branch circuit," Optical Fiber Communication Conference and National Fiber Optic Engineers Conference (OFC), pp. 3, 2006.

[15] S. Kamei, M. Ishii, A. Kaneko, T. Shibata and M. Itoh, "Cyclic-Frequency Router With Improved Performance Based on Arrayed-Waveguide Grating," journal of Lightwave Technology, vol. 27, no. 18, pp. 4097-4104, 15 September 2009.

[16] H. White, M. Ding, Q. Cheng, A. Wonfor and R. V. Penty, "Advanced photonic routing sub-systems with efficient routing control," Transparent Optical Networks (ICTON), 17th International Conference on Budapest, pp. 1-4, 2015.

[17] S. K. Raghuvanshi, A. Kumar, S. Kumar, "1×4 Signal Router Using 3 Mach-Zehnder Interferometers," Opt. Eng., vol. 52, no. 3, pp. 035002, 2013.

[18] Santosh Kumar, Sanjeev Kumar Raghuvanshi, Ajay Kumar, "Implementation of optical switches using Mach-Zehnder interferometer," Optical Engineering, vol. 52, no. 9, pp. 097106, September 2013.

[19] Rabeya Khatun, Raqibul Hossen, Kazi Tanvir Ahmmed, "Implementation of a 1x16 Router Using 2x2 Mach-Zehnder Interferometer Electro-Optic Switch," 2nd International Conference on Electrical Information and Communication Technology (EICT), pp. 295-300, December 2015.

[20] Rabeya Khatun, A. Zahed Chowdhury, "Performance Evolution of a 2x2 MZI Electro-Optic Switch Using Ti:KNbO<sub>3</sub> as Waveguide at 1.55 μm," 3rd International Conference on Optical Engineering and Information & Communication Technology, 2016, inpress.

# A Highly Efficient InGaN Single Junction Solar Cell Using MATLAB

Nargis Akter<sup>1</sup>, Sanjida Sharmin<sup>1</sup>, Rahima Afrose<sup>1</sup>

<sup>1</sup>Department of Computer Science and Engineering  
International Islamic University Chittagong  
Chittagong, Bangladesh  
[nargis.cuet@gmail.com](mailto:nargis.cuet@gmail.com),  
[ssharmin114@gmail.com](mailto:ssharmin114@gmail.com)  
[jiucrahima@gmail.com](mailto:jiucrahima@gmail.com)

M.A.Matin<sup>2</sup>, N. Amin<sup>3</sup>

<sup>2</sup>Department of Electrical and Electronic Engineering  
Chittagong University of Engineering and Technology  
Chittagong, Bangladesh  
[imamatin@yahoo.com](mailto:imamatin@yahoo.com)

<sup>3</sup>Department of Electrical, Electronic and System  
Engineering, Universiti Kebangsaan Malaysia  
Bangi, Selangor, Malaysia  
[nowshad@eng.ukm.my](mailto:nowshad@eng.ukm.my)

**Abstract**—Though the expenditure of world energy is increasing exponentially, it is obvious that a solution of renewable energy must be utilized. In order to fulfill the energy demand of the mankind, utilization of the huge energy of the sun by transforming it into electricity is an emerging alternative way. Recently developed InGaN is a direct band gap solar photovoltaic material that has an amazing tunable band gap of 0.7 eV to 3.4 eV and a high optical absorption coefficient over  $10^5$  /cm. In this paper, numerical simulations has been done using MATLAB to explore the unknown potential of this promising material to design a high performance InGaN solar cell. All the required parameters for simulation were determined from the theory, literature and in some cases reasonable estimation. This simulation were done with different ratio of In and Ga content for the single junction solar cell and found a high conversion efficiency of 27.3% with this InGaN compound material.

**Keywords**—Renewable energy; Solar photovoltaic; InGaN; MATLAB; Conversion efficiency.

## I. INTRODUCTION

Worldwide civilization requires low-priced, dependable and sustainable energy sources. With the increased technological development, the energy expenditure has enlarged steadily. More and more energy consumption is expected in future to withstand the present human development. Solar cells is the best way to utilize energy from the sun that is exactly the boundless source of renewable and clean energy. The initial efforts for progress of photovoltaic (PV) cells were focused towards space applications, and PV cells are still today the main source of power in space. InGaN based PV cells are the most potential candidate for solar energy conversion into electricity as there are possibilities of higher cell conversion efficiency and low cost fabrication. InGaN has near the ideal band gap of 0.7 eV to 3.42 eV [1, 2, 3] and higher optical absorption coefficient greater than  $10^5$ /cm, which indicates the better absorption of the sun spectrum. It is a very potential material for ultra-thin solar cells in space application. The layers of an InGaN solar cell might be deposited using the

various techniques, namely Metal Organic Chemical Vapor Deposition (MOCVD), Molecular Beam Epitaxy (MBE), Metal Organic Vapor Phase Epitaxy (MOVPE) [4]. In 2007, Xiaobin Zhang published the conversion efficiency of single junction InGaN solar cell was 20.284% [5] and the same group published the efficiency of 24.95% in 2008 [6]. In 2011, S. Ben Machiche has achieved efficiency of 24.88% for a single junction InGaN solar cell [7]. The III-V group materials are widely used for tandem materials cells for the space application, in 2009 InGaP/GaAs double Junction and InGaP/GaAs/Ge triple Junction cells were designed. Triple junction structure of GaInP/GaAs/Ge shown efficiency of 41.6% [8] but it should be noted that the 0.66eV indirect band gap energy of Ge is not optimal band gap of lower sub cell of a triple junction cell. In recent times, in 2012 a latest structure of GaInP/GaAs/GaInNAs shows efficiency of 44%, which is the world highest [9]. But the problem of this structure is more complex quardinary alloy system of the cell and the toxicity and the cost of As material are the biggest barrier of these material system.

However, there were no major work using MATLAB with this excellent material though it can save time and cost by designing high efficient cell. There are scopes to minimize the thickness to save materials and to increase the conversion efficiency with improved short circuit current density ( $J_{sc}$ ), open circuit voltage ( $V_{oc}$ ) and fill factor ( $FF$ ) with different proportion of In(x) in  $In_xGa_{1-x}N$  material system [10]. All the above ideas were modeled in this work and numerical analysis was done by using MATLAB to achieve the best possible structure of InGaN single junction solar cell for higher efficiency which is the basic component of tandem solar cell. The conversion efficiency has been found in this research work were 27.3% for the single junction solar cell from MATLAB Simulation.

## II. MODELING AND MATLAB SIMULATION

Numerical simulation is the first way to calculate the effect on cell performance [10] and to test the possibility of the proposed structure. Modeling is widely used in the analysis of solar cells due to its complex and very costly fabrication method. Figure.1 illustrates the proposed structure of aInGaN based single junction solar cell. From Fig. 1, it is clear that this structure consists a p layer and an n layer InGaN along with a TCO and back contact to achieve thin InGaN layer.

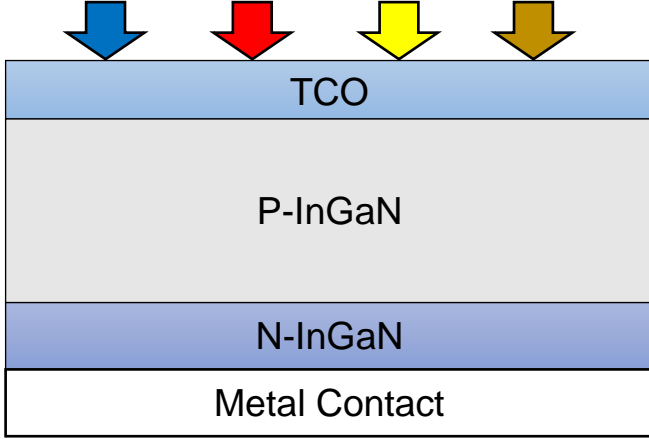


Fig.1: Proposed structure of single junction solar cell

MATLab simulations were done in this work to design the cell structure and the required equations were collected from the theory of solar cells. The equations required for this simulations are shown here.

The Short circuit current density,  $J_{sc} = J_n^p + J_p^n$  [11]

Where  $J_n^p$  and  $J_p^n$  are the photocurrent collected by p type and n type materials. The total the photocurrent collected by p type material is equal to

$$J_n^p = \int_0^{\lambda_1} j_n(\lambda) d\lambda$$

Where  $\lambda_1$  is the absorption wavelength of InGaN which can be varied from 0.7eV to 3.4 eV. The photo generated electron current density is

$$j_n(\lambda) = qF(\lambda)[1 - R(\lambda)] \frac{a_n(\lambda)}{\alpha_n(\lambda)^2 - 1} \beta_n \left[ b_n + a(\lambda) - \exp\left(\frac{-Z_p a_n(\lambda)}{L_n}\right) \left[ [b_n + a_n(\lambda)] \cosh\left(\frac{Z_p}{L_n}\right) + [1 + b_n a_n(\lambda)] \sinh\left(\frac{Z_p}{L_n}\right) \right] \right]$$

Where q is the absolute value of electronic charge,

$$\beta_n = [\cosh\left(\frac{Z_p}{L_n}\right) + b_n \left(\frac{Z_p}{L_n}\right)].$$

Spectral distribution of the solar flux is

$$F(\lambda) = 3.5 * 10^{21} \lambda^{-4} \left[ e\left(\frac{hc}{KT_1 \lambda} - 1\right) \right]^{-1}$$

Where h is plank's constant, c is the velocity of light.

For n type material, total photocurrent collected is

$$J_p^n = \int_0^{\lambda_1} j_p(\lambda) d\lambda$$

Where  $\lambda_1$  is the absorption wavelength of InGaN which can be varied from 0.7eV to 3.4 eV. The photo generated electron current density is

$$j_p(\lambda) = qF(\lambda)[1 - R(\lambda)] \frac{a_p(\lambda)}{\alpha_p(\lambda)^2 - 1} \beta_p \left[ b_p + a(\lambda) - \exp\left(\frac{Z_n a_p(\lambda)}{L_p}\right) \left[ [b_p + a_p(\lambda)] \cosh\left(\frac{Z_n}{L_p}\right) + [1 + b_p a_p(\lambda)] \sinh\left(\frac{Z_n}{L_p}\right) \right] \right]$$

Where,  $\beta_p = [\cosh\left(\frac{Z_n}{L_p}\right) + b_p \left(\frac{Z_n}{L_p}\right)]$

Open circuit voltage  $V_{oc}$  is defined as

$$V_{oc} = \frac{KT}{q} \ln\left(\frac{J_{sc}}{J_0} + 1\right) \quad [12]$$

Where  $j_0$  is the reverse saturation current and the equation is,

$$J_0 = Q \left( \frac{D_n}{L_n N_A} + \frac{D_p}{L_p N_D} \right) n_i^2 \quad [13]$$

Where

$$n_i^2 = N_c N_v e \left( -\frac{E_g}{KT} \right)$$

$N_c$  and  $N_v$  are the effective density of state.  $N_A$  and  $N_D$  are the doping concentration of p type and n type materials. The equation of mobility of electron is

$$\mu_i(N) = \mu_{min,i} + \frac{\mu_{max,i} - \mu_{min,i}}{1 + \left(\frac{N}{N_{g,i}}\right)^{\gamma_i}} \quad [14]$$

The equation of fill factor is[14]

$$FF = \frac{v_{oc} - \ln(v_{oc} + 0.72)}{v_{oc} + 1}$$

Where,  $v_{oc} = \frac{q}{nKT} V_{oc}$ , n is the ideality factor that can be considered 1.

Finally the efficiency of a solar cell is related with short circuit current density, open circuit voltage and fill factor of a cell.

$$\eta = J_{sc} \cdot V_{oc} \cdot FF$$

The power input is 1000 W/m<sup>2</sup> at 1 sun.

Table 1 show all material parameters used in this modeling, which were determined based on literature, theory or in some cases reasonable estimations to get better cell performance.

TABLE 1 PARAMETER USED IN SIMULATION

Parameters for Simulation	Unit of measure	Value
Surface recombination velocity for electron (S <sub>n</sub> )	cm s <sup>-1</sup>	1000
Surface recombination velocity for hole (S <sub>p</sub> )	cm s <sup>-1</sup>	1000
Surface reflection coefficient (R <sub>s</sub> )		0.1
Absorption coefficient (α <sub>i</sub> )	cm <sup>-1</sup>	5x10 <sup>5</sup>
Effective density of state at conduction band (N <sub>c</sub> )	cm <sup>-3</sup>	1.40x10 <sup>18</sup>
Effective density of state at valence band (N <sub>v</sub> )	cm <sup>-3</sup>	4.04x10 <sup>19</sup>
Acceptor concentration (N <sub>A</sub> )	cm <sup>-3</sup>	10 <sup>16</sup>
Donor concentration (N <sub>D</sub> )	cm <sup>-3</sup>	10 <sup>16</sup>
Electron mobility (μ <sub>n</sub> )		955
Hole mobility (μ <sub>p</sub> )		169.8
Ideality factor		1

### III. RESULT AND DISCUSSIONS

The number of parameters that can be varied is more than 50 in a solar cell. So it is ambiguous to solve such variable model. This numerical analysis has been done aiming to improve the cell performance of the InGaN single junction solar cell structure. All the required equations were simulated using MATLAB to find the stable structure of a single junction InGaN solar cell.

The dependency of the cell performance on the ratio of In in In<sub>x</sub>Ga<sub>1-x</sub>N from 0% to 100% has been simulated by MATLAB. It has been observed from the simulation result shown in Fig. 2 that the efficiency is highest in the range of Indium ratio of 55% to 75% corresponding the following equation of band gap with Indium proportion. [15, 16]

$$E_g(x) = 0.7x + 3.4(1-x) - 1.43x(1-x)$$

Where E<sub>g</sub> is the band gap and x is the proportion of In in In<sub>x</sub>Ga<sub>1-x</sub>N.

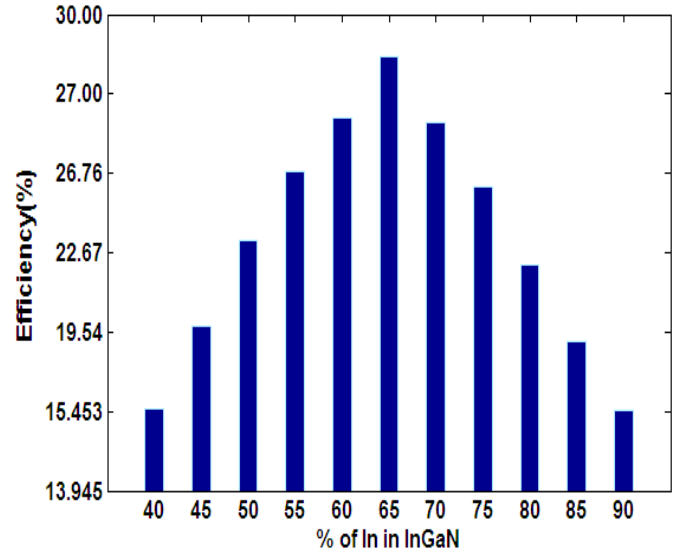


Fig.2: Efficiency vs percentage of In in InGaN of the proposed single junction solar cell

Fig.3 shows the output J-V characteristic curve of the designed cell. After doing rigorous simulation, efficiency of 27.3% was found (J<sub>sc</sub>=34.15mA/cm<sup>2</sup>, V<sub>oc</sub>=0.89V and FF=0.88). MATLAB is more effective tools that requires less time to simulate more data. Rigorous simulation can be done from which best result can be fitted. In AMPS, for each data we need to simulate the cell separately. But in MATLAB, it can be done by using the equation with the range of data and then best cell structure can be selected.

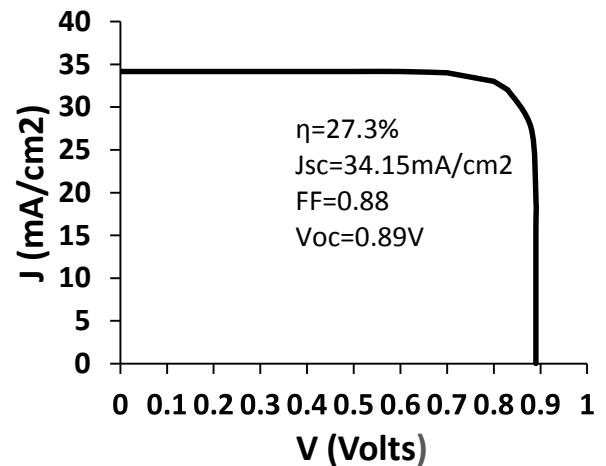


Fig.3: J-V curve of the proposed InGaN single junction solar cell

A single junction solar cell of InGaN material has been designed with conversion efficiency of 27.3% ( $J_{sc}=34.15\text{mA/cm}^2$ ,  $V_{oc}=0.89\text{V}$ ,  $FF=0.88$ ). Here MATLAB is introduced to design such kind of InGaN solar cell. Though the fabrication method is very complex and costly, MATLAB simulation is useful to design this highly efficient cell that can save time and cost. This designed basic cell of InGaN with its tunable bandgap can be used to design multijunction tandem solar cells for space application.

### References

- [1] Wu J, Walukiewicz W, Yu K M, Ager J W III, Haller E, Lu H, Schaff W J, Saito Y and Nanishi Y 2002 Appl. Phys. Lett. 80 3967.
- [2] Xiao H L, Wang X L, Wang J X, Zhang N H, Liu H X, Zeng Y P, Li J M and Wang Z G 2005 J. Cryst. Growth 276 401
- [3] N. Akter, M.A. Matin, N.Amin, "A high performance  $\text{In}_x\text{Ga}_{1-x}\text{N}$  single junction solar cell from numerical analysis", IEEE conference on Clean Energy and Technology (CEAT), 2013.
- [4] "Characterization of InGaN based photovoltaic devices" www.sciencedirect.com/science/article/pii/S004060901200733X, June 2012.
- [5] "Simulation of  $\text{In}_{0.65}\text{Ga}_{0.35}\text{N}$  single junction solar cells" Journal of Physics D: Applied Physics, doi:10.1088/0022-3727/40/23/031.
- [6] "Xiaoming; Shen Shuo; Lin Fubin; Li Yiming; Wei Shuiku; Zhong Haibin; Wan Jiangong Li "Simulation of the InGaN-based tandem solar cells" Photovoltaic Cell and Module Technologies II, edited by Bolko von Roedern, Alan E. Delahoy, Proc. of SPIE Vol. 7045, 70450E, (2008) · 0277-786X/08/\$18 · doi: 10.1117/12.793997
- [7] "Potential of  $\text{In}_x\text{Ga}_{1-x}\text{N}$  Photovoltaic Tandem" Revue des Energies Renouvelables Vol. 14 N° 1 (2011) 47-56.
- [8] Takamoto, T.; Kodama, T.; Yamaguchi, H.; Agui, T.; Takahashi, N.; Wasio, H.; Hisamatsu, T.; Kaneiwa, M.; Okamoto, K.; Imaizumi, M.; Kibe, K. InGaP/GaAs solar cells. In Proceedings of the IEEE 4th World Conference on Photovoltaic Energy Conversion, Waikoloa, HI, USA, May 2006; pp. 1769-1772.
- [9] "Solar spectrum conversion for photovoltaics using nanoparticles" igitur-archive.library.uu.nl/milieu/2012-1102-00548/UUindex.html.
- [10] Nargis Akter, "Design and Simulation of Indian Gallium Nitride Multijunction Tandem Solar Cells", International Journal of Research in Engineering and Technology (IJRET) ISSN: 2321-7308. Volume 3, Issue 1, PP. 315-321, January, 2014.
- [11] Matin, M.A., Amin, N., Zaharim, A. & Sopian, K. 2010b. A Study towards the Possibility of Ultra Thin CdS/CdTe High Efficiency Solar Cell from Numerical Analysis", WSEAS Transaction on Environment and Development 8(6): 572-580.
- [12] [https://en.wikipedia.org/wiki/Theory\\_of\\_solar\\_cells#Photogeneration\\_of\\_charge](https://en.wikipedia.org/wiki/Theory_of_solar_cells#Photogeneration_of_charge)
- [13] P. Singh, S. N. Singh, M. Lal, M. Husain, "Temperature dependence of I-V characteristics and performance parameters of silicon solar cell", Solar Energy Materials and Solar Cells 92 (2008) 1611-1616.
- [14] M. A. Contreras, T. Nakada, A. O. Pudov, R. Sites, "ZnO/ZnS(O,OH)/Cu(In,Ga)Se<sub>2</sub>/Mo solar cell with 18.6% efficiency", Proceedings of the third world conference of photovoltaic energy conversion, 2003, pp. 570-573.
- [15] T.T. Mnatsakanov, M.E. Levinshtein, L.I. Pmorteveva, S.N. Yurkov, G.S. Simin, M.A. Khan, Carrier mobility model for GaN, Solid-State Electron. 47 (2003), 111-115.
- [16] N. Posthuma, J. Vander Heide, G. Flamand, J. Poortmans, "Emitter formation and contact realization by diffusion for germanium



# An Analysis of the Problems for Health Data Integration in Bangladesh

Shahidul Islam Khan; Abu Sayed Md. Latiful Hoque  
Department of Computer Science and Engineering (CSE)  
Bangladesh University of Engineering and Technology (BUET)  
Dhaka, Bangladesh  
nayeemkh@gmail.com; asmlatifulhoque@cse.buet.ac.bd

**Abstract**— Discovering the hidden knowledge from different health data repositories requires the integration of health data from widely diversified sources. While integration, maintaining record linkage is a critical research issue for developing countries such as Bangladesh. Researchers have given different solutions to this problem that are applicable for developed countries where electronic health record of patients are maintained with identifiers like social security number (SSN), Universal Patient Identifier (UPI), etc. These algorithms cannot be used for integrating health data in Bangladesh because of many missing data, different ID used for the same patient in same or different systems and high amount of noise in other patient information. In this paper, we have defined the constraining factors of healthcare data available in Bangladesh and other developing countries. We have analyzed the practical problems of collecting and integrating healthcare data in Bangladesh to build up its National Health Data Warehouse (NHDW). We have also provided some important recommendations to boost the integration process and also to support record linkage.

**Keywords**—Data Integration; Health Data Warehouse; Record Linkage; Bangladesh

## I. INTRODUCTION

Integrated health data repositories or health data warehouse are proven to be beneficial in many fields such as mining health patterns, evidence-based medicine, personalized treatments etc. [1]-[5]. Significantly large volume of medical records and associated documents are generated by health investigative equipment every day. These worthy healthcare data are reserved in different healthcare information systems such as Picture Archiving and Communications System, Hospital Information System, Radiology Information System etc. in public hospitals, private clinics, and diagnostic centers. Data requires for making proper medical decisions are trapped within the fragmented and heterogeneous healthcare delivery systems that are not integrated appropriately. So it is very much essential to integrate these health records into one place—a single data warehouse.

To get most out of Integrated Health Data Repositories (IHDR), linkage of records is essential. Uncovering fruitful knowledge (e.g., finding correlation among diseases) from health dataset requires maintaining record linkage. Record linkage is a mechanism to find out record pairs from multiple information systems which refer to the same object in reality. Given two databases of records, the record-linkage procedure

determines all pairs that are similar to each other. The likeness of two records is defined using domain-specific matching over individual attributes. Record linkage is indispensable to join datasets based on entities that may or may not share common identifiers [6], [7].

Numerous techniques have been proposed by the researchers for record linkage in the medical domain. These techniques are shown to be efficient for IHDR of the modern world where health records typically contain PID, correctly inputted name, date of birth, ZIP codes of the patients. But in the cases of developing countries like Bangladesh current linkage techniques cannot be implemented properly. Some common problems of developing countries are illiteracy and dense population. Thus available health data suffers from lacking patient identity in any form (e.g., medical card no., SSN, NID) as well as correct names and DOB of the patients.

Bangladesh government took the initiative to develop National Health Data Warehouse (NHDW) in 2009 with the help of German Donor GIZ. The objective of the warehouse is to build a digital data storage that will eliminate the disparity between the available medical recordsets and will also support interoperability. Healthcare data from different organizations under Directorate General of Health Services (DGHS) of Bangladesh Government are gathered using DHIS2 and OpenMRS; both are open source software. The warehouse provides a gangplank for reporting and data mining functions that could be used by the decision makers at different levels to monitor health improvements at all levels down to Upazila health complexes [8], [9].

In this paper, we have analyzed different problems for healthcare data integration in Bangladesh to develop a national level health data warehouse for the citizen. We have also provided some guidelines to boost up the integration process.

## II. CONSTRAINTS OF HEALTH DATA IN BANGLADESH AND OTHER DEVELOPING COUNTRIES

Developing countries are those with low, lower middle or upper middle incomes. There are some common socio-economic characteristics found in the developing countries of the world that have a similar impact on healthcare facilities and health data. These characteristics include Lower per-capita income, higher population growth rates, and low level of urbanization [10], [11]. This implies poor health, inadequate education, and the majority of the people lives in

---

This research is supported by the ICT Division, Ministry of Posts, Telecommunications and Information Technology, Government of the People's Republic of Bangladesh.

the rural area. Above socio-economic conditions made an impact in the available health care data of Bangladesh and other developing countries in the following ways.

a) Health records without unique Patient ID: people do not have medical cards with unique health ID. Health care centers do not have provision to store National ID numbers or Social Security Numbers (SSN).

b) Misspelled names: Many people in real do not know their full name and unable to pronounce their name correctly even in the mother tongue. The Same person provides a different version of their name in the health care facilities. The problem can be understood from the table below.

TABLE I. AMBIGUITY IN PATIENTS' NAME IMPUTATION

Actual Patient Name	Inputted Name
Abul Hossain	Mr. Abul Hossain
	Mr. Md. Abul Hosen
	Mohammad Abul Hossain
	Abul Hosen
	Abul Hossen
	Mr. Abul
	Md. Hosen
	Md. Hossain

c) No actual date of birth: Enormous people do not know their actual birth date because of lacking of birth registration. For several years, they provide same age (e.g., 43 years) to hospitals and diagnostic centers. A lot of people do not know their actual date of birth in Bangladesh. This is a very common scenario for aged rural people with less education.

d) Missing attribute values: As Bangladesh and other developing countries have the dense population and inadequate facilities, in all health centers there are long queues of patients. So many necessary attribute values cannot be inputted for processing a high number of patients in limited time.

e) Error in data: less qualified staffs for inputting patients' data. This leads to unintentional wrong input data.

So patients' health records in Bangladesh contain more noisy data with more missing values and without unique patient identification numbers. The situation is depicted in Fig. 1. These makes techniques of developed countries for record linkage inappropriate for Bangladesh and more specialized technique to address the situation.

ID	PATIENT NAME	BIRTH YEAR	M STATUS	Gender	PHONE/MOBILE	Test Date	Test Name	Result
NC11509778	MR. TANVIR HASAN	1985	U	M	01677111948	18-Jun-14	S. Creatinine	1.35
NC21509575	MR. TANVEER HASAN	1985			7111948		HbA1c	5.9
778607	MR. TANVIR HOSSEN		U	M	01677111948		HbA1c	5.7
NC214194512	MRS. AMENA BEGUM	1982	M	F	01677111948		CBC	4.2
214154503	MRS. AMINA BEGUM		M	F	000	25-Jan-15	HbA1c	7.6
RC114080069	MRS. AMENA BEGUM	1959		F	01677117513	13-Apr-16	SGPT	33
RC154088403	MRS. AMINA BEGOM	1962	M	F	01677117513	12-Jan-13	S. Creatinine	1.4

Fig. 1. Status of available patient records in Bangladesh

### III. HEALTH DATA GENERATION AND STORAGE IN BANGLADESH

The patient visit cycle to different hospitals, diagnostic centers, and private practitioners' chamber is illustrated in Fig.2 to Fig. 5. The patient visit to different health service providers can be grouped as follows.

#### 1) Patient treatment cycle in Bangladesh

##### a) Patient visits hospitals

There are two types of hospitals in Bangladesh, Government hospitals and private hospitals. According to Directorate General of Health Services (DGHS), the total number of government hospitals under DGHS is 592 [12], [13]. According to the list provided by Bangladesh Private Clinic and Diagnostic Owners Association (BPCDOA), the only Government approved association of private hospital owners, there are 2761 private hospitals in Bangladesh [14], [15].

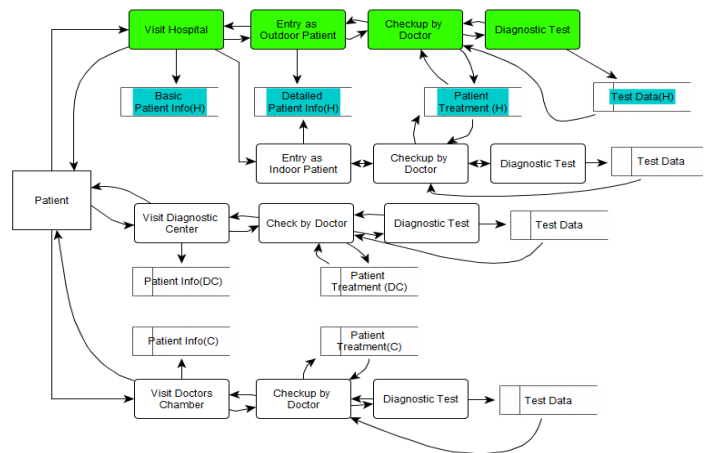


Fig. 2. Patient treatment in a hospital as an outdoor patient

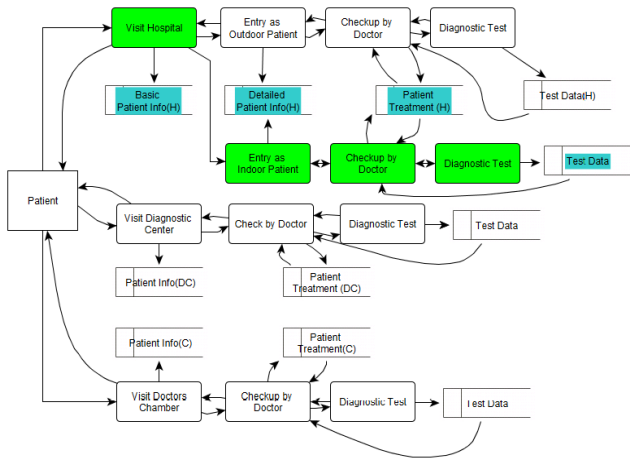


Fig. 3. Patient treatment in a hospital as an indoor patient

Patients normally visit a hospital’s outdoor or OPD unit, where the person in the reception notes down the basic information of the patient. Then the corresponding doctor checked the patient and write up the treatment notes. If necessary, the doctor gives some pathological tests that the patient performed in the diagnostic unit inside the hospital or any outside diagnostic center. The test results are stored in the centers where a test is performed. In almost all hospitals, there is no patient tracking system with unique patient ID. The irony is that the number of times same patient visits same hospital for treatment or diagnosis, his or her records will be recorded each time as a different patient with different ID or serial number.

*b) Patient visits Diagnostic Centers*

According to Bangladesh Private Clinic and Diagnostic Owners Association (BPCDOA, there are more than 8000 private diagnostic centers in Bangladesh registered by the Government. A patient may visit any diagnostic center to perform some routine health checkups to know his health conditions. These tests include Blood sugar, Cholesterol level test etc. In almost all Diagnostic Centers (more than 99%), every time when same patient visits, he is treated as a new patient and his records are stored as a new entry with no relationship or linking with the previous records of the same patient (Fig. 4).

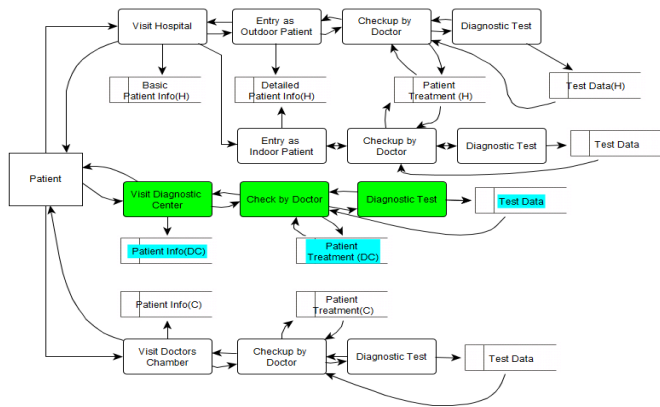


Fig. 4. Patient treatment in a diagnostic center

*c) Patient visits Personal Chamber of Doctors*

There are about 75700 Registered MBBS doctors and 6800 Dental doctors in Bangladesh [16]. Most of the doctors have private chambers where they consult patients after office hours. A patient can visit a doctor’s chamber for treatment. The doctor may recommend some pathological tests. Here also the patients are not tracked with unique ID and no linkage is maintained among the test records of a single patient (Fig. 5).

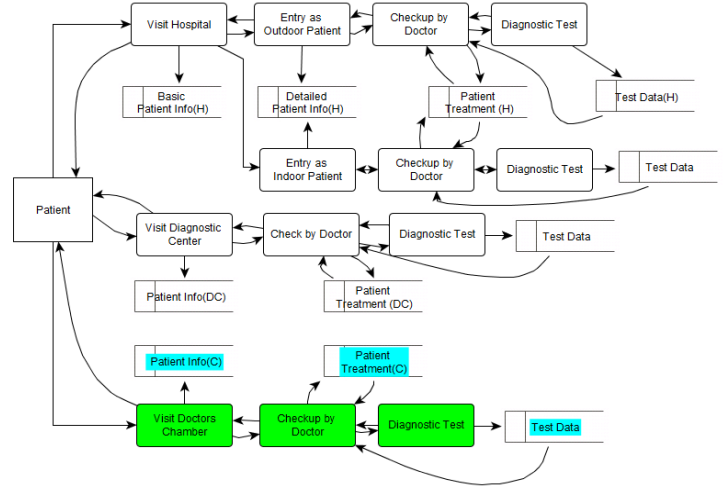


Fig. 5. Patient treatment in a doctor’s private chamber

*2) Record linkage problem*

Based on the patient cycles as described above, different cases arise.

Case 1: Patient  $P_1$  visits hospital  $H_1$  at timestamp  $T_1$  for event  $e_1$  with ID  $concat(P_1H_1T_1e_1)$

Case 2: Patient  $P_1$  visits hospital  $H_1$  at timestamp  $T_2$  for event  $e_1$  with ID  $concat(P_1H_1T_2e_1)$

.....  
 Case i: Patient  $P_1$  visits hospital  $H_k$  at timestamp  $T_i$  for event  $e_1$  with ID  $concat(P_1H_kT_ie_1)$

.....  
 Case n: Patient  $P_1$  visits hospital  $H_k$  at time stamp  $T_n$  for event  $e_1$  with ID  $concat(P_1H_kT_ne_1)$

Now the question is how many possible records that can be evolved in the lifetime of a patient?

Let RL is the total health records for the lifetime of a single patient.

$$So RL \subseteq H \times T \times e$$

We can estimate an upper limit of RL as follows:

Let life span of a person =  $y$  years

Average visit to any health care facility per month =  $v$

Visit per year =  $12v$

Total health care visits in life span of a person  $T = 12vy$

Average Life expectancy in Bangladesh: Male-70years and Female-72years [17].

If we consider  $y=71$  and  $v=3/month$

$$So T = 12 \times 3 \times 71 = 2556 \text{ times}$$

If one visit creates one record,  $RL=2556$

In Bangladesh perspective, health records of a person are stored either in electronic form or hard copy format and 2556 different records of the same person are stored with 2556 different identities. These records are highly distributed in terms of time (e.g., doing pathological tests in different times), space (e.g., outdoor, indoor or lab), data type (e.g., MS Excel or Oracle), and locations (e.g., different hospitals).

For extraction of fruitful knowledge from health data, it is the first requirement to accumulate health records from widely variable sources. Privacy of patients needs to be preserved as health data have high sell values [18]. While accumulation, these records cannot be mapped with the patients because of storing patient records every time with different identities. Record linkage problem is to find an optimum reliable mapping of each patient to his health record throughout the lifespan.

#### IV. RECOMMENDATIONS

Followings are our recommendations to improve the usability, performance, and security of the National Health Data Warehouse (NHDW) of Bangladesh.

1. It is very important to include all healthcare providers, regardless public or private, in the NHDW soon. If the coverage of the national data repository reaches 100%, then the Govt. will be able to take more fruitful administrative and management decisions.
2. Data quality is very important because utilization of the data will improve the service delivery. Policy makers can be benefited by using quality data for taking better decisions. There is scope to improve the quality of the available data in the warehouse. For future data collection, data entry personnel at Upazila level should be given more training.
3. Patient information collection forms in all hospitals, clinics, diagnostic centers, research centers etc. need to be standardized and necessary fields should be included.
4. As health records are stored in different medical centers in different formats (e.g., MS Excel, Oracle, MySQL, etc.), this heterogeneity needs to be addressed properly by adopting efficient Extract, Transform, and Load (ETL) mechanism.
5. For privacy reason, no medical record can be stored at any level, from diagnostic centers to NHDW, with *personally identifiable attributes* of the patients.

#### V. CONCLUSION

Health data warehouse development is a complex and time-consuming process but plays a vital role in delivering quality health services. To extract knowledge from different health data sources requires the integration of healthcare data from various diversified sources like hospitals, clinics, diagnostic centers, research centers etc. Preservation of record linkage using identifiable attributes of patients in national health data warehouse is very important for knowledge discovery. Researchers have given different solutions of health data integration and record linkage that are applicable for developed countries where electronic health record of patients are maintained with different identifiers. Their solutions are

inappropriate for integrating health data in Bangladesh because of many missing data, different ID used for the same patient in same or different systems and high amount of noise in other patient information. Bangladesh government is developing Health Data Warehouse at the national scale. In this paper, we have characterized the factors constraining health care data available in Bangladesh. We have discussed the problems of collecting and integrating healthcare data in Bangladesh to build up its National Health Data Warehouse. We have also provided guidelines to boost the integration process and also to support record linkage.

#### REFERENCES

- [1] T.R. Sahama, and P.R. Croll, "A Data Warehouse Architecture for Clinical Data Warehousing," Australasian Workshop on Health Knowledge Management and Discovery, 2007.
- [2] J.A. Lyman, K. Scully, and J.H. Harrison, "The development of health care data warehouses to support data mining," Clin Lab Med. 28,1 2008, pp. 55-71
- [3] O. Maimon, and L. Rokach, Data Mining and Knowledge Discovery Handbook, 2<sup>nd</sup> Edition, Springer 2010.
- [4] J. H. Boyd, S.M. Randall, A. M. Ferrante, J.K. Bauer, A. P. Brown, and J.B. Semmens, "Technical challenges of providing record linkage services for research", BMC Medical Informatics and Decision Making 2014, 14:23
- [5] S. I. Khan and A.S.M.L. Hoque, "Towards Development of National Health Data Warehouse for Knowledge Discovery", Intelligent Systems Technologies and Applications, Springer, Vol. 385, pp.413-421, 2016.
- [6] J. Liang, L. Chen, and S. Mehrotra, "Efficient Record Linkage in Large Data Sets," In Proc. of the Eighth International Conference on Database Systems for Advanced Applications, 2003.
- [7] J. H. Weber-Jahnke, and C. Obry "Protecting privacy during peer-to-peer exchange of medical documents", Inf Syst Front (2012), Springer, 14:87-104.
- [8] A Quiet Revolution: Strengthening the Routine Health Information System in Bangladesh, published by giz, accessed from [http://health.bmz.de/good-practices/GHPC/A\\_Quiet\\_Revolution/HIS\\_Bangladesh\\_long\\_EN.pdf](http://health.bmz.de/good-practices/GHPC/A_Quiet_Revolution/HIS_Bangladesh_long_EN.pdf).
- [9] S. I. Khan and A.S.M.L. Hoque, "Privacy and security problems of national health data warehouse: a convenient solution for developing countries", In Proc. 2nd International Conference on Networking systems and Security IEEE, (2015) 157-162;
- [10] The United Nations Educational, Scientific and Cultural Organization (UNESCO), Principal characteristics of the least developed countries, <http://unesdoc.unesco.org/images/0004/000483/048315Eb.pdf>
- [11] Diana Kendall, Sociology in Our Times, cengage, 11<sup>th</sup> Ed, 2015.
- [12] HEALTH BULLETIN 2014, 2nd Edition, DGHS, Ministry of Health and Family Welfare, Government of the People's Republic of Bangladesh
- [13] <http://www.dghs.gov.bd/index.php/en/health-program-progress/hpnsdp-2011-16/84-english-root/ehealth-eservice/497-hpnsdp-2011-16-brief>. Accessed 20 Feb 2015.
- [14] [http://www.bpcdoa.com/clinics\\_and\\_diagnostics.html](http://www.bpcdoa.com/clinics_and_diagnostics.html). Accessed 22 Feb 2015.
- [15] Government of the People's Republic of Bangladesh, Ministry of Health and Family Welfare, Human Resources Development Unit, HRD Data Sheet-2011.
- [16] <http://bmdc.org.bd/doctors-info/>
- [17] WHO, Global Health Observatory Data Repository: Life expectancy-Data by country, 2015.
- [18] S. I. Khan, and A.S.M.L. Hoque, "Digital Health Data: A Comprehensive Review of Privacy and Security Risks and Some Recommendations" Computer Science Journal of Moldova.24.2 (2016): 273-292.

# A Prospective Model of Bangladesh Electricity Market

S. M. G. Mostafa<sup>1</sup>, Jai Govind Singh<sup>2</sup>, H. Masrur  
Energy Filed of Study, SERD  
Asian Institute of Technology  
Pathumthani-12120, Thailand  
E-mail: <sup>1</sup>mostafa.93eee@gmail.com, <sup>2</sup>jgsingh@ait.ac.th

Md. Shahid Ullah  
Department of Electrical and Electronic Engineering  
International Islamic University Chittagong (IIUC)  
Chittagong-4203, Bangladesh  
E-mail: shahideee04@gmail.com

**Abstract**— The traditional vertically integrated utility company combines the generation, transmission, distribution and customer service in a seamless operation that makes no detailed distinctions about the costs of each of these four activity levels. The target of deregulation of electricity market is to create an open access to assure perfect competition among purchasers and sellers and establish a reliable, secure and affordable electrical power system. So electric markets around the globe are undertaking unique changes related to deregulation to improve the efficiency of electricity power markets. Independent System Operator (ISO) and Power Exchange (PX) play very crucial role on unbundled power market. The integrated single buyer electricity market model of Bangladesh has very limited access of retail competition that lead to monopoly business of electricity. In this paper we propose a structure for the vertically unbundled electricity market of Bangladesh on the basis of existing electricity market around the world.

**Keywords**— *Deregulated power market; Independent System Operator (ISO); Power Exchange (PX); monopolistic utility company*

## I. INTRODUCTION

The traditional power sectors were completely vertically integrated and market was controlled by unbundled utility companies. But nowadays the restructuring in the electricity market is booming sharply around the globe. In 1980 first test performance in deregulation of electricity market was started in Chile. Then it was spread whole world along with some Latin American countries. Due to deregulation in power sectors the integrated structures were reformed. Hence, perfect competitions among various level of operation in electrical industry were introduced. There are various reasons and aims to deregulate the electricity markets in different countries [1]. The main target of deregulation power market is removing restrictions and regulations to achieve competitive affordable prices without sacrificing adequacy, system reliability and security. Moreover, unbundled market promotes generators to run efficiently to sustain in industry and regain the expenses., incorporating the applicable criteria that follow.

Restructuring aimed to increase competition and thereby efficiency. Apart from privatization, the reform typically included breaking up the integrated monopoly [2]. Electricity market introduces competition among generation entities so that the price of electricity is decided in real time (e.g. hourly

or half hourly) by the supply and demand situation. The deregulated power market performs their contracts in either pool or bilateral or both markets.

The reasons behind restructuring of electricity market defer country to country. Different Asian country such as Japan, China, India, Singapore, Thailand, and South Korea has taken outstanding steps to unbundle their power market. The process and mechanism of deregulated market is very difficult due to numerous entity and their obligatory regulations, different market management policies, ancillary service market, congestion management, market power, and highly volatile nature of electricity prices.

There is various research are done on unbundled electricity market around the world. In [3]-[5], the authors were suggested some models structure for deregulated market. In this paper we proposed a structure to deregulate existing power market of Bangladesh based on Nordpool and Indian electricity market.

## II. REFORMATION OF BANGLADESH POWER SECTOR

### A. Earliest Reformation of Bangladesh Electricity

In 1977, the initial reformation was taken in the history of Bangladesh electricity in distribution. Later 1977 Bangladesh Power Development Board (BPDB) merely assigned for the distribution in urban areas and the rural areas were under the supervision of new entity Rural Electrification Board (REB). But the vast reformation was taken place of Bangladesh electricity sector from 1990s to 2000s. The Private Sector Power Generation Policy was acted at 1996 and hence few numbers of Independent Power Producers (IPP) were added in generation. Consequently, a new era of competition was begun. These IPPs reduced the monopoly nature of BPDB in generation. As soon as these IPPs showed intense contribution over BPDB regulated power plants and hence their contribution to the grid also plumed. After that Public-Private-Partnership (PPP) power plants came in operation. Power cell was begun its journey in 1995 under the MPEMR to conduct reform power sectors and at the same time to encourage private power development significantly [6].

First, Starting with the generation then transmission & distribution and retail all were taken care by the Bangladesh Power Development Board (BPDB) in monopoly business mode under the direct authorization of Ministry of Power,

Energy and Mineral Resources (MPEMR). The line of operation was single line from generation to retail, as shown in the Fig.1.

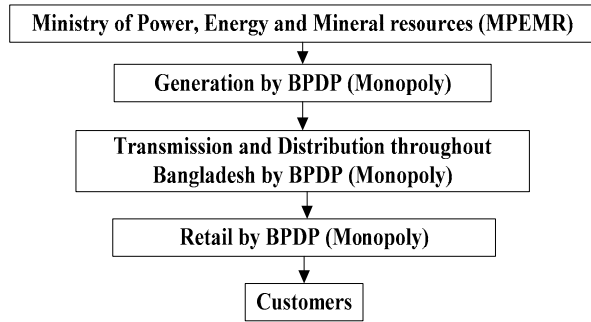


Fig. 1. Monopoly vertically bundled power market in Bangladesh .

### B. Initial Steps for Restructuring

In order to meet the immediate demand Bangladesh Government also took the initiative for Quick Rental Plant-(QRP) most of them are privately owned. Another major scheme was Corporatization of Ashugonj Power Station (APSCL) in 2002. These initiatives actually brought a message towards the generation and other sectors that, competition in a sector can lead to improve the efficiency and profit with a quality service and creates scope of improvements in the other segments. Moreover, introduction of IPP in generation sector has encouraged the transmission & distribution to privatize them. Dhaka Electric Supply Authority (DESA) and Dhaka Electricity Supply Company Ltd. (DESCO) have formed in 1991 and 1994 respectively and hence operation of BPDB has further reduced. Later on in 2003 West Zone Power Distribution Company (WZPDC) was created. Presently DESA is known as Dhaka Power Distribution Company (DPDC). Dhaka is taken care by DESCO & DPDC and REB undertaken distribution in the rural areas and west zone by WZPDC. Consequently 4,100 km asset of was handed over REB. For this reason, it increased in demand from 110 MW in 1997 to 575 MW in 2003 of 8 Palli Bidyut Samities (PBSs). In addition, it reduced system losses [6]. Power Grid Company of Bangladesh (PGCB) was created in 1996 to divide transmission section and finally it owned 100% transmission asset from BPDP. National Load Dispatch Center (NLDC) performed its task under cooperation with PGCB. In December 2002, transmission assets of DESA had transferred to PGCB. So, PGCB completely became accountable for building new transmission assets [7].

Power Division founded on 25 March 1998 by the MPEMR vide Cabinet Division Notification No. CD-4/1/94Rules/23(100) and then whole management of power sector rested on it. A better functioning market it needs an independent regulator. Considering this on March 13, 2003 Bangladesh Energy Regulatory Commission (BERC) was formed to control Gas, Electricity and Petroleum products of Bangladesh. Regulatory Commission was founded in April 2004, and became operative. Chief Electrical Inspector (CEI) was created to ensure the human safety, standards of equipment & issuing licenses to all working in electricity industry [6]. As a result of this restructuring there are notable changes in the electricity sector pattern. A simplified pictorial

representation of electricity sector subsequent to this restructuring is given below.

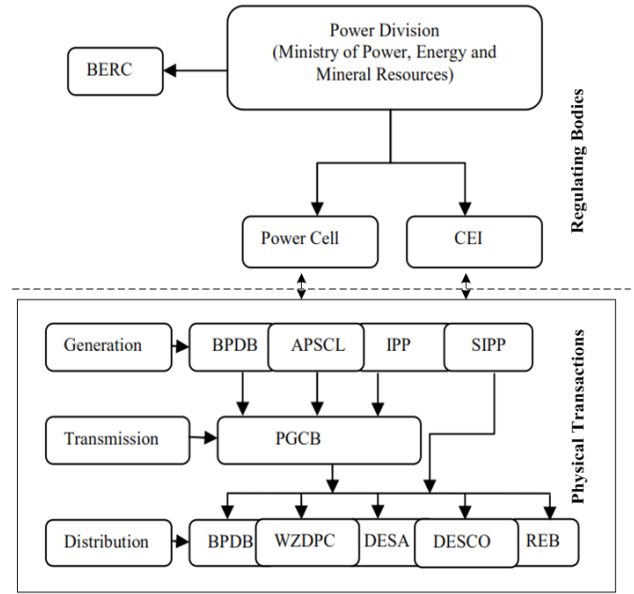


Fig. 2. Initial restructuring of electricity market of Bangladesh [2].

### C. Motivation Towards Deregulated Electricity Market

In unbundled electricity market it is very difficult to isolate costs related to generation, transmission and distribution. Hence, an aggregated cost tariff imposed to customers. In Bangladesh BERC enacts the regulated aggregated tariff on consumers by satisfying government rules and guidelines. Due to this monopolistic nature, the customers have no provision of choice. Moreover, in existing electricity paradigm there is very narrow scope for retail completion. If electricity market is open for all, more IPPs, SIPPs, PPPs, and other private sector will compete to enter into the market. More level playing field will create for retailers. The retailers vie not only for offered price but also on the other facilities to the customers. As a result, better plans, quality and reliability of power will be assured, price of electricity will reduce and there will be huge scope to additional generation. Customer will have more choices for retailers and retailers will give better service than what the monopolistic do. India has their deregulated market with three power exchange (PX). The opening of the Bangladesh's power market would allow importing/exporting electricity through pool or bilateral contract like Nordpool power market. Asian Power Grid (APG) is going to embark by 2020 to fulfill the power requirement to its member states country by strengthening and/or restructuring their respective power market industry. So, deregulated power market will create great possibilities for Bangladesh.

## III. DEREGULATED ELECTRICITY MARKET MODELING

Unbundling of electricity market is a process to reform the rules and regulation to remove the monopoly nature to run the electric sectors. It mainly lessens risk because both business and government accepted it. The ultimate focus of open power market is that competition could lead to a lessening in

electricity prices and could enhance the advent of new ideas and technologies. Due to the power system restructuring the traditional vertically unbundled power market could be reformed in following way-

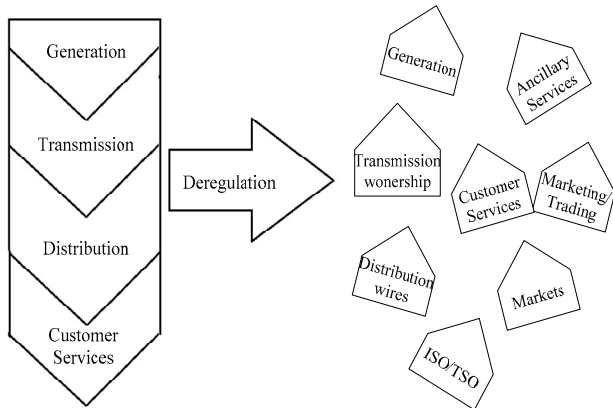


Fig. 3. Disintegrations of vertically integrated utility structure.

#### A. Power Exchange (PX)

The PX provides a platform that satisfy the both supply and demand considering bidding prices by maintaining the power pool. It selects the market clearing price (MCP) and fixes schedules through assimilating bids from both electricity sellers and buyers. If transmission system becomes congested, then it modifies the schedules and sends it to ISO or TSO. The timing span of pool market lasts 30 minutes to 7 days or more. The quite prevalent Day-Ahead Market (DAM) to assist electricity marketing one day earlier from the day of operation. Additionally, an hour-ahead market (HAM) is also offer further chances for power transaction to makeup short term discrepancy. In the E&W electricity market both the ISO and PX roles exist within the National Grid Company (NGC). Besides these the PXs furnish Adjustment Markets for varying commitments originating from the result of the DAM [8]. PX will enhance confidence among the market contestants and will enhance the strength of the market. To avoid risk, bilateral transactions are carried out.

#### B. Scheduling Coordinators (SCs)

SCs accumulate the both sellers and buyers in energy transactions using protocols which are quite different from pool rules. In the contrary, SCs may be built new market policies after being enrolled with current regulations. Basically it drives a forward market along with makes suitable scheduling through bidding process to purchase and electricity commodity. In this way SCs fixes the market clearing price (MCP) for energy transactions. Moreover, ISO gets suitable schedule from it and reordered it in case of necessity. SCs are an inevitable parameter in California electricity market but in E & W it is not permitted to function [8].

#### C. Independent System Operator (ISO)

There is numerous ISO design are available around the globe but no one is particularly satisfying the common basic requirements. Essentially, it is mandatory task of ISO to ensure reliable and secure operation that each and every contestant

must have free and non-discriminatory access in unbundled electricity power market through proper scheduling and action.

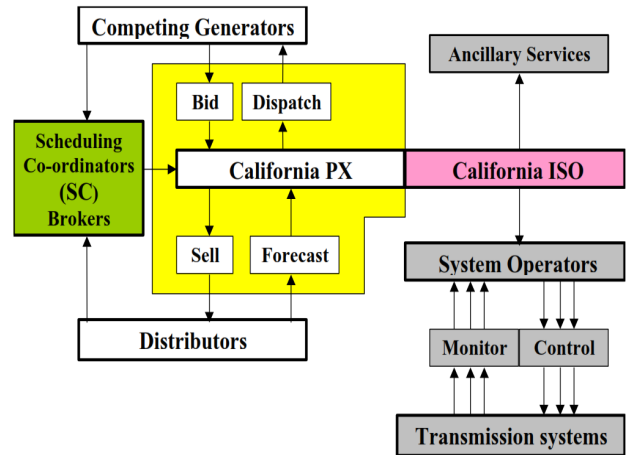


Fig. 4. The California ISO and Power market.

The principal roles of the ISO could be characterized into reliability-related functions and market-related activities. The ISO should accomplish system security monitoring functions and re-dispatch electricity generation as essential to remove real-time transmission congestion and to maintain system reliability, including taking all necessary emergency actions to maintain the security of the system in both normal and abnormal operating conditions. It should be noted that an ISO does not involve with financial activities rather than it is a market enabler. All kinds of power market oriented activities of an ISO should be in accordance with clear, comprehensible guidelines and protocols [9].

### IV. PROPOSED ELECTRICITY MARKET MODEL

There is different market model existing around the world such as E & W, California, Chile, New Zealand, Nordpool, India etc. electricity market, but no one is completely fit to any definite market model. Actually the market model of a particular country is influenced by the political, Social, economic and existing electricity power structures. But it is true that all existing electricity market model is created to assure perfect competition and maintain reliability and quality of affordable electricity supply.

#### A. Market Restructuring

Power exchange creates a room where electricity is traded based on bidding pricing, scheduling, and settlement of transaction on the real time. In Bangladesh there is no specific model of Electricity market.

Power Cell can perform its function as a PX and we can have called it as Bangladesh Electrical power Exchange (BEX). It can be made on the basis of Nordpool power exchange (Denmark, Finland, Norway, Iceland, Sweden [10]) which is the most successful international power exchange in the world. Under the guidance of Power Division, BERC sets the functioning strategy of Power Cell. Power Grid Company

of Bangladesh (PGCB) can act as Independent Service Operator (ISO) because it has 100 percent transmission assets.

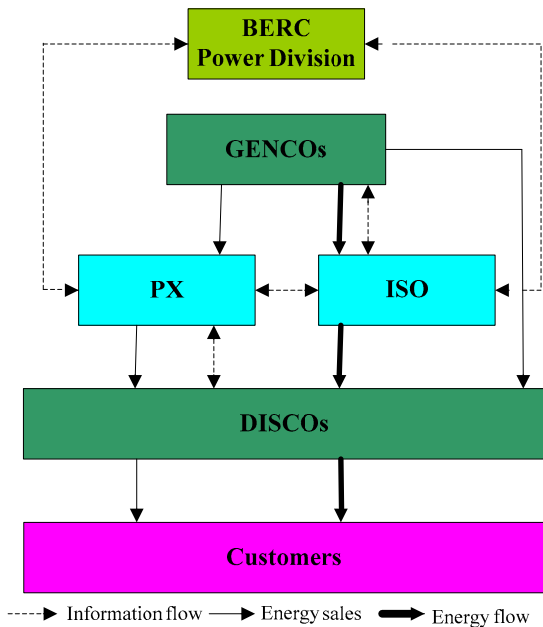


Fig. 5. Proposed Market structure model for Bangladesh.

BEX can have two sub markets such as Day Ahead Market (DAM) and Term Ahead Market (TAM) to perform its trading. DAM will offer 24 hours trading with double side bidding from both sellers (GENCOs) and purchasers (DISCOs). In this proposed model BPDP, ASPCL, IPP, Small Independent Power Projects (SIPP) are the GENCOs and BPDP, WZDPC, DESA, DESCO, REB etc. are the DISCOs. But TAM offers week ahead, year ahead or seasonal contract. Power Cell (BEX) should be coordinates with National Load Dispatch Center (NLDC) to get network information to maintain the traded schedules. However, some generation companies such as IPP, SIPP can directly sell power to some whole sell retailers directly.

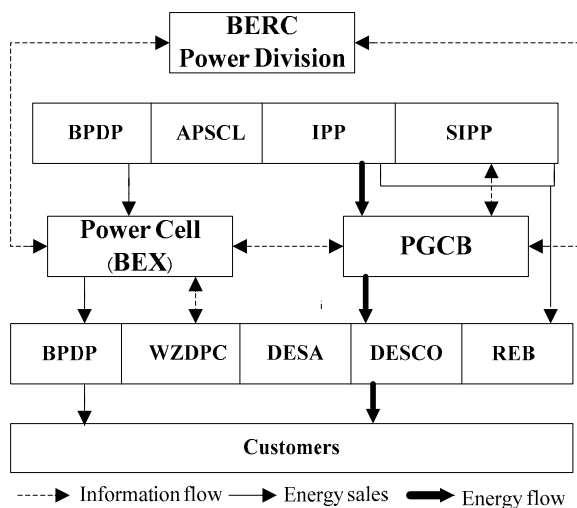


Fig. 6. Proposed deregulated power market of Bangladesh.

### B. Power Exchange Functioning Model

The function of DAM of proposed BEX can be depicting as: At the beginning it will collect the Available Transfer Capability (ATC) from NLDC. At the time of bidding it will collect all bidding prices and offers from all sellers (GENCOs) and buyers (DISCOs). After matching the bids, the Market Clearing Price (MCP) and corresponding MCV are determined. The Power Exchange (BEX) will send finalized schedules to NLDC when it is ready. Finally, NLDC will send the schedule to corresponding sellers or buyers. Then it will be considered that power is delivered in between 00h to 24hours.

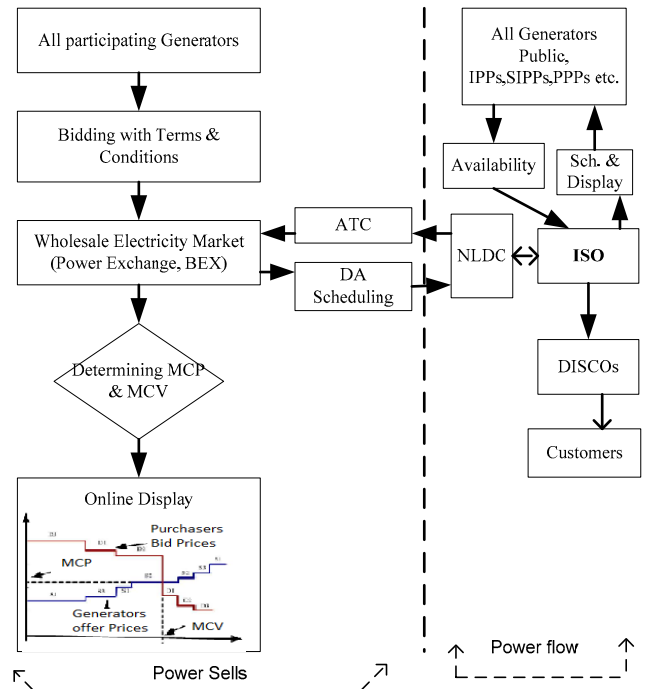


Fig. 7. Operation of proposed electricity market model.

### C. Retail Market Competition

Introducing retailers play very important role to enhance competition in retail sectors. Recently, in deregulated market distribution companies are became restricted to maintain the distribution network and furnishing all facilities for supplying electricity. However, retail marketers are isolated from distribution companies and supply electricity power to end customers (Fig. 8). Retailers, stated as Market customers in the spot market, purchase this electricity from the spot market and then sell it to End Users. The main target of retail market competition is that the profit must distribute to trivial customers instead of capturing by monopolistic Discos or even retail marketers. Small customers viable to enter to real pricing fixation, hence get the real cost of energy per hour.

Sophisticated metering system can be useful to have retail competition. On the contrary, retail competitors may provide a contract with certain amount rate to their consumers conferring on their single load profile. So, consumers can hedge the uncertainties of spot prices and simultaneously can buy electricity very close to the wholesale market rate, adding with various losses in distribution network.



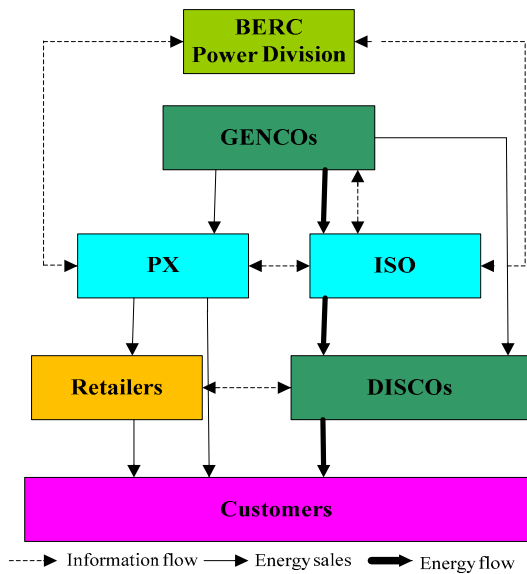


Fig. 8. Proposed deregulated market model with retailers.

The retailers can buy their consumers metered amount of electricity power from the native distributors through hedging tools i.e. Contract for Difference (CfD). CfD is financial tool where suppliers are paid a certain price in a fixed time period that is amalgamation of short-term market price and adjustment with the buyers with difference.

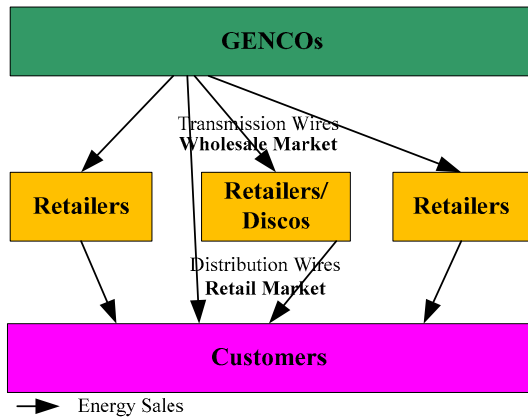


Fig. 9. Retail competitions in proposed unbundled power market.

It is found in numerous cases that power produces in generation companies are not directly supply to the end users rather than it bought and resold several times. These lead to “sales for resale” and build wholesale electricity market. To become a participant, it is necessarily need to own neither any generation entity nor serves to end users-solely buying electricity on open market and resells it. Wholesale market should be open to anybody who can assure required. permission, can viable to generate power, connected to the grid and find a party who is agreed to buy. These include competitive sellers and marketers that are linked with Power utilities, IPPs are not connected with a utility, as well as some

excess generation sold by traditional vertically unbundled utilities. All of these participants vie with each other on the wholesale market.

## V. CONCLUSION

This paper depicts an over view of Bangladesh power sector and proposed a model for vertically unbundled electricity market. Moreover, it provides the idea of operation of proposed Power Exchange (BEX). This BEX will perform DA market with proper price signal and it will furnish real time nondiscriminatory information to all market competitors via internet enabled electric board. It is true that deregulation of electricity market will create better level playing field for all competitors, maintain perfect competition and greater customer benefits. As a result, the producers of electricity market will try to sell power at a marginal cost that lowering the electricity prices and improve the power quality and better reliability.

## ACKNOWLEDGMENT

The first author would like to thanks ADB-JSP for providing scholarship to pursue his master degree and carry out this work at Asian Institute of Technology, Thailand.

## REFERENCES

- [1] Prabavathi, M., & Gnanadass, R., “Bidding strategies for Indian restructured power market,” Proceedings of IEEE International Conference on Circuit, Power and Computing Technologies, ICCPCT 2013, 568–573.
- [2] Joskow, Paul L., “Introducing Competition into Regulated Network Industries:from Hierarchies to Markets in Electricity,” Industrial and Corporate Change,1996, 5(2), 341–382.
- [3] A.K.David, N.Leeprachanon, S.S.Murthy and F.Liu, “Transition to an electricity market: A model for developing countries”, IEEE Transactions on Power Systems, vol.17, no.3, pp.885-894, Aug. 2002.
- [4] Bajpai, P., & Singh, S. N., “An electric power trading model for Indian electricity market,” 2006 IEEE Power Engineering Society General Meeting. <http://doi.org/10.1109/PES.2006.1709055>.
- [5] S.N. Singh, S.C. Srivastava, “Electric power industry restructuring in India: present scenario and future prospect”, in Proc. of IEEE International Conference on Electric Utility Deregulation, Restructuring and Power Technologies (DRPT 2004), vol.1, pp.20-23, April 2004.
- [6] Gupta, S. Das, “Bangladesh Power Sector Reform and Multidimensional Reflections,” Recent Researches in Environment and Biomedicine, 2007.
- [7] South Asia Regional Initiative for Energy. [http://www.sarienergy.org/pagefiles/countries/bangladesh\\_energ\\_detail.asp](http://www.sarienergy.org/pagefiles/countries/bangladesh_energ_detail.asp).
- [8] Loi Lei Lai, “Power System Restructuring and Deregulation: Trading, Performance and Information Technology,” 6.1 Transmission open access, 2001, 172-185.
- [9] Song, Y. H., Wang, X., & Liu, J. Z., “Operation of Restructured Power Systems 1. 1 System Operation in a Competitive Environment, 1–13.
- [10] Svento, R., Markets, M. E., & Energy, G., “The Effects of Nuclear Power Investments in Real-Time Pricing Framework,” Green Energy and Technology, 2012, 105, 45–53.

# Design & Implementation of an UAV (Drone) with Flight Data Record

Tuton Chandra Mallick , Mohammad Ariful Islam Bhuyan, Mohammed Saifuddin Munna

Department of Electrical and Electronic Engineering

Premier University, Chittagong

Chittagong- 4203, Bangladesh.

tuton.soc@gmail.com , arif.ajfts@yahoo.com , munna.puc@gmail.com

**Abstract**— This paper proposed the development of an autonomous unmanned aerial vehicle (UAV) which is controlled by wireless technology through graphical user interface (GUI). This proposed design capable to fly autonomously and also capable to track pre loaded mission automatically. Proposed mathematical model and artificial algorithm control technique by which quad rotor can capable to fly autonomously, trajectory tracking, graceful motion and accurate altitude hold performance. In this system author used IMU 9DOF (3-axis accelerometer, 3-axis gyroscope & 3-axis magnetometer) which ensure it smooth movement, graceful motion and trajectory tracing. GPS system and barometric sensor make it more efficient in autonomous mode. Several PID loops designed to get better stability and performance in different mode. All signals are processed by a powerful high speed controller board which makes it more efficient and effective. This work aimed to design a quad copter that will try stable its position according to preferred altitude. Also here stability check has been done with pitch and roll. All data and result discussed at the end of paper.

**Keywords**—autonomous UAV system, inertial measurement unit, graphical user interface, PID controls loops, stability and performance.

## I. INTRODUCTION

At present world drone technology is very familiar & versatile technology. Drone can drift in air .We can also use wireless camera with it. So that we can use it to do different types of tasks. Nowadays Drones are used in long range wars as a weapon and also as a helper of fighter in the war. Scientist use drone as a part of their research assistant. Drones not only help us in society but also a threat for us, as because many of developed countries use it as their weapon of destruction. So drones have their ability to predetermined work so that it becomes important in today's world. [1]

Drone has many importances but it also creates some questions about privacy. So for this issue many governments declared some rules and regulation to fly drone in different purposes. A mature quad rotor system can use for educational and experimental porpoise [2], [3]. Photo shoot for films & drama are also use drone.

At past drones was used only by military in their war. But day by day it is now used in various household works as it operation and control become easy day by day. Developed

world and also developing world use it for their own purposes. Uses of drone are rapidly increased for both public & Private sector. Peoples of Canada & North America now use drone as their assistant of housework & office work. At present not only in Canada but also in others countries drone technology increasing day by day.

For the domestic user they have to pay attention on government rules regarding use of drone. For this propose small & cost effectives drones are available in markets. Its popularity increased day by day.

### A. Applications of UAV( Drone)

There are some many important activates of drones. Which are:

- National security
- As a long range weapon of military war
- Public safety
- Environmental research
- Scientific research
- Small household work.

### B. Related Works

In recent years many scientist works into this area of UAV. As in reference paper [5], [6], [7], Samir Bouabdallah et al. make a good number of research on smart controlling if UAV. This author also used back stepping method [7]. For a better solution in stability & smooth controlling many scientists used PID and root locus method [8]. PD controller is also a very popular method for control drone & robotic arm [9]. Many scientist use PD control as their experimental platform [1], [10]

## II. PROPOSED DESIGN

### A. System Overview

To desing a stable multicopter we need maintain some physics, mathmatics and aeirodynamic term. Aerodynamic help to define its movement and inertial motion. In the other hand mathematical calculation helps to manipulate required lift

force, angular position, graceful motion and trajectory definition.

We designed drone's body according with dynamics and also designed artificial algorithm to make it autonomous and well behaved. Hardware system consists of different sensors, powerful controller unit and electronic equipments so on. For a desire movement controller takes data from different sensors. 3-axis accelerometer and 3-axis gyroscope provide data of its orientation, acceleration and angular rate. Then these data processed and compare with reference and desire value. This operation performs with the help of PID loop. Several PID loops used in these case like pitch control, roll control, yaw control, hover, altitude holding and orientation control. IMU (inertial measurement unit) provides real altitude, angular movement and orientation. After that required pulse sends to ESC (Electronic Speed Controller) for desire speed of rotation. Magnetometer provides real time direction with the global magnetic field reference. Barometric pressure sensor also provides real time altitude. GPS (global position system) module helps to make system autonomy. It helps find out any coordinate and reach to this coordinate. Telemetry kit helps to observe flight data wirelessly from ground station. It also send mission file and communicate with air part like USB serial mode (TTL mode).

In ground part consists of powerful ground station. PC/Laptop used for sending data through telemetry and coding or data logging from air part. Another radio transmitter used to switch different mode and operate in manual mode.

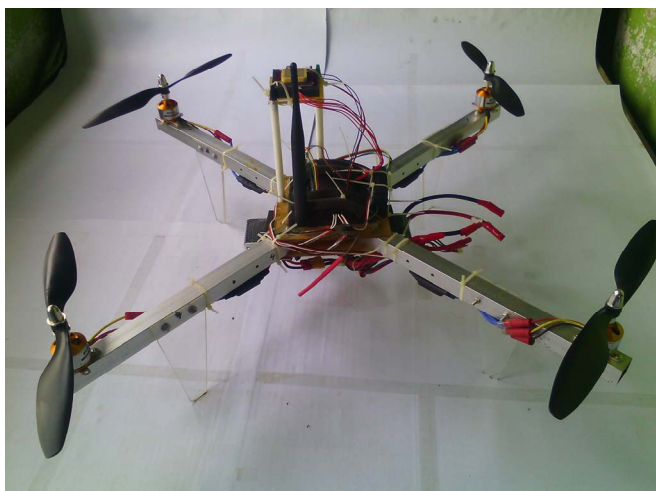


Figure 1. System Overview of Autonomous Unmanned Aerial Vehicle

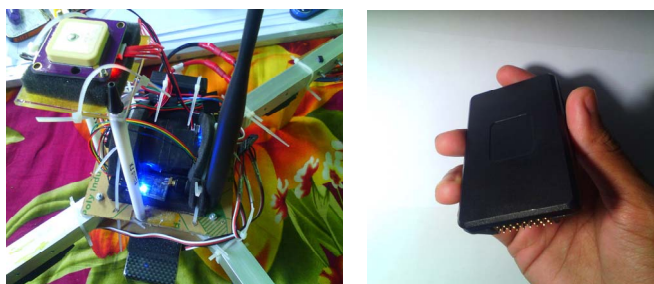


Figure 2. Air part hardware system in alive. Right figure shows Processing unit of an autonomous UAV.

### B. System Block Diagram

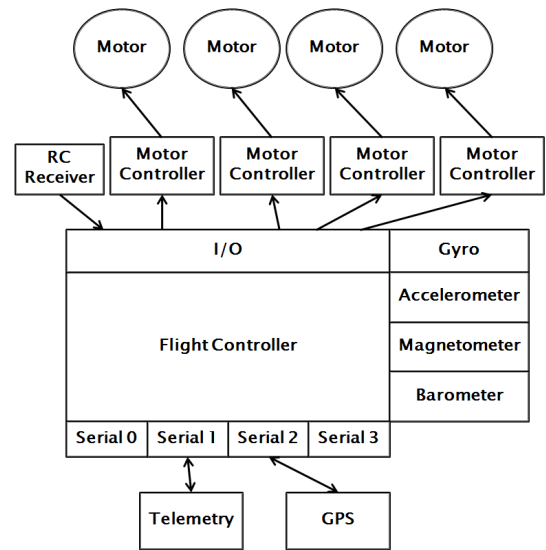


Figure 3. Proposed block diagram of UAV's air part.

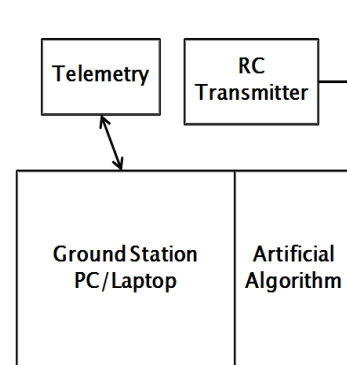


Figure 4. Proposed block diagram of UAV's ground station.

## III. SYSTEM MODELING

To design a stable multi-rotor copter we have to concentrate its structure and dynamics. We have to develop a firmware in which contains different control strategy, mode of operation, data evaluation and different PID loops for stability:

### A. Body Dynamics

Body dynamic of multi-rotor copter governs the response of attitude control. Let consider a multi-rotor copter frame. We can derive expression in two coordinate system i.e. one is inertial coordinates and another one is body fixed coordinates.

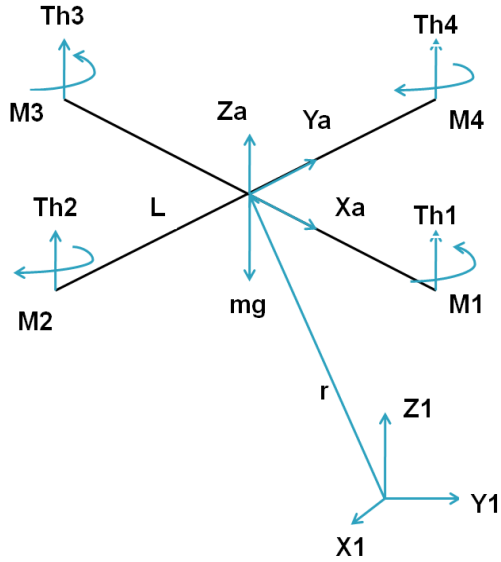


Figure 5. Force diagram of quad copter.

$U1$  is summation of the thrust of every individual motor.  $Th1$ ,  $Th2$ ,  $Th3$  and  $Th4$  are thrust generated by front, rear, left and right motor respectively.  $m$  is Quad-copter mass,  $g$  is marked as the gravity acceleration and  $L$  is the lever distance of Quad-copter.  $x$ ,  $y$  and  $z$  are the three axis position.  $\phi$ ,  $\theta$ ,  $\psi$  are three Euler angles representing pitch, roll and yaw.

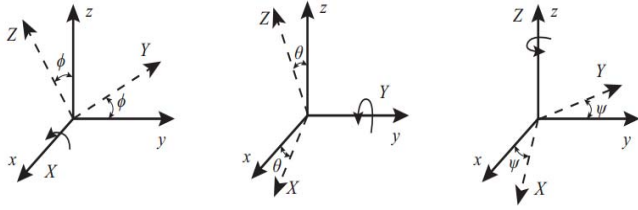


Figure 6. Attitude control definition.

From the Fig. 6 we get transformation matrix with defined attitude angles:

$$R(\theta, \phi, \psi) = \begin{bmatrix} c\psi c\theta & c\psi s\theta\psi - s\psi c\theta & c\psi s\theta\phi + s\psi s\phi \\ s\psi c\theta & s\psi s\theta\psi + c\psi c\theta & s\psi s\theta\phi - s\psi s\phi \\ -s\theta & c\theta\phi & c\theta\psi \end{bmatrix} \quad (1)$$

Where  $s$  represents  $\sin$ ,  $c$  represents  $\cos$ , and  $\phi$ ,  $\theta$ ,  $\psi$  stands for attitude angles of roll, pitch, and yaw respectively.

Direct inputs are RPM commands for every motor in body fixed coordinates. So the resultant outputs are  $Z$  directional thrusts in body fixed coordinates. Attitude & position is only concern of our outputs.  $U1$ ,  $U2$ ,  $U3$  and  $U4$  are four control variables used to eliminate this gap. Each of the affects the attitude, rotation in roll angle, rotation in pitch angle and yaw angle respectively.

$$U = \begin{cases} U1 = Th1 + Th2 + Th3 + Th4 \\ U2 = (Th3 - Th1)L \\ U3 = (Th2 - Th4)L \\ U4 = M1 + M3 - M2 - M4 \end{cases} \quad (2)$$

Here  $Th_i$  is thrust generated by four motor,  $M_i$  are momentums, and  $L$  is lever length.

By applying the force and moment balance laws, motion formulations are given as

$$\begin{aligned} \ddot{x} &= \{U1(\sin\psi\sin\phi + \cos\psi\sin\theta\cos\phi) - K1\dot{x}\} / m \\ \ddot{y} &= \{U1(\sin\psi\sin\theta\cos\phi - \cos\psi\sin\phi) - K2\dot{y}\} / m \\ \ddot{z} &= (U1\cos\phi\cos\theta - K3\dot{z}) / m - g \end{aligned}$$

Where  $k_i$  is drag coefficient (assume zero since drag is negligible at low speed).

The angle  $\phi_d$  and  $\psi_d$  can determine as follows from Fig.7,

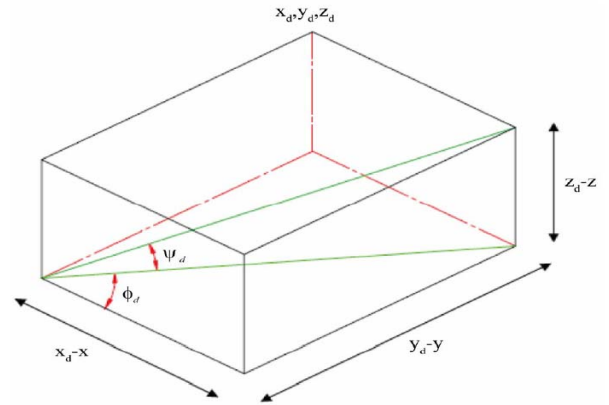


Figure 7. Angle movement of quad copter.

$$\begin{aligned} \phi_d &= \tan^{-1} \frac{y_d - y}{x_d - x} \\ \psi_d &= \tan^{-1} \frac{z_d - z}{\sqrt{(x_d - x)^2 + (y_d - y)^2}} \end{aligned}$$

The second derivatives of each angle given as

$$\begin{aligned} \ddot{\phi} &= U2 / I_{xx} \\ \ddot{\theta} &= U3 / I_{yy} \\ \ddot{\psi} &= U4 / I_{zz} \end{aligned}$$

Where  $I_{xx}, I_{yy}, I_{zz}$  is rotary inertia around X, Y, Z axis respectively

### B. Aerodynamics Effect

The thrust T produced by each motor is calculated as

$$T = \rho C_T A w_m^2 R^2$$

Where

$C_T$  : thrust coefficient

$\rho$  : Air density

A: rotor disk area

R: blade radius

Propeller diameter & pitch-

$$D \sim \tau, p \sim \tau$$

$$\tau \sim E$$

Where, d: diameter of propeller,  $\tau$  : torque, E: energy

Frame parameters-

$$\text{Blade tip speed, } v \sim \sqrt{R}$$

$$\text{Lift, } F \sim R^3$$

$$\text{Inertia, } m \sim R^3, I \sim R^5$$

$$\text{Acceleration, linear } a \sim 1, \text{ angular } a \sim \frac{1}{R}$$

Where, R: frame center to motor distance

### C. Dynamics of Rotor

The dynamics of DC motor is generally described as

$$L_i \frac{di}{dt} + Ri + k_e w_m = u$$

$$J \frac{dw_m}{dt} = \tau - \tau_d$$

Where

$L_i$  : Coefficient of inductance

i: armature current

R: armature resistance

$k_e$  : back emf constant

$w_m$  : speed of motor

u: armature voltage

J: inertia of motor

$\tau$  : torque of motor

$\tau_d$  : load

### D. System PID Control

PID (proportional-integral-derivative) is a closed-loop control system. It helps to get our results as much as close to the actual result by responding to our inputs. Scientist uses it while controlling drone or robot for achieves stability.

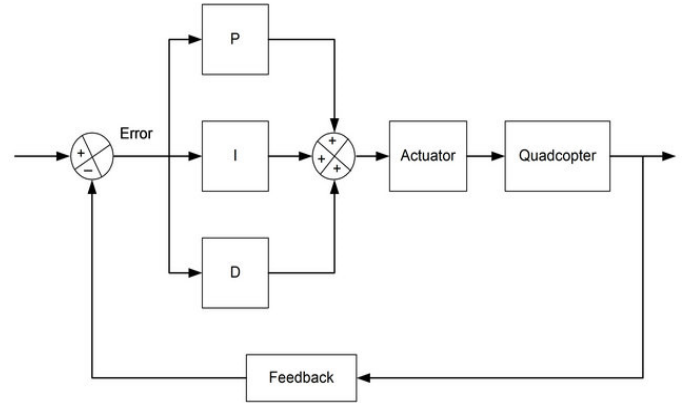


Figure 8. PID loop for system.

PID basically works with three algorithms.

- P depends on the present result
- I on the accumulation of past errors.
- D is prediction of future errors based on current data.

Different coding systems are available based on these algorithms.

Per axis PID structure shown in Fig.9. For controlling quadcopter or any types of multicopters, output of sensors (like the pitch angle) is very much needed. From the sensor data we can easily estimate the error (how far we are from the desired pitch angle, e.g. horizontal, 0 degree). Then we can use PID algorithms for eliminating errors

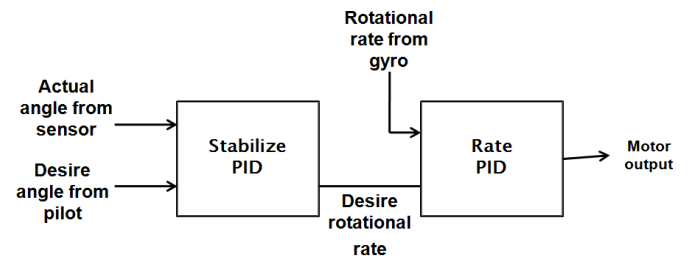


Figure 9. Per axis PID structure.

#### IV. RESULTS AND IMPLEMENTED DESIGN

##### A. On flight Simulation Data

All the data collected after 18-20 experimental flight of implemented UAV.

Fig. 10, indicates the altitude hold performance. This is one of the important curves which indicate the stability and behavior of our drone. Here Holt for desire altitude and Alt for altitude at which drone travels. This curve contains several mode of operations characteristics. When we shift from stabilize (manual) mode to hover mode or GPS lock mode then DAlt curve generate and then altitude calculated from IMU unit and also generate the barometer altitude curve shown in Fig. 11, as blue line. Alt and DAlt line lies close together that means altitude hold performance is good in different modes.

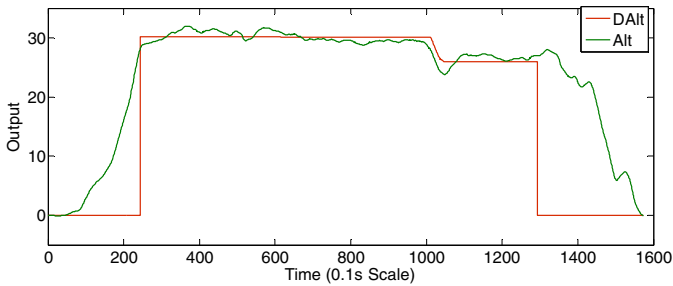


Figure 10. Altitude hold performance data in different mode.

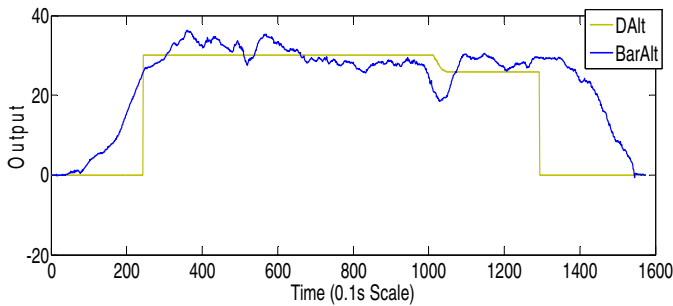


Figure 11. Altitude hold performance with barometer.

Fig. 12, shows the pitch response and Fig. 13, shows the roll response of UAV in different modes. Here, DesPitch and DesRoll for desire pitch and roll respectively. And only pitch and roll indicate the pitch roll response. If we observe the curves than we see that pitch and roll curve is similar to desire pitch and roll curve. We see in stabilize (manual) mode and altitude hold mode we get some spike which indicate pitch & roll action. Though stabilize mode is manual mode so we change pitch manually. In altitude hold mode- altitude maintain automatically but pitch & roll is also manual control. In loiter mode that means in GPS lock mode- all parameters controlled automatically without human interface. So in loiter mode spike is less which indicate it holds a constant coordinate with stability.

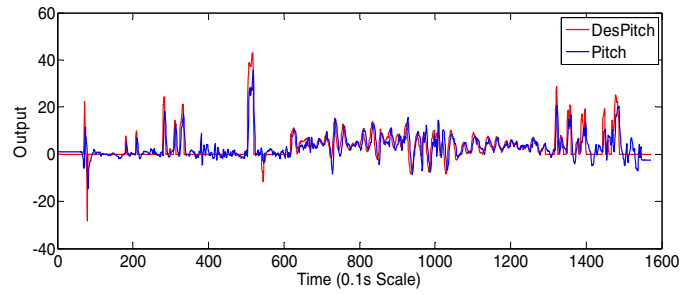


Figure 12. Response of pitch in different mode.

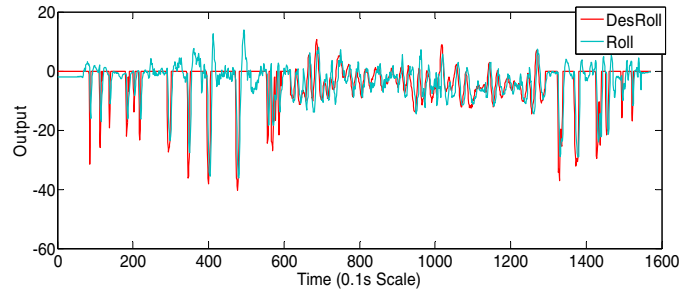


Figure 13. Response of roll in different mode.

Fig. 14, shows the throttle response in different modes. We see that throttle fluctuate in manual mode due to manual control of throttle fluctuation. In autonomous mode throttle automatically control by processor unit. So throttle response does not fluctuate significantly.

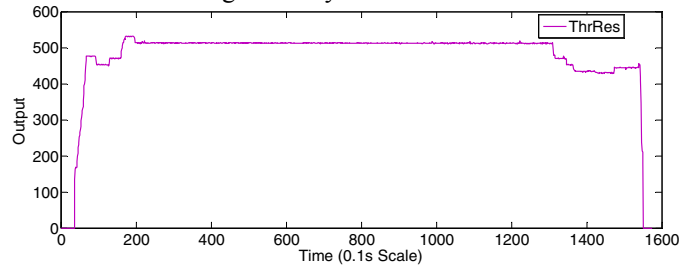


Figure 14. Throttle response of proposed design in different mode.

##### B. Implemented Design

Total hardware design of proposed UAV is given below.

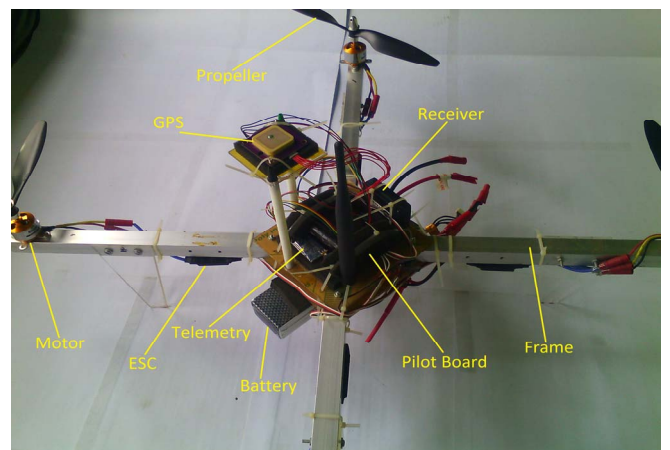


Figure 15. Real view of implemented design.

## V. CONCLUSION

From all of curve analysis we can conclude that overall performance of our system is stable. This system is capable to fly in different mode without complexity. It's performance, movement, orientation, motion, stability also good. This drone is capable to fly in several modes. The main modes are manual mode, hover mode, auto mode and return to launch mode. In manual mode drone is controlled by remote device and in others mode drone flies autonomously. This system have facility to see flight data by using powerful ground station and user can upload or override a mission in real time flight condition when a mission running. The distance between motor to motor is 0.61m. The overall total weight of implemented design is 1.46kg and its carrying capacity is 0.5kg.

## REFERENCES

- [1] N. Michael, D. Mellinger, Q. Lindsey, and V. Kumar, "The grasp multiple micro-uav testbed," *Robotics & Automation Magazine, IEEE*, vol. 17, no. 3, pp. 56–65, 2010.
- [2] V. Kumar and N. Michael, "Opportunities and challenges with autonomous micro aerial vehicles," in *Int. Symp. on Robotics Research*, 2011.
- [3] D. Mellinger, M. Shomin, and V. Kumar, "Control of quadrotors for robust perching and landing," in *International Powered Lift Conference, October 5-7, 2010*, 2010.
- [4] The standing Senate Committee on National Security and Defense - Evidence, April 23, 2012.
- [5] S. Bouabdallah, R. Siegwart, S. Bouabdallah, and R. Siegwart, "Backstepping and sliding-mode techniques applied to an indoor micro quadrotor," in *Robotics and Automation, 2005. ICRA 2005. Proceedings of the 2005 IEEE International Conference on*. Ieee, 2005, pp. 2247–2252.
- [6] S. Bouabdallah and R. Siegwart, "Full control of a quadrotor," in *Intelligent Robots and Systems, 2007. IROS 2007. IEEE/RSJ International Conference on*. Ieee, 2007, pp. 153–158
- [7] S. Bouabdallah, "Design and control of quadrotors with application to autonomous flying," *Lausanne Polytechnic University*, 2007.
- [8] P. Pounds, R. Mahony, and P. Corke, "Modelling and control of a quadrotor robot," in *Proceedings Australasian Conference on Robotics and Automation 2006*. Australian Robotics and Automation Association Inc., 2006.
- [9] Q. Lindsey, D. Mellinger, and V. Kumar, "Construction of cubic structures with quadrotor teams," *Proc. Robotics: Science & Systems VII*, 2011.
- [10] R. Mahony, V. Kumar, and P. Corke, "Multirotor aerial vehicles: Modeling, estimation, and control of quadrotor," *Robotics & Automation Magazine, IEEE*, vol. 19, pp. 20 – 32, 2012.

# Performance Measurement of Different Backoff Algorithms in IEEE 802.15.4

Md. Mohibur Rahaman

Department of Computer Science & Engineering, University of Chittagong, Chittagong-4331, Bangladesh.  
Email:mohib.csecu@yahoo.com

Mohammad Sanaullah Chowdhury

Department of Computer Science & Engineering, University of Chittagong, Chittagong-4331, Bangladesh.  
Email:sana1691@gmail.com

Kazi Ashrafuzzaman

Department of Electrical Engineering & Computer Science, University of Calgary, Canada.  
Email:ashraf@cu.ac.bd

Mohammad Osiur Rahman

Department of Computer Science & Engineering, University of Chittagong, Chittagong-4331, Bangladesh.  
Email:osiur\_rahman@yahoo.com

**Abstract**—The Low Rate Wireless Personal Area network (LR-WPAN), that is IEEE 802.15.4 is extensively used for many areas of applications. The Slotted CSMA/CA mechanism is used by the standard in its contention access period (CAP) in beacon enabled mode. The protocol supported a binary exponential backoff (BEB) algorithm. In this paper, we investigate the saturation throughput, mean frame service time or delay and energy of this standard using the existing BEB algorithm and compares it with three other backoff schemes—exponential increase exponential decrease (EIED), exponential increase linear decrease (EILD), and exponential increase multiplicative decrease (EIMD) algorithm. From simulation results, it is obtained that EIED, EILD, EIMD performs better than BEB for higher loads that is EIED, EILD, EIMD has better throughput, less delay, using minimal power. The EIED propagates the highest throughput, less delay and minimal energy used among all of these schemes.

**Keywords**—IEEE 802.15.4; backoff algorithms; contention access period; CSMA/CA.

## I. INTRODUCTION

The standard that is IEEE 802.15.4 is aimed for Low Rate Wireless Personal Area network (LR-WPANs) [1]. This is a well-known light, cost effective communication network standard. The standard permits wireless connectivity in applications with confined power. The primary objectives of the protocol are cost effective wireless communication with moderate data rates, feasible data transfer, ease of installation, smaller-range operation and a legitimate battery life. It sustains a light and yieldable protocol. The standard support light weight devices that consume subtle power.

Throughput considered to be one of the most important aspect for analysing MAC performance metrics. The other aspects are delay and energy. The prime application area of this standard is the implementation of Wireless Sensor Networks (WSNs), which are systems with miniature devices deployed in an area. WSNs are used for monitoring some physical phenomena and/or for reporting the information achieved through wireless links upon reception of queries or detection of events to one or more sinks.

The standard IEEE 802.15.4 Medium Access Control (MAC) allows two types of channel access mechanisms. The first one is non-beacon and the second one is beacon enabled mode. The first mode employs an un-slotted carrier sense multiple access with collision avoidance (CSMA/CA). However, the second mode that is beacon enabled mode uses superframes separated by periodic beacons. The superframe consists of contention access period (CAP) which works non-persistent slotted CSMA/CA in a distinguished manner. This protocol employs a channel access mechanism and binary exponential backoff (BEB) scheme. The saturation throughput and delay results for the CAP using this protocol of the standard can be found in the reference [2].

The BEB are also spreadly used in many standards, for example, in IEEE 802.11. The purpose of BEB is to sets the medium but it responds rapidly to the tokens of network congestion. It is achieved by doubling the channel intercession time (backoff period) every time a node tastes a failure to deliver a frame. For every successful transmission of packets the channel intercession time reduces quickly to its minimum value. The effect of cutback in the backoff period can conduct to performance degeneration when there are a large amount of contending nodes, as it causes excessive collisions latterly a effective transmission. As a consequence, two types of schemes that point out a gradual cutting in a backoff period latterly any significant transmission. One of the scheme that is the first algorithm known as exponential increase exponential decrease (EIED) [3]. EIED increases the backoff period by power of 2 (two) latterly a collision and halves it after a successful transmission. The second scheme is named exponential increase linear decrease (EILD) algorithm. EILD also increases the backoff period by power of 2 (two) after collision, but linearly decreases the backoff period latterly a significant transmission. Also there exists a third scheme known as exponential increase multiplicative decrease (EIMD) [4]. In reference [4], the authors analyzed and compared the performance of the three backoff algorithms for IEEE 802.11 – BEB, EIED and EILD.



But the backoff scheme is different in the IEEE 802.15.4[5]. Hence, it is significant to inquire the performance of the other backoff algorithms along with the existing BEB for this standard. To the best of our knowledge, the performances of other backoff algorithms are yet to be found for this standard.

In this paper, we investigate and compare the performances (that is throughput, delay and energy) of the slotted CSMA/CA protocol in the IEEE 802.15.4 MAC using the different backoff mechanisms - EIED, EILD and EIMD along with the BEB.

The organization of residual of the paper is as follows. IEEE 802.15.4 MAC protocol is explained in section II. The different backoff algorithms are described in section III. The results are discussed in the next section. Finally, we conclude the paper in section V.

## II. THE IEEE 802.15.4 MAC PROTOCOL

In this part, we discuss the MAC protocol in the IEEE 802.15.4 in brief. More particulars of the procedure of the protocol can be found in [1] and [6].

The IEEE 802.15.4 MAC specifies two modes: beacon-enabled and non-beacon-enabled. Non-beacon mode uses a non-slotted CSMA with collision avoidance (CSMA/CA) protocol for accessing the channel. If the channel is busy, the node will backoff and attempt to access the channel in an upcoming slot. If the channel is idle, the transmission of a frame will begin right away. The method has been extensively studied in the literature [7].

On the other hand, in the beacon mode, a coordinator transmits a beacon periodically and forms a superframe. The superframe structure is shown in Fig. 1. The superframe can have two portions: active and inactive. It consists of a beacon, contention access period (CAP), contention free period (CFP), and an inactive period. The inactive period is optional. The CAP and CFP collectively form the active part. All communication among the nodes should go on during the active portion. The CFP is divided into guaranteed time slots (GTS). The coordinator allocates GTS to those nodes with their GTS request approved. The allocation of the GTS to the nodes is done by the scheduling procedure decided by the coordinator.

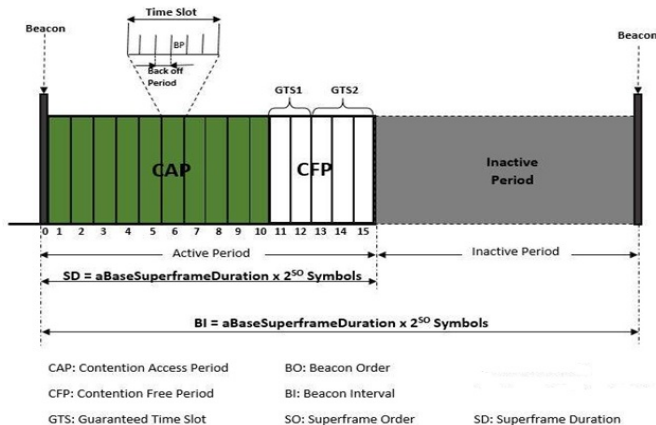


Fig. 1. The superframe of IEEE 802.15.4 and Backoff period in the CAP

In the CAP, a slotted CSMA/CA protocol is used with binary exponential backoff scheme. Each frame need to maintain three variables before it is transmitted successfully. They are - the contention window ( $CW$ ), the current backoff

exponent ( $BE$ ) and the number of random backoff stages experienced ( $NB$ ).

The  $CW$  defines the number of slots that require to be clear of activity ahead of the start of a transmission. It is set to 2 before each transmission attempt. If the channel is assessed to be busy, the  $CW$  is reset to 2. The  $BE$  is associated with how many slots a node must wait before attempting to evaluate the channel. The  $NB$  is the number of times the node requires to wait while attempting the ongoing transmission. It is set to 0 before each fresh transmission. The IEEE 802.15.4 slotted CSMA/CA works as follows and is depicted in Fig. 2

- Step 1: The parameters  $CW$ ,  $BE$  and  $NB$  are initialized.
- Step 2: The node waits for a random number of slots taken from a uniform distribution over  $[0, 2^{BE} - 1]$ .
- Step 3: Carry out a clear channel assessment (CCA). Then the MAC sub-layer proceeds if the remaining steps can be finished before the end of the CAP period. If it is not, it will try again at the beginning of the CAP in the next superframe.
- Step 4: In case of busy channel, both the  $NB$  and  $BE$  are incremented by 1. Make sure that the value of  $BE$  is not more than  $aMaxBE$ , and  $CW$  is initialized to 2. The CSMA/CA must return back to the step 2 if the value of  $NB$  is less than or equal to the value of the  $macMaxCSMABackoffs$ . Otherwise, the CSMA/CA ends with the status - Channel\_Access\_Failure.
- Step 5: In case of idle channel, the  $CW$  is decremented by 1. If the  $CW$  is equal to 0, begin transmission on the boundary of the next slot. Otherwise, it must go to the step 3.

The standard specifies the following default parameter values:  $amacMinBE=3$ ,  $aMaxBE=5$  and  $NB_{max} = 5$ . If the node succeeds in accessing the channel during the backoff procedure, it will return the  $CW$ ,  $BE$  and  $NB$  to the default values for the initial transmission in the next superframe.

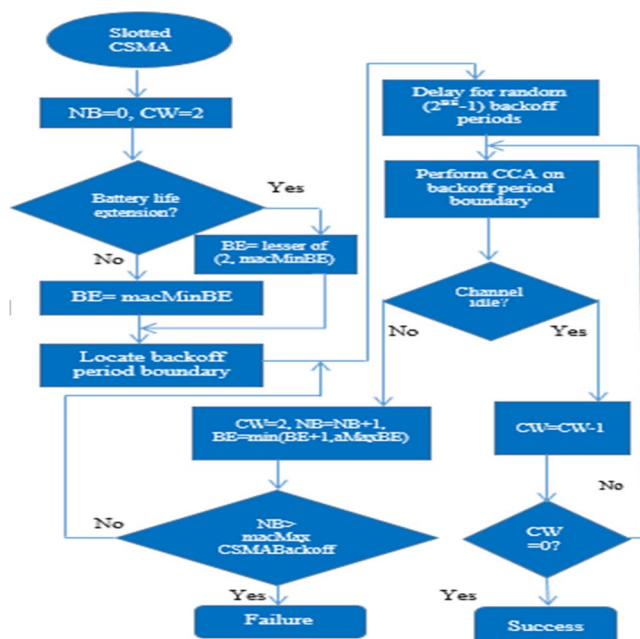


Fig. 2. Slotted CSMA/CA mechanism for IEEE 802.15.4

### III. DIFFERENT BACKOFF ALGORITHMS

In previous section, we have described about the backoff algorithm for the IEEE 802.15.4 which is known as BEB. In this section, we briefly discuss three more backoff algorithms namely EIED, EIMD and EILD. Then we adopt these algorithms in the slotted CSMA/CA of IEEE 802.15.4.

#### A. Exponential Increase Exponential Decrease Algorithm

*Step1:* Initialization-minimum backoff exponent, maximum backoff exponent, maximum number of backoffstages.

*Step2:* At the First Transmission Attempt

- Set: Backoff Period Set to the Minimum.

*Step3:* For Each Collision or Unsuccessful Transmission

- EIED doubles the Backoff Period
- It retries until maximum number of backoff occurs

*Step4:* For Each Successful Transmission

- EIED halves the Backoff Period

*Step5:* End

#### B. Exponential Increase Multiplicative Decrease Algorithm

*Step 1:* Initialization-minimum backoff exponent, maximum backoff exponent, maximum number of backoffstages.

*Step 2:* At the First Transmission Attempt

- Set: Backoff Period Set to the Minimum.

*Step 3:* For Each Collision or Unsuccessful Transmission

- EIMD doubles the Backoff Period
- It retries until maximum number of backoff occurs

*Step 4:* For Each Successful Transmission

- EIMD decrease the Backoff Period by a Factor(here 1.5).

*Step 5:* End

#### C. Exponential Increase Linear Decrease Algorithm

*Step1:* Initialization-minimum backoff exponent, maximum backoff exponent, maximum number of backoffstages.

*Step 2:* At the First Transmission Attempt

- Set: Backoff Period Set to the Minimum.

*Step3:* For Each Collision or Unsuccessful Transmission

- EILD doubles the Backoff Period
- It retries until maximum number of backoff occurs

*Step4:* For Each Successful Transmission

- EILD decrease the Backoff Period Linearly, that is current Backoff period=Backoff period-1.

*Step5:* End

### IV. RESULTS AND DISCUSSIONS

In this part, we present simulation results and compare the saturation throughputs, delay and energy by applying the four backoff algorithms in slotted CSMA/CA of IEEE 802.15.4.

The simulation results presented in this section are obtained using the same simulator used in [2] for the BEB. We extend the simulator adding other backoff algorithms. It is a discrete event simulator using C++ that closely ensues the MAC layer procedure of the IEEE802.15.4. We have used two scenario – the first one is the using the default values in the standard and other one is using different parameter values as shown in the Table I

Table I Simulation parameters

Parameters	Scenario 1 (Default Values)	Scenario 2
amacMinBE(minimum backoff exponent)	3	4
aMaxBE(maximum backoff exponent)	5	9
NB <sub>max</sub> (maximum number of backoffstages)	5	5

The Fig. 3, Fig. 5, and Fig. 7 shows the normalized throughput, mean frame service time or delay and energy respectively for all the four backoff algorithms using the scenario 1. The result using BEB is similar to the reference [2]. The EIED algorithm outperforms the other three. As the load (number of nodes) increases, the relative performance of the EIED increases. That is, it has better throughput, less delay using low energy than others (shown in Fig. 3, Fig. 5, Fig. 7). However, other three schemes – BEB, EILD and EIMD show almost similar throughputs (Fig. 3) for the default parameters. But EILD and EIMD has less delay (Fig 5) and low energy used (Fig. 7) than BEB. This implies, EIED would be better choice among all for this scenario (default parameter values).

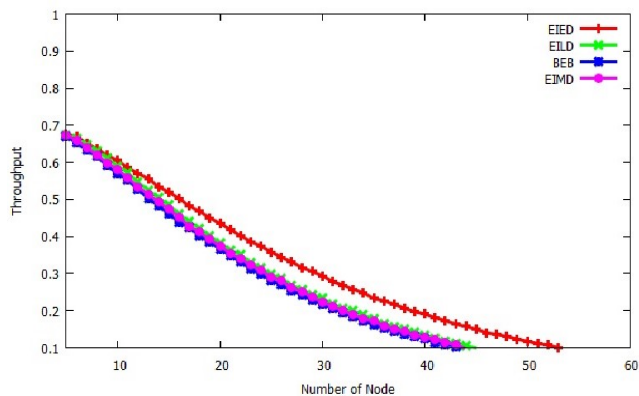


Fig. 3. Normalized Saturation Throughput ( $amacMinBE=3, aMaxBE=5$  and  $NB_{max}=5$ ).

On the other hand, the Fig. 4, Fig. 6, Fig. 8 shows the performance results scenario 2 as the values are given at the Table I. The throughputs of BEB are better up to a certain number of nodes (around 25) (Fig. 4). As a consequence BEB has less delay and low energy used for lower number of nodes. After that, the performance is decreased. This concludes that for higher load, BEB would not be good choice. However, the EIED closely performs same as BEB up to the first 25 nodes and takes lead afterwards. So EIED has better throughput (Fig. 4), less delay (Fig. 6) and minimal energy used (Fig. 8) when the number of nodes increased. It outperforms other backoff algorithms for higher number of nodes. The EILD and EIMD also has better throughput than the BEB (Fig. 4) for higher amounts of nodes. So that EILD and EIMD also has less delay (Fig. 6) and low energy (Fig. 8) used than BEB for higher number of nodes. It happens because of taking a random number from a small distribution range yield a higher collision probability. In BEB, after a successful transmission, it decreases the backoff window into the minimum. Hence, the distribution range is small and collision probability is higher. But in the cases of EIED, EILD and EIMD, it decrease the backoff window into halves, linearly, and by a factor (here 1.5) respectively. As a result, a larger distribution range produced and collision probability become lower. If collision

probability is less, that results less delay and if less delay occurs which leads to minimal energy used. Therefore, the throughputs, delay and energy of EIED, EILD, and EIMD algorithm are better than that of BEB algorithm after certain amount of nodes.

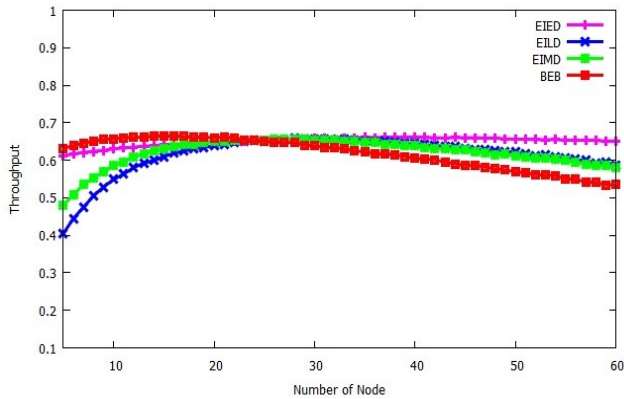


Fig. 4. Normalized Saturation throughput ( $a_{macMinBE} = 4$ ,  $a_{MaxBE} = 9$  and  $N_{B_{max}} = 5$ )

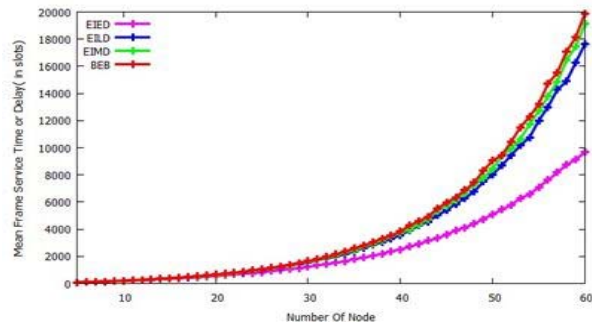


Fig. 5. Delay vs. no. of nodes ( $a_{macMinBE} = 3$ ,  $a_{MaxBE} = 5$  and  $N_{B_{max}} = 5$ )

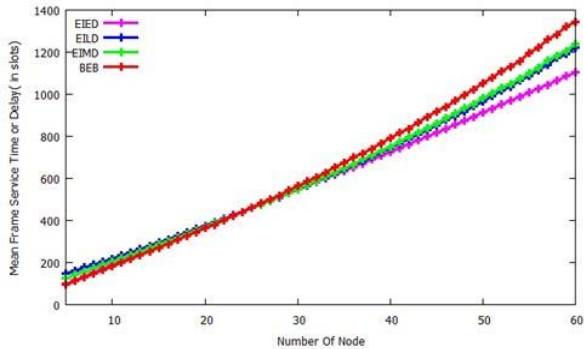


Fig. 6. Delay vs. no. of nodes ( $a_{macMinBE} = 4$ ,  $a_{MaxBE} = 9$  and  $N_{B_{max}} = 5$ )

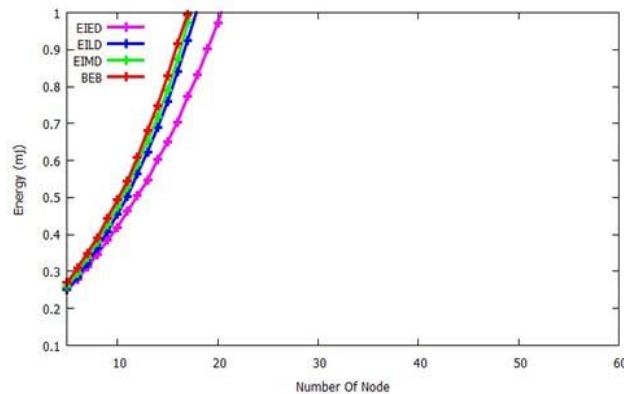


Fig. 7. Energy vs. no. of nodes ( $a_{macMinBE} = 3$ ,  $a_{MaxBE} = 5$  and  $N_{B_{max}} = 5$ )

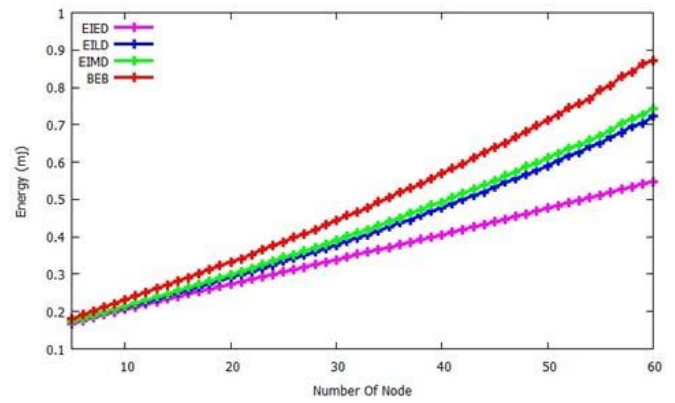


Fig. 8. Energy vs. Number of Node ( $a_{macMinBE} = 4$ ,  $a_{MaxBE} = 9$  and  $N_{B_{max}} = 5$ ).

## V. CONCLUSION

We have compared the throughputs, delay and energy of existing BEB algorithm with three other backoff algorithms - EIED, EILD, EIMD for the slotted CSMA/CA in IEEE 802.15.4 MAC. Simulation results show that EIED algorithms give better throughputs, less delay and low energy used over BEB, EILD and EIMD. For the higher load, the EIED, EILD, EIMD perform better than that of the BEB algorithm.

## REFERENCES

- [1] LAN/MAN Standards Committee. "Part 15.4: wireless medium access control (MAC) and physical layer (PHY) specifications for low-rate wireless personal area networks (LR-WPANs)." *IEEE Computer Society* (2003).
- [2] Kazi Ashrafuzzaman and SUP KWAK KYUNG. "On the performance analysis of the contention access period of IEEE 802.15. 4 MAC." *IEEE communications letters* 15.9 (2011): 986-988.
- [3] Song, Nai-Oak, et al. "Enhancement of IEEE 802.11 distributed coordination function with exponential increase exponential decrease backoff algorithm." *Vehicular Technology Conference, 2003. VTC 2003-Spring. The 57th IEEE Semiannual*. Vol. 4. IEEE, 2003.
- [4] Vukovic, Ivan N., and Natt Smavatkul. "Saturation throughput analysis of different backoff algorithms in IEEE802. 11." *Personal, Indoor and Mobile Radio Communications, 2004. PIMRC 2004. 15th IEEE International Symposium on*. Vol. 3. IEEE, 2004.
- [5] Ling, Xinhua, et al. "A renewal theory based analytical model for the contention access period of IEEE 802.15. 4 MAC." *IEEE Transactions on Wireless Communications* 7.6 (2008): 2340-2349.
- [6] Zheng, Jianliang, and Myung J. Lee. "Will IEEE 802.15. 4 make ubiquitous networking a reality?: a discussion on a potential low power, low bit rate standard." *IEEE Communications magazine* 42.6 (2004): 140-146.
- [7] Kleinrock, Leonard, and Fouad Tobagi. "Packet switching in radio channels: Part I-carrier sense multiple-access modes and their throughput-delay characteristics." *IEEE transactions on Communications* 23.12 (1975): 1400-1416.

# A Compact Triangular Shaped Microstrip Patch Antenna with Triangular Slotted Ground for UWB Application

M. A. Ullah<sup>1</sup>, F. B. Ashraf<sup>1</sup>, T. Alam<sup>1,2</sup>, M. S. Alam<sup>2</sup>, S. Kibria<sup>1</sup>, M. T. Islam<sup>1</sup>

<sup>1</sup>Dept. Of Electrical, Electronic and Systems Engineering,  
Universiti Kebangsaan Malaysia (UKM), Malaysia

<sup>2</sup>Dept. of CSE, International Islamic University Chittagong (IIUC), Bangladesh  
Email: tariqul@ukm.edu.my

**Abstract**— This paper is aimed to present a very small sized patch antenna for UWB applications. The antenna used microstrip feed-line. This antenna is very small in dimension. The total size of the antenna is  $20 \times 18 \text{mm}^2$ . Triangular slots in the partial ground plane, are used to get a better bandwidth. The antenna has  $\text{VSWR} < 2$  over the bandwidth. The whole designing and simulation process of the antenna is done by CST Microwave Studio software.

**Keywords**— UWB; Patch antenna; Triangular slotted ground; Compact patch antenna; CST MWS

## I. INTRODUCTION

Ultra Wide Band is used to provide greater bandwidth and high data transmission rate. Its short range characteristics make it useful for WPAN, WBAN and some other indoor applications [1]. Researchers got interested in UWB antennas since the Federal Communications Commission of the US approved 3.1-10.6GHz spectrum for commercial use. As an important design parameter, compact size of the UWB antenna has been always a requirement for mobile units [2].

A lot of UWB antenna has been proposed since past years, but not many of them are compact in size. The antennas presented in [3-16] has been investigated for UWB applications, but these antennas are not compact enough for integrating in smaller devices and other applications where small size is an important design requirement. Another study on the Ultra Wide Band Application is investigated [9] and it also does not serves a compact size.

Though, these designs covered the UWB frequency well, but the question of a smaller sized antenna remained. So, considering the applications and comparing the size, in this study presents a very small sized microstrip patch antenna with triangular slots in its partial ground, for UWB applications. The antenna covers 3.32-9.12 GHz, which provides a bandwidth of 5.8 GHz. The main focus of this study was to design a UWB patch antenna with a smaller dimension. As a result, this antenna's dimension is  $20 \times 18 \text{mm}^2$  which is smaller considering the UWB specifications and some other previous designs.

## II. DESIGN OF THE ANTENNA

The configuration of the proposed UWB microstrip patch antenna is shown in figure 1. The FR4 is used as substrate material and the width of the substrate is 1.63 mm. The patch width is kept 0.035 mm. The width of the feed line is different over the whole feed line. On the backside of the antenna, the partial grounding technique is applied to triangular slots within the ground plane. The partial ground plane has an impact behind providing wide bandwidth.

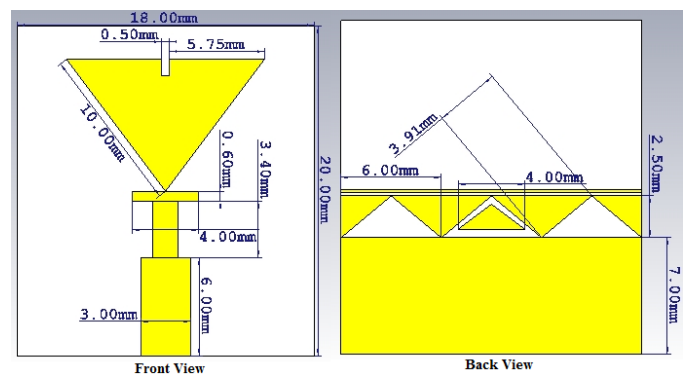


Fig. 1. Specifications of the proposed antenna.

## III. RESULTS AND DISCUSSIONS

The proposed triangular shaped microstrip patch antenna is designed and simulated under CST Microwave Studio environment. From figure 1, it can be seen that, the width of feed line is changed after 6 mm from the feed point. Certainly, varying the width of the second feed line provides different return loss. The width of the second part of the feed line is 4mm, which provided a good return loss [11]. To get a good impedance matching, the width varying technique worked well.

Partial ground is used for the antenna for grounding purpose. The triangular shaped slots are used to enhance the bandwidth for the antenna. The total ground plan of the antenna has a total size of 10mm in the backside.

The difference between the ground plane and the radiating patch is increased when different slots are cut on the ground plane. As a result, impedance bandwidth is improved [4].

Figure 2 shows the VSWR of the studied antenna from the simulated results. From the curve, it can be seen that the Voltage Standing Wave Ratio has remained less than 2, over 3.32 to 9.12 GHz of the bandwidth.

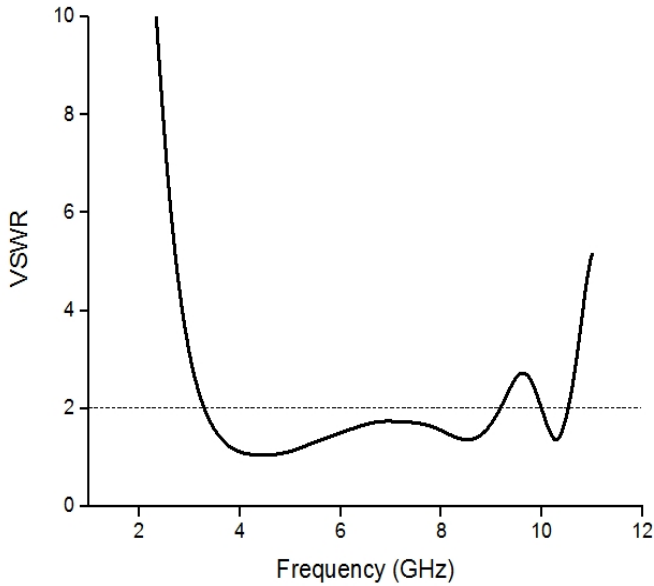


Fig. 2. VSWR of the proposed antenna.

Figure 3 illustrates the return loss of the proposed UWB antenna, and it can be seen that, the mentioned operating bandwidth remained under -10dB of the return loss curve. The return loss is resonant at 4.46 GHz. The coupling between triangular shaped radiating patch and triangular slotted partial ground helped the proposed antenna to achieve the operating bandwidth.

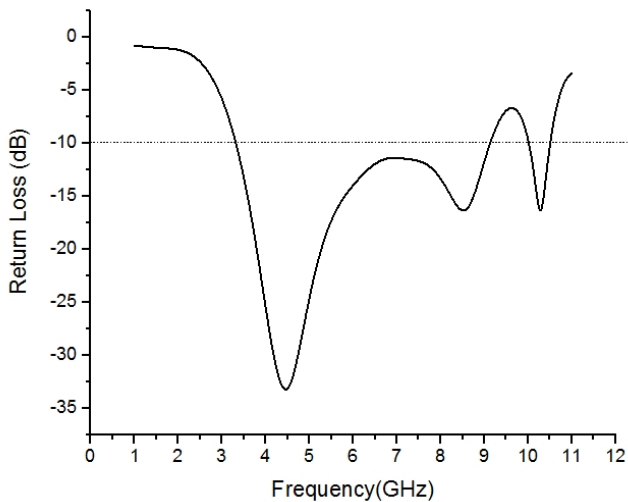


Fig. 3. Return loss of the proposed antenna.

Figure 3 shows the peak gain curve. The peak gain is about 1.5dB, which is acceptable for an UWB patch antenna having a very small size. Over the whole bandwidth the average gain about 1.49dB.

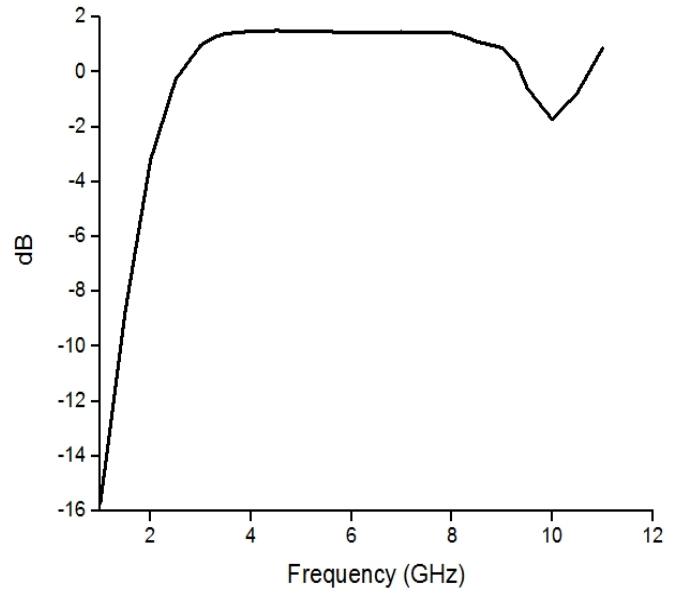
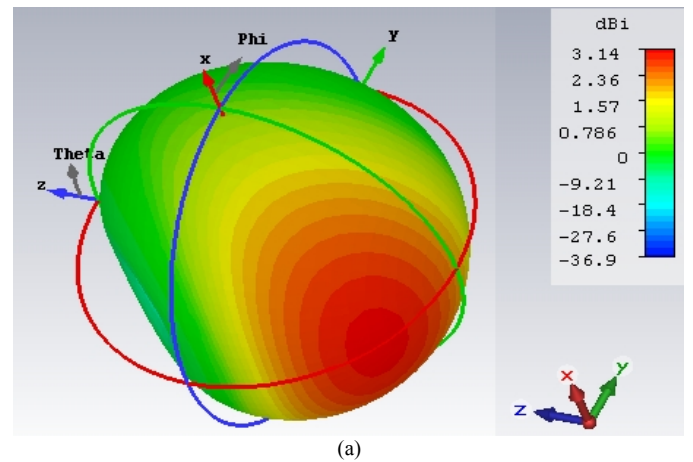
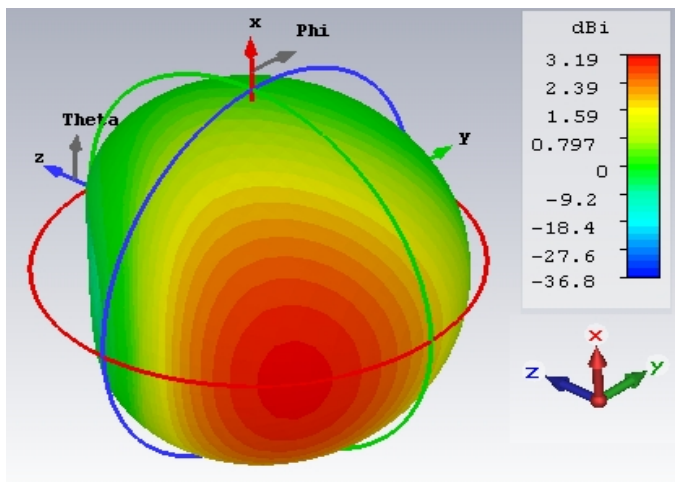


Fig. 4. Peak gain of the proposed antenna.

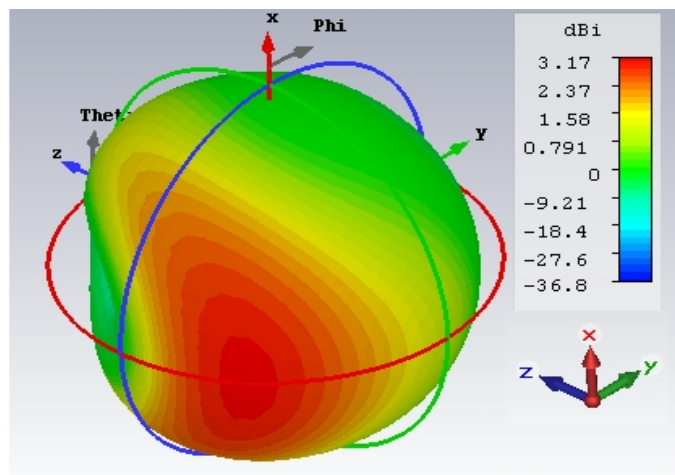
The radiation patterns of the proposed antenna are also studied at different frequencies. Fig. 5 shows radiation patterns of the antenna at different frequencies. Over the operating bandwidth the radiation patterns remain almost like monopole antenna. From these figures, it can be seen that, the radiation patterns remained consistent with the change of frequency. But after crossing the operating bandwidth, its radiation pattern changes into more like bidirectional at 10GHz.



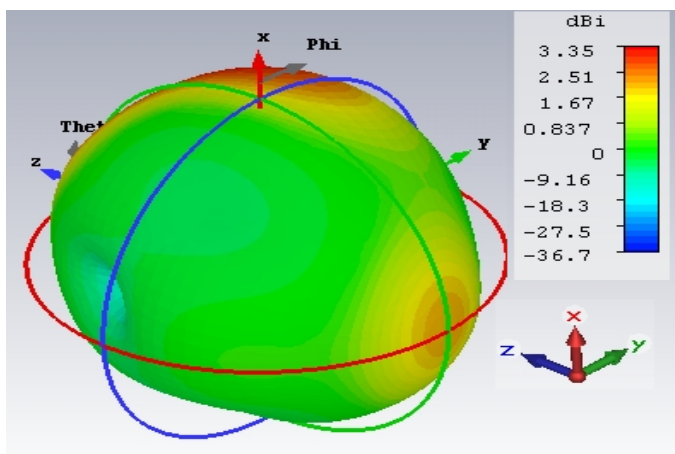
(a)



(b)



(c)

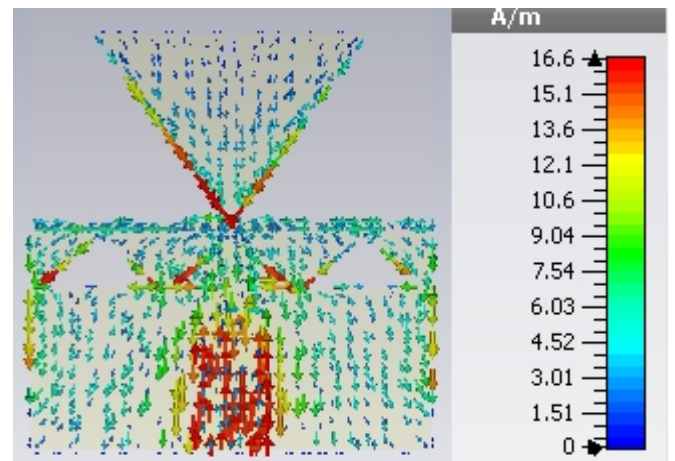


(d)

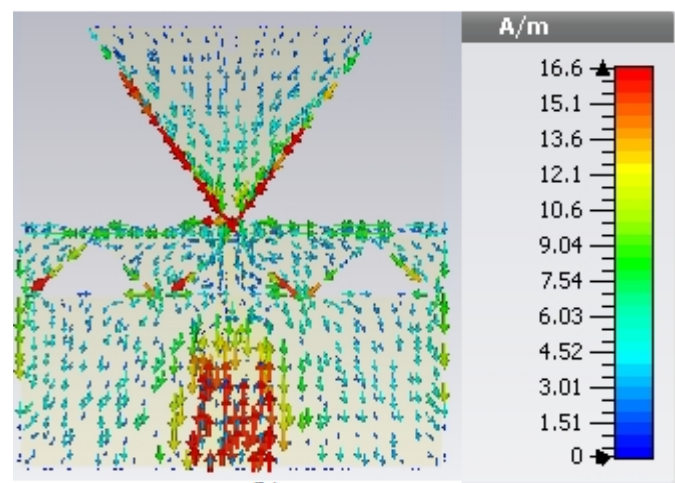
Fig.5. The 3D radiation patterns for the proposed antenna at (a) 4.46 GHz, (b) 5 GHz, (c) 7GHz and (d) 10 GHz.

Fig. 6 illustrates the surface current distribution of the proposed antenna, at different frequencies. In figure 6, current distribution at (a) 4.46 GHz and (b) 5 GHz is shown. It can be seen that, the surface current is maximum at the left and right edge of the triangular patch along with the feed line. And there is also concentrated current along the edge of the triangular slots and lesser in the upper edge of the radiating patch. Uniformly distributed current is seen in other parts. And

strong current exists around the feed point and more than half of the length of the feed line.



(a)



(b)

Fig. 6. Surface current distribution of the proposed antenna.

Table 1 represents a comparison among different antenna studied with this proposed antenna. Total dimension and bandwidth of the reference antennas are compared to the proposed antenna in the table.

TABLE I. COMPARISON

Ref. Antenna	Total Dimension (L×W)	Bandwidth (GHz)
[3]	40×32 mm <sup>2</sup>	2.8-16.5
[5]	35×31 mm <sup>2</sup>	3.6-11.06
[7]	30×22 mm <sup>2</sup>	2.95-15.45
[8]	26×28 mm <sup>2</sup>	3.7-18
[9]	39×40 mm <sup>2</sup>	2.6-12.3
[10]	35×30 mm <sup>2</sup>	2.5-11.21
[12]	28×24 mm <sup>2</sup>	3.5-12
[13]	40×30 mm <sup>2</sup>	2.3-11.4
[15]	34×36 mm <sup>2</sup>	3.05-10.83
Proposed UWB Antenna	20×18 mm <sup>2</sup>	3.32-9.12

#### IV. CONCLUSION

The proposed UWB microstrip fed patch antenna serves its purpose well. Comparing the antenna size is  $20 \times 18$  mm, it would be highly efficient for the applications of smart devices and gadgets. Considering its total size the antenna provides  $VSWR < 2$  and covers the UWB frequency from 3.32GHz to 9.12 GHz which could be useful for numerous applications. As one of the main key points behind this study was to design a smaller UWB antenna, the simulation results show this smaller version does not dissatisfy at all.

#### REFERENCES

- [1] Verbiest, J.R., and Vandenbosch, G.A.E.: 'A novel small-size printed tapered monopole antenna for UWB WBAN', *IEEE Antennas Wirel. Propag. Lett.*, 2006, 5, (1), pp. 377-379.
- [2] Federal Communication Commission, "First order and report: Revision of part 15 of the Commission's rules regarding UWB transmission systems," April 22, 2002.
- [3] J. Zhang, X.L. Sun, S.W. Cheung, T.I. Yuk and Z.B. Ni, "CPW-Coupled-Fed Elliptical Monopole Antenna for UWB Applications", *Radio and Wireless Symposium (RWS)*, 2012 IEEE.
- [4] Alam, T., et al. "Dual elliptical patch antenna design on low cost epoxy resin polymer substrate material." *International Journal of Applied Electromagnetics and Mechanics* 49.1 (2015): 23-29.
- [5] Islam Md. Rafiqul, Alam AHM Zahirul, M. Feroze Akbar J. Khan, Shaker Alkaraki, "Design of microstrip patch antenna using slotted partial ground and addition of stairs and stubs for UWB application", *Cyber Journals: Multidisciplinary Journals in Science and Technology, Journal of Selected Areas in Telecommunications (JSAT)*, May Edition, 2012.
- [6] Alam, T., Mohammad Rashed Iqbal Faruque, and Mohammad Tariqul Islam. "Broadband triangle shape printed antenna for mobile wireless communication." *Theory and Applications of Applied Electromagnetics*. Springer International Publishing, 2015. 287-294.
- [7] R. Azim, M. T. Islam and N. Misran, "Design of a Planar UWB Antenna with New Band Enhancement Technique", *Applied Computational Electromagnetics Society Journal*. Oct2011, Vol. 26 Issue 10, p856-862. 7p.
- [8] L. Liu, S.W. Cheung, R. Azim, M. T. Islam, "A compact circular-ring antenna for ultra-wideband applications.", *Microwave and Optical Technology Letters*, Volume 53, Issue 10, October 2011, Pages 2283-2288.
- [9] R. Azim, M. T. Islam and N. Misran, "Microstrip Line-fed Printed Planar Monopole Antenna for UWB Applications", *Arabian Journal for Science and Engineering*, September 2013, Volume 38, Issue 9, pp 2415-2422.
- [10] B. Tahar, K. Djamel, H. Abdesselam, "A simple small size disk microstrip patch antenna with a rectangular aperture for ultra wide band application", *Control, Engineering & Information Technology (CEIT)*, 2015 3rd International Conference on, 25-27 May 2015.
- [11] Alam, T., Faruque, M.R.I. & Islam, M.T. "A corded shape printed wideband antenna design for multi-standard mobile applications" *Telecommun Syst* (2016) 62: 511. doi:10.1007/s11235-015-0090-x
- [12] G. Shrikanth Reddy, S. K. Mishra, S. Khariche, and J. Mukherjee, "High gain and low cross-polar compact printed elliptical monopole uwb antenna loaded with partial ground and parasitic patches", *Progress In Electromagnetics Research B*, Vol. 43, 151-167, 2012.
- [13] Gaurav K. Pandey, Hari S. Singh, Pradutt K. Bharti, and Manoj K. Meshram, "Design of wlan band notched uwb monopole antenna with stepped geometry using modified ebg structure", *Progress In Electromagnetics Research B*, Vol. 50, 201-217, 2013.
- [14] Alam, T., Mohammad Rashed Iqbal Faruque, and Mohammad Tariqul Islam. "Printed circular patch wideband antenna for wireless communication." *Informacije MIDEM* 44.3 (2015): 212-217.
- [15] H. S. Mewara, M. M. Sharma, Mayank Sharma, Ajay Dadhich, "A novel ultra-wide band antenna design using notches, stepped microstrip feed and beveled partial ground with beveled parasitic strip", *Applied Electromagnetics Conference (AEMC)*, 2013 IEEE.
- [16] Sharma, Manmohan, Akram Alomainy, and Clive Parini. "Fidelity pattern analysis of a CPW-fed miniature UWB antenna using different excitation pulses." *IEEE Antennas and Wireless Propagation Letters* 14 (2015): 494-498.

# Rotation Invariant Power Line Insulator Detection Using Local Directional Pattern and Support Vector Machine

Taskeed Jabid

Department of Computer Science and Engineering  
Sogang University  
Seoul, Republic of Korea  
[taskeed@ewubd.edu](mailto:taskeed@ewubd.edu)

Md. Zia Uddin

Department of Computer Education  
Sungkyunkwan University  
Seoul, Republic of Korea  
[ziauddin@skku.edu](mailto:ziauddin@skku.edu)

**Abstract**— Detecting and localizing insulator plays a vital role in any power line monitoring system. In this work, we present a novel method for rotation invariant insulator detection. Rotation invariance is achieved by an efficient approach for estimating rotation angle of all insulator of an image. Sliding window based local directional pattern (LDP) feature is extracted from the image and support vector machine is used for classing each of those sliding window. We demonstrate our approach on an evaluation set of 325 real-world insulator images captured from a moving vehicle and evaluate our results with respect to a manually created ground-truth. The performance of our insulator detector is comparable to other state-of-the-art detectors.

**Keywords**— *Insulator detection, rotation estimation, local directional pattern(LDP), support vector machine (SVM).*

## I. INTRODUCTION

Periodic inspection of different parts of power line is one of the most important jobs in power system operation. Insulators are the key component among those parts and regular inspection of insulators is essential for an uninterrupted power distribution. However, manual inspection is very much labor-intensive, time-consuming and dangerous [1]. It requires inspectors to climb the transmission line tower which also can be limited by the adverse environmental condition. Therefore, it is necessary to develop an automatic insulator inspection system which can accurately detect insulators from an image taken from a vehicle or helicopter. Because without accurate localization and segmentation of the insulator, it is not possible to carry out further defects analysis [2]. Number of researches has been conducted regarding automatic insulator detection from aerial images. A novel approach based on discriminative training of local gradient-based descriptors is proposed by Oberweger et al. [3]. Their method utilizes a subsequent voting scheme for localization to detect insulators in aerial images. Another insulator detection algorithm based on local features and spatial orders for aerial images is proposed by Liao and An [4]. They introduce a new multiscale and multifeature (MSMF) descriptor to represent the local features. Special shape features of insulator are also used to identify an insulator. In

[5], insulator's Haar-like rectangular feature was used to express the insulator and fed to an AdaBoost algorithm for classification. Instead of real aerial insulator images, the paper adopted synthesized 3D insulator images built with 3DMax software as positive samples to train the classifier. Test results showed great improvement of recognition rate which is up to 80% due to their obvious features compared with the real insulator images. Bingfeng Li et al. [6] used insulator's shape features derived from vertical profile projection curve to recognize them. For classifier, SVM is selected as the learning algorithm which also achieved solid recognition results, e.g. more than 90% recognition rate. Wang et al. [2] proposed a novel insulator recognition method for images taken by Unmanned Aerial Vehicles (UAVs) with highly cluttered background, which adopts Support Vector Machine (SVM) as a classifier to distinguish insulator from the cluttered background based on Gabor features.

Though numbers of works are conducted regarding automatic insulator detection from aerial image, high acquisition cost of aerial image makes the system less implementable. Besides this capturing aerial images is not feasible during some adverse environmental condition where vehicle based image acquisition is feasible. Therefore, many insulator detection works is proposed using images taken from ground vehicle. As example, Li et al. [7] used the improved MPEG-7 edge histogram descriptor (EHD) technique to recognize the insulator from video taken from ground. In order to reduce the time cost and improve the accuracy of recognition, they also applied used Kalman filter to forecast the target position of the insulators. V. Murthy et al. [8] compute the condition indices for overhead power distribution line insulators to overcome difficulties related to vehicular applications in video surveillance. They utilize wavelet-transform based feature extraction and SVM for subsequent condition analysis of insulators.

Developing a successful insulator monitoring system is challenged by the fact that a large variation exist in the appearance of insulator. Therefore, it is very difficult to develop a universal insulator detection system which can be effective in all scenarios. As a result, all existing insulator detection methods work well in certain scenario which cannot



be applied to other situations. Among various challenges, cluttered background and insulators appearance in arbitrary in plane and out plane rotational angle is most common in insulator images which hampers detection accuracy. In this work we present a novel insulator recognition method which works on highly cluttered images with arbitrary orientation. The proposed system can overcome the insulator's rotation problem by estimating rotation and rotate back the images

accordingly so that insulators always appeared horizontal with the image axis. A robust insulator detector is developed which is invariant to insulator size and combinations, partial overlap, illumination, and background clutter using local directional pattern (LDP) feature and Support Vector Machine (SVM) classifier. Figure 1 elucidates every steps of the proposed insulator detection procedure.

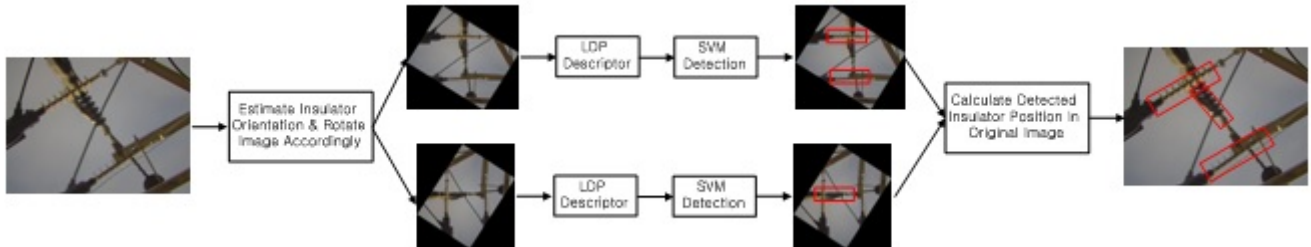


Fig. 1. An overview of rotation invariant insulator detection method

## II. ROTATION INVARIANT INSULATOR DETECTION

A rotation invariant insulator detection method is proposed in this paper. In perspective of object detection problem, insulator can be considered a weakly textured object which may appear in arbitrary orientation in the image. The object of interest that is insulator may be surrounded by clutter and/or by other object. However, insulators have a rigid form with repetitive geometric structure and a distinctive circular shape of each cap, which are properties that can be utilize. Lisin et al advocates the use of local feature for describing the shape of a rigid object during object detection work [9]. In accordance to that, we propose a local feature insulator detection which preceded by a novel insulator rotation estimator for achieving rotation invariant detection. Over the two decades, the scale-invariant feature transform (SIFT) descriptor [10] has been shown to outperform a set of existing descriptors. SIFT tries to align a local coordinate system to the dominant gradient direction at each detected interest point. However in presence of much background clutter, image dominant gradient orientation may provide erroneous information. Therefore, many object detectors skip this and use the non-invariant dense features. In our proposed work, we use local directional pattern (LDP) feature to represent the insulator appearance. A novel rotation estimator aids us to align the insulator with the image axis. The axis-aligned insulator is then detected by proposed LDP based support vector machine (SVM) detector.

### A. Insulator Rotation Estimation

Insulator is a rigid object with repeating structures known as insulator caps. Because shape of each cap is identical to each other, it is more likely that corner points will originated from the same location of each cap (Figure 2(a)). Consequently, line formed by those corner points will correspond with the insulator orientation. We therefore apply Hough-based line estimation to estimate the orientation of this straight line.

**Corner Detection:** At first step of rotation estimation, Harris corner detector [11] is used to detect corner points from

the given image. The Harris corner detector is a popular interest point detector due to its strong invariance to rotation, scale, illumination variation and image noise. The Harris corner detector is based on the local auto-correlation function of a signal; where the local auto-correlation function measures the local changes of the signal with patches shifted by a small amount in different directions. Given a shift  $(\Delta x, \Delta y)$  and a point  $(x, y)$ , the auto-correlation function is defined as,

$$C(x, y) = \sum_W [I(x_i, y_i) - I(x_i + \Delta x, y_i + \Delta y)]^2 \quad (1)$$

Where  $I(\cdot, \cdot)$  denotes the image function and  $(x_i, y_i)$  are the points in the window  $W$  centered on  $(x, y)$ .

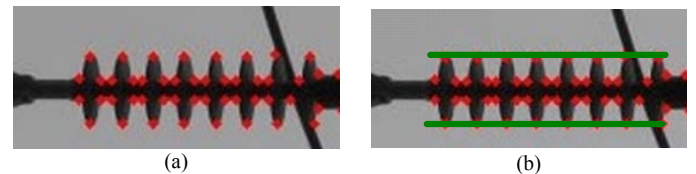


Fig. 2. (a) Detected corner points from an insulator. (b) Detected corner points fall into straight lines

**Hough Transformation:** Hough transformation is applied on the detected corner points to estimate the line formed by most number of corner points. Hough transformation is used to find imperfect instances of objects within a certain class of shapes by a voting procedure [12]. The idea behind the method is simple: parametric shapes in an image are detected by looking for accumulation points in the parameter space. If a particular shape is present in the image, then the mapping of all of its points into the parameter space must cluster around the parameter values which correspond to that shape [13]. This approach maps distributed and disjoint elements of the image into a localized accumulation point. Therefore, if some caps do not produce any corner points, the line will still be detected, on the evidence of their visible points. Hough transformation provides number of lines' orientation with their

corresponding voting score. As multiple insulators may appeared in different orientation in the image, selecting orientation of the single line with most vote may not sufficient. In addition, in background other object with strong repeating structure can exist. Therefore multiple orientations from Hough space need to be picked for correctly estimate all the insulators' orientation. Consequently after selecting the straight line with highest vote in Hough accumulator, we also select other straight lines which Hough accumulator value crosses a specific percentage ( $T_H$ ) of highest voting score.

### B. Insulator Detection

Insulators are weakly textured object and most of the time surrounded by clutter. In addition, it has a rigid form with repetitive geometric structure. It also maintains a fixed aspect ratio as long as the images are taken with reasonable viewing angle. All of these properties of insulators inspired us to use local directional pattern (LDP) feature to detect the insulators.

Local Directional Pattern (LDP): The local directional pattern (LDP) [14][15] is an eight bit binary code assigned to each pixel of an input image. This pattern is calculated by comparing the relative edge response value of a pixel in different directions. For this purpose, we calculate eight directional edge response value of a particular pixel using Kirsch masks [16] in eight different orientations (M0~M7) centered on its own position.

With eight directional masks, we obtain eight edge response value  $m_0, m_1, \dots, m_7$ , each representing the edge significance in its respective direction. The response values are not equally important in all directions. The presence of a corner or an edge shows high response values in some particular directions. Therefore, we are interested to know the  $k$  most prominent directions in order to generate the LDP. Here, the top- $k$  directional bit responses  $b_i$  are set to 1. The remaining  $(8-k)$  bits of 8-bit LDP pattern are set to 0. Finally, the LDP code is derived by (2).

$$LDP_k = \sum_{i=0}^7 b_i(m_i - m_k) \times 2^i, b_i(a) = \begin{cases} 1 & a \geq 0 \\ 0 & a < 0 \end{cases} \quad (2)$$

where,  $m_k$  is the  $k$ -th most significant directional response.

After computing all the LDP code for each pixel  $(r,c)$ , the input image  $I$  of size  $M \times N$  is represented by a LDP histogram  $H$  using equation (3). The resultant histogram  $H$  is the LDP descriptor of that image.

$$H(i) = \sum_{r=1}^M \sum_{c=1}^N f(LDP_k(r,c), i); f(a,i) = \begin{cases} 1 & a = i \\ 0 & a \neq i \end{cases} \quad (3)$$

where,  $i$  is the LDP code value. For a particular value of  $k$ , the histogram  $H$  has  $C_k^8$  number of bins.

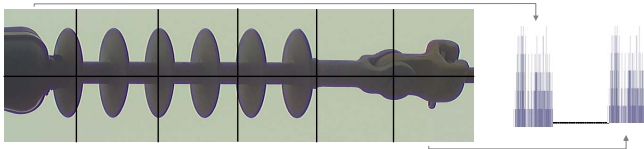


Fig. 3. A insulator image is divided into small regions from which LDP histograms are extracted and concatenated.

**Support Vector Machine (SVM):** Many previous object recognition works used Support Vector Machine (SVM); here we also evaluate our proposed insulator detection system using SVM. SVM [17] is a popular supervised machine learning technique which performs an implicit mapping of data into a higher dimensional feature space. After that it finds a linear separating hyperplane with maximal margin to separate data from this higher dimensional space.

Given a training set of labeled examples  $T = \{(x, y), i = 1, \dots, M\}$  where  $x_i \in R^n$  and  $y_i \in \{-1, 1\}$ , the new test data will be classified by equation (4)

$$f(x) = \text{sign}\left(\sum_{i=1}^M \alpha_i y_i K(x_i, x) + b\right) \quad (4)$$

where  $\alpha_i$  are Lagrange multipliers of dual optimization problem,  $b$  is a bias and  $K(\cdot, \cdot)$  is a kernel function. SVM allows domain-specific selection of the kernel function. Though new kernels are being proposed, the most frequently used kernel functions are the linear, polynomial, and Radial Basis Function (RBF) kernels.

### III. EXPERIMENTAL RESULT

In this section we present and discuss the results of the evaluation. To the best of our knowledge, there is currently no publicly available dataset for insulator detection. Therefore we use our own evaluation set, which contains 325 images (size  $2592 \times 1944$ px) with 500 labelled insulators. For evaluation and training we use a segmented ground-truth, which is generated by manually tag the insulators.

#### A. Rotation Estimation

In the image there may be multiple insulators in different orientations. Hence, we evaluate how many insulators' rotation is correctly estimated by our proposed rotation estimator. As Hough transformation provides number of orientation estimation, selecting more estimation may increase number of correct estimation. However, it also increase wrong estimation which in turns requires unnecessary image rotation and increase the processing time. Therefore, we need to choose how many estimated orientation should be picked from each image. For this, we choose orientation of highest vote and also those orientations which's vote crosses a certain percentage ( $T_H$ ) of highest vote. The Table I shows the relationship between varying percentages with rotation estimation performance. We found that initially choosing only the strongest orientation can estimate only 71% insulators' orientation. Consequently, as we relaxing the threshold more and more orientated insulator becoming correctly estimated. Conversely, it also starts to estimate some background object's orientation. As a result precision going down though recall rates improves. However, lowering the threshold below 50% do not estimate any more insulator's orientation correctly rather estimates more background object's orientation. As a result the recall unchanged but precision getting lower. Hence threshold 50% is used to get optimum trade-off between precision and recall during orientation estimation.

TABLE I. ROTATION ESTIMATION WITH VARYING THRESHOLD (TH)

Threshold (TH)	Recall	Precision
100%	71.29%	81.82%
75%	78.43%	68.97%
50%	92.71%	72.73%
25%	92.71%	55.54%

### B. Insulator Detection

We evaluate the insulator detector on our evaluation set, where each insulator is marked by a rotated rectangle. In order to evaluate the localization of our method we use the well-known Pascal score [18], which is calculated from the overlap of our generated bounding box  $B_{cl}$  to the ground-truth  $B_{gt}$

$$\text{by } P(B_{cl}, B_{gt}) = \frac{\text{area}(B_{cl} \cap B_{gt})}{\text{area}(B_{cl} \cup B_{gt})}. \text{ An object is considered}$$

detected if  $P(B_{cl}, B_{gt}) > 0.5$

As objective we want to maximize the number of correct detections and minimize the number of false detections. The two used evaluation metrics are precision, the fraction of correct detections to the total number of detections made by our detector, and recall, the fraction of correctly detected objects to the number of annotated objects. Our proposed method achieved recall rate 94.24% with 89.54% precision. The comparison of recall and precision with other method is shown in Table II which clearly demonstrates the effectiveness of the method.

TABLE II. COMPARISON OF PRECISION AND RECALL

Method	Recall	Precision
Oberweger et al [3]	98%	33%
Liao and An [4]	91%	87%
Wu and An [1]	86.47%	85.59%
Proposed Method	94.24%	89.54%

Table 2 demonstrates that recall rate of our proposed method is better than all other method except method proposed by Oberweger et al. However their precision rate becomes as low as 33% when their approach achieved highest recall rate. Contrary, our system can achieve close to their recall rate by maintaining precision rate approximately 90%. To further analyze the performance of our proposed method, we use precision recall (PR) curve. The following figure shows precision recall curve of our method and method proposed by Oberweger et al. The precision recall curve of proposed method is above their method which exhibits the superiority of the proposed system.

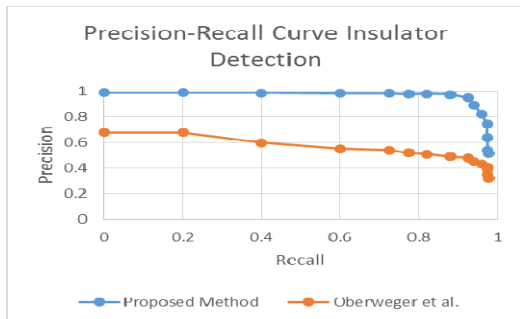


Fig. 4. Precision-recall curve (PRC) for insulator detection.

## IV. CONCLUSION

In this work we have presented a rotation invariant approach for insulator. We introduce a novel technique to estimate the insulator's rotation effectively which allows using a single insulator detector for detecting multiple insulators appearing in different orientation. The results of the experiment show that the performance of the proposed LDP based method is better than other competing methods. The proposed approach system can be employed in power distribution system for better monitoring. In future, we target to achieve real-time monitoring and recognition using further efficient feature extraction and recognition techniques.

## References

- [1] Q. Wu and J. An, "An active contour model based on texture distribution for extracting inhomogeneous insulators from aerial images", IEEE Trans. Geosci. Remote Sens., vol. 52, no. 6, pp. 3613-3626, 2014.
- [2] X. Wang and Y. Zhang, "Insulator Identification from Aerial Images Using Support Vector Machine with Background Suppression" in Proc. International Conf. on Unmanned Aircraft Systems, 2016. pp. 892 – 897.
- [3] M. Oberweger, A. Wendel, and H. Bischof, "Visual recognition and fault detection for power line insulators," in Proc. 19th Computer Vision Winter Workshop, 2014, pp. 1–8.
- [4] S. Liao, J. An, "A robust insulator detection algorithm based on local features and spatial orders for aerial images," IEEE Geosci. Remote Sens. Lett. Vol. 12, no. 5, pp. 963–967, 2015.
- [5] Y. Zhai, Y. Wu, H. Chen, and X. Zhao, "A method of insulator detection from aerial images," Sensors & Transducers, vol. 177, no. 8, 2014.
- [6] B. Li, D. Wu, Y. Cong, Y. Xia, and Y. Tang, "A method of insulator detection from video sequence," in 2012 International Symposium on Information Science and Engineering (ISISE), 2012, pp. 386–389.
- [7] W. G. Li, G. Ye, F. Huang, S. Wang, and W. Z. Chang, "Recognition of insulator based on developed MPEG-7 texture feature," in Proc. IEEE ICISP, 2010, pp. 265–268.
- [8] V.S. Murthy, K. Tarakanath, D.K. Mohanta, S. Gupta, "Insulator condition analysis for overhead distribution lines using combined wavelet and support vector machine (SVM)," IEEE Transactions on Dielectrics and Electrical Insulation, vol. 17, no. 1, pp. 89–99, 2010
- [9] D.A. Lisin, M.A. Mattar, M.B. Blaschko, E.G. Learned-Miller, M.C. Benfield, Combining local and global image features for object class recognition, IEEE CVPR, 2005.
- [10] D. G. Lowe. Object recognition from local scale-invariant features. International Conference on Computer Vision, pages 1150-1157, 1999.
- [11] C. Harris and M. Stephens, "A Combined Corner and Edge Detector," Proc. Alvey Vision Conf., pp. 147-151, 1988.
- [12] Duda, R. O. and P. E. Hart, "Use of the Hough Transformation to Detect Lines and Curves in Pictures," Comm. ACM, Vol. 15, pp. 11–15, 1972.
- [13] Danko Antolovic, "Review of the Hough Transform Method, With an Implementation of the Fast Hough Variant for Line Detection"
- [14] Jabid T, Kabir MH, Chae O: Local Directional Pattern (LDP) A Robust Image Descriptor for Object Recognition: in Proceedings of the IEEE Advanced Video and Signal Based Surveillance (AVSS), August 29 - September 1, Boston, USA, 2010; pp. 482–487.
- [15] T. Jabid, MH. Kabir, O. Chae, "Facial expression recognition using local directional pattern (LDP)", IEEE International Conference on Image Processing, 2010; pp. 1605–1608.
- [16] R. A. Kirsch. "Computer determination of the constituent structure of biomedical images". Comput. Eiorned. Res., vol. 4, pp. 315-328, 1971.
- [17] C. Cortes and V. Vapnik, "Support vector networks", Machine Learning, Vol.20, No. 3, pp. 273-297, 1995.
- [18] Mark Everingham, Luc J. Van Gool, Christopher K. I. Williams, John M. Winn, and Andrew Zisserman. The Pascal Visual Object Classes (VOC) Challenge. IJCV, 88(2):303–338, 2010.

# Occlusion Handling and Human Detection Based on Histogram of Oriented Gradients for Automatic Video Surveillance

Shayhan Ameen Chowdhury<sup>1</sup>, Mohammed Nasir Uddin<sup>2</sup>, Mir Md. Saki Kowsar<sup>1</sup>, Kaushik Deb<sup>1\*</sup>

<sup>1</sup>Dept. of Computer Science and Engineering, Chittagong University of Engineering & Technology (CUET), Chittagong-4349, Bangladesh

<sup>2</sup>Dept. of Computer Science and Engineering, Jagannath University, Dhaka-1100, Bangladesh

Email: shayhan@yahoo.com, nasir@cse.jnu.ac.bd, sakikowsar@cuet.ac.bd, <sup>1\*</sup>debkaushik99@cuet.ac.bd

**Abstract**—Human detection in a video surveillance system has vast application areas including suspicious event detection and human activity recognition. In the current environment of our society suspicious event detection is a burning issue. For that reason, this paper proposes a framework for detecting humans in different appearances and poses by generating a human feature vector. Initially, every pixel of a frame is represented as an incorporation of several Gaussians and use a probabilistic method to refurbish the representation. These Gaussian representations are then estimated to classify the background pixels from foreground pixels. Shadow regions are eliminated from foreground by utilizing a Hue-Intensity disparity value between background and current frame. Then morphological operation is used to remove discontinuities in the foreground extracted from the shadow elimination process. Partial occlusion handling is utilized by color correlogram to label objects within a group. After that, the framework generates ROIs by determining which of the foregrounds represent human by considering conditions related to human body. Finally, Histogram of Oriented Gradients (HOG) feature is extracted from ROI for classification. Various videos containing moving humans are utilized to evaluate the proposed framework and presented outcomes demonstrate the adequacy.

**Keywords**—human detection; shadow elimination; partial occlusion handling; color correlogram; histogram of oriented gradients (HOG)

## I. INTRODUCTION

The escalation of computer vision usages impelled human detection as an active research field. Human detection in a video surveillance system has vast application areas including human locomotion characterization, fall detection for patients and intelligent gestural user interface (wiimote, kinect, smart TV). Human detection is a deep-seated and demanding issue because of two challenges: 1) Humans Intra-class divergences like appearance, clothing, skin color and pose; 2) External issues like uneven illumination and cluttered background. Current human detection frameworks can be decomposed into two processes. One process employs sliding window, while other process employs a part-based detection.

The sliding window based process can be improved in two areas: Composing more discerning features to improve

detection rate and use effective training methods to learn improved classifiers. Widely used features involve Haar wavelet, HOG [11], shapelet, edge orientation histogram (EOH), edgelet, region covariance [6] and LBP.

In [3], a hybrid local transformation feature is proposed that integrates various regional features LBP, LBP and HOG. The proposed feature show robustness to local illumination changes. However, the high dimensionality of the hybrid feature increases computational complexity. Polar coordinate based shape feature is generated and used SVM for classification in [2]. However, detection of the system is limited to upper part of human body. Salient object features are captured by integrating intensity variation of every pixel with texture related features in [1]. Although these multidimensional features occupy large-scale knowledge about the object, the proposed method determined some key thresholds based on hypothesis. Which made the method fragile when dealing with issues related to outdoor environment such as illumination changes and background clutter. Several classifiers have been approached for human detection. Most efficient human detection classifiers commonly employ different variations of boosting algorithms [7], different forms of SVMs or Neural networks. Contrary to whole body human detection frameworks, human parts based detection [4], [5] is better suited to handle partial human occlusions. Nonetheless, the enhanced detection efficiency also increases the computational cost. For instance, the multiple kernel learning (MKL) framework presented in [9] approximately takes 67 seconds to process each frame. Background subtraction [8], [10] has been an active research field for a long time. However, the efficiency of these processes significantly reduced when ROI becomes motionless for extended periods.

This paper proposes a framework to detect occluded humans by extracting foreground from background using background subtraction process. The main emphasis of this paper is to eliminate shadow regions from foreground to find accurate ROI. Shadows can be defined as portion of regions in a video frame that are not directly illuminated by light source. As a result, shadow regions contain same hue (pure color) as background with different intensity value. Based on these properties a hue-intensity disparity value is computed for every

foreground pixel to detect and eliminate shadow regions in foreground. Then occluded foregrounds are labeled individually by utilizing color correlogram. Finally, HOG feature is extracted for each ROI and sent to linear SVM for human detection.

Rest of the paper is summarized as follows. The proposed framework for occlusion handling and human detection is described in Section II. Section III discusses the simulation results. Finally, Section IV encloses the concluding remarks.

## II. PROPOSED FRAMEWORK FOR OCCLUSION HANDLING AND HUMAN DETECTION

In this section the proposed framework has been described in details. The proposed framework consists of six main stages: (1) Converting from RGB to Gray and HSI, (2) Subtracting background, (3) Eliminating shadow regions, (4) Labeling, occlusion handling and filtering, (5) Extracting HOG features and (6) Classification. Fig. 1 shows the proposed framework for occlusion handling and human detection.

### A. Converting from RGB to Gray and HSI

The RGB frame is converted to grayscale and HSI frame. The grayscale and HSI frame is used for background subtraction and shadow eliminate process respectively.

### B. Subtracting background

Instead of representing all the pixel values by same dispersion, values of each pixel are modeled as a mixture of Gaussians to describe numerous backgrounds. Based on the consistency and the variance of each Gaussian dispersion, the framework decides foreground pixels. At any given time the history of a specific pixel,  $(x_0, y_0)$  is known as (1).

$$\{V_1, \dots, V_t\} = \{F(x_0, y_0, m) : 0 < m \leq t\} \quad (1)$$

Where  $F$  is an array of frames and  $V_t$  represents the intensity value of a pixel at time  $t$ . The previous occurrences of a pixel are represented by a combination of  $J$  Gaussian dispersions. The likelihood of finding value  $V_t$  in the representation is presented in (2).

$$P(V_t) = \sum_{i=1}^J w_{i,t} * N(V_t, \mu_{i,t}, \Sigma_{i,t}) \quad (2)$$

Where  $J$  denote the quantity of Gaussian dispersions.  $\Sigma_{i,t}$ ,  $\mu_{i,t}$  and  $w_{i,t}$  denote co-variance matrix, mean and weight at time  $t$  of  $i^{\text{th}}$  Gaussian respectively.

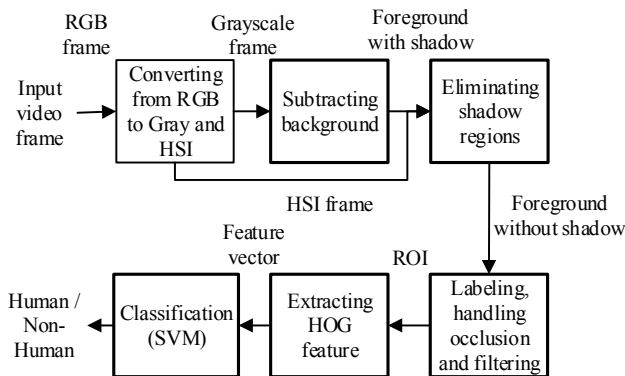


Fig. 1. The proposed framework for occlusion handling and human detection.

And  $N$  represent the probability density of Gaussian dispersion. The  $J$  dispersions are ranked by  $w_j/\sigma_j$  and first  $B$  dispersions are considered as background representation which is presented in (3).

$$B = \text{argmin}_b(\sum_{i=1}^b w_i > Th) \quad (3)$$

Where  $Th$  denotes the marginal allocation of the background representation. Foreground detection is accomplished by identifying pixels corresponding to foreground. A pixel is considered foreground pixel if the pixel intensity value  $V_t$  is beyond  $2.5 * \sigma$  from all  $B$  dispersions. However, if  $V_t$  is within 2.5 standard deviations of one or more dispersions, then the dispersion with the highest ranking i.e.  $w_j/\sigma_j$  value is updated using (4).

$$w_{j,t} = (1 - \alpha)w_{j,t} + \alpha \quad (4)$$

If  $V_t$  is not within  $2.5 * \sigma$  of any dispersion, then the dispersion with the lowest ranking replaced with a new one with  $V_t$  as mean.

### C. Eliminating shadow regions

The accuracy of ROI construction relies on generating accurate foreground extraction. As shadows of an object continually follow the object, background subtraction process considers these shadows as foreground. Beside, these shadows also preserve the geometric properties of an object as a result; those shadows can be misclassified as human. For detecting shadow regions a Hue-Intensity disparity ( $D_{HI}$ ) value between background and current frame for every pixel is calculated. For pixel  $X$ ,  $D_{HI}$  value is defined as (5).

$$D_{HI}(X) = C * H_{Diff}(X) + \left| \log_e \left( \frac{I_{X,Bg}}{I_{X,Curr}} \right) \right| \quad (5)$$

Where  $I_{X,Curr}$  and  $I_{X,Bg}$  represent the Intensity of pixel  $X$  for current and background frame respectively,  $C$  is a constant and  $H_{Diff}(X)$  denotes the hue difference between background and current frame for pixel  $X$ , which is calculated by (6).

$$H_{Diff}(X) = \min \left( \frac{|hue_{Curr}(X) - hue_{Bg}(X)|}{360 - |hue_{Curr}(X) - hue_{Bg}(X)|} \right) \quad (6)$$

Where  $hue_{Curr}(X)$  and  $hue_{Bg}(X)$  express hue of pixel  $X$  for current and background frame respectively. The Hue-Intensity disparity value is used to detect shadow regions by (7).

$$Shadow(X) = \begin{cases} 1, & \text{if } D_{HI}(X) < T \text{ AND } FS(X) == 1 \\ 0, & \text{otherwise} \end{cases} \quad (7)$$

Here  $FS(X)$  denotes the value of pixel  $X$  for  $FS$  image.  $FS$  image is the output of background subtraction process containing foreground(s) with shadows and  $T$  is a threshold value. For a shadow pixel  $Y$ , value of  $D_{HI}(Y)$  will be zero as the hue of current and background frame for pixel  $Y$  will be same. And the proposed method can detect shadow region if the intensity ratio of background and current frame for pixel  $Y$  is at most 2.5. So, threshold  $T$  is defined as (8).

$$T = C * 0 + |\log_e(2.5)| \approx 0.91 \quad (8)$$

Finally, the shadow regions are eliminated to construct foreground without shadow ( $FWS$ ) image by using (9).

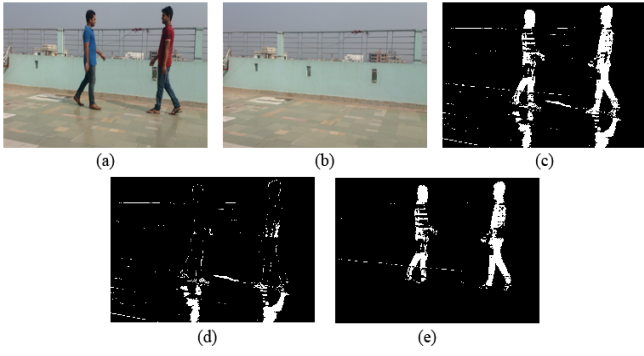


Fig. 2. Processing example of shadow elimination process: (a) current frame, (b) background frame, (c) foreground with shadow image (d) shadow region and (e) foreground without shadow image.

Fig. 2 illustrates the processing example of shadow elimination process.

$$FWS = FS * (1 - Shadow) \quad (9)$$

#### D. Labeling, handling occlusion and filtering

From the FWS image the framework detects occlusion events. An occlusion event is defined as, if binary large object (BLOB) number in the previous frame is greater than the BLOB number in the current frame and one of the BLOBs in current frame overlaps with more than one BLOBs in the previous frame. After detecting an occlusion event the framework label individual BLOB in a group by computing likelihood of each pixel belonging to a particular BLOB with the utilization of back-projection histogram and color correlogram. Fig. 3 shows the processing example of occlusion handling process.



Fig. 3. Processing example of occlusion handling. Left and right column represents input frame and labeled frame respectively. (a) & (b) before occlusion, (c) & (d) during occlusion and (e) & (f) after occlusion.



Fig. 4. Various types of video frames: (a) different appearances, (b) different poses, (c) uneven illuminations and (d) under occlusion.

After correctly labeling grouped objects morphological closing operation is applied to remove holes in the foreground. Then connected component labeling and filtering is used to find ROIs and remove non-human regions. After that, the framework considers circumstances associated with human body which must be fulfilled by the labeled object in order to consider as ROI. The filtering conditions are aspect ratio and solidity of the labeled object.

#### E. Extracting HOG feature

To extract Histogram of Oriented Gradients (HOG) [11] feature, each ROI is resized into  $128 \times 64$  pixels. Then, gradient orientation and magnitude is extracted for each ROI by performing a convolution with a horizontal and vertical kernel represented by  $[-1 \ 0 \ 1]$  and  $[-1 \ 0 \ 1]^T$  respectively. After that, the gradient image is divided into cells of  $8 \times 8$  pixels. For each cell a histogram is computed by sampling the gradient orientation ( $0^\circ$ - $180^\circ$ ) into 9 equal size bins. Each bin represents the magnitude of the corresponding orientations. After generating histogram for each cell,  $2 \times 2$  cells are grouped into blocks with 50% overlap to make the feature illumination invariant. Then, all block histograms are concatenated to generate feature vector. Finally, the feature vector is normalized with L2-norm to generate HOG feature. The size of HOG feature is  $9 \times 7 \times 15 \times 4 = 3780$ .

#### F. Classification

Finally, the HOG feature vector is sent to a linear SVM for human detection. SVM is a supervised margin classifier. For two grouped training dataset, linear SVM intends to find maximum-margin hyperplane, which leads to largest separation between the groups.

### III. EXPERIMENTAL RESULTS

In this section, experimental results of the proposed framework for occlusion handling and human detection are explained. Experiments are performed on Intel Core i5 3.20 GHz CPU and 4 GB RAM memory using MATLAB environment. Videos have been captured with a static camera at a rate of 25 fps and a resolution of  $320 \times 240$  pixels (QVGA) in urban, suburban and rural environments. Most of the humans in the data set are upright standing or walking. Some cases of partial occlusions occur, including humans walking across other objects or other human. The proposed framework is trained with 140 frames and tested on 1280 frames.

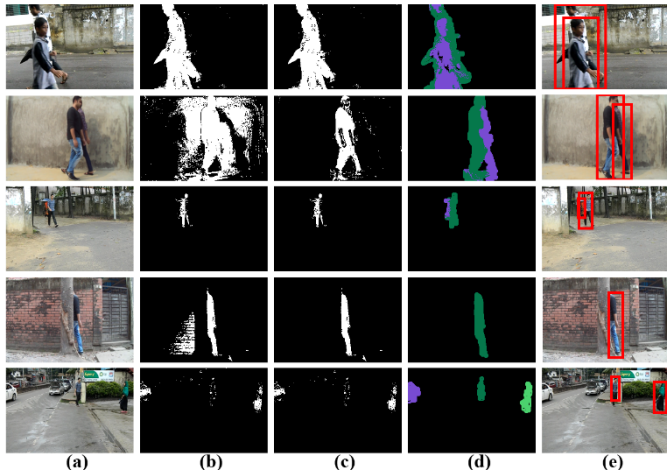


Fig. 5. Processing example of occlusion handling and human detection: (a) input RGB frame, (b) foregrounds with shadows, (c) foregrounds without shadows (d) labeled foreground(s) and (e) detected object(s).

For testing, different types of indoor and outdoor frames are utilized, which contain humans in different appearances, poses, uneven illuminations and under occlusion as shown in Fig. 4. Furthermore, these test sets are independent from the training sequences. Fig. 5 illustrates the processing example of the proposed framework for occlusion handling and human detection. In Fig 5, input RGB frame contain human with human occlusion (i.e. first three rows), human occluded by tree (i.e. fourth row) and human with moving non-human object (i.e. fifth row).

The precision (Prec) and recall (Rec) value is computed from various types of video frames which are captured from different environment and illumination conditions. Table I shows the precision and recall value at various environmental conditions. In Table I TP, FP and FN denotes True Positive, False Positive and False Negative respectively. The proposed framework shows higher response to indoor and outdoor video frames and also provide satisfactory results for video frames containing complex background. Results extracted from the proposed framework are compared with [2]. The comparison is performed with respect to precision and recall value as shown in Table II. According to results shown in Table II the proposed framework significantly outperforms [2]. The method presented in [2] is not capable of detecting human in different appearances, poses, uneven illuminations and under occlusion. The recall value presented in the Table II shows that the proposed framework is robust enough to handle video of low contrast as well as normal condition.

TABLE I. PRECISION AND RECALL VALUE AT DIFFERENT ENVIRONMENT CONDITIONS

Frame type	Environmental conditions	Total frame	Prec (%)	Rec (%)	Avg. time(s)
Indoor	Normal condition, uneven illumination and low contrast	433	94.7	93.4	0.46
Outdoor		615	93.2	92.8	
Complex Background	Normal illumination	232	91.3	89.3	
	<b>Average</b>	1280	93.1	91.8	

TABLE II. COMPARISON OF RESULTS BETWEEN PROPOSED FRAMEWORK AND [2]

Framework	TP	FP	FN	Prec (%)	Rec (%)
The proposed framework	1039	78	92	93.1	91.8
[2]	754	116	312	86.7	70.3

#### IV. CONCLUSION

This paper proposed a framework for occlusion handling and human detection, with the goal to detect humans from continuous frame sequences with higher adaptability. Initially, the RGB frame is converted to grayscale and HSI frame. Then background subtraction is performed to extract foreground regions. After that, shadow elimination process is used to remove shadow regions from foreground to find the accurate ROI. Then labeling is utilized by using color correlogram for occlusion handling and filtering is employed to remove noises. Finally, HOG feature vector is extracted from ROI and sent to linear SVM for detecting human region. The proposed framework is limited to detect humans from videos provided by a stationary camera. This framework may not provide better results if small portion of an occluded human is visible. This work will be extended to detected humans from moving background. And also focus will be given to implement human part-based detection for better occlusion handling.

#### REFERENCES

- [1] Y. Ma, L. Deng, X. Chen and N. Guo, "Integrating Orientation Cue With EOH-OLBP-Based Multilevel Features for Human Detection," IEEE Trans. Circuits Syst. Video Technol., vol. 23, no. 10, pp. 1755 - 1766, Oct. 2013.
- [2] R. Tong, D. Xie and M. Tang, "Upper Body Human Detection and Segmentation in Low Contrast Video," IEEE Trans. Circuits Syst. Video Technol., vol. 23, no. 9, pp. 1502 - 1509, Sept. 2013.
- [3] B. Jun, I. Choi, D. Kim, "Local Transform Features and Hybridization for Accurate Face and Human Detection," IEEE Trans. Pattern Recognit. Mach. Intell., vol. 35, no. 6, pp. 1423 - 1436, June 2013.
- [4] P. F. Felzenszwalb, R. B. Girshick, D. McAllester, and D. Ramanan, "Object detection with discriminatively trained part based models," IEEE Trans. Pattern Recognit. Mach. Intell., vol. 32, no. 9, pp. 1627-1645, Sep. 2010.
- [5] B. Wu and R. Nevatia, "Detection and segmentation of multiple, partially occluded objects by grouping, merging, assigning part detection responses," Int. J. Comput. Vis., vol. 82, no. 2, pp. 185-204, Apr. 2009.
- [6] S. Paisitkriangkrai, C. Shen, and J. Zhang, "Fast pedestrian detection using a cascade of boosted covariance features," IEEE Trans. Circuits Syst. Video Technol., vol. 18, no. 8, pp. 1140-1151, Aug. 2008.
- [7] Y. Chen and C. Chen, "Fast human detection using a novel boosted cascading structure with meta stages," IEEE Trans. Image Process., vol. 7, no. 8, pp. 1452-1464, Jul. 2008.
- [8] K. Kim, T. Chalidabhongse, D. Harwood, and L. Davis, "Real-time foreground-background segmentation using codebook model," J. RealTime Imag., vol. 11, pp. 172-185, Jun. 2005.
- [9] A. Vedaldi, V. Gulshan, M. Varma, and A. Zisserman, "Multiple kernels for object detection," in Proc. IEEE 12th Int. Conf. Comput. Vision, , pp. 606-613, 2009.
- [10] Y. Liu, H. Yao, W. Gao, X. Chen, and D. Zhao, "Nonparametric background generation," in Proc. Int. Conf. Pattern Recognit., vol. 4, pp. 916-919, Sep. 2006.
- [11] N. Dalal and B. Triggs, "Histograms of oriented gradients for human detection," in Proc. IEEE Int. Conf. Comput. Vision Pattern Recognit., pp. 886-893, 2005.

# Grid-voltage Synchronization Algorithm for Grid Tied Renewable Energy Sources During Adverse Grid Fault Condition

Khaled Syfullah Fuad

Department of Computer Science & Engineering  
Britannia University, Bangladesh

Md Rahmat Ullah Chowdhury

Department of Electrical & Electronic Engineering  
International Islamic University Chittagong, Bangladesh

Eklas Hossain

Department of Electrical Engineering & Renewable Energy  
Oregon Institute of Technology, USA

**Abstract**—Grid-voltage synchronization algorithm performs the main role during unbalanced and distorted grid fault condition to measure the positive- and negative-sequence values of grid voltage at the point of common coupling for grid-tied renewable energy sources. Power control during severe grid conditions mostly depends on these measured values. Three-phase synchronous reference frame phase-locked loop (SRF-PLL) is the most conversant methods for grid-voltage synchronization. Decoupled Double Synchronous Reference Frame PLL (DDSRF-PLL) is one of the most advanced synchronization algorithm. In this paper, calculation for power control during unbalanced grid condition are given for active and reactive power and performance of DDSRF-PLL is evaluated under adverse grid fault conditions.

**Index Terms**—active and reactive power, decoupling network, grid-connected converter, phase-locked loop.

## I. INTRODUCTION

In the next generation power system, microgrid is a preferable option due to a number of appreciable reasons. At first, most of the industries, professional organizations, and academic institutions require reliable power back up because of the uncertain and interrupted power supply from the utility grid. The available power backups such as private generation, energy storage systems, and diesel engine are very expensive. By adopting microgrid system, it is possible to get rid of that and to experience a cost effective and reliable solution during power crisis. Apart from that, considering wider picture, it is possible to save billions of dollars if few hundred summer peak hours can be managed by load shifting or load shaving techniques. Besides that, reliability is one of the key justifications to adopt microgrid system in larger scale. China has already introduced microgrid systems widely and experienced appreciable performance with sustainability. Since the energy security is one of the prime concerns to the power industry, microgrids can offer that desired fidelity to the entire system. It-due to smaller operating zone and easy control technique- is possible to solve the cyber security problem by the microgrid system [1]-[5].

During different kind of faults, positive- and negative-sequence values of unbalanced grid voltage must be estimated by grid-voltage synchronization algorithm. As we can see from Fig. 1, frequency ( $\omega$ ), phase angle ( $\theta$ ) and magnitudes of the positive- ( $\mathbf{u}_{abc}^+$ ) and negative-sequence ( $\mathbf{u}_{abc}^-$ ) parameters of the grid voltage is detected by grid synchronization block. Phase-locked loop (PLL) is a well known method for grid-synchronization.

In forthcoming sections in this paper: 1) power control during unbalanced grid condition are given for active and reactive power; 2) PLL is studied, modeled and its performance is evaluated; 3) Decoupled Double Synchronous Reference Frame PLL (DDSRF-PLL) is studied, modeled and its performance is justified under different fault conditions according to modern grid codes.

## II. CHARACTERIZATION OF THREE-PHASE VOLTAGE

Balanced three-phase voltage  $abc$  can be expressed as [15],

$$\mathbf{u}_{abc}(t) = \begin{bmatrix} u_a(t) \\ u_b(t) \\ u_c(t) \end{bmatrix} = \begin{bmatrix} U_a \cos(\omega t + \phi_a) \\ U_b \cos(\omega t - \frac{2\pi}{3} + \phi_b) \\ U_c \cos(\omega t + \frac{2\pi}{3} + \phi_c) \end{bmatrix} \quad (1)$$

where  $U_a$ ,  $U_b$  and  $U_c$  denotes the peak value of  $u_a(t)$ ,  $u_b(t)$  and  $u_c(t)$  phase voltages, respectively. The unbalanced three-phase system in (1) is decomposed with zero-, positive- and negative-sequence and written below as,

$$\mathbf{u}_{abc}(t) = \underbrace{\begin{bmatrix} U_+ \cos(\omega t + \phi^{+1}) \\ U_+ \cos(\omega t - \frac{2\pi}{3} + \phi^{+1}) \\ U_+ \cos(\omega t + \frac{2\pi}{3} + \phi^{+1}) \end{bmatrix}}_{\mathbf{u}_{abc}^+} + \underbrace{\begin{bmatrix} U_- \cos(\omega t + \phi^{-1}) \\ U_- \cos(\omega t + \frac{2\pi}{3} + \phi^{-1}) \\ U_- \cos(\omega t - \frac{2\pi}{3} + \phi^{-1}) \end{bmatrix}}_{\mathbf{u}_{abc}^-} + \underbrace{\begin{bmatrix} u_0(t) \\ u_0(t) \\ u_0(t) \end{bmatrix}}_{\mathbf{u}_{abc}^0} \quad (2)$$

where  $U_+$  and  $U_-$  are the maximum value of the positive and negative sequence components and  $\mathbf{u}_{abc}^+$ ,  $\mathbf{u}_{abc}^-$ ,  $\mathbf{u}_{abc}^0$  represent



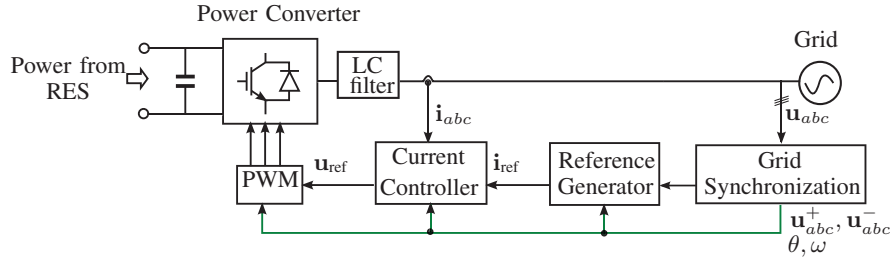


Fig. 1. Control of a grid connected three-phase power converter by means of grid-voltage synchronization algorithm.

positive-, negative- and zero-sequence voltages of three-phase voltage.

### A. Space Vectors

$\mathbf{u}$  is the space vector in synchronous coordinates, symbolized by boldface and its components are expressed with subscripts  $d$  and  $q$ . The space vector in stationary reference frame  $\alpha\beta$ ,  $\mathbf{u}^s$  is symbolized with superscript  $s$  and subscripts  $\alpha$  and  $\beta$  are used to denote the components of vector [13].  $\mathbf{u}^s$  is expressed for positive- and negative-sequence components as,

$$\mathbf{u}^s = \underbrace{U_+ \begin{bmatrix} \cos(\omega t) \\ \sin(\omega t) \end{bmatrix}}_{\mathbf{u}_+^s} + \underbrace{U_- \begin{bmatrix} \cos(-\omega t + \phi^{-1}) \\ \sin(-\omega t + \phi^{-1}) \end{bmatrix}}_{\mathbf{u}_-^s} \quad (3)$$

where  $\mathbf{u}^s$  consist of two sub-vectors;  $\mathbf{u}_+^s$ , having angular frequency  $\omega$  and  $\mathbf{u}_-^s$ , having negative  $-\omega$ .

### B. Voltage Dip or Sag

Different type of voltage dip are categorized as 1. Three-phase and three-phase-to-ground fault (type A); 2. Single-phase-to-ground fault (type B); 3. Phase-to-phase fault (type C) and 4. Two-phase-to-ground fault (type E) [17]-[18].

Dispersion of these four type of voltage dips rise another three new voltage dips. Which are: 1. dispersion of type C (type D); 2. dispersion of type E (type F) and 3. dispersion of type F (type G). For a demonstration, type C can be expressed by the following equation:

$$\begin{bmatrix} U_+ \\ U_- \\ U_0 \end{bmatrix} = \begin{bmatrix} \frac{1}{2}(1+D) \\ \frac{1}{2}(1-D) \\ 0 \end{bmatrix} U_{pf} \quad (4)$$

here pre-fault voltage is symbolized by  $U_{pf}$  and phase angle jump is denoted by  $D$ .

## III. POWER MANAGEMENT STRATEGIES UNDER UNBALANCED GRID CIRCUMSTANCES

Precise control approaches are required for managing the exchange of the instantaneous active and reactive power with the grid during adverse grid-fault circumstances. The instantaneous active power,  $p$ , can be expressed in synchronous coordinates, provided or emptied by a grid-connected three-phase power converter as [6],

$$p = \frac{3}{2} \mathbf{u}^T \mathbf{i} = \frac{3}{2} (u_d i_d + u_q i_q) \quad (5)$$

here the current vector  $\mathbf{i} = [i_d \ i_q]^T$  and ‘ $T$ ’ denotes transpose of matrices. For positive- and negative-sequence components of both voltage and current, (5) will be,

$$\begin{aligned} p &= \frac{3}{2} [(\mathbf{u}^+)^T + (\mathbf{u}^-)^T] [\mathbf{i} + \mathbf{i}] \\ &= \frac{3}{2} \underbrace{[(\mathbf{u}^+)^T \mathbf{i}^+ + (\mathbf{u}^-)^T \mathbf{i}^-]}_P + \underbrace{\frac{3}{2} [(\mathbf{u}^+)^T \mathbf{i}^- + (\mathbf{u}^-)^T \mathbf{i}^+]}_{\tilde{p}} \end{aligned} \quad (6)$$

here subscripts ‘+’ express positive and ‘-’ negative sequence variables, respectively. The part of equation above  $P$  and  $\tilde{p}$  represent the average and oscillatory value of  $p$ , respectively in (6). On the other hand, instantaneous active power,  $q$ , is defined as,

$$q = \frac{3}{2} \mathbf{u}^T \mathbf{J} \mathbf{i} = \frac{3}{2} (u_q i_d - u_d i_q) \quad (7)$$

where  $\mathbf{J} = \begin{bmatrix} 0 & -1 \\ 1 & 0 \end{bmatrix}$  [15]. Now, considering the symmetrical components of both voltage and current and (7) will be,

$$\begin{aligned} q &= \frac{3}{2} [(\mathbf{u}^+)^T + (\mathbf{u}^-)^T] [\mathbf{J} \mathbf{i}^+ + \mathbf{J} \mathbf{i}^-] \\ &= \frac{3}{2} \underbrace{[(\mathbf{u}^-)^T \mathbf{J} \mathbf{i}^+ + (\mathbf{u}^+)^T \mathbf{J} \mathbf{i}^-]}_Q + \underbrace{\frac{3}{2} [(\mathbf{u}^+)^T \mathbf{J} \mathbf{i}^- + (\mathbf{u}^-)^T \mathbf{J} \mathbf{i}^+]}_{\tilde{q}} \end{aligned} \quad (8)$$

here part of equation above  $Q$  and  $\tilde{q}$  represent the average and oscillatory value of  $q$ , respectively.

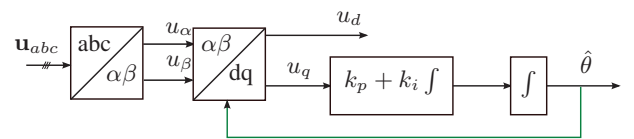


Fig. 2. Block diagram of a three-phase PLL system.

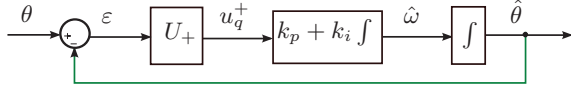


Fig. 3. Linearized control loop

#### IV. THREE PHASE SYNCHRONOUS REFERENCE FRAME PLL SYSTEM

The most traditional method, three-phase synchronous reference frame (SRF) based on phase locked loop (PLL), together referred as SRF-PLL. SRF-PLL can detect positive-sequence values of three-phase system. A conventional block diagram of a three-phase PLL is given in Fig. 2. The input frequency and phase angle can be tracked down by the PLL frequency and phase angle, respectively [9]. The loop filter represents a proportional-integral (PI) controller, where  $k_p$  is proportional and  $k_i$  is integral gain, respectively. The amplitude and phase angle of  $\mathbf{u}^s$  obtained from (3) as,

$$|\mathbf{u}^s| = \sqrt{U_+^2 + U_-^2 + 2U_+U_- \cos(-2\omega t + \phi^{-1})} \quad (9a)$$

$$\theta = \omega t + \tan^{-1} \left( \frac{U_- \sin(-2\omega t + \phi^{-1})}{U_+ + U_- \cos(-2\omega t + \phi^{-1})} \right) \quad (9b)$$

$u_q$  has a linear connection with the feedback variable  $\hat{\theta}$ , which is shown in Fig. 2. This character aid to develop the idea of linearized control model given by Fig. 3 and explained thoroughly in [9],[11] and [16]. The system can be written as,

$$\frac{\hat{\theta}(s)}{\theta(s)} = \frac{2\xi_{\text{PLL}}\omega_{\text{PLL}}s + \omega_{\text{PLL}}^2}{s^2 + 2\xi_{\text{PLL}}\omega_{\text{PLL}}s + \omega_{\text{PLL}}^2} \quad (10)$$

$$\frac{\varepsilon(s)}{\theta(s)} = \frac{s^2}{s^2 + 2\xi_{\text{PLL}}\omega_{\text{PLL}}s + \omega_{\text{PLL}}^2} \quad (11)$$

The value of  $k_p$  and  $k_i$  can be selected from  $\omega_{\text{PLL}} = \sqrt{U_+k_i}$  and  $\xi_{\text{PLL}} = \frac{k_p}{2} \sqrt{\frac{U_+}{k_i}}$ , where  $\omega_{\text{PLL}}$  is control loop frequency and  $\xi_{\text{PLL}}$  is damping constant [9],[11], [16].

#### A. SRF-PLL under Balanced and Unbalanced Circumstance

SRF-PLL is modelled by using MATLAB/Simulink and simulated to justify under balanced and unbalanced circumstance. The voltage is defined for balanced circumstance as  $U_+ = 100$  V,  $U_- = 0$  V,  $\phi^{-1} = 0$  and  $\omega = 2\pi 50$  rad/s. On the other hand, for unbalanced circumstance as  $U_+ = 100$  V,  $U_- = 30$  V,  $\phi^{-1} = 0$  and  $\omega = 2\pi 50$  rad/s and occurs after 0.05 s, where  $U_{\text{pf}} = 100$  V. The values for the PI controller parameters for the simulation below are  $k_p = 44.42$  and  $k_i = 9.87 \times 10^4$ , justification given in [8]; gives  $\xi_{\text{PLL}} \approx 1/\sqrt{2}$  and control loop bandwidth  $\omega_{\text{PLL}} \approx 2\pi 500$  rad/s.

Fig. 4(a) and 4(b) depicts the simulation result under balanced and unbalanced condition, respectively. The input parameters  $\omega$  and  $\theta$  is accurately tracked down by the PLL  $\hat{\omega}$  and  $\hat{\theta}$ , respectively. During unbalanced circumstance Fig. 4(b) shows that,  $u_q \approx 0$  with larger bandwidth  $\omega_{\text{PLL}} \approx 2\pi 500$  rad/s. And The values of  $u_d$  and  $\hat{\theta}$  are polluted with oscillation. As we can see from (9a) and (9b) that this oscillation  $2\omega$  is the result of negative sequence appears in unbalanced condition. So for the control of power converters, the conventional SRF-PLL technique cannot be used.

#### V. DECOUPLED DOUBLE SYNCHRONOUS REFERENCE FRAME PLL

In Decoupled Double synchronous reference frame PLL (DDSRF-PLL),  $\mathbf{u}^s$  is thrown on two distinct SRF's as shown in Fig. 5 [11].  $dq^+$  reference frame having  $\hat{\omega}$  is integrated with  $\mathbf{u}_+^s$  and another  $dq^-$  reference frame having  $-\hat{\omega}$  is integrated with  $\mathbf{u}_-^s$ . A cross-feedback decoupling network in Fig. 5, simply cancels the oscillating term of both axes and can estimate the dc values of both positive and negative reference frames. As a consequence,  $\mathbf{u}_{abc}^+$  and  $\mathbf{u}_{abc}^-$  of unbalanced three-phase system can be track out accurately [6]. Symbols with

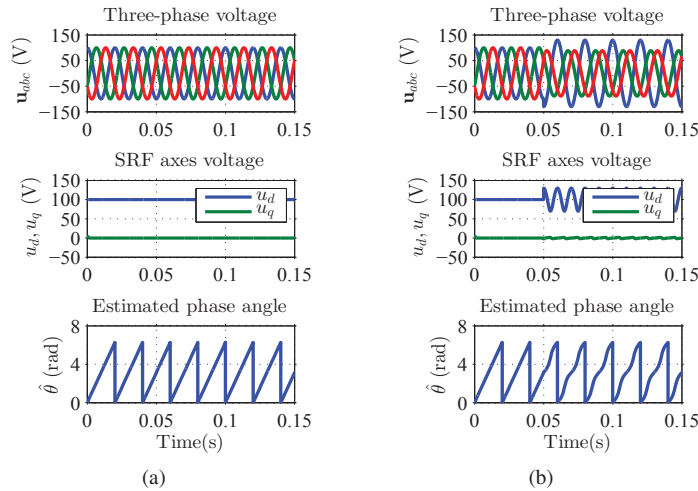


Fig. 4. SRF-PLL during (a) balanced and (b) Unbalanced circumstance.

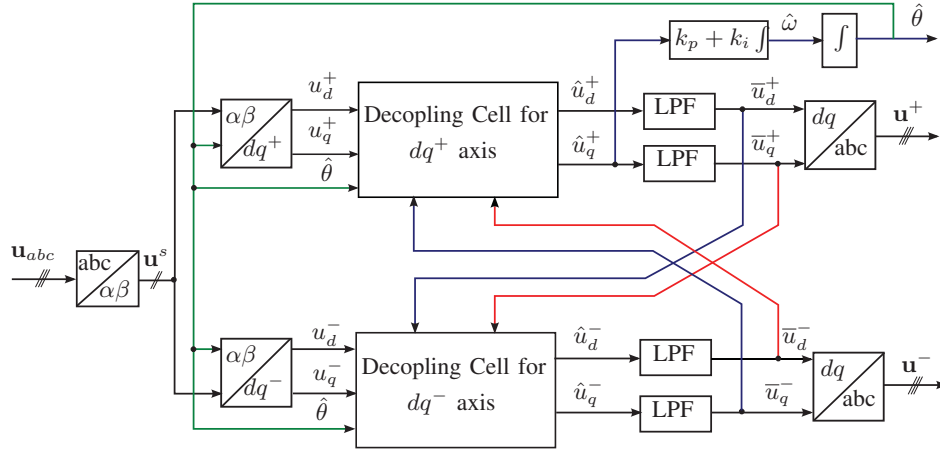


Fig. 5. Block diagram of DDSRF-PLL.

'hat' express the estimated value from the system. In Fig. 5, low pass filter (LPF) block perform filtering and expressed by equation as [12],

$$LPF(s) = \frac{\omega_f}{s + \omega_f} \quad (12)$$

where, LPF cut-off frequency is given by  $\omega_f = \frac{\omega}{\sqrt{2}}$  [12].

#### A. DDSRF-PLL During Different Grid fault Condition

DDSRF-PLL synchronization algorithms is modelled in Matlab Simulink environment. The values for the PI controller parameters for the simulation below are  $k_p = 2.22$  and  $k_i = 246.7$ , justification given in [13]; gives  $\xi_{PLL} \approx 1/\sqrt{2}$  and reduced control loop bandwidth  $\omega_{PLL} \approx 2\pi 25$  rad/s. Under unbalanced voltage condition, DDSRF-PLL cancels the  $2\omega$

oscillation and perfectly detects  $\mathbf{u}_{abc}^+$  and  $\mathbf{u}_{abc}^-$  values [10]. During jumps for amplitude and frequency, DDSRF-PLL also accurately detect  $\mathbf{u}_{abc}^+$  and  $\mathbf{u}_{abc}^-$  values of the voltage [10].

1) *During Harmonic-distorted Circumstances and Voltage Sags:* To justify DDSRF-PLL under severe utility harmonic-distorted condition, the input voltage is characterized with an unbalanced fifth harmonic component as:  $U_+ = 100$  V,  $U_- = 30$  V,  $U_{+5} = 10$  V,  $U_{-5} = 10$  V,  $\omega = 50$  Hz and  $U_{pf} = 100$  V. Fig. 6(a) shows the performance of DDSRF-PLL. Here we can see that estimation of  $\hat{\theta}$  verily flawless under this harmonic polluted circumstance. It is reasonable because of the low-pass nature of (12) and the values are given for the simulation are  $\omega_{PLL} \approx 2\pi 25$  rad/s and  $\xi_{PLL} \approx 1/\sqrt{2}$ . The frequency and  $\mathbf{u}_{abc}^-$  detection is disturbed because of the voltage harmonic pollution. This shows that DDSRF-PLL performance is not

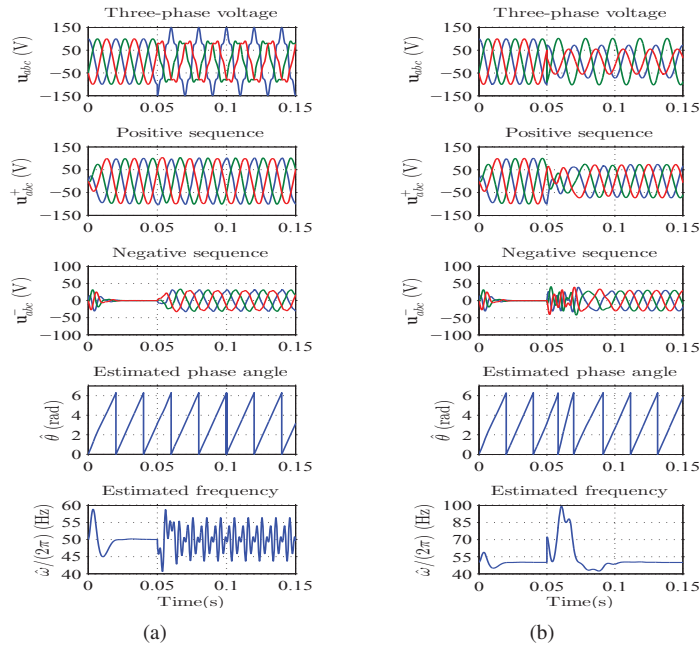


Fig. 6. Output of DDSRF-PLL (a) during harmonic-distorted circumstance; (b) during dip type C.

acceptable during harmonic-distorted circumstance.

DDSRF-PLL is examined for every classified voltage dips from A-G mentioned in section II having  $D = 0.5\angle 0^\circ$ . DDSRF-PLL can accurately detect the voltage components of the unbalanced systems except type C [10]. A voltage dip type C is applied as input voltage having  $D = 0.5\angle -30^\circ$ ,  $U_+ = 73\angle -9.9^\circ$  V,  $U_- = 25\angle 23.8^\circ$  V,  $\omega = 50$  Hz and  $U_{pf} = 100$  V. Output graph of DDSRF-PLL is shown in Fig. 6(b). DDSRF-PLL exhibits high overshoot for the detection of  $\hat{\omega}$  and as a consequence, it also unable to correctly detect  $\hat{\theta}$ . It also exhibits slow dynamics and oscillation in case of  $\mathbf{u}_{abc}^+$  and  $\mathbf{u}_{abc}^-$  estimation. So, during sudden phase angle jumps in the grid voltage, performance of DDSRF-PLL is not upto the mark.

## VI. CONCLUSION

In this paper, the importance of grid voltage synchronization algorithm is presented at the beginning for interconnected RES. Active and reactive power calculation during unbalanced grid fault condition are also presented. The most conversant method, SRF-PLL for grid voltage synchronization is modeled and tuned accordingly. Its performance under the unbalanced condition is not really acceptable according by modern grid codes. There are some limitations for DDSRF-PLL which can be enhanced further, particularly performances during harmonic-distorted condition and phase angle jumps. Unless DDSRF-PLL satisfies modern grid codes by displaying exceptional dynamics response and adequate fault ride through (FRT) operation during grid faults.

## REFERENCES

- [1] Hossain, E., Kabalci, E., Bayindir, R. and Perez, R. *Microgrid testbeds around the world: State of art*, Energy Conversion and Management 86 (2014) 132-153.
- [2] Hossain, E., Kabalci, E., Bayindir, R. and Perez, R. *A Comprehensive Study on Microgrid Technology*, International Journal of Renewable Energy Research, Vol.4, No.4, 2014 1094-1107.
- [3] Kabalci, E., Hossain, E. and Bayindir, R. *Microgrid test-bed design with renewable energy sources*, International Conference on Power Electronics and Motion Control Conference and Exposition (PEMC), 2014, Pg. No. 907-911.
- [4] Kabalci, E., Bayindir, R. and Hossain, E. *Hybrid microgrid testbed involving wind/solar/fuel cell plants: A desing and analysis testbed*, Renewable Energy Research and Application (ICRERA), 2014 International Conference on, Milwaukee, WI, 2014, pp. 880-885. doi: 10.1109/ICRERA.2014.7016511.
- [5] Bayindir, R. and Hossain, E., Kabalci, E. and Billah, K. *Investigation on North American Microgrid Facility*, International Journal of Renewable Energy Research, Vol.5, No.2, 2015 558-574.
- [6] Teodorescu, R., Liserre, M. and Rodriguez, P. *Grid Converters for Photovoltaic and Wind Power Systems*. John Wiley and Sons, Inc., UK, 2011. ISBN 9780470057513.
- [7] Blaabjerg, F., Teodorescu, R., Liserre, M., Timbus, A. *Overview of control and grid synchronization for distributed power generation systems*. IEEE Transactions on Industrial Electronics, vol. 53, no. 5, pp 1398-1409, October 2006.
- [8] Abdalrahman, A., Zekry, A., Alshazly, A. *Simulation and Implementation of Grid-connected Inverters*. International Journal of Computer Applications (0975 - 8887), vol. 60, no.4, December 2012.
- [9] Chung, S. *A phase Tracking System for Three phase Utility Interface Inverters*. IEEE Transactions on Power Electronics, vol. 53, no. 3, May 2000.

- [10] Fuad, K. *Grid-voltage Synchronization Algorithms Based on Phase-locked Loop and Frequency-locked Loop for Power Converters*. Aalto University publication, Finland, June 2015.
- [11] Rodriguez, P., Sainz, L., Bergas, J. *Synchronous Double Reference Frame PLL applied to a Unified Power Quality Conditioner*. 10th International Conference on Harmonics and Quality of Power, vol.02, pp 614-619, October 2002.
- [12] Rodriguez, P., Pou, J., Bergas, J., Candela, J., Burgos, R. and Boroyevich, D. *Decoupled double synchronous reference frame PLL for power converters control*. IEEE Transactions on Power Electronics, vol. 22, no. 2, pp. 584-592, 2007.
- [13] Rodriguez, P., Luna, A., Munoz-Aguilar, A., Etxeberria-Otadui, I., Teodorescu, R. and Blaabjerg, F. *A Stationary Reference Frame Grid Synchronization System for Three-phase Grid-connected Power Converters Under Adverse Grid Conditions*. IEEE Transactions on Power Electronics, vol. 27, no. 1, January 2012.
- [14] Franklin, G., Powell, J., Emami-Naeini, A. *Feedback control of Dynamic Systems*. Englewood Cliffs, NJ: Prentice-Hall, 2009.
- [15] Harnefors, L. *Control of Variable-speed Drives*. " Applied Signal Processing and Control, Department of Electronics, Mlardalen University " , Sweden, 2003.
- [16] Gardner, F. *Phaselock Techniques*. John Wiley and Sons, Inc., USA, 1979. ISBN 0-471-04294-3.
- [17] Bollen, M. and Gu, I. *Signal Processing for Power Quality Disturbances*. Hoboken, NJ, USA: Wiley-IEEE Press, 2006, ch. 8.
- [18] Bollen, M. *Understanding Power Quality Problems: Voltage Sags and Interruptions (Power Engineering Series)*. Piscataway, NJ: IEEE Press, 2000.
- [19] Altin, M., Gksu, O., Teodorescu, R., Rodriguez, P., Jensen, B.-B. and Helle, L. *Overview of Recent Grid Codes for Wind Power Integration*. 12th International Conference on Optimization of Electrical and Electronic Equipment (OPTIM), 2010 , pp. 1152-1160, May. 20-22, 2010.

# Experimental Verification of Regenerative Braking Characteristics by Applying Different Motor Armature Voltage

S.M. Baque Billah,<sup>1,\*</sup> Dr. Kazi Khairul Islam,<sup>1</sup> and Shahadat Hossain<sup>2</sup>

<sup>1</sup>Department of Electrical and Electronic Engineering, Islamic University of Technology (IUT)  
Gazipur, Bangladesh

<sup>2</sup>Department of Electrical and Electronic Engineering, University of Science and Technology Chittagong  
Chittagong, Bangladesh

\*baque.ustc06@gmail.com

**Abstract**—Simpler design of control system is the key advantage of DC motor. In recent decade, however, use of dc motor in battery-operated electric vehicles (BEV) are declined spectacularly. Without significant improvement of efficiency of such system the use of dc motor in BEV will be objectionable. Regenerative braking is the possible way to improve the efficiency. In this paper a novel regenerative braking mechanism for electric vehicles based on DC motor is proposed. The performance of the proposed braking system has been evaluated experimentally for different motor armature voltage. For this a prototype model of BEV has been used. Simulation results show that the proposed regenerative braking technique is feasible and effective. Also this research provides a new possibility of cost effective equipments and simplest system for regenerative braking to improve the drive distance of electric vehicles.

**Keywords**—regenerative; braking; efficiency; vehicle; armature voltage; DC motor.

## I. INTRODUCTION

Now fuel consumption of Gasoline Vehicles (GVs) is about 60% of total world oil. Due to global warming and rising cost of petrol price hybrid and battery-operated electric vehicles (BEV) are getting admired. It is believed that Electric vehicles (EVs) will replace the existing GV's and dominate the market due to some factors like zero carbon emission, less expensive and quiet maneuver. Basically AC and DC motor are the main part of different types of EVs [1], including two-, three- and four-wheelers. Manufacturer prefers AC motor instead of DC motor in EVs because of its high efficiency [2-4]. However, researches till see the potentiality of DC motor in EVs as AC motor are highly expensive with respect to DC motor. For that "Commuter Cars" has taken initiative and manufacture Tango T600 utilizing FB1-4001 DC motor but does not have regenerative braking mechanism [5]. As regenerative braking is an energy recovery process which create braking torque to slows a vehicle by energy conversion (kinetic to electrical energy) and feeding it back to the battery [6-7]. So Tango T600 is not efficient with respect to AC-motor vehicles. If the feasibility and efficiency of DC motor based EVs need to improve, than designing of regenerative braking system for this vehicles is so much important. To solve this problem in [8] they design a regenerative braking

system using series wound brushed DC motor. They have achieved braking efficiency around 26.34%. For better improvement in [9] they proposed Two-speed DCT (Dual Clutch Transmission) based braking energy recovery system. However both described method in [8] and [9] need power electronics switching devices which is complex and also complex mechanical gear system. So to achieve simplicity and cost effective efficient braking system some new method need to be established and its urgent [10]. Thus DC motor terminal voltage control based new regenerative braking system is proposed in this paper. Based on proposed method regenerative braking can be achieved by applying different motor terminal voltage. This new method does not required complex power electronics switching devices but only a low cost rotary mechanical switch which will select different voltage from different battery cell based on brake pedal position. For experimental verification a permanent magnet DC motor based prototype model of EVs are used.

The material is organized as follows. Section II presents the theory behind the proposed method. In section III structure of prototype EVs, collection of braking parameters from this EVs and also how those parameters represents braking characteristics based on simulation are explained. Section IV presents the comparison and simulation results. After comparison, results show that proposed method is feasible and effective. Compared to series-wound DC motor based regenerative braking system, proposed braking system is superior due to its simplicity and high efficiency

## II. REGENERATIVE BRAKING BASED ON DIFFERENT MOTOR ARMATURE VOLTAGE

The speed of dc motor is controlled using variable armature voltage and rotational speed is proportional to motor terminal voltage [11-12]. High voltage will generate high rotational speed and low voltage will low speed. Two different armature voltages  $V_{a1}$  and  $V_{a2}$  will be considered. Those voltages will generate two different speeds  $N_1$  and  $N_2$  RPM simultaneously. If  $V_{a1} > V_{a2}$  then  $N_1 > N_2$  also. Now if a motor feed with  $V_{T1}$  voltage then its RPM will be  $N_1$ . During this running condition if the motor armature voltage  $V_{a1}$  is changed to  $V_{a2}$  using different Battery cell then motor will experience a braking torque  $T_b$  until its speed reduced to  $N_2$ . For this

braking torque motor will works as a generator (Regenerative mode) and charge the battery cell (Which voltage is  $V_{a2}$ ) until motor achieve the speed  $N_2$ . This braking torque  $T_b$  is proportional to difference of rotational speed ( $N_1-N_2$ ) and the storage energy of battery during charging time is also proportional to ( $N_1-N_2$ ). Basically here the extra rotational or kinetic energy is converted into electrical energy and return back to the system. Using this technique a simple and effective regenerative braking system can be developed which is proposed here. To prove this technique a prototype model of EVs are used and braking parameters are taken from this prototype model and simulated in MATLAB which is farther described in section III.

### III. EXPERIMENTS

For experimental verification of proposed method a prototype EVs is used. This prototype was designed in lab and consists of one flywheel, permanent magnet DC motor, Array of battery cell, mechanical break, DC volt meter, DC ammeter, newly designed rotary mechanical switch named as electric brake.

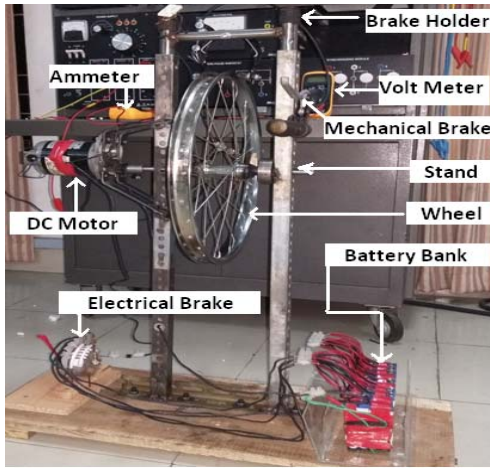


Fig. 1. Prototype EVs.

Fig.1 shows the actual constructions of prototype EVs. The rotary mechanical switch that means the electrical brake consists of a brake pedal, selector pin and contact leads. Battery bank is directly connected with contact leads of electrical brake. Based on brake pedal position electrical brake will able to select different voltage from battery bank and feed it to motor armature. Fig.2 and Fig. 3 shows the construction of newly designed electric brake and electrical connections of prototype EVs respectively.

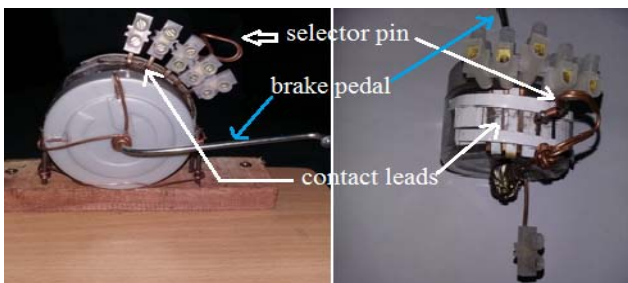


Fig. 2. Electrical brake of EVs (rotary mechanical switch)

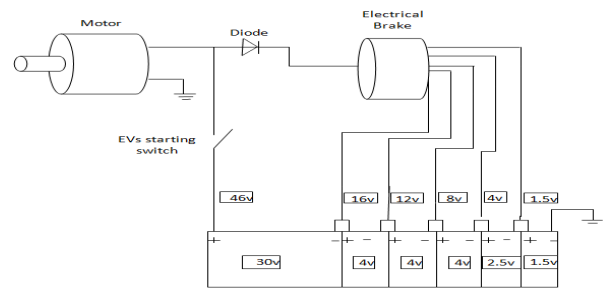


Fig. 3. Electrical connections of prototype EVs

In section II it was mentioned that,

$$N_1 \propto V_{a1} \quad (1)$$

$$N_2 \propto V_{a2} \quad (2)$$

And

$$T_{b2} \propto N_1 - N_2 \quad (3)$$

At (3)  $T_{b2}$  is the braking torque at  $V_{a2}$  voltage when motor armature voltage shifted from  $V_{a1}$  to  $V_{a2}$  where  $V_{a2} < V_{a1}$ .

From (1) and (2) it is clear that

$$(N_1 - N_2) \propto (V_{a1} - V_{a2}) \quad (4)$$

Using (3) and (4)

$$T_{b2} \propto (V_{a1} - V_{a2}) \quad (5)$$

Relation (5) indicates that, at motor higher armature voltage difference will create higher braking torque. Now let  $V_{ra}$  is a rated motor armature voltage. For braking if reflect on 3 different voltages like  $V_{a1}$ ,  $V_{a2}$  and  $V_{a3}$  where

$$V_{ra} > V_{a1} > V_{a2} > V_{a3} \quad (6)$$

Then braking torques will act like

$$T_{b3} > T_{b2} > T_{b1} \quad (7)$$

In (7)  $T_{b1}$  is the braking torque when motor armature voltage shifted from  $V_{ra}$  to  $V_{a1}$  and similarly  $T_{b2}$ ,  $T_{b3}$  for  $V_{ra}$  voltage to  $V_{a2}$  and  $V_{a3}$  voltage respectively. Higher braking torque means higher deceleration of vehicles and lower the braking time required to stop the vehicle. So if  $T_1$ ,  $T_2$  and  $T_3$  are the braking time during regenerative braking for  $V_{a1}$ ,  $V_{a2}$  and  $V_{a3}$  armature voltage respectively then from (7) it is cleared that

$$T_1 > T_2 > T_3 \quad (8)$$

During generator action of motor, as generated voltage of armature is directly proportional to motor rotational speed. So motor armature voltage ( $V_{ar}$ ) will represent the characteristics of motor rotational speed. Now it's logical to characterize the braking characteristics of both mechanical and regenerative braking of prototype EVs by using generated armature voltage as motor is coupled with flywheel. In this section mechanical

and regenerative braking characteristic parameters are measured in terms of armature voltage. Regenerative braking characteristics are compared with mechanical braking and regenerated energies are estimated from the charging current during regenerative braking. For doing this 2 mechanical braking condition are observed like mechanical hard and medium brake. In regenerative braking based on proposed method 8v, 4v and 1.5v are taken to feed the armature or motor terminal.

**A. Mechanical Braking characteristics**

In fig. 4 mechanical hard is presented. Calculated mechanical hard braking time of this prototype is  $T_{mhb}=.85s$ . That means prototypes take .85s to decelerate. Same way fig.5 shows the mechanical medium brake.

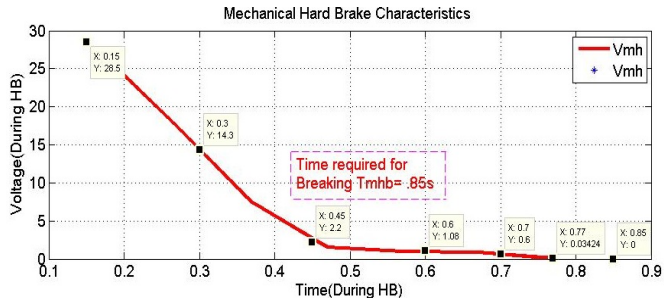


Fig. 4. Mechanical Hard brake.

Here calculated braking time  $T_{mmb}=4.0s$ . All values of motor armature voltage during braking are mentioned both in fig.4 and fig.5.

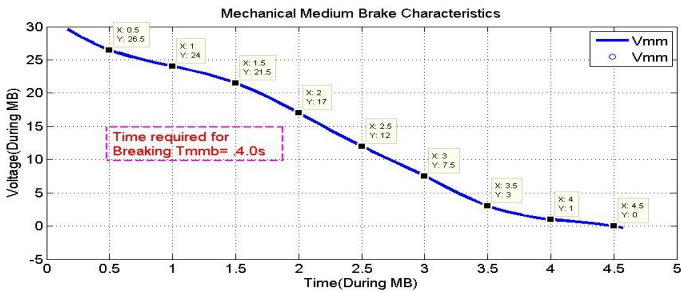


Fig. 5. Mechanical Medium brake.

**B. Regenerative Braking**

Proposed method of regenerative braking based on 8 volt is presented in Fig.6. From figure it's clear that regenerative braking time during 8 volt  $T_{rb8} = 4.75s$

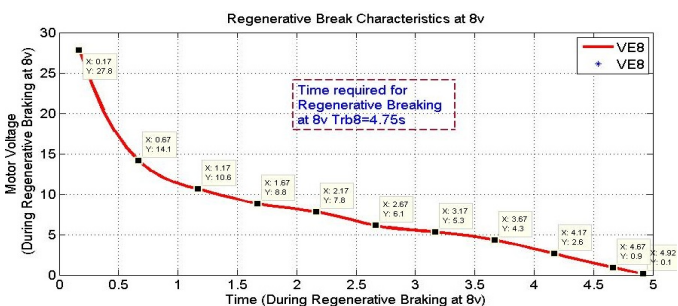


Fig. 6. Regenerative Braking at 8v.

Similarly 4v and 1.5v are presented in fig. 7 and fig. 8. where estimated braking time  $T_{rb4} = 2.75s$  and  $T_{rb1.5} = 1.15s$  respectively.

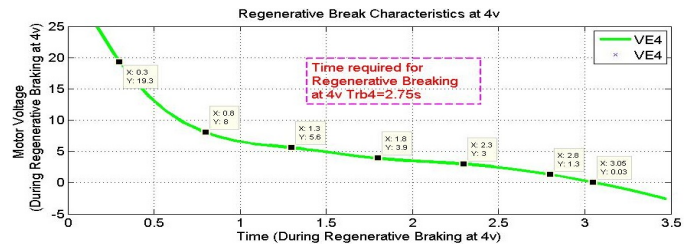


Fig. 7. Regenerative Braking at 4v.

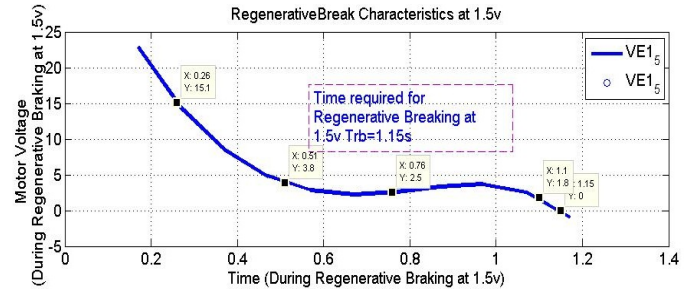


Fig. 8. Regenerative Braking at 1.5v.

**C. Comparison of mechanical and proposed braking**

For justify the effectiveness of regenerative braking it's compared with conventional mechanical braking system. Comparison shows that 1.5v braking is closed to mechanical hard brake and 8v braking is closed to medium brake. Fig. 9 and Fig. 10 clearly illustrate those observations.

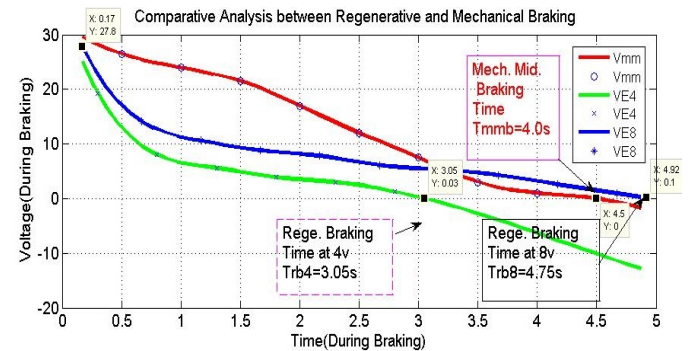


Fig. 9. Comparison with medium brake.

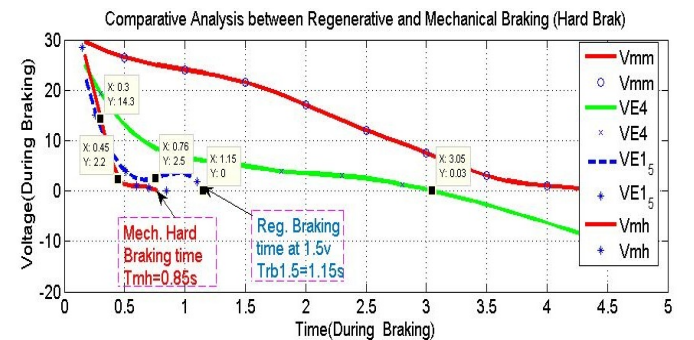


Fig. 10. Comparison with hard brake.

#### IV. RESULT

From simulated figure it's obvious that proposed method is feasible because it follows the relation (8). That means regenerative braking time

$$T_{rb8} > T_{rb4} > T_{rb1.5}$$

For efficiency estimation, braking current is observed during 1.5v regenerative braking, because most of the times vehicles use hard breaks. Braking current during 1.5v is presented in Fig.11.

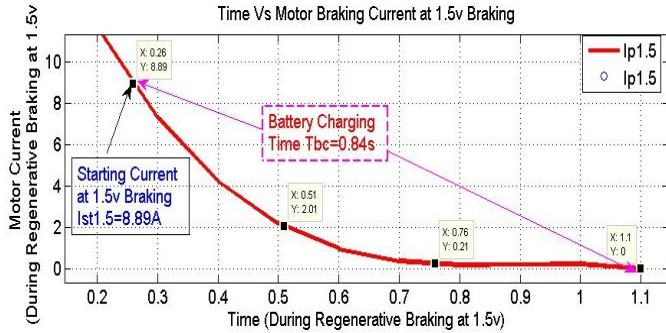


Fig. 11. Regenerative Braking current at 1.5v braking.

From the experimental data the calculated energy recovery and power during 1.5v braking are:

Power of regenerative Braking,  $P_{RB1.5(av)}$ : 66.5438w  
 Energy of regenerative braking,  $E_{RB1.5(av)}$  : 94.492j

By observing the motor current consumption pattern, the characteristics curve of prototype EVs is constructed. Fig. 12 shows this characteristics curve.

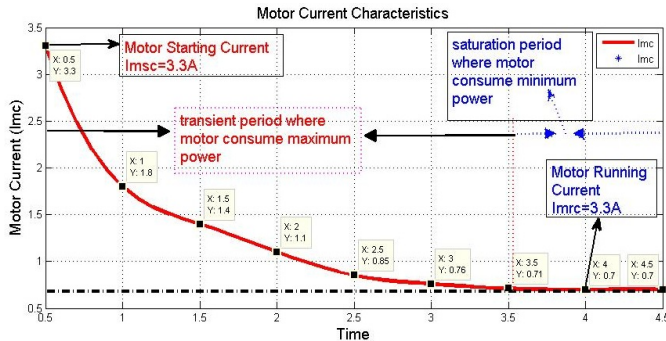


Fig. 12. current characteristics of Prototype Evs.

After analysis the calculated powers which will always consumed by the Prototype EVs are:

Power at starting time,  $P_{st(av)}$  : 34.936w

Power at Running Condition,  $P_{r(av)}$  : 21.49w

Total Power,  $P_{t(av)} = P_{st(av)} + P_{r(av)} = 56.426w$

Total Energy Used,  $E_{st(av)} = 220.625j$

From calculation it is very much clear that Efficiency of this proposed method is 42.829% .so proposed method will

increase the driving range around 42.829% that means 42.829% further than without regenerative braking and also 15% more than proposed method in [8].So proposed system is batter then the system proposed in [8] .

#### V. CONCLUSION

In this paper armature voltage control based regenerative braking system are proposed and compared by simulation .After simulation authors finds that proposed method can increase driving range around 43%. Finally this paper proves that regenerative braking based on motor armature voltage control is more effective and efficient then series-wound Dc motor based regenerative braking system and also comparative with AC Motor based EVs.

#### References

- [1] B. Fahimi and T. Sebastian, "Guest editorial special section on automotive electromechanical converters," IEEE Transactions on Vehicular Technology, vol. 56, no. 4, 2007, pp. 1470–1476.
- [2] I. Husain and MS. Islam, "Design, modeling and simulation of an electric vehicle system," SAE Technical Papers Series 1999-01-1149, International Congress and Exposition. Detroit, Michigan, March 1-4, 1999.
- [3] H. Bausch, A. Greif, B. Lange, R. Bautz, "A 50 kW/15000 rpm switched reluctance drive for an electric vehicle: Current control and performance characteristics," ICEM 2000, 28-30 August, Espoo, Finland, pp. 603-607.
- [4] H. Bausch, A. Greif, A.B.A. Nickel, "A switched reluctance and an induction machine in a drive train for an electrical vehicle under the conditions of car application," ICEM 2000, 28-30 August, Espoo, Finland, pp. 1313-1316
- [5] Commuter Car Corporation, 2008, Commuter Cars Specification, [Online]. Available: <<http://www.commutercars.com/>>
- [6] A. Caratti, G. Catacchio, C. Gambino and N. C. Kar, "Development of a predictive model for regenerative braking system," *Transportation Electrification Conference and Expo (ITEC 2013)*, Detroit, MI, 2013, pp. 1 – 6.
- [7] J. Guo, J. Wang and B. Cao, "Regenerative braking strategy for electric vehicles," *Intelligent Vehicles Symposium*, Xijian, China, 2009, pp. 864 – 868.
- [8] Y. Xiao, M. Nemeč, L. J. Borle, V. Sreeram and H. H. C. Iu, "Regenerative braking of series-wound brushed DC electric motors for electric vehicles," *2012 7th IEEE Conference on Industrial Electronics and Applications (ICIEA)*, Singapore, 2012, pp. 1657-1662. doi: 10.1109/ICIEA.2012.6360991.
- [9] J. Ruan, P. Walker and B. Zhu, "Experimental Verification of regenerative braking energy recovery system based on electric vehicle equipped with 2-speed DCT," *Power Electronics, Machines and Drives (PEMD 2014), 7th IET International Conference on*, Manchester, 2014, pp.1-8. doi: 10.1049/cp.2014.0356
- [10] X. Liu, C. Liu, M. Lu and D. Liu, "Regenerative braking control strategies of switched reluctance machine for electric bicycle," *International Conference on Electrical Machines and Systems ICEMS 2008*, Wuhan, China, 2008, pp. 3397 – 3400.
- [11] M. H. Rashid, "Dc Drives," in *Power Electronics Circuits, Devices and Applications*, 2nd ed. New Delhi, India: Prentice Hall, 1998, pp. 493-540.
- [12] M. H. Rashid, "Dc Drives," in *Power Electronics Circuits, Devices and Applications*, 3rd ed. New Delhi, India: Prentice Hall, 2004, pp. 640-691.



# Manipulation of structural, electrical and magnetic properties on zinc substitution in cobalt nanoferrite

S. Nasrin<sup>a\*</sup>

Department of Physics  
University of Chittagong  
Chittagong 4331, Bangladesh  
e-mail: shamima\_phys@yahoo.com

F.-U.-Z. Chowdhury<sup>c</sup>  
Department of Physics

Chittagong University of Engineering & Technology  
Chittagong 4349, Bangladesh

M. Moazzam Hossen<sup>b</sup>

Department of Computer Science & Engineering  
International Islamic University Chittagong  
Chittagong 4203, Bangladesh

S. Manjura Hoque<sup>d</sup>  
Materials Science Division  
Atomic Energy Centre,  
Dhaka 1000, Bangladesh

**Abstract**— Using wet chemical co-precipitation method cobalt-zinc nanoparticles ( $Co_{1-x}Zn_xFe_2O_4$ , with  $x = 0.2, 0.4, 0.6$  and  $0.8$ ) were synthesized and sintered at 1200 °C. The single phase spinel formation of all the samples has been confirmed by X-ray diffraction pattern. The scanning electron microscopy (SEM) was utilized for surface morphology study of samples. Impedance spectroscopy and initial permeability studies for all compositions have been performed in the frequency range 1 kHz to 120 MHz. We observed that the initial permeability remains more or less stable up to certain higher frequency range. The DC electrical resistivity demonstrates a definite break that has been explained in the light of conduction mechanism.

**Keywords**— Co-Zn ferrite; X-ray diffraction; Scanning electron microscopy; Magnetic properties; Electrical properties

## I. INTRODUCTION

By the reaction of non-magnetic metal oxides with magnetic materials spinel type ferrites which are ceramic materials are usually formed. Typically spinel type ferrites are naturally super lattices. They possess crystal structure with general formula  $AB_2O_4$ . This type of crystal structure contains tetrahedral A-site and octahedral B-site. Based on chemical composition and cation distribution, these materials show different sorts of structural, magnetic and electric properties. A variety of cations can be positioned in A and B-sites to alter its electric and magnetic properties. As these materials contain significant magnetic and electric properties, so these materials are currently not only used in industrial areas but also in research areas. They also prove their promising role in biomedical applications such as in ferrofluids, magnetic drug transportation, in cancer healing, etc. [1]. Having  $Zn^{2+}$  ions in tetrahedral and  $Fe^{3+}$  in octahedral sites,  $ZnFe_2O_4$  form a normal spinel structure with whereas with  $Co^{2+}$  ions in octahedral sites and  $Fe^{3+}$  ions uniformly dispersed between tetrahedral and octahedral sites,  $CoFe_2O_4$  form inverse spinel structure [2]. Therefore, Zn -substitution in  $CoFe_2O_4$  might have deformed spinel structures based upon the amount of the predecessor solutions. Due to substitution of  $Co^{2+}$  with  $Zn^{2+}$  leads to improve magnetic properties of nanocrystalline ferrites that has also observed by Arulmurugan et al. [3].

The current work deals with the preparation and characterization of nanoparticles of zinc substituted cobalt

ferrite,  $Co_{1-x}Zn_xFe_2O_4$ , ( $x = 0.2, 0.4, 0.6$  and  $0.8$ ) via wet chemical co-precipitation method. The samples were characterized using X-ray diffractometry (XRD), scanning electron microscope (SEM), electrical and magnetic measurements.

## II. EXPERIMENTAL

### A. Sample preparation

$Co_{1-x}Zn_xFe_2O_4$  nanoferrites have been prepared via wet chemical co-precipitation method. Analytical grade salts,  $CoCl_2 \cdot 6H_2O$ ,  $Zn(NO_3)_2 \cdot 6H_2O$  and  $FeCl_3$ , were used for the preparation of ferrites. Sodium hydroxide ( $NaOH$ ) has been employed as co-precipitating means and was added into the 8 M of  $NaOH$  solution with nonstop stirring. To complete the ferritization process of Co based ferrites, the particles were heated at 90 °C for 1 h. After centrifuging at 13000 rpm for 20 min and rigorous washing, the precipitate was collected. The calcined powders (80 °C for 72 h) were compressed uniaxially into disk-shaped (about 7.6-8.1 mm diameter, 0.9-1.0 mm thickness) and toroid-shaped (about 9.9-13.7 mm outer diameter, 6.2-8.7 mm inner diameter, and 1.85-2.85 mm thickness) samples. After that at 1200 °C in air, the samples were sintered for 180 min. For heating, the temperature rate was 7°C/min. The disk-shaped and toroid-shaped samples were used for characterization.

### B. Measurements

The structural characterization of the sintered powder was done by powder XRD technique using a Phillips X-pert Pro X ray diffractometer with Cu- $K\alpha$  radiation ( $\lambda = 1.5418 \text{ \AA}$ ). At room temperature, XRD scans, from 25-70° with a step size of 0.02°, have been taken for all the samples. The microstructures of the samples were studied by using Philips XL-30 scanning electron microscope. From frequency from 1 kHz to 120 MHz, initial permeability has been measured by using an Impedance Analyzer (Wayne Kerr 6500B). The temperature dependent (ranging room temperature to 300 °C) dc electrical resistivity has been performed by two probe method using a programmable Keithley Electrometer (Model 6514).

### III. RESULTS AND DISCUSSION

#### A. XRD analysis

The XRD patterns of all the samples of  $Co_{1-x}Zn_xFe_2O_4$  ( $x = 0.2, 0.4, 0.6$  and  $0.8$ ) sintered at  $1200^\circ\text{C}$  have been depicted in Fig. 1. The major peaks in the XRD patterns are indexed with ( $hkl$ ) values. The XRD patterns of the samples show sharp, intense and well-defined reflections of planes (220), (311), (400), (422), (511) and (440) which reveal single-phase spinel structure. The XRD spectra contains no extra peak that corresponds to other crystallographic phase [4, 5, 6, 7]. This single phase cubic spinel structure corresponds to the space group  $Fd\bar{3}m$  for all the sintered samples.

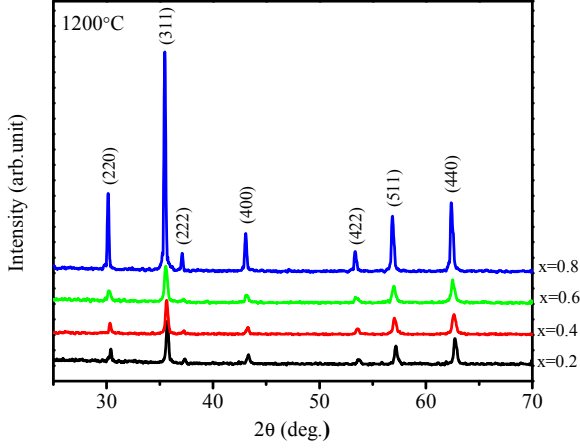


Fig. 1 X-ray diffraction patterns of  $Co_{1-x}Zn_xFe_2O_4$  at  $1200^\circ\text{C}$

#### B. Scanning electron microscopy

The typical SEM micrographs of  $Co_{1-x}Zn_xFe_2O_4$  sintered at  $1200^\circ\text{C}$  has been shown in Fig. 2. From the microstructures it can be seen that the grain size varies with zinc content in the  $Co_{1-x}Zn_xFe_2O_4$  system. Furthermore, the grains of the samples appear to be non-uniform with some agglomerations containing more than one grain.

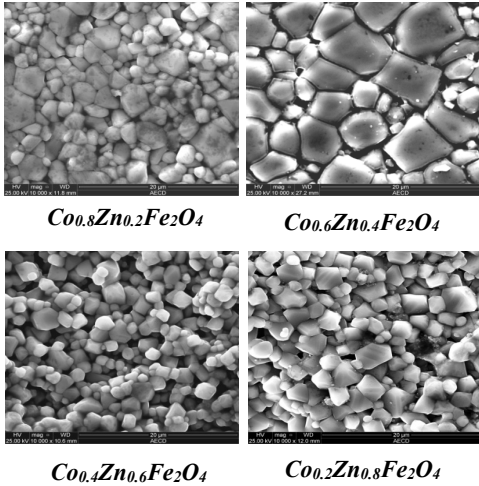


Fig. 2. SEM micrographs of  $Co_{1-x}Zn_xFe_2O_4$  at  $1200^\circ\text{C}$

#### C. Magnetic measurements: Initial permeability

The initial permeability ( $\mu'$ ) within the frequency range 1 kHz-120 MHz for  $Co_{1-x}Zn_xFe_2O_4$  ( $x = 0.2, 0.4, 0.6$  and  $0.8$ ) samples sintered at  $1200^\circ\text{C}$  has been presented in Fig. 3. It was observed that  $\mu'$  remains fairly stable up to a particular frequency characterized by the onset of resonance [8]. The stable values of  $\mu'$  over a certain frequency range reveal that the ferrite samples are stable in the frequency range. This characteristic is very much desirable for wideband video recording and broadband pulse transformers. This trend of the curve is clearly visible for all the compositions. The values of  $\mu'$  in the low frequency region rise with the increase of zinc content. For  $Co_{0.2}Zn_{0.8}Fe_2O_4$  system, the increase of  $\mu'$  is clear. Beyond this, the curves suddenly fall to a very low value. This stability up to certain higher range and then the sudden fall to an extremely small value is known as dispersion of initial permeability. This is due to either domain wall displacement or domain rotation or combined contribution of both of these [9]. At the lower frequency range, magnetizing process and loss mechanism significantly depend on the domain wall motion. With the rise of frequency, the wall motion damped and out of phase with the applied field. This sort of occurrence is found in  $Ni-Zn$  ferrites [10] and  $Li-Zn$  ferrites [11].

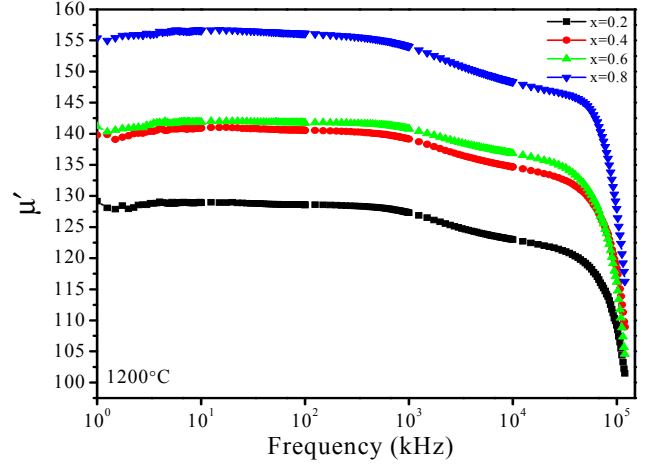


Fig. 3. Frequency dependence of the real part of the initial permeability,  $\mu'$  for different value of  $x$  at  $1200^\circ\text{C}$ .

#### D. Electric measurements: dc electrical resistivity

At  $1200^\circ\text{C}$  sintering temperature, the dc electrical resistivity has been found to decline with the rise of  $Zn^{2+}$  ions for all ferrites (Fig. 4). In ferrites, the conductivity is due to the existence of  $Fe^{2+}$  and the metal ions ( $Co^{3+}$ ). The presence of  $Fe^{2+}$  results in n-type behavior and  $Co^{3+}$  in p-type behavior [12]. In n-type ferrites, the conduction mechanism is due to the electron hopping between  $Fe^{2+}$  and  $Fe^{3+}$  at B sites. On the other hand, the conduction in the p-type specimens is due to the jumping of holes between  $Co^{3+}$  and  $Co^{2+}$  ions. In the  $Co-Zn$  ferrite system, the  $Fe^{3+}$ ,  $Co^{2+}$  and  $Zn^{2+}$  are distributed among octahedral (B-sites) and tetrahedral (A-sites) sites of the face centered cubic lattice. Early reports on such systems have attributed the anomaly either to the Curie temperature or alteration in the conduction mechanism,

however, in this case the anomaly arises according to the change in the conduction mechanism.

With the addition of zinc, the resistivity of the sample decreases due to existence of  $Fe^{2+}$  ions [13]. Consequently the electrical conductivity in ferrites is controlled by the increase in the number of ferric and ferrous ions at B-sites. As a result, resistivity reduces with the increase of  $Zn^{2+}$  ion concentration [14]. This similar fashion of resistivity has been reported earlier by Ghazanfar *et al* [15]. The plots of resistivity versus temperature are marked by a change in slope for all ferrites. Jonker have carried out similar studies on  $Co_{1-x}Fe_{2+x}O_4$  observed two regions of conductivity [16]. The region contained  $Co^{2+}$  and  $Co^{3+}$  ions shows low conductivity, while the region contained  $Fe^{2+}$  and  $Fe^{3+}$  ions shows high conductivity. The existence of cobalt on the octahedral site of the spinel favors a conduction mechanism  $Co^{2+} + Fe^{3+} \leftrightarrow Co^{3+} + Fe^{2+}$ . The substitution of zinc influences this conduction mechanism.

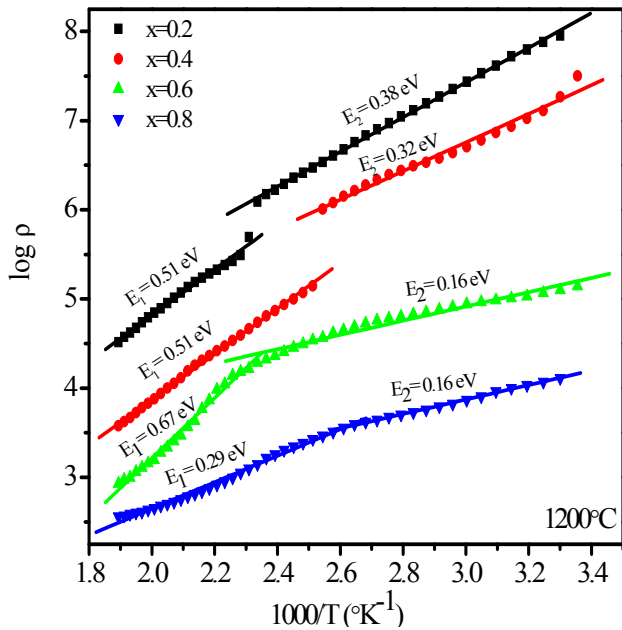


Fig. 4. Variation of resistivity

This, in fact, explains the predominant conduction mechanism in cobalt ferrite. The resistivity ( $\rho$ ) at absolute temperature ( $T$ ) is expressed by the relation:

$$\rho = \rho_0 \exp\left(\frac{\Delta E}{kT}\right),$$

where  $k$  represent Boltzmann constant and  $\Delta E$  is the activation energy difference of ferromagnetic ( $E_f$ ) and paramagnetic ( $E_p$ ) regions. This activation energy releases electron from  $Fe^{2+}$  to the neighboring ions which contributes electrical current either by jumping or by hopping mechanism.

From the linear plots of  $\log \rho$  and  $1000/T$  (Fig. 4), the activation energies for the two regions ( $E_f$  and  $E_p$ ) of the sintered samples have been calculated from the slope) using the formula [17]:  $\Delta E = slope \times 4.606 \times 8.62 \times 10^{-5}$  eV and tabulated in the Table 1.

TABLE I. ACTIVATION ENERGY OF  $Co_{1-x}Zn_xFe_2O_4$  SYSTEM SINTERED AT 1200°C

Temperature (°C)	Zn <sup>2+</sup> Content, x	E <sub>p</sub> (eV)	E <sub>f</sub> (eV)	ΔE = E <sub>p</sub> - E <sub>f</sub> (eV)
1200	0.2	0.51	0.38	0.13
	0.4	0.51	0.32	0.19
	0.6	0.67	0.16	0.51
	0.8	0.29	0.16	0.13

#### IV. CONCLUSIONS

The  $Co_{1-x}Zn_xFe_2O_4$  ferrites have been successfully prepared by wet chemical co-precipitation method. The formation of single phase spinel structure evidently revealed by the X-ray diffraction studies. The initial permeability decreases with the increase in zinc content and the ferrite samples show good high frequency stability up to around 10 MHz. The activation energy increases from 0.13 to 0.51 eV with the zinc content (up to 0.6), whilst it decreases on further increase in zinc content. The zinc substitution has remarkable effect on the structural, electrical and magnetic properties of cobalt ferrite.

#### ACKNOWLEDGEMENT

The authors are thankful to Materials Science Division, Atomic Energy Centre, Dhaka 1000, Bangladesh, for providing experimental facilities. We acknowledge the financial support provided by Chittagong University of Engineering and Technology (CUET), Chittagong 4349, Bangladesh.

#### REFERENCES

- [1] K. Raj, R. Moskowitz and R. Casciari, "Advances in Ferrofluid Technology" Journal of Magnetism and Magnetic Materials, Vol. 149, No. 1-2, pp. 174-180, 1995.
- [2] D. S. Mathew and R.-S. Juang, "An Overview of Structure and Magnetism of Spinel Ferrite Nanoparticles and their Synthesis in Microemulsions" Journal of Chemical Engineering, Vol. 129, No. 1-3, pp. 51-65, 2007.
- [3] R. Arulmurugan, B. Jeyadevan, G. Vaidyanathan and S. Sendhilnathan, "Effect of Zinc Substitution on Co-Zn and Mn-Zn Ferrite Nanoparticles Prepared by Co-Precipitation" Journal of Magnetism and Magnetic Materials, Vol. 288, pp. 470-477, 2005.
- [4] N. H. Vasoya, V. K. Lakhani, P. U. Sharma, K. B. Modi, Ravi Kumar and H. H. Joshi, "Study on the electrical and dielectric behaviour of Zn-substituted cobalt ferrite/aluminates" Journal of Physics: Condensed Matter, Vol. 18, pp. 8063-8092, 2006.
- [5] A. Hassadeea, T. Jutarosagaa, W. Onreabroya, "Effect of zinc substitution on structural and magnetic properties of cobalt ferrite" Procedia Engineering, Vol. 32, pp. 97 - 602, 2012.
- [6] Ahmed Saied Faheim, Abd El Fattah Mustafa KhourshidAlaa- ELdin, A EL-Hammady Abdul Rahman and Abdullah Badawi, "Effect of Zn Substitution on the Characterization of Cobalt Ferrite Nano Particles Prepared Co-precipitation Method" Journal of Nanomaterials & Molecular Nanotechnology, Vol. 4, Issue 1, pp. 1 - 6, 2015.
- [7] S. Nasrin, S. Manjura Hoque, F.-U.-Z. Chowdhury, M. Moazzam Hossen, "Influence of Zn substitution on the structural and magnetic properties of  $Co_{1-x}Zn_xFe_2O_4$  nano-ferrite" IOSR Journal of Applied Physics (IOSR-JAP), Vol. 6, Issue 2, pp. 58 - 65, 2014.

- [8] N. Bloembergen, "Magnetic Resonance in Ferrites" Proceedings of the Institute of Electronic and Radio Engineers, Vol. 44, pp. 1259-1269, 1956.
- [9] G. T. Rado, R. W. Wright and W. H. Emerson, "Ferro-magnetism at Very High Frequencies. III. Two Mechanisms of Dispersion in a Ferrite" Physics Review, Vol. 80, No. 2, pp. 273-280, 1950.
- [10] J. Smit and H. P. Wijn, "Ferrites" Wiley, New York (1959) pp. 268.
- [11] T. Nakamura, T. Miyamoto and Y. Yamada, "Complex Permeability Spectra of Polycrystalline Li-Zn Ferrite and Application to EM-Wave Absorber" Journal of Magnetism and Magnetic Materials, Vol. 256, No. 1-3, pp. 340-347, (2003).
- [12] B. Vishwanathan and V. R. K. Murthy, "Ferrite Materials, Science and Technology" New Delhi: Narosa Publishing House, 1990.
- [13] M. U. Islam, T. Abbas, S. B. Niazi, Z. Ahmed, S. Sabeen and M. A. Chaudhry, "Electrical Behavior of Fine Particle, Co-Precipitation Prepared Ni-Zn Ferrites" Solid State Communications, Vol. 130, No. 5, pp. 353-356, 2004.
- [14] M. E. Shabashy, "DC Electrical Properties of Zn-Ni Ferrites" Journal of Magnetism and Magnetic Materials, Vol. 172, No. 1-2, 188-192, 1997.
- [15] U. Ghazanfar, S. A. Siddiqui and G. Abbas, "Study of Room Temperature dc Resistivity in Comparison with Activation Energy and Drift Mobility of NiZn Ferrite" Materials Science and Engineering: B, Vol. 118, No. 1-3, pp. 132-134, 2005.
- [16] G. H. Jonker, "Analysis of the semiconducting properties of cobalt ferrite" J. Phys. Chem. Solids, Vol. 9, No. 2, pp. 165-175, 1959.
- [17] N. Jahan, F.-U.-Z. Chowdhury and A.K.M. Zakaria, "Structural and electrical properties of chromium substituted nickel ferrite by conventional ceramic method" Materials Science-Poland, Vol. 34, No. 1, pp. 185-191, 2016.

# HSV and Template Matching Based Bengali Road Sign Recognition Technique

Mohsina Binte Asad

Department of Computer Science and Engineering  
Sylhet Engineering College  
Sylhet, Bangladesh

Fatema Jannat Sharna

Department of Computer Science and Engineering  
Sylhet Engineering College  
Sylhet, Bangladesh

Nashid Alam

Department of Computer Science and Engineering  
Sylhet Agricultural University  
Sylhet, Bangladesh

M. Jahirul Islam

Department of Computer Science and Engineering  
Shahjalal University of Science and Technology  
Sylhet, Bangladesh  
e-mail: jahir-cse@sust.edu

**Abstract**— Road sign recognition plays an exigent role for easy, immune and suitable driving. In this paper, a road sign detection system is developed to automatically recognize Bengali road signs. The proposed method is based on HSV transformation along with a template matching technique to detect and recognize circular, triangular, rectangular and octagonal signs and it covers all existing Bengali road signs. The localization phase requires 2.846 seconds for color information processing and recognition phase requires 5 or 6 seconds in average. The system consists of two stages and they are sign localization and recognition. In localization stage, the sign is labeled based on its color information. Original image is converted into HSV image. After applying proper thresholding value, the HSV image is converted into binary image. Then hole filling operation is used. After that the biggest blobs are detected and then the sign is cropped out by calculating both maximum and minimum values of rows and columns of the matrix containing labels for the connected components in binary image. In recognition step, the sign is recognized using Template Matching which is done by creating a small template from cropped image, a pixel by pixel matching of template with every possible pixel of main image using a similarity matrix normalized cross correlation to find the pixel giving maximum match. The whole system was tested over 30 unique signs collected from Sylhet Metropolitan City. The proposed system shows 83.33% accuracy (25/30) in recognition step.

**Keywords**— Bengali Road Sign Localization, Recognition, HSV Transformation, Color Image Thresholding, Template Matching.

## I. INTRODUCTION

Road sign recognition is very important for driving properly and safely. Serious accidents may occur while driving on road when driver do not notice and recognize the sign beside the road. Sometimes driver do not notice the sign because of less concentration. Taking with people sitting beside him, taking on cell phone, interesting object may prevent drivers from noticing road sign. Tiredness, snoozing, lack of sensation, nervousness, anxiety also impede drivers from observing road signs. So serious accidents, traffic jams, mess occurs every day. For automotive and robotic vehicle that

automatically drive on road, road sign recognition plays a vital role. S. Maldonado-Bascón et al. [1] propose a method to evaluate the signaling of the road based on support vector machines (SVMs) which is able to run in real time. R. Azad et al. [2] worked on Detection and Recognition of Road Signs in Optimized Method based on support vector machines (SVMs) classifier. Z.T. Kardkov'acs et al. [3] focus on real-time traffic sign recognition based on feature extraction techniques used with data mining classifiers. Md. S. Hossain et al. [4] reviews on Traffic Road Sign Detection and Recognition for automotive vehicles based on BFS. S.H. Hsu et al. [5] describe an automatic road sign recognition system by using Matching Pursuit (MP) filters. An algorithm is proposed by Swathi M. et al. [6] which is based on color segmentation, morphological functions and use of discriminative features. A. Adam et al. [7] describe an automatic road sign detection and classification system based on Support Vector Machines and hog descriptors. Y. Chen et al. [8] worked on detection and recognition of traffic signs based on HSV vision model and shape features.

In this paper, we propose a novel approach for road sign detection and recognition based on HSV Transformation and Template Matching technique. There are some common problems that are involved in road sign detection such as various lighting conditions of the scene in a natural environment, variation in size, different weather conditions producing bright spot, shadows, time of the day or night etc. Sometimes posters, banners are attached to signs. The shape of road signs are corrupted due to presence of many years, destruction or sometimes covered up due to presence of other objects. Road signs also exist in hundred of variance often different from legally defined standard. Sign also appear in clustered scene and imperfect shape. So we developed a method based on color using HSV. Because HSV is invariant to lighting conditions and quite similar to the way in which human perceive color. It is also suitable for color segmentation. We work on still images collected from Sylhet Metropolitan city captured by mobile phone. All signs are

summarized in Fig. 1. Besides HSV Transformation we also applied SURF (Speeded Up Robust Feature) which is a feature based method. SURF is mainly used for image registration, reconstruction but we applied that in a different way for road sign localization. The accuracy of SURF for road sign localization is 80.95% and the process is not robust and computation is not in real time, it also varies in different lighting conditions. For this reason we propose HSV Transformation as our method which is greater than the localization rate in SURF.



Fig. 1: Some Unique Bengali Road Signs

## II. MATERIALS AND METHOD

In this paper, we present a system for localization and recognition of road signs that has been successfully applied to Bangladeshi road signs. The whole system is divided into two stages: 1) localization and 2) recognition. The general diagram of the proposed method is shown in (Fig. 2). In our proposed method first the captured image is preprocessed by converting from RGB to HSV. Image is then binarized by a color thresholding value. Flood fill operation on background pixel of input binary image is done by hole filling operation. Finally the road sign is localized. Afterwards, the sign is cropped out by calculating both maximum and minimum values of rows and columns of the matrix containing labels for the connected components in binary image. Then the extracted sign is recognized by template matching process, template stored on the database.

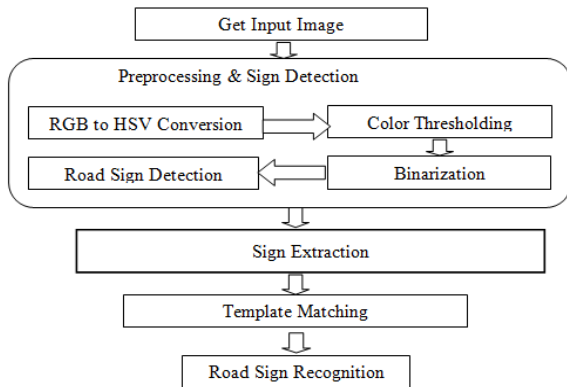


Fig. 2: Block Diagram of Proposed Method

Preprocessing is carried out on the image for making the image suitable for work, so that the main processing on the

image becomes easier. This steps involves image converting from RGB to HSV, color thresholding, hole filling and finally the sign localization that is shown in Fig. 3.

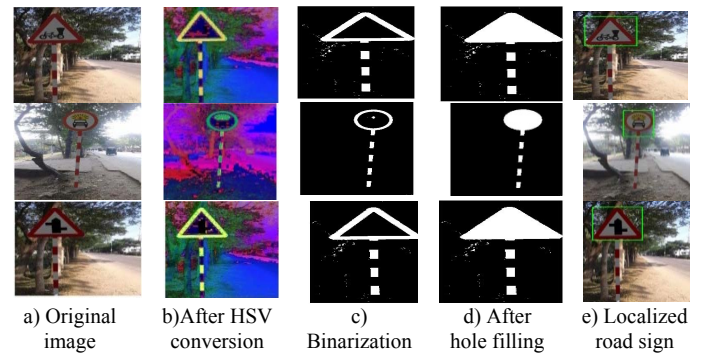


Fig. 3: Stages of Preprocessing and Sign Localization

HSV is quite similar to the way in which humans perceive color and much more suitable for color segmentation because it gives unique information for different component of colors. Moreover, the hue value is invariant for illumination which makes HSV color space as one of the best choices for color segmentation. The purpose of thresholding is to classify pixels of an image into ‘foreground pixels’ and ‘background pixels’. As our main concern is the sign which is the foreground of the image, the foreground has to be subtracted from background by removing the complex background, which we have done by color thresholding. By matching certain criteria level, a pixel is called a ‘foreground pixel’ which is the required object pixel if its color is close enough to a reference color, if not it will be a ‘background pixel’. The HSV color range for red road sign is as follows: Hue is less than 0.05 or Hue is greater than 0.95, Saturation is greater than 0.5 and Value is greater than 0.01.

The algorithm for binary image creation by color thresholding is described in Algorithm-01. To find the red pixel in the image after the HSV transformation these ranges of values are used as the thresholds. Then, the red pixel is converted to binary image that is shown in Fig. 3(c).

### Algorithm-01: Binary Image Creation By Color Thresholding

**Input:** Captured image

**Begin**

1. Read Input Image
2. Convert RGB image into HSV image.
3. Set the value Hue less than 0.05 or greater than 0.95
4. Set the value Saturation greater than 0.5
5. Set Value greater than 0.01

**End**

Hole filling operation fill image regions and holes. A hole is a set of background pixel that cannot be reached by filling

in the background from the edge of the image. It performs a flood fill operation on background pixels of the binary image starting from the point specified in locations. Matlab command “imfill” used for this operation. In binary image the red rim of the object are translated into white pixel. As our sign is located in white pixel the hole filling operation is used to fill the region inside white pixel rim. Some of the experimental results are shown in Fig. 3(d).

A red color pixel will be translated to white color, the rest of the colors are black color. The binary image is then labeled according to each pixel’s 8-connectivity. The pixels labeled 0 are the background and the pixels labeled 1 make up the object. Then from the connected components (object) that have fewer than 1000 pixels are removed by area opening operation. The matlab command “bwareaopen” is used for this operation. The algorithm for road sign localization is described in Algorithm-02. This operation helps to remove unexpected objects from binary image and this way we get our required sign by removing all the unexpected objects. Then the required sign is labeled successfully by measure properties of image regions by “regionprops”. It measure a set of properties for each connected component (object) in binary image, which must be a logical array, hence the road sign localized. The localized sign is shown in Fig.3 (e).

**Algorithm-02: Road Sign Localization by HSV Transformation**

**Input:** Captured image  
Begin

1. Convert RGB image into HSV image.
2. Find Red pixel by thresholding.
3. Convert into binary image.
4. Fill the hole of binary image.
5. Label the Road sign.

End

At this stage all the connected components of binary image, which we get from previous step are labeled. Matlab command “bwlabel” is used for this operation. This operation returns a matrix L, of the same size as BW (binary image). The elements of L are integer values greater than or equal to 0. The pixels labeled 0 are the background. The pixels labeled 1 make up one object; the pixels labeled 2 make up a second object, and so on. Our main target is to find the pixels labeled 1. Finally, the sign is cropped out by calculating both maximum and minimum value of row and column of the matrix of the same size as binary image containing labels for the connected components in BW. Now the extracted sign is further processed and do a pixel by pixel matching of the extracted sign with the template stored in database, placing (center of) the template at every possible pixel of the cropped image. Then, using a similarity metric, like normalized cross correlation, find the pixel giving maximum match. That maximum match is the place which has a pattern most similar to the template. The Algorithm of Template matching is described at **Algorithm-03**. The experimental results of template matching are shown in Fig. 4.

**Algorithm-03: Template matching Technique of Sign Recognition**

**Input :** Template Images  
Begin

1. Load Template Images
2. Do a pixel by pixel matching of Template image and complemented image.
3. Use similarity metric normalized cross correlation.
4. Find the pixel giving maximum match.
5. Take the maximum match as output.

End

The algorithm of road sign recognition is described in **Algorithm -04**.

**Algorithm-04: Road Sign Recognition by Template Matching**

**Input:** Extracted road sign  
Begin

1. Convert image into gray scale image.
2. Crop sign from binary image.
3. Label removes on gray scale image.
4. Convert this into binary image.
5. Complement the image.
6. Template Matching
7. Road sign is successfully recognized

End.

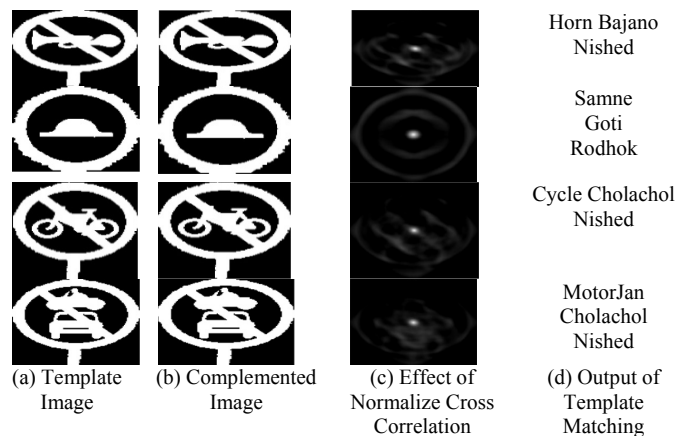


Fig.4: Steps of Template Matching

III. RESULT ANALYSIS

In this paper, we have tested 30 unique road signs. Among them 25 unique road signs were segmented successfully using our proposed method. To demonstrate the capability of our system, we perform two different experiments. The first one is the road sign localization and the second one is the road sign recognition, it includes recognizing the road sign under different view and variant lighting conditions. Some of the recognized road signs and the elapsed time are shown in Fig. 5. Our system is tested mostly in the streets of Sylhet Metropolitan City. Only 30 unique road signs are available

here. The localization phase is tested over 116 individual road signs. The percentage of road signs which are correctly localized shown in Table I. In the recognition process, the system is tested over 76 road signs. The percentage of the road signs correctly recognized is shown in Table II. Performance of our overall system described below.

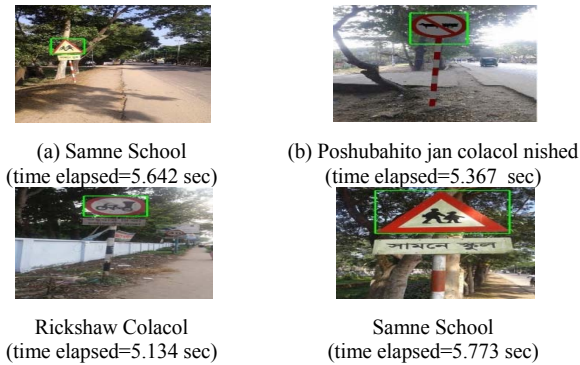


Fig. 5: Some Recognized Road Signs

TABLE I: LOCALIZATION PHASE (TOTAL IMAGE: 116)

Good Quality images: 99		Bad Quality images: 17	
True Positive	True Negative	False Positive	False Negative
99	8	7	2
Accuracy =85.34%			

The false negative and false positive will be 2.02% and 7.07% respectively that is shown in Table I.

TABLE II: RECOGNITION PHASE (TOTAL IMAGE: 76)

Correct Output	Incorrect Output	Accuracy (%)
63	13	82.89%

TABLE III: COMPARATIVE ANALYSIS OF ROAD SIGN LOCALIZATION AND RECOGNITION

Author reference and year	Methods	Number of Images used for experiments	Good/Acceptable (%)
Adam et al.(2014) [7]	Support vector machines and hog descriptors	207 training data (Only testing purpose on STOP sign)	94.34%
Azad et al.(2014) [2]	Support vector machines (SVMs) classifier	375	93%
<b>Proposed Method</b>	Localization by HSV and recognition using template matching technique	76 (Available unique sign 30 used for experiment among them 25 are recognized )	83.33%

Adam et al. (2014) [7] detected and classified Greek road signs based on Support Vector Machines (SVM) and HOG descriptors. They only worked on STOP sign which is hexagonal shape. Variety of shapes and signs are not considered here. On the other hand, we proposed a method on Bengali road signs based on HSV Transformation and Template Matching. We worked on 30 unique signs (Total images 116) of different shapes. Although, Template Matching is old method, there is no previous works on road sign recognition based on template matching in Bangladesh.

## IV. CONCLUSIONS

In this paper, a complete methodology for road sign localization and recognition is presented and described. In the localization phase, A special focus is given in the examination of the proficiency of extracting ROIs by HSV Transformation under noisy and complex scenario. In the recognition phase, template matching is used to recognize the road signs effectively. Our system is able to recognize 25 unique signs out of 30 unique signs. The computation time of the localization phase is 2.846 seconds for color information processing and then extracting the road sign image, whereas the recognition operation using template matching method requires about 5 to 6 seconds in average on Intel Core i3 4030U, 1.96 GHz CPU with 4GB RAM. The success rate of our proposed algorithm is 83.33%. All the implementation and appraisal of experimental results was carried out using MATLAB (R2014a) on Windows 8 Version 8.1. Experimental results show that the proposed method exhibits a better performance. Experimental results imply that our system is accurate because it allows us to localize different geometric shapes, i.e., circular and triangular in different conditions such as distant Image, blur Image, close image, variant lighting condition, complex scenario, different positions.

## REFERENCES

- [1] S.M. Bascón, S. L. Arroyo, P. G. Jiménez, H. G. Moreno, and F. L.Ferreras, "Road-Sign Detection and Recognition Based on Support Vector Machines," IEEE Intell. Trans. Syst., vol. 8, no. 2, June 2007.
- [2] R. Azad, B. Azad, Babak, and I.T Kazerooni, "Optimized Method for Iranian Road Signs Detection and Recognition". International Journal of Research in Computer Science, eISSN 2249-8265 vol. 4, Issue 1 (2014), pp.19-26,2014.
- [3] Z.T. Kardkov'acs, Z. Par'oczi, E. Varga, A. Siegler, and P. Lucz, "Real-time Traffic Sign Recognition System," UI Res. Ltd., Budapest, Hungary Conference: Cognitive Infocommunications (CogInfoCom), 2011 2<sup>nd</sup> International Conference.
- [4] M.S. Hossain, and Z. Hyder, "Traffic Road Sign Detection and Recognition for Automotive Vehicles," International Journal of Computer Applications (0975 – 8887) vol. 120 ,no. 24, Jun. 2015 .
- [5] S.H. Hsu, and C.L. Huang, "Road sign detection and recognition using matching pursuit Method". Image and Vision Computing 19 (2001), 119–129, June 2000.
- [6] M. Swathi, and R. Nisha, "A Robust System for Automatic Road Sign Detection and Recognition," International Journal of Advanced Research in Biology, Ecology, Science and Technology (IJARBEST), Vol. 1, Issue 2, May 2015.
- [7] A. Adam, and C. Ioannidis, "Automatic Road-Sign Detection and Classification Based on Support Vector Machines and HOG Descriptors," ISPRS Annals of the Photogrammetry, Remote Sensing and Spatial Information Sciences, Volume II-5, June 2014.
- [8] Y. Chen, Y. Xie, and Y. Wang, "Detection and Recognition of Traffic Signs Based on HSV Vision Model and Shape features," Journal of Computers, Vol. 8, No.5, May 2013.
- [9] M. Lalonde, and Y. Li. 'Raod sign Recognition - survey of the State of art, technique report for sub-project 2.4', CRIM-IIT-95/09-35.
- [10] Linda G. Shapiro and George C. Stockman 'Computer Vision' ©2001 by Prentice Hall Inc.
- [11] D.S. Singh, and Dr. G. Dixit, "Traffic Sign Detection Using Feature Based Method". International Journal of Advanced Research in Computer Science and Software Engineering, vol.5, Issue 2, February 2015.



# Analytical Study of High Efficient Cu(In,Ga)Se<sub>2</sub> Solar Cell with In<sub>2</sub>S<sub>3</sub> Buffer Layer

Mohammad Sijanur Rahaman Robin<sup>1</sup>, Khurshedul Islam Meheraj<sup>1</sup>, MD. Shakawat Zaman Sarker<sup>2</sup>,  
Electrical and Electronic Engineering, International Islamic University Chittagong, Chittagong-4314, Bangladesh<sup>1</sup>  
Electrical and Electronic Engineering, Uttara University, Dhaka-1230, Bangladesh<sup>2</sup>  
Email: sijan.robin24@gmail.com

**Abstract**—This paper represents a lucid numerical analysis of thin film Cu(In,Ga)Se<sub>2</sub> (CIGS) solar cell with In<sub>2</sub>S<sub>3</sub> (Indium Sulphide) buffer layer by using SCAPS-1D. The effect of band gap, concentration and thickness of both Cu(In,Ga)Se<sub>2</sub> absorber layer and In<sub>2</sub>S<sub>3</sub> buffer layer are investigated in this simulation. This study is focused to analyze electrical performances of In<sub>2</sub>S<sub>3</sub> buffer layer based Cu(In,Ga)Se<sub>2</sub> solar cell for a better substitute of toxic CdS buffer layer. The optimum thickness has found 40 nm for In<sub>2</sub>S<sub>3</sub> buffer layer and 3000 nm for Cu(In,Ga)Se<sub>2</sub> absorber layer. In addition, the optimum band gap of CIGS and In<sub>2</sub>S<sub>3</sub> layer has attained 1.10 eV and 2.6 eV subsequently and 25.03% efficiency has achieved along with 0.75 V open circuit voltage (V<sub>oc</sub>), 39.435 mA/cm<sup>2</sup> short circuit current density (J<sub>sc</sub>) and 84.62% Fill Factor (FF).

**Keywords**—CIGS, In<sub>2</sub>S<sub>3</sub>, band gap, efficiency.

## I. INTRODUCTION

CIGS (Copper Indium Gallium diselenide) solar cells are now leading the thin film solar cells market due to its low manufacturing cost and high efficiency compared to other thin film solar cells. The highest lab efficiency of CdS/CIGS solar cell is 21.7% by “Solar Energy and Hydrogen Research (ZSW)” [1] and 22.3% by “Solar Frontier” [2]. It is an adulterant of copper indium diselenide (CIS) and copper gallium diselenide (CGS) which can be denoted as [Cu(In<sub>x</sub>Ga<sub>1-x</sub>)Se<sub>2</sub>] CIGS. By tuning the In:Ga ratio  $x$ , the band gap of CIGS can be tuned from 1.0 eV to 1.7 eV [3].

CdS (Cadmium Sulphide) buffer layer contains toxic element Cadmium (Cd), so the excessive use of CdS in CIGS solar cells indirectly lead to serious environmental problems [4]. Moreover, the fabrication technique of the CdS as buffer layer is not compatible with other layers, resulting in a complex fabrication process for CIGS solar cells [4].

Various buffer layers have been researched in CIGS cell i.e. ZnS, ZnSe, In(OH)<sub>3</sub>, In<sub>2</sub>S<sub>3</sub>, In<sub>x</sub>S<sub>y</sub>, ZnInSe<sub>x</sub>, ZnMgO, ZnO, SnO<sub>2</sub>, SnS<sub>2</sub>. Among them In<sub>2</sub>S<sub>3</sub> is a very auspicious one and  $\beta$ -In<sub>2</sub>S<sub>3</sub> buffer layer has been applied as an ideal substitute for CdS to avoid the use of toxic Cd and to obtain an environment friendly photovoltaic system [5]. The In<sub>2</sub>S<sub>3</sub> band gap ranges from 2.1 to 2.9 eV or higher values when oxygen or sodium elements is doped with it partially [5]. It has found in some report that the optical band gap of pure  $\beta$ -In<sub>2</sub>S<sub>3</sub> in thin film form was only from 2.0 eV to 2.2 eV [6] [7]. However, In<sub>2</sub>S<sub>3</sub>

based CIGS cell has reached efficiency of 15.7% efficiency by CBD (Chemical Bath Deposition) process [8] and the highest efficiency 16.4% [9] is achieved by ALCVD (Atomic Layer Chemical vapor Deposition) process.

The purpose of this study is to observe performance of CIGS solar cell with In<sub>2</sub>S<sub>3</sub> buffer layer and to find out the optimum performance of alternative buffer layer which can replace the toxic CdS. We study the effect of band gap, concentration and thickness of both CIGS absorber layer and In<sub>2</sub>S<sub>3</sub> buffer layer.

## II. METHODOLOGY

### A. CIGS solar cell structure and cell parameters

The CIGS solar cell structure used is ZnO:Al/i-ZnO/In<sub>2</sub>S<sub>3</sub>/CIGS/Mo/substrate. Transparent conductive oxide (TCO) has been used as window layer. It is a bi-layer which comprises of intrinsic Zinc-Oxide (i-ZnO) and Aluminum doped ZnO (ZnO:Al). ZnO:Al has 95% transmission [10]. Molybdenum (Mo) is the back contact of this CIGS solar cell. It has a metal work function of 4.95 eV [11]. Its thickness depends on the required resistance of the solar cell. Solar cells are mostly fabricated on soda-lime glass (SLG) substrate. The highest efficiency of CIGS cell is obtained on glass [2].

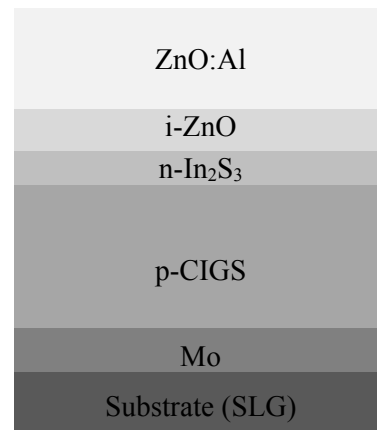


Fig. 1. Schematic structure of CIGS solar cell used in the simulation.

Numerical method helps to test the results and optimize the process parameters on the device without fabrication. In this study, CIGS solar cells are modeled using the latest version

(3.0.0.2) of SCAPS (Solar Cell Capacitance Simulator) which is a one dimensional simulator developed at the university of Gent [12]. The semiconductor parameters used in this simulation is given in Table I. The CIGS solar cell is simulated with solar spectrum AM 1.5G, 100mW/cm<sup>2</sup> power density and 300 K of temperature. The function of current density versus voltage (J-V) characteristic curve has used for extraction of electrical parameters such as V<sub>oc</sub>, J<sub>sc</sub>, FF and efficiency. In this study band gap, concentration and thickness of both CIGS and In<sub>2</sub>S<sub>3</sub> have been observed and all the other parameters remain constant.

TABLE I  
Material properties for basic CIGS cell materials

Layer properties				
Layer	ZnO:Al	i-ZnO	In <sub>2</sub> S <sub>3</sub>	CIGS
Thickness (nm)	200	50	40-200	500-3000
E <sub>g</sub> (eV)	3.3	3.3	2.1-2.8	1.01 - 1.69
χ <sub>e</sub> (eV)	4.45	4.45	4.65-3.95	4.35 - 3.69
ε <sub>r</sub>	9	9	13.5	13.6
N <sub>c</sub> (cm <sup>-3</sup> )	2.20×10 <sup>18</sup>	2.20×10 <sup>18</sup>	1.80×10 <sup>19</sup>	2.20×10 <sup>18</sup>
N <sub>v</sub> (cm <sup>-3</sup> )	1.80×10 <sup>19</sup>	1.80×10 <sup>19</sup>	4.00×10 <sup>13</sup>	1.80×10 <sup>19</sup>
μ <sub>e</sub> (cm <sup>2</sup> /Vs)	100	100	400	100
μ <sub>h</sub> (cm <sup>2</sup> /Vs)	31	31	210	25
N <sub>D</sub> (cm <sup>-3</sup> )	1.00×10 <sup>20</sup>	1.00×10 <sup>18</sup>	1.00×10 <sup>16</sup> - 1.00×10 <sup>18</sup>	0
N <sub>A</sub> (cm <sup>-3</sup> )	0	0	10	1.00×10 <sup>16</sup> - 2.00×10 <sup>18</sup>
Parameter	ZnO:Al	i-ZnO	In <sub>2</sub> S <sub>3</sub>	CIGS
Type	Donor	Donor	Acceptor	Donor
σ <sub>n</sub>	1.00×10 <sup>-15</sup>	1.00×10 <sup>-15</sup>	1.00×10 <sup>-15</sup>	5.00×10 <sup>-17</sup>
σ <sub>p</sub>	5.00×10 <sup>-13</sup>	5.00×10 <sup>-13</sup>	5.00×10 <sup>-13</sup>	1.00×10 <sup>-13</sup>
Contact properties				
Contact	Mo	ZnO:Al		
SN <sub>0</sub> (cm/s)	1.00×10 <sup>7</sup>	1.00×10 <sup>7</sup>		
SP <sub>0</sub> (cm/s)	1.00×10 <sup>7</sup>	1.00×10 <sup>7</sup>		
φ <sub>m</sub> (eV)	4.95	4.4		
Transmittivity	0.20	0.95		

TABLE II  
Overall sign of CIGS cell material properties

Overall properties	
Bandgap	E <sub>g</sub>
Electron affinity	χ <sub>e</sub>
Dielectric relative permittivity	ε <sub>r</sub>
Conduction band effective density	N <sub>c</sub>
Valence band effective density	N <sub>v</sub>
Electron mobility	μ <sub>e</sub>
Hole mobility	μ <sub>h</sub>
Donor density	N <sub>D</sub>
Acceptor density	N <sub>A</sub>
Capture cross section of electrons	σ <sub>n</sub>
Capture cross section of holes	σ <sub>p</sub>
Surface recombination velocity of electron	SN <sub>0</sub>
Surface recombination velocity of hole	SP <sub>0</sub>
Metal work function,	φ <sub>m</sub>

### III. RESULTS AND DISCUSSIONS

#### A. Effect of CIGS absorber layer band gap

In this study CIGS band gap has varied from 1.01eV to 1.69 eV while other parameters are remain constant. Fig. 2 shows that V<sub>oc</sub> has increased with the band gap and it has

saturated at 0.853 V over the band gap value of 1.42 eV, whereas J<sub>sc</sub> and FF decrease rapidly and efficiency increases for a while then it started to decrease. Photons which are carrying energy larger than band gap, will contribute to electron hole pair formation and remaining photons which are carrying energy lesser than the band gap will be wasted. That's why efficiency has increased for a while with the band gap and then it has decreased after a certain value. The highest efficiency that is obtained from this simulation is 21.297% at 1.10 eV.

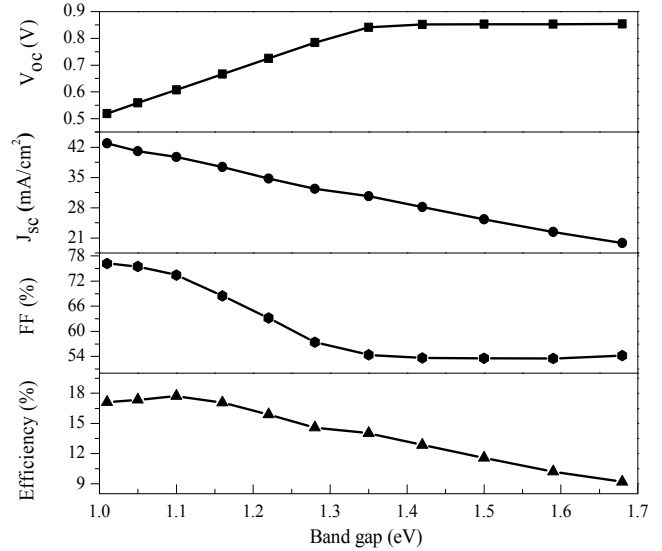


Fig.2. Solar cell electrical parameters with variable CIGS band gap.

Fig. 3 depicts the quantum efficiency of CIGS solar cell with variable band gap. Conduction band is varies with band gap. For a high band gap materials it is much higher compared to a low band gap material. Hence for higher band gap, more photons energy will require to free the electrons. That's why absorption rate is reduced due to higher band gap as well as long wavelengths.

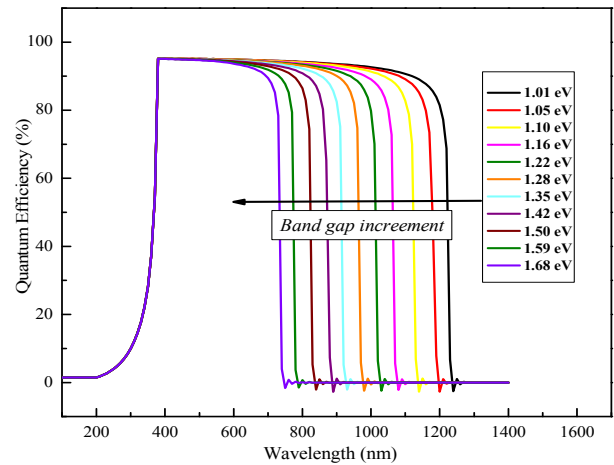


Fig.3. Quantum efficiency with variable CIGS band gap.

#### B. Effect of CIGS absorber layer concentration

In this section, CIGS concentration is varied from 1×10<sup>16</sup> cm<sup>-3</sup> to 2×10<sup>18</sup> cm<sup>-3</sup> and the optimum CIGS band gap 1.01 eV

is set. As we increase the concentration FF,  $V_{oc}$  increases rapidly and  $J_{sc}$  reduces slightly which in turns lead to the rise in efficiency from 17.72% to 23.89% as shown in Fig. 4.

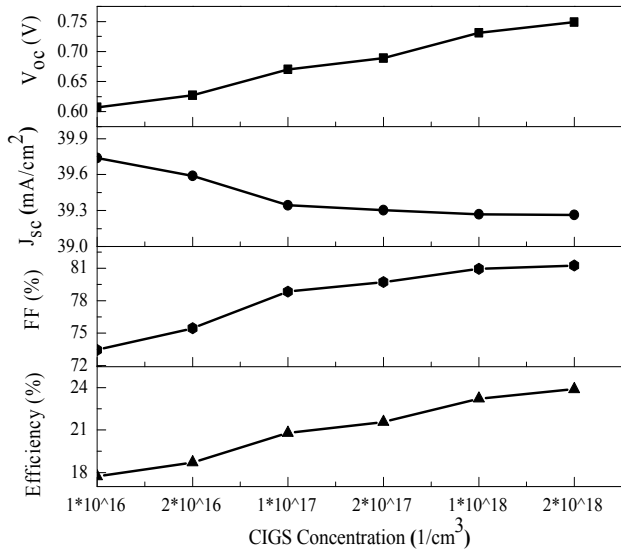


Fig.4. Solar cell electrical parameters with variable CIGS Concentration.

C. Effect of CIGS absorber layer thickness

CIGS solar cell output parameters have shown an upward trend with the rise in thickness as exhibits in Fig.5. Its thickness has varied from 500nm to 3000nm while the CIGS concentration is set  $2 \times 10^{18} \text{ cm}^{-3}$  and other parameters remain same. When the thickness of CIGS absorber layer has increased, more photons will be absorbed here which results growth in  $V_{oc}$ ,  $J_{sc}$ , FF and efficiency. The optimum thickness of absorber layer has found 3000 nm in this simulation.

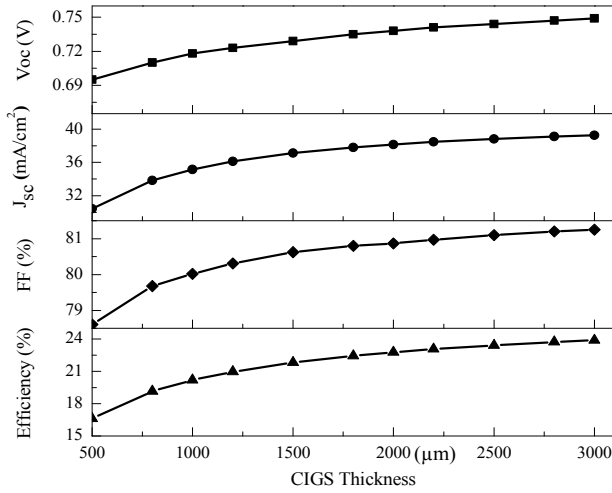


Fig.5. Solar cell electrical parameters with variable CIGS Thickness.

Fig. 6 depicts the quantum efficiency of the solar cell with variable CIGS absorber layer thickness. Thicker absorber layer quantum efficiency is much higher than the thinner one as shown in Fig.6. Because, in thicker absorber layer generation process held very far from back contact while in thin absorber layer it is much nearer to back contact.

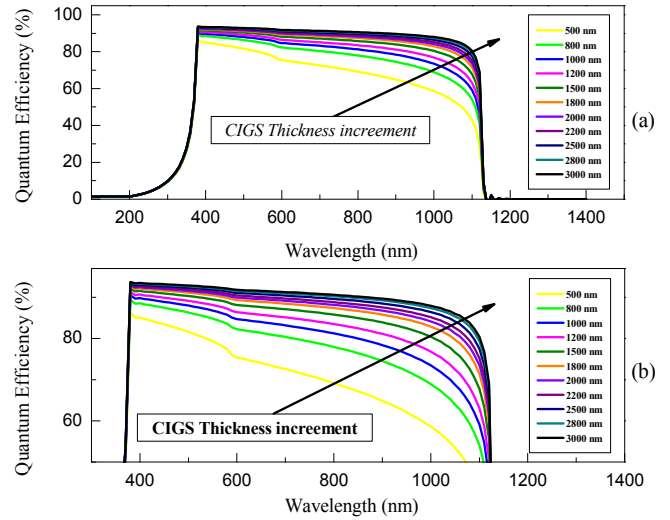


Fig.6. Quantum efficiency with variable CIGS Thickness (a) in full scale (b) in optimized scale.

D. Effect of  $\text{In}_2\text{S}_3$  buffer layer band gap

In this part, the band gap of  $\text{In}_2\text{S}_3$  has been varied from 2.1 eV to 2.8 eV whereas the optimum CIGS thickness is set at 3000 nm.  $V_{oc}$  is plateaued with the rise in band gap and a slight increment in  $J_{sc}$ . However efficiency increases with band gap and peaks at 2.6 eV with 25.03% highest efficiency. This is because of higher bandgap of n-type region will allow maximum number of photons to be absorbed in the absorber layer. Further increment in band gap results reduction in efficiency and with 2.8 eV efficiency reaches at 17.32% as given in Fig.7.

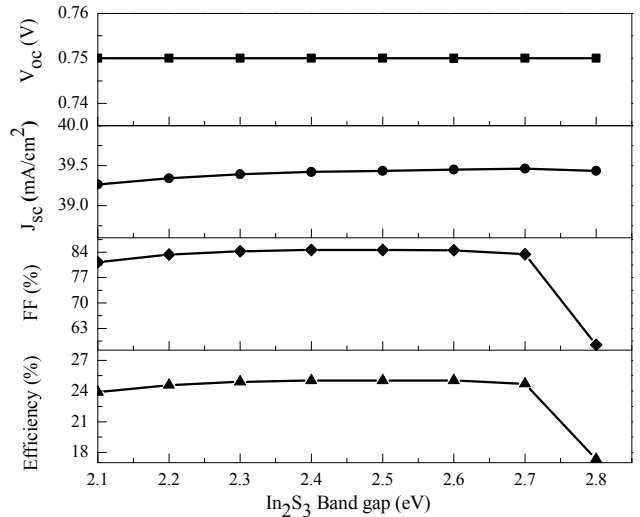


Fig.7. Solar cell electrical parameters with variable  $\text{In}_2\text{S}_3$  band gap.

E. Effect of  $\text{In}_2\text{S}_3$  buffer layer concentration

It can be seen from Fig. 8 on increasing the concentration efficiency rises swiftly. In this section  $\text{In}_2\text{S}_3$  concentration varied from  $1 \times 10^{16} \text{ cm}^{-3}$  to  $1 \times 10^{18} \text{ cm}^{-3}$  and its band gap is set at 2.5 eV. With the rise in concentration  $J_{sc}$  and also FF increases gradually whereas  $V_{oc}$  remain constant at 0.75 V.

#### IV. CONCLUSION

The electrical performances of CIGS solar with variation in band gap, concentration and thickness of both absorber layer and buffer layer has been carried out through numerical analysis.  $\text{In}_2\text{S}_3$  has shown great performances as buffer layer which can be a better substitute of toxic CdS. The optimum band gap of CIGS and  $\text{In}_2\text{S}_3$  layer has detected 1.10 eV and 2.6 eV respectively.  $\text{In}_2\text{S}_3$  thickness increment results fall in efficiency, whereas the opposite scenario has seen in case of CIGS and optimum layer thickness is found 40 nm and 3000 nm accordingly. 25.03% efficiency with 84.62% FF has perceived in  $\text{In}_2\text{S}_3/\text{CIGS}$  solar cell. These results can be helpful to fabricate a desired  $\text{In}_2\text{S}_3/\text{CIGS}$  solar cell. But some other parameters need to be investigated in further studies.

#### REFERENCES

- [1] Theresa Magorian Friedlmeier, Philip Jackson, Andreas Bauer, Dimitrios Hariskos, et al., "Improved Photocurrent in  $\text{Cu}(\text{In,Ga})\text{Se}_2$  Solar Cells: from 20.8% to 21.7% Efficiency," *IEEE Journal of Photovoltaics*, vol. 5, pp. 1487-1491, 2015.
- [2] Martin A. Green, Keith Emery, Yoshihiro Hishikawa, Wilhelm Warta and Ewan D. Dunlop "Solar cell efficiency tables (version 48)," *Progress Photovoltaics journal*, vol. 24, pp. 905-913, 2016.
- [3] Clas Persson, "Thin-film  $\text{ZnO}/\text{CdS}/\text{CuIn}_{1-x}\text{Ga}_x\text{Se}_2$  solar cells: anomalous physical properties of the  $\text{CuIn}_{1-x}\text{Ga}_x\text{Se}_2$  absorber," *Brazilian Journal of Physics*, vol. 36, no. 3B, pp. 948-951, 2006.
- [4] D. Hariskos, S. Spiering, M. Powalla, "Buffer layers in  $\text{Cu}(\text{In,Ga})\text{Se}_2$  solar cells and modules," *Thin Solid Films*, vol.480-481, pp.99- 109, 2005.
- [5] Barreau N, Marsillac S, Bernede J C, Assmann L., "Evolution of the band structure of  $\beta\text{-In}_2\text{S}_3\text{-}3x\text{O}_3x$  buffer layer with its oxygen content," *Journal of Applied Physics*, vol 93, pp, 5456-5459, 2003.
- [6] Barreau N, Bernede J C, Marsillac S, Mokrani A., "Study of low temperature elaborated tailored optical band gap  $\beta\text{-In}_2\text{S}_3\text{-}3x\text{O}_3x$  thin films," *Journal of Crystal Growth*, vol. 235, pp. 439-449, 2002.
- [7] Nomura R, Konishi K, Matsuda H., "Single-source organometallic chemical vapour deposition process for sulphide thin films: Introduction of a new organometallic precursor  $\text{BuIn}(\text{SPri})_2$  and preparation of  $\text{In}_2\text{S}_3$  thin films," *Thin Solid Films*, vol. 198, pp. 339-345,1991.
- [8] D. Hariskos, M. Ruckh, U. Rqhle, T. Walter, H.W. Schock, J. Hedstrfm, L. Stolt, "A novel cadmium free buffer layer for  $\text{Cu}(\text{In,Ga})\text{Se}_2$  based solar cells", *Solar Energy Materials and Solar Cells*, vol. 41-42, pp. 345-353, 1996.
- [9] Naghavi N, Spiering S, Powalla M, Cavana B, Lincot D., "High-efficiency copper indium gallium diselenide (CIGS) solar cells with indium sulfide buffer layers deposited by atomic layer chemical vapor deposition (ALCVD)," *Progress Photovoltaics journal*, vol. 11, pp. 437-443, 2003.
- [10] Shou-Yi Kuoa, Wei-Chun Chena,b, Fang-I Laic, Chin-Pao Chengb, Hao-Chung Kuod, et al., "Effects of doping concentration and annealing temperature onproperties of highly-oriented Al-doped ZnO films," *Journal of Crystal Growth*, vol. 287, pp. 78-84, 2006.
- [11] P. Ranade, H. Takeuchi, T.-J. King, and C. Hu, "Work function engineering of molybdenum gate electrodes by nitrogen implantation," *Electrochemical and Solid-State Letters*, vol.4 (11), pp.G85-G87, 2001.
- [12] M. Burgelman, P. Nollet and S. Degrave, "Modelling polycrystalline semiconductor solar cells", *Thin Solid Films*, vol. 361-362, pp.527-532, 2000.
- [13] A. Bouloufa, K. Djessas, A. Zegadi, "Numerical simulation of  $\text{CuIn}_x\text{Ga}_{1-x}\text{Se}_2$  solar cells by AMPS-1D," *EMRS 2006 Conference Proceedings of Symposium O on Thin Film Chalcogenide Photovoltaic Materials*, vol. 515, issue 15, pp. 6285-6287, 2007.

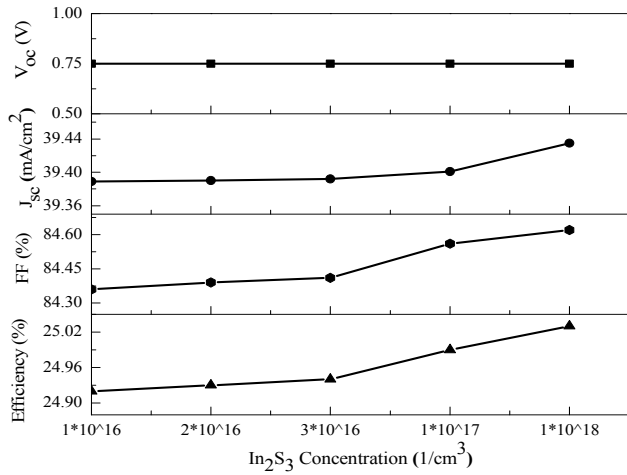


Fig.8. Solar cell electrical parameters with variable  $\text{In}_2\text{S}_3$  Concentration.

#### F. Effect of $\text{In}_2\text{S}_3$ buffer layer thickness

In this section,  $\text{In}_2\text{S}_3$  buffer layer has been varied from 40 nm to 200 nm. Efficiency and  $J_{sc}$  has decreased with rise in  $\text{In}_2\text{S}_3$  thickness, and  $V_{oc}$  remain same at 0.75 V and a slight increment in FF has observed. Due to buffer layer increment, more energy carrying photons will be absorbed in this layer. It will reduce the number of photons which could reach the absorber layer. Hence the efficiency has been decreased from 25.03% to 23.38% as illustrates in Fig. 9. .

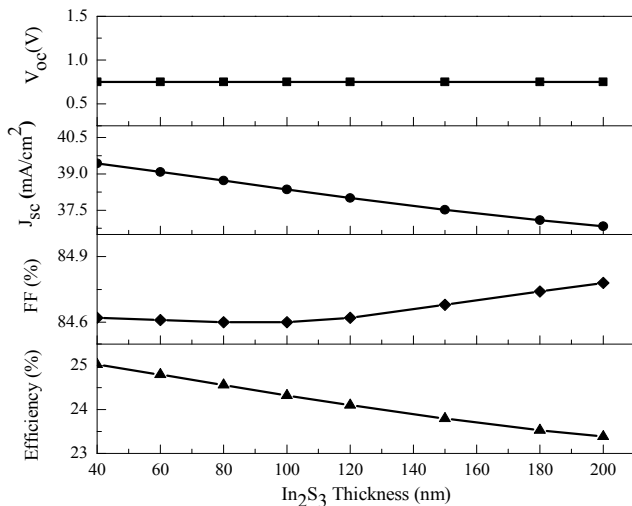


Fig.9. Solar cell electrical parameters with variable  $\text{In}_2\text{S}_3$  Thickness.

$\text{In}_2\text{S}_3$  based proposed CIGS cell efficiency has reached over the previous best efficiency.

TABLE III  
Proposed simulated  $\text{In}_2\text{S}_3/\text{CIGS}$  cell parameters and previous study

	Efficiency (%)	$V_{oc}$ (V)	FF (%)	$J_{sc}$ ( $\text{mA}/\text{cm}^2$ )
Proposed $\text{In}_2\text{S}_3/\text{CIGS}$	25.03	0.75	84.62	39.43
CBD process [8]	15.70	0.59	74.60	35.50
ALCVD process [9]	16.40	0.66	78.00	31.50
AMPS simulation [13]	16.00	0.65	75.20	32.57

# Segmentation Analysis on Magnetic Resonance Imaging (MRI) with Different Clustering Techniques: Wavelet and BEMD

Lamia Iqbal Dolon, Aditi Ghosh, Touhidul Alam, Mohammed Shamsul Alam, Md. Khaliluzzaman\*, Ahmed Imteaj and Mohammad Mahadi Hassan

Dept. of Computer Science and Engineering, International Islamic University Chittagong, Chittagong - 4203, Bangladesh  
lamiaiq04@yahoo.com, aditighosh510@gmail.com, touhid13@gmail.com, alam\_cse@yahoo.com, \*khalil\_021@yahoo.co.in, imtu\_1992@yahoo.com, mahadi\_cse@yahoo.com

**Abstract**— Tumor creates as a lopsided mass of tissues that can be condensed or liquid-filled. It can grow in any part of body. A tumor sometimes can cause to cancer as it will grow in deadly form or sometimes it doesn't mean to be like cancer or like so serious condition. Tumors have lots of names and their name have been categorized by their various shapes and their containing material. This paper is based on the previous works of image segmentation analysis with different techniques like wavelet process and bidimensional empirical mode decomposition (BEMD). For the brain tumor treatment, tumor detection is very important and so for tissue extraction. The artificial brain images have been used for this experiment. By that, the segmentation of noisy MR images has done almost perfectly. As for MR image segmentation for better treatment purpose the previous works on MR segmentation should be acknowledged. By that the most useful algorithm like the previous FCM algorithm can be found and more specific way of noisy image segmentation can also be detect. Gradually from that the new techniques or ways will be explored in future work. By comparing the techniques, a better method can be establish of image segmentation.

**Keywords**—MRI segmentation; fuzzy C-Means; wavelet; BEMD; FCM

## I. INTRODUCTION

By means of position, tumors have been divided into two types: the one is primary position and another is secondary position. At the beginning stage of polyp, it is called primary position. When the polyp extends into the body parts and starts to rise by its own character then the position will be called secondary position. The main cause of brain stroke is the tumor which directly affects the Cerebral Spinal Fluid. Doctors are more concern about the reduction of strokes rather than the treatment of tumors. So for the correct treatment, it is very important to localize the tumor position and study about it for the cure. Transformation based image dispensation has been supported by Fourier transformation and there is a more current revolution which is known as wavelet image transformation. Now it is upgrading itself for more informal to poultice, conduct and study about MRI. Empirical Mode Decomposition is an improved function that is able to gain all known features and time-frequency domain of all non-stationary and non-linear facts and usually it does not exercise any pre-determine filter or wavelet functions.

In pervious, a lot of work has been done over the MRI segmentation using SOMN technique, wavelet, texture

mapping etc. In our paper, we have elucidated on some of the previous work of MRI segmentation field for clarifying the method in an enhanced manner.

## II. SEGMENTATION BY SELF-ORGANIZING MAP NETWORKING (SOMN)

For detection and segmentation of Alzheimer's disease (AD) on the basis of structural information of abnormal and normal tissues, Sampath *et al.* worked on it [1]. For Alzheimer's disease image segmentation, they worked their method using Self-Organizing Map Network. That paper represents adaptive fuzzy inference System (ANFIS) for Alzheimer's Disease MRI image classification. In noisy medical image, they used Fuzzy C-Means (WFCM) algorithm specifically wavelet transformation. For comparing the result, they used Fuzzy C-Means (FCM) and Kernelized Fuzzy C-Means (KFCM) methods. Their system achieved accuracy of classification about 98% and attained almost exact results of segmentation. But as for image segmentation they used Wavelet Fuzzy C- Means (WFCM), which is not always accurate in segmentation. Its accuracy possibility is about 88% in modern technique [1]. So for better segmentation, we have to apply more advance process.

Suchendra *et al.* worked on Segmentation of multispectral MRI. In their work, they focused on the application of the HSOM to the division into segments of multispectral MRI of the humanoid brain. The HSOM outcome is a generalized way which implies to a multi perseverance segmentation of the involvement multispectral MR image. Their results indicate that with an appropriate abstraction tree traversal criterion, it is possible to map different tissue classes to nodes at different levels in the abstraction tree [2]. But they can't show the fine-tuning and more exhaustive testing of the HSOM on anatomically for more diverse MR image sets.

## III. IMAGE PROCESSING BY WAVELET

As for brain tumor segmentation, Alan *et al.* worked in their paper [3] on the basis of Fuzzy C-Means algorithms and K-Means clustering and about its range calculation. Their proposed method has four sections specifically Pre-processing, image segmentation using FCM and k-means, estimated reasoning and ffeatures abstraction. Their proposed method had examined whit clarifying the algorithm. Signal noises

were abridged. They used by their proposed method of fuzzy C-Means and K-Means algorithms. In pre-processing step, it completes sieving of clutter signals and further relies on the input appearance and improving boundaries of the appearance. At the final steps, the polyp area has premeditated by the help of the completion manner by making the dark pixels more darker and snowy pixel perkier. Formally K-means will not be more efficient to locate the brain cells in a mass figures. For any noisy MRI it will be hard to remove for the K-means process.

Noreen *et al.* worked in their paper about MR image segmentation by using Wavelets and Fuzzy C-Means. Their work is based on the image segmentation obtained by MRI, is a challenging task as for the inherent signal noises and inhomogeneity. Their paper represents a method of segmented MR images and that is vigorous in contradiction of noise. Wavelet transformation (DWT) has been applied to MRI image to excerpt great details and after some dispensation on high pass image. The processing that includes the FCM dissection algorithm functional to the Kirch's edge detection mask wavelet transformed image. In paper, they extracted the high filtered image by wavelets and Kirch's edge detection [5]. Usually MR images are dispersed; incorrect brink collection can cause an absconding polyp portion or tab a lot in decent physical forms as polyps [4]. These types of methods are not that much dependable. For human body, it provides improved imagining of soft muscles. But the Discrete DWT is not much effective because the discrete value can miss some important value which may be useful for the survey.

Sindhujal *et al.* worked for wavelet based transformation in [6]. They proposed that the elastography is the developing image segmentation modality that scrutinizes the toughness of the tissue for locating and classifying breast tumors. In breast cancer, for improving the survival rate Computer-aided recognition speeds up the diagnostic process. They also proposed for the breast cancer detection system. In diagnosis of breast cancer, mammography and sonography are mainly used. In the proposed work, wavelet transform is used for exemplifying the consistency topographies since multi-scale image analysis has been offered by the wavelet transform. The combination of feature extraction has been examined by the optimal feature selection algorithm Sequential Floating Forward Selection Algorithm (SFFS). This hints up to 70% to 90% breast surgeries on gentle diseases, leads to uneasiness and apprehension counting redundant outlays to the patients. But in now-a-days there are many modern methods which also effective for these purposes.

#### IV. CLUSTERING FUNCTION:FUZZY C-MEANS (FCM)

A work on medical appearance segmentation by using the combination of Fuzzy C-means clustering and watershed transformation has been done by Kue *et al.* [7]. The new image segmentation technique that combines the watershed and fuzzy C-Means clustering algorithm that proposed to minimize the objectionable section over segmentation. The numbers of region are specially connected group of pixels. Idyllically, the appraised collections are correspondence expressively to the areas of the image. FCM clustering is one of the well-known undersized image segmentation. These paper only worked by fuzzy C-Means algorithm. In these system fuzzy C-Means also divided in different types, which

can easily remove noise. Only fuzzy C-Means may be not efficient for this purpose.

Gupta *et al.* worked on a paper that was on medicinal image segmentation using Fuzzy C-Means (MRI images) [8]. The perspective of their paper was to examine numerous segmentation procedures in the area of medical. The output metaphors are gotten by means of MRI as for detecting tumor and also by using Fuzzy C-Means. Their real motivation was to advance the commutated gained time and classify its efficiency. This method's result had been simulated in MATLAB. In their method, for adjusting thresholding algorithm the fuzzy coding method has been changed in the segmentation process with the combination of clustering.

Mahesh *et al.* suggested a technique for image segmentation by using Fuzzy C-Means Clustering [9]. Their paper represents a review of various technologies used in image segmentation of medical field. Firstly, they talked about Fuzzy C-Means (FCM) algorithm. Secondly, they detailed about Low Depth of Field (DOF). The last method they stated is Self Organizing Map (SOM) algorithm, an important method for medical image segmentation. The technique is separated into two parts. The first part consists of an image from the database and the second part consist of accurately find the main tissue structures in image volumes. In this paper they only introduced with the different techniques but not with the accurate solution process or any implementation process [9]. So this can be only used for introduction to image segmentation techniques.

Thamaraichelvi *et al.* worked on a paper where they focus comparatively analysis, which has three diverse kinds of segmentation techniques [10]. It contains K-Means clustering, Pulse Coupled Neural Network segmentation methods and Fuzzy C-Means clustering. In accordance with the assessment of outcomes, this paper accomplishes that the main downsides of K-Means clustering method are that it stretches high significance of misclassified figures. Subsequently segmentation procedure and likewise it is time consuming than others. However, the PCNN technique has also great assessment of exactness, it has computational complexity and it is also time consuming. It is hoped that their future work will emphasis on refining the dissection accuracy through feature abstraction and encompassing the Fuzzy C-Means bunching segmentation procedure to embrace bias alteration and kernel purposes.

Ravindraiah *et al.* worked on a survey of image segmentation algorithms that are based on Fuzzy C-Means Clustering [11]. On about anatomy, imaging modality provides detailed information. To give a comprehensive reference source which is involved in Fuzzy C-Means based medical image processing is the main purpose of their survey. Fuzzy C-Means clustering used for the inquiry of image input data and edifice models. In those circumstances, fuzzy clustering is superior to durable clustering. Fuzzy C-Means algorithm is extensively used for segmentation process of extrication a digital image that displays dissimilar reasons that have identical possessions such as color, gray level, texture etc. These proposal have tried to develop by fuzzy C-Means, but not with as a fully good survey.

Archana *et al.* proposed a work that compacts with the perception for instinctive brain tumor recognition [12]. The

composition of the brain was observed by the result value of MRI or CT scan. Now-a-days, MRI is a trusted way to know the tested value and for this in their paper they have taken MRI scanned values for the better study of the process. In their paper, fuzzy C-Means and K-Means algorithm was used for dissection. Their anticipated method is in [12]. As they proposed the method using Fuzzy C-Means algorithm and K-Means Clustering but it didn't possible to develop the process in 3D assessment [12].

#### V. ANALYSIS BY TEXTURE

For Classification and Segmentation of Brain Tumor using Texture Analysis Qurat-ul-ain *et al.* focused on this [13]. They proposed the system on bases of image segmentation by the brain tumor diagnosis, which is a very crucial task. Their projected structure contains the numerous stages. Initial phase contains the consistency feature abstraction from brain MR images. On the foundations of texture feature using the base classifier, the next phase categorizes brain images. Afterward, cataloguing polyp section is mined from images are stable as malevolent two phase dissection. Quantifiable outcomes demonstrate their projected method completed competently and precisely. Suggested scheme is almost precise for detecting the tumor location in the brain. The texture feature extraction procedure is used for the resolved method of feature abstraction from brain MRI. Proposed system recycled Cluster Validity which is the technique of appraising quantitatively the fallouts of a clustering algorithm. Texture method is a 2D foundation. It is the backdated method. Now-days it is not that much affected.

#### VI. SEGMENTATION BY EMPIRICAL MODE DECOMPOSITION

There is another paper about empirical mode decomposition which shows solicitations on indicator and appearance handling and this work is done by Jean-Claude Nunes *et al.* [14]. In this paper, they recommend some topical works on data analysis and amalgamation based on Empirical Mode Decomposition (EMD). Firstly, focused on an undeviating 2D extension which stimulates the procedure with solicitation to texture study, and Brownian motion synthesis. Secondly, displayed a logical variety created on PDE in 1D space is accessible. The 2D-sifting process which worked in two steps: first one extrema detection and second one surface interpolation. The Hilbert–Huang transform is applied by them, which consist of two parts: empirical mode decomposition, and the Hilbert spectral scrutiny to texture exploration. The monogenic indicator projected by Felsberg *et al.* is a 2D generalization of the systematic gesture that the Hilbert transform is replaced by Riesz transformation. These native possessions were attained by the edifice multi-vector such as anticipated by Felsberg and Sommer.

Gulam *et al.* proposed a paper on MRI segmentation based on Fuzzy C-Means Clustering and Bi-dimensional Empirical Mode Decomposition. This paper presents an application of Fuzzy C-Means (FCM) bunching by expending wavelet and BEMD mode. Signal to noise ratio (SNR) value is calculated from the previous clustering date to the best segmentation technique. The experiment with synthetic Brain Web images has verified the effectiveness and sturdiness of the methodology in segmenting medical images with noise ratio. The primitive techniques are based on a time consuming manual segmentation which is process besides being

susceptible to human error. Their proposed method is illustrated in [15]. From their method, it is noted that BEMD decomposition approach is better than the wavelet algorithm for the use of decomposition before applying the segmentation algorithm such as FCM. As they used BEMD with wavelet algorithm for future more advance technique its efficiency can be improved more [15].

#### VII. OTHER RELATED WORKS

In [16], Ashour *et al.* worked on Cuckoo search algorithm which is a record transmute founded method. Their work was the base of computed tomography image augmentation with the CS. To appraise numerous ailments such as polyps and vascular abrasions, Computed Tomography (CT) is reflected as a vibrant medical imaging modality. In their exertion, by using log transform in an optimization framework a medical image augmentation algorithm has been proposed. For optimization they used CS algorithm. Their method's enactment is calculated on a lower difference CT image data set. The outcomes obviously indicate that the associated to PSO Cuckoo Search founded method has greater conjunction and suitability ethics as it is a quicker method.

Ourda *et al.* worked with the aim of better segmentation of MR brain real images in [17]. Images of medical sector play a very important role in research. For this reason, they worked for the brain image segmentation which gained from magnetic resonance images. The works have been done by the use of guesstimate and expansion with modalities blending scheme. Their aggregation was performed by merging operatives. To certify their effectiveness, they have tested their method on real MR brain images and they found that modalities fusions have improved the segmentation quality of brain images.

Hussain *et al.* worked in a paper which is based on the Dissection of Brain Tissues by MRI images by applying Dynamic Neuro-Fuzzy System [18]. In that paper, for the precise separation of normal and pathological muscles in the MRI brain images an efficient method is proposed by them. They examined the usual MR images and compulsive tissues such as Edema and Polyp.

Ahmed *et al.* Worked on an MRI based paper and their paper designates a process for instinctive brain polyp separation for the abstraction of polyp skins. With both Perona and Malik anisotropic, it combines dissemination model for input image improvement and K-Means bunching method for assemblage tissues fitting to a precise collection. They used enhanced image and clean image for the better result and they achieved success in a good means [19].

With a fully spontaneous algorithm Roy *et al.* worked to locate brain polyps by spending symmetry inquiry. Here first they locate the polyp position, fragment the tumor and estimate the expense of the polyp. By considering modular and multi-step approaches impersonating, the delinquent of subdividing polyp in MR images can be positively lectured the human visual scrutiny process [20]. The detection of polyps is often an indispensable initial stage to decrypt the separation delinquent definitely.

Landgren *et al.* who worked on a paper based on separation of MR images [21]. They suggested for the segmentation which is a significant assignment in all kinds of

doppelgänger scrutiny. In that paper, a full computer assisted diagnosis system is presented where the aim is to find anomalous scratches in scintigraphy images of the kidneys. The segmentation has done using a region based snake where the data term is determined by virtual image forces derived from the image intensities. Tumors are visible PET images, but it can be difficult to interpret the exact anatomical position in these images. CT images give a better anatomical view and by matching a CT image with a PET image, the location of the tumor can be identified. But it is not effective because the contamination is exaggerated for people, which decreases the density of bones.

### VIII. PROPOSED METHOD

As by reviewing some previous works on image segmentation based on MRI, it is shown that those works had advantages and also with some disadvantages. The main problems of average works are noise problems and are not efficient enough as they used old methods by that time. The proposed method is on the bases of noisy MR images. For better segmentation and for better image result, by the proposed method in future we will compare decomposition techniques between BEMD and Wavelet. As BEMD is a new method on image processing field and a time consuming process. On the other hand, Wavelet is an efficient method for satisfactory output images. By comparing between them the best way of image segmentation with noise will be come out.

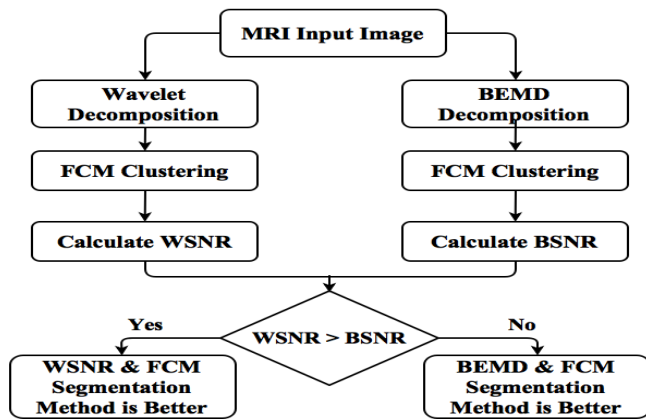


Fig. 1. Workflow of the proposed method.

### IX. CONCLUSIONS

To establish a better technique, we analyzed image segmentation with wavelet decomposition and BEMD. There may be casing in the part of the brain or malevolent completed the intellect. Assume there could be corpus in the brain, at that time Fuzzy C-means procedure is sufficient to citation it from the brain cubicles. If there remains any clamor ratio in the MR image, then it will be detached earlier in the procedure. In our future work, we will focus on the enactment of brain polyp dissection and also will be appraised founded in Fuzzy c-means assembling. The SNR of the segmented image generated from BEMD and FCM will give the higher value for noisy MR Image. So BEMD decomposition approach will be better than the wavelet algorithm for the use of decomposition before applying the segmentation algorithm such as FCM.

### References

- [1] Sampath, R. and Saradha, A., Alzheimer's, 2015. Disease Image Segmentation with SOMN, journal of software, Vol. 5, pp. 670-680.
- [2] Bhandarkar, Suchendra M., and Premini Nammalwar. "Segmentation of multispectral MRI using a hierarchical self-organizing map." In *Computer-Based Medical Systems, 2001. CBMS 2001. Proceedings. 14th IEEE Symposium on*, IEEE, 2001, pp. 294-299.
- [3] Jose, A., Ravi, S. and Sambath, M., 2014. Brain tumor segmentation using k-means clustering and fuzzy c-means algorithms and its area calculation. *International Journal of Innovative Research in Computer and Communication Engineering*, Vol. 2, No. 3, pp.3496-3501.
- [4] Noreen, N., Hayat, K. and Madani, S.A., 2011. MRI segmentation through wavelets and fuzzy C-means. *World Applied Sciences Journal*, Vol.13, pp.34-39.
- [5] Robb, R.A., 1999. Biomedical imaging, visualization, and analysis. John Wiley & Sons, Inc..
- [6] Sindhuja, A. and Sadasivam, V., 2014. Wavelet based segmentation using optimal statistical features on breast images. *ICTACT J. Image Video Process*, Vol. 4, pp.853-857.
- [7] Sawant, H.K. and Vaishali, D.S., 2011. Breast tumor analysis using texture features and wavelet transform with dynamic neural network based training. *J. Inf. Knowl. Res. Comput. Eng*, Vol.1, pp.46-51.
- [8] Chuang, K.S., Tzeng, H.L., Chen, S., Wu, J. and Chen, T.J., 2006. Fuzzy c-means clustering with spatial information for image segmentation. *computerized medical imaging and graphics*, Vol. 30, No.1, pp.9-15.
- [9] Yambal, M. and Gupta, H., 2013. Image segmentation using fuzzy C means clustering: a survey. *International Journal of Advanced Research in Computer and Communication Engineering*, Vol. 2, No. 7.
- [10] Thamarachelvi, B. and Yamuna, G., 2014. APPLICATION OF VARIOUS SEGMENTATION TECHNIQUES FOR BRAIN MRI-A COMPARATIVE STUDY. *International Journal of Advances in Engineering & Technology*, Vol. 7, No. 5, pp.1434.
- [11] Ravindraiah, R. and Tejaswini, K., A Survey of Image Segmentation Algorithms Based On Fuzzy Clustering. *International Journal of Computer Science and Mobile Computing*, Vol. 2, No.7, pp.200-206, 2013.
- [12] Lala, A., Gupta, J.K. and Shringirishi, M., 2013. Implementation on K-means Clustering and Fuzzy C-means Algorithm For Brain Tumor Segmentation. *International Journal of Computer Engineering & Science*, Vol. 3, No. 1, pp.27-33.
- [13] Qurat-Ul-Ain, G.L., Kazmi, S.B., Jaffar, M.A. and Mirza, A.M., 2010. Classification and segmentation of brain tumor using texture analysis. *Recent Advances In Artificial Intelligence, Knowledge Engineering And Data Bases*, pp.147-155.
- [14] Nunes, J.C. and Deléchelle, E., 2009. Empirical mode decomposition: Applications on signal and image processing. *Advances in Adaptive Data Analysis*, Vol. 1, No. 1, pp.125-175.
- [15] Sarowar G., Khaliluzzaman M., Technical Writer's Handbook University Science, pp 23-28, 2015
- [16] Ashour, A.S., Samanta, S., Dey, N., Kausar, N., Abdesslemkaraa, W.B. and Hassanien, A.E., 2015. Computed Tomography Image Enhancement Using Cuckoo1Search: A Log Transform Based Approach. *Journal of Signal and Information Processing*, Vol. 6, No. 3, p.244, 2015.
- [17] Ouarda, A.S.S.A.S., MR Brain Real Images Segmentation Based Modalities Fusion and Estimation Et Maximization Approach. *International Journal of Advanced Computer Science & Applications*, Vol. 1, No. 7, pp.267-273.
- [18] Hussain, S.J., Savithri, T.S. and Devi, P.S., 2012. Segmentation of tissues in brain MRI images using dynamic neuro-fuzzy technique. *International Journal of Soft Computing and Engineering*, Vol. 1, No. 6, pp.2231-2307.
- [19] Ahmed, M.M. and Mohamad, D.B., 2008. Segmentation of brain MR images for tumor extraction by combining kmeans clustering and perona-malik anisotropic diffusion model. *International Journal of Image Processing*, Vol. 2, No. 1, pp.27-34.
- [20] Roy, S., Dey, A., Chatterjee, K. and Bandyopadhyay, S.K., 2012. A New Efficient Binarization Method for MRI of Brain Image. *Signal & Image Processing*, Vol. 3, No. 6, pp.35.
- [21] Hillengass, J., Weber, M.A., Kilk, K., Listl, K., Wagner-Gund, B., Hillengass, M., Hielscher, T., Farid, A., Neben, K., Delorme, S. and Landgren, O., 2014. Prognostic significance of whole-body MRI in patients with monoclonal gammopathy of undetermined significance. *Leukemia*, 28(1), pp.174-178.



# Variation of structural and mechanical properties as 20 wt% ZrO<sub>2</sub> added to Al<sub>2</sub>O<sub>3</sub> for biomedical application

M. Moazzam Hossen <sup>a\*</sup>,

<sup>b</sup> Department of Computer Science & Engineering,  
International Islamic University Chittagong,  
Chittagong 4203, Bangladesh  
E-mail: mhossen65@yahoo.com

F.-U.-Z. Chowdhury <sup>c</sup>,

<sup>c</sup> Department of Physics,  
Chittagong University of Engineering & Technology,  
Chittagong 4349, Bangladesh

S. Nasrin <sup>b</sup>,

<sup>b</sup> Department of Physics,  
University of Chittagong,  
Chittagong 4331, Bangladesh

A. K. M. Abdul Hakim <sup>d</sup>

<sup>d</sup> Department of glass and ceramic engineering,  
Bangladesh University of Engineering & Technology,  
Dhaka 1000, Bangladesh

**Abstract**—Employing slurry method, 20 wt % of ZrO<sub>2</sub> has been prepared by incorporating high purity nanocrystalline  $\alpha$ -alumina powder and sintered at 1600°C for two hours. XRD pattern confirmed the existence of m and t phase of 20 wt % of ZrO<sub>2</sub> compared to pure alumina. The theoretical and bulk density increases with the doping of zirconia, whereas porosity declines with the similar change of zirconia. By using SEM, the surface morphology of the samples has been studied. The effect of zirconia content on hardness and elastic modulus were examined. Maximum hardness and elastic modulus has been observed for pure alumina. Moreover, flexural strength shown increasing trend with the rise of zirconia content. An alternative design of Al<sub>2</sub>O<sub>3</sub>-ZrO<sub>2</sub> composites can be employed for improved structural and mechanical properties for biomedical application rather than using pure alumina at 1600°C.

**Keywords**— Alumina-Zirconia composite; X-ray diffraction; Scanning electron microscopy; Elastic Modulus; Flexural strength.

## I. INTRODUCTION

As Alumina has some outstanding characteristics e.g. high mechanical strength, excellent corrosion, wear resistance and thermal stability, so these properties make this material a prominent candidate for biomedical application. In spite of this alumina has some limitations such as poor fracture toughness or brittleness. To overcome this weakness, many ways have been employed including making it composite materials. To make composite materials, commonly used material is zirconia. By transforming phase, fracture toughness can be enhanced. Depending on the transformation from tetragonal-to-monoclinic, the mechanical properties are changes according to service conditions such as temperature or applied loads. Therefore, to get stable tetragonal phase at room temperature, zirconia needs dopants like yttria or magnesium oxide. In turn, these will converted to monoclinic phase and give volume expansion in the structure along with compressive strain. In addition, fine zirconia particles hinder crack propagation of

the matrix during sintering that advances fracture toughness for a certain extent, as reported elsewhere [1-2, 3].

Moreover, ZTA composites is an essential class of toughened structural ceramics which employ tetragonal to monoclinic martensitic transformation toughening and microcrack toughening and by this technique the strength and toughness have been improved [4-6]. Particle size of Al<sub>2</sub>O<sub>3</sub> and ZrO<sub>2</sub> plays an significant role to achieve required toughening achieved in this composites, as a large fraction of ZrO<sub>2</sub> remained in the metastable tetragonal phase and relative dispersion of Al<sub>2</sub>O<sub>3</sub> and ZrO<sub>2</sub> in the matrix [7]. As the particle size becomes fine to finer, then it improve the possibilities of Al<sub>2</sub>O<sub>3</sub> and ZrO<sub>2</sub> distribution and it also raises the opportunity of ZrO<sub>2</sub> remaining in metastable tetragonal phase [8]. Compare to pure alumina, addition of zirconia in pure alumina remarkably change its mechanical properties.

The current work deals with change of the structural and mechanical properties of Al<sub>2</sub>O<sub>3</sub>-ZrO<sub>2</sub> composites by employing slurry method. Various ZTA composites have been prepared. Phase analysis was done by X-ray Diffraction (XRD) patterns and microstructures were analyzed by SEM. Various Physical properties density and porosity and mechanical properties including microhardness, elastic modulus and flexural strength were examined.

## II. EXPERIMENTAL

### A. Sample Preparation

The raw powders  $\alpha$ - Al<sub>2</sub>O<sub>3</sub> powder and yttria-stabilized ZrO<sub>2</sub> (3 mol %)(Inframat<sup>®</sup> Advanced Materials<sup>™</sup>, USA) that has been used in this work were the nanocrystalline form.  $\alpha$ - Al<sub>2</sub>O<sub>3</sub> powder has crystallite size ~40 nm and particle size ~150 nm and and yttria-stabilized ZrO<sub>2</sub> (3 mol %) has average particle size 30-60 nm. By employing unitary method, 20 wt % of ZrO<sub>2</sub> and related powders were weighed by keeping the total weight same.

To compare the properties of 20 wt % of ZrO<sub>2</sub>

composite, samples of pure  $Al_2O_3$  sample was also prepared. First of all, using zirconia ball as grinding media mechanical milling was done in distilled water for 24 hours in ball milling. The slurry of the powder was dried at  $100^\circ C$  for next one day. Then the dried slurry were crushed to make it in powder form and after it passed through a plastic sieve. For uniform distribution, the powder was handmilled for several hours. Final form of powder was compressed at about 55 MPa with mixing polyvinyl alcohol (PVA) used as binder, in a bar whose dimension is  $5 \times 6 \times 50$  mm. To remove this PVA, green samples were heated in a muffle furnace at  $600^\circ C$  with heating rate  $6^\circ C/min$  for 3 hours. Then, pure alumina and 20% ZTA was sintered at  $1600^\circ C$  in a box furnace for two hours. The heating ramp was  $20^\circ C/min$ . Using the ratio weight/volume, the bulk densities of the sintered samples were calculated. For hardness measurement, this bar was placed longitudinally with a 325 grit-resin bonded diamond wheel at a depth of  $5 \mu m/pass$ . For flexural strength measurement, samples with dimensions  $3 \times 4 \times 35$  mm were prepared.

### B. Measurements

Powder X-ray diffractometry (XRD) technique confirmed Phase identification by employing BRUKER X-Ray Diffractometer (Model D8 Advance) using Cu-K $\alpha$  radiation ( $\lambda = 1.54 \text{ \AA}$ ) as source. With step size  $0.02^\circ$ , scan has been performed from  $20^\circ$  to  $75^\circ$ . Using the following equation, the volume fraction of zirconia ( $V_m$ ) has been calculated:

$$V_m = \frac{I_{(\bar{1}\bar{1}1)_m} + I_{(111)_m}}{I_{(\bar{1}\bar{1}1)_m} + I_{(111)_m} + I_{(111)_t}}$$

Employing actual density of raw powders and their weight percentages by the rule of mixtures, theoretical density  $\rho_o$  of the sample was calculated [9]:

$$\rho_o = \rho_A V_A + \rho_Z V_Z$$

where  $\rho_A, \rho_Z$  are the density and  $V_A, V_Z$  are the volume fraction of  $Al_2O_3$  and  $ZrO_2$  respectively. Here, Values of  $\rho_A = 3.97 \text{ gm/cm}^3$  and  $\rho_Z = 6.10 \text{ gm/cm}^3$  have been used to calculate  $\rho_o$ . Using the following formula, the bulk density  $\rho_b$  has been determined:

$$\rho_b = \frac{m}{\pi r^2 h}$$

Where  $m$  is the mass,  $r$  the radius and  $h$  the height of the sample.

The porosity  $P$  of the sintered sample has been calculated using the following relation:

$$P = \left(1 - \frac{\rho_b}{\rho_o}\right) \times 100\%$$

B Philips XL-30 scanning electron microscopy

(SEM) has been used to investigate microstructures for the samples of different compositions. Mean linear intercept length  $\bar{l}$  has been used to determine the ASTM grain size number,  $G$ , by using the linear intercept method:

$$G = -3.2877 + 6.6439 \log_{10} \bar{l}$$

where  $\bar{l}$  is in millimeters at  $1 \times$  Magnification.

with the help of ASTM C1327-99, hardness was determined [10]. After measuring diagonal length measurement, Vickers hardness (GPa) has been calculated, by using following equation [11, 12]:

$$H_v = 0.0018544 \times \frac{F}{d^2}$$

Where  $F$  is the load in N and  $d$  is the average length of the two diagonals of the indentations in mm.

Using the Dewey-Mackenzie relation, porosity dependent Elastic Modulus can also be measured [13]:

$$E = E_o(1 - 2P)$$

Where  $E$  and  $E_o$  are the effective elastic modulus of the porous composites and the elastic modulus of the dense composites, respectively and  $P$  is the porosity of the sample.

By using three-point bending method (Hounsfield Model H10KS-universal test machine), the flexural strength of the specimen was determined. The flexural strength was calculated from the following equation.

$$\sigma_{flexural} = \frac{3WL}{2BD^2}$$

where  $W$  is the load (N),  $B$  is the width (mm) and  $D$  is the thickness (mm) of the sample.

## III. RESULT AND DISCUSSION

### A. XRD analysis

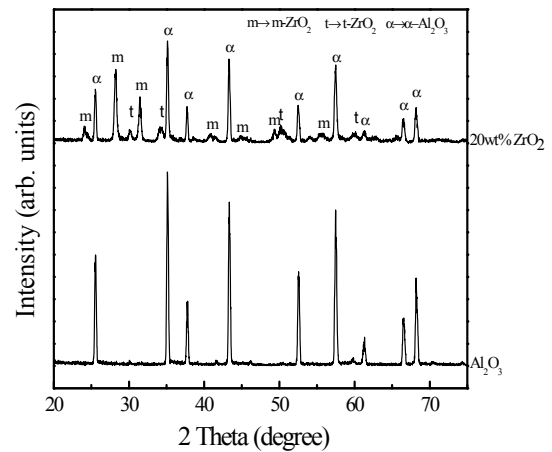


Fig. 1. XRD pattern of  $Al_2O_3$  and 20 wt%  $ZrO_2$  composite sintered at temperature  $1600^\circ C$

From XRD spectra, it has been observed that  $\alpha$  phase is only present in pure alumina, whereas  $\alpha$ -phase, tetragonal and monoclinic phases are present in ZTA composites. It has been seen that in the pure  $\text{Al}_2\text{O}_3$ , m- $\text{ZrO}_2$  phase and t- $\text{ZrO}_2$  phase are absent, while in the 20 wt%  $\text{ZrO}_2$  composite more m- $\text{ZrO}_2$  phase is observed than t- $\text{ZrO}_2$  phase. On the other hand, it is much easier to transform t- $\text{ZrO}_2$  to m- $\text{ZrO}_2$  that dominates transformation toughening. Moreover, the particle size of  $\text{Al}_2\text{O}_3$  and  $\text{ZrO}_2$ , the  $\text{ZrO}_2$  amount remained in the metastable tetragonal phase and the relative distribution of  $\text{Al}_2\text{O}_3$  and  $\text{ZrO}_2$  in the matrix controls the extent of toughening accomplished in the composites[14, 15, 16]. Due to the existence of the hard alumina matrix, at room temperature more monoclinic phase is retained and this phase is responsible for flexural strength that is improved by transformation toughening mechanism.

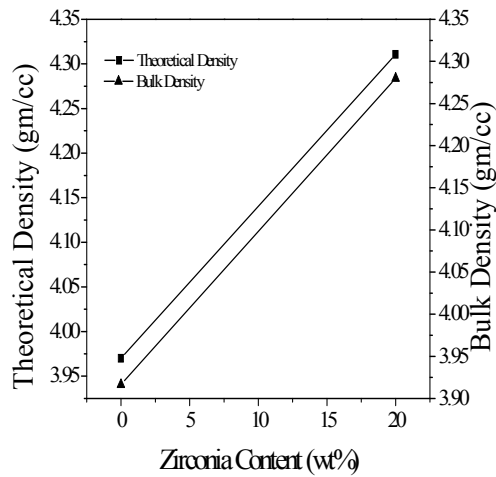


Fig. 2. Variation of theoretical and bulk density of  $\text{Al}_2\text{O}_3$  and 20 wt%  $\text{ZrO}_2$  composite at  $1600 \cdot \text{C}$

The result of density as a function of zirconia content has been shown in Fig. 2. Continuous increase in density is due to existence of  $\text{ZrO}_2$  in the samples. The theoretical density of  $\text{Al}_2\text{O}_3$  is 3.97 gm/cc, whereas that of ZTA composites is around 4.311 gm/cc. therefore the effective density values of the alumina-zirconia increase with increasing  $\text{ZrO}_2$  content and a compact structure is formed than pure alumina. At high temperature such as in  $1600^\circ\text{C}$ , pores are eliminated, instantaneous grain growth takes place with grain boundary diffusion and lattice diffusion, which results more compact materials. Moreover, increasing zirconia content, density increases more linearly than that of pure alumina.[15, 16].

The effect of  $\text{ZrO}_2$  content on the relative density and porosity of ZTA composites has been shown in Fig. 3. It is seen that the porosity is decreased with  $\text{ZrO}_2$  content. It resembles that the composites are in more compressed form at the higher zirconia content. During sintering, diffusion

process is going on and as the intervening porosity diffuses out and it reduces the amount porosity.

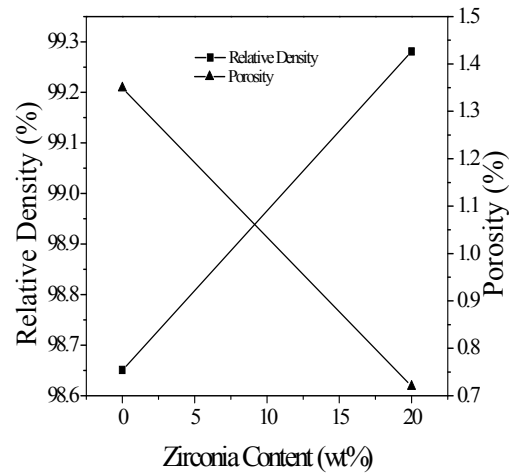


Fig. 3. Variation of relative density and porosity of  $\text{Al}_2\text{O}_3$  and 20 wt%  $\text{ZrO}_2$  composite at  $1600 \cdot \text{C}$

#### B. Scanning electron microscopy

The SEM micrographs of the pure alumina and ZTA composites containing 20 wt%  $\text{ZrO}_2$  at  $1600^\circ\text{C}$  has been shown in Fig. 4. (a)–(b). The grain is coarser of pure  $\text{Al}_2\text{O}_3$  than that of 20% ZTA composites as shown in Fig. 5. (a). From the micrograph, it has been observed that, microstructures are highly homogeneous but contains some agglomerates, pores or abnormally grown alumina grains. In the micrograph, the  $\text{Al}_2\text{O}_3$  and  $\text{ZrO}_2$  grains are distinguished as dark and whitish color respectively. Here alumina grains are surrounded zirconia grains.

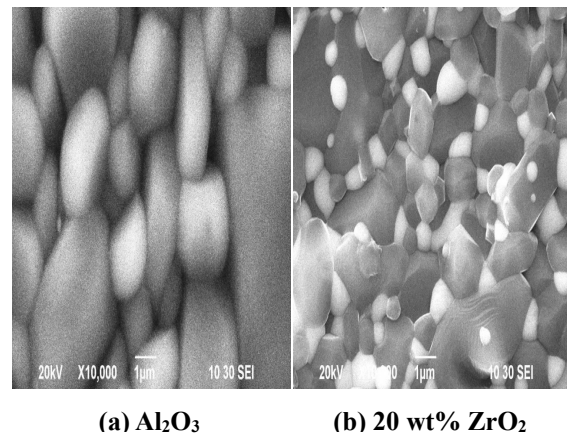


Fig. 4. Microstructure of  $\text{Al}_2\text{O}_3$  and 20 wt%  $\text{ZrO}_2$  composite sintered at temperature  $1600^\circ\text{C}$

According to microstructure, rounding the alumina matrix,  $\text{ZrO}_2$  particles are homogeneously distributed. As  $\text{ZrO}_2$  particles show pinning effect round  $\text{Al}_2\text{O}_3$  particles, so it hinders the growth of  $\text{Al}_2\text{O}_3$  particles. As a result, the grain size of  $\text{Al}_2\text{O}_3$  decreases considerably with the increase of

zirconia content. Moreover, fine  $ZrO_2$  grains perform as grain refiner that make  $Al_2O_3$  grains smaller than before. This in turn increase in density that enhance its mechanical properties. To improve mechanical properties especially for application in dental implant, dense material with fine particle and refined microstructure are essential [15, 16].

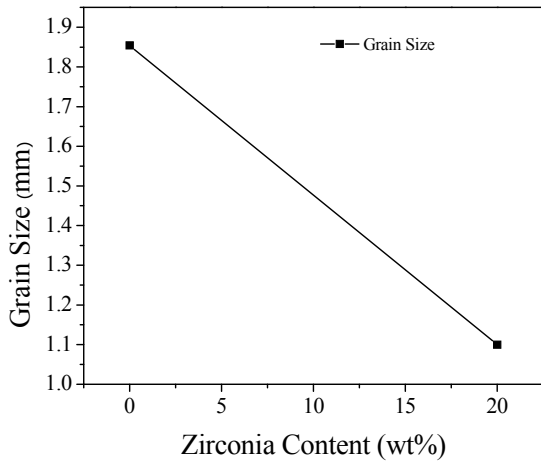


Fig. 5. Grain size of  $Al_2O_3$  and 20 wt%  $ZrO_2$  composite at 1600 °C

It has been seen from Fig. 5. that the grain size of pure alumina and 20% ZTA differ significantly from each other. With the increase of zirconia, then the grain size decline appreciably. By employing linear intercept method, grain size have been calculated that have been found around  $1.85\mu m$  for pure  $Al_2O_3$  and that of  $1.099\mu m$  for 20 wt% of ZTA at sintering temperature 1600°C for 2 hours.

#### C. Hardness and elastic modulus

In Fig. 6, The Vickers hardness of ZTA composites at sintering temperature 1600°C as a function of zirconia content has been shown. As zirconia contains lower hardness than alumina, so it resist the densification of alumina phase. As a result, hardness declines with the rise of  $ZrO_2$  content. In addition, the increase of zirconia content coarses zirconia grain that form subsequent porosity. At 1600°C, maximum hardness shows 19.76GPa, which is observed for pure Alumina. However, at same temperature, minimum hardness shows 11.52GPa, that is observed for 20 wt%  $ZrO_2$ .

The total volume fraction of alumina and zirconia and their modulus of elasticity make the elastic modulus of the composite. By decreasing pore volume fraction in the composite, densification of the composites can be improved that in turn improve modulus of elasticity. As alumina consist higher modulus of elasticity compared to zirconia, so the samples containing pure alumina have the highest modulus of elasticity, whereas samples containing 20 wt% zirconia has

lower levels of modulus of elasticity at 1600°C.

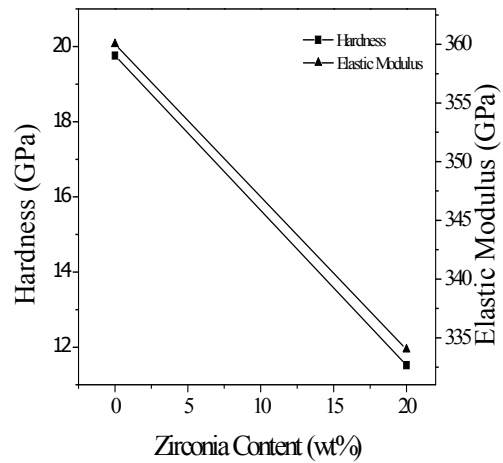


Fig. 6. Variation of Hardness and Elastic Modulus of  $Al_2O_3$  and 20 wt%  $ZrO_2$  composite at 1600 °C

#### D. Flexural Strength

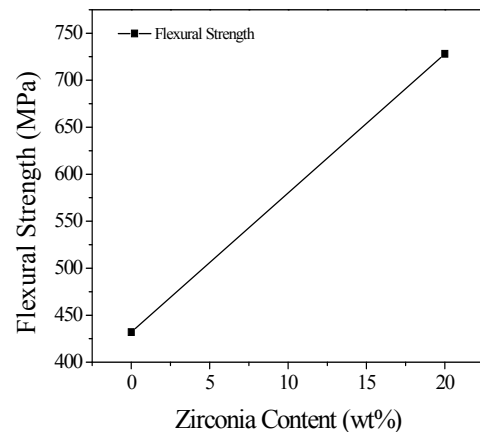


Fig. 7. Variation flexural strength of  $Al_2O_3$  and 20 wt%  $ZrO_2$  composite at 1600 °C

The Flexural strength increases linearly with increasing zirconia content that has shown in Fig. 7. The value of flexural strength was around 432 MPa for pure  $Al_2O_3$  and that of 728 MPa for 20 wt% of ZTA sintered at 1600°C for 2 hours. The variation of flexural strength of  $Al_2O_3$ - $ZrO_2$  composite can be explained by the martensitic transformation and frontal process zone mechanisms. If the grain size is much smaller than critical size, then the stress-induced transformation from tetragonal zirconia to monoclinic zirconia never take place, so it does not show any variation in the value of flexural strength. Typically, in transformation-toughened composites, the role of grain size on flexural strength is a complex phenomenon [15, 16, 17].

#### IV. CONCLUSION

Using slurry method, the Zirconia-toughened alumina (ZTA) composite has been successfully prepared and sintered at 1600°C for 120 min. Structural and mechanical properties are controlled by the addition of zirconia content. From XRD spectra, the phases of  $\alpha$ -Al<sub>2</sub>O<sub>3</sub>, t and m-ZrO<sub>2</sub> in both pure Al<sub>2</sub>O<sub>3</sub> and ZTA composites, respectively was identified clearly. The addition of ZrO<sub>2</sub> increases the density of ZTA composites, while porosity decreases for the same change of zirconia than pure alumina. The microstructures of pure alumina and 20% ZTA composites sintered at 1600°C have been shown in SEM images. It reveals that the grains of pure alumina and 20% ZTA composites are uniform and finer. It is also seen that the grain size of ZrO<sub>2</sub> reduces with the increasing number of ZrO<sub>2</sub> content. Hardness and elastic modulus have been found to be decreased with the addition of ZrO<sub>2</sub>. The flexural strength increases with increasing zirconia content. Increased value of flexural strength of Al<sub>2</sub>O<sub>3</sub>-ZrO<sub>2</sub> composite has been found than that of pure alumina. The value of the flexural strength depends on martensitic transformation and frontal process zone mechanisms. The zirconia addition in pure Al<sub>2</sub>O<sub>3</sub> was found to have a considerable effect on structural and mechanical properties.

#### ACKNOWLEDGEMENT

The authors are thankful to PP and PDC, BCSIR and Materials Science Division, Atomic Energy Centre, Dhaka 1000, Bangladesh, for providing experimental facilities. We also acknowledge the financial support provided by Chittagong University of Engineering and Technology (CUET), Chittagong 4349, Bangladesh.

#### REFERENCES

- [1] Tuan, W.H., Chen, R.Z., Wang, T.C., Cheng, C.H. & Kuo, P.S. Mechanical properties of Al<sub>2</sub>O<sub>3</sub>/ZrO<sub>2</sub> composites. *J. Eur. Ceram Soc.* 22(16), pp. 2827-2833, 2002.
- [2] Sadangi, R.K., Shukla, V. & Kear, B.H.. Processing and properties of ZrO<sub>2</sub>(3Y<sub>2</sub>O<sub>3</sub>) Al<sub>2</sub>O<sub>3</sub> nanocomposites. *Int. J. Refract. Met. H.* 23(4-6), pp. 363-368, 2005.
- [3] Chen, P.L. & Chen, I.W. In-situ alumina/ aluminate platelet composites. *J. Am. Ceram. Soc.* 75(9):pp. 2610-2612, 1992.
- [4] H. Mills and S. Blackburn., et al., "Zirconia toughened aluminas by hydro-thermal processing", *J. Eur. Soc.*, 20, pp. 1085-1090, 2000.
- [5] A. Bleier. and C. G. Westmoreland, et al., "Effects of pH and particle size on the processing of and the development of microstructure in Alumina-Zirconia composites", *J. Am. Ceram. Soc.*, 74, pp. 3100-11, 1991.
- [6] T. Suzuki, Y. Sakka, K. Nakano and H. Hiraga, "Effect of ultra-sonication on colloidal dispersions of Al<sub>2</sub>O<sub>3</sub> and ZrO<sub>2</sub> in pH controlled suspensions", *JIM* 39, pp. 682-689, 1998.
- [7] A. Bleier, P. F. Becher, C. G. Westmoreland and K. B. Alexander, et al., "Effect of aqueous processing conditions on the microstructure and transformation behaviour in Al<sub>2</sub>O<sub>3</sub>- ZrO<sub>2</sub> (CeO<sub>2</sub>) composites", *J. Am. Ceram. Soc.*, 75, pp. 2649-58, 1992.
- [8] R. C. Garvie, et al., "Occurrence of metastable tetragonal zirconia as a crystallite size effect", *J. Phys. Chem.*, 69, pp. 1238-43, 1965.
- [9] P. Bansal, S. R. Choi "Processing of Alumina-Toughened ZrO<sub>2</sub> Composite", NASA/TM -212451, 2003.
- [10] T. Suzuki, Y. Sakka, K. Nakano and H. Hiraga, "Effect of ultra-sonication on colloidal dispersions of Al<sub>2</sub>O<sub>3</sub> and ZrO<sub>2</sub> in pH controlled suspensions", *JIM* 39, pp. 682-689, 1998.
- [11] Maria Cecilia, Carlos Nelson EliasI, Jamil Duailibi FilhoII, Leandra Guimarães de OliveiraIII, "Mechanical properties of Al<sub>2</sub>O<sub>3</sub>- ZrO<sub>2</sub> composites for composite abutments", *Mat. Res.*, Vol. 7, No. 4, pp. 643-649, 2004.
- [12] C. Santos, R. C. Souza, J. K. M. F. Daguano, C. N. Elias, S. O. Rogero, " Development of ZrO<sub>2</sub> -Al<sub>2</sub>O<sub>3</sub> Composite", The 51st Brazilian Congress on Composites, 2007.
- [13] Willi Pabst, Eva Gregorova, Gabriela Ticha, Eva Tynova, "Effective Elastic Properties of Al<sub>2</sub>O<sub>3</sub> - ZrO<sub>2</sub> Composite Composites Part 4. Tensile Modulus of Porous Al<sub>2</sub>O<sub>3</sub> and ZrO<sub>2</sub>", *Composites - Silikáty* Vol. 48, No.4, pp. 165-174, 2004.
- [14] A. Bleier, P. F. Becher, C. G. Westmoreland and K. B. Alexander, "Effect of aqueous processing conditions on the microstructure and transformation behavior in Al<sub>2</sub>O<sub>3</sub> - ZrO<sub>2</sub> (CeO<sub>2</sub>) composites", *J. Am. Ceram. Soc.*, Vol. 75, pp. 2649-58, 1992.
- [15] M. Moazzam Hossen<sup>1\*</sup>, F.-U.-Z. Chowdhury<sup>2</sup>, M. A. Gafur<sup>3</sup>, A. K. M. Abdul Hakim<sup>4</sup>, M. Belal Hossen<sup>2</sup>, "Effect of Zirconia Substitution on Structural and Mechanical Properties of ZTA Composites" *IOSR Journal of Mechanical and Civil Engineering (IOSR-JMCE)*, Volume 11, Issue 2 Ver. 1, pp. 01-07, 2014.
- [16] Moazzam Hossen<sup>1\*</sup>, F.-U.-Z. Chowdhury<sup>2</sup>, M. A. Gafur<sup>3</sup>, A. K. M. Abdul Hakim<sup>4</sup>, S.Nasrin<sup>5</sup>, " Investigation of mechanical properties of Al<sub>2</sub>O<sub>3</sub>-20 wt% ZrO<sub>2</sub> composites as a function of sintering temperature" *European Scientific Journal*, vol.10, No.9, pp. 399-411, 2014.
- [17] G. Orange, G. Fantozzi, P. Homerin, F. Thevenot, A. Leriche, "Thermomechanical Properties of Zirconia-Toughened Alumina Materials: Effect of Microstructure and Temperature on Toughening Mechanisms", *Advances in Composites, Vol24B, Science and Technology of Zirconia III*, Edited by A. Somiya, N. Yamamoto, H. Yanagida, The American Composite Society, Inc. O. H. Westerville, pp. 1075-8, 1988.

# Solar Energy as an Alternative of IPS in Bangladesh

Anis Haque

Department of Electrical and Computer Engineering  
University of Calgary, Calgary, Canada

**Abstract**—The use of IPS in Bangladesh is rapidly increasing because of the shortfall in electricity generation. The entire energy loss by an estimated total number of IPS units would be as high as 46 GWh/year. This paper has proposed an alternative solar system to make it sustainable and cost effective. It compares a stand-alone rooftop solar system and a 100 kWp centrally managed grid-connected system in Chittagong. The technical details of the grid-connected system has been discussed. It also provides a comparison with the same system installed in Berlin, Germany.

**Keywords**—IPS; energy loss; solar energy; energy policy; photovoltaics; grid-connected solar system;

## I. INTRODUCTION

With a 162.9 million populations in Bangladesh, a small saving or wastage by each person in the country may make an enormous impact on the country's economy and overall growth. The country's overall electricity coverage has increased from 55.3% in 2010 to 71.0% in 2015. The current installed capacity of 14.1 GW is still far below the total electricity demand of the area that has access to electricity [1]. The country's energy sector, particularly electrical energy, has to grow exponentially because of the facts: the population growth in Bangladesh is 1.2%, the per capita energy demand is increasing, and the shortfall in electricity generation is still very large. As of 2015, system loss acknowledged by Bangladesh Power Development Board is 13.6% although it is widely accepted that the actual system loss would be higher. The consumers generally add a tremendous number to the bigger picture of system loss as because none of the household equipment or devices operates at 100 % efficiency. However, this might be improved by making high efficiency equipment available and affordable to the consumers and by motivating people to avoid low efficiency equipment. If the 71% electricity users reduced electricity wastage by an equivalent amount of only Tk 1.00 per person per week, the country could save 602 crores taka in one year.

The IPS (Instant Power Supply), one of the increasingly popular household equipment, wastes a large amount of electricity, which could be easily avoided. This would need incorporation of more renewable energy, such as solar, with a visionary energy policy to be adopted by the country.

## II. THE ENERGY WASTAGE IN IPS

An IPS system is primarily a charger, which stores electricity from the grid. When the grid becomes unavailable it supplies the stored energy back to the designated household

loads. The major modules of an IPS are ac to dc converter with step down transformer and rectifier, battery charging unit, dc to ac converter and a step up transformer as shown in figure 1.

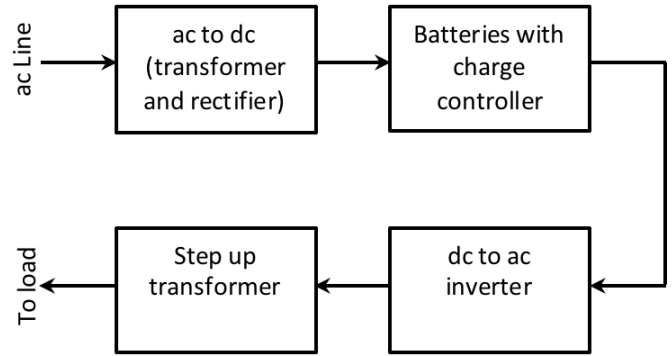


Fig. 1. Major modules in an IPS unit.

Transformer losses include hysteresis loss, eddy current loss and copper loss depend on many other factors [2]. The IPS manufacturers in Bangladesh use different types of transformers. It is noteworthy that in addition to the country's leading IPS manufacturers, these are also made by local technicians without proper specifications and knowledge. The transformers made by the leading manufacturers have an average efficiency of only 86.0%.

Battery performance depends on many factors which include type of batteries, charging-discharging rate, internal resistance, operating voltage, temperature and physical conditions [3,4,5]. The lithium-ion batteries have higher efficiency than the lead-acid batteries and their efficiency ranges vary widely. It is not known what type of batteries are mostly used in the IPS units in Bangladesh. This study assumes that half of the IPS batteries are lead-acid type and the other half are of lithium-ion type. Also, the average efficiency of the lithium-ion batteries is 90.0% and the same for lead-acid batteries is 82.0%. This concludes that an overall efficiency of all the batteries used in IPS units in Bangladesh is 86.0%.

The inverter, that converts dc to ac, has generally higher efficiency. However, that may vary widely depending on the technology used and the manufacturer. Taking the average of some 20 common inverters, the average efficiency of the inverters used in IPS units has been considered 92.0%.

With the above numbers, the overall average efficiency of an IPS unit in Bangladesh is estimated by

$$\eta = 0.86 \times 0.86 \times 0.92 \times 0.86 = 0.585 = 58.5\%.$$

In other words, 41.5% electrical energy loss in each IPS unit. In order to estimate the total energy loss from all the IPS units in the country, let's estimate that: (a) only 2% of the total of

17.8 million households in Bangladesh use an IPS, (b) the average size of all the IPS units is 500 W, which can run 1 TV, 2 fans and 3 tube lights, and (c) that each IPS unit remains functional for 1.0 hour per day. Thus, each 500W IPS unit requires  $(500W/0.585 \times 1h \times 365 \text{ days})$  312 kWh of energy per year from the grid. Based on the above estimates, a total of 356,000 IPS units would require 110 GWh/year of energy. Shockingly, 41.5% of this energy, which is 46.1 GWh/year, is lost. Apart from improving the efficiency of IPS modules through quality research, solar energy could be considered as an alternative in Bangladesh.

### III. SOLAR ENERGY: AN ALTERNATIVE SOURCE

The energy received in one hour of sunshine on the earth's surface is sufficient to meet the annual energy demand of the entire world. A relatively lower conversion efficiency of PV technology makes it difficult to promote. However, use of solar energy instead of IPS would save a significant amount of energy loss, where, unlike the IPS units, the energy from the sun to feed the IPS is absolutely free.

#### A. Solar IPS system

People have thought about 'Solar IPS', where the input of the battery charging unit in figure 1 is solar energy generated by the respective household [6]. Since the PV panels produce dc energy at relatively lower voltages, the first transformer stage in the IPS block diagram is not required. This would increase the overall average efficiency to 68.0% in addition to the free solar energy. The solar IPS system is the same as a stand-alone PV system.

A stand-alone system in Chittagong has been studied using a widely accepted industry level software. A 500W supply to the IPS unit in Chittagong requires 850 Wp to be installed, which is at a performance ratio of 58.8%. Although it sounds promising, there are some major drawbacks of this Solar IPS system. The annual average PSH (Peak Sun Hour) of Chittagong is 5.13. To charge the 500 W IPS this stand-alone solar system would need only an annual average of 1 hour of PSH equivalent sunshine. This means electricity generated by rest of the 4.13 hours of PSH equivalent sunshine, which is 80.5% of the total solar electricity generation, will not be used anywhere as the PV system is connected to the IPS only. It is possible to install much lower than 850 Wp solar panels to ensure the optimal use of available PSH. However, that might not guarantee power availability in some days when the sun would not shine well or an additional storage would be required. Secondly, most of the roofs would be tree covered, creating shading on the solar panel. This would not only reduce the power generation but would create a hot spot [7]. Thirdly, theft, as it is pretty common in Bangladesh, would be a serious issue for the homeowners. In addition, some losses, such as wire loss, for this small scale system would add up largely. Thus, an alternative of the Solar IPS is needed to make the system efficient at large.

#### B. A Central Grid-Connected Solar System

This study proposes a central grid-connected system installed and maintained by the government or the respective

organization in the country. Instead of purchasing IPS the homeowners may invest an equivalent amount of money to a central grid-connected solar system. The investment could be made at different level i.e., 10, 20, 30 kWh/month, and the investors would get credit on their monthly electricity bill based on their appropriate share of investment. If the price of residential electricity is Tk 4.5 per kWh at the higher slab, a homeowner invested 20 kWh/month would receive a credit of Tk 90.00 per month. Such central grid-connected systems could be installed on abundant land such as riverside.

A 100 kWp grid-connected system in Chittagong area was designed to evaluate the annual energy yield by the proposed central grid-connected system. The system was defined as follows.

Solar module used	: 210 Wp at STC
Total number of solar modules	: 476
Module area	: 775 m <sup>2</sup>
Total nominal power	: 99.96 kW
Inverter type	: String inverter
Number of strings	: 34 (in parallel)
Number of modules in series	: 14
Number of inverters	: 18
Tilt angle	: 30° (south facing)
Tracking system	: No tracking (fixed angle)

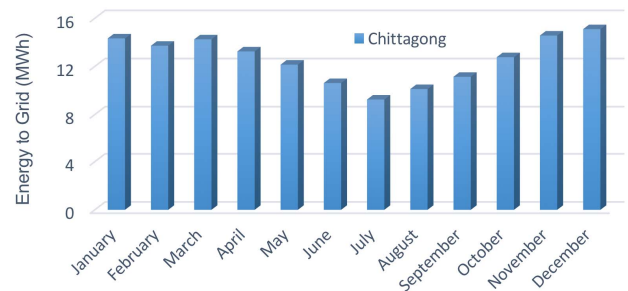


Fig. 2. Available energy to grid produced by a 100 kWp system installed in Chittagong.

As shown in figure 2, the 100 kWp system in Chittagong would supply 151.27 MWh/year of electrical energy to the grid, which translates to 12.61 MWh/month on an average. This amount of energy is equivalent to energy supplied by 829 units of 500W IPS that has been considered in this study. Considering US\$ 2.50/W of total installation cost of a grid-connected system, the cost of the 100 kWp grid-connected solar system would be Tk 1,75,00,000. As a comparison, the price of 829 unit of 500W IPS would be (Tk 31,000 × 829) Tk 2,57,00,000 [8]. It is noteworthy that the IPS units have an average warranty of two years after which most of the batteries, the most expensive component in an IPS, would need to be replaced. On the contrary, the solar system has a life of about 25 years and there is no battery required in a grid-connected system. This suggests that the energy produced by the grid-

connected solar system would be at least ten times cheaper than the energy supplied by the IPS units.

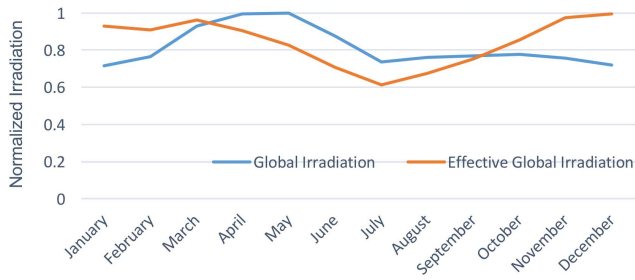


Fig. 3. Normalized global irradiation and effective global irradiation in Chittagong.

It would be interesting to notice in figure 2 that the energy yield in summer is less than the energy yield in winter although Bangladesh is situated in the northern hemisphere. This is because of the fact that the effective global irradiation in Chittagong drops in the summer which is not very common in many locations. The global irradiation is defined as the energy received by a horizontal surface on the ground. It can be expressed in kWh/m<sup>2</sup>. The effective global irradiation drops depending on several factors such as far and near shadings, IAM (Incidence Angle Modifier) and soiling losses. Figure 3 helps understand how the global irradiation and the effective global irradiation in Chittagong vary by month.

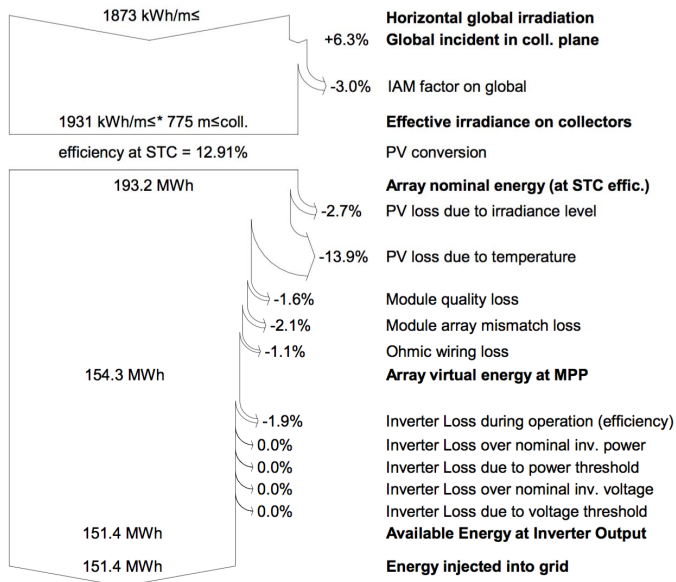


Fig. 4. The loss diagram of the 100 kWp grid-connected system.

In addition, the higher temperature in the summer months largely reduces the effective efficiency of the solar panels. A detail of all losses in the 100 kWp grid-connected system is shown in the loss diagram in figure 4.



Fig. 5. Available energy to grid produced by the same 100 kWp system installed in Berlin.

Germany, the world leader in photovoltaic energy, does not have more potential than what Bangladesh has. In order to make it easily understandable, the energy yield by the same 100 kWp grid-connected system installed in Berlin is presented in figure 5. As seen by comparing this with figure 2, the available energy in Chittagong is much higher than the same in Berlin. The annual available energy in Berlin is 92.6 MWh which is 151.27 MWh in Chittagong. The global irradiation in Germany is less than what is available in Bangladesh. In addition, Germany’s solar energy production is affected by the country’s snowfall in the winter.

#### IV. DISCUSSION AND CONCLUSION

The above sections clearly demonstrate that a grid-connected solar system is more efficient and cost effective than the commonly used IPS system in Bangladesh. In addition, the proposed centrally managed grid-connected system would not suffer from shading. The security of the sites, preventing possible theft, would easily be provided. Maintenance would also be cheaper as it is centrally located. Another great advantage of installing such systems by the river is an increased energy production because of the surrounding sand. All of the above calculations are done with an albedo value of 0.2, which means the surroundings are grass covered. In case of sand, the albedo value would increase to 0.6 or higher. This increases the annual energy production in Chittagong from 151.27 MWh to 154.7 MWh. However, the additional dust coverage may reduce the amount of energy incident on the solar panels. The breakeven point for such system would be 7-8 years.

Realistically, installation of additional solar plants would not provide instantaneous and complete solution to frequent load shedding problem, which is the reason for IPS system becoming increasingly popular in Bangladesh. It will certainly help reduce the country’s shortfall in electricity generation. It is believed that because of the incentive in their monthly



electricity bill, the proposed alternative system would encourage people to accept the consequences of load shedding to some extent. The government may also consider imposing additional taxes on IPS system as because it is a silent but giant killer of the much needed electricity in the grid. This would discourage people to use IPS system. Furthermore, a portion of the lost energy in the IPS system could be credited to the investors in the solar plants.

As of November 2015, the country's total installed capacity of solar energy is 145 MW off-grid. The good news is that the government has a plan to increase the installed capacity of solar plants to 1.74 GW by the year 2021 [1]. The proposed system is believed to help achieve the goal through public participation and by giving ownership. It would also help reduce a giant loss in electricity.

#### REFERENCES

- [1] A presentation by the Government of the People's Republic of Bangladesh at the United Nations Office for Sustainable Development, "A paradigm shift in Bangladesh energy sector towards SDG-7: a few insights of energy statistics in Bangladesh," Incheon, South Korea, Nov 17, 2015. [[http://www.unosd.org/content/documents/14698\\_SDGs-Incheon-2015-Bangladesh.pdf](http://www.unosd.org/content/documents/14698_SDGs-Incheon-2015-Bangladesh.pdf)]
- [2] J. C. Olivares-Galvan, P. S. Georgilakis, and R. Ocon-Valdez, "A review of transformer losses," *Electric Power Components and Systems*, vol. 37, pp. 1046-1052, 2009.
- [3] E. M. Krieger and C. B. Arnold, "Effects of undercharged and internal loss on the rate dependency of battery charge storage efficiency," *Journal of Power Sources*, vol. 210, pp. 286-291, 2012.
- [4] V. Svoboda, H. Wenzl, R. Kaiser, A. Jossen, I. Baring-Gould, J. Manwell, P. Lundsager, H. W. Bindner, T. Cronin, P. B. Nørgård, A. Ruddell, A. Perujo, K. Douglas, C. Rodrigues, A. Joyce, S. Tselepis, N. Borg, F. Nieuwenhout, N. Wilmot, F. Mattera, and D. U. Sauer, "Operating conditions of batteries in off-grid renewable energy systems," *Solar Energy*, vol. 81, pp. 1409-1425, 2007.
- [5] C. J. Rydh and B. A. Sanden, "Energy analysis of batteries in photovoltaic systems. Part II: Energy return factors and overall battery efficiencies," *Energy Conversion and Management*, vol. 46, pp. 1980-2000, 2005.
- [6] BRAC Solar: [www.brac.net](http://www.brac.net)
- [7] H. Patel and V. Agarwal, "MATLAB-based modeling to study the effects of partial shading on PV array characteristics," *IEEE Transactions on Energy Conversion*, vol. 23, pp. 302-310, 2008.
- [8] Rahim Afroz: <http://www.rahimafroz-ips.com/price.html> (as of Aug 08, 2016).

# Design and Simulation of Piezoelectric Cantilever Beam Based on Mechanical Vibration for Energy Harvesting Application

<sup>1</sup>Md. Naim Uddin, <sup>1,2</sup>Md. Shabiul Islam, <sup>1</sup>Jahariah Sampe,  
<sup>1</sup>Institute of Microengineering & Nanoelectronics (IMEN),  
<sup>1</sup>Universiti Kebangsaan Malaysia (UKM) 43600, Bangi, Selangor,  
<sup>2</sup>Multimedia University, 63100 Cyberjaya, Malaysia.

<sup>3</sup>Sawal H. Md Ali  
<sup>3</sup>Department of Electrical, Electronic and Systems Engineering,  
<sup>3</sup>Faculty of Engineering and Built Environment, 43600 UKM Bangi, Selangor, Malaysia.

<sup>4</sup>M.S. Bhuyan  
<sup>4</sup>Department of Computer Science and Engineering,  
<sup>4</sup>Stamford University Bangladesh Dhaka, Bangladesh.

**Abstract**—This paper presents design and simulation of a piezoelectric cantilever beam for energy harvesting using mechanical ambient vibration. Ambient vibration energy used by the developed piezoelectric cantilever beam can be converted into electrical energy using piezoelectric effect as a piezoelectric energy harvester. The piezoelectric cantilever beam was consisted of copper substrate, two piezoelectric layers, and a base. The two piezoelectric layers were placed at the top and bottom faces of the copper substrate. The 3D design of the beam was performed by using SolidWorks. The simulation of the piezoelectric harvester was performed by COMSOL Multiphysics where Finite Element Method (FEM) was used. During the analysis, mechanical and electrical properties of the energy harvester were analysed. In the mechanical properties analysis, maximum vertical displacement of 70.9  $\mu\text{m}$  and maximum stress of  $7.96 \times 10^5 \text{ N/m}^2$  were obtained at resonant frequency of 345.75 Hz. A maximum output power of 14.85  $\mu\text{W}$  and voltage of 595.5 mV was obtained from the harvester at 12.6 k $\Omega$  under the acceleration of 1 g ( $g = 9.81 \text{ m/s}^2$ ) at resonant frequency of 345.75 Hz. This energy harvester can be used for numerous purpose in the field of sensors and wireless sensor networks.

**Keywords**—Energy harvesting, Cantilever beam, Vibration, Piezoelectric effect, Simulation, FEM, Acceleration.

## I. INTRODUCTION

With the boost of advance technology in electronic systems such as wireless sensors, researchers have focused on improvement of smaller volume and durable power sources. Batteries as a conventional power sources has some draw backs due to its higher volume and a limited lifetime [1, 2]. To mitigate the energy sources issue, energy harvesting is an attractive way to extracting energy from environmental renewable energy sources such as wind, solar, geothermal, and tidal [3]. Moreover, ambient mechanical vibration can be recycled to generate electrical energy for wireless sensor networks, chemical sensors [4] and health monitoring [5-7]. Vibration driven energy harvesters efficiently convert vibration energy into electrical energy using three electromechanical transduction processes: electrostatic, electromagnetic, and piezoelectric [1] [8-11]. Among those transduction methods, piezoelectric transducers have attained much attention due to the simplicity in

configuration and higher conversion efficiency [12, 13]. In piezoelectric transduction, there are some piezoelectric materials namely Lead Zirconate Titanate (PZT), Polyvinylidene Fluoride (PVDF), [14] Aluminium nitride (AlN) [5]. When those piezoelectric materials have set under the condition of mechanical energy then electrical energy will be generated and vice versa as shown in Fig. 1. [15].

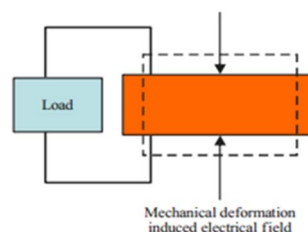


Fig. 1. Piezoelectric effect on piezoelectric materials [15].

Ambient mechanical vibration sources provide lower frequencies ( $< 1000 \text{ Hz}$ ). In order to utilize ambient vibration properly, resonant frequency of piezoelectric energy harvester should be less than the range. Moreover, maximum energy can be harvested efficiently when energy harvester driven at the resonant frequency [16]. Due to flexibility, lower resonant frequency and high stress generation, cantilever beam structure is more preferred. Previous researcher [1] harvested 101 mV and 0.32  $\mu\text{W}$  using a PZT cantilever beam across a resistive load of 16 k $\Omega$ .

In this research work, a cantilever beam was analysed to achieve mechanical properties such as resonant frequency, displacement and stress generation and electrical properties such as voltages and power output. During the analysis SolidWorks was used to design 3D cantilever beam and the FEM simulation was performed using COMSOL Multiphysics. A maximum output power of 14.85  $\mu\text{W}$  and voltage of 595.5 mV was achieved from the harvester at 12.6 k $\Omega$  under the acceleration of 1 g at resonant frequency of 345.75 Hz.

The authors gratefully acknowledge that this study was financially supported by UKM, through the grant funded under GUP 2014-023

## II. PIEZOELECTRICITY THEORY, DESIGN OF THE PZT BEAM AND SIMULATION USING COMSOL OF THE HARVESTER

### A. Piezoelectricity Theory (Piezoelectric Effect)

In piezoelectric mechanism, if piezoelectric material is physically deformed by pressure, vibration or force then it will create induced electrical field. In contrast, if electrical energy is applied then mechanical deformation will induce [15, 17]. The electrical charge density generated by the piezoelectric cantilever can be calculated by using the following piezoelectric constitutive equation.

$$\left. \begin{aligned} S_1 &= s_{11}^E T_1 + d_{31} E_3 \\ D_3 &= d_{31} T_1 + \epsilon_{33}^T E_3 \end{aligned} \right\} \quad (1)$$

Where  $S_1$  and  $T_1$  is the strain and stress in the length direction of the piezoelectric layer;  $D_3$  is the electrical charge density;  $d_{31}$  is the piezoelectric strain constant,  $s_{11}^E$  is the elastic compliance in a constant electric field;  $\epsilon_{33}^T$  is the dielectric constant of the piezoelectric material under constant stress conditions, and  $E_3$  is the electric field developed in the “3” direction [11]. From the equation (1), it is clear that charge density is proportional to the developed stress.

### B. Design of PZT beam

The piezoelectric cantilever beam was designed using SolidWorks as shown in Fig. 2. The cantilever beam structure was consisted of two materials; copper as substrate and PZT-5H as piezoelectric layers. The substrate material was in the middle position while PZT-5H was put top and bottom surface of the substrate. Copper is also used for the base part of the beam. The properties of PZT-5H and copper have been shown in Table I. The dimension (length  $\times$  width  $\times$  thickness in mm) of piezoelectric layers was  $12 \times 2.5 \times 0.03$ . The dimension (length  $\times$  width  $\times$  thickness in mm) of copper substrate was  $15 \times 2.5 \times 0.1$ . After 12 mm from fixed base in length direction, the thickness of the substrate was increased and the thickness of the free end become 0.16 mm. The dimension (length  $\times$  width in mm) of base was  $2 \times 2.5$ . There were two different thicknesses of the base part. The thickness was 0.25 mm at the joint location of piezo-layers and base. The thickness of other side was 0.5 mm. The substrate, piezoelectric layers and base of the beam was assembled using assembly operation in SolidWorks.

### C. Simulation using COMSOL

The designed 3-D model can be imported to the COMSOL Multiphysics in order to analysis its mechanical and electrical properties. In solid mechanics physics, the boundary condition for the beam such as free end, fixed end, applied vibration and damping of the beam materials have been set up. The base part of the beam was kept constant. The rest of the beam was under free conditions. After applying vibration the free part can be displaced. Mechanical damping for both PZT-5H and Copper layers was set 0.001. The applied acceleration vibration sources for the beam was kept 1 g.

During the boundary conditions of electrostatics physics, the top and bottom surface of the piezoelectric layers was used as terminal. The rest two faces of the layers was used as ground. The electrostatics physics was coupled with electrical circuit physics so that electrical response of the beam can be obtained.

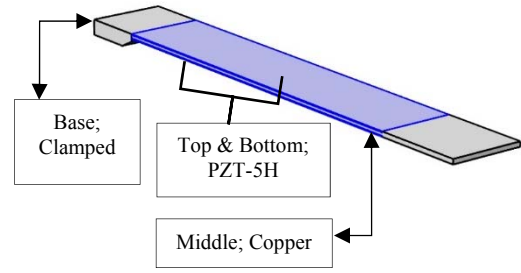


Fig. 2. Bi-layered piezoelectric cantilever beam.

TABLE I. MATERIAL PROPERTIES OF THE PZT-5H AND COPPER

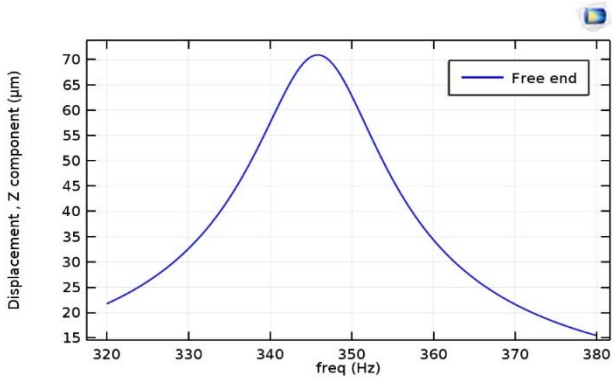
Properties	Materials	
	PZT-5H	Copper
Young's modulus ( Pa )	$62 \times 10^9$	$70 \times 10^9$
Poisson's ratio	0.31	0.33
Density ( kg/m <sup>3</sup> )	7500	2700

After that, tetrahedral mesh with fine element size were used for the discretization of the beam. Eigen frequency analysis was performed to determine eigenvalue of the beam. Finally, three frequency domain analyses were conducted for the cantilever beam and they are frequency dependence, acceleration dependence and load dependence.

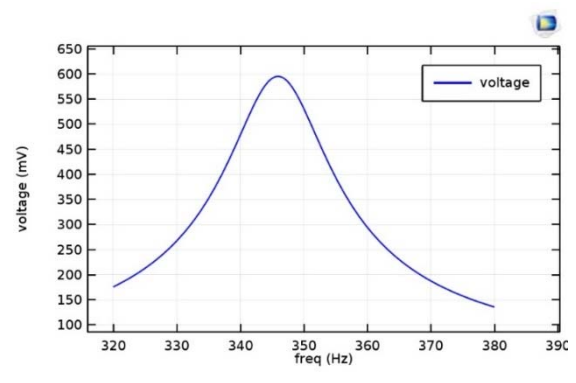
## III. RESULTS AND DISCUSSION

A piezoelectric cantilever beam has been studied to obtain its mechanical and electrical properties. Piezoelectric cantilever beam can be used as an energy harvester. The energy conversion from the mechanical energy to electrical energy will maximum when the piezoelectric cantilever beam will be driven at its resonant frequency. Mechanical properties of the beam such as displacement and stress were analysed with respect to frequency. In the displacement analysis, vertical displacement of the beam was measured in the frequency domain of 320 Hz – 380 Hz as shown in Fig. 3(a). From the figure, it is shown that the free end of the beam was displaced and reached to a peak at 345.75 Hz.

The maximum displacement value was  $70.9 \mu\text{m}$  at the resonant frequency of 345.75 Hz which is shown at Fig. 3(b). After that, the displacement value decreased and reached to a minimum value around  $15 \mu\text{m}$  at 380 Hz. The stress generation in the beam was  $7.96 \times 10^5 \text{ N/m}^2$  at the resonant frequency of 345.75 Hz. The colour contour of von Mises stress is shown in Fig. 3(c). Electrical properties of the beam such as voltage output with respect to frequency range, voltage output with respect to applied acceleration and power output with respect to load resistance was analysed. As the piezoelectric cantilever beam was driven under vibration force, a voltage output can be provided due to piezoelectric effect. The generation of voltage output was analysed in the frequency domain analysis of 320 Hz – 380 Hz at vibration acceleration of 1 g as shown in Fig. 4(a). The voltage generation was obtained around 170 mV at 320 Hz. The value gradually was increasing until it reached maximum of 595.5 mV at resonant frequency of 345.5 Hz. After that the voltage generation was decreasing and reached to a value around

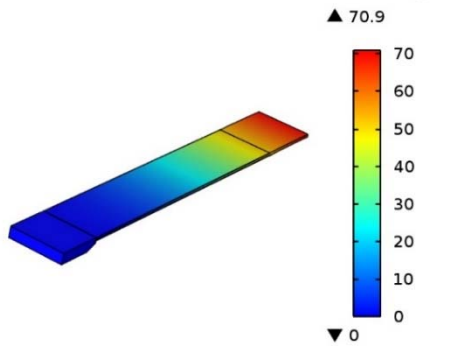


(a)

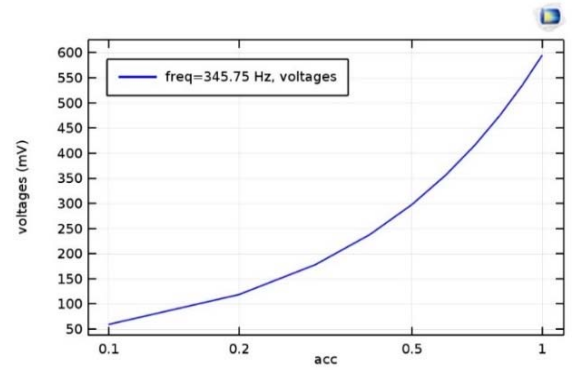


(a)

freq=345.75Hz; Displacement, Z component (µm)

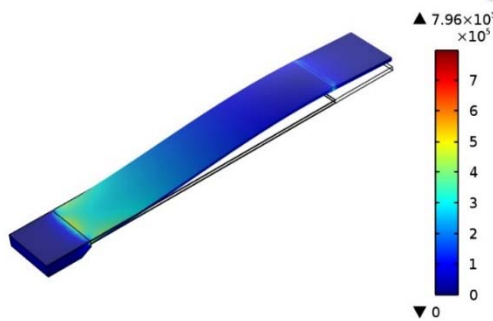


(b)

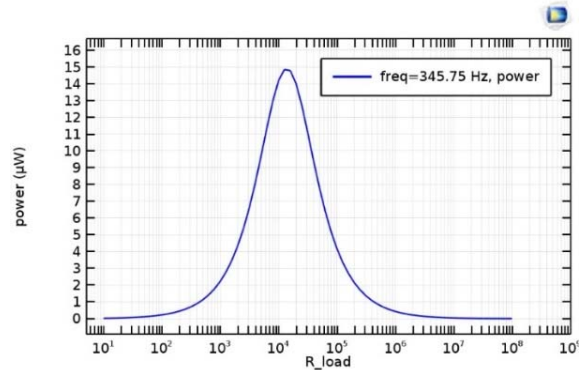


(b)

freq=345.75Hz; von Mises stress (N/m<sup>2</sup>)



(c)



(c)

Fig. 3. Mechanical properties of the beam: (a). Vertical displacement curve of the beam, (b). Vertical displacement contour at resonant frequency of 345.75 Hz, and (c). von Mises stress contour at resonant frequency of 345.75 Hz.

Fig. 4. Electrical properties of the beam: (a) voltage output with respect to frequency range, (b) voltage output with respect to acceleration, and (c) power output with respect to load resistance.

140 mV at the frequency of 380 Hz. The acceleration dependence of the harvester also analysed from 0.1 g – 1 g acceleration as shown in Fig. 4(b). The voltage output was increased with the increasing acceleration. Moreover, the power output was analysed in the load resistance range of  $10^1 \Omega$  -  $10^8 \Omega$  under the acceleration of 1g as shown in Fig. 4(c). The power output was increased by increasing of the load resistance up to 12.6 k $\Omega$ .

A maximum power output of 14.85  $\mu$ W was achieved with a load resistance of 12.6 k $\Omega$  at resonant frequency of 345.75 Hz. After that peak point, power output was diminishing. So the optimal resistive load for the harvester is 12.6 k $\Omega$ .

#### IV. CONCLUSION

In this study, the mechanical properties and electrical properties of a piezoelectric cantilever beam was investigated

under the condition of mechanical vibration. When the vibration acceleration sources of 1 g was applied to the beam, mechanical properties such as resonant frequency displacement and stress was achieved of the beam. The maximum displacement and stress was obtained 70.9  $\mu\text{m}$  and  $7.96 \times 10^5 \text{ N/m}^2$  at resonant frequency of 345.75 Hz consequently. The piezoelectric beam was set up such a way that it provided mechanical vibration energy into electrical energy as an energy harvester. From the harvester, maximum voltage of 595.5 mV power output of 14.85  $\mu\text{w}$  was achieved at 12.6 k $\Omega$  under the acceleration of 1 g at resonant frequency of 345.75 Hz.

## REFERENCES

- [1] D. Shen, J.-H. Park, J. H. Noh, S.-Y. Choe, S.-H. Kim, H. C. Wickle, and D.-J. Kim, "Micromachined PZT cantilever based on SOI structure for low frequency vibration energy harvesting," *Sensors and actuators A: physical*, vol. 154, no. 1, pp. 103-108, 2009.
- [2] F. F. Zulkifli, J. Sampe, M. S. Islam, and M. A. Mohamed, "Architecture of Ultra Low Power Micro Energy Harvester Using RF Signal for Health Care Monitoring System: A Review," *American Journal of Applied Sciences*, vol. 12, no. 5, pp. 335, 2015.
- [3] N. A. A. Semsudin, J. Sampe, M. S. Islam, M. Zain, and A. Rifqi, "Architecture of ultra-low-power micro energy harvester using hybrid input for biomedical devices," *Asian Journal of Scientific Research*, vol. 8, no. 2, pp. 212-224, 2015.
- [4] N. V. Lavrik, M. J. Sepaniak, and P. G. Datskos, "Cantilever transducers as a platform for chemical and biological sensors," *Review of scientific instruments*, vol. 75, no. 7, pp. 2229-2253, 2004.
- [5] Y. Jiang, S. Shiono, H. Hamada, T. Fujita, K. Higuchi, and K. Maenaka, "Low-frequency energy harvesting using a laminated PVDF cantilever with a magnetic mass," *Power MEMS*, vol. 375378, 2010.
- [6] S. Roundy, and P. K. Wright, "A piezoelectric vibration based generator for wireless electronics," *Smart Materials and structures*, vol. 13, no. 5, pp. 1131, 2004.
- [7] Y. Song, C. H. Yang, S. K. Hong, S. J. Hwang, J. H. Kim, J. Y. Choi, S. K. Ryu, and T. H. Sung, "Road energy harvester designed as a macro-power source using the piezoelectric effect," *International Journal of Hydrogen Energy*, 2016.
- [8] M. Bhuyan, B. Majlis, M. Othman, S. H. M. Ali, C. Kalaivani, and S. Islam, "Development of a Fluid Actuated Piezoelectric Micro Energy Harvester: Finite Element Modeling Simulation and Analysis," *Asian Journal of Scientific Research*, vol. 6, no. 4, pp. 691, 2013.
- [9] M. Bhuyan, B. Majlis, M. Othman, S. H. M. Ali, C. Kalaivani, and S. Islam, "Bluff Body Fluid Interactions Modelling for Micro Energy Harvesting Application." p. 012024.
- [10] M. Bhuyan, B. Majlis, M. Othman, S. H. M. Ali, and S. Islam, "Finite Element Analysis of a Fluid Flow Based Micro Energy Harvester," *Research Journal of Applied Sciences*, vol. 8, no. 10, pp. 507-515, 2013.
- [11] L.-j. Gong, X. Shen, and J.-q. Li, "Experimental investigation of energy harvesting from triple-layer piezoelectric bender." pp. 1-6.
- [12] J. C. Park, J. Y. Park, and Y.-P. Lee, "Modeling and characterization of piezoelectric-mode MEMS energy harvester," *Journal of Microelectromechanical Systems*, vol. 19, no. 5, pp. 1215-1222, 2010.
- [13] Md. Naim Uddin, Md. Shabiul Islam, J. Sampe, and M. S. Bhuyan, "Modeling of MEMS Based Piezoelectric Cantilever Design Using Flow Induced Vibration for Low Power Micro Generator: A Review," *Asian Journal of Scientific Research*, vol. 9, no. 2, pp. 71-81, March 15, 2016.
- [14] D. Vatansver, R. Hadimani, T. Shah, and E. Siores, "An investigation of energy harvesting from renewable sources with PVDF and PZT," *Smart Materials and Structures*, vol. 20, no. 5, pp. 055019, 2011.
- [15] C.-Y. Sue, and N.-C. Tsai, "Human powered MEMS-based energy harvest devices," *Applied Energy*, vol. 93, pp. 390-403, 2012.
- [16] J.-Q. Liu, Hua-Bin Xu, Zheng-Yi Mao, Xin-Hui Shen, Xiu-Cheng Chen, Di Liao, Hang Cai, Bing-Chu, "A MEMS-based piezoelectric power

generator array for vibration energy harvesting," *Microelectronics Journal*, vol. 39, no. 5, pp. 802-806, 2008.

[17] Chalasani Sravanthi, and J. M. Conrad, "A survey of energy harvesting sources for embedded systems." pp. 442-447.

# A Comprehensive Study and Performance Based Evaluation on Routing Protocols of WiMAX

Farzana Shabnam\*, Aparna Saha, Rifat Binte Sobhan, Tanmoy Debnath

Department of Electrical & Electronic Engineering, BRAC University  
Dhaka, Bangladesh

fshabnam@bracu.ac.bd

**Abstract**— Worldwide Interoperability for Microwave Access (WiMAX) technology is a subdivision of the vast field of wireless communications, which breaks the restrictions of DSL, cable-modem or T1 infrastructure based wire line of our broadband Internet connections [1]. Wireless networking has become an important area of research in academic and industry. The four high-speed intensive applications such as high-speed data, video, voice and streaming media are being served properly by the WiMAX network, which overcomes the term digital divide. It has a number of spearhead applications with at-home and dynamic internet accessibility along with large geographical coverage and relatively low expense to pursuit. Routing overhead, unidirectional link support, delay, throughput, QoS support and multicast are the analysable terms by whom we can define the WiMAX protocols. To attain best use of this technology selection of suitable protocol is very important. In our paper, most imperative protocols of 802.16 WiMAX network called AODV, DSDV and OLSR is ventilated as well as further criticized in accordance with their performance on WiMAX where AODV is a reactive (on demand) protocol and both DSDV and OLSR are proactive.

## I. INTRODUCTION

Broadband wireless access (BWA) is known as favourable salvation for 'last mile' access technology over cable-modem based connection and IEEE802.16 standard WiMAX serves BWA with a large geographical area, a huge quantity of subscriber and most importantly with maximum possible speed at the same time [1]. WiMAX towers established in different locations of the community consisting of transmitter and receiver, in short transceivers. WiMAX signal are sent back and forth to the towers which are connected to other n<sup>th</sup> devices like computer, mobiles anything that can receive ethernet connection like routers. Further, WiMAX has come to every one of us with many possibilities of using Internet in a cost effective way at the same time having a better Internet experience than the previous DSL, T1 or cable-modem oriented broadband Internet connections. Other great thing about WiMAX is the standard called the mobile WiMAX. By this facility, people on motion can get the access to the same WiMAX connection of intended towers that they all put together in mesh format. WiMAX actually fill in the gaped what we actually have in the DSL, cable and T-1. It also features with a minimum overhead for transmitting data, connection oriented wide area network, huge bandwidth, channel capacity with at most one hundred users with promising connection speed [2]. In addition to that, large ecosystem, low IPR cost, low cost devices, wireless link with microwave, licensed spectrum and point-to-point (P2MP) architecture are the advantages owe by WiMAX. It was initially designed to achieve 30 to 40 megabyte per second data rates where in 2011 it speeded up to 1Gbit/second.

Different protocols of WiMAX are serving different criteria of wireless connections accordingly to improve the routing efficiency and it is required to select a suitable protocol, which will reduce the routing overhead due to rerouting instability problem. The WiMAX protocols are AODV, DSR, DSDV, OLSR, ZRP, LAR, LANMAR, STAR, DYMO, PAODV, CBRP, TORA, ODMRP, CAMP, and CBT so on [1]. Among them, we have selected three routing protocols named AODV, DSDV, OLSR to analyse the few categories like routing overhead, throughput, multicast route, delay etc.

In the section (II), the subsections A, B and C describe the routing mechanism, discovery and maintenance of three different routing protocol: AODV, DSDV and OLSR.

In the following section (III), the factors of analysis are described such as routing overhead process, unidirectional link support, average delay, throughput, QoS support, multicast and reactivity based on which preferable routing protocol should be chosen. At the very last before we conclude in section (IV), a performance comparison between the protocols AODV, DSDV and OLSR is elucidated along with a table. Finally, in section (V), we conclude our paper.

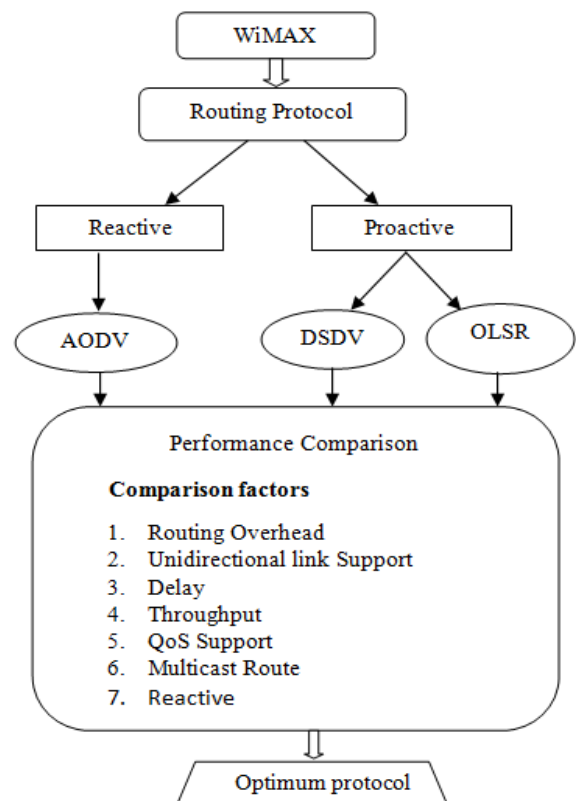


Fig.1 Workflow of the paper

## II. WiMAX ROUTING PROTOCOLS

### A) Ad hoc On-Demand Distance Vector Routing Protocol (AODV):

The reactive routing protocol, AODV is considered as a hop to hop routine approach which is a fusion of on-demand and distance vector. AODV works in accordance with the source and if route discovery is needed by the source, this protocol initiates the process as well as terminates when all routes are evaluated by the source [2].

In order to ensure loop freedom, AODV also comes up with the advantages like low network utilization and destination sequence. It is considered as a reactive protocol signifying that it only search or asking a route when needed and it declines to preserve routes for the inactive nodes.

#### Route Discovery:

While sending packets to completely new destination, source floats a route or path request (RREQ) packets to all the nearby nodes and then they forward to other nodes until the destination node is discovered and the process is called path exploration process [1], [2]. A node sequence number and broadcast ID and a most updated sequence number concerned to the desired end terminal are maintained in the RREQ [2]. In this searching process the initial TTL value got incremented as long as the threshold value is reached. The intermediate nodes establish a reversed path in order to get a brand-new route to the destination and at the same time the nodes unicast a reply (RREP) to the source nodes. Finally, when the RREP arrives at the final source node, source to destination route is established [1].

#### Maintenance:

In an active session, if source node moves, relaunch is possible. At the same time if any in between nodes or destination moves, a route error message (RERR) is auto created and sent to source node following the intermediate nodes. Further propagation decision is taken by the concerned source node whether to reinitiate or terminated [1].

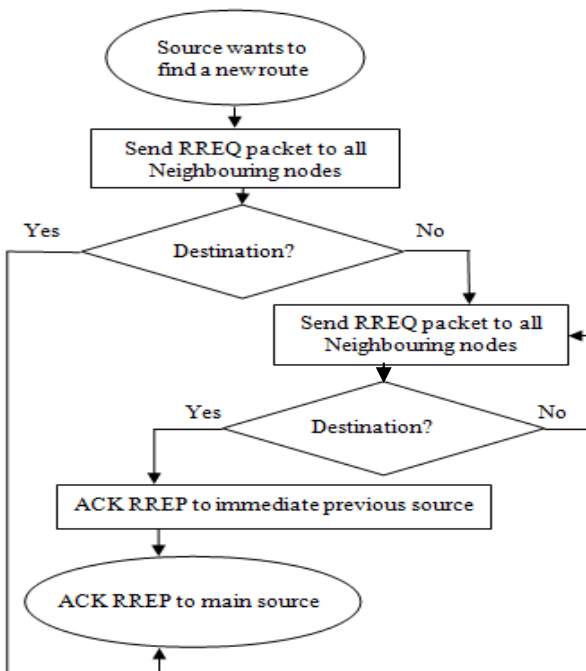


Fig 2 Workflow of AODV Routing Protocol

### B) Destination-Sequenced Distance-Vector Routing (DSDV):

This protocol is a hop-by-hop distance vector routing protocol that wishes periodical broadcast of each node-to-node direction built upon the idea of classical Bellman-Ford routing mechanism [4]. DSDV is a table-driven algorithm that shows routing updates of the analysis of periodical broadcast. This algorithm concerns to the routing loop problem salvation mostly.

#### Route Discovery:

A sequence number is present in the routing table for each entry where could be even or odd. If a link status appeared in the routing table, then the sequence number is considered as even otherwise odd. The destination node creates this sequence number, which is used to transmit the subsequent update by the emitter [3], [5]. Route information is shared among all the nodes by transmitting full dump occasionally and the updates of incremental repeatedly. The reactive routing protocol like DSDV maintains a systematic update in the routing table, which needs the power of a battery and smaller bandwidth even if in the case of idle network. Before the network converges again, a completely new sequence number is essential as per the changes come up in the topology of the network. Thus, this protocol is not compatible for extreme dynamic network.

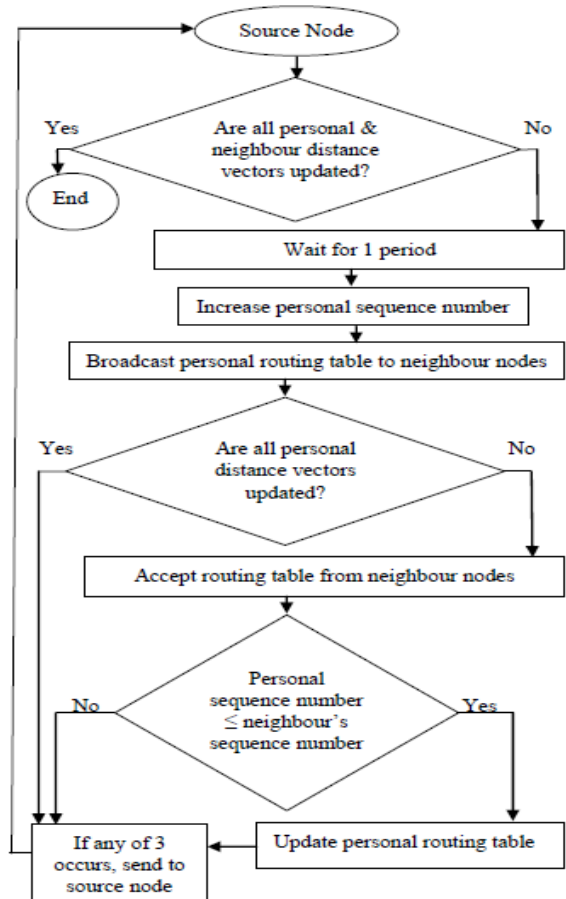


Fig.3 Workflow of DSDV Routing Protocol

#### Maintenance:

DSDV preserves a routing table to reach the destination for each and every source node which contains the information of

the next hop, number of the hops and the sequence number appointed by the destination node. To avoid unnecessary loop formation, the sequence number is there to differentiate the faded routes from the most recent one. The sources always update their immediate neighbours by the periodical transmission of routing table. Further, it also transmits the routing table significant modifications in the table occurs [6]. There are two types of update of the routing table named time-driven and event-driven. Meanwhile the updates can be transmitted in two different ways such as ‘full dump’ and ‘incremental’.

### C) Optimized Link State Routing (OLSR) Routing Protocol:

The proactive routing protocol, OLSR maintains a routing table for all of its nodes. This routing table contains route information of each node which routes are always available in the network when needed. OLSR is also known as pure link state protocol. The three functions of OLSR are packet forwarding, topology determination and sensing neighbor. In the network, information about the neighbor is achieved through packet forwarding and sensing neighbor functions. These functions offer the effective way of flooding the message using Multi-point Relays (MPR). Nodes select MPRs in the whole network system for forwarding the control traffic. The reasons behind the selection of MPRs is to create a route for each of its two-hop neighbor through a node selector. Because of its proactive nature, it exchanges the messages in a periodic way like HELLO and Topology Control messages through MPR. For controlling the overhead of this protocol, OLSR uses some important parameters like HELLO interval parameters, TC interval parameter, MPR coverage parameter and T-C redundancy parameter. Thus, only the small sub sets are declared instead of all links.

#### Route Discovery:

The unidirectional link supporting protocol like OLSR usually transmits two kinds of routing control messages- HELLO and TC (Topology Control) from time to time [6]. One hop neighbourhood data is received by the HELLO message which mentions information about the neighbours as well as link status [1]. Furthermore, it may be broadcasted toward one-hop neighbours with the goal to generate of its own one-hop neighbourhood and two-hop neighbourhood for each node.

In light of that neighbourhood information, every node does a selection of a set of one-hop neighbours. Those selected one-hop neighbour nodes are known as Multi-Point Relay (MPR) where each node gets access to all nodes within its two-hop neighbourhood [1]. The selected MPRs are exposed in the HELLO message so that those nodes could know about their selection. Then, each of the nodes send TC message to state its MPR selectors and MPR advances it all the way through the network. In addition, all of its nodes that point out the final hop to reach the destination [6] build a topology table. Subsequently, a routing table is built and updated proactively based on the topology table and lowest metric.

#### Maintenance:

The intervals of sending HELLO and TC message are the parameter to determine the performance of OLSR. If the interval is overlong, the multicast route and QoS supporting protocol like OLSR takes additional time to identify the

breakdown of the route and re-launch new route. Moreover, data packet that is sent through the broken path or route can be lost [6]. On the contrary, when the interval is short, a quicker adjustment to alterations is attained with the cost of enhanced routing control overhead. Again additional routing control message indicates that because of congestion few HELLO and TC will be lost. However, OLSR might infer this incorrectly as degrading link quality. Performance degradation can be caused by this wrong analysis [6].

Fig.4 mainly describes the control of the network. Based on the control of the network, Source node can send any data to the destination.

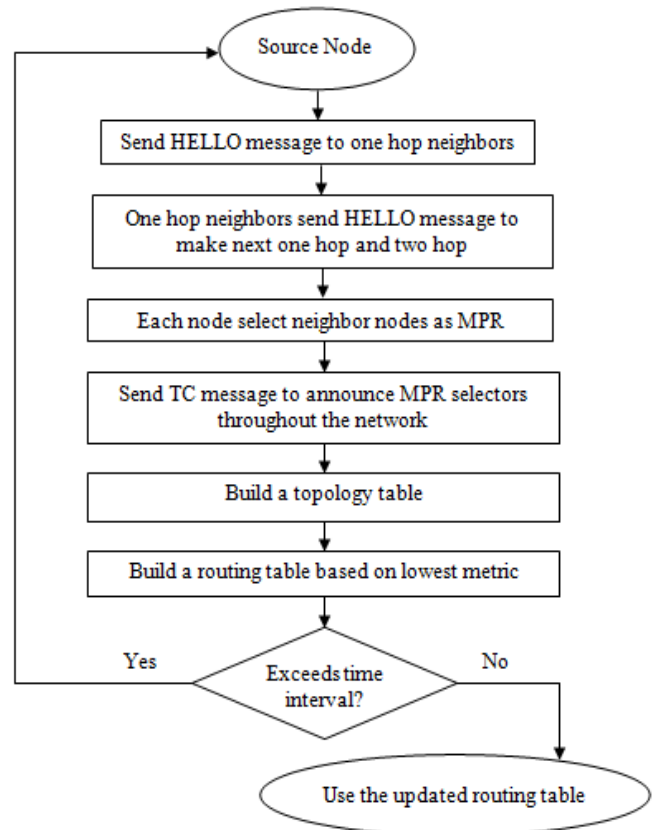


Fig.4 Workflow of OLSR Routing Protocol

### III. FACTOR OF ANALYSIS

**Routing Overhead:** Routing algorithms auto generates very small size packets to get the up-to-date information about network routes. For examples, to know whether the neighbour is active or not a ACK packet is sent known as routing packet which is considered as a routing overhead. In any routing protocol, the lesser the routing overhead the more efficient protocol it is.

**Unidirectional Link Support:** Unidirectional Link Detection is a protocol of Layer 2 (Data Link Layer) which is used to prevent Layer 2 loops. It works with Layer 1 mechanisms to determine the physical configuration of the cables and detect unidirectional links. In order for this protocol to work, both neighbouring devices must support the protocol and on respective ports it must be enabled. It complements the Spanning Tree Protocol, which is used to remove switching loops. Before forwarding loop is created, the protocol detects the unidirectional links. Auto-negotiation looks after physical signalling and fault detection at Layer 1. Unidirectional Link Detection does other tasks that auto-negotiation cannot do like



detecting the identities of neighbours and shutting down misconnected ports. When both auto-negotiation and unidirectional Link Detection are enabled, Layer 1 and 2 work together to prevent physical and logical unidirectional connections and the malfunctioning of other protocols.

**Average Delay:** The time interval for an intact message to reach the destination node successfully from the source is called average delay. The term delay usually depends on many other factors for instance Propagation Time (PT), Queuing Time (QT), Transmission Time (TT) and Processing Delay (PD) [6].

**Throughput:** It estimates how a data can be send node-to-node direction throughout the network. In a communication channel throughput measures the average rate of successive message delivery [6].

**QoS Support:** Quality of service (QoS) represents the overall performance for telephony or computer network. It has become an important consideration for supporting various network applications. Particularly it refers to the performance seen by the users of the network. The network applications can be voice over IP, multimedia services such as video streaming or conferencing and many more. Quality of service is used as a key element in designing the WiMAX medium. By using QoS mechanisms, network administrators can monitor network resources effectively which ensures the required level of network services. QoS ensures desired services by ensuring sufficient bandwidth, controlling latency and jitter and reducing data loss.

**Multicast:** Multicast routing is a way in which data is distributed by multicast IP routing protocols to many recipients. For example, audio or video streaming is broadcasted by multicast IP routing protocols. In this process, a source sends a single copy of data to a single multicast address and it is distributed to an entire group of recipients afterwards.

#### IV. COMPARISON

In terms of the capability of controlling the connection through periodic exchange of information, AODV is considered the foremost. The performance of DSDV is better in case of the mobility ratio and the speed of movement just like DSR. OLSR continuously updates the routes in the routing table as this protocol is effective for traffic patterns. In case of traffic pattern, a huge subset of nodes are communicating with the other subset and changing the pairs [source, destination] over time. In case of overhead, DSDV requires higher number of routing overhead packets while transmitting than the other two protocols. OLSR has the lesser number of routing overhead than DSDV but higher than AODV. In the different scenarios of mobility, OLSR always maintains the updates of the link status through MPR which reduces the routing overhead. With higher number of nodes, AODV functions better than DSDV. In real time traffic AODV is more desirable over DSDV. The performance of DSDV is the best in case of less number of nodes and mobility. The OLSR routing protocol works most efficiently in the dense system network. In terms of delay, AODV works efficiently in the dense network whereas average delay is high

in DSDV and OLSR demonstrate less delay than AODV due to their proactive manner.

TABLE 1  
Comparison between different parameters of AODV, DSDV and OLSR

Parameter	AODV	DSDV	OLSR
Routing Overhead	Low	Higher	High
Unidirectional Link Support	No	No	Yes
Delay	Higher	High	Low
Throughput	High	Higher	Low
QoS Support	No	No	Yes
Multicast Route	No	No	Yes
Reactive	Yes	No	No

#### V. CONCLUSION

WiMAX is for everyone and it goes everywhere. That means the four high speed intensive applications like as high speed data, video, voice and streaming media are served properly by the WiMAX network which overcome the term digital divide. This paper is a survey on the different routing protocols of WiMAX and will be a guideline for the future researchers in this field. The three of the most intelligent protocols of WiMAX AODV, DSDV and OLSR have been discussed here, as these are the most on demand routing protocol. As stated by those, DSDV protocol has the best performance according to their internal mechanism and it changes information periodically. AODV perform better than OLSR. Then again, DSDV and OLSR have more end-to-end and has high packet delivery ratio than the other two. DSDV has the higher pdf in mobility. Based on the above details, differences, scenario, parameters, flowchart maintenance, assumption and result AODV can be considered as the fastest efficient routing protocol.

#### REFERENCES

- [1] Anwar, F., Azad, M., Rahman, M., & Uddin, M. M. (2008). Performance Analysis of Ad hoc Routing Protocols in Mobile WiMAX Environment. *IAENG International Journal of Computer Science*, 35(3). Available: [http://www.iaeng.org/IJCS/issues\\_v35/issue\\_3/IJCS\\_35\\_3\\_13.pdf](http://www.iaeng.org/IJCS/issues_v35/issue_3/IJCS_35_3_13.pdf), [July 21, 2016 ]
- [2] Rasheed, M. R., Khan, M. K., Naseem, M., Ajmal, A., & Hussain, I. M. (2010). Performance of routing protocols in WiMAX networks. *International Journal of Engineering and Technology*, 2(5), 412
- [3] Perkins, C. E., & Bhagwat, P. (1994, October). Highly dynamic destination-sequenced distance-vector routing (DSDV) for mobile computers. In *ACM SIGCOMM computer communication review* (Vol. 24, No. 4, pp. 234-244). ACM.
- [4] L. R. Ford Jr. and D. R. Fulkerson, *Flows in Networks*, Princeton Univ. Press, 1962.
- [5] Boukerche, A. (2004). Performance evaluation of routing protocols for ad hoc wireless networks. *Mobile Networks and Applications*, 9(4), 333-342.
- [6] S.Mohapatra, P.kanungo."Performance analysis of AODV, DSR, OLSR and DSDV routing protocols using NS2 simulator" in international conference on communication technology and system design 2011 (vol.3 0,pp.69-76)
- [7] Kong, P. Y., Wang, H., Ge, Y., Ang, C. W., Wen, S., Pathmasuntharam, J. S., ... & Dien, H. V. (2008, March). A performance comparison of routing protocols for maritime wireless mesh networks. In *2008 IEEE Wireless Communications and Networking Conference* (pp. 2170-2175). IEEE.

# Enhancement the Performance of Molybdenum Telluride Solar Cells with Zinc Telluride BSF

Mrinmoy Dey<sup>1,2\*</sup>, Maitry Dey<sup>3</sup>, M. A. Matin<sup>1,2</sup> and Nowshad Amin<sup>4,5</sup>

<sup>1</sup>Department of Electrical and Electronic Engineering, Chittagong University of Engineering and Technology, Chittagong-4349, Bangladesh

<sup>2</sup>Renewable Energy Laboratory (REL), Chittagong University of Engineering and Technology, Chittagong-4349, Bangladesh

<sup>3</sup>Department of Electrical and Electronic Engineering, Premier University, Chittagong-4203, Bangladesh

<sup>4</sup>Solar Energy Research Institute (SERI), The National University of Malaysia, 43600 Bangi, Selangor, Malaysia

<sup>5</sup>Department of Electrical, Electronic and Systems Engineering, The National University of Malaysia, 43600 Bangi, Selangor, Malaysia

\*mrinmoycuet@gmail.com

**Abstract**—The binary semiconductor compound Molybdenum telluride ( $\text{MoTe}_2$ ) is For high efficiency and better thermal stability, Molybdenum telluride ( $\text{MoTe}_2$ ) is considered as potential solar cell. AMPS (Analysis of Microelectronic and Photonic Structures) simulator is used to investigate the cell performance parameters for ultra-thin  $\text{MoTe}_2$  PV cell. In this research work, it has been explored that the cell conversion efficiency of  $\text{MoTe}_2$  PV cell is improved with the insertion of Zinc Telluride ( $\text{ZnTe}$ ) as back surface field (BSF) above the back contact metal. The highest conversion efficiency of 25.29% was found for  $\text{ZnTe}$  BSF with only 0.7  $\mu\text{m}$  of absorber layer whereas it was 17.06% for no BSF with 1  $\mu\text{m}$  thickness of absorber layer. The thermal stability of  $\text{MoTe}_2$  PV cell with  $\text{ZnTe}$  BSF showed better stability.

**Keywords**— Thermal Stability, Ultra-thin,  $\text{MoTe}_2$ , Photovoltaic cell, AMPS,  $\text{ZnTe}$  BSF.

## I. INTRODUCTION

Molybdenum Ditelluride ( $\text{MoTe}_2$ ) is commonly known as Molybdenum Telluride and it is considered by the researchers as potential candidate for cost effective, highly efficient, stable PV cells and green energy for thin film technology in earth. Subsequently, some research groups are doing extensive research work to explore the hidden potentiality on  $\text{MoTe}_2$  PV cells. The binary semiconductor material  $\text{MoTe}_2$  has direct band gap 1.1 eV and the work function is 4.7 eV [1]. The percentage of mass distribution for  $\text{MoTe}_2$  material is 27.32% molybdenum (Mo) and 72.68% tellurium (Te).

The higher performance of PV cell, preservation of absorber layer material and better thermal stability are the challenges for  $\text{MoTe}_2$  PV cell research work. During the production of efficient  $\text{MoTe}_2$  PV cells, tellurium pressure or

vapour is often play significant role. In this study, Cadmium Sulphide (CdS) window layer is selected with  $\text{MoTe}_2$  as absorber layer to form CdS/ $\text{MoTe}_2$  PV cells. In this research work, the possibility of ultra-thin  $\text{MoTe}_2$  PV cell is investigated with the addition of potential BSF layer at the back contact for higher performance and better cell stability. Many research groups are researching extensively on CdTe solar cells to explore the hidden potentiality by the insertion of back surface field between the absorber layer and back contact metal. The performance of CdS/CdTe solar cell is improved through adding  $\text{ZnTe}$  BSF discussed by Dey et. al [2],  $\text{ZnTe}$  BSF as discussed by Dey et. al [3], GeTe BSF as discussed by Dey et. al [4], PbTe BSF as discussed by Matin and Dey [5] and SnTe BSF as discussed by Dey et. al [6]. The insertion of suitable BSF layer placement between the back contact and absorber layer in the proposed cell showed better performance to design this ultra-thin high performance  $\text{MoTe}_2$  PV cell.

In this research work, numerical analysis is done by well known AMPS simulator to examine the performance of ultra-thin CdS/ $\text{MoTe}_2$  cell structure with  $\text{ZnTe}$  BSF layer to explore the hidden potentiality of  $\text{MoTe}_2$  PV cells with improved cell performance parameters. Both the higher cell conversion efficiency (25.08%) and better thermal stability were achieved in the modified proposed cell structure ( $\text{SnO}_2/\text{Zn}_2\text{SnO}_4/\text{CdS}/\text{MoTe}_2/\text{ZnTe}/\text{Ni}$ ) with less than 1  $\mu\text{m}$  of absorber layer.

## II. MODELING AND SIMULATION

To represent the complicated system in a simplified mode, PV cell model is supportive by avoiding the non useful features. Consequently, all the significant parameters are considered and the non important ones are ignored, then a good model can be constructed for analysis. AMPS-1D

simulator is widely used more than 200 research groups for designing PV cell structure [7]. The conventional structure of CdS/MoTe<sub>2</sub> PV cell is shown in Fig. 1 for numerical analysis to investigate the different parameters of cell performance.

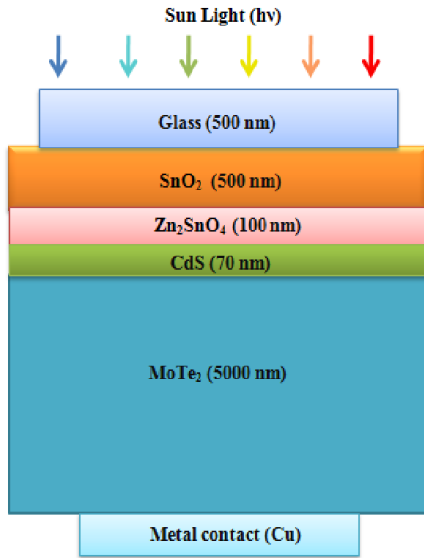


Fig.1 Modeling of conventional MoTe<sub>2</sub> PV cell

In this research work, the model of conventional MoTe<sub>2</sub> PV cell consists of Stannic Oxide (SnO<sub>2</sub>) as TCO (Transparent conducting oxide) layer, Zinc Stannate (Zn<sub>2</sub>SnO<sub>4</sub>) as buffer layer, CdS as window layer and finally MoTe<sub>2</sub> as absorber layer. The hidden potentiality of CdS/MoTe<sub>2</sub> cell structure can be explored by adding the potential ZnTe BSF layer in between absorber layer and back contact metal.

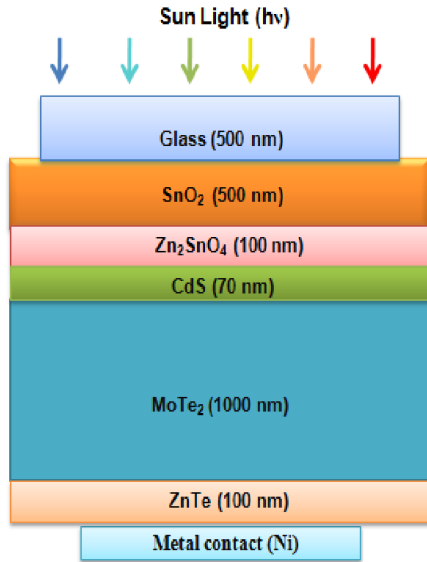


Fig.2 Proposed cell structure of MoTe<sub>2</sub> PV cell

In this study, the used materials with different parameters are shown in Table I which are chosen based on experimental data, literature values or in some cases reasonable estimations [3, 8, 9].

TABLE I THE MATERIAL PARAMETERS USED FOR THE NUMERICAL ANALYSIS OF THE PROPOSED CELLS

Parameters	n-CdS	p-MoTe <sub>2</sub>	p-ZnTe
Thickness, W (μm)	0.01-0.1	0.1-10	0.1
Permittivity, ε/ε <sub>0</sub>	9	13	14
Electron mobility, μ <sub>c</sub> (cm <sup>2</sup> /Vs)	350	110	70
Hole mobility, μ <sub>p</sub> (cm <sup>2</sup> /Vs)	50	426	50
Carrier concentration, n, p (cm <sup>-3</sup> )	1×10 <sup>17</sup>	1×10 <sup>17</sup>	7.5×10 <sup>19</sup>
Band gap, E <sub>g</sub> (eV)	2.42	1.10	2.25
Density of state in conduction band, N <sub>c</sub> (cm <sup>-3</sup> )	1.8×10 <sup>19</sup>	1×10 <sup>15</sup>	7.5×10 <sup>17</sup>
Density of state in valence band, N <sub>v</sub> (cm <sup>-3</sup> )	2.4×10 <sup>18</sup>	1×10 <sup>17</sup>	1.5×10 <sup>19</sup>
Electron affinity, χ (eV)	4.50	4.20	3.65

### III. RESULTS AND DISCUSSION

#### A. Optimization of Conventional Cell

The numerical analysis was done by AMPS-1D simulator in conventional CdS/MoTe<sub>2</sub> PV cell to optimize the thickness of CdS window layer as well as thickness and doping concentration of MoTe<sub>2</sub> absorber layer to overcome the challenges of thin film PV cells. Fig. 3 shows the variation of thickness for CdS window layer from 10 nm to 100nm to investigate the performance of MoTe<sub>2</sub> PV cells without BSF layer. From the numerical analysis considering the conversion efficiency and current technology, CdS layer is reduced to 70 nm in the cell structure of CdS/MoTe<sub>2</sub> PV cell for optimization of window layer along with 500 nm TCO layer and 100 nm Zn<sub>2</sub>SnO<sub>4</sub> buffer layer.

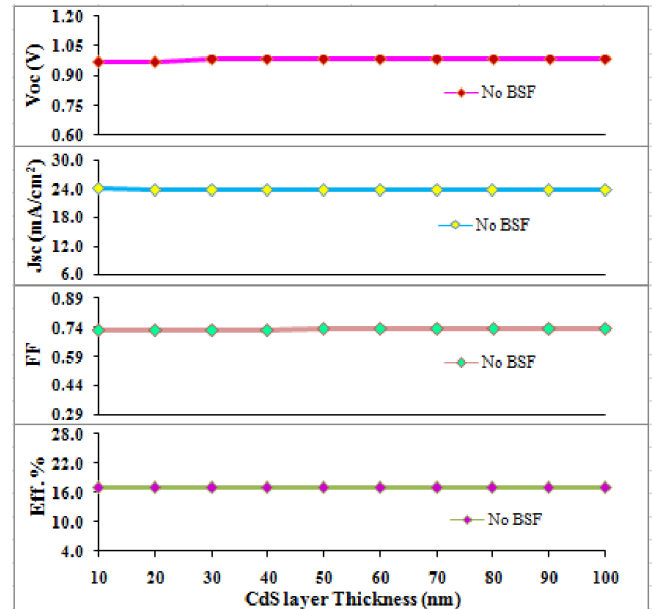


Fig.3 Effect of the CdS thickness variation on cell performance of the conventional cell

The main challenge of thin film PV cell is to preserve the absorber layer material for GW range solar power generation. Fig. 4 illustrates the thickness variation of absorber layer from 100 nm to 10  $\mu\text{m}$  to examine the performance of MoTe<sub>2</sub> PV cells. The MoTe<sub>2</sub> absorber layer is optimized to 1  $\mu\text{m}$  with 500 nm TCO layer, 100 nm Zn<sub>2</sub>SnO<sub>4</sub> buffer layer and 70 nm CdS window layer in the CdS/MoTe<sub>2</sub> PV cell structure to design in ultra-thin range.

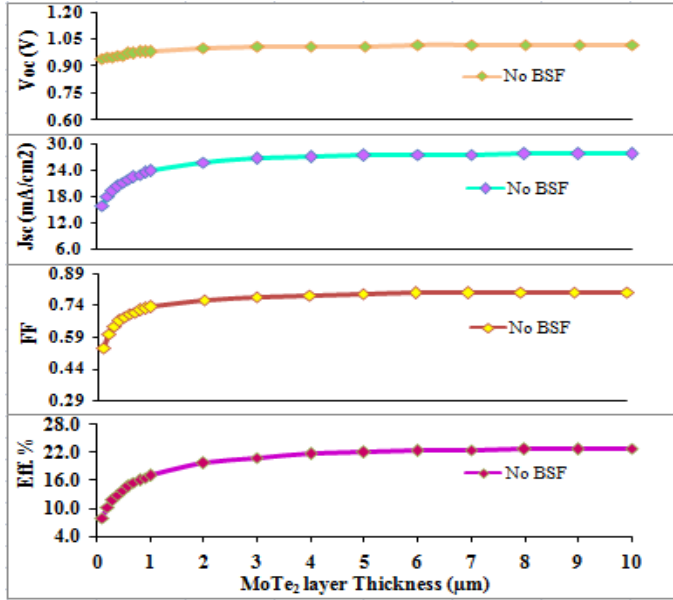


Fig.4 Effect of the MoTe<sub>2</sub> thickness variation on cell performance of the conventional cell

The performance parameters of PV cell are depends on the amount of doping concentration. The effect of doping concentration variation for absorber layer is shown in Fig. 5. For this purpose, the doping concentration of MoTe<sub>2</sub> layer is varied from 10<sup>13</sup> cm<sup>-3</sup> to 10<sup>17</sup> cm<sup>-3</sup> and the highest cell conversion efficiency is found for higher doping concentration of 10<sup>17</sup> cm<sup>-3</sup> which is now practically achievable.

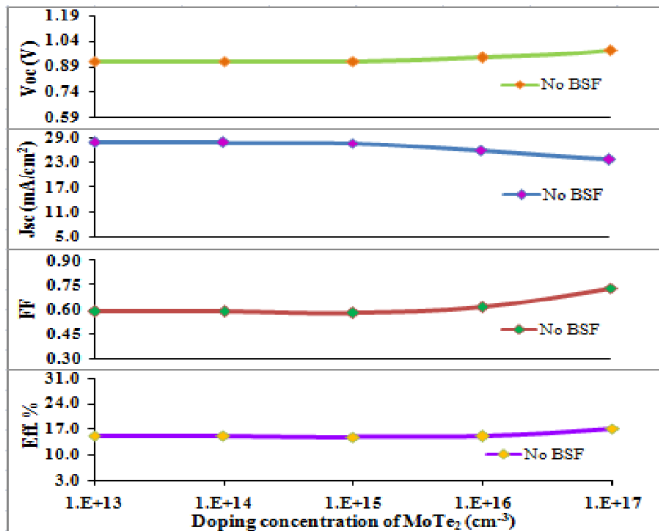


Fig.5 Effect of the doping concentration of MoTe<sub>2</sub> on cell performance of the conventional cell

### B. Effects of ZnTe BSF Insertion

In this research work, the conventional MoTe<sub>2</sub> PV cell is modified into proposed cell which consists of SnO<sub>2</sub> layer, Zn<sub>2</sub>SnO<sub>4</sub> buffer layer, CdS window layer as well as 1  $\mu\text{m}$  thickness of absorber layer with 10<sup>17</sup> cm<sup>-3</sup> doping concentration. The modification of conventional cell is completed by adding a high band gap material ZnTe ( $E_g = 2.25$  eV) of 100 nm thickness placed above the back contact metal to improve the cell conversion efficiency, thermal stability and preserve the absorber layer also by reducing back surface recombination velocity in between the absorber and BSF layer. Table II shows the effects of ZnTe BSF insertion on MoTe<sub>2</sub> PV cell with 1  $\mu\text{m}$  thickness of absorber layer. With the insertion of ZnTe BSF layer, the magnitude of cell performance parameters is higher compared to conventional cell structure.

TABLE II THE OUTPUT PARAMETERS OF PROPOSED CELL WITHOUT BSF LAYER AND WITH BSF LAYER

Structure/parameters	V <sub>oc</sub> (V)	J <sub>sc</sub> (mA/cm <sup>2</sup> )	FF	Eff. (%)
Base case	0.98	23.740	0.730	17.06
ZnTe BSF	1.07	27.91	0.842	25.16

Numerical analysis has been done in the proposed cell to investigate the possibility to lower thickness of absorber layer. The simulation results are shown in Fig. 6 that the cell performance parameters are varied with the variation of absorber layer thickness from 0.1  $\mu\text{m}$  to 5  $\mu\text{m}$ . It is depicted in Fig. 6 that the cell conversion efficiency is getting increased in the 1 $\mu\text{m}$  range of absorber layer with highly doped ZnTe BSF. This is because for the improved values of open circuit voltage, fill factor and current density.

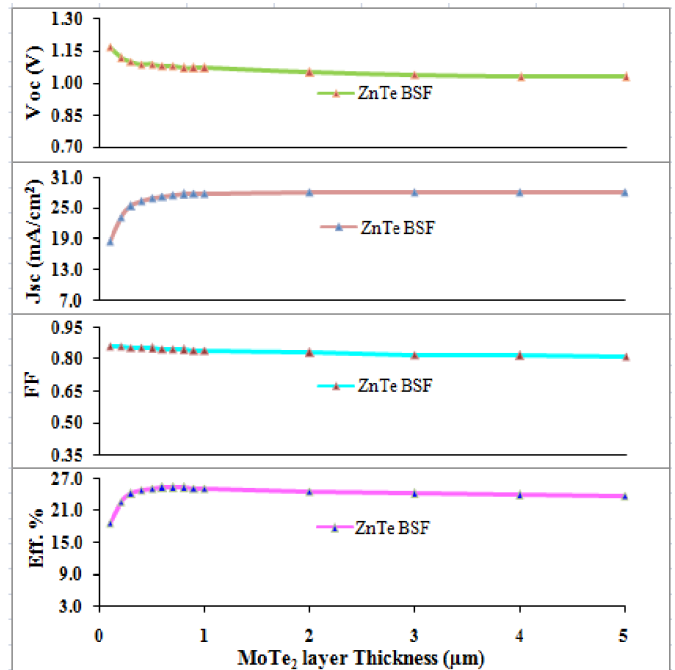


Fig.6 Variation of absorber layer thickness in the proposed cell with ZnTe BSF

It is found from the numerical analysis that the conversion efficiency is 17.06% for conventional structure of MoTe<sub>2</sub> PV cell without BSF layer. The highest conversion efficiency 25.29% (FF = 0.847,  $V_{oc}$  = 1.08 V and  $J_{sc}$  = 27.61 mA/cm<sup>2</sup>) is achieved at only 0.7 μm of absorber layer with 100 nm of ZnTe BSF layer which is approximately 8% greater than the conventional cell structure. These results of cell performance with the addition of ZnTe BSF layer are agreeable to the related published work [8]. The cell performance is improved by reducing back surface recombination velocity through highly doped p-type BSF layer.

### C. Effects of Operating Temperature

The thermal stability is important parameter for PV cell and it is determined by the performance of cell under higher operating temperature. In this case, the operating temperature plays a significant role to test the cell performance parameters of the proposed cell with compared to conventional cell structure. From the numerical analysis, the potentiality of ZnTe BSF layer insertion in the proposed cell structure of CdS/MoTe<sub>2</sub> PV cell is observed. The effect of operating temperature is shown in Fig. 7 for both MoTe<sub>2</sub> PV cell without and with ZnTe BSF. The performance of MoTe<sub>2</sub> PV cell is examined for both without and with ZnTe BSF at operating temperature ranging from 25°C to 160°C. The cell performance parameters are decreased at higher operating temperature and the degradation of conversion efficiency is decreased in the proposed MoTe<sub>2</sub> PV cell by adding the potential ZnTe BSF.

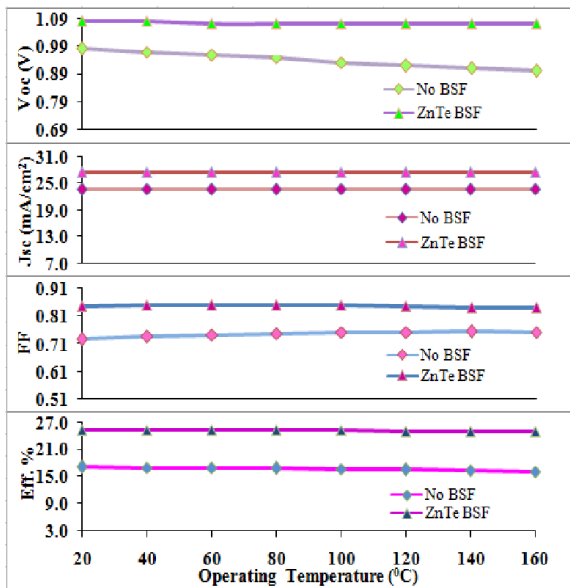


Fig. 7 Effect of temperature on cell performances of MoTe<sub>2</sub> cell with and without ZnTe BSF

The normalized efficiency has been calculated for MoTe<sub>2</sub> PV cell with and without ZnTe BSF. Fig. 8 shows that the normalized efficiency is decreased at higher operating temperature for both cases. In case of no BSF insertion in MoTe<sub>2</sub> PV cell, the normalized efficiency is linearly decreased with the increased of operating temperature ranging from

25°C to 105°C. By adding the ZnTe BSF, the normalized efficiency of the proposed cell is almost constant in the operating temperature ranging from 25°C to 55°C with a TC of 0.24%/°C and then from 55°C to 105°C the normalized efficiency is linearly decreased at a temperature co-efficient of -0.34%/°C which shows better stability in the proposed with ZnTe layer.

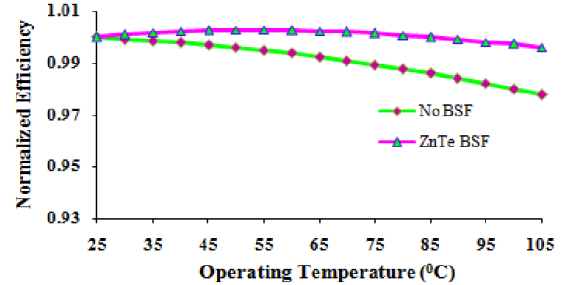


Fig. 8 Effect of operating temperature on normalized efficiency

### IV. CONCLUSION

The effect of ZnTe BSF insertion has been investigated in the proposed ultra-thin MoTe<sub>2</sub> PV cell to achieve higher cell conversion efficiency with lower thickness of absorber layer. The performance of MoTe<sub>2</sub> PV cell with ZnTe BSF showed best cell conversion efficiency of 25.29% (FF = 0.847,  $V_{oc}$  = 1.08 V and  $J_{sc}$  = 27.61 mA/cm<sup>2</sup>) at 0.7 μm thickness of MoTe<sub>2</sub> absorber layer. The cell conversion efficiency of baseline case MoTe<sub>2</sub> PV cell is 17.06% (FF = 0.730,  $V_{oc}$  = 0.98 V and  $J_{sc}$  = 23.74 mA/cm<sup>2</sup>) without ZnTe BSF layer. With the addition of ZnTe BSF, the conversion efficiency is increased upto 8%. Moreover, the thermal stability is better at higher operating temperature in case of ZnTe BSF placing between the absorber layer and back contact metal.

### ACKNOWLEDGMENT

The authors would like to thank the Department of Electrical and Electronic Engineering (EEE) and Renewable Energy Laboratory (REL) of Chittagong University of Engineering and Technology (CUET), Bangladesh.

### REFERENCES

- [1] T. Löher, Y. Tomm, C. Pettenkofer, A. Klein and W. Jaegermann, "Structural dipoles at interfaces between polar II-VI semiconductors CdS and CdTe and non-polar layered transition metal dichalcogenide semiconductors MoTe<sub>2</sub> and WSe<sub>2</sub>," *Semiconductor Science and Technology*, vol. 15, no. 6, pp. 514–522, 6 March, 2000.
- [2] Mrinmoy Dey, Maitry Dey, M. A. Matin and Nowshad Amin, "Design of High Efficient and Stable Ultra-Thin CdTe Solar Cells with ZnTe as a Potential BSF," in *Proceedings of the 3<sup>rd</sup> International Conference on Green Energy and Technology*, Dhaka, Bangladesh, September 2015.
- [3] Mrinmoy Dey, M. A. Matin and Maitry Dey, "Arsenic Telluride BSF for High Performance and Stable ultra-thin CdTe PV cell," *International Journal of Research in Computer Engineering and Electronics*, vol. 4, no. 2, July 2015.
- [4] Mrinmoy Dey, M. A. Matin, Nipu Kumar Das and Maitry Dey, "Germanium telluride as a BSF material for high efficiency ultra-thin

CdTe solar cell,” in *Proceedings of the 9<sup>th</sup> International Forum on Strategic Technology*, pp. 334-338, Cox’s Bazar, Bangladesh, October 2014.

- [5] M. A. Matin and Mrinmoy Dey, “High performance ultra-thin CdTe solar cell with Lead Telluride BSF,” in *Proceedings of the 3<sup>rd</sup> International Conference on Informatics, Electronics & Vision*, pp. 1-5, Dhaka, Bangladesh, May 2014.
- [6] Mrinmoy Dey, Maitry Dey, M. A. Matin and Nowshad Amin, “Design of high performance and ultra-thin CdTe solar cells with SnTe BSF from numerical analysis,” in *Proceedings of the 18<sup>th</sup> International Conference on Computer and Information Technology*, Dhaka, Bangladesh, December 2015.
- [7] H. Zhu, A. K. Kalkan, J. Hou, and S. J. Fonash, “Applications of AMPS-1D for solar cell simulation,” *AIP Conference Proceedings*, vol. 462, pp. 309–314, March 1999.
- [8] Mrinmoy Dey, Maitry Dey, M. A. Matin and Nowshad Amin, “High performance and stable molybdenum telluride PV cells with Indium Telluride BSF,” in *Proceedings of the 4<sup>th</sup> International Conference on Developments in Renewable Energy Technology*, Dhaka, Bangladesh, January 2016.
- [9] Mrinmoy Dey, Maitry Dey, M. A. Matin and Nowshad Amin, “Design of Highly Stable and Efficient Molybdenum Telluride PV Cells with Arsenic Telluride BSF,” in *Proceedings of the 3<sup>rd</sup> International Conference on Electrical Engineering and Information & Communication Technology*, Dhaka, Bangladesh, September 2016.

# *In vitro, in vivo* and *in silico* drug-drug interaction study between Vildagliptin and Bisoprolol fumarate.

Kazi Ashfak Ahmed Chowdhury<sup>✉\*</sup>, Mohammad Shah Hafez Kabir<sup>✉</sup>, Mohammed Munawar Hossain, Tanvir Ahmad Chowdhury, Nishan Chakrabarty

Department of Pharmacy, International Islamic University Chittagong, Chittagong-4203, Bangladesh

<sup>✉</sup>these two authors are equally contributed

## ABSTRACT

**Objective:** Aim of the present study to evaluate the *in vitro, in vivo* and *in silico* drug-drug interaction between Vildagliptin and Bisoprolol fumarate.

**Methods:** Interaction between Vildagliptin and Bisoprolol fumarate has been studied in a system of water at a fixed 37°C at pH 1.0, 3.0 and 6.8 by using spectral observation, Job's method of continuous variation, Ardon's method. *In silico* complexation was measured by NMR prediction and DDI-CPI analysis.

**Results:** From spectrophotometric study, Vildagliptin and Bisoprolol fumarate give different spectra when Vildagliptin mixed with Bisoprolol fumarate in 1:1 mixture, intensity of spectra of Vildagliptin transform surprisingly due to interaction. The jobs plot was attained by plotting absorbance difference (D) against the mole fraction of the each drug at pH 1, 3, and 6.8. Vildagliptin moderate for 1:1 mixture with Bisoprolol fumarate and slightly lower spectra indicate the formation of 1:1 mixture of Vildagliptin with Bisoprolol fumarate. The value of stability constant for the drug-drug system at pH 1.0, 3.0 and 6.8 are 1.875 0.7778 and 1.2000 respectively. From the IR report it also proved that Vildagliptin and Bisoprolol fumarate produced interaction. In this OGTT test at 1:1, 1:2 and 2:1 complex blood glucose level decrease compared to Vildagliptin. Because when drug-drug interaction happened, then drug cannot exhibit its main activity. That's why in this test complex showed different activity. In *in silico* methods, results showed that the drugs interact with each other.

**Conclusion:** So, a careful concern is desired during simultaneous administration of Vildagliptin with Bisoprolol fumarate.

**Keywords:** Drug-drug interaction, Vildagliptin, Bisoprolol fumarate, Ardon's, Jobs method, OGTT.

## 1. INTRODUCTION

It is often necessary to take more than one drugs at a time and some level of medication collaboration happens with attending utilization of medications. Drug interactions can cause serious harm to the patient, sometimes causes serious adverse reactions and nowadays become an obvious concern for the health care providers. For instance, drug interactions, especially with medications having a narrow therapeutic range, may have serious adverse outcomes. A literature search in Medline and Embase database from 1990 to 2006 illustrated that drug-drug interactions (DDIs) were detained accountable for 0.054 % of the emergency department (ED) visits, 0.57 % of the hospital admissions, and 0.12 % of the re-hospitalizations [1]. It is conceivable that medication connection can be helpful or hindering. The utilization of various medications may give synergism, for example, expanding the viability of helpful impact, diminishing measurement however holding the same adequacy to maintain a strategic distance from poisonous quality, or minimizing the medication resistance [2]. Drug-drug interactions are the important cause of therapeutic problems and increased number of hospital admissions within Asia, where Bangladesh has a leading position. It is because of lack of knowledge about it. Both physicians and medicine taker (patient) are not concern it. As a result, these problems rising dangerously. The United States (US) withdraw half of drugs from the market, because of safety reasons, during the period 1999-2003, was associated with important drug interactions [3]. The unfavorable impacts of medications which are an outcome of drug interactions can be averted by making proper move. It was estimated that more than three-quarters of clinically significant drug interactions can be avoided [4]. For adequate management of drug-drug interactions, the access to appropriate information sources is very important for health professionals [5].

But problem seriously arise when new drugs come in the market, where lack of information included in its descriptions. So, drug-drug interaction (DDI) or drug-food interaction (DFI) is challenging sector, where huge amount of medicine are present in the market. Bur multiple drug treatment is a typical and helpful practice for the treatment of ailments where two or more medications are given in the meantime or simultaneously. For this reason DDI should measure selective group of drugs with new medicine.

The prime object of this project was to clarify the potential drug-drug interactions (DDIs) as a contributing factor towards drug safety because these drugs have narrow TI and any kind of potential interaction may leads to toxic or sub-therapeutic effect. The main focus of this work was to identify whether there is any interaction between Vildagliptin (anti-diabetic drug) and Bisoprolol fumarate (beta-blockers) present or not. The present study was to find out the DDIs as well as to establish the stability of the complexes, which could be formed after interaction between Vildagliptin and Bisoprolol fumarate at various pH. The values of stability constants were determined by using Job's continuous-variation analysis, Ardon's spectrophotometric measurement methods and IRAffinity-1S FTIR spectrophotometer. DDI also measured with *in vivo* Oral glucose tolerant test (OGTT). *In silico* complexation was measured by NMR prediction and DDI-CPI analysis.

## 2. MATERIALS AND METHODS

### 2.1 Drugs and chemicals

Vildagliptin and Bisoprolol fumarate were collected from a renowned pharmaceutical company. All chemicals and reagents were of analytical grade.

### 2.2 Equipment

UV-visible spectrophotometer, pH meter (Hanna-HI981.7, USA), analytical balance (Model No. LF 224 DR, Shinko Denshi Co Ltd, Japan), a thermostatic water bath (Shimadzu, Japan), IRAffinity-1S spectrophotometer (Shimadzu, USA) and Rapid View™ (California, USA) were used for the test.

### 2.3 Preparation of standard solutions

Vildagliptin ( $1 \times 10^{-3}$  M) and Bisoprolol fumarate ( $1 \times 10^{-4}$  M) were dissolved in distilled water to prepare the stock solutions.

### 2.4. *In vitro* studies

#### 2.4.1 Absorbance Spectra Analysis

In observation of the spectra, the absorption characteristics of Vildagliptin and Bisoprolol fumarate and their 1:1 mixture in the solutions of buffers [6] pH 1.0, 3.0 and 6.8 were contrasted and those of each interacting species. The concentrations of the specimen were kept at extremely dilute levels for every situation and the estimations made utilizing UV-VIS spectrophotometer. The spectra of the working standard arrangements ( $1 \times 10^{-3}$  M) were recorded between 400 - 200 nm. The spectra were contrasted and those of the immaculate examples for every situation.

#### 2.4.2 Job's Spectrophotometric Method

According to this method [7]: [8] the absorbance of sequence of Vildagliptin ( $1 \times 10^{-3}$ ) with Bisoprolol fumarate ( $1 \times 10^{-4}$ ) in different molar ratios 1:9, 2:8, 3:7, 4:6, 5:5, 6:4, 7:3, 8:2, 9:1 were measured by keeping the total mole consistent. The absorbances of solutions were measured at 244 nm utilizing UV-VIS spectrophotometer. The watched absorbance of the mixtures at different mole fractions was subtracted from whole of the qualities with the expectation of free drugs (Vildagliptin and Bisoprolol fumarate). The absorbance difference (D) was then plotted against the mole fractions of the medication in the mixtures. On the off chance that the development consistent

is sensibly great, two straight lines of various inclines that meet at a mole proportion that relates to the consolidating proportion in the complex are gotten.

### 2.4.3 Ardon's spectrometric method

In this method, [9, 10] concentrations of Vildagliptin was diverse while observe the concentrations of Bisoprolol fumarate fixed at  $1 \times 10^{-4}$  M. The study performed in buffer at pH 1.0, 3.0 and 6.8. The absorbances of solutions were measured at 244 nm using UV-VIS spectrophotometer. The Ardon's equation was used is given below-

$$\frac{1}{(D - \epsilon_A C)} = \frac{1}{KC (\epsilon_{\text{com}} - \epsilon_A) [B]^n} + \frac{1}{C (\epsilon_{\text{com}} - \epsilon_A)}$$

Where, D = Absorbance of the mixture, B = Molar concentration of the Vildagliptin. C = Molar concentration of the Bisoprolol fumarate  $\epsilon_{\text{com}}$  = Molar extinction co-efficient of the complex,  $\epsilon_A$  = Molar extinction co-efficient of the Vildagliptin.

The value of n was chosen as 1, which is an essential condition for validation of the method. The value for  $1 / (D - \epsilon_A C)$  was plotted versus  $1 / D$  to get the straight lines.

The stability constant of the complex was given by the relation,  $K = \text{intercept} / \text{slope}$

It is to be mentioned that this method is only valid for the systems where 1:1 complexes are found.

### 2.4.4 Drug-drug interaction measured by IRAffinity-1S FTIR spectrophotometer

The IRAffinity-1S FTIR spectrophotometer has been planned in view of educating and general research labs. Notwithstanding its conservative plan, it offers full usefulness for all FTIR strategies, including transmission, diffuse reflection, and attenuated total reflection (ATR). Spectra were recorded on IRAffinity-1S FTIR spectrophotometer (Shimadzu, USA) apparatus in the range of  $350\text{-}4600 \text{ cm}^{-1}$ . The spectrum was a mean of ten consecutive scans on the same sample. Spectra recorded for Vildagliptin, Bisoprolol and their 1:1 complex.

### 2.5 In vivo study

#### 2.5.1 Hypoglycemic effect in glucose induced hyperglycemic mice (OGTT)

This test was performed according to the established method [11] with minor modification. 1<sup>st</sup> group was treated as normal control group, 2<sup>nd</sup> group treated with Vildagliptin (50mg/kg, p.o.), 3<sup>rd</sup> group were treated with Bisoprolol fumarate (50mg/kg, p.o.), 4<sup>th</sup> group were treated with Vildagliptin (50mg/kg, p.o.)+ Bisoprolol fumarate (50mg/kg, p.o.) of 1:1 mixture, 5<sup>th</sup> group were treated with 1:2 mixture, and 6<sup>th</sup> group were treated with 2:1 mixture respectively. Glucose solution (1 g/kg) was administered at first. Then drugs and complex solutions were administered to the glucose fed mice. Serum glucose level of blood test from tail vein was evaluated by utilizing Glucometer (Rapid View™) at 0, 60 min, 120 min, and 180 min. Percent decrease of blood glucose level after 120 min measured by following equation,

$$\% \text{ decrease} = \frac{\text{Blood Glucose level at 0 min} - \text{Blood Glucose level at 180 min}}{\text{Blood Glucose level at 0 min}} \times 100$$

### 2.6 In silico studies

#### 2.6.1 Structural studies

Vildagliptin and Bisoprolol fumarate were acquired from Pubchem compound vault (<http://www.ncbi.nlm.nih.gov/pccompound>). The structures were drawn utilizing the Chem sketch package 11.0 having a place with the ACD chem. Lab. Then the structures opened with the Accelrys Discovery Studio Visualizer and performed the interaction. The found complex molecule of Vildagliptin and Bisoprolol fumarate then saved.

#### 2.6.2 NMR Prediction

H-1 and C-13 NMR prediction was done by Chem office 2002.

#### 2.6.3 DDI-CPI analysis

Users need to upload a drug molecule in mol2 organize with charges and hydrogens included. At the point when the client presents a medication atom, our server checks the arrangement appropriateness and ascertains the association profile of this medication towards all existent drugs [12].

#### 2.7 Statistical analysis

Statistical programs used were GRAPHPAD PRISM®, which also used for graph preparation. The outcomes were factually broke down utilizing reshaped measures analysis of variance with Dunnett's test by using SPSS (version 22.0).  $P < 0.05$  and  $P < 0.01$  were considered as statistically significant.

## 3. RESULTS

### 3.1 Spectral study

The drugs concentrated on indicated retention in UV-VIS area. The atomic types of Vildagliptin when mixed with Bisoprolol fumarate demonstrated a few changes in assimilation qualities of this molecule (Bisoprolol fumarate) incorporating a few moves in the ingestion maxima. Consequently modification in ghastly example might be viewed as a pointer for the essential communication among these drugs (Figure 1).

### 3.2 Study of Job's method

The molar proportions of the complexes of Vildagliptin with Bisoprolol fumarate were assessed by Job's method for consistent variety. The watched absorbance qualities were measured in pH 1.0, 3.0 and 6.8 at different focuses ( $0.1 \times 10^{-3}$  to  $0.9 \times 10^{-3}$  M) Vildagliptin with Bisoprolol fumarate of at 244 nm. The Job's plots at pH 1.0, 3.0 and 6.8 were acquired by plotting absorbance contrasts against the mole part of the medication (Vildagliptin) which are exhibited in Figure 2.

### 3.3 Effect of Vildagliptin on Bisoprolol fumarate using Ardon's method

Ardon's plot confirmed the formation of 1:1 complex of Vildagliptin and Bisoprolol fumarate at pH 1.0, 3.0 and 6.8, since the method is valid only for 1:1 complexes. The values of  $1 / [\text{drug}]$  by using the Ardon's equation:

$$\frac{1}{(D - \epsilon_A C)} = \frac{1}{KC (\epsilon_{\text{com}} - \epsilon_A) [B]^n} + \frac{1}{C (\epsilon_{\text{com}} - \epsilon_A)}$$

The data for Ardon's gave straight lines with intercept which are presented in Figure 3 indicates the formation of 1:1 complexes for the system at both pH.

### 3.4 Estimation of Stability Constant

The value of stability constant for the complexation of Vildagliptin with Bisoprolol fumarate at pH 1.0, 3.0 and 6.8 were gotten from the spectral data utilizing Ardon's plot. The qualities for security steady were ascertained from the inclines and captures of the straight lines from these plots. It was seen from the Ardon's condition that the estimations of solidness consistent was given as [(intercept)/(slope)] of straight line so got. i. e.  $k = (\text{capture}) / (\text{incline})$ . The estimation of intercept and slope were ascertained by Least Squares Method utilizing the accompanying equation:

$$y = mx + C$$

The values of stability constants for the drug-drug system at pH 1.0, 3.0 and 6.8 presented in the table 1.

### 3.5 Drug-drug interaction measured by IRAffinity-1S FTIR spectrophotometer

I R of the Vildagliptin, Bisoprolol fumarate was determined by FTIR spectra. Physical of drugs and their mixture were characterized by FTIR spectral analysis. From the results, it was concluded that there was moderate interference between Vildagliptin and Bisoprolol fumarate. Because a slight change of spectra occurred in their 1:1 complex. All of the spectra showed in Figure 4.

### 3.6 In vivo drug interactions study of Vildagliptin with Bisoprolol fumarate was evaluated by Oral Glucose Tolerance Test

All the treatments significantly reduce blood glucose level in 30 min after administration. Most significant reduction ( $P < 0.01$ ) was observed for Vildagliptin and the complex (2:1) at 120 min. Other complexes (1:1 and 1:2) also reduced the blood glucose level, but these are less than the (2:1) complex. Bisoprolol fumarate reduced negligible blood glucose level after 180 min of the treatment. All results are presented in Table 2, Figure 5 and Figure 6.

### 3.7 In silico studies

#### 3.7.1 Structural studies

The structure of the complex of Vildagliptin with Bisoprolol fumarate found from the Accelrys Discovery Studio Visualizer was presented in Figure 7.

#### 3.7.2 NMR Prediction

NMR Prediction from Chem office 2002 presented in Figure 8. In this figure, it is clear that the interaction between happened, because found structure of complex showed different NMR report then its mother compounds.

#### 3.7.3 DDI-CPI analysis

The output results from DDI-CPI analysis showed in Table 3. In this analysis, Vildagliptin showed 1.000 interaction confidence towards Bisoprolol fumarate.

## DISCUSSION

Initial evidence for complexation of Vildagliptin with Bisoprolol fumarate originated from contrasts between the spectra of the medications and those of their mixtures in buffer solutions. Every compound has its interesting sub-atomic structure or electronic design which is in charge of assimilation of light. Clearly every compound has its one of a kind sub-atomic structure or electronic setup which is in charge of retention of light as bright or visible form [13, 14]. The molecular species of Vildagliptin and Bisoprolol fumarate when independently mixed demonstrated a few changes in retention attributes



incorporating a few moves in the absorption maxima of buffer mixes and in addition their 1:1 mixture in buffer solution of pH 1.0, 2.0 and 6.8 at an altered focus (1 X 10<sup>-3</sup> M). The modification in spectral pattern might be viewed as a marker for connection between these medications.

In Job's plot, at pH 1.0, 2.0 and 6.5, various concentrations comprising 1 X 10<sup>-3</sup> M to 9 X 10<sup>-3</sup> M of Vildagliptin were interacted with Bisoprolol fumarate. The breakdown in the curve at different concentrations of Vildagliptin indicates the presence of drug interaction.

The Ardon's plots have been utilized to assess the stability constants and it has been watched that when estimations of 1/(D - CεA) are plotted against 1/Drug (Figure 3), these lines are acquired complying with the Ardon's equation. The estimations of stability constants at various pH are appeared in table 3. Stability constants data demonstrated that Vildagliptin-Bisoprolol fumarate framework shaped generally more grounded buildings at all pH conditions.

The stability constants obtained from the Ardon's plot for the systems (Vildagliptin with Bisoprolol fumarate) were found to show mild drug interaction at pH 2.0 and show stable complex at pH 1.0 and show moderate stable complex at pH 6.8 as the stability constant is greater than 1, which is an indication of drug interaction.

The spectrum of 1:1 complex is slightly different from pure Vildagliptin and pure Bisoprolol fumarate. Spectrum of 1:1 complex is near to Bisoprolol fumarate. That means presence of Bisoprolol fumarate interrupt Vildagliptin spectrum. Because, when ever any type of interaction happened between two drugs, then different type of spectrum found. So IR report proved that, between Vildagliptin and Bisoprolol fumarate an interaction happen. But this interaction is moderate.

In this OGTT test at 1:1, 1:2 and 2:1 complex blood glucose level decrease compared to Vildagliptin. Because when drug-drug interaction happened, then drug cannot exhibit its main activity. That's why in this test complex showed different activity.

From the results of *in silico* methods used, they exhibited the presence of interaction by showing different parameters. In structural study of the drugs, they formed a complex, which conclude that they have attraction towards them. It also proved by other two methods also. In NMR prediction spectra, deviant spectra showed by the complex compound and DDI-CPI analysis also predicted that Vildagliptin had 1.000 interaction confidence towards Bisoprolol fumarate.

## CONCLUSION

By all the trial information appeared above we can conclude that the interaction of Vildagliptin with Bisoprolol fumarate show diminish in free drug concentration of both drug which ultimately results in decrease affinity towards receptors and it is clear that one or both drug may show diminished pharmacological activity. The complex of Vildagliptin and Bisoprolol fumarate shows different spectra and *in vivo* process it was also causes difference in decrease of blood glucose level. All *in vitro* and *in vivo* report showed that Vildagliptin and Bisoprolol fumarate produced complex between them which can lower the concentration of free drug in plasma and may causes some undesirable effect. In *in silico* methods, results showed that the drugs interact with each other. It can in this way be presumed that a cautious thought is required during concurrent administration of Vildagliptin with Bisoprolol fumarate.

## Competing interests

The authors declare that they have no competing interests.

## References

- [1] M. L. Becker, M. Kallewaard, P. W. Caspers, L. E. Visser, H. G. Leufkens, and B. H. Stricker, "Hospitalisations and emergency department visits due to drug-drug interactions: a literature review," *Pharmacoepidemiol Drug Saf*, vol. 16, no. 6, pp. 641-51, 2007.
- [2] T. C. Chou, "Theoretical basis, experimental design, and computerized simulation of synergism and antagonism in drug combination studies," *Pharmacol Rev*, vol. 58, no. 3, pp. 621-81, 2006.
- [3] S. M. Huang and L. J. Lesko, "Drug-drug, drug-dietary supplement, and drug-citrus fruit and other food interactions: what have we learned?," *J Clin Pharmacol*, vol. 44, no. 6, pp. 559-69, 2004.
- [4] E. N. van Roon *et al.*, "Clinical relevance of drug-drug interactions : a structured assessment procedure," *Drug Saf*, vol. 28, no. 12, pp. 1131-9, 2005.
- [5] V. Bergk, W. E. Haefeli, C. Gasse, H. Brenner, and M. Martin-Facklam, "Information deficits in the summary of product characteristics preclude an optimal management of drug interactions: a comparison with evidence from the literature," *European Journal of Clinical Pharmacology*, vol. 61, no. 5-6, pp. 327-35, 2005.

- [6] M. S. H. K. Kazi Ashfaq Ahmed Chowdhury, Tanvir Ahmad Chowdhury, Mohammed Munawar Hossain, A.T.M. Mostafa Kamal, Md. Rafi-Uz-Zaman Akanda, Abul Hasanat, "In vitro drug-drug interaction study between Montelukast Sodium and Amlodipine Besylate at gastric and intestinal pH," *International Journal of Pharmacy*, vol. 5, no. 3, pp. 1003-1009, 2015.
- [7] Job P. Job's method of continuous variation. *Ann Chim* 1928; 10(9): 113.
- [8] M. Mohiuddin, Z. Azam, M. S. Amran, and M. A. Hossain, "In vitro study on the interaction of caffeine with gliclazide and metformin in the aqueous media," *J. Pharmacol. Toxicol*, vol. 4, no. 5, pp. 194-204, 2009.
- [9] M. Ardon, "340. Oxidation of ethanol by ceric perchlorate," *Journal of the Chemical Society (Resumed)*, pp. 1811-1815, 1957.
- [10] M. A. Sayeed and S. Rana, "In vitro and invivo drug-drug interaction study between ketotifen fumarate and chlorpheniramine maleate at gastric and intestinal pH," 2015.
- [11] F. Xia *et al.*, "Castration-induced testosterone deficiency increases fasting glucose associated with hepatic and extra-hepatic insulin resistance in adult male rats," *Reproductive Biology and Endocrinology*, vol. 11, no. 1, pp. 1-11, 2013.
- [12] H. Luo *et al.*, "DRAR-CPI: a server for identifying drug repositioning potential and adverse drug reactions via the chemical-protein interactome," *Nucleic acids research*, p. gkr299, 2011.
- [13] S. Saha, R. Begum, A. Rahman, M. Z. Sultan, M. S. Amran, and M. A. Hossain, "Evaluation of in vitro Interaction of Metformin with Ibuprofen in Aqueous Medium," *Bangladesh Pharmaceutical Journal*, vol. 16, no. 2, pp. 189-194, 2015.
- [14] M. Ahsan *et al.*, "The study of in vitro interaction of ciprofloxacin with paracetamol and zinc in aqueous medium," *Journal of Scientific Research*, vol. 4, no. 3, pp. 701-708, 2012.

## Tables

**TABLE 1: Stability constant of Vildagliptin with Bisoprolol fumarate at different pH.**

System	pH	Stability Constants
Interaction of Vildagliptin with Bisoprolol fumarate	1.0	1.8750**
	3.0	0.7778*
	6.5	1.2000**

Values are the mean of triplicate experiments and represented as mean. Values in the same column with different superscripts (\*) are significantly different \*P < 0.05 and \*\*P < 0.01. Student's t test was performed to analyze this data set.

**Table 2: Effect of Vildagliptin with Bisoprolol fumarate and their mixtures of 1:1, 1:2 and 2:1, on glucose induced hyperglycemia (mmol/L) in normal mice.**

Group	0 hour	1st hour	2nd hour	3rd hour	% decrease
<b>Control</b>	9.4±0.063	9.96±0.25	10.3±0.27	9.74±0.144	-
<b>Vildagliptin</b>	10.3±0.307	8.46±0.835*	6.74±0.612*	7.48±0.406**	27.38
<b>Bisoprolol fumarate</b>	9.24±0.845	9.92±0.789*	9.24±0.64	9.04±0.658	2.16
<b>Mixture (1:1)</b>	10.94±0.271	8.7±0.152*	9.52±0.166	10.12±0.189*	7.50
<b>Mixture (1:2)</b>	9.32±0.26	9.58±0.351	8.92±0.373*	8.83±0.534*	5.26
<b>Mixture (2:1)</b>	10.24±0.299	9.38±0.649*	9.1±0.378*	8.48±0.471**	17.19

Values are presented in mean±SEM (n=5). Values with different superscripts in same column are significantly different from control at each specific hour after the administration of Vildagliptin with Bisoprolol fumarate and their mixture of different ratio. For \*P>0.05 and \*\*P<0.01. One-way ANOVA followed by Dunnett's multiple comparison was performed to analyze this comparison. "-" means no decrease.

**Table 3: Results from DDI-CPI analysis for Vildagliptin with Bisoprolol fumarate.**

Input drug	Existant drug	Interaction confidence
Vildagliptin	Bisoprolol fumarate	1.000

**Figures**

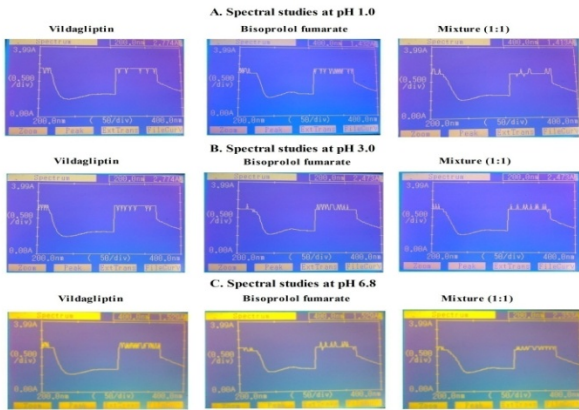


**Figure 1:** Spectral studies of Vildagliptin, Bisoprolol fumarate and their (1:1) mixture for A. pH 1.0, B. pH 3.0, and C. pH 6.8.

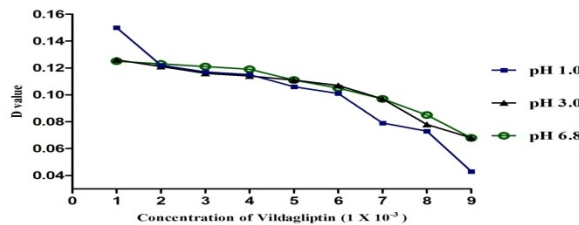


**Figure 2:** Job's plot for complexation of Vildagliptin with Bisoprolol fumarate at 244 nm.

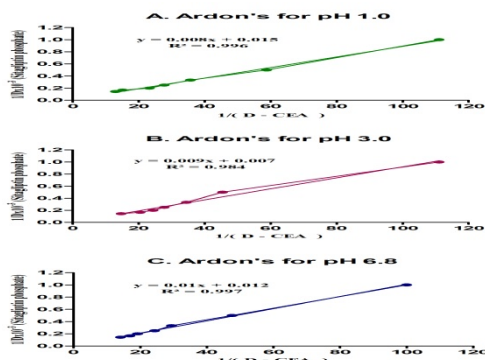


**FIGURE 3:** Ardon's plot for complexation of Vildagliptin with Bisoprolol fumarate at 244 nm for A. pH 1.0, B. pH 3.0 and C. pH 6.8.

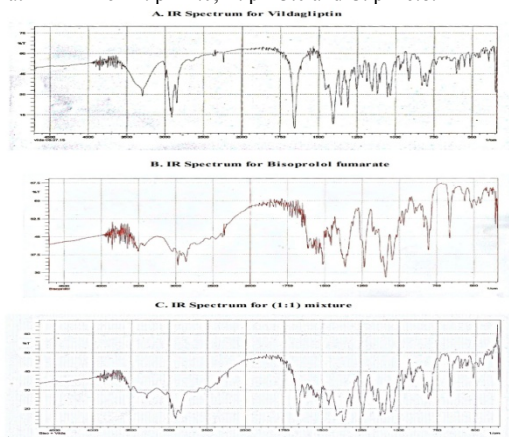


**Figure 4:** IR Spectrum for, A. Vildagliptin, B. Bisoprolol fumarate and C. their (1:1) mixture.

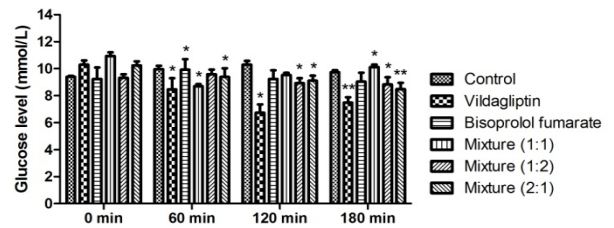


**Figure 5:** Effect of Vildagliptin with Bisoprolol fumarate and their mixtures of 1:1, 1:2 and 2:1 ratio, on glucose induced hyperglycemia (mmol/L) in normal mice. Values are presented in mean±SEM (n=5).

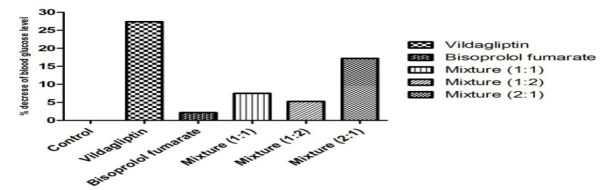


**Figure 6:** Percentage decrease of blood glucose level after treatment with Vildagliptin with Bisoprolol fumarate and their mixture of 1:1, 1:2 and 2:1 ratio, on glucose induced mice.

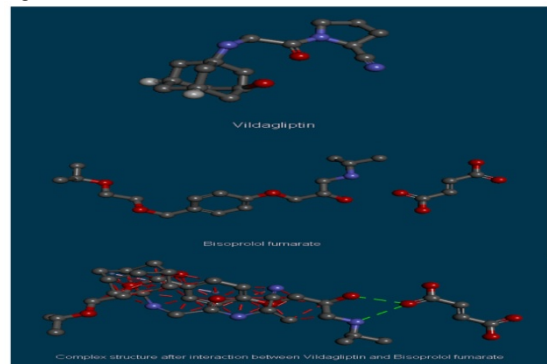


**Figure 7:** Structures of Vildagliptin, Bisoprolol fumarate and their interacted complex compound.

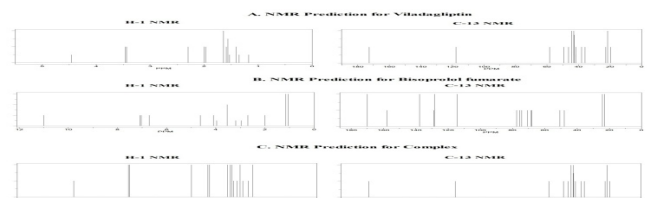


**Figure 8:** H-1 NMR and C-13 NMR prediction for, A. Vildagliptin, B. Bisoprolol fumarate and C. Complex of Vildagliptin and Bisoprolol fumarate.

# *In vitro* reconstitution of mutant catalytic domains of *Enterococcus hirae* V-ATPase

Md. Jahangir Alam

Department of Genetic Engineering and  
Biotechnology

Shahjalal University of Science and Technology,  
Sylhet-3114, Bangladesh  
and

Department of Biological Science and Technology,  
Tokyo University of Science, Katsushika-Ku, Tokyo  
Japan

e-mail: jalambioruahoo.com

Ichiro Yamato

Department of Biological Science and Technology,  
Tokyo University of Science, Katsushika-Ku, Tokyo  
Japan.

**Abstract**— Vacuolar ATPase (V-ATPase) of *Enterococcus hirae* is composed of a soluble functional domain V<sub>1</sub> and an integral membrane domain V<sub>o</sub>, where V<sub>1</sub> and V<sub>o</sub> domains are connected by a central stalk and two peripheral stalks. We identified 120 interacting residues of A<sub>3</sub>B<sub>3</sub> heterohexamer with D-subunit in DF heterodimer in the crystal structures of A<sub>3</sub>B<sub>3</sub> and A<sub>3</sub>B<sub>3</sub>DF. In this study, we constructed two mutant forms of A-subunit of *E. hirae* V-ATPase, viz. AR475A and ALV476-7AA. Mutant AR475A and ALV476-7AA proteins were successfully expressed as His-tagged soluble proteins in *Escherichia coli* BL21 (DE3) cells without IPTG induction at 30°C for 12 hours incubation and afterward, purified by gel filtration chromatography. After removing His-tag by the treatment of His-TEV protease, mutant proteins were purified and reconstituted mutant A<sub>3</sub>B<sub>3</sub> heterohexamers. Both mutant heterohexamers formed catalytic domain (V<sub>1</sub> moiety- AR475A<sub>3</sub>B<sub>3</sub>DF and ALV476-7AA<sub>3</sub>B<sub>3</sub>DF complex, respectively) with DF heterodimer independent of nucleotides.

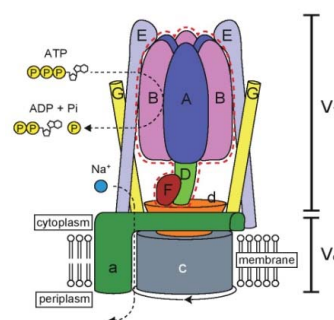
**Keywords**— Site-directed mutation, reconstitution, catalytic domain, V-ATPase, *Enterococcus hirae*.

## I. INTRODUCTION

Vacuolar ATPase (V-ATPase) functions as a proton pump in the acidic organelles and plasma membranes of eukaryotic cells and bacteria [1, 2]. This acidic environment is essential for such processes as receptor-mediated endocytosis, intracellular targeting of lysosomal enzymes, protein processing and degradation [1]. F-, V-, and A-ATPases possess an overall similar structure composed of a catalytic portion (F<sub>1</sub>-, V<sub>1</sub>-, or A<sub>1</sub>-ATPase) and a membrane-embedded ion-transporting portion (F<sub>o</sub>-, V<sub>o</sub>-, or A<sub>o</sub>-), and have a similar reaction mechanism as rotary motors [1]. V-ATPases are also found in bacteria, such as *Thermus thermophilus* and *Enterococcus hirae*. *T. thermophilus* V-ATPase physiologically functions as an ATP synthase [3], whereas, *E. hirae* V-ATPase is not an ATP synthase and instead acts as a primary ion pump

similar to eukaryotic V-ATPases, which transports Na<sup>+</sup> or Li<sup>+</sup> instead of H<sup>+</sup> [4-8].

A



B



Fig. 1. A. A model of V-ATPase from *Enterococcus hirae* created by Arai et al. 2013 [9]. V<sub>1</sub> indicates catalytic part (consisting of A<sub>3</sub>B<sub>3</sub>DF), V<sub>o</sub> indicates membrane part (consisting of c-ring and a subunit). Peripheral stalk consists of E and G subunits and central stalk consists of D, F, and d subunits. B. Crystal structure of nucleotide-free A<sub>3</sub>B<sub>3</sub>DF [9].

V-ATPase of *Enterococcus hirae* is composed of a soluble functional domain V<sub>1</sub> (A<sub>3</sub>B<sub>3</sub>DF) (Fig. 1) and an integral membrane domain V<sub>o</sub> (ac), where V<sub>1</sub> and

V<sub>o</sub> domains are connected by a central stalk, composed of D-, F-, and d-subunits, and two peripheral stalks (E- and G-subunits) (Fig. 1A). In this study, we constructed two mutant forms of A-subunit of *E. hirae* V-ATPase, viz. A<sub>R475A</sub> and A<sub>LV476-7AA</sub>, and reconstituted mutant A3B3 heterohexamers. Both mutant heterohexamers formed catalytic domains (V1 moiety- A<sub>R475A</sub>3B3DF and A<sub>LV476-7AA</sub>3B3DF complex, respectively) with DF heterodimer.

## II. METHODS

Purification of mutant A<sub>R475A</sub>, A<sub>LV476-7AA</sub>, and wild-type B monomers were performed as described previously [10]. Reconstitution of mutant A<sub>R475A</sub>3B3 and A<sub>LV476-7AA</sub>3B3 heterohexamers were performed as described [10, 11]. Basic native PAGE was used to check the reconstitution of A<sub>R475A</sub>3B3 and A<sub>LV476-7AA</sub>3B3 heterohexamers. These mutant heterohexamers were purified by gel filtration chromatography. For the formation of wild-type and mutant catalytic domains (V1 moiety- A3B3DF complex), purified wild-type and mutant A3B3 heterohexamers and synthesized DF heterodimer were incubated on ice for 1 hour and the formation of the complexes were analyzed by native-PAGE as reported earlier [10, 11].

## III. RESULTS AND DISCUSSION

### A. Expression, purification of mutant A-subunit and reconstitution of mutant heterohexamers

Mutant A<sub>R475A</sub> and A<sub>LV476-7AA</sub> proteins were successfully expressed and purified by using *Escherichia coli* expression system. A<sub>R475A</sub> and A<sub>LV476-7AA</sub> proteins were purified by using Ni Sepharose 6 fast flow column and gel filtration chromatography (Fig. 2). Purification of the mutants was confirmed by SDS-PAGE (Fig. 2). The mutant A<sub>R475A</sub> and A<sub>LV476-7AA</sub> subunits reconstituted A<sub>R475A</sub>3B3 and A<sub>LV476-7AA</sub>3B3 heterohexamers respectively with wild-type B-subunit in nucleotide dependent manner (data not shown).

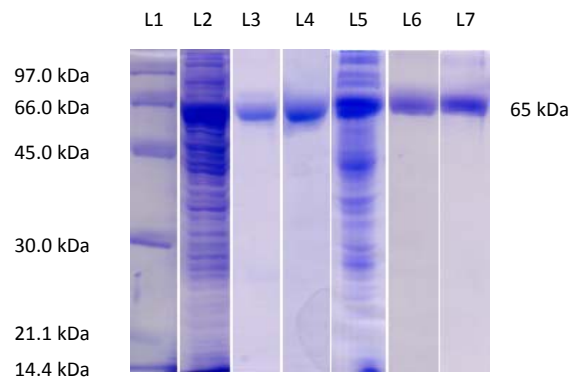


Fig. 2. SDS-PAGE pattern for the expression and purification of A<sub>R475A</sub> and A<sub>LV476-7AA</sub> proteins. SDS-PAGE pattern stained with

Coomassie Brilliant Blue. L1- Low molecular weight marker; L2- pET23d-HisA<sub>R475A</sub>-soluble fraction; L3- His-tag removed (by the treatment of His-TEV Protease) A<sub>R475A</sub>; L4- Gel filtration purified A<sub>R475A</sub>; L5- pET23d-HisA<sub>LV476-7AA</sub> soluble fraction; L6- His-tag removed (by the treatment of His-TEV Protease) A<sub>LV476-7AA</sub>; and L7- Gel filtration purified A<sub>LV476-7AA</sub>. 1μg of protein was loaded in each lane.

### B. Reconstitution of mutant catalytic domains

Both A<sub>R475A</sub>3B3 and A<sub>LV476-7AA</sub>3-B3 heterohexamers formed catalytic domain i.e. V1 moiety (A<sub>R475A</sub>3-B3DF and A<sub>LV476-7AA</sub>3B3DF complex, respectively) of V-ATPase with DF heterodimer. When A<sub>R475A</sub>3B3 heterohexamer was incubated with DF heterodimer in the absence of AMP-PNP, A<sub>R475A</sub>3B3DF complex was formed with remaining slight amount of unbound A<sub>R475A</sub>3B3 heterohexamer (Fig. 3, Lane 6).

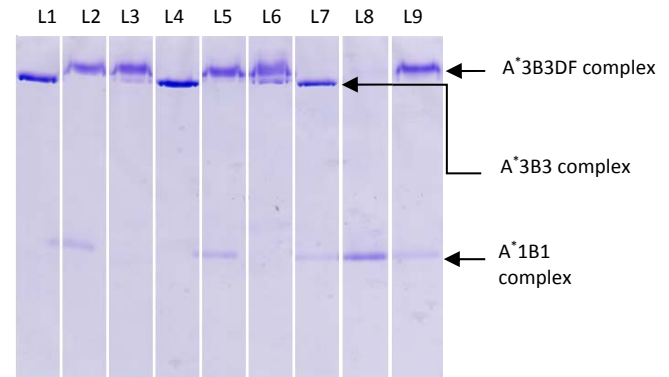


Fig. 3. Basic native PAGE pattern for the reconstitution of catalytic domain (A\*3B3DF complex) from reconstituted A\*3B3 heterohexamer and synthesized DF heterodimer of *Enterococcus hirae* V-ATPase. L1- Wild-type A3B3 heterohexamer; L2- Wild-type A3B3 heterohexamer with DF heterodimer in the presence of 2 mM AMP-PNP; L3- Wild-type A3B3 heterohexamer with DF heterodimer; L4- A<sub>R475A</sub>3B3 heterohexamer; L5- A<sub>R475A</sub>3B3 heterohexamer with DF heterodimer in the presence of 2 mM AMP-PNP; L6- A<sub>R475A</sub>3B3 heterohexamer with DF heterodimer; L7- A<sub>LV476-7AA</sub>3B3 heterohexamer; L8- A<sub>LV476-7AA</sub>3B3 heterohexamer with DF heterodimer in the presence of 2 mM AMP-PNP; and L9- A<sub>LV476-7AA</sub>3B3 heterohexamer with DF heterodimer. 1μg of protein was loaded in each lane.

\*Wild-type (L1, L2, & L3), and mutant (L4, L5, and L6 for A<sub>R475A</sub>, and L7, L8, and L9 for A<sub>LV476-7AA</sub>) A3B3 heterohexamers.

However, when this complex was incubated with 2 mM AMP-PNP, most of the complex formed catalytic domain/ V1 moiety, although trace amount of A<sub>R475A</sub>1B1 complex was observed in native PAGE (Fig. 3, Lane 5). These findings are in consistent with the observations of wild-type A3B3DF complex (Fig. 3, Lane 1-3) [10]. On the other hand, when A<sub>LV476-7AA</sub>3B3 heterohexamer was incubated with DF heterodimer in the presence of 2 mM AMP-PNP, it

completely dissociated, didn't produce catalytic domain-  $A_{LV476-7AA}3B3DF$  complex and migrated at the position of  $A_{LV476-7AA}1B1$  complex in native PAGE (Fig. 3, Lane 8), but in the absence of nucleotides it formed catalytic domain and some amount of  $A_{LV476-7AA}1B1$  complex (Fig. 3, Lane 9).

#### IV. CONCLUSION

Mutant catalytic domains (V1 moiety-  $A_{R475A}3B3DF$  and  $A_{LV476-7AA}3B3DF$ ) were useful to understand protein-protein interactions and ATPase activities which would be helpful to become conscious about the rotation mechanism of V-ATPases.

### **References**

- [1] M. Forgac, *Nat Rev Mol Cell Biol*; 8: 917—929, 2007.
- [2] T. H. Stevens and M. Forgac, *Annu Rev Cell Dev Biol*; 13: 779—808, 1997.
- [3] L. K. Lee, A. G. Stewart, M. Donohoe, R. A. Bernal, and D. Stock, *Nat Struct Mol Biol*; 17: 373—378, 2010.
- [4] T. Murata, K. Igarashi, Y. Kakinuma, and I. Yamato, *J Biol Chem*; 275: 13415—13419, 2000.
- [5] T. Murata, I. Yamato, Y. Kakinuma, A. G. W. Leslie, and J. E. Walker, *Science*; 308: 654—659, 2005.
- [6] T. Murata, I. Yamato, Y. Kakinuma, M. Shirouzu, J. E. Walker, S. Yokoyama, and S. Iwata, *Proc Natl Acad Sci, USA*; 105: 8607—8612, 2008.
- [7] Y. Furutani, T. Murata, and H. Kandori, *J Am Chem Soc*; 133: 2860—2863, 2011.
- [8] K. Mizutani, M. Yamamoto, K. Suzuki, I. Yamato, Y. Kakinuma, M. Shirouzu, J. E. Walker, S. Yokoyama, S. Iwata, and T. Murata, *Proc Natl Acad Sci, USA*; 108: 13474—13479, 2011.
- [9] S. Arai, S. Saijo, K. Suzuki, K. Mizutani, Y. Kakinuma, Y. Ishizuka-Katsura, N. Ohsawa, T. Terada, M. Shirouzu, S. Yokoyama, S. Iwata, I. Yamato, and T. Murata, *Nature* 493: 703-707, 2013.
- [10] S. Arai, I. Yamato, A. Shiokawa, S. Saijo, Y. Kakinuma, Y. I. Katsura, M. Toyama, T. Terada, M. Shirouzu, S. Yokoyama, S. Iwata, and T. Murata, *Biochem Biophys Res Comm*; 390: 698-702, 2009.
- [11] M. J. Alam, I. Yamato, S. Arai, S. Saijo, K. Mizutani, Y. I. Katsura, N. Ohsawa, T. Terada, M. Shirouzu, S. Yokoyama, S. Iwata, Y. Kakinuma, and T. Murata, *SpringerPlus*; 2:689, 2013.

# Phytochemical and biological investigation on *Artocarpus chaplasha* Roxb.

Sanjida.Sharmin, Fakir Shahidullah Tareq  
Dept. of Pharmaceutical Chemistry, Faculty of Pharmacy  
University of Dhaka,  
Dhaka, Bangladesh.

Choudhury Mahmood Hasan, Monira Ahsan  
Dept. of Pharmaceutical Chemistry, Faculty of Pharmacy  
University of Dhaka,  
Dhaka, Bangladesh.

**Abstract**—The methanolic extract of the stem bark of *Artocarpus chaplasha* Roxb.(Family: Moraceae) was investigated for the isolation of pure compounds and determination of few biological activities. A mixture of two compounds cycloartenyl acetate and lupeol acetate were isolated from it. The crude methanol extract as well as its petroleum ether, chloroform, carbon tetrachloride and aqueous soluble fractions were studied for antioxidant, cytotoxic and antimicrobial activities. Among the different fractions, the aqueous soluble partitionate was found to have most potent antioxidant activity as compared to tertbutyl-1-hydroxytoluene. Antimicrobial screening of the different fractions was performed using the disc diffusion method. In these tests, the chloroform soluble fraction and carbon tetrachloride soluble fraction of methanolic extract exhibited moderate antimicrobial activity (range of zone of inhibition 8-12 mm). In brine shrimp lethality test, the carbon tetrachloride soluble extract exhibited the highest level of cytotoxicity.

**Keywords**— *Artocarpus chaplasha*; chemical constituents; antioxidant; antimicrobial; cytotoxicity

## I. INTRODUCTION

*Artocarpus chaplasha* Roxb (Syn: *Artocarpus melinoxylus* Gagnep.) is a member of the family Moraceae and is native to north-eastern India, lower Burma and the Andaman and Nicobar Islands. [1] It is a tall deciduous tree which reaches a height of 30-40 m, with a girth of 3-5 m. The tree has edible fruits. The timber is of good quality and the leaves are used for elephant fodder. They are Perennial plants. Common names of this plant include Chaplash, Chaplis, Chapalis, Lutta, Cham, Sam, Taungpeinne, Toung-peing-nai. Chaplash. It can be found at elevations up to 1650 m. It is adapted to moist conditions and requires a fairly well-marked monsoon climate. The tree is shade-bearing in youth, although it requires a fair amount of light for its later development. Wood production of this tree may be 15-40 m<sup>3</sup>/ha/year. Its bark is used to cure skin problems and powdered heals sores. On the other hand, its dry leaves are used to treat swelling of lymph glands. Its fruits help to develop appetite. [2]

## II. MATERIALS AND METHOD

### A. General experimental procedure

The <sup>1</sup>H NMR spectra were obtained using a Varian Unity 500 spectrometer (500 MHz) instrument in CDCl<sub>3</sub>. For NMR studies deuterated chloroform was used and the δ values for <sup>1</sup>H spectra were referenced to the residual non deuterated solvent signals.

### B. Plant materials collection

The stem bark of *Artocarpus chaplasha* Roxb was collected from the Botanical; garden of Dhaka, Bangladesh in November, 2012. A voucher specimen had been maintained in the National herbarium of Bangladesh under the accession number DACB-38271. The bark samples were cut into small pieces and sun dried for 7 days and then dried in oven for 24 hours at 40°C to remove moisture completely.

### C. Extraction and isolation

The air-dried and powdered stem bark (1.3 kg) of *Artocarpus chaplasha* was soaked in 3L of methanol for 15 days at room temperature and then filtered using a cotton plug, followed by filter paper (Whatman number 1 filter paper). A rotary evaporator was used to remove the solvent and make the solution concentrated. After complete evaporation of the solvent a solid residue of around 14 gm was obtained. Then the sample was subjected to Vacuum liquid chromatography [3] for the initial rapid fractionation of the crude methanolic extract. The column was first eluted with 100% Petroleum ether. Then the polarity of the mobile phases was progressively increased using a increasing concentration of ethyl acetate and passed through the column, until it reached to 100% ethyl acetate and 0% petroleum ether. For the initial screening of the VLC fraction extracts Thin layer chromatographic technique [4] was used and the compounds – 1 and 2 (9 mg), were isolated from the VLC extracts of 20% ethyl acetate in petroleum ether followed by TLC using Merck pre-coated TLC plates (Silica gel 60, F254), eluting with petroleum ether:n-Hexane (40 : 60).

An aliquot (5.0 g) of the concentrated methanolic extract was fractionated by the modified Kupchan partitioning method [5] into petroleum ether (2.0 g), carbon tetrachloride (0.75 g), chloroform (0.5 g) and aqueous (1.75 g) soluble fractions for biological activity.

#### D. Antioxidant activity

The antioxidant activities or free radical scavenging activities of the extractives were determined by DPPH assay which was developed by Brand-Williams *et al.*[6]. In this method, 1, 1-diphenyl-2-picrylhydrazyl (DPPH) is used to determine free radical scavenging activity. 2.0 ml of different partitionates of methanolic at different concentrations were mixed with 3.0 ml of a DPPH in methanol solution (20 µg/ml). Then the mixtures were kept in dark for 20 minutes for reaction. Finally, absorbance of the different solution was determined at 517 nm and the inhibition percentage was calculated from the formula:  $[(A_0 - A_1)/A_0] \times 100$ . Here  $A_0$  = the absorbance of the control and  $A_1$  = the absorbance of the test sample.

#### E. Antimicrobial screening

The antimicrobial activity of the partitionates against 10 bacteria was evaluated by using disc diffusion method [7] (Table-2). Bacteria were collected as pure cultures, from the Institute of Nutrition and Food Sciences (INFS), University of Dhaka, Bangladesh. 400 µg/ml of solutions of test samples (chloroform, aqueous, petroleum ether and carbon tetrachloride soluble partitionates of methanolic extract) were prepared by dissolving measured amount of the samples in particular volume of respective solvents. Then completely dry and sterilized filter paper discs (6 mm diameter) were taken and soaked in known amount of the test substance using micropipette and the residual solvents were allowed to evaporate completely. A positive control (standard solution of ciprofloxacin with a concentration of 40 µg/disc) and negative control (blank discs soaked in respective solvents) were also done. The plates of pure culture impregnated with discs were then allowed to keep at 4° C for 24 hours to ensure maximum diffusion of all of the test materials and standard solution. Finally, the plates were incubated at 37° C for 24. Then the diameter of zone of inhibitions were measured in mm to determine the antimicrobial activity.

#### F. Evaluation of cytotoxicity

The general cytotoxic property of the plant extractives were determined using Brine shrimp lethality bioassay [8] [9], technique. In a single day assay, DMSO solutions of the samples were applied against *Artemia salina*. 4 mg of the extractives were dissolved in DMSO in separate vessels and then solutions of decreasing concentrations (400, 200, 100, 50, 25, 12.50, 6.25, 3.125, 1.563 and 0.781 µg/ml) were obtained by serial dilution. In this test, varying concentrations of vincristine sulphate (10, 5, 2.5, 1.25, 0.625, 0.3125, 0.15625, 0.078125 and 0.0390 µg/ml) were used as positive control.

### III. RESULTS AND DISCUSSION

**Compound 1:** <sup>1</sup>H NMR (500 MHz, CDCl<sub>3</sub>): δ 4.56 (1H, dd, J = 9.0, 6.5 Hz, H-3), 0.94 (3H, s, Me-18), 0.32 (1H, s, Me-19a), 0.56 (1H, s, Me-19b), 0.88 (3H, d, J = 9.0 Hz, Me-21), 5.08 (3H, t, J = 9.0 Hz, Me-24), 1.67 (3H, s, Me-26), 1.59 (1H, s, Me-27), 0.87 (1H, s, Me-28), 0.88 (3H, s, Me-29), 0.83 (3H, s, Me-30), 2.03 (3H, s, Me-2').

**Compound 2:** <sup>1</sup>H NMR (500 MHz, CDCl<sub>3</sub>): δ 4.46 (1H, dd, J = 6.0, 10.5 Hz, H-3), 0.84 (3H, s, Me-23), 0.83 (3H, s, Me-24), 1.01 (3H, s, Me-25), 0.82 (3H, s, Me-26), 0.77 (3H, s, Me-27), 0.94 (1H, s, Me-28), 4.55 (1H, s, Me-29a), 4.67 (3H, s, Me-29b), 1.67 (3H, s, Me-30), 2.03 (3H, s, Me-2').

Chromatographic separation using VLC and TLC and purification over silica gel of the methanol extract of *Artocarpus chaplasha* revealed a total of two compounds (**1** and **2**) in a mixture. The structures of isolated compounds were established by NMR data analysis, comparison with published values and co-TLC with authentic samples.

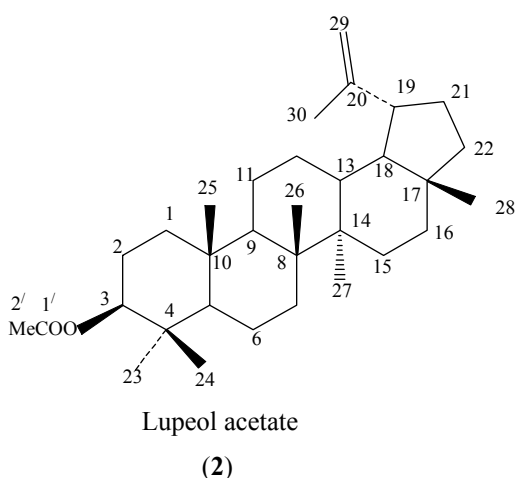
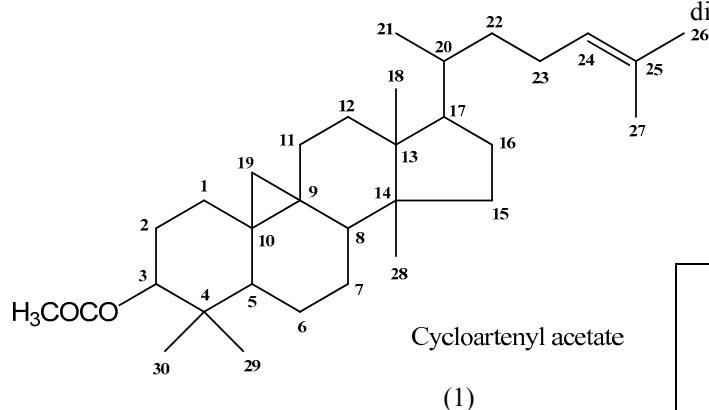
Mixture of Compound **1** and **2** (11 mg); was isolated as white powder. Compounds were obtained as white needle from the Gel Permeation column fractions from VLC fraction [n-hexane: Toluene (85: 15)] of crude methanolic extract of *Artocarpus chaplasha*. It was visualized as a spot under short wavelength of UV light (254 nm). Moreover, It appeared as a purple spot on TLC (silica gel PF<sub>254</sub>) when the plate was sprayed with vanillin sulphuric acid followed by heating at 110° C for 3-7 minutes. The R<sub>f</sub> value of the compound was 0.54 in n-Hexane–toluene (85:15) on silica gel PF<sub>254</sub> plate. Compounds were found to be soluble in n-Hexane, ethyl acetate and chloroform.

The <sup>1</sup>H NMR spectrum (500 MHz, CDCl<sub>3</sub>) showed two upfield doublets at δ 0.32 and δ 0.55 characteristic of non-equivalent protons of cyclopropyl methylene group and could be ascribed to 19a and 19b respectively. A double doublet at δ 4.46 with a large coupling constant (3H, dd, J = 6.0, 10.5 Hz) ascribed the 3α-proton indicating the presence of acetyl group at 3β-position which is further confirmed by the presence of methyl group at δ 2.03. The upfield methyl signals were appeared at δ 0.83, δ 0.88, δ 0.87, δ 0.88.

The above spectral features are in close agreement to those observed for cycloartenol [10] except that instead of H-3α proton δ 3.23 a deshielded signal at δ 4.46 appeared which is characteristic for the presence of an acetate group on this position. Further the spectrum showed a triplet at δ 5.08 and two downfield methyls at δ 1.67 and δ 1.59 which could be assigned to H-24, Me-26 and Me-27 respectively suggesting an unsaturation at C-24. On this basis, the identity of the first compound was confirmed as cycloartenyl acetate (**1**).

The remaining proton signals indicated a lupine triterpene. The <sup>1</sup>H NMR spectrum (500 MHz, CDCl<sub>3</sub>) showed two broad signals at δ 4.67 and δ 4.55 characteristic of exocyclic olefinic protons and could be assigned to H-29b and H-29a respectively. The tertiary methyl at δ 0.84, δ 0.83, δ 1.01, δ 0.82, δ 0.94 and δ 1.67 could be assigned to Me-24, Me-25, Me-26, Me-27, Me-28 and Me-30 respectively. The α-proton at C-3 appeared at δ 4.56 instead of δ 3.23 indicated that 3β OH has been acetylated which is further confirmed by the presence of acetyl methyl at δ 2.02.

On the basis of the above findings the second compound was characterized as lupeol acetate (2) [11].



antimicrobial activity (40-42 mm) exhibited by ciprofloxacin (Table 2). However, the chloroform soluble fraction, petroleum ether soluble fraction and the negative control disc did not show any inhibition of microbial growth.

**Table 2. Antimicrobial activity of *Arocarpus chaplasha* extractives and ciprofloxacin**

Test organisms	Diameter of the zone of inhibition (mm)				
	PE	CL4	CL	AQ	Ciprofloxacin
Gram positive bacteria					
<i>Bacillus aureus</i>	-	8	11	-	37
<i>Bacillus megaterium</i>	-	-	9	-	35
<i>Bacillus subtilis</i>	-	-	9	-	45
<i>Staphylococcus aureus</i>	-	7	11	-	40
<i>Sarcina lutea</i>	-	-	-	-	20
<i>Bacillus polymyxa</i>	-	-	-	-	40
Gram negative bacteria					
<i>Escherichia coli</i>	-	-	-	-	46
<i>Pseudomonas aureus</i>	-	-	-	-	-
<i>Salmonella paratyphi</i>	-	-	-	-	-
<i>Salmonella typhi</i>	-	-	-	-	-
<i>Shigella boydii</i>	-	-	-	-	27
<i>Shigella dysenteriae</i>	-	-	-	-	45
<i>Klebsiella pneumonia</i>	-	-	-	-	17
<i>Shigella flexi</i>	-	-	11	-	-
<i>Proteus vulgaris</i>	-	-	10	-	40

**Table i: IC<sub>50</sub> values of the standard partitionates of *Artocarpus chaplasha* in DPPH**

Samples	IC <sub>50</sub> value (µg/ml)
BHT (standard)	20.96
PEF	61.12
CTF	21.52
CLF	19.20
AQ	11.54

BHT = Tert- butyl-1-hydroxytoluene

Among the different fractions tested for antioxidant activity (Table 1), the aqueous soluble fraction (IC<sub>50</sub>=11.54) of the methanolic extract of *A. chaplasha* showed the highest antioxidant property and other fractions showed moderate free antioxidant property.

In the antimicrobial screening, the methanolic crude extract and its aqueous soluble fractions showed moderate antimicrobial activity with an average zone of inhibition ranging from 10-12 mm each as compared to the standard

The results of brine shrimp lethality testing after 24 hours of exposure to the samples and the positive control, vincristine sulphate are represented in Table 3. The LC<sub>50</sub> value was found to be for 1.15 µg/ml petroleum ether fraction and 1.6µg/ml for aqueous soluble fraction of the methanol as compared to the standard sample, vincristine sulphate (LC<sub>50</sub> value = 0.451 µg/ml).



**Table iii. LC<sub>50</sub> values of the standard sample and partitionates of *Arocarpus chaplasha* in brine shrimp leothalics assay**

Test Samples	LC <sub>50</sub> values (µg/ml)
VS (standard)	0.451
PEF	1.15
CTC	2.33
CLF	2.09
AQ	1.69

VS = Vincristine sulphate, PEF = Petroleum ether soluble fraction of the methanolic extract of stem bark of *A. chaplasha*, CTC = Carbon tetrachloride soluble fraction of the methanolic extract of the stem bark of *Arocarpus chaplasha*, CLF = Chloroform soluble fraction of the methanolic extract, AQ= Aqueous soluble fraction of the methanolic extract of the stem bark.

#### IV. CONCLUSION

Traditionally used medicinal plants could important sources for the development of potential lead compounds. These lead compounds may be used for the synthesis of new drugs. Our attempt was to identify new compounds in this plant that revealed two compounds and all of them are previously established. Moreover, the crude methanol extract and aqueous soluble fractions of the plant exhibited moderate antimicrobial activity; the aqueous soluble materials demonstrated the highest toxicity and most potent antioxidant activity. This is only a preliminary study and a more detailed study is under progress.

#### REFERENCES

- [1] Seibert, B. & Jansen, P.C.M., *Artocarpus* J.R. & G. ForsterIn: Verheij, E.W.M. and Coronel, R.E. (Editors). "Plant Resources of South-East Asia No. 2: Edible fruits and nuts. Pudoc, Wageningen, The Netherlands", pp. 79-83, 1991.
- [2] Deepa D. Nair, A.K. Gupta, HIMANGSHU Bikash Das Atanu Chakraboti; Medicinal plant in Tripura, 2009, [http://books.google.com.bd/books?id=74Q74U7GTQC&pg=PT45&lpg=PT45&dq=artocarpus+chaplasha+medicinal+use&source=bl&ots=QwK8526jz\\_&sig=NlccVZDTMbZfo9pbGtIEzk\\_dvQ&hl=en&sa=X&ei=pdqgUISbMlfrQfm04BY&redir\\_esc=y#v=onepage&q&f=false](http://books.google.com.bd/books?id=74Q74U7GTQC&pg=PT45&lpg=PT45&dq=artocarpus+chaplasha+medicinal+use&source=bl&ots=QwK8526jz_&sig=NlccVZDTMbZfo9pbGtIEzk_dvQ&hl=en&sa=X&ei=pdqgUISbMlfrQfm04BY&redir_esc=y#v=onepage&q&f=false)
- [3] Pelletier, S.W.; Chokshi, H.P.; Desai, H.K. "Separation of diterpenoid alkaloid mixtures using vacuum liquid chromatography". *J. Nat. Prod.* 1986, vol. 49, pp 892-900.
- [4] Liu Q.T, Kinderlerer J.L, "Preparative thin-layer chromatographic separation and subsequent gas chromatographic-mass spectrometric analysis of monoacylglycerols derived from butter oil by fungal degradation", *Journal of Chromatography A.*; 855 (2):617-624, 1999.
- [5] Vanwagenen, B. C., Larsen, R., Cardellina II, J. H., Randazzo, D., Lidert Z. C. and Swithenbank, C., Ulosantoin, a potent insecticide from the sponge *Ulosaruetzleri*, *J. Org. Chem.* 58, pp 335-337, 1993.
- [6] Brand-Williams, W., Cuvelier M.E. and Berset C. "Use of free radical method to evaluate antioxidant activity", *Lebensm. Wiss. Technol.* 28, pp 25-30, 1995.
- [7] Bauer, A. W., Kirby, W. M. M., Sherris J. C. and Turck, M. "Antibiotic susceptibility testing by a standardized single disc method". *Am. J. Clin. Pathol.* 45, pp 493-496, 1966.
- [8] McLaughlin J. L. and Rogers, L. L., "The use of biological assays to evaluate botanicals". *Drug Info. J.* 32, 1998, pp 513-524.
- [9] Meyer, B. N., Ferrigni, N. R., Putnam, J. E., Jacobsen, J. B., Nicholsand, D. E. McLaughlin, J. L. "Brine shrimp: a convenient general bioassay for active plant constituents", *Planta Med.* 45, 31-34, 1982.
- [10] Asl BARLA, H`usniye B IRMAN2, S`ukran K`ULT`URand Sevil "OKS`UZ; *Turk J Chem* 30 (2006) , 325 { 332.T`UB\_ITAK }
- [11] A.K Jamal, W.A.Yaacob and Laily B.Din. "A Chemical Study on *Phyllanthus reticulatus*.*Journal of Physical science*", Vol.19(2)45-50, 2008.

# Evaluation of in vitro anti-inflammatory activity of *Leea rubra* by membrane stabilization assay and against the denaturation of protein

Afrina Azad

Department of Pharmacy  
International Islamic University Chittagong (IIUC),  
Chittagong 4203, Bangladesh  
Email: afrina.ru.pharm@gmail.com

Shahnaj Parvin and Ekramul Islam

Department of Pharmacy,  
University of Rajshahi (RU),  
Rajshahi, Bangladesh  
Email: shahnaj\_parvin@ru.ac.bd, ekrams74@yahoo.com.au

**Abstract— Objective:** To evaluate the in vitro anti-inflammatory effect of n-hexane and methanolic extract of *Leea rubra* by membrane stabilization assay and against the denaturation of protein. **Methods:** The extract at different concentrations was incubated with red blood cell and egg albumin in controlled experimental conditions and subjected to determination of absorbance to assess the anti-inflammatory property. Aspirin was used as the reference drug. **Results:** The present findings exhibited a concentration dependent anti-inflammatory activity and inhibition of protein (albumin) denaturation by the *Leea rubra* methanolic extract. **Conclusions:** From the present study it can be concluded that *Leea rubra* possessed marked in vitro anti-inflammatory effect against the membrane stabilization assay and denaturation of protein.

**Keywords—** *Leea rubra*, Anti-inflammatory, Membrane stabilization, Denaturation, Aspirin

## I. INTRODUCTION

Inflammation is part of the complex biological response of vascular tissues to harmful stimuli, such as pathogens damaged cells, or irritants [1]. The term inflammation is derived from the Latin word—Inflammaré, means burn. Any form of injury to the human body can elicit a series of chemical changes in the injured area. The cardinal signs of inflammation are heat, redness, swelling, pain and loss of function. Inflammation usually involves a sequence of events which can be categorized under three phases viz. acute transient phase, delayed sub-acute phase and chronic

proliferate phase. Inflammation results in the liberation of endogenous mediators like histamine, serotonin, bradykinin, prostaglandins etc. In order to comprehend the inflammatory process, antagonists of mediators are generally employed in both Ayurveda and Allopathic treatment. Most of the anti-inflammatory drugs now available are potential inhibitors of cyclooxygenase (COX) pathway of arachidonic acid metabolism which produces prostaglandins. Prostaglandins are hyperalgesic, potent vasodilators and also contribute to erythema, edema and pain. Hence for treating inflammatory diseases analgesic and anti-inflammatory agents are required. These points to the utilization of plants possessing anti-inflammatory and analgesic properties. Now day's herbal drugs are routinely used for curing diseases rather than chemically derived drugs having side effects. The drugs used in inflammatory disorders may be either with analgesic and insignificant anti-inflammatory effects or with analgesic and mild to moderate anti-inflammatory activity. An array of drugs are available in the market to treat these disorders but only very few are free from toxicity. It is very important that profound research with ethnobotanical plants possessing anti-inflammatory and analgesic properties can definitely open up new vistas in inflammatory disorders. Purified natural compounds from plants can serve as template for the synthesis of new generation anti-inflammatory drugs with low toxicity and higher therapeutic value [2].

*Leea rubra* is a member of the Vitaceae family. Usually flowers and fruits as a shrub about 1-2 m tall, occasionally to 3 m. Grows in disturbed areas of lowland and upland rain forest and monsoon forest. Also occurs in SE Asia and Malesia.

## II. MATERIALS AND METHODS

### A. Plant material

The leaves of *Leea rubra* Blume were collected from the district of Bandarban, Bangladesh. The plant was identified by Dr. Shaikh Bokhtiar Uddin, Associate Professor, Dept. of Botany, Chittagong University. The fresh leaves were thoroughly washed with water and dried in shade. Then leaves were cut into small pieces if necessary to make it suitable for grinding purpose and finally dried in an oven at 40-45°C for 36 hrs. The materials were grinded separately into coarse powder with the help of a grinder and stored in an air tight container for further use.

### B. Drugs and chemicals

Aspirin was procured from Beximco Pharmaceuticals Ltd. All the other chemicals were of analytical grade obtained commercially. Double distilled water from all-glass still was used throughout the study.

### C. Preparation of methanolic extract

Powdered plant materials (leaves) having a weight of about 10 gm were taken in an amber colored reagent bottle with 50ml of n-Hexane. This was kept for overnight with occasional shaking and stirring. The whole mixture was then filtered and discarded the supernatant.

Then the residue was taken and mixed with methanol and water at a ratio 4:1 (where, total volume is 50ml) and kept it for overnight. The whole mixture was then filtered through cotton and then through Whitman No.1 filters paper and collected the supernatant (Filtrate-1). Further the residue was mixed with methanol and water at a ratio 4:1 (total volume is 50ml) and kept at 2-3 hours. The whole mixture was then filtered through cotton and then through Whitman No.1 filters

paper and collected the filtrate (Filtrate-2). Then combine the two filtrate (Filtrate-1 & Filtrate-2)<sup>[3]</sup>

### D. Evaluation of in vitro anti-inflammatory activity

D.1. Human red blood cell membrane cell (HRBC) membrane Stabilization method :

The human red blood cell membrane stabilization method (HRBC) has been used as a method to study the *in-vitro* anti-inflammatory activity<sup>[4]</sup>. NSAIDs were used as standard and anti-inflammatory activity was expressed as percentage of RBC lysis. HRBC or erythrocyte membrane is analogous to the lysosomal membrane<sup>[5]</sup> and its stabilization implies that the extract may as well stabilize lysosomal membranes. Various methods are employed to screen study drugs, chemicals, herbal preparation that exhibit anti-inflammatory properties or potentials. In the present study, stabilization of erythrocyte membranes exposed to heat and hypotonic solution were employed due to its simplicity and reproducibility. The hemoglobin content in the suspension was estimated using spectrophotometer at 560 nm.

Preparation of blood sample:

The blood sample was collected from healthy human volunteer who had not taken any NSAIDs for 2 weeks prior to the experiment. It was centrifuged at 2500rpm for 5min and the supernatant was removed. The cell suspension was washed with sterile saline solution (0.9% w/v NaCl) and centrifuged at 2500rpm for 5mins. This was repeated three times till the supernatant was clear and colorless and the packed cell volume was measured. The cellular component was reconstituted to a 40% suspension (v/v) with phosphate buffer saline (10mM, P<sup>H</sup>7.4)

Heat-induced haemolysis

$$\% \text{ inhibition of haemolysis} = 100 \times \left[ 1 - \frac{OD_2 - OD_1}{OD_3 - OD_1} \right]$$

Hypotonicity-induced haemolysis

% of stabilization activity

$$=100-\left[\frac{\text{test absorbance}-\text{test control absorbance}}{\text{blank absorbance}}\right]\times 100$$

#### D.2. Evaluation of egg albumin denaturation:

Denaturation of tissue proteins is one of the well documented causes of inflammatory and arthritic diseases. In the present investigation, the in vitro anti-inflammatory effect of CME of *Leea rubra* Blume (Leaves Powder) was evaluated against denaturation of egg albumin. The percentage inhibition of protein denaturation was calculated by using the following formula:

% inhibition of haemolysis

$$= 100 \times \left[ 1 - \frac{OD_2 - OD_1}{OD_3 - OD_1} \right]$$

### III. Results and Discussion

The methanolic extract of *Leea rubra* was studied, in vitro anti-inflammatory activity by HRBC membrane stabilization method and egg albumin denaturation assay. Phytochemical analysis revealed that methanolic extract of *Leea rubra* contains alkaloids, saponins, tannins, glycosides, steroids phenols, flavonoids. The results obtained demonstrate that the extract has significantly concentration dependently inhibits RBC haemolysis. For hypotonicity induced haemolysis, at the concentration of 100 and 1000 µg/ml, CME showed 7.91% and 85.11% protection, respectively, whereas aspirin at above concentration showed 49.60% and 79.25% inhibition of RBC haemolysis (Table-1). And for heat induced haemolysis, at the concentration of 100 and 500 µg/ml, CME showed 36.05% and 65.95% protection, respectively, whereas aspirin at above concentration showed 12.50% and 64.75% inhibition of RBC haemolysis (Table-2). The egg albumin denaturation assay also exhibited a concentration dependent inhibition of protein (albumin) denaturation by CME throughout the concentration range of 100 to 1000 µg/ml. Aspirin at the concentration range of 100 to 1000 µg/ml was used as reference drug which also exhibited concentration dependent inhibition of protein denaturation (Table-3).

**Table 1- Effect of CME and Aspirin of *Leea rubra* Blume on hypotonicity- induced haemolysis of RBC membrane**

Treatment	Concentration	%Inhibition
-----------	---------------	-------------

<i>Leea rubra</i>	100	7.91±1.738
leaves	400	51.34±0.657
methanolic	1000	85.11±0.230
extract	100	49.60±0.529
Aspirin(Drug)	1000	79.25±0.362

Control: 1.149

**Table 2- Effect of CME and Aspirin of *Leea rubra* Blume on heat- induced haemolysis of RBC membrane**

Treatment	Concentration	%Inhibition
<i>Leea rubra</i>	100	36.05±0.532
leaves	300	45.80±2.378
methanolic	500	65.95±0.498
extract	100	49.60±0.308
Aspirin(Drug)	500	79.25±0.135

Control: 0.965

**Table 3- Effect of CME and Aspirin of *Leea rubra* Blume on egg albumin denaturation.**

Treatment	Concentration	%Inhibition
<i>Leea rubra</i>	100	9.05±1.471
leaves	750	36.05±1.36
methanolic	1000	46.44±1.65
extract	100	49.60±1.29
Aspirin(Drug)	1000	79.25±2.39

Control: 1.890

### CONCLUSION

This study has provided some scientific justification for the folkloric use of the leaves of the plant for the treatment of inflammatory conditions, pain and infection.

### Acknowledgment

I would like to express my heartfelt thanks to Dr. Mst. Shahnaj Parvin, Professor, Department of Pharmacy, University of Rajshahi, for her constant supervision. Dr. Md. Ekramul Islam, Professor, Department of Pharmacy, University of Rajshahi, for his valuable suggestions and open hearted co-operation during my research work. My special

thanks to department of Pharmacy, University of Rajshahi for Providing the adequate facilities to carry out my project work.

#### REFERENCES

1. Ferrero-Miliani L, Nielsen OH, Andersen PS, Girardin SE: Chronic inflammation: importance of NOD2 and NALP3 in interleukin-1beta generation. *Clin. Exp. Immunol.* 2007, 147 (2):1365-2249.
2. Ravikiran AG, Elumalai M, Eswaraiah C, Naresh V: An annual review of anti-inflammatory medicinal plants. *Inter. J. of Phytoth.* 2012, 2(1):23-27.
3. C. Asha Poorna, M.S. Resmi and E.V. Soniya. *In vitro* Antioxidant Analysis and the DNA Damage Protective Activity of Leaf Extract of the *Excoecaria agallocha* Linn Mangrove Plant. *INTECH.* 156.
4. Tjolsen A; Berge OG, Hanskaar S Rosland JH, Hole K. The formalin test; an evaluation of the method. *Pain* 1992;51:5-7
5. Prempeh ABA, Mensah-Attipoe J. Crude aqueous extract of the root stem bark of *zanthoxylum xanthoxyloides* inhibits white blood cells migration in acute inflammation. *Ghana. Med. J.* 2008; 42(3): 117-119.

# Antimicrobial Activities of Isolated Probiotics and Their Metabolites against Some Pathogenic Microorganisms

Mohammed Abu Sayeed, Altaf Hossen and Md. Jakaria

Department of Pharmacy,  
International Islamic University Chittagong (IIUC),  
Chittagong 4203, Bangladesh

**Abstract**— The study was aimed to finding the antimicrobial activities among probiotics isolated from different yoghurts and their metabolites against some common bacterial pathogens. The nutrient agar media overlay method (Disc diffusion Method) was used to determine the presence of antibacterial effects among the isolated probiotics. Probiotics produced potential antibacterial activities against several pathogenic bacteria and fungi. The maximum antibacterial property (13.5 mm of zone of inhibition) of bacterial strain found against *Salmonella paratyphi*. Conversely, bacterial metabolites produced maximum effect (10.3 mm of zone of inhibition) against *Staphylococcus aureus*. The antibacterial effect is one of the most important criteria for probiotics selection, and the verified antibacterial activities of the probiotics supports the development of these functional foods as a key to the enhancement of health in the consuming public.

**Keywords**—Probiotics, yoghurts, *Salmonella paratyphi*, *Staphylococcus aureus*, antimicrobial effects

## I. INTRODUCTION

Probiotics defined as the microorganisms (in most cases, bacteria) that are supposed to provide health benefits when consumed [1-2]. They are also known as “friendly bacteria” or “good bacteria.” Nowadays, the term probiotic is used to name ingested microorganisms associated with benefits for humans and animals [3]. In medicine, probiotics are living microorganisms, which are incorporated into different kinds of foods due to their health-promoting effects. Due to lack of no side effects, probiotics are used for long times in food ingredients for human as well as to feed the animals. In addition, probiotics are suitable because of being naturally found in the intestinal tract as intestinal flora of healthy humans and in foods.

In the present day, the members of the genera *Lactobacillus*, *Bifidobacterium* and *Streptococcus* are the most familiar probiotics used in commercial fermented and non-fermented dairy products [4]. The properties against bacteria are one of the most significant selection criteria for probiotics [5]. The antimicrobial effects of lactic acid bacteria are formed by producing some substances such as organic acids (lactic, acetic, propionic acids), carbon dioxide, hydrogen peroxide,

diacetyl, low molecular weight antimicrobial substances and bacteriocins [6].

A number of studies have found probiotic consumption to be useful in the treatment of many types of diarrhea, including antibiotic-associated diarrhea in adults, travelers' diarrhea, and diarrheal diseases in young children caused by rotaviruses. The most commonly studied probiotic species in these studies have been found to be *Lactobacillus GG*, *L. casei*, *B. bifidum* and *S. thermophilus* [7]. The aim of this study was to determine the presence of antibacterial effects among the probiotics isolated from different yoghurts against some common bacterial pathogens.

## II. MATERIALS AND METHODS

### A. Yoghurts, Probiotics, Media and Pathogen Strains

Yogurt was collected from different brand sources such as; Arong sour yoghurt, Rosmela sour and sweet yoghurt, Rajdani sweet yoghurt and Eglo sweet yoghurt. 100µl of each samples were taken by the micropipette from each tube, then incorporate into Petri-dish. Samples were spread out into Petri-dishes. Then nutrient agar media was to be given in each Petri-dish and kept in incubator for 24-48 hour. Cultures in solid media were visually inspected for growth rate and colony characteristics. Several types of colonies were seen in the Petri-dishes. The Probiotic properties were determined by several tests like Resistance to low pH and Resistance to 1% bile salt etc. Carbohydrate Fermentation Test, Glucose fermentation test, Tolerance Against 6.5% Sodium Chloride and protein nature tests were also performed. The isolated bacteria were gram stained for the study of microscopic morphology. The test pathogens were gram positive bacteria like *Bacillus cereus*, *Bacillus subtilis*, Gram negative bacteria *Salmonella paratyphi*, *Vibrio parahemolyticus*, *Staphylococcus aureus*, *Escherichia coli*, *Shigella dysenteriae*, *Sarcina lutea* and fungi like *Candida albicans*, *Aspergillus niger* etc.

### B. Determination of Antimicrobial Effects

The selected pathogens were maintained in nutrient agar media at 25<sup>o</sup> C. The test antimicrobial activity, prepared standard discs (isolates) as the concentration of 20µl of each sample.

Determination of antimicrobial activity of isolated metabolites against different pathogenic microorganisms from subculture also was performed. The blank discs were kept in covered Petri dishes and then subjected to dry heat sterilization for 1hr at 150°C. After completion of sterilization, both the sterilized glass materials and discs were kept in a laminar hood for 30 minutes. UV light was switched on before working in laminar hood to avoid any accidental contamination. Isolated metabolites were re-suspended by adding 0.5 ml phosphate buffer (pH-7.1) and shaking vigorously for dissolve of metabolites. For each disc 20µl sample were applied. In Nutrient agar plates, 500µl pathogenic subcultures were spread.

The prepared metabolites discs were placed gently on the solidifier agar plates where contains the pathogenic organism with the help of a sterile forcep to ensure complete contact with medium surface. This was sufficient time for the material to diffuse to a considerable area of the medium. Finally, the plates were incubated at 37°C for 24 hrs [8].

### III. RESULTS AND DISCUSSION

#### A. Macroscopic and Microscopic Properties Of Isolated Probiotics

The probiotics isolates were cream colored, circular, convex and moist with smooth edges. Microscopic smear of gram staining of the Colonies showed gram-positive, non-sporeforming short bacilli in pairs or in chains. The results were those expected of *Streptococci sp*, *Lactobacillus sp* and *Bifidobacterium sp. found in yoghurt*. When slides were observed under light microscope, it was shown 8 (eight) colonies gave blue (violet) colour among 15 colonies. So, they were gram positive (+ve) bacteria and other colonies were discarded. Selected colonies were given new code (Table 1).

Table 1. Gram staining result of isolates

Strain code	Colour	Gram stain	New code
ATY-1	Blue	+	1
ATY-2	Blue	+	2
ATY-3	Red	-	×
ATY-4	Blue	+	3
RTY-1	Blue	+	4
RTY-2	Red	-	×
RTY-3	Red	-	×
RTY-4	Blue	+	5
EMY-1	Blue	+	6
EMY-2	Red	-	×
EMY-3	Red	-	×
RMY-1	Blue	+	7
RMY-2	Blue	+	8
RMY-3	Red	-	×
DMY	Red	-	×

#### B. Antimicrobial Activities of Selected Strains

All strains of probiotic bacteria were found from experiments. These strains were catalase negative, survived against low pH (pH 3.0 & 1.0) during 3 hours and against 1% bile salt during 4 hours, show antimicrobial activity against different types of pathogenic bacteria. The bacterial strains had antagonistic effect against pathogenic bacteria. The zone of inhibition in mm was shown in Table 2. In antimicrobial activity test, all 8 strains were given effect against all pathogenic bacteria. But strain no. 1 did not given effect against *Bacillus subtilis*. Beside *Bacillus sereus*, bacterial strain no. 6 & 1 produced maximum zone of inhibition (10.75mm & 9.6mm) but against *Bacillus subtilis*, no. 3 & 2 strains produced maximum zone of inhibition (8.35mm & 7.45mm). Maximum inhibition of *Salmonella paratyphi* occurred by 7 & 6 number of strains and inhibition area were 13.55mm & 9.35mm respectively. Strains no. 7 & 8 produced maximum inhibition (12.85mm & 10.55mm) against *Vibrio parahemolyticus*. For *Staphylococcus aureaus*, strains 5 & 6 produced higher inhibition (15.00mm & 10.9mm) than other strains. Against *E.coli*, strains 3 & 5 produced maximum inhibition (12.85.55mm & 12.15mm) respectively. Higher inhibitions of *Shigella dysenteriae* occurred by 4 & 7 number strains and inhibited area are 8.3mm and 8.05mm. Strains 8 & 7 produced maximum inhibition (9.2mm & 9.1.6mm) against *Sarcina lutea*. For *Candida albicans*, higher inhibition are caused by strains 3 & 4 respectively and inhibited area in slide calipers were 10.95mm & 8.55mm. Against *Apergillus niger*, strains 5 & 4 produced maximum zone of inhibition (7.8mm & 7.75mm) than others strains. Among all strains, 15.0mm was maximum zone of inhibition against *Staphylococcus aureaus* and effective strains are 8 number strain.

#### C. Antimicrobial Activities of Bacterial Metabolites

Bacteriocin or bacterial metabolites show significant inhibitory action against pathogenic bacteria. Isolated metabolites were diluted by using 500µl phosphate buffer (pH-7.1). Disc contains 20µl metabolites samples and 500µl pathogenic bacteria were spread in agar plate. Then all dishes were kept in incubator for 24 hour's. Isolated bacterial metabolites were considered for antimicrobial test against 10 pathogenic bacteria. We observed that all 8 different metabolites were produced zone of inhibition against given pathogenic bacteria but 3, 4 number metabolites have no any activity against *Shigella dysenteriae*. Antibacterial activity of metabolites is given in Table 3.

Against *Bacillus sereus*, metabolites 6 & 2 produced maximum zone of inhibition (8.05mm & 8.2mm). Against *Bacillus subtilis*, 2 & 3 number metabolites produced maximum zone of inhibition (9.8mm & 9.8mm). Maximum inhibition of *Salmonella paratyphi* occurred by 4 & 6 number of metabolites and inhibition area were 8.8mm & 8.4mm respectively. Metabolites 7 & 5 produced maximum inhibition (8.05mm & 7.6mm) against *Vibrio parahemolyticus*. For *Staphylococcus aureaus*, metabolites 2 & 3 produced higher inhibition (9.05mm & 8.9mm) than other metabolites. Against

*E. coli*, metabolites 8 & 7 produced maximum inhibition (9.55mm & 7.75mm) respectively. Higher inhibition of *Shigella dysenteriae* occurred by 8 & 1 number metabolites and inhibition area were 8.55mm and 7.6 mm. Metabolites 5 & 1 produced maximum inhibition (8.1mm & 7.6mm) against *Sarcina lutea*. For *Candida albicans*, higher inhibition were caused by metabolites 8 & 7 respectively and inhibition area in slide calipers were 9.1mm & 8.3mm. Against *Apergillus niger*, metabolites 8 & 7 produced maximum zone of

inhibition (7.7mm & 7.35mm) than others metabolites. Among all metabolites, 9.8mm is maximum zone of inhibition against *Bacillus subtilis* and effective metabolites were 2 & 3 numbers metabolite.

Table 2: Zone of inhibition of isolates against pathogenic bacteria

Pathgenic Organisms		Zone of Inhibition in mm							
Name	Code	Strain Code of Selected Bacteria							
		1	2	3	4	5	6	7	8
<i>Bacillus sereus</i>	1	9.6±4.8	6.8±0.6	6.9±0.8	7.3±0.0	7.4±1.0	10.7±5.0	6.65±1.1	9.6±4.4
<i>Bacillus subtilis</i>	3	–	7.4±2.7	8.35±3.3	7.4±0.2	7.0±0.6	6.2±0.2	6.65±0.3	6.1±0.0
<i>Salmonella paratyphi</i>	4	7.9±0.8	7.5±1.6	6.33±0.5	6.7±1.2	7.4±1.4	9.35±3.3	13.5±8.9	11.5±0.0
<i>Vibrio parahemolyticus</i>	6	7.95±2.3	6.3±0.0	6.4±0.0	6.3±0.1	6.65±1.1	7.85±2.5	12.8±4.2	10.5±4.6
<i>Staphylococcus aureus</i>	8	7.4±2.6	8.65±2.3	7.35±0.5	9.15±1.7	15±0.6	10.9±0.9	6.1±0.0	7.5±0.8
<i>E.coli</i>	9	7.65±1.1	7.9±0.4	12.85±4.2	9.8±3.7	12.1±0.5	7.7±0.4	7.6±0.0	6.8±0.0
<i>Shigella dysenteriae</i>	10	7.55±0.5	7.5±2.2	7.1±0.0	8.3±2.8	7.05±1.7	6.4±0.0	8.05±0.7	6.5±0.8
<i>Sarcina lutea</i>	12	7.8±0.0	6.25±0.3	6.3±0.0	7.6±0.0	6.15±0.1	7.8±0.0	9.1±0.0	9.2±0.0
<i>Candida albicans</i>	15	8.5±1.2	9.5±2.4	10.95±0.3	8.85±0.5	7.7±1.0	8.2±0.2	6.15±0.1	7.35±2.4
<i>Asergillus niger</i>	16	6.75±0.3	7.2±0.0	7.2±1.8	7.75±1.1	7.8±1.4	7.7±0.0	7.7±0.8	6.8±0.8

Values are presented as the Mean ± SE (n=3)

Table 3: Inhibitory result of metabolites against pathogenic bacteria

Pathgenic Organisms		Zone of Inhibition in mm							
Name	Code	Strain Code of Isolated Metabolites							
		1	2	3	4	5	6	7	8
<i>Bacillus sereus</i>	1	6.85±0.1	8.2±0.8	6.75±1.1	7.9±0.0	6.95±1.3	8.05±0.3	7.6±1.0	6.7±1.2
<i>Bacillus subtilis</i>	3	7.8±0.0	9.8±1.5	9.8±1.5	7.25±0.7	7.8±1.8	7.5±0.8	7.35±1.9	7.9±1.4
<i>Salmonella paratyphi</i>	4	7.25±0.9	7.25±0.9	8.05±1.1	8.8±0.8	8.65±3.8	7.6±1.4	8.4±1.4	8.4±1.6
<i>Vibrio parahemolyticus</i>	6	7.4±2.6	7.1±2.0	6.95±0.3	7.15±1.9	7.6±2.6	7.35±0.1	8.05±0.5	7.5±2.5
<i>Staphylococcus aureus</i>	8	9.05±3.0	10.3±0.0	8.9±0.0	6.85±1.1	6.65±1.1	7.35±1.9	8.1±0.4	7.0±3.3
<i>E.coli</i>	9	7.6±2.2	7.55±2.7	6.5±0.8	6.45±0.5	6.15±0.1	6.7±1.2	7.7±0.9	9.5±2.0
<i>Shigella dysenteriae</i>	10	7.6±1.4	6.9±0.0	–	–	6.2±0.2	6.45±0.5	6.8±0.0	8.5±0.7
<i>Sarcina lutea</i>	12	7.6±1.8	6.7±0.2	7.3±1.2	7.35±0.9	8.1±3.6	7.3±1.6	6.95±0.5	7.0±1.6
<i>Candida albicans</i>	15	8.15±1.3	7.8±0.6	8.25±1.9	7.75±2.7	7.25±1.3	7.3±1.2	8.3±0.4	9.1±1.0
<i>Aspergillus niger</i>	16	6.5±0.8	6.93±1.3	7.0±0.3	6.1±0.0	6.1±0.0	6.1±0.0	7.35±2.1	7.7±1.8

Values are presented as the Mean ± SE (n=3)

Due to the exceptional properties, probiotic bacteria may also have competed for nutrients [9], and at the same time produced hydrogen peroxide and bacteriocins that performed as antibiotic agents [10]. Excluding, bacteriocins, numerous probiotics also competent of reuterine production that is well-known to act as an antibacterial compound [11].

Finally, the capacity of the probiotics incorporated in bioyoghurts to inhibit the growth, or even kill certain selected pathogens confirms the health benefits one derives from the consumption of these yoghurts. Taking of these products can help protect one from occurrences of diarrhea, food poisoning and even systemic and enteric infections. The verified antibacterial effects of the probiotics supports the development



of these functional foods as a key to the improvement of the health in the consuming public.

### **Acknowledgment**

The authors are grateful to the Department of Pharmacy, East West University for valuable support during the progression of laboratory work.

### **References**

[1] C. Hill, F. Guarner, G. Reid, G.R. Gibson, D.J. Merenstein, B. Pot, L. Morelli, R.B. Canani, H.J. Flint, S. Salminen, P.C. Calder, M.E. Sanders, "Expert consensus document. The International Scientific Association for Probiotics and Prebiotics consensus statement on the scope and appropriate use of the term probiotic", *Nature reviews. Gastroenterology & hepatology*, 11(8): 506-14.

[2] G.T. Rijkers, "Health benefits and health claims of probiotics: Bridging science and marketing", *British Journal of Nutrition*, 106(9): 1291-6.

[3] A. Magdalena, "Probiotics in food: health and nutritional properties and guidelines for evaluation", *FAO Food and Nutrition paper 85*, 2006, pp. 1-50.

[4] K. Heller, "Probiotic bacteria in fermented foods: Product characteristics and starter organisms", *Am. J. Clin. Nutr.*, 2001, 73, 374S-79S.

[5] T.R. Klaenhammer, M.J. Kullen, "Selection and design probiotics", *Int. J. Food Microbiol.*, 1999, 50, 45-57.

[6] A.C. Quwehand and S. Vesterlund, "Antimicrobial components from lactic acid bacteria. *Lactic Acid Bacteria*", *Microbiological and Functional Aspects*, Marcel Dekker Inc., New York, USA 2006.

[7] E. Isolauri, M. Juntunen, T. Rautanen, P. Sillanauke, T. Koivula, "A human *Lactobacillus* strain (*Lactobacillus casei* sp. Strain GG) promotes recovery from acute diarrhea in children", *Pediatrics*, 1991, 88, 90-7.

[8] S.F. Barefoot and T.R. Klaenhammer, "Purification and characterization of the *Lactobacillus acidophilus* bacteriocin lactacin B". *Antimicrob. Agents Chemother.*, 1984, 26, 328-34.

[9] P. Marteau, P. Pochart, B. Flourie, P. Pellier, L. Santos, J.F. Desjeux, J.C. Rambaud, "Effect of chronic ingestion of a fermented dairy product containing *Lactobacillus acidophilus* and *Bifidobacterium bifidum* on metabolic activities of the colonic flora", *Am. J. Clin. Nutr.*, 1990, 52, 685-88.

[10] D. Wolfson, "A probiotics primer". *Nutrition Science News*, 1999.

[11] B. Ray, "Health benefits of beneficial bacteria". *Fundamental Food Microbiology*, CRC Press, USA, 1996, pp. 107, 194-97.

# ***Labisia Pumila* Regulates the Expressions of Bone-Related Genes and Pro-Inflammatory Cytokines in Postmenopausal Osteoporosis Rat Models**

Nadia Mohd Effendy <sup>1,2</sup> and Ahmad Nazrun Shuid <sup>1,†\*</sup>

<sup>1</sup> Department of Pharmacology, Faculty of Medicine, Pusat Perubatan Universiti Kebangsaan Malaysia, 56000 Cheras, Kuala Lumpur, Malaysia, E-Mail: nadiaeffendy@yahoo.com

<sup>2</sup> Department of Pharmacology, Faculty of Medicine, Universiti Sains Islam Malaysia, Jalan Pandan Utama, Pandan Indah, 55100 Kuala Lumpur

† *These authors contributed equally to this work.*

\* Author to whom correspondence should be addressed; E-Mail: anazrun@ppukm.edu.my ; Tel.: +603-91459576; Fax: +603-91459547.

---

**Abstract:** Background: *Labisia pumila var. alata* (LP) has shown potential as an anti-osteoporotic agent in recent years. The crude extract of LP was reported to reverse trabecular microarchitecture changes induced by ovariectomy. The mechanism is still unclear but it may be elucidated by examining the bone molecular pathways. This study aimed to evaluate the bone-related genes and pro-inflammatory cytokines expressions to provide a mechanistic overview on how the different LP extracts could prevent degenerative bone changes. Methods: Forty-eight female Sprague-Dawley rats were randomly divided into sham-operated (Sham), ovariectomized control (OVX), ovariectomized and given oestrogen at 64.5µg/kg (ERT), ovariectomized and given LP aqueous extract at 100 mg/kg (LP<sub>aq</sub>), ovariectomized and given LP methanol extract at 100 mg/kg (LP<sub>met</sub>) and ovariectomized and given LP ethanol extract at 100 mg/kg (LP<sub>et</sub>) All treatments were given daily via oral gavages for nine weeks. Rats were then euthanized and femora dissected out for genes and cytokines expressions analysis. Results: Among the extracts, LP<sub>aq</sub> was found to produce the highest expressions of OPG, osteocalcin, osterix, osteonectin and ALP. LP<sub>aq</sub> was also shown to down-regulate the expressions of RANKL, MMP9, M-CSF as well as cytokine IL-

1β. Conclusion: Aqueous extract is the best extract of LP which may exert anti-osteoporosis activity by regulating the bone-related genes and cytokines expressions.

**Keywords:** *Labisia pumila*; osteoporosis; postmenopausal, bone; gene expression; cytokine

---

## 1. Introduction

Osteoporosis is a disease which causes bone loss and fractures that leads to severe pain, deformity and in certain cases secondary complications resulting in death (Johnell and Kanis, 2006). The disease is classified clinically to be either primary or secondary osteoporosis. Primary osteoporosis refers to both bone loss occurring in post-menopausal women (type I) and bone loss owing to the normal ageing process (type II). Secondary osteoporosis refers to bone loss that ensues as a secondary effect to other diseases or drugs treatment. Post-menopausal osteoporosis (type I) is the most common form of the disease which occurs when estrogen is deficient following menopause (Riggs *et al.*, 2002). Osteoporosis generally affects women (75%) to a greater extent than men (25%). This gender imbalance is contributed by three primary factors: firstly, women achieve a lower peak BMD than men; secondly, the bone density in women declines rapidly following menopause due to estrogen deficiency; and thirdly, in most populations, women have a longer life expectancy than men, and as a consequence there is a steadily increasing proportion of elderly women (Peter, 2013).

Osteoporotic fractures reduced the quality of life and cause financial burden to society, hence it should be prevented. The available pharmacological anti-osteoporotic agents for postmenopausal osteoporosis includes estrogen replacement therapy (ERT), biphosphonates, strontium ranelate and teriparatide (Stevenson *et al.*, 2005; Marcea *et al.*, 2012). Although they are known to be effective, they are not free of side-effects (Varenna, 2013). Calcium and vitamin D are commonly prescribed but have also been

associated with an increased risk of cardiovascular diseases (Bolland *et al.*, 2011). This has led to a search for new agents with anti-osteoporotic activities but with minimal side effects.

*Labisia pumila* (LP), a herb used for women's health for many generations, was recently found to possess estrogen-like effects on bone (Melissa *et al.*, 2012). LP or also known traditionally as *Kacip Fatimah* is available in three common varieties which are *Labisia pumila* var. *alata*, *Labisia pumila* var. *pumila* and *Labisia pumila* var. *lanceolata* (Ariffin, 2005). LP is used by the locals to treat menstrual irregularities, promote uterine contraction after delivery, promote sexual health (Bodeker, 1999) as well as treating rheumatism and sickness in bones (Fasihuddin *et al.*, 1995; Jamal *et al.*, 1998). Studies have confirmed that LP exerted phytoestrogenic effects which may explain its therapeutic benefits on women's health (Fazliana, 2010). The phytoestrogenic property of LP is contributed by the presence of compounds such as alkaloid, flavonoids, saponins, tannins and triterpenes (Nadia *et al.*, 2014). Other than phytoestrogenic effects, LP also exerts anti-oxidative and anti-inflammatory properties. These actions may contribute to the therapeutic values of LP on bone.

Previous study done by Nazrun *et al.* (2012) reported that LP supplementation at the dose of 17.5mg/kg was able to increase bone formation marker and reduce bone resorption marker in ovariectomized rats. Nadia *et al.* (2014) reported that supplementation of LP crude extract at the dose of 100 mg/kg daily was able to reverse all the OVX-induced trabecular bone changes as quantified by micro-computed tomography (micro-CT) analysis. These have led to the belief that LP may provide as alternative to conventional anti-osteoporotic agents. Despite its positive effects on bone, these studies did not provide sufficient data to determine the anti-osteoporosis mechanisms of LP. Therefore, studies are needed to provide better understanding of the mechanisms involved in LP- protection against osteoporosis.

Osteoporosis occurs due to an imbalance in bone remodeling where bone resorption outweighs the bone formation processes. Estrogen plays an important role in maintaining this balance via several mechanisms (Khosla, 2007; Maria *et al.*, 2013). The main mechanism is via direct effects on osteoblasts and osteoclasts. Estrogen exerts pro-apoptotic effects on osteoclasts and anti-apoptotic effects on

osteoblasts (Manolagas, 2000). Hence, estrogen deficiency will result in disturbance of the balance between bone resorption and formation in favour of the former. This will consequently lead to increased rate of bone remodeling that leads to bone loss (Manolagas *et al.*, 2002). Indirectly, estrogen acts on several bone-related genes and cytokines known to play important roles in bone remodeling (Collin-Osdoby *et al.*, 2001; Clowes *et al.*, 2005).

The main proteins involved in controlling the balance between osteoblast and osteoclast activities are receptor activator of nuclear factor- $\kappa$ B ligand (RANKL) and osteoprotegerin (OPG), which are encoded by gene TNFSF11 and TNFRSF11b, respectively. Previous studies have reported that estrogen deficiency will cause the activation of T cell, which will then stimulate RANKL production and increase the rate of osteoclastogenesis (Eghbali-Fatourehchi *et al.*, 2003). OPG on the other hand, will act as an anti-osteoclastogenic factor, which is a negative feedback regulator to bone resorption (Jabbar *et al.*, 2011). There are also postulations of inflammatory components taking part in the pathogenesis of postmenopausal osteoporosis (Yun and Lee, 2004; Ganesan *et al.*, 2005). Recently, there were numerous reports of raised pro-inflammatory cytokines in osteoporotic patients (Koh *et al.* 2005). In view of all these reports, there is a need to measure the related genes and cytokines expressions to give insight on the mechanisms involved in the bone protective effects of LP extracts. To the best of our knowledge, this is the first study on the molecular mechanisms of the different LP extracts against osteoporosis.

## **2. Results**

### *2.1. Bone Formation-Related Genes Expression*

The median fluorescence intensity (MFI) of all the genes were normalised to the expression of GAPDH. BGLAP gene, which expressed osteocalcin protein showed a significantly higher expression in the Sham, ERT and LP<sub>aq</sub> groups compared to the OVX group (Figure 1b). The expressions of gene SP7 (osterix) were significantly higher only in the LP<sub>aq</sub> group compared to the OVX group (Figure 1c). There were significantly higher expressions of SPARC gene (osteonectin) in the LP<sub>aq</sub> and LP<sub>met</sub> groups compared to the OVX group (Figure 1d). ALP1 gene showed significantly higher expressions in the

Sham and LPaq groups compared to the OVX group (Figure 1e). These results have clearly shown that LPaq supplementation was the most effective LP extract in up-regulating the expressions of osteoblast-related genes. The methanolic extract of LP (LPmet) also significantly increased the expressions of several bone formation genes albeit not as effective as the aqueous extract (LPaq). There were no significant differences in the expressions of RUNX2, COL1 $\alpha$ 1 and IBSP genes between the groups.

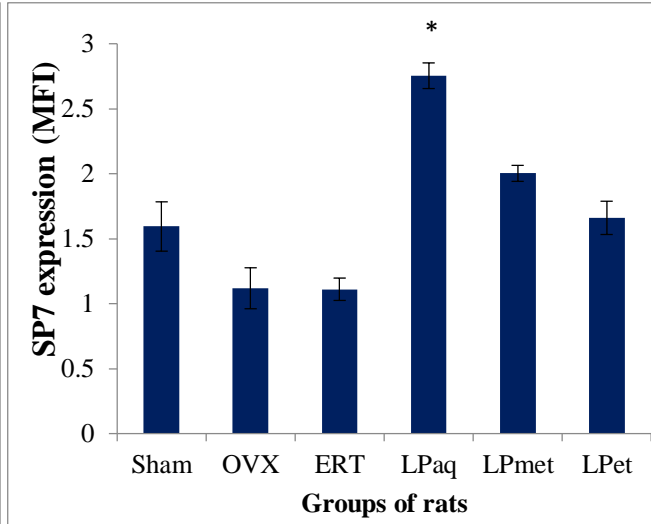
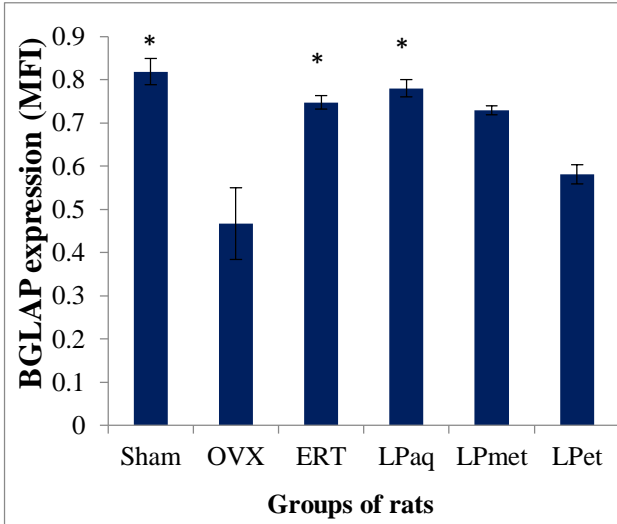


Figure 1a

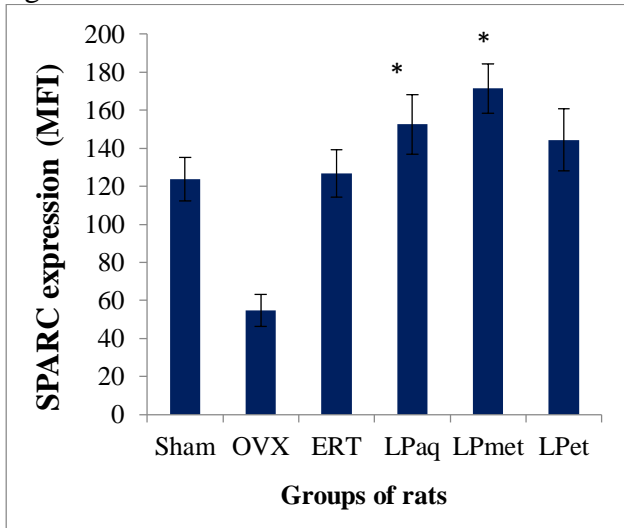


Figure 1c

Figure 1b

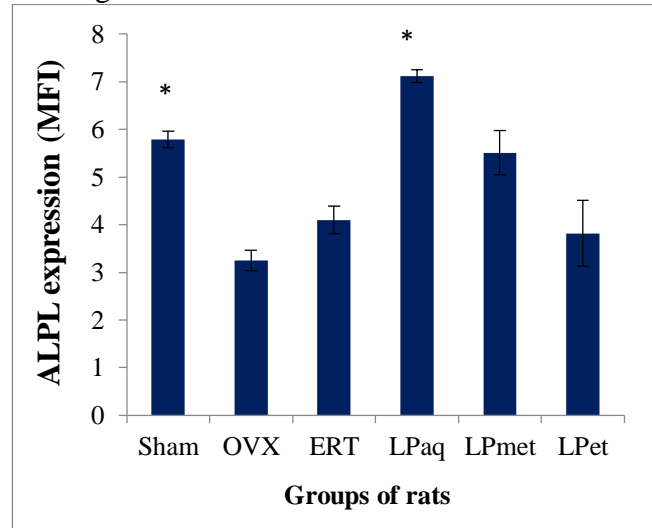


Figure 1d

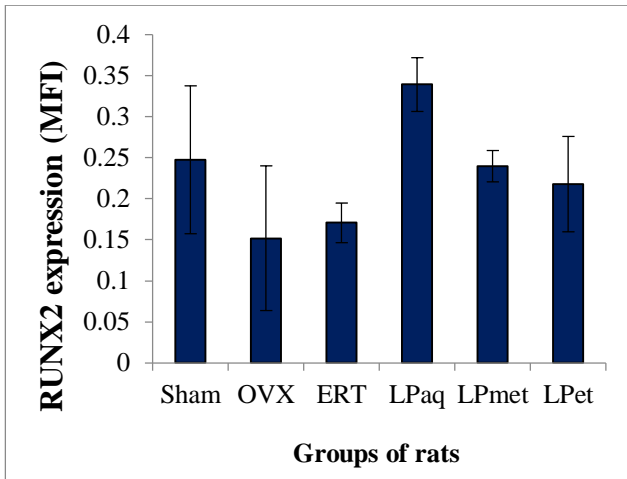


Figure 1e

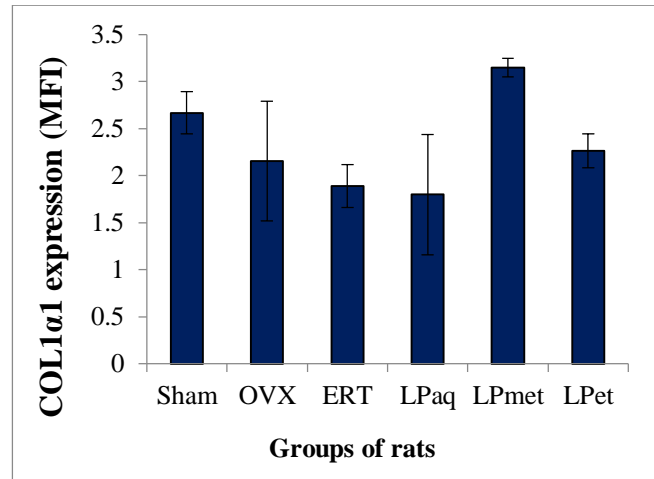


Figure 1f

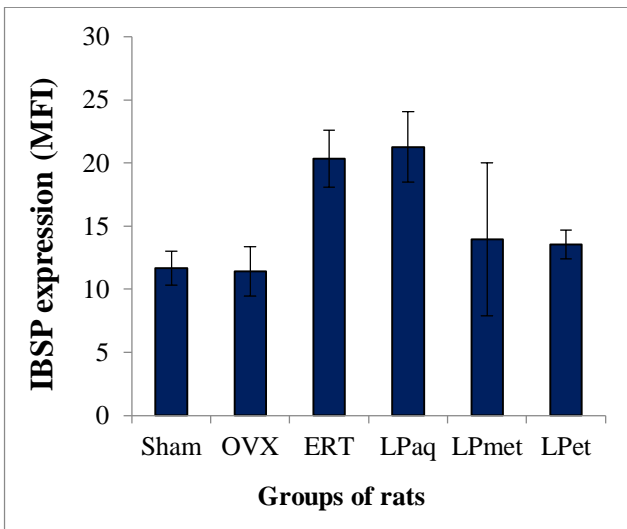


Figure 1g

**Figure 1** The median fluorescence intensity (MFI) of genes normalized to GAPDH. The bar charts (a – g) show the relative expression of genes related to osteoblasts/ bone formation. Values are shown as mean  $\pm$  SEM.

\* indicates significant difference compared to the OVX group. The statistical significance value is set at  $P < 0.05$ .

Sham: sham-operated, OVX: ovariectomized control group, ERT: estrogen (Premarin 64.5  $\mu\text{g}/\text{kg}$ )-supplemented group, LPaq: aqueous extract of LP-supplemented group, LPmet: methanol extract of LP-supplemented group, LPet: ethanol extract of LP-supplemented group

## 2.2. Osteoclast-Related Genes Expression

Osteoclast-related genes expressions were normalized to the expression of GAPDH. The expressions of RANKL, which is the most important gene in bone resorption were significantly lower in the ERT

and LPaq groups compared to the Sham and OVX groups (Figure 2a). The OPG gene expressions of the femoral bones were significantly higher in the ERT, LPaq and LPmet groups compared to the OVX group (Figure 2b). The ERT and LPaq groups also showed significantly lower expressions of MMP9 (Figure 2c) and CSF1 (Figure 2d) compared to the Sham and OVX groups. Supplementation of extract aqueous LP was able to suppress the bone resorption-related gene expressions as effective as ERT. There were no significant differences in the expression of CTSK and ACP5 between all the groups.

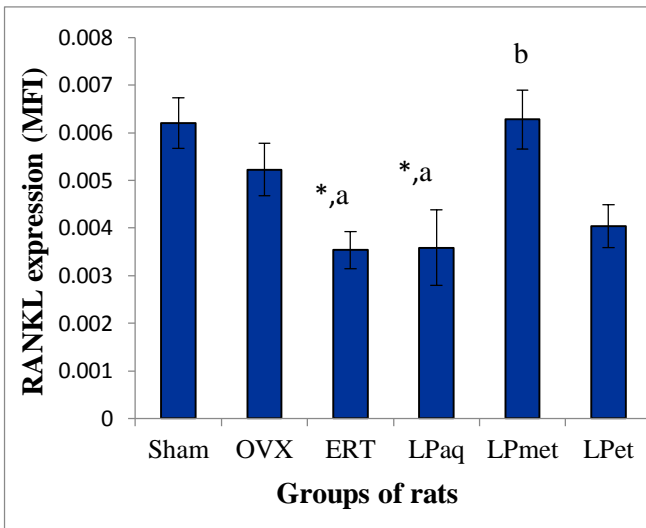


Figure 2a

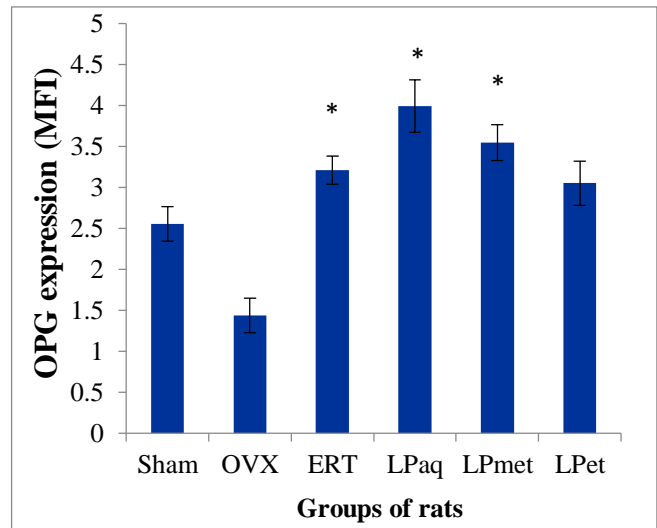


Figure 2b

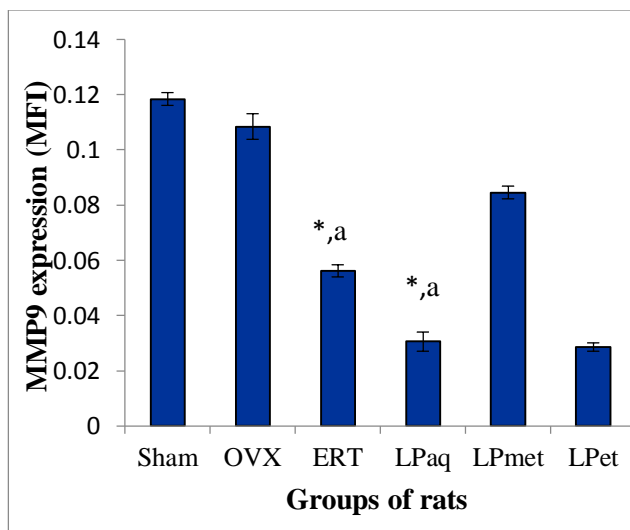


Figure 2c

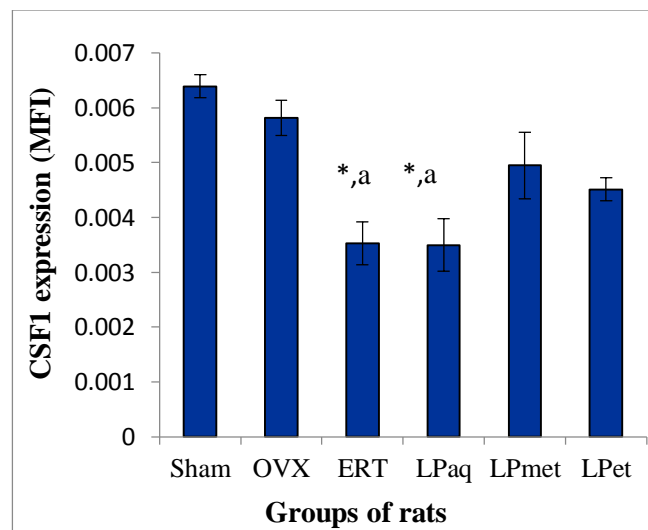


Figure 2d



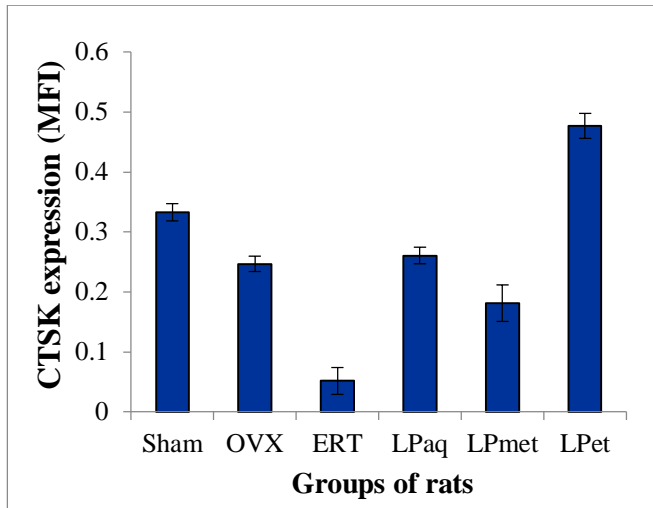


Figure 2e

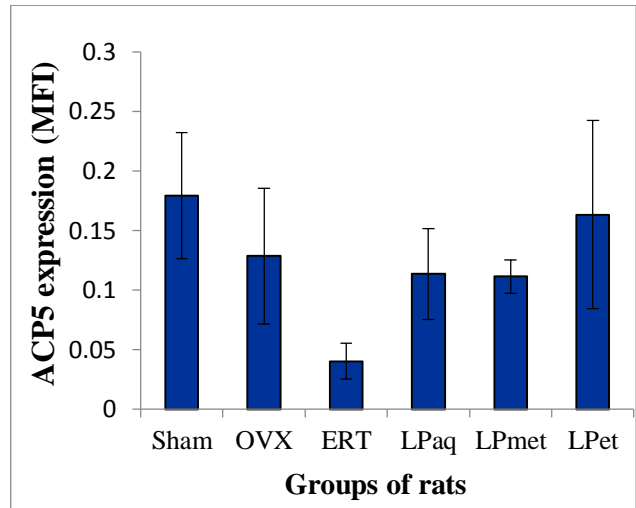


Figure 2f

**Figure 2.** The median fluorescence intensity (MFI) of genes normalized to GAPDH. The bar charts (a – f) show the relative expression of genes related to osteoclasts/ bone resorption. Values are shown as mean  $\pm$  SEM.

\* indicates significant difference compared to the Sham group. <sup>a</sup> indicates significant difference compared to OVX group. <sup>b</sup> indicates significant difference compared to ERT. The statistical significance value is set at  $P < 0.05$ .

Sham: sham-operated, OVX: ovariectomized control group, ERT: estrogen (Premarin 64.5  $\mu$ g/kg)-supplemented group, LPaq: aqueous extract of LP-supplemented group, LPmet: methanol extract of LP-supplemented group, LPet: ethanol extract of LP-supplemented group.

### 3.3. Pro-Inflammatory Cytokines Expression

The TNF- $\alpha$  expression of the femoral bones were significantly lower in rats supplemented with ethanol extract of the LP group compared to the OVX group (Figure 3a). The Sham, ERT and LPaq groups showed significantly lower expressions of IL-1 $\beta$  compared to the OVX group (Figure 3b) but no significant changes were seen in the expression of IL-1 $\alpha$  (Figure 3c). There were no significant differences in the expressions of IL-6 and IFN- $\gamma$  between all the groups.

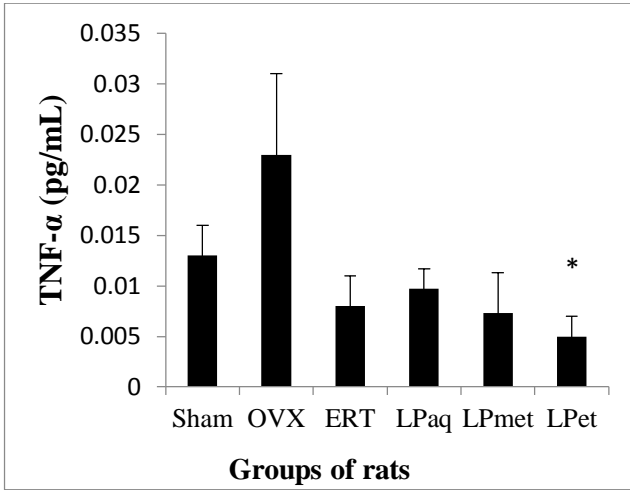


Figure 3a

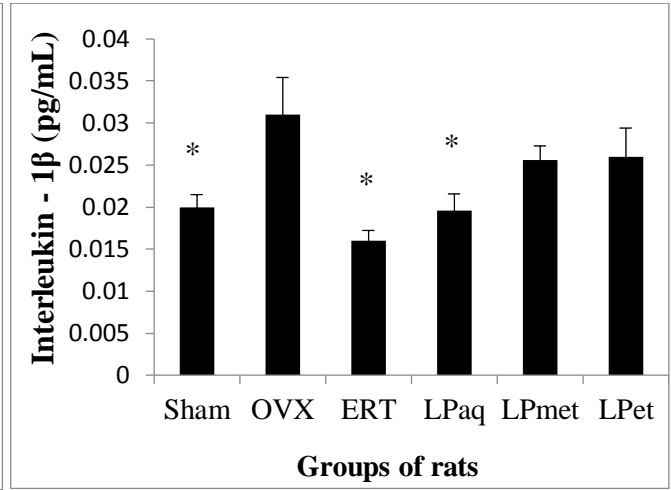


Figure 3b

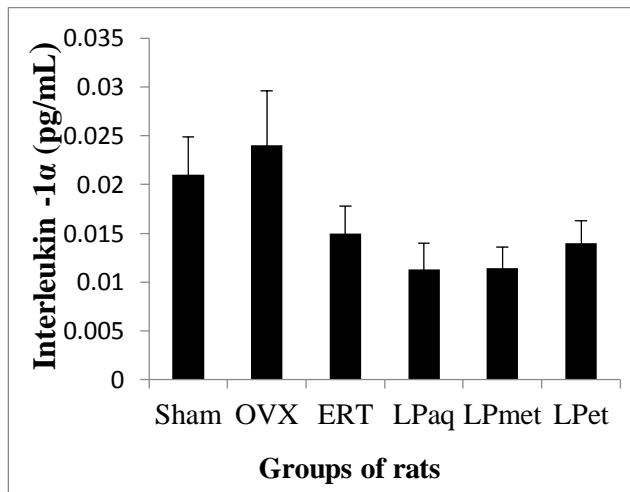


Figure 3c

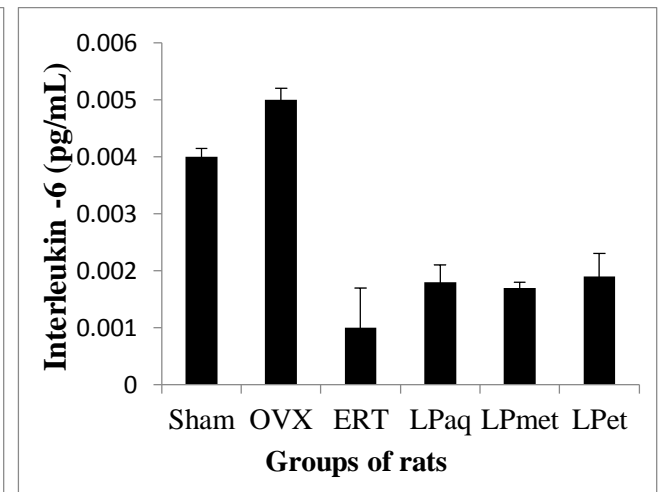


Figure 3d

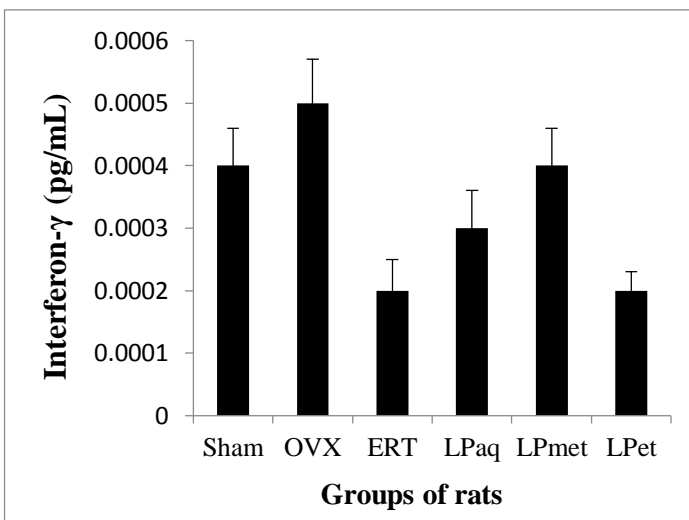


Figure 3e

**Figure 3** The median fluorescence intensity (MFI) of pro-inflammatory cytokines. The bar charts (a-e) show the expression of pro-inflammatory cytokines relative to protein concentration. Values are shown as mean  $\pm$  SEM.

\* indicates significant difference compared to the OVX group. The statistical significance value is set at  $P < 0.05$ .

Sham: sham-operated, OVX: ovariectomized control group, ERT: estrogen (Premarin 64.5  $\mu\text{g}/\text{kg}$ )-supplemented group, LP<sub>aq</sub>: aqueous extract of LP-supplemented group, LP<sub>met</sub>: methanol extract of LP-supplemented group, LP<sub>et</sub>: ethanol extract of LP-supplemented group.

### 3. Experimental Section

#### 3.1. Animals and Treatment

The study was approved by Universiti Kebangsaan Malaysia Animal Ethics Committee (ethical approval number: FP/FAR/2011/NAZRUN/30-NOVEMBER/415-NOVEMBER-2011-MAY-2012). A total of 48 female Sprague-Dawley rats aged 4 to 5 months weighing between 200 to 250g were obtained from the Universiti Kebangsaan Malaysia Laboratory Animal Research Unit. The rats were housed in plastic cages at temperature of  $29 \pm 3^\circ\text{C}$  under natural day/night cycle. They were fed with commercial food pellets (Gold Coin, Port Klang, Malaysia) and deionised water *ad libitum*. They were allowed to adapt to the new environment for a week prior to the study. They were then randomly divided into six groups of sham-operated (Sham), ovariectomized control (OVX), ovariectomized and given oestrogen (Premarin) at 64.5  $\mu\text{g}/\text{kg}$  (ERT), ovariectomized and given *Labisia pumila* aqueous extract at 100 mg/kg (LP<sub>aq</sub>), ovariectomized and given *Labisia pumila* methanol extract at 100 mg/kg (LP<sub>met</sub>) and ovariectomized and given *Labisia pumila* ethanol extract at 100 mg/kg (LP<sub>et</sub>) All the treatments were given daily via oral gavages for nine weeks. At the end of the treatment, rats were euthanized via inhalation of overdosed diethyl ether.

#### 3.2. *Labisia Pumila* Var. *Alata* (LP) Extracts and Estrogen (ERT)

Raw powdered form of LP was supplied by Delima Jelita Herbs (Alor Setar, Kedah). The whole plant of *Labisia pumila* var. *alata* was grinded and dried prior to extraction. Three different extracts were

prepared; aqueous, methanol and ethanol. The extraction procedures were done according to the methods by Harborne (1973). To prepare the aqueous extract, samples of dried, grounded LP were extracted with Soxhlet apparatus (Buchi Labortechnik, Switzerland) in water at 100 °C for 4 hours. The extraction ratio between the dried, grounded raw material and water was 1:10 by mass. Following extraction, the solid residue was removed by filtration and the liquid part was transferred into rotary evaporator for evaporation process. The residue was then immediately freeze dried using Buchi Spray Drier (Buchi Labortechnik, Switzerland) to produce LP powdered form.. To prepare the methanolic and ethanolic extracts of LP, samples of dried, grounded LP were extracted with Soxhlet apparatus in methanol or ethanol respectively at 100 °C for 4 hours. The extraction ratio between the dried, grounded raw material and methanol or ethanol was 1:10 by mass. Following extraction, the solid part was removed by filtration and the liquid part was evaporated at 78 °C. Each of the LP extract was dissolved in deionised water and given accordingly to their assigned groups via oral gavages at the dose of 100 mg/kg rat weight daily at 9 am for 9 weeks.

Oestrogen Premarin® (Wyeth-Ayerst, Canada) tablet which contains 0.625 mg of conjugated oestrogen was crushed, dissolved in deionised water and given via oral gavage at the dose of 64.5 µg/kg rat weight daily at 9 am for 9 weeks.

### 3.3. Gene Expression Analysis

A sample of approximately 20 mg of trabecular bone (relatively size of a rice grain), specifically around the metaphysis area of the distal right femur was biopsied from each rats to measure the bone-related gene expressions. The bone sample was then homogenized in buffer provided by the manufacturer using a high-speed homogenizer containing magnetic beads (Omni Bead Ruptor 24, Kennesaw, USA) at 25°C for 2 cycles of 20 seconds each. The tissue lysate was incubated at 65°C for an hour and centrifuged at 13,000 rpm for 10 minutes to precipitate the debris. The expression of osteoblast and osteoclast-related genes of the femur was quantified using QuantiGene Plex 2.0 technique

(Panomics/Affymetrix, Santa Clara, CA). Osteoblast is the bone-forming cells, while osteoclast is the bone-resorbing cells. The genes of interest with their accession numbers were listed in Table 1.

The supernatant of the tissue lysate was loaded into a 96-well plate preloaded with capture reagent and probe set. Oligonucleotide probe sets for each gene of interest were designed by the manufacturer. Hybridization with pre-amplifier, amplifier and biotinylated label was performed after an overnight incubation at 54°C. Luminescence signal proportional to mRNA captured by the beads was measured using Luminex 200 analyser (Bio-Rad, CA, USA) and was converted into mean fluorescence intensity (MFI). The expressions of the genes were normalized to the expression of housekeeping gene, glyceraldehydes-3-phosphate dehydrogenase (GAPDH).

#### *3.4. Pro-Inflammatory Cytokines Analysis*

Procarta Immuno Assay kit (Panomics/ Affymetrix, CA, USA) was used to simultaneously detect multiple cytokines in rats' bone, according to the manufacturer's instruction. This technique was based on the multi-analite fluorescent microsphere beads technology which involved separation of tagged antibody-coated beads. Metaphyseal area of distal femur from each rat was biopsied and homogenized using Omni Bead Ruptor. The tissue lysate was incubated in ice for 5 minutes prior to centrifugation. Antibody beads were added to each well of the filter plate and washed using wash buffer. Bone tissue supernatant was then added to each well, incubated for at least one hour at room temperature, and washed with buffer. Then, 25 µL per well of the detection antibody was added and the filter plate was shaken at 500 rpm for 30 minutes at room temperature. After adding Streptavidin-PE, the signals were detected using a Luminex 200 analyser. The cytokines measured in this study were tumor necrosis factor- $\alpha$  (TNF- $\alpha$ ), interleukin (IL)-1 $\alpha$ , IL-1 $\beta$ , IL-6 and interferon (IFN)- $\gamma$ .

#### *3.5. Statistical analysis*

The data was analysed using Statistical Package for Social Sciences software (SPSS 21.0, Chicago, USA). Distribution of the data was tested using the Shapiro-Wilk test and all data were found to be normally distributed. To determine significant difference between all the variables, tests used were the analysis of variance (ANOVA), followed by Tukey's HSD as the post hoc test. P-values of < 0.05 were considered to be statistically significant. All the results were expressed as mean  $\pm$  standard error of the mean (SEM).

**Table 1.** Genes of interest

<b>Gene</b>	<b>Scientific symbol</b>	<b>NCBI accession number</b>	<b>Probe set area</b>
<b>Bone formation-related</b>			
Runt related transcription factor 2	RUNX2	XM_346016	314- 820
Bone gamma-carboxyglutamate protein 2/ osteocalcin	BGLAP	NM_013414	31- 374
Secreted acidic cyctein rich glycoprotein/ osteonectin	SPARC	NM_012656	106- 676
Sp7 transcription factor/ osterix	SP7	NM_181374	737- 1280
Alkaline phosphatase	ALP1	NM_013059	908- 1313
Collagen type 1 alpha 1	COL1 $\alpha$ 1	NM_053304	2888- 3291
Integrin binding sialoprotein	IBSP	NM_012587	385-867
<b>Bone resorption-related</b>			
Osteoprotegrin/Tumor necrosis factor receptor superfamily, member 11b	OPG/TNFRSF11b	NM_012870	261- 701
RANKL/Tumor necrosis factor ligand superfamily member 11	RANKL/TNFSF11	NM_057149	246- 884
Cathepsin K	CTSK	NM_031560	386- 774
Matrix metalloproteinase 9	MMP9	NM_031055	1565- 1988
Colony stimulating factor 1/M-CSF	CSF1	NM_023981	345- 864
Acid phosphatase 5, tartrate resistant	ACP5	NM_019144	438- 807

#### 4. Discussion

Postmenopausal osteoporosis is more prominent compared to other types of osteoporosis because it contributes the most to the economic burden caused by osteoporosis (Ray *et al.*, 1997). Following the increasing annual rate of postmenopausal osteoporosis, wide ranges of conventional treatments are

available nowadays such as ERT, alendronate, risedronate and strontium ranelate. Despite their effectiveness, prolonged use of these medications may lead to serious adverse effects (Ferguson, 2004). In recent years, *Labisia pumila* (LP) was reported as potential alternative to conventional treatments for postmenopausal osteoporosis (Nadia *et al.*, 2012).

Previous studies have reported that LP supplementation at the dose of 17.5mg/kg was able to improve bone histomorphometric parameters (Fathilah *et al.*, 2012a). In the following study, two different doses of LP (20 mg/kg and 100 mg/kg) were given for different duration of treatment (three, six and nine weeks). It was reported that supplementation LP at the dose of 100 mg/kg for nine weeks was the best regimen in reversing the OVX-induced bone changes (Nadia *et al.*, 2014). This dose was considered safe as toxicity studies revealed that the LD50 of LP was more than 5.0 g/kg (Wan Ezumi *et al.*, 2007). According to other studies, LP was found to exhibit no-adverse-effect-level (NOAEL) at the dose of 50 mg/kg in sub-acute (Singh *et al.*, 2009), 1000 mg/kg in sub chronic (Taneja, 2004) and 800 mg/kg in reproductive toxicity studies (Wan Ezumi *et al.*, 2007). In human, the effective doses taken by women are around 500 to 1000 mg daily. Hence, the dose of 100 mg/kg used in our study is considered safe. Based on previous studies, the bioactive compounds contributing to LP's therapeutic effects were mostly found in aqueous, methanolic and ethanolic extracts (Khairul *et al.*, 2004; Chua *et al.*, 2011). Therefore, these three different extracts were selected to be used in our study to determine which is the best extract that offers bone protection and to evaluate the molecular mechanisms involved in preventing postmenopausal osteoporosis.

Osteoblast and osteoclast-related genes work together in maintaining the balance of bone remodeling. The most important transcription factors are OPG and RANKL, which are encoded by gene TNFRSF11b and TNFSF11, respectively. RANKL binds to receptor RANK on osteoclast surfaces and stimulates osteoclastic differentiation and activity to resorb bone (Chafik *et al.*, 2011). OPG on the other hand acts as an anti-osteoclastogenic factor which binds antagonistically to RANKL and indirectly reduces bone loss. Previous studies have reported an increased expression of RANKL but decreased expression of OPG in ovariectomized rats, which resulted in bone loss (Zhou *et al.*, 2010; Qi-Guang *et al.*, 2011). This

study has shown that ERT and LPaq significantly suppressed RANKL expression and increased OPG expression in ovariectomised rats.

Postmenopausal osteoporotic women demonstrated reduced expression of osteoblast-related genes (Jabbar *et al.*, 2011). This was believed to be contributed by estrogen deficiency, which led to down regulation of OPG and inhibition of other bone formation-related gene expressions. In the current study, we found that LPaq significantly increased the expression of genes encoding osteocalcin, osteonectin, osterix and alkaline phosphatase of ovariectomised rats. ERT and LPaq also significantly reduced the expressions of MMP9 and CSF1 genes of ovariectomised rats. This is an important finding since MMP9 is a protein which stimulates the early phase of bone resorption processes by removing the collagenous layer on bone surface, prior to mineralization (Delaisse *et al.*, 2000).

Previous studies have confirmed that osteoclasts-related gene expressions were increased significantly in postmenopausal osteoporotic women (Darja *et al.*, 2007). Estrogen deficiency in postmenopausal women stimulates the expression of RANKL. Consequently, RANKL will up-regulate the expression of other downstream osteoclast-related genes such as MMP9 and CTSK (Pang *et al.*, 2005). Macrophage colony stimulating factor (M-CSF), encoded by gene CSF1 plays an important role in inhibiting osteoclasts apoptosis, resulting in accelerated bone loss (Wilson *et al.*, 2009). This is in line with our findings where M-CSF was up-regulated in the OVX group. The expressions of CTSK and ACP5 were also lower in the estrogen treated groups, albeit not significant when compared to the OVX group.

LP has long been known for its phytoestrogenic property. Bioactive compounds such as alkaloids, saponins, triterpens and tannins that are responsible for its estrogenic activity are polar in nature. Hence, they are highly expressed in more polar solvent (Melissa *et al.*, 2013). This may elicit that aqueous extract of LP contain more bioactive compounds compared to other less polar extract. Previous studies have also shown that aqueous extract of LP contains the most antioxidative compounds such as flavonoids, isoflavonoids and phenol compared to other types of LP extracts (Norhaiza *et al.* 2009; Chua *et al.* 2011; Melissa *et al.* 2012]. Other than that, in other previous study, aqueous extract of LP was



found to increase the ALP activity which reflect high estrogenic activity. Study done by Khairul et al. (2004) reported that aqueous extract of LP showed the highest inhibition against free radicals, followed by methanol and ethanol extracts. These have reflected that aqueous extract of LP possessed phytoestrogenic and anti-oxidative activities. Hence, these may be the reasons why aqueous extract (LP<sub>aq</sub>) was the most effective LP extract compared to methanol (LP<sub>met</sub>) or ethanol(LP<sub>pet</sub>) extracts in increasing the expression of bone formation-related genes and reducing the expression of bone resorption-related genes. This meant that LP<sub>aq</sub> may possess the highest bioactive compounds compared to LP<sub>met</sub> and LP<sub>pet</sub>.

The effectiveness of LP supplementation can be associated with its phytoestrogenic and antioxidative properties. LP was found to inhibit estradiol binding to antibodies raised against estradiol, making it to function similarly to oestrogen (Husniza, 2002). LP was reported to contain flavonoids, saponins, tannins and triterpenes, which were speculated to contribute to its phytoestrogenic properties (Ayida *et al.*, 2007; Avula *et al.*, 2010). Flavonoids were found to increase the expression of OPG, resulting in increased osteoblasts differentiation (Sharan *et al.*, 2009). The ability of flavonoids to up-regulate osteoblasts activity may be reflected by the bone-forming effects of LP in our study. The bioactive compounds present in LP may also contribute to its anti-oxidative property. Norhaiza *et al.* (2009) reported that LP was a strong antioxidant due to the presence of flavonoids, beta-carotene, ascorbic acid and phenolic compounds.

The estrogen deficiency condition in postmenopausal osteoporosis has been associated with oxidative stress (Almeida et al., 2007; Sendur et al., 2009). Similarly, ovariectomy can stimulate the production of free radicals which may progress to oxidative stress (Muthusami et al., 2005). Previous studies have shown that oxidative stress could inhibit the expression of osteoblast-related genes such as OPG and enhance the expression of osteoclast-related genes such as RANKL and MMP9 (Maziere *et al.*, 2010; Hyeon *et al.*, 2013). All these changes were seen in our ovariectomized rat model used in the current study. As expected, the estrogen-deficient state after ovariectomy may have induced oxidative stress in the rats of the OVX group which resulted in the up-regulation of bone resorption-related genes. Previous

study by Nadia et al. (2014b) reported that supplementation of LP crude extract was able to increase the anti-oxidative enzymes levels and reduced lipid peroxidation in femoral bones of ovariectomized rats. Hence, the anti-oxidative property of LP could have played a major role with our present findings. This property may have scavenged free radicals to maintain the bone remodeling molecular pathways. Khairul et al. (2004) reported that aqueous extract of LP has the strongest ability to scavenge free radicals, followed by methanolic and ethanolic extract. The superior anti-oxidant ability of aqueous extract of LP was also reported by other studies which found it to contain the highest anti-oxidative compounds compared to other extracts (Norhaiza *et al.*, 2009; Chua *et al.*, 2011).

The pathogenesis of postmenopausal osteoporosis could also be linked with inflammation. In recent years, it was shown that the levels of pro-inflammatory cytokines such as TNF- $\alpha$ , IL-1, IL-6, IL-17 and IFN- $\gamma$  were elevated in postmenopausal osteoporotic women (Lorenzo *et al.*, 2000; Young-Mi *et al.*, 2010). Elevated pro-inflammatory cytokines stimulated the expression of RANKL and M-CSF, which would enhanced the differentiation of osteoclasts and increased the rate of bone resorption (Riggs, 2000; Mundy, 2007). TNF- $\alpha$  could also work synergistically with RANKL as they both have anti-apoptotic effects on osteoclasts.

In our present study, only treatment with the ethanolic extract of LP (LP<sub>et</sub>) significantly decreased TNF- $\alpha$  expression of ovariectomised rats. Similar finding was reported by Choi *et al.* (2010), which showed that the ethanolic extract of LP was able to inhibit TNF- $\alpha$  expression of dermal cells. On the other hand, only treatments with ERT and LP<sub>aq</sub> significantly lowered the IL- $\beta$  expression of ovariectomised rats. In general, there was a decreasing trend of IL-1 $\alpha$ , IL-6 and IFN- $\gamma$  expressions with LP supplementations, albeit not statistically significant. Both IL- $\alpha$  and IL- $\beta$  played a role in regulation of bone remodeling but it was reported that IL-1 $\beta$  exerted a more significant effect on bone compared to IL- $\alpha$  (Nguyen *et al.*, 1991; Gillespie, 2007). In summary, with the abilities of LP to inhibit the expressions of TNF- $\alpha$  and IL-1 $\beta$ , it can be assumed that LP's anti-osteoporotic effect is contributed by its anti-inflammatory property.

## 5. Conclusions

Aqueous extract of LP was the best form of extract and as effective as ERT in regulating the molecular pathways of bone remodeling. It was able to up-regulate the bone formation-related genes expressions, down regulate the bone resorption-related genes expressions and down regulate the pro-inflammatory cytokines expressions. Further studies are warranted to provide a more detail and conclusive mechanisms of LP.

## Acknowledgments

This study was made possible through the grant provided by the Faculty of Medicine, Universiti Kebangsaan Malaysia (UKM DLP-2011-044). The authors would like to thank Mr Fadhlullah Zuhair, Mrs Juliana Abdul Hamid, Ms Nurul Hafizah Abas and Mrs Farhana Mohd Fozi from the Department of Pharmacology for their technical assistance. We also thank Dr Thuan Bui from i-DNA Biotechnology Sdn. Bhd. for his assistance during the QuantiGene 2.0 and Procarta analysis.

## Conflicts of Interest

The authors declare to have no conflicts of interest whatsoever. The authors are responsible for the content and writing of this paper.

## References

1. Johnell, O. and J.A. Kanis, 2006. An estimate of the worldwide prevalence and disability associated with osteoporotic fractures. *Osteoporos. Int.*, 17(12):1726-1733. DOI: 10.1007/s00198-006-0172-4.
2. Riggs, B.L., S. Khosla and L.J. Melton 3<sup>rd</sup>, 2002. Sex steroids and the construction and conservation of the adult skeleton. *Endocrinol. Rev.*, 23: 279–302. DOI: 10.1210/er.23.3.279.
3. Peter, M.B, 2013. Osteoporosis – an increasingly important issue for both young and aging citizens of Malaysia. *Int. e-Journal Sci., Med. Edu.* 7(1): 1-3.

4. Stevenson, M., M.L. Jones, E. De Nigris, N. Brewer, S. Davis and J. Oakley, 2005. A systematic review and economic evaluation of alendronate, etidronate, risedronate, raloxifene and teriparatide for the prevention and treatment of postmenopausal osteoporosis. *Health Technol. Assess.*, 9:1–160. DOI: <http://dx.doi.org/10.3310/hta9220>.
5. Marcea, M, G. Jia, K. Theresa and B. George, 2012. Biphosphonates for Osteoporosis- Where do we go from here? *New Engl. J. Med.*, 366: 2048-2051. DOI: 10.1056/NEJMp1202619.
6. Varena, M., F. Bertoldo, M.D. Monaco, A. Giusti, G. Martini and M. Rossini, 2013. Safety profile of drugs used in the treatment of osteoporosis; a systematical review of the literature. *Reumatismo* 65(4): 143-166. DOI: 10.4081/reumatismo.2013.143.
7. Bolland, M.J., A. Grey, A. Avenell, G.D. Gamble and I.R. Reid, 2011. Calcium supplements with or without vitamin D and risk of cardiovascular events: reanalysis of the Women's Health Initiative limited access dataset and meta-analysis. *BMJ*, 342:d2040. DOI: 10.1136/bmj.d2040.
8. Melissa, P.S.W, V. Navaratnam and C.Y. Yin, 2012. Phytoestrogenic property of *Labisia pumila* for use as an estrogen replacement therapy agent. *Afr. J. Biotechnol.* 11(50): 11053-11056. DOI: 10.5897/AJB12.160.
9. Ariffin, N., 2005. *Penyembuhan semula jadi dengan herba*. PTS Litera Utama, Kuala Lumpur, Malaysia.
10. Bodeker, G., 1999. *Health and Beauty from the Rainforest: Malaysian Traditions of Ramuan*. Editions Didier Millet Pty, Kuala Lumpur, Malaysia.
11. Fasihuddin, A., A.H. Rahman and R. Hasmah, 1995. Medicinal plants used by bajau community in sabah. In: *Trends in Traditional Medicine Research*, K. L., Chan et al., (Eds.). The School of Pharmaceutical Sciences, University of Science Malaysia, Penang, Malaysia, pp: 493–504.

12. Jamal, J.A., P.J. Houghton and S.R. Milligan, 1998. Testing of *labisia pumila* for oestrogenic activity using a recombinant yeast screen. *J. Pharm.Pharmacol.*, 50(S9): 79. DOI: 10.1111/j.2042-7158.1998.tb02279.x.
13. Fazliana, M, 2010. Studies on *Labisia pumila* var. *alata* extract with phytoestrogenic effects: impact on biological activities and gene expression, Karolinska Institutet, Stockholm, Sweden, pp: 1-4.
14. Nadia, M.E., M.K. Fadhli, S. Ima Nirwana and A.S. Nazrun, 2014. The effects of *Labisia pumila* on postmenopausal osteoporotic rat model: dose and time-dependent micro-CT analysis. *J. X-Ray Sci Technol.*, 22: 503-518. DOI: 10.3233/XST-140441.
15. Nazrun, A.S, P.L. Lee, M. Norliza, M. Norazlina and S. Ima Nirwana, 2011. The effects of *Labisia pumila* var. *alata* on bone markers and bone calcium in a rat model of post-menopausal osteoporosis. *J. Ethnopharmacol.*, 133(2): 538–542. DOI: 10.1016/j.jep.2010.10.033.
16. Khosla, S., 2007. Estrogen and the death of osteoclasts: a fascinating story. *BoneKEY-Osteovision*, 4:267–272. doi:10.1138/20070275.
17. Maria, A., I. Srividhya, M.M. Marta, M.B. Shoshana, H. Li, A. Elena, O. Melda, X. Jinhu, S.W. Robert, L.J. Robert, A.C. O'Brien and S.C. Manolagas, 2013. Estrogen receptor- $\alpha$  signalling in osteoblast progenitors stimulates cortical bone accrual. *J. Clin. Invest.*, 123(1): 394-404. DOI: 10.1172/JCI65910.
18. Manolagas, S.C., 2000. Birth and death of bone cells: basic regulatory mechanisms and implications for the pathogenesis and treatment of osteoporosis. *Endocr.Rev.* 21(2): 115–137. DOI: <http://dx.doi.org/10.1210/edrv.21.2.0395>.
19. Manolagas, S.C, S. Kousteni, R.L. Jilka, 2002. Sex steroids and bone. *Recent Prog. Horm. Res.* 57: 385-409. PMID:12017554.

20. Collin-Osdoby, P., L. Rothe, F. Anderson, M. Nelson, W. Maloney and P. Osdoby, 2001. Receptor activator of NF- $\kappa$ B and osteoprotegerin expression by human microvascular endothelial cells, regulation by inflammatory cytokines, and role in human osteoclastogenesis. *J. Biol. Chem.*, 276(23): 20659–20672. DOI: 10.1074/jbc.M010153200.
21. Clowes, J.A., B.L. Riggs and S. Khosla, 2005. The role of the immune system in the pathophysiology of osteoporosis. *Immunol. Rev.*, 208: 207-227. DOI:10.1111/j.0105-2896.2005.00334.x.
22. Eghbali-Fatourehchi, G., S. Khosla, A. Sanya, W.J. Boyle, D.L. Lacey and B.L. Riggs, 2003. Role of RANK ligand in mediating increased bone resorption in early postmenopausal women. *J. Clin. Invest.*, 111(8): 1221-1228. DOI: 10.1172/JCI200317215.
23. Jabbar, S., J. Dury, J.N. Fordham, H.K. Datta, R.M. Francis and S.P. Tuck, 2011. Osteoprotegerin, RANKL and bone turnover in postmenopausal osteoporosis. *J. Clin. Pathol.*, 64(4): 354-357. DOI: 10.1136/jcp.2010.086595.
24. Yun, A.J. and P.Y. Lee, 2004. Maladaptation of the link between inflammation and bone turnover may be a key determinant of osteoporosis. *Med. Hypotheses.*, 63: 532-537. PMID: 15288383.
25. Ganesan, K., S. Teklehaimanot, T.H. Tran, M. Asuncion and K. Norris, 2005. Relationship of C-reactive protein and bone mineral density in community-dwelling elderly females. *J. Natl. Med. Assoc.*, 97: 329-333. PMID:15779496.
26. Koh, J.M., Y.H. Kang, C.H. Jung, S. Bae, D.J. Kim, Y.E. Chung and G.S. Kim, 2005. Higher circulating hsCRP levels are associated with lower bone mineral density in healthy pre- and postmenopausal women: evidence for a link between systemic inflammation and osteoporosis. *Osteoporos. Int.*, 16(10): 1263-1271. DOI: 10.1007/s00198-005-1840-5.

27. Harborne, J.B., 1973. Photochemical Methods: A Guide to Modern Techniques of Plant Analysis. Chapman A. & Hall, London, pp: 279.
28. Ray, N.F., J.K. Chan, M. Thamer and L.J. Melton 3<sup>rd</sup>, 1997. Medical expenditures for the treatment of osteoporotic fractures in the United States in 1995: report from the National Osteoporosis Foundation. *J. Bone Miner. Res.* 12(1): 24-35. DOI: 10.1359/jbmr.1997.12.1.24.
29. Ferguson, N., 2004. Osteoporosis in Focus. Pharmaceutical Press, Oxford, pp: 229.
30. Nadia, M.E., A.S. Nazrun, M. Norazlina, N.M. Isa, M. Norliza and S. Ima Nirwana, 2012. The anti-inflammatory, phytoestrogenic and antioxidative role of *Labisia pumila* in prevention of postmenopausal osteoporosis. *Adv. Pharmacol. Sci.*, 2012: 706905. DOI: 10.1155/2012/706905.
31. Fathilah, S.N., A.S. Nazrun, M. Norazlina, M. Norliza and Ima Nirwana, 2012a. *Labisia pumila* protects the bone of estrogen-deficient rat model: A histomorphometric study. *J. Ethnopharmacol.*, 142: 294-299. DOI: 10.1016/j.jep.2012.04.029.
32. Wan Ezumi, M.F., S. Siti Amrah, A.W.M. Suhaimi and S.S.J. Mohsin, 2007. Evaluation of the female reproductive toxicity of aqueous extract of *Labisia pumila* var. *alata* in rats. *Indian J. Pharmacol.*, 39: 30–32. DOI: 10.4103/0253-7613.30760.
33. Singh, G.D., M. Ganjoo, M.S. Youssouf, A. Koul, R. Sharma, S. Singh, P.L. Sangwan, S. Koul, D.B. Ahamad and R.K. Johri, 2009. Sub-acute toxicity evaluation of an aqueous extract of *Labisia pumila*, a Malaysian herb. *Food Chem. Toxicol.*, 47: 2661–2665. DOI: 10.1016/j.fct.2009.07.031.
34. Taneja, S.C., 2004. Sub-Chronic (90 days) Oral Toxicity Studies of Aqueous Extract of *Labisia pumila* in Wistar Rats (250,500&1000 mg/kg b. wt. only). Indian Institute of Integrative Medicine, Jammu, India.

35. Khairul, F.K., M.N. Haniza and I. Zahari, 2004. Antioxidative properties of various extracts of *Labisia pumila* Kacip Fatimah. In: Proceedings Of The Seminar On Medicinal And Aromatic Plants. Forest Research Institute, Malaysia., 20-21 July 2004.
36. Chua, L. S., N. Abdul, S.Y. Lee, C.T. Lee, M.R. Sarmidi and R. Abdul, 2011. Flavonoids and phenolic acids from *Labisia pumila* (Kacip Fatimah). *Food Chem.*, 127(3): 1186-1192. DOI: 10.1016/j.foodchem.2011.01.122.
37. Chafik, G., M.C. Rita, L. Katrin, S. K. Lindsay, W. Klaus Grätz and E.W. Franz, 2011. Gene Regulation: Inhibition of Osteoclast Differentiation and Bone Resorption by *N*- Methylpyrrolidone. *J. Biol. Chem.*, 286:24458-24466. DOI: 10.1074/jbc.M111.223297.
38. Zhou, J., S. Chen, H. Guo, L. Xia, H. Liu, Y. Qin and C. He, 2010. Pulsed electromagnetic field stimulates osteoprotegerin and reduces RANKL expression in ovariectomized rats. *Rheumatol. Int.*, 33(5): 1135-1141. DOI: 10.1007/s00296-012-2499-9.
39. Qi-Guang, M., Z. Zhong-Min, X. Song, L. Ming, Z. Rong-Ping, Z. Li, J. Chun-Hong, W. Zhi-Hua, J. Da-Di and B. Xia0-Chun, 2011. Metformin stimulates osteoprotegerin and reduces RANKL expression in osteoblasts and ovariectomized rats. *J. Cell. Biochem.*, 112(10): 2902–2909. DOI: 10.1002/jcb.23206.
40. Delaisse, J.M., M.T. Engsig, V. Everts, M.C. Ovejero, M. Ferreras, L. Lund, T.H. Vu, Z. Werb, B. Winding, A. Lochter, M.A. Karsdal, T. Troen, T. Kirkegaard, T. Lenhard, A.M. Heegard, L. Neff, R. Baron and N.T. Foged, 2000. Proteinases in bone resorption: obvious and less obvious roles. *Clin. Chim. Acta*, 291: 223-234. DOI: 10.1016/S0009-8981(99)00230-2.
41. Darja, B.L., R. Komadina, J. Prezelj, B. Ostanek, Z. Trosk and J. Marc, 2007. Expression of bone resorption genes in osteoarthritis and in osteoporosis. *J. Bone Miner. Metab.*, 25(4): 219-225. DOI: 10.1007/s00774-007-0753-0.



42. Pang, M., A.F. Martinez, J. Jacob, W. Balkan and B.R. Troen, 2005. RANK ligand and interferon gamma differentially regulate cathepsin gene expression in pre-osteoclastic cells. *Biochem. Biophys. Res. Commun.*, 328: 756-763. DOI:10.1016/j.bbrc.2004.12.005.
43. Wilson, S.R., C. Peter, P. Saftig and D. Bromme, 2009. Cathepsin K activity-dependent regulation of osteoclast actin ring formation and bone resorption. *J. Biol. Chem.*, 284(4): 2584-2592. DOI: 10.1074/jbc.M805280200.
44. Melissa, P.S.W., V. Navaratnam and C.Y. Yin, 2013. Estrogenic assessment of *Labisia pumila* extracts using a human endothelial cell line. *Int. J. Pharm. Pharma. Sci.*, 5(2): 448-452. ISSN- 0975-1491.
45. Husniza, H., 2002. Estrogenic and Androgenic Activities of Kacip Fatimah (*Labisia pumila*). Abstracts of Research Projects, Institute of Medical Research, Ministry of Health Malaysia, Kuala Lumpur, Malaysia.
46. Al-Wahabi, A., W.M. Wan Nazaimoon, H.S. Farihah and A.L. Azian, 2007. Effect of Ovariectomy, *Labisia pumila var alata* Treatment and Estrogen Replacement Therapy on the Morphology of Adipose Tissue in Ovariectomized Sprague Dawley Rats. *J. Med.*, 1(1): 1-7.
47. Avula, B., Y.H. Wang, Z. Ali, T.J. Smillie and I.A. Khan, 2010. Quantitative determination of triperpene saponins and alkenated-phenolics from *Labisia pumila* by LCUV/ELSD method and confirmation by LC-ESI-TOF. *Planta Med.*, 77(15): 1742-1748. DOI: 10.1055/s-0030-1271037.
48. Sharan, K., J.A. Siddiqui, G. Swarnkar, R. Maurya and N. Chattopadhyay, 2009. Role of phytochemicals in the prevention of menopausal bone loss: evidence from in vitro and in vivo, human interventional and pharmacokinetic studies. *Curr. Med. Chem.*, 16: 1138-1157. DOI: 10.2174/092986709787581806.

49. Norhaiza, M., M. Maziah and M. Hakiman, 2009. Antioxidative properties of leaf extracts of a popular Malaysian herb, *Labisia pumila*. *J. Med. Plants Res.*, 3(4): 217–223. ISSN: 1996-0875.
50. Almeida, M., L. Han, M. Martin-Millan, L.I. Plotkin, S.A. Stewart, P.K. Roberson, S. Kousteni, C.A. O'Brien, T. Bellido, A.M. Parfitt, R.S. Weinstein, R.L. Jilka and S.C. Manolagas, 2007. Skeletal involution by age-associated oxidative stress and its acceleration by loss of sex steroids. *J. Biol. Chem.*, 282: 27285–27297. DOI: 10.1074/jbc.M702810200.
51. Sendur, O.F., Y. Turan, E. Tastaban and M. Serter, 2009. Antioxidant status in patients with osteoporosis: A controlled study. *Joint Bone Spine*, 76(5): 514-518. DOI: 10.1016/j.jbspin.2009.02.005.
52. Muthusami, S., I. Ramachandran, B. Muthusamy, G. Vasudevan, V. Prabhu, V. Subramaniam, A. Jagadeesan and S. Narasimhan, 2005. Ovariectomy induces oxidative stress and impairs bone antioxidant system in adult rat. *Clin. Chim. Acta.*, 360: 81-86. DOI: 10.1016/j.cccn.2005.04.014.
53. Mazière, J.C., V. Savitsky, A. Galmiche, C. Gomila and Z. Massy Z, 2010. Oxidized low density lipoprotein inhibits phosphate signalling and phosphate-induced mineralization in osteoblasts: involvement of oxidative stress. *Biochim. Biophys. Acta*, 1802(11): 1013-1019. DOI:10.1016/j.bbadis.2010.07.010.
54. Hyeon, S., H. Lee, Y. Yang and W. Jeong, 2013. Nrf2 deficiency induces oxidative stress and promotes RANKL-induced osteoclast differentiation. *Free Radic. Biol. Med.* 65: 789-799. DOI: 10.1016/j.freeradbiomed.2013.08.005.
55. Nadia, M.E. and A.S. Nazrun, 2014. Time and dose-dependent effects of *Labisia pumila* on bone oxidative status of postmenopausal osteoporosis rat model. *Nutrients*, 6: 3288-3302.
56. Lorenzo, J., 2000. Interactions between immune and bone cells: new insights with many remaining questions. *J. Clin. Invest.*, 106(6): 749-752. DOI: 10.1172/JCI11089.

57. Young-Mi, L., F. Noriyuki, M. Hiroko, Y. Hisataka and I. Iwakura , 2010. IL-1 plays an important role in the bone metabolism under physiological conditions. *Int. Immunol.*, 22(10): 805-816. DOI: 10.1093/intimm/dxq431.
58. Riggs, B.L., 2000. The mechanisms of estrogen regulation of bone resorption. *J. Clin. Invest.*, 106(10): 1203-1204. DOI: 10.1172/JCI11468.
59. Mundy, G.R., 2007. Osteoporosis and inflammation. *Nutr. Rev.*, 65: S147- S151. DOI: 10.1111/j.1753-4887.2007.tb00353.x.
60. Choi, H.K., D.H. Kim, J.W. Kim, S. Ngadiran, M.R. Sarmidi and C.S. Park, 2010. *Labisia pumila* extract protects skin cells from photoaging caused by UVB irradiation. *J. Biosci. Bioeng.*, 109(3): 291-296. DOI: 10.1016/j.jbiosc.2009.08.478.
61. Nguyen, L., F.E. Dewhirst, P.V. Hauschka and P. Stashenko, 1991. Interleukin-1 beta stimulates bone resorption and inhibits bone formation in vivo. *Lymphokine Cytok. Res.* 10: 15-21. PMID: 1873357.
62. Gillespie, M.T., 2007. Impact of cytokines and T lymphocytes upon osteoclast differentiation and function. *Arthritis Res. Ther.*, 9: 103. DOI: 10.1186/ar2141.

# Future drug delivery technologies: Benchtop to industry

Md Jasim Uddin<sup>1\*</sup>, Irin Sultana<sup>1</sup>, Ayesha Amin Nipa<sup>1</sup>, M. Mohi Uddin Chowdhury<sup>1</sup>, Dennis Douroumis<sup>2</sup>

<sup>1</sup>Department of Pharmacy, Southern University Bangladesh, 22 Shaheed Mirza Lane (East), Mehedibagh Road, Chittagong, Bangladesh.

<sup>2</sup>Faculty of Engineering and Science, University of Greenwich, Medway Campus, Chatham Maritime, Kent ME4 4TB, UK.

\*Corresponding author: Tel: +8801812756110; e-mail: [dr.jasim@southern.edu.bd](mailto:dr.jasim@southern.edu.bd) (Dr. Md Jasim Uddin, Assistant Professor, Southern University Bangladesh)

**Abstract**— Transmucosal buccal drug delivery system is considered as a future drug delivery technology, always assist to enhance patient compliance mainly for paediatric and geriatric community. The studies aim to develop buccal delivery for delivering a hydrophilic drug, flucoxacillin sodium, across the mucosal route. The buccal films comprised of a bio-adhesive polymer, plasticizer and drug. Optimised films were characterised by measurement of weight, length and width, hardness, thickness, surface pH, moisture content and uptake, swelling study, folding resilience, hydration and entrapment efficiency. Drug release studies were performed for different polymer-plasticizer-drug ratios. Concentration of polymer and plasticizer were influenced on the development, evaluation and release rate of flucoxacillin sodium from the buccal films. In conclusion, these studies reveal that buccal delivery of flucoxacillin sodium can be an alternative route in comparison to conventional route for patient compliance.

**Keywords**— Buccal delivery, Solvent casting, Drug release.

## INTRODUCTION

Oral drug delivery is the most popular route due its safe and easy administration. But oral route is not always preferable due to the hepatic first pass effect, enzymatic degradation and inactivation at gastric pH. Compared to other mucosal sites (i.e. intestinal, nasal and rectal); the oral mucosa possesses higher vascularity, less enzyme activity and are less susceptible to irritation and damage. The oral mucosa route can be employed for both local and systemic administration of drugs (Boateng et al., 2013, Boateng & Okeke., 2014). Previous studies have also shown that microneedles-mediated transdermal drug delivery are capable of piercing skin in a painless and simple manner making them appropriate for patients who suffer from needlephobia (Nir et al., 2003; Simonsen et al., 1999). As a painless manner, either microneedles mediated transdermal delivery (e.g. anticancer drug) (Uddin et al., 2015) or buccal (e.g. Buprenorphine, Fluticasone Propionate etc.) (Ammar et al., 2016; Bai et al., 2016); or even sublingual (e.g. granisetron hydrochloride, apomorphine etc.) (Bilbault et al., 2016; Kalia et al., 2016) delivery have been used successfully in advanced drug delivery technologies.

In order to overcome these disadvantages related to the oral drug delivery and injections, it is necessary to develop an alternative drug delivery system. This research work involves in the physicochemical characterizations of solvent casted buccal films and the release profile of a drug from different amounts of polymer-plasticizer ratios. A model *beta*-lactam antibiotic of the penicillin class, flucoxacillin sodium, was chosen as a model drug. The effect of diverse variables (amounts of polymer, plasticizer and drug) and formulation type on drug release characteristics were also investigated. These will facilitate to understand the relationship between drug release characteristics, prepared from mucoadhesive polymer.

## MATERIALS AND METHODS

### Materials

A model *beta*-lactam antibiotic of the penicillin class, Flucoxacillin sodium (FluNa)(Molecular Weight: 493.3 Da), was kindly gifted by Albion Laboratories Ltd. (Chittagong, Bangladesh). Polymer X (PolyX) (Molecular Weight 1261.4 Da), Plasticizer Y (PlasY) (Molecular Weight 92.0 Da), Calcium chloride, Potassium chloride, sodium hydroxide and potassium dihydrogen phosphate were purchased from Merck Ltd. (Damstadt, Germany). Nutrient agar media was obtained from HiMedia Laboratories Ltd. (Mumbai, India).

### Preparation of blank and drug loaded films

Polymer and plasticizer were dissolved in distilled water prior adding of drug molecule and casting of the films. PolyX and PlasY were dissolved slowly into distilled water at room temperature and left for 1 hour in a shaker (Huafeng, China) to achieve complete dissolution and clear solution. The resulting gel formulations were left to place for 24 hours to remove all air bubbles that entrapped in the solutions. Clear formulations was poured into the petri dishes (90 mm in diameter) and dried in an oven (Genlab Limited, Cheshire,UK) at 40°C for 24 hrs. The model *beta*-lactam antibiotic of the penicillin class, FluNa, was used to develop a homogeneous and reproducible drug-loaded buccal film. Drug-loaded buccal films were prepared as above with the addition of FluNa to the clear gel solutions before drying in the oven. The composition of blank- and drug-loaded formulations are shown in Table 1.

**Table 1.** Optimised blank- and drug-loaded buccal films prepared with various amounts of polymers and plasticizer.

Formulation/ Film Type	Polymer: Plasticizer	Weight ratios	Total excipients content (% w/v)	% FluNa loading (w/w)
F1	PolyX:PlasY	1:1	8%	-
F2	PolyX:PlasY	2:1	12%	-
F3	PolyX:PlasY	3:1	16%	-
F4	PolyX:PlasY	1:1	8%	11.1
F5	PolyX:PlasY	2:1	12%	7.7
F6	PolyX:PlasY	3:1	16%	5.9
F7	PolyX:PlasY	1:1	8%	20
F8	PolyX:PlasY	2:1	12%	14.3
F9	PolyX:PlasY	3:1	16%	11.1

#### Measurement of weight, length & width, hardness and thickness

Blank- and drug-loaded buccal films (27 X 15 mm) were cut by using stainless steel cutter. All blank- and drug-loaded films from each formulation (n=3) were weighed for individual weight individually using digital balance (Shende et al. 2016). Length & width (Fig.1) of the optimised films (n=3) were measured using slide calipers. All films (n=3) were investigated for hardness using Monsanto hardness tester. Finally, thickness of the buccal films (n=3) were measured at five different places on the film using manual screw gage and calculated for mean±standard deviations (SD) (Kumar et al., 2013; Yehia et al., 2009).

#### Folding resilience

Folding resilience of the films (n=3) were determined manually for the blank- and drug-loaded films. It was calculated approximately by continually folding a small strip of film at the same place till it breaks. The patch folded at the same place without breaking and will propose the value of folding resilience (Boateng et al., 2013; Khana et al., 1997).

#### Moisture content

All buccal films were weighed separately and hold in a desiccator at room temperature for 24 hours, filling with calcium chloride granules. Films were re-weighed again. The percentage (%) of moisture content was determined using following method (Reddy et al., 2012):

$$\% \text{ Moisture content} = \frac{[\text{Initial weight} - \text{Final weight}]}{\text{Final weight}} \times 100.$$

#### Moisture uptake

Individually weighed films were exposed to the saturated solution of potassium chloride (84% relative humidity) after leaving in desiccators for 24 hours, until a stable weight was attained. The percentage of moisture uptake is calculated from following equation (Madhvi et al., 2013):

$$\% \text{ Moisture uptake} = \frac{[\text{Final weight} - \text{Initial weight}]}{\text{Initial weight}} \times 100.$$

#### Surface pH & Swelling Index (SI)

Surface pH of all buccal films (n=3) were investigated using a digital pH meter (Hanna Instrument Inc., USA) after an hour on an agar plate (2% w/v) in an incubator maintained at 37±0.2°C. Swelling index (SI) was also measured using the same parameters. Swelling index was calculated using following formula (Nair et al., 2013; Perioli et al., 2004; Wu et al., 2016):

SI =  $\frac{W_s - W_d}{W_d} \times 100$ ; where W<sub>d</sub>= Dry weight of buccal film .W<sub>s</sub>= Weight of film after swelling.

#### Percent Elongation

A film sample stretches with the application of stress. The percent elongation of the buccal films were calculated using the following formula (Madhvi et al., 2013):

Percent Elongation =  $\frac{L - L_0}{L_0} \times 100$ ; Where, L= Increase in length of buccal film, L<sub>0</sub>=Initial length of buccal film.

#### Hydration and entrapment efficiency

All films (F4 to F9) (n=3) were dissolved in 50 ml of phosphate buffer pH 6.5 at 50 rotation per minute (r.p.m) until entire dissolution. The buffer solution was manufactured from KH<sub>2</sub>PO<sub>4</sub> and NaOH(0.1M) to get a pH of 6.5 simulating salivary conditions. The entrapment efficiencies of the films were calculated using following formula (Boateng et al., 2013; Shende et al., 2016; Okeke & Boateng, 2016):

% Drug entrapment efficiency=  $\frac{[\text{Initial weight} - \text{Final weight}]}{\text{Initial weight}} \times 100$ .

#### In vitro release studies of drug-Loaded oral films

In vitro release studies of FluNa-loaded buccal films were investigated using 50 ml of phosphate buffer of pH 6.5 at 37°C at 50 r.p.m for an hour. At planned intervals (0-60 minutes), 10 ml of aliquots were taken out from the media and analysed at 219 nm using UV-spectrophotometer (Boekel & Co., Hamburg, Germany) for the quantification of FluNa. Aliquots were replaced with fresh buffer medium at the different intervals to uphold sink condition (Boateng et al., 2009, 2013; Kianfar et al., 2012; Shende & Gaud., 2009).

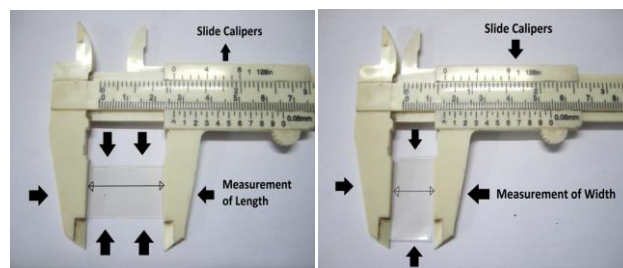


**Fig. 1.** Measurement of length and width of transmucosal buccal film using slide calipers.

## RESULTS AND DISCUSSION

For the rationale of the research, FluNa-loaded mucoadhesive buccal films were manufactured with PolyX and PlasY system using a solvent casting method. Un-plasticized blank film with PolyX was brittle in nature and firm to remove from the petri dishes. PlasY was dissolved to the formulations, to make the buccal films more elastic and remove its brittleness. The optimal amount of PlasY was 1% (w/w) in both the blank and drug-loaded films. Drug-loaded films were easier to remove from the petri dishes than the blank films. All films were transparent, except F6 and F9 (drug-loaded), the concentration of PolyX and FluNa was higher than other formulations (Table.2a). Initially, blank films were optimised for physicochemical characterization. Film defects, such as irregular film size, defects on the edge, observation of small particulate, fungal contamination, film hole, rough surface, gel dumping in one side (Fig.2), were investigate during this research. However, Uniform, transparent, clear, well distributed films were developed using appropriate amount of polymer and plasticizer (Fig.3). Physicochemical characterization was performed to study the properties of each buccal film. Increasing the amount of PolyX, PlasY and FluNa, weight of the film increased rapidly (Table.2a). Length and width of the films showed almost constant size and shape after cut in specific size and shape. Hardness of the film was checked to ensure the films have appropriate flexibility to apply onto the mucosal route (Table.2a). Thickness of the film were in range between 0.10 to 0.14 mm which indicate the formation of thin buccal film (Table.2b). Folding resilience of the films were F1>F2>F3 (blank), F4>F5>F6 and F7>F8>F9 (drug loaded). PolyX and PlasY influenced on the folding resilience of each film, high the ratios of plasticizer exhibit upper folding resilience (Table.2c). This trend also same for percent moisture content and uptake. Hydrophilic drug and polymer has a great ability to contain and uptake moisture from the enviroment. Surface pH was in the range between 6.5-6.8 for all formulations (Table.2c). An acidic or alkaline pH may irritate the buccal mucosa and affect the degree of polymer hydration. Therefore, the surface pH of the buccal films were selected to optimise both the mucoadhesion and drug release (Wu et al., 2016). All formulations were dissolved after completely an hour for hydrophilic drug and polymer, ability to swell rapidly (Table.2d). Plasticizer has direct influence on the plastic properties or elongation properties (Table.2d). The entrapment efficiencies of the drugs were 93%-98% for all formulations.

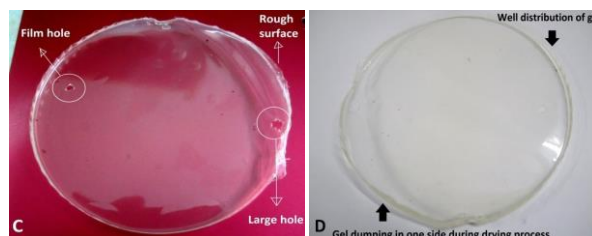
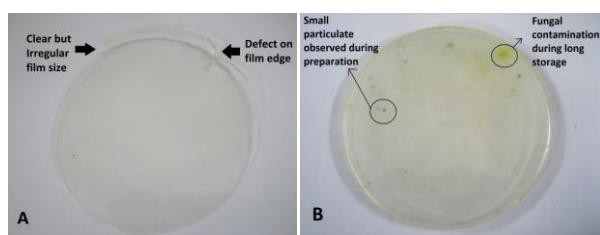


**Fig.2.** Digital photographs of manufacturing defects during the optimising of the blank buccal films.

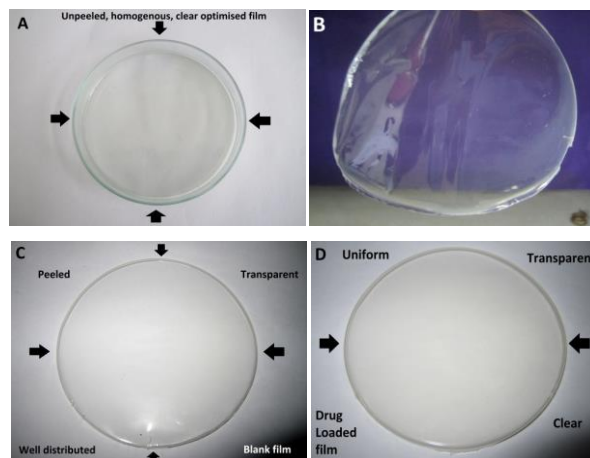


**Fig.3.** Digital images of solvent casted optimized blank- and drug-loaded films for the delivery of antibiotics.

**Table.2a.** Physicochemical characterisation of mucoadhesive buccal film (Visual appearance, Weight, Length & Width, Hardness).

Formulation/ Film Type	Visual appearance	Weight of film (mg) ±SD	Length of film (mm) ±SD	Width of film(mm) ±SD	Hardne ss (kg- cm) ±SD
F1 (Blank)	Transparent	154.0±3.2	27.2±0.3	15.0±0.5	5.0±0.2
F2 (Blank)	Transparent	242.1±3.1	26.8±0.6	15.2±0.3	8.0±0.1
F3 (Blank)	Transparent	332.0±0.6	27.0±0.5	15.2±0.3	8.0±0.3
F4 (Drug Loaded)	Transparent	165.3±2.5	27.5±0.3	15.2±0.2	10.2±0. 3
F5 (Drug Loaded)	Transparent	257.1±2.1	27.5±0.2	15.5±0.1	10.4±0. 1
F6 (Drug Loaded)	Semi- Transparent	338.0±2.9	27.5±0.1	15.5±0.2	10.5±0. 3
F7 (Drug Loaded)	Transparent	185.4±3.8	27.5±0.3	15.5±0.1	10.5±0. 3
F8 (Drug Loaded)	Transparent	272.3±4.0	27.5±0.3	15.2±0.2	10.5±0. 4
F9 (Drug Loaded)	Semi- Transparent	365.1±7.0	27.5±0.1	15.0±0.0	10.3±0. 3

**Table.2b.** Physicochemical characterisation of mucoadhesive buccal film (Thickness at the five places).

Formulation/ Film Type	Thickness of film (mm ±SD)				
	Upper left	Below left	Middle centre	Upper right	Upper right
F1 (Blank)	0.11±0.02	0.13±0.01	0.12±0.01	0.11±0.01	0.10±0.01
F2 (Blank)	0.11±0.01	0.11±0.02	0.11±0.01	0.10±0.02	0.12±0.01
F3 (Blank)	0.11±0.01	0.11±0.01	0.11±0.01	0.10±0.01	0.12±0.01
F4 (Drug Loaded)	0.11±0.02	0.11±0.01	0.12±0.02	0.10±0.02	0.11±0.02

F5 (Drug Loaded)	0.11±0.01	0.10±0.01	0.11±0.01	0.10±0.01	0.11±0.01
F6 (Drug Loaded)	0.10±0.01	0.11±0.01	0.11±0.01	0.11±0.02	0.11±0.01
F7 (Drug Loaded)	0.12±0.01	0.12±0.02	0.12±0.02	0.10±0.01	0.11±0.02
F8 (Drug Loaded)	0.12±0.01	0.11±0.01	0.14±0.04	0.11±0.02	0.12±0.01
F9 (Drug Loaded)	0.11±0.01	0.12±0.01	0.12±0.02	0.11±0.02	0.11±0.01

**Table.2c.** Physicochemical characterisation of mucoadhesive buccal film (Folding resilience, Percent moisture content, Percent moisture uptake & Surface pH).

Formulation/ Film Type	Folding resilience (in number) ±SD	% Moisture content ±SD	% Moisture uptake ±SD	Surface pH
F1 (Blank)	125.0±1.0	13.3±1.5	25.0±3.0	6.6±0.1
F2 (Blank)	120.0±1.0	25.3±1.5	53.0±1.3	6.6±0.1
F3 (Blank)	114.7±0.6	59.0±1.0	65.6±3.1	6.7±0.2
F4 (Drug Loaded)	116.3±0.6	18.2±1.8	22.1±2.8	6.5±0.0
F5 (Drug Loaded)	110.7±3.1	27.2±0.8	35.2±3.5	6.5±0.0
F6 (Drug Loaded)	101.3±2.5	52.8±1.7	50.6±5.9	6.6±0.1
F7 (Drug Loaded)	117.3±1.5	17.7±0.4	27.1±3.5	6.6±0.1
F8 (Drug Loaded)	105.3±1.0	18.8±1.6	48.5±8.7	6.5±0.1
F9 (Drug Loaded)	80.2±2.5	56.7±2.2	65.2±7.4	6.6±0.1

**Table.2d.** Physicochemical characterisation of mucoadhesive buccal film (Swelling index, Percent elongation, Hydration & Entrapment efficiency).

Formulation/ Film Type	% Swelling index after hour 1±SD	% Elongation ±SD	Hydration Time (min)	% Entrapment efficiency
F1 (Blank)	100±0.0	105.2±3.0	5-10	-
F2 (Blank)	100±0.0	118.0±3.2	7-15	-
F3 (Blank)	100±0.0	101.6±2.0	15-20	-
F4 (Drug Loaded)	100±0.0	104.6±0.9	5-10	93.3±2.8
F5 (Drug Loaded)	100±0.0	105.9±1.2	7-15	94.6±3.7
F6 (Drug Loaded)	100±0.0	108.6±1.1	15-20	96.7±2.3
F7 (Drug Loaded)	100±0.0	104.5±0.9	5-10	95.0±3.3
F8 (Drug Loaded)	100±0.0	104.1±0.7	7-15	96.2±2.5
F9 (Drug Loaded)	100±0.0	112.2±1.5	15-20	97.0±1.2

To study the release profile of FluNa at different polymer concentrations, FluNa-loaded transmucosal buccal films were tested into phosphate buffer at pH 6.5 and the release profile for each formulation was examined for an hour. FluNa was chosen in order to investigate the effect of drug hydrophilicity, entrapment efficiencies and formulation. Fig.5a shows the release of the FluNa where the increase of PolyX ratio, resulted in slower release rates for 1:1 and 2:1 PolyX/PlasY ratios. The release rates were 71% and 45% being release after 30 mins while at 3:1 ratio controlled release was observed. After 60 minutes all formulations (F4-F6) showed complete release of FluNa. Similar results were observed for FluNa-loaded formulation (F7-F9), the dissolution of PolyX was the rate-limiting factor for the drug release (Fig.5b). The FluNa

release patterns are related to those of F4-F6 but with slightly quicker rate most probably because of the higher water solubility of both FluNa and PolyX. However, FluNa release rates were significantly lower at the beginning, until the full hydration of film into the buffer medium.

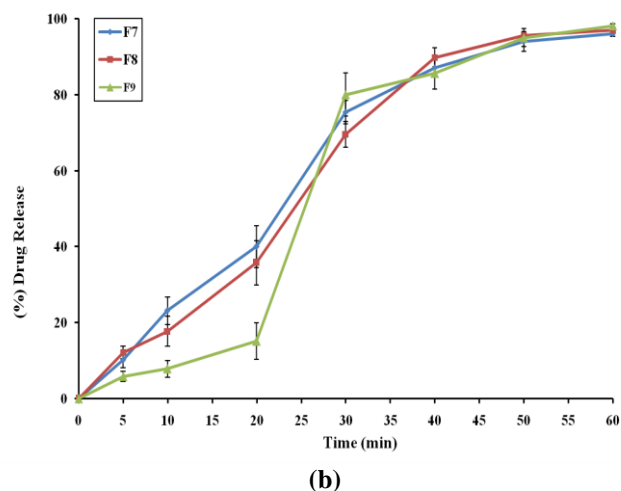
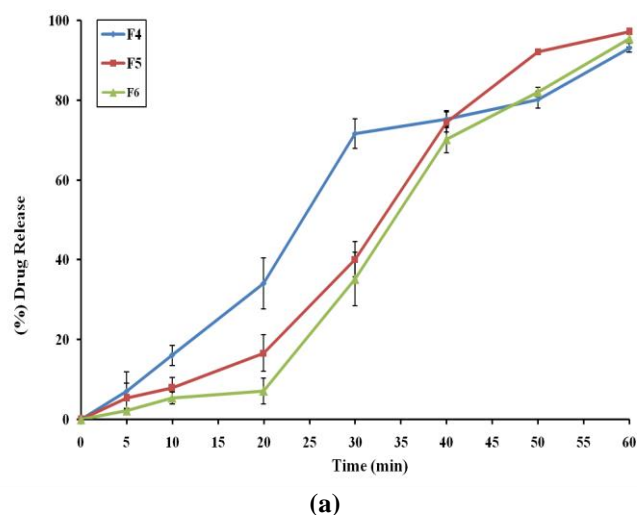


**Fig.5.** *In vitro* release profile of FluNa loaded different (a) formulations (F4-F6), (b) formulations (F7-F9).

The empty amount is therefore expected to be full by the external liquid diffusing into the buccal film and thereby increasing the dissolution of the film. In addition, the thick film surface produced on the swollen film surface is competent of avoiding disintegration and controlling additional water diffusion (Yehia et al., 2009).

## CONCLUSIONS

In conclusion, buccal films were loaded with various amounts of FluNa and successfully released from the films. The optimisation of blank buccal films were uniform, reproducible and accurate in terms of drug loading and drug release profile. The hydrophilic drug, FluNa, showed fast release profiles with most of the substances released within an hour. This release

phenomenon was achieved using PolyX, a polymer with high solubilising capacity, which increased the drug release rates. Transmucosal buccal film is a new technology for delivering a wide range of active pharmaceutical substances compare to conventional approaches and can be further used for protein and peptide delivery.

#### ACKNOWLEDGMENT

This research work was funded and organised by Southern University Bangladesh, Chittagong.

#### REFERENCES

Ammar, H.O., Ghorab, M.M., Mahmoud, A.A. and Shahin, H.I., 2016. Design and *In Vitro/In Vivo* Evaluation of Ultra-Thin Mucoadhesive Buccal Film Containing Fluticasone Propionate. *AAPS PharmSciTech*, pp.1-11.

Bai, S.A., Xiang, Q. and Finn, A., 2016. Evaluation of the Pharmacokinetics of Single-and Multiple-dose Buprenorphine Buccal Film in Healthy Volunteers. *Clinical therapeutics*, 38(2), pp.358-369.

Bilbault, T., Taylor, S., Walker, R., Grundy, S.L., Pappert, E.J. and Agro, A., 2016. Buccal mucosal irritation studies of sublingual apomorphine film (APL-130277) in Syrian golden hamsters. *Therapeutic Delivery*, 7(9), pp.611-618.

Boateng, J., Mani, J. and Kianfar, F., 2013. Improving drug loading of mucosal solvent cast films using a combination of hydrophilic polymers with amoxicillin and paracetamol as model drugs. *BioMed research international*, 2013.

Boateng, Joshua S. and Okeke, Obinna (2014). Chitosan-based films for the sustained release of peptides: a new era in buccal delivery? *Therapeutic Delivery*, 5 (5). pp. 497-500. ISSN 2041-5990.

Kalia, V., Garg, T., Rath, G. and Goyal, A.K., 2016. Development and evaluation of a sublingual film of the antiemetic granisetron hydrochloride. *Artificial cells, nanomedicine, and biotechnology*, 44(3), pp.842-846.

Khana, R., Agarwal, S.P. and Ahuja, A., 1997. Preparation and evaluation of muco-adhesive buccal films of clotrimazole for oral Candida infections. *Indian Journal of pharmaceutical sciences*, 59, pp.299-305.

Kumar, S.K., Nagabhushanam, M.V. and Rao, K.S., 2013. Formulation development and *in vivo* evaluation of zolmitriptan oral dissolving films.

Madhavi, B.R., Murthy, V.S., Rani, A.P. and Kumar, G.D., 2013. Buccal Film Drug Delivery System-An Innovative and Emerging Technology. *J Mol Pharm Org Process Res*, 1(3), pp.1-6.

Nair, A.B., Kumria, R., Harsha, S., Attimarad, M., Al-Dhubiab, B.E. and Alhaider, I.A., 2013. In vitro techniques to evaluate buccal films. *Journal of Controlled Release*, 166(1), pp.10-21.

Nir, Y., Paz, A., Sabo, E., Potasman, I., 2003. Fear of injections in young adults: prevalence and associations. *Am. J. Trop. Med. Hyg.* 68, 341-344.

Okeke, O.C. and Boateng, J.S., 2016. Composite HPMC and sodium alginate based buccal formulations for nicotine

replacement therapy. *International journal of biological macromolecules*, 91, pp.31-44.

Perioli, L., Ambrogi, V., Angelici, F., Ricci, M., Giovagnoli, S., Capuccella, M. and Rossi, C., 2004. Development of mucoadhesive patches for buccal administration of ibuprofen. *Journal of controlled release*, 99(1), pp.73-82.4.

Shende, P.K., Gaud, R.S., Bakal, R. and Yeole, Y., 2016. Clove Oil Emulsified Buccal Patch of Serratiopeptidase for Controlled Release in Toothache. *Journal of Bioequivalence & Bioavailability*.

Siddiqui, M.N., Garg, G. and Sharma, P.K., 2011. A short review on "A novel approach in oral fast dissolving drug delivery system and their patents". *Advances in Biological Research*, 5(6), pp.291-303.

Simonsen, L., Kane, A., Lloyd, J., Zaffran, M., Kane, M., 1999. Unsafe injections in the developing world and transmission of bloodborne pathogens: a review. *Bull. World Health Organ.* 77, 789-800.

Uddin, M.J., Scoutaris, N., Klepetsanis, P., Chowdhry, B., Prausnitz, M.R. and Douroumis, D., 2015. Inkjet printing of transdermal microneedles for the delivery of anticancer agents. *International journal of pharmaceutics*, 494(2), pp.593-602.

Wu, W., Chen, W. and Jin, Q., 2016. Oral Mucoadhesive Buccal Film of Ciprofloxacin for Periodontitis: Preparation and Characterization. *Tropical Journal of Pharmaceutical Research*, 15(3), pp.447-451.

Yehia, S.A., El-Gazayerly, O.N. and Basalious, E.B., 2009. Fluconazole mucoadhesive buccal films: in vitro/in vivo performance. *Current drug delivery*, 6(1), pp.17-27.